

Alma Mater Studiorum – Università di Bologna

**DOTTORATO DI RICERCA IN NANOSCIENZE PER LA  
MEDICINA E L'AMBIENTE**

Ciclo XXXIII

Settore Concorsuale: 03/B1

Settore Scientifico Disciplinare: CHIM/03

**Survey of methodologies of pharmaceutical interest  
for quantification of crystal form  
via X-Ray Powder Diffraction**

Presentata da: Laura Dall'Olio

Coordinatore Dottorato

Prof. Dario Braga

Supervisore

Prof.ssa Lucia Maini

Co-supervisore

Dr. Marco Curzi  
PolyCrystalLine S.p.A.

Esame finale anno 2021



# TABLE OF CONTENT

<b>PREFACE.....</b>	<b>7</b>
---------------------	----------

## **Chapter 1**

### **CRYSTAL FORMS**

<b>1 Polymorphism importance in pharmaceutical field .....</b>	<b>9</b>
<b>2 Crystal forms.....</b>	<b>13</b>
2.1 Polymorphs .....	13
2.2 Solvates/Hydrates.....	14
2.3 Cocrystal .....	16
2.4 Organic Salts .....	16
2.5 Amorphous phase.....	17
<b>3 Reference .....</b>	<b>19</b>

## **Chapter 2**

### **COCRYSTAL SCREENING OF ALLANTOIN**

<b>1 Introduction.....</b>	<b>22</b>
1.1 Allantoin.....	22
1.2 Cocrystals.....	26
1.3 CSD modules .....	27
<b>2 Aim.....</b>	<b>29</b>
<b>3 Experimental procedure .....</b>	<b>29</b>
3.1 Reagent and Standards .....	29
3.2 Application CSD modules .....	30
3.3 Characterization of Allantoin .....	37
3.4 Characterization of Alphanta .....	38
3.5 Solubility and pH.....	39
3.6 EvHT (evaporation at 60°C).....	39
3.7 Precipitation at low temperature .....	40
3.8 Slurry.....	43
3.9 Grinding .....	44
3.10 Kneading .....	44
3.11 Thermal characterization of mixtures.....	45
<b>4 Conclusion .....</b>	<b>48</b>
<b>5 Appendix A .....</b>	<b>49</b>
<b>6 Appendix B .....</b>	<b>51</b>
6.1 EvHT results .....	51
6.2 Precipitation results.....	53
6.3 Slurry.....	55
6.4 Grinding .....	61
6.5 Kneading .....	63

<b>7</b>	<b>Appendix C .....</b>	<b>68</b>
<b>8</b>	<b>References.....</b>	<b>71</b>

**Chapter 3**

**EVALUATION OF ERRORS AND ABERRATIONS AFFECTING THE ANALYSIS BY X-RAY POWDER DIFFRACTION**

<b>1</b>	<b>Introduction.....</b>	<b>74</b>
1.1	X-ray powder diffraction (XRPD) .....	74
1.2	XRPD errors.....	76
<b>2</b>	<b>Aim.....</b>	<b>83</b>
<b>3</b>	<b>Experimental procedure.....</b>	<b>83</b>
3.1	Instrumental aberrations .....	83
3.2	Systematic errors .....	86
<b>4</b>	<b>Conclusion .....</b>	<b>92</b>
<b>5</b>	<b>References.....</b>	<b>93</b>

**Chapter 4**

**UNIVARIATE QUANTITATIVE METHODS BY X-RAY POWDER DIFFRACTION**

<b>1</b>	<b>Introduction.....</b>	<b>95</b>
1.1	Quantitative analysis in X-Ray Powder diffraction.....	95
1.2	Univariate analysis .....	98
<b>2</b>	<b>Aim.....</b>	<b>101</b>
<b>3</b>	<b>Limit test .....</b>	<b>101</b>
3.1	Aim.....	101
3.2	Experimental procedure .....	101
3.3	Results.....	103
3.4	Conclusion.....	105
<b>4</b>	<b>Quantitative of starting material in co-crystal .....</b>	<b>106</b>
4.1	Aim.....	106
4.2	Experimental procedure .....	106
4.3	Results.....	107
4.4	Conclusion.....	111
<b>5</b>	<b>Quantification of crystalline polymorphs .....</b>	<b>112</b>
5.1	Aim.....	112
5.2	Experimental procedure .....	112
5.3	Results.....	113
5.4	Conclusion.....	115
<b>6</b>	<b>References.....</b>	<b>116</b>

## Chapter 5

### QUANTIFICATION BY STANDARD ADDITION METHOD IN X-RAY DIFFRACTOMETRY: A COMPARISON OF UNIVARIATE AND MULTIVARIATE ANALYSES

<b>1</b>	<b>Introduction.....</b>	<b>118</b>
1.1	Multivariate analysis.....	118
<b>2</b>	<b>Aim.....</b>	<b>121</b>
<b>3</b>	<b>Quantification methods of paracetamol form II in tachifludec.....</b>	<b>122</b>
3.1	Paracetamol polymorphism.....	122
3.2	Experimental procedure.....	124
3.3	Data evaluation and results.....	129
<b>4</b>	<b>Quantification methods of crystalline and amorphous lactose.....</b>	<b>137</b>
4.1	$\alpha$ -lactose polymorphism.....	137
4.2	Experimental procedure.....	138
4.3	Data evaluation and results.....	142
<b>5</b>	<b>Quantification method of crystalline lactose and hpmc.....</b>	<b>147</b>
5.1	Experimental procedure.....	147
5.2	Data evaluation and results.....	149
<b>6</b>	<b>Conclusion.....</b>	<b>154</b>
<b>7</b>	<b>References.....</b>	<b>155</b>

## Chapter 6

### DIRECT DERIVATION OF THE CRYSTALLINE FRACTION OF HIGHLY POTENT ACTIVE PHARMACEUTICAL INGREDIENTS BY X-RAY POWDER DIFFRACTION

<b>1</b>	<b>Introduction.....</b>	<b>158</b>
<b>2</b>	<b>Material and Methods.....</b>	<b>160</b>
2.1	Materials.....	160
2.2	Sample preparation and data collection.....	160
2.3	Data analysis.....	161
<b>3</b>	<b>Results.....</b>	<b>162</b>
3.1	Method <i>a</i> .....	162
3.2	Method <i>b</i> .....	164
3.3	Method <i>c</i> .....	166
3.4	Kapton film.....	167
<b>4</b>	<b>Discussion.....</b>	<b>168</b>
<b>5</b>	<b>Conclusions.....</b>	<b>171</b>
<b>6</b>	<b>References.....</b>	<b>172</b>
<b>7</b>	<b>Supplementary data.....</b>	<b>174</b>
7.1	The intensity–composition (IC) equation.....	174
7.2	Instrument and measure settings.....	174
7.3	Integration methods.....	175
7.4	Standard reference material.....	176

7.5	Method a .....	178
7.6	Method b .....	185
7.7	Method c.....	192
7.8	Method b - Kapton.....	196

## **Chapter 7**

### ***DIRECT DERIVATION OF THE CRYSTALLINE FRACTION OF FORMULATION DEPOSITED ONTO DRUG COATED BALLOON BY X-RAY POWDER DIFFRACTION***

<b>1</b>	<b>Introduction.....</b>	<b>200</b>
1.1	Drug-coated balloon catheter.....	200
1.2	Drug polymorphism .....	201
<b>2</b>	<b>Aim.....</b>	<b>205</b>
<b>3</b>	<b>Experimental procedure .....</b>	<b>206</b>
3.1	Lactose – HPMC .....	206
3.2	Drug Coated Balloon .....	219
<b>4</b>	<b>Conclusion .....</b>	<b>238</b>
<b>5</b>	<b>References.....</b>	<b>240</b>
	<b><i>CONCLUSION.....</i></b>	<b><i>243</i></b>

## PREFACE

The interest on crystal forms of APIs arises from the different properties, as such as solubility, dissolution rate, and bioavailability which they exhibit. A strategy to improve the properties of compound, is the formation of cocrystal involving API and a coformer. In this PhD project, a cocrystal screening of cosmetic API allantoin and some coformers of cosmetic interest was performed. The screening was preceded by statistical analysis of possible cocrystals of allantoin using CSD- materials. Potentially, allantoin can be involved in cocrystal formation with the selected coformers. Nevertheless, experimental results disagree with the statistical analysis and no cocrystal were obtained. The unique known crystalline form of DL-allantoin has been shown to be extremely stable and not available to make interaction with other molecules.

The PhD thesis is focused mainly on quantitative method of API crystalline forms via X-Ray Powder Diffraction because the high request of the pharmaceutical companies to establish the quantity of polymorphic impurities or partially recrystallization of amorphous. These information are fundamental to guarantee the quality and efficacy of the drug product during and after the manufacturing process. The polymorph of the drug product must be qualitatively and quantitatively evaluated to monitor the potential transition of the polymorphic form in another. Therefore, the development of solid-state quantitative analysis method is essential for control products' stability. X-Ray Powder Diffraction (XRPD) is the main technique applied for qualitative and quantitative determination of the polymorphs.

The systematic and accidental errors, which may impact the analysis, have been studied to avoid such errors during the analysis. As evidenced also during the real case of quantitative analysis investigated, the preparation of homogeneous calibration standards, is extremely challenging for solid-state mixtures, but it is fundamental to achieve satisfactory results.

In the PhD thesis different approaches of quantitative analysis are reported: univariate, multivariate method with or without internal standard.

Frequently, the content of a crystal form is precisely quantified in a wide range with construction of a calibration curve and it is possible to reach the low weight fraction of 1%.

I presented the example of quantification of a polymorphic impurity (paracetamol form II) in the commercial preparation of Tachifludec which contains paracetamol form I. The main issue in univariate method is the identification of a specific peak of the analyte among the several peaks due to the excipients which can interfering with the analyte. Although a specific peak was present, its intensity was not sufficient for quantification of low percentage (< 15%). The presence of several peaks due to the formulation was overcome by applying the standard addition method (SAM) and the tachifludec formulation was spiked with paracetamol form II. The data were evaluated by univariate and multivariate method NAS and the best results were obtained with the application of the multivariate method NAS. These approaches were also evaluated in the case of mixture amorphous-crystalline. Two different standards were used: mixtures of  $\alpha$ -lactose monohydrate/amorphous lactose and  $\alpha$ -lactose monohydrate/Hydroxy propyl methyl cellulose (HPMC). In the last case it was studied the potential use of stable amorphous surrogate as Hydroxypropyl methyl cellulose (HPMC) instead to the unstable real amorphous in crystallinity degree determination. The univariate analysis was applied to five different peaks of  $\alpha$ -lactose monohydrate but only two signals gave satisfactory results with  $R^2$  values. It is worth noting that the  $\alpha$ -lactose monohydrate is affected by preferential orientation, which significantly decreases the reliability of the calibration curve. Even in these cases, multivariate method achieved the best results succeeding into overcoming of inhomogeneity problem that mostly affects the univariate analysis.

The novel XRPD quantification method based on the whole pattern Direct derivation (DD) based on intensity-composition equation was applied to determine crystallinity degree of binary mixture containing HPMC as amorphous and monohydrate  $\alpha$ -lactose in percentage  $\leq 15\%$  w/w. The quantification method was evaluated in three scenarios: method a) the unit cell parameters of the crystalline form are available, method b) the structural information is unknown, but the patterns of pure crystalline and amorphous references are available, and method c) only the mixtures' patterns are available. The obtained results in the three different scenarios evidence comparable and reasonable relative errors (<20%) in methods a and b, while in method c the crystalline degree was underestimated with relative errors ranged up to 40%. Method a and b achieved more accurate results than method c because it was possible to better describe the crystalline phase with a high number of peaks. Method b was evaluated in sample covered by containment system as the Kapton® film to

evaluate the analysis of highly potent compounds. In this last case an accurate quantification was achieved removing the matrix effect by subtracting the Kapton® film signal from the total signal.

Finally, I evaluated three different methods: autoscale, USP and direct derivation (DDQM), for the crystallinity degree determination of three sample (Test 02, Test 03, and Test 04) of formulation containing highly potent API deposited on catheter balloon. To evaluate the best approach for the quantification of the drug coated balloon (DCB) the three methods were assessed with mixtures on HPMC and  $\alpha$ -lactose monohydrate analysed in the same way into a glass capillary. The quantification of the DCB samples presented several difficulties: 1) the amount of powder for each samples was around 10-15mg so it was impossible add an internal standard, 2) the filling of the capillary is particularly challenging; 3) the preparation of known samples is prevented by the absence of suitable amount of amorphous and crystalline references precluding the assessment of the precision and accuracy of the methods; 4) the nature of API itself because it is highly potent and it has non-stoichiometric hydrate behaviour, so the crystal structure can slightly change from sample to sample.

The three quantitative methods gave different quantification of the crystalline material. With the autoscale method, all the DCB samples showed crystallinity degree comparable to the crystalline reference, however the difference plot was very noisy because of the mismatch of the crystalline peak positions in the reference and the samples, so it was not considered reliable. The USP method required a correction factor based on the 100% crystalline reference and gave a crystallinity around the 81%-97%, while the DDQM gave a crystallinity between 59%-71%. The results of USP method and DDQM method are not comparable between them but they are consistent inside the method. Both methods agree to determine the sample Test 03 as the most crystalline sample and the other sample Test 02 and Test 04 with a comparable crystallinity degree. Nevertheless, the DDQM method was considered the best method to estimate the crystallinity degree of formulation onto DCB because of the directly determination without application of a correct factor needed for the USP method and of the possible application of Pawley function and hence determination of the changing in unit cell parameter after manufacturing.

# CHAPTER 1

## CRYSTAL FORMS

### 1 POLYMORPHISM IMPORTANCE IN PHARMACEUTICAL FIELD

The term polymorphism derived from the Greek words *polus* (πολύ) meaning much/many and *morphē* (μορφή) meaning form, in chemistry it denotes the physical phenomenon consisting, essentially, in the possibility of a compound to exist in different crystalline forms. Crystals are characterized by the order arrangement of the atoms in the three dimensions. Usually they are described by a structural unit, called unit cell, which is repeated regularly in three dimensions in space<sup>1,2</sup>. In polymorphs the same atoms or molecules are arranged differently in the unit cell, yielding to different crystal phases. Crystalline solids are usually very stable, have a well-defined melting point value and often exhibit different behavior in different measurement directions, i.e., they are generally anisotropic. Compounds can exist as amorphous solid, which is characterized by highest density of imperfections, and it is commonly described as a liquid with a very high density. Amorphous compounds are less stable than crystalline solids and do not present melting point. Generally, they show hygroscopic behavior, i.e., absorb water from the atmosphere in ambient humidity conditions, and they are isotropic, which means they have the same physical properties in all directions. Alongside amorphous and crystalline polymorphs, several different crystal forms related to a target compound are studied. We can distinguish solvates or pseudo-polymorphs which commonly appear during the polymorph screening, salts and cocrystal, as represented in Figure 1 and described following.

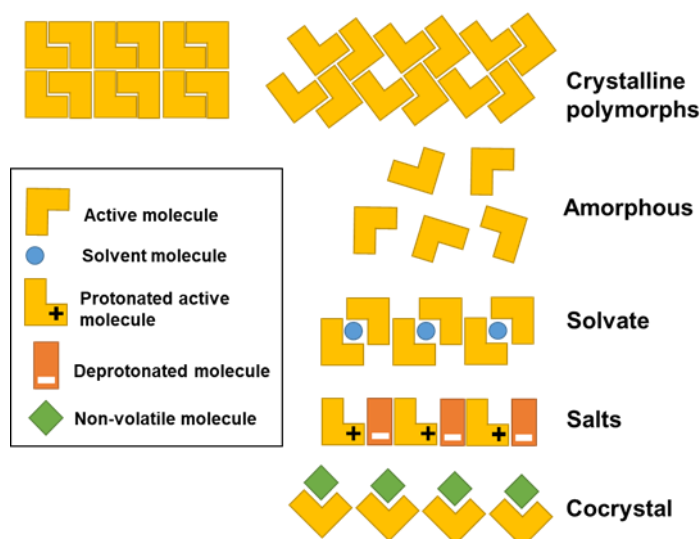


Figure 1. Solid-state forms

Polymorphism phenomenon and the study of the different crystal forms is extremely important in industry, especially in pharmaceutical. Guideline for the investigation, determination, development, manufacturing, and control of the different crystal structures of a new drug are issued by ICH (International Conference on Harmonization) and FDA (Food and Drug Administration). These organizations underline the importance to study polymorphism and solvate formation of new drug and to control this phenomenon during the whole process because of differences in forms could affect the quality and performance of the new drug products.<sup>3,4</sup> ICH Q6 provides guidance on how and when the polymorphic forms should be investigated and controlled also considering the impact of the polymorph on the performance of the relevant final drug product (solid or liquid dosage) (Figure 4).<sup>3</sup> The first step is to conduct a polymorph screening to find out all the multiple crystalline forms of the new drug, extremely probable considering the statistic. In fact, Stahly G.P., in his paper reveals that 90% of organic compounds exist as amorphous and multiple crystalline forms and about 50% of molecules has solvates and hydrated forms.<sup>5</sup> In the mid1990s, polymorph screening was proposed as procedure to find the form with the most advantageous bioavailability. The goal of polymorph screening is to find all potential crystal forms by small-scale study and to select a stable form that can be manufactured and formulated into

dosage products.<sup>6</sup> The guideline does not report a procedure for the polymorph screening which needs to be tailored on the properties of the target molecule. Several techniques can be used to obtain new crystal form as such as crystallization by shock cooling, evaporation, precipitation, vapor diffusion, slurry (suspension equilibrium), crystallization from melt, humidity induced transformation, sublimation, desolvation, salting out, pH change, lyophilization, etc.<sup>1</sup> Once polymorphs had been identified and isolated, their characterization shall be carried out by single crystal (SCXRD) and powder (XRPD) X-Ray diffraction, thermal analysis as differential scanning calorimetry (DSC) and thermogravimetric analysis (TGA), microscopy, solid-state nuclear magnetic resonance (SSNMR), infrared (IR) spectroscopy and Raman one.

X-Ray diffraction is the main technique for the study of polymorphism. The XRPD diffractogram of crystalline phase is characterized by sharp peaks, while amorphous phase gives only a halo. Hence, XRPD readily distinguishes between crystalline and amorphous phases. Additionally, XRPD pattern is characteristic of each crystalline phase, as a fingerprint of the crystalline structure. In fact, United States Pharmacopeia (USP) reports XRPD as leading technique for identification of the crystalline phases. In addition to qualitative phase analysis, USP also indicates XRPD for quantitative phase analysis of crystalline fractions. X-Ray diffraction allows the determination of the crystalline structure giving information about the unit cell parameters and the position of the atoms. On the other hand, when the crystal structure is known it is possible to calculate XRD pattern with corrected position and intensity (devoid of preferred orientation). Single crystal X-Ray diffraction is the principal technique for solving crystalline structures, but it requires a single crystal with suitable size, not always available, alternatively even powder XRD is able to determine the crystalline structure. However, it is more challenging due to reflection overlap, hard background determination and possible preferred orientation phenomenon, especially for organic compounds, which have large lattice, and low symmetry and scattering properties.<sup>7,8</sup>

Other useful techniques for the polymorph characterization are FT-IR and FT-Raman spectroscopy, whose spectra are molecular structure fingerprint and are sensitive to conformation and environment as such as different interactions. FT-IR and FT-Raman are complementary technique because FT-IR is based on absorption of infrared light by molecule that changes a dipole moment (asymmetric mode), while FT-Raman is based on scattering of laser radiation due to change in the polarization of the molecule (symmetric mode).<sup>9</sup> Both qualitative and quantitative analysis can be performed using FT-IR and FT-Raman spectroscopy.

Other powerful but lesser-known technique is SSNMR, based on the resonance frequency of nuclei (<sup>13</sup>C, <sup>15</sup>N, <sup>31</sup>P, <sup>25</sup>Mg, and <sup>23</sup>Na) in a strong magnetic field. It is complex and highly cost technique, though it gives wide structural and dynamic information about both crystalline and amorphous materials and even formulations. Among all, it provides information about crystalline structure, solid state chemical reactivity, interaction between API (active pharmaceutical ingredient) and excipients, and it can be used in quantification analysis.

9-11

Differential scanning calorimetry (DSC) and thermalgravimetric analysis (TGA) are destructive techniques that investigate the thermal behavior of compounds. DSC measures the different heat absorbed or released by analyzing the temperature difference between reference (empty pan) and sample during heating and cooling. The temperature and energy involved in melting, crystallization, solid-solid reaction, and evaporation events can be easily determined. TGA measures the change in mass of a sample during a heating cycle. It is useful in the solvates and hydrates study and in determination of their stoichiometric and stability. Microscopic techniques are used to evaluate the morphology, shape, and particle size of the crystalline (Figure 2). Additionally, polarized light microscopy (PLM) studies the different optical properties of materials and it can mainly be used to readily discriminate between amorphous and crystalline materials, because amorphous phase (isotropic) propagates light in the same way in all directions and completely extinguished the light, while crystalline phase (anisotropic) extinguishes the light only in two directions and they appears colored (Figure 3).<sup>1</sup>



**Figure 2. Image of prism crystal by optical microscopy**

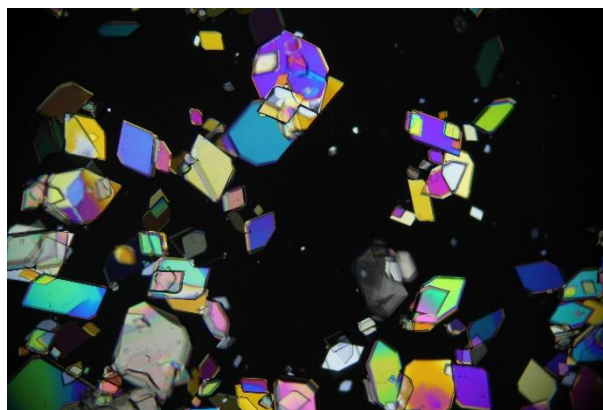


**Figure 3. Image of crystalline phase by PLM**

A combination of several techniques is usually recommended to obtain suitable and deep characterization of drug substance. Physical characterization is a crucial aspect of evaluating the performance, efficacy, and stability of materials under development and of selecting the best polymorph for the drug product. Properties, as such as solubility, stability, and melting point, of the new crystalline forms impact differently on quality of the drug product depending on the intended dosage form. The polymorphic form is important in dosage choice, the manufacturing process, and formulation.<sup>6</sup> In pharmaceutical practice, the solid phase is the widely preferred phase for the easiness of handle and its stability and the compliance of the patient. The administration of drug products occurs commonly via oral dosing, in which solid state of the ingredients significantly affect the performance.<sup>12,13</sup> Lipinski et al. point out that in oral administered drug with a dose of 1 mg/kg and solubility greater than 65  $\mu\text{g/mL}$  absorption is unaffected, while solubility less than 10  $\mu\text{g/mL}$  limits absorption.<sup>14</sup> Hence, ICH requires control of drug substance polymorph in case of solid dosage form and liquid containing undissolved drug substance to avoid adverse effect on drug product performance and quality.<sup>3</sup> The strategy of control, such as appropriate tests and acceptance criteria are determined case by case. Byrn et al. provide different flow charts for different common types of solid (polymorphs, solvates, amorphous). Generally, when single polymorph is routinely produced from manufacturing process, they recommend a qualitative test to differentiate and control the form, e.g., XRPD or DSC. Otherwise, when the manufacturing process provides mixture of forms, quantitative tests are needed to determinate the composition, in particular, limit test should be performed to control the presence of particular form below acceptable amount.<sup>15</sup> Furthermore, control of polymorph of APIs is necessary after manufacturing of the drug product because of possible changes in its crystal form, such as amorphization, crystallization, polymorphic transition or alteration in chemical composition (desolvation or salt-free base/acid transition) can occurred during the process or the storage. Several stresses undergo during the manufacturing process of drug product for example mechanical stress (e.g. milling, compression), thermal stress (e.g. freezing, drying, melting) and interaction with other components, may induce phase transition.<sup>1</sup> In case of a drug substance sensitive to polymorphic alteration, its stability should be monitored during its production and storage to assure reproducibly and stability of the final product. Especially, the check of drug polymorph is crucial in case of high risk of adverse effect in efficacy and quality of formulation. Nevertheless, the entity of the tests and acceptance criteria should be assessed on a case-by-case basis, considering the characteristic of the drug.<sup>16</sup> FDA reports that concern about the polymorph in the drug product is not in needed “if the most thermodynamically stable polymorphic form is used or the same form is used in a previously approved product of the same dosage form” and it estimates that “Drug product performance testing (e.g., dissolution testing) can generally provide adequate control of polymorph ratio changes for poorly soluble drugs [...] Only in rare cases would polymorphic form characterization in the drug product be recommended”.<sup>4</sup>

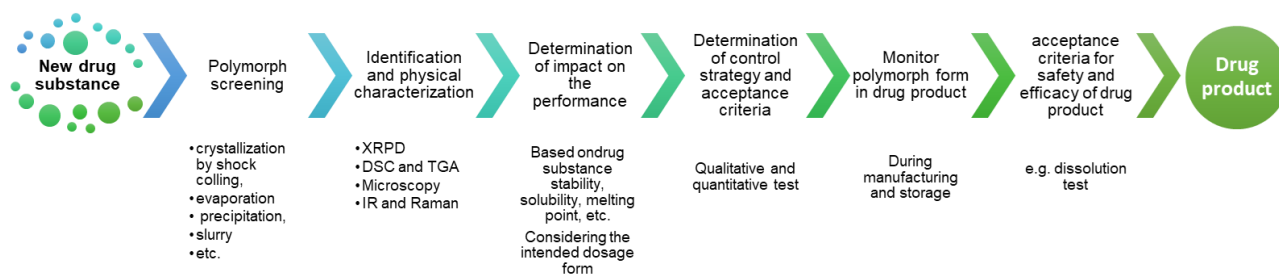


**Figure 4. Flow of drug substance polymorph evaluation based on ICH and FDA guideline**

The formation of different polymorphs is primarily lead by the kinetic and thermodynamic of the system. In fact, polymorphs are solid phases with distinct Gibbs free energy, enthalpy, and entropy due to the definite molecular interactions in crystal lattices. It is worth noting that the difference of free energy between polymorphs are small, 90% of polymorphs differ by less than 4 kJ/mol (or 1 kcal/mol), however, the structural difference between the polymorphs and the resulting different free energy lead to different properties, such as stability and solubility.<sup>6,13,17</sup> Additionally, polymorphs present differences in other several properties, as such as dissolution rate, compressibility, and handling, that can drastically affect the properties of pharmaceutical product and its manufacturing process. In Table 1 are set out thoroughly all the different properties that differ among crystal forms<sup>1,18–20</sup>.

**Table 1. Different physical properties of polymorphs**

<b>Packing properties</b>	Molar volume and density Refractive index Conductivity: electrical and thermal
<b>Thermodynamic properties</b>	Hygroscopicity Melting and sublimation temperatures Internal or structural energy Enthalpy Heat capacity Entropy Free Energy and Chemical Potential Thermodynamic Activity Vapor Pressure Solubility
<b>Spectroscopic properties</b>	Electronic state transitions Vibrational state transitions Nuclear spin state transitions
<b>Kinetic properties</b>	Dissolution rate Rates of solid-state reactions Stability
<b>Surface properties</b>	Surface free energy Interfacial tensions Crystal habit Hardness
<b>Mechanical properties</b>	Tensile strength Compressibility, tableting Handling, flow, and blending

In the formulation of a pharmaceutical product the physical-chemical stability, solubility, and bioavailability of API are considered fundamental aspects.

Generally, the most stable crystalline form (lowest free energy) leads the choice of the pharmaceutical industry for drug products thanks to its stability. The possibility of interconversion between the various forms can have very serious consequences on the life of a product. The risk of significant impact on product performance due to polymorph transition is high for poorly soluble and unstable drug substance.<sup>12</sup> Despite their poor stability, amorphous and metastable solids have attracted the attention of pharmaceutical industries because, thanks to their high free energy, they have higher solubility and dissolution rate, which give medical benefits as bioavailability and drug delivery. These properties could be used to increase the absorption and performance of poorly soluble drugs. In fact, poor bioavailability of drug substance (<20%) can result poorly controlled pharmacological effects, and poorly controlled toxic effects.<sup>12</sup> Generally, different polymorphs show different solubility less than 10 times, while largest difference (up to several hundred times) is observed between amorphous and crystalline phases. Solvates are always less soluble in the solvation solvent, thus, hydrates are less soluble in water than the anhydrous solid.<sup>12,21</sup> As demonstrated by Kobayashi et al., the solubility of anhydrous Form I and III of carbamazepine is 1.5–1.6 times more soluble than dihydrate form.<sup>22</sup>

Therefore, the research and characterization of the crystal forms of a molecule, such as polymorphs, salts, solvates or cocrystals, expand the choice of the most suitable solid form for the development of a new drug and has relevant implications in the manufacturing. The desired crystal form is chosen also taking into account all the manufacturing process, in fact, another critical factor of developability is the ability to scale-up the manufacturing of the selected crystal form. The manufacturing process of drug substance and product should be reproducible and with a reasonable cost.<sup>12</sup> The knowledge of the solid-state properties of APIs in the first steps of drug development, avoids problems related to their production and optimizes the drug product manufacturing process.

The pharmaceutical companies invest wide resources, time, and cost, to deeply study and develop drug products, hence they are concerned to protect their own inventions by patent. Additionally, the polymorphism is potentially of great business-wise importance for pharmaceutical industry thanks to the patentability of the crystalline forms, which show the three requirements for US patent: utility, novelty, and non-obviousness. The potential difference in properties of different polymorphs allows to claim the crystal form in patent. In recent years, increasingly economic and regulatory pressure, the cost of the discovery of even more rare new drugs, and the constant expiration of drugs' patents has led the pharmaceutical industry to focus on patents' lifecycle of their existing drug products. Typically, pharmaceutical companies implement the strategy of claiming new crystalline form usually 4-6 years after the issue of the original patent to extend its protection.<sup>23</sup>

Concluding, the polymorph screening of pharmaceutical compounds and the characterization of the crystal forms of the APIs lead to choose the best crystal form for the pharmaceutical formulation and constitute a strategic patent defense tool for drugs.<sup>24,25</sup>

## 2 CRYSTAL FORMS

### 2.1 Polymorphs

Polymorphism occurs when compounds with the same chemical composition arrange atoms or molecules in different crystalline structures characterized by long range order with different inter- and intra-molecular interaction network and consequently different level of free energy and solid-state stability, that makes them desirable for active pharmaceutical ingredients.<sup>17</sup> Cruz-Cabeza et al. report that polymorphism is independent of most molecular properties except for chirality and flexibility of the molecules.<sup>17</sup> Crystalline form can be found in configurational and conformational polymorphs related to flexibility of the molecules. Configurational polymorphs, called also packing polymorphisms, have different crystalline structure with distinct molecular interaction networks but equivalent molecule conformation. Typically, conformational polymorphism occurs with molecules with rigid conformation, for instance carbamazepine that exists in four different polymorphs with equivalent molecular conformation, hydrogen bond network and consequently similar free energy (difference within 0.7 kcal/mol).<sup>26</sup> Contrarily, in conformational polymorphism the molecules show multiple conformations, the flexibility of the molecular structure allows manifold interaction, different packing, and various crystalline structures. An example of conformational polymorph is ritonavir form I and II, which respectively show the molecule in cis and trans conformation around carbamate bond. The different molecular conformations lead to dissimilar hydrogen bonds and different crystalline structures. These differences

resulting in different properties, as such as morphology and solubility. In case of ritonavir, the forms have divergent solubility affecting their performance and additionally different morphology, form I has plate-like shape while form II shows acicular shape.<sup>27</sup>

To describe the thermodynamic relationship of polymorphs, we can consider a dimorphic system with form A and B in isobaric condition. The pair of polymorphs can form an enantiotropic or monotropic system. In an enantiotropic system, a reversible transition between polymorphs A and B exists at define temperature before the melting points of both polymorphs. At this transition point ( $T_t$ ) the free energy of the two polymorphs is equal  $G_A = G_B$  and they undergo solid-solid transition (Figure 5 right side).

In the case of monotropic system, only one of the polymorphs is stable in all the temperature, that is characterized by the lowest free energy value below the melting point of both polymorphs. As reported in left side of Figure 5, the free energy of polymorph B is always lower than one of polymorph A  $G_B < G_A$ .<sup>19,28</sup>

The polymorph with the lower free energy (higher melting temperature) is the thermodynamic stable form. The metastable form should convert to stable form at any temperature but, the conversion is kinetically avoided.<sup>29</sup> It is important to establish the stability of the polymorphs. Generally, slurry experiments allow to identify the thermodynamic stable polymorph. As the same way, antisolvent diffusion and slow recrystallization are used to obtain more stable forms. On the contrary, metastable forms are generally obtained by fast crystallization, as such as high supersaturation, precipitation with antisolvent, quench-cooling, and pH change.

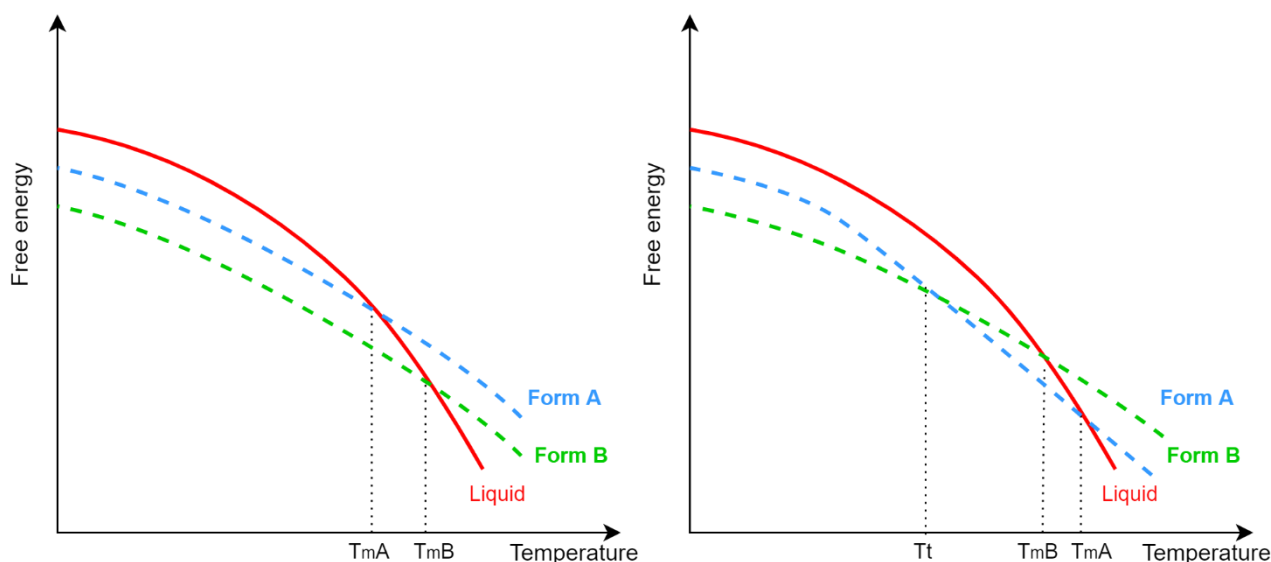


**Figure 5. Energy-temperature plot for monotropic (left side) and enantiotropic (right side) system.**

An extensive polymorph screening on the target API is important to assure consistent and reproducible production of the desired form, and to avoid the appearance of a new polymorph on the late stages of bulk drug process development as in the case of ritonavir.

The occurrence of the more stable and dramatically less soluble form II of ritonavir in batch of more soluble form I, affected the effectiveness of the drug product. Production of pure batch of the metastable form I had been impossible for the concomitant crystallization of the two forms due to competing kinetic and thermodynamic factors which forced the Abbot to rethink to the manufacturing process.<sup>27,30</sup>

## 2.2 Solvates/Hydrates

Solvates are crystalline form containing into crystal lattice a molecule of solvent, when the solvent is water the crystalline form is called hydrate.

Large number of pharmaceutical compounds are solvates and hydrates, often called pseudo-polymorphs. The propensity of API and solvent molecules to crystallize in solvate form depends on their molecular structures and tendency to form hydrogen bonds. Water is extremely receptive to form hydrates thanks to its small size and propensity to form hydrogen bonds both as donor and acceptor. In fact, a survey of the Cambridge Structural Database demonstrated the more frequency of hydrates than solvates with organic solvents, about 30% of drug substances can form hydrates.<sup>31</sup> Moreover, wide use of water during the manufacturing process

promotes the formation of hydrates. Mostly, hydrates are of great interest in pharmaceutical field due to stabilization effect of water and safety concern about organic solvent toxicity, not suitable for drug substance. Based on structural aspect of the interaction between water and API, hydrates are classified in three different classes. Class I) the water molecules are isolated from other water molecules. Water molecules interact only with API through hydrogen bond and van der Waals interactions. Hydrates of class I are identifiable by DSC, TGA and infrared spectroscopy. These hydrates show sharp endothermic peak and weight loss in small range due to dehydration in DSC and TGA respectively and hydroxyl bands in IR spectroscopy. <sup>6</sup> Class II) water molecules interact both with API and adjacent molecules of water. These hydrates are called channel hydrate due to the formation along crystallographic axis of channels or layers where water molecules are located. Hydrates of class II are divided in channel and planar hydrate based on hydration and dehydration behavior. Exposed at high humidity, channel hydrates can host additional water molecules into the channels expanding the crystal lattice in all the directions changing the unit cell dimension, this can be observed with the shift of crystalline reflection in XRPD pattern. While, in planar hydrates the water molecules are in layers between drug molecules and the exposition at high humidity causes expansion of crystal lattice only along an axis. Generally, channel hydrates are nonstoichiometric hydrates, while in planar hydrates the amount of water in layers change stoichiometrically in accordance with relative humidity. <sup>6</sup> Stoichiometric hydrates show hydrate/dehydration transition point at critical RH%. In nonstoichiometric hydrates water molecules can move into or out of the crystal lattice without occur in solid state transition and the form is stable in a wide range of RH%. Figure 6 reports an example of XRPD pattern of nonstoichiometric hydrates, red pattern was collected at 60%RH, while collection of the green pattern was performed after stability at 75%RH. The XRPD comparison points out the shift in position of the peaks in the range 8-14°2 $\theta$  and around 20°2 $\theta$  due to the increased of relative crystalline planes while the peaks in the range 14-19°2 $\theta$  are superimposable. Class III) are metal-ion coordinated hydrates in which water molecules form strong ion-water bonds. <sup>31</sup>

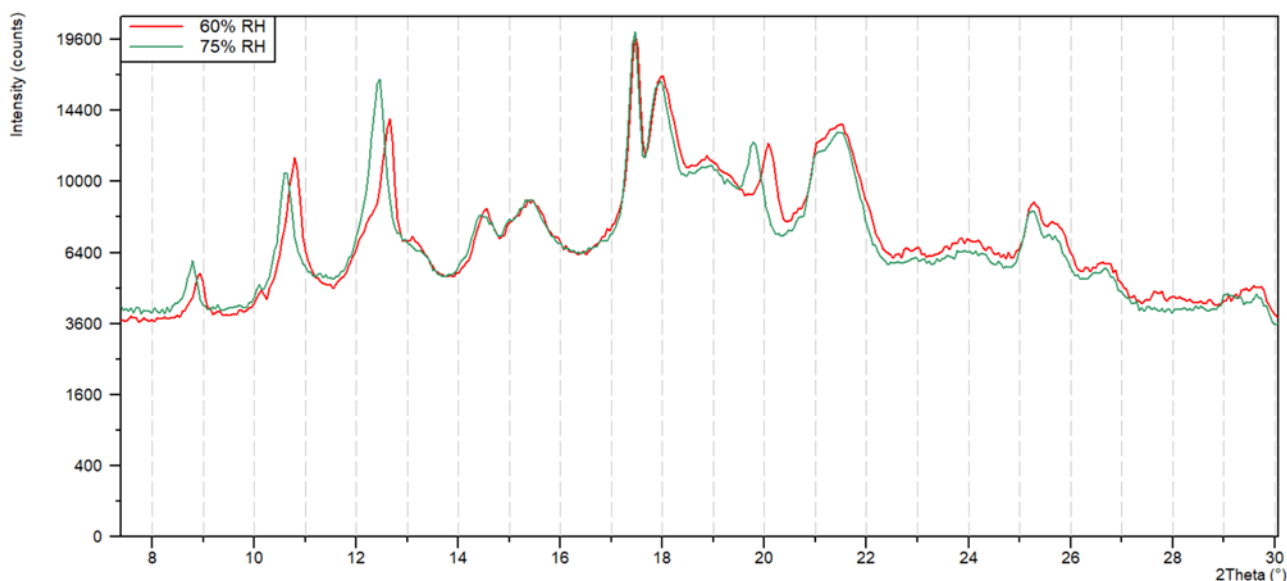


**Figure 6. Example of nonstoichiometric hydrate. Red pattern was collected at 60%RH while collection of the green pattern was performed at 75% RH.**

Different physical, chemical, and mechanical properties are observed between hydrates/solvates and anhydrous crystal forms and between hydrates of different stoichiometry. It is worth noting that hydrates are less soluble in water than the anhydrous form which are commonly two times more soluble. Additionally, mechanical properties of the powder are affected by hydration state, for instance different compressibility of anhydrous and dihydrate forms of dibasic calcium phosphate. <sup>32</sup>

Typically, solvates and hydrates arise during slurring, refluxing, wet granulation, or exposition to solvent vapor. Exposure to solvent vapor can also lead to the formation of solvates. Hydration states of a compound can be studied by moisture sorption experiments with DVS (Dynamic vapor sorption) analysis or by exposure to high humidity. Karl Fisher titration measures the amount of water present in a powder. TGA can measure the amount of weight loss during desolvation/dehydration process and in connection with EGA (evolved gas analysis) it is possible to identify the solvent. Desolvation/dehydration is an endothermic event detectable by

DSC. Using at hot stage microscopy desolvation/dehydration can be directly observed. Study of crystalline structure by SCXRD allows the determination of the presence of solvent/water, its location in the crystalline lattice, the interaction involves and the classification of the hydrates. XRPD, FT-IR and FT-Raman monitors the transition of the phases.

## 2.3 Cocrystal

Cocrystal is a multicomponent crystal containing within the crystal lattice two or more components in neutral and solid state, generally in a stoichiometric ratio, linked via non-ionic interactions, typically hydrogen bond interactions, but also van der Waals forces and  $\pi$ - $\pi$  interactions. Considerable number of APIs potentially can form cocrystal because of their propensity to interact through hydrogen bonds. When cocrystal is constituted by an API and the other molecule, named coformer, pharmaceutically acceptable for safety reason, it is labeled as pharmaceutical cocrystal.<sup>33</sup> FDA reports “drug products that are designed to contain a new co-crystal are considered analogous to a new polymorph of the API. A co-crystal that is composed of two or more APIs (with or without additional inactive cofomers) will be treated as a fixed-dose combination product and not a new single API”.<sup>34</sup>

For safety reason the choice of possible cofomers is limited at small group of amino acids, acids, bases, nucleotides, or vitamins. However, cocrystals are very attractive for their significantly different physical and chemical properties compared to pure starting materials. Cocrystal formation can enhance the performance of API, as such as stability, solubility, bioavailability, and efficacy. An example, cocrystal of tramadol and celecoxib shows improvement in safety of tramadol and in bioavailability of celecoxib compared to the drugs dosing separately.<sup>33</sup> Additionally, cocrystal formation is extremely promising especially for neutral molecules with non-ionizable functional groups in which salt formation is not applicable. It was demonstrated that cocrystals, as well as salts, may show polymorphism and form various polymorphs and hydrates. Among others, carbamazepine-saccharin and carbamazepine-nicotinamide cocrystals have shown two polymorphs each other.<sup>35</sup>

Several methods yield to the formation of cocrystal including solid state methods, as such as mechanical synthesis (grinding and kneading) and extrusion, solution methods (isothermal slurry conversion, evaporation, spray drying, and precipitation), and supercritical fluid methods.<sup>36</sup>

Cocrystal are characterized using SCXRD and SSNMR to define molecular interaction and stoichiometry to confirm the cocrystal structure, by thermal analysis DSC and TGA to determine melting point and presence of solvent, and spectroscopy FT-IR and FT-Raman.

## 2.4 Organic Salts

Several compounds contain ionizable groups and can constitute salt with appropriate ions via acid – base reaction. The condition for forming of salt is pKa difference greater than 2 between compound and counter ion. Salt formation is important in pharmaceutical industry because is a simple way to change and improve physical and chemical properties. The 50% of drug substances in the market are salts.<sup>6</sup> Salts for pharmaceutical purpose must include safely counter ions of which toxicity has fully examined. Additionally, safety assessment of salt is required for regulatory approval to initiate clinical studies and marketing.<sup>6</sup>

Formation of salts leads to several advantages: poorly soluble drugs may increase solubility and bioavailability, taste masking, improvement of physical properties (melting temperature, crystallinity, and hygroscopicity) and mechanical ones, augmentation of chemical stability, overcoming of formulation problems (incompatibility with excipients), improvement of purity, as such as enantiomeric purity, as in the case of chiral compound clopidogrel. Only S enantiomer of clopidogrel shows biological activity additionally R enantiomer has poor tolerability, the selective formation of salt of 10- L-camphorsulfonic acid with S enantiomer of clopidogrel resolves the racemic mixture.<sup>37</sup>

Nevertheless, the stability and solubility of salts depends on the pH of aqueous solution. The pH value in which salt reaches the maximum solubility and the transition in free form occurs is labeled pH<sub>max</sub>. Salts resulting from weak base are stable at pH values below pH<sub>max</sub>, while salts of weak acid are stable at pH higher than pH<sub>max</sub>. For this reason, in formulation it is fundamental to consider the stability of the salt and its pH solubility profile. For example, precipitation and redissolution may occur in gastrointestinal tract or humidity can promote

transition in free form. In solid dosage form, salt with low hygroscopicity and high crystallinity is preferable to avoid changes due to interaction with water in excipients and environment.<sup>38</sup>

First, fundamental information to conduct a salt screening is the knowledge of pKa of the drug substance to choose suitable counter ions based on their pKa and drug-ion pKa difference. The salts are characterized mainly with XRPD and spectroscopy technique, as such as FT-Raman. SCXRD and SSNMR are extremely useful to define the crystalline structure and determine the formation of salt or cocrystal. Moreover, dissolution testes at different pH to study the pH solubility profile are essential.<sup>1</sup>

## 2.5 Amorphous phase

ICH and FDA define polymorph as different forms of the same drug substance which differ in their physical properties and report “Polymorphism may also include solvation or hydration products (also known as pseudo-polymorphs) and amorphous forms” including amorphous phase in polymorphism phenomenon.

The amorphous phase is characterized by lack of long-range order. Compared to crystalline phases, it has higher molecular energy and greater molecular mobility, so we can say that it has microscopically properties of a liquid, with macroscopic mechanical properties of a solid.

Amorphous phase is characterized by high level of free energy that results in wide solubility and potentially greater dissolution rates and oral bioavailability compared to corresponding crystal. Conversely, its high free energy involves in chemical and physical instability, as demonstrated by Pikal et al.<sup>39</sup>

The properties of amorphous phase related to its free energy are explained by the free energy versus temperature plot (Figure 7). At temperature below of melting temperature ( $T_m$ ) the solid phase is the thermodynamically stable form because of it has lower free energy than the liquid phase while at temperature higher than the melting point the liquid phase is stable. Slowly cooling the liquid phase at temperature below  $T_m$  crystallization can occurred. However, quench colling the liquid, the formation of crystal nuclei can be avoided, and the system follow the supercooled liquid line shown in Figure 7. Decreasing the temperature, the molecular mobility decreases and the viscosity of liquid increases, until glass transition temperature ( $T_g$ ) in which unstable glassy state forms with amorphous characteristics. Glass transition temperature is a kinetic transition, hence  $T_g$  depends on the rate of cooling and equilibrium of supercooled liquid. Experimentally,  $T_g$  can be determined by differential scanning calorimetry (DSC).<sup>6</sup>

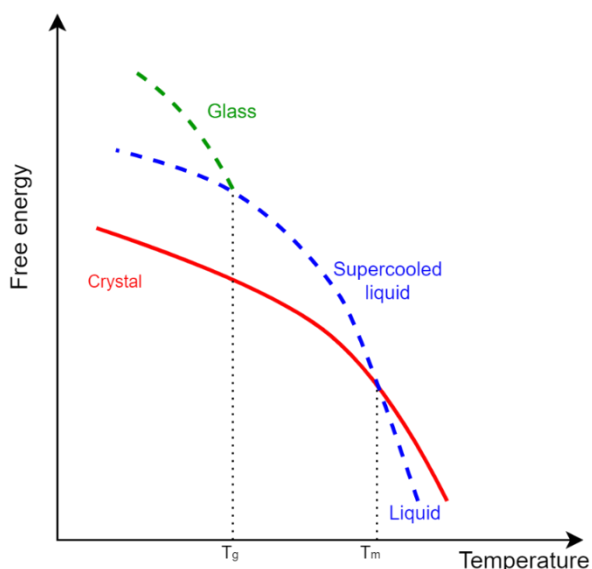


Figure 7. Free energy plot

As reported, amorphous phase can be form by melting the crystal and rapidly cooling the liquid to avoid recrystallization, this procedure is called vitrification or quench-cooling. However, amorphous can be formed through other methods. Generally, formation of amorphous state requires fast changing, as such as in temperature, to avoid generation of high order of the molecules, or introduction of sufficient energy to break

crystal structure. Following some examples of amorphous preparation procedure are reported. Amorphous can be formed from solution by inducing a rapid precipitation with use of anti-solvent, swift changing in pH or temperature. Amorphization can be promoted by grinding, although its efficacy is disputed for the ambiguous distinction between true amorphous solid and microcrystalline powder with particle size  $\leq 100 \text{ \AA}$ , hardly distinguishable by main technique XRPD and DSC.<sup>40</sup> The most used amorphization methods are lyophilization and spray-drying. In the first case amorphization occurs by rapidly freezing a solution and successively sublimation of frozen solution and drying to eliminate residual solvent to obtain highly soluble product. Spray-drying consists in rapid drying through heat atmosphere of atomized concentrated solution to increase the surface area in contact with the hot gas. In this way, it is possible to produce powder with good flow properties and spherical particle with desired size, usually small size for inhalation dosage forms.<sup>1</sup>

In pharmaceutical field numerous amorphous compounds, both excipient and API, are used. Hence, the study of the amorphous phase is important because of its advantageous high solubility and, on the contrary, its inconvenient instability. In case of poor soluble drug, the amorphous phase is desirable to enhance solubility, bioavailability, and performance of the drug product. For example, amorphous form of the antibiotic novobiocin shows solubility rate 70 times greater than its crystalline form. For this reason, amorphous phase is preferable because it is readily absorbed and it reaches the therapeutic blood level, in contrast to crystalline form that is not effective due to its poor absorption.<sup>41</sup>

Nevertheless, as reported by Fukuoka et al, amorphous phase is generally unstable and it tendentially crystallizes.<sup>42</sup> Therefore, crystalline phase is usually preferable despite its low solubility.

Therefore, it is fundamental characterized amorphous phase to know its crystallization tendency, surface chemistry and molecular mobility. Additionally, it is important to quantitatively determine the crystalline fraction in largely amorphous substance or formulation to, for instance, avoid dramatically decrease of solubility and guarantee the performance of the product. Deeply characterization of amorphous phase requires combination of technique, especially XRPD, DSC and DVS. In case of amorphous phase XRPD shows diffusive halo as opposed to sharp peaks detected for crystalline materials, XRPD pattern is largely used for amorphous-crystalline quantitative analysis.<sup>43</sup> DSC gives information about Tg, and crystallization temperature (Tc), respectively marked in thermogram by change of the baseline due to change in heat capacity and exothermic peak.<sup>44</sup> Amorphous phase has high hygroscopicity, its exposure at high humidity induces absorption of water and increase in molecular mobility and potentially crystallization. DVS allows to study the amorphous behavior in different %RH and gives information about its stability.

### 3 REFERENCE

- (1) Hilfiker, R.; Von Raumer, M. *Polymorphism: In the Pharmaceutical Industry*; Wiley-VCH Verlag GmbH & Co. KGaA: Weinheim, Germany, 2006.
- (2) Vippagunta, S. R.; Brittain, H. G.; Grant, D. J. W. Crystalline Solids. *Adv. Drug Deliv. Rev.* **2001**, *48* (1), 3–26. [https://doi.org/10.1016/S0169-409X\(01\)00097-7](https://doi.org/10.1016/S0169-409X(01)00097-7).
- (3) International Conference on Harmonization. *ICH Q6A - Specifications: Test Procedures and Acceptance Criteria for New Drug Substances and New Drug Products: Chemical Substances*; 1999.
- (4) FDA The United States Food and Drug Administration. Guidance for Industry. ANDAs: Pharmaceutical Solid Polymorphism. Chemistry, Manufacturing and Controls Information. *Journal of Generic Medicines*. 2007.
- (5) Stahly, G. P. Diversity in Single-and Multiple-Component Crystals. The Search for and Prevalence of Polymorphs and Cocrystals. *Cryst. Growth Des.* **2007**, *7* (6), 1007–1026. <https://doi.org/10.1021/cg060838j>.
- (6) Byrn, S. R.; Zografi, G.; Chen, X. *Solid-State Properties of Pharmaceutical Materials*; John Wiley & Sons, I., Ed.; 2017; Vol. 26. <https://doi.org/10.1080/0889311x.2019.1698555>.
- (7) USP-NF United States Pharmacopeia and National Formulary. (941) Characterization of Crystalline and Partially Crystalline Solids BY X-Ray Powder Diffraction (XRPD). 2019.
- (8) Altomare, A.; Cuocci, C.; Moliterni, A.; Rizzi, R. Single Crystal and Powder XRPD Techniques: An Overview. In *Inorganic Micro- and Nanomaterials*; 2013; pp 57–92.
- (9) Newman, A. W.; Byrn, S. R. Solid-State Analysis of the Active Pharmaceutical Ingredient in Drug Products. *Drug Discov. Today* **2003**, *8* (19), 898–905. [https://doi.org/10.1016/S1359-6446\(03\)02832-0](https://doi.org/10.1016/S1359-6446(03)02832-0).
- (10) Geppi, M.; Mollica, G.; Borsacchi, S.; Veracini, C. A. Solid-State NMR Studies of Pharmaceutical Systems. *Appl. Spectrosc. Rev.* **2008**, *43* (3), 202–302. <https://doi.org/10.1080/05704920801944338>.
- (11) Vogt, F. G. Evolution of Solid-State NMR in Pharmaceutical Analysis. *Future Med. Chem.* **2010**, *2* (6), 915–921. <https://doi.org/10.4155/fmc.10.200>.
- (12) Huang, L. F.; Tong, W. Q. Impact of Solid State Properties on Developability Assessment of Drug Candidates. *Adv. Drug Deliv. Rev.* **2004**, *56* (3), 321–334. <https://doi.org/10.1016/j.addr.2003.10.007>.
- (13) Cui, Y. A Material Science Perspective of Pharmaceutical Solids. *Int. J. Pharm.* **2007**, *339* (1–2), 3–18. <https://doi.org/10.1016/j.ijpharm.2007.04.021>.
- (14) Lipinski, C. A.; Lombardo, F.; Dominy, B. W.; Feeney, P. J. Experimental and Computational Approaches to Estimate Solubility and Permeability in Drug Discovery and Development Settings. *Adv. Drug Deliv. Rev.* **2012**, *64* (SUPPL.), 4–17. <https://doi.org/10.1016/j.addr.2012.09.019>.
- (15) Byrn, S.; Pfeiffer, R.; Ganey, M.; Hoiberg, C.; Poochikian, G. Pharmaceutical Solids: A Strategic Approach to Regulatory Considerations. *Pharmaceutical Research: An Official Journal of the American Association of Pharmaceutical Scientists*. 1995, pp 945–954. <https://doi.org/10.1023/A:1016241927429>.
- (16) Raw, A. S.; Furness, M. S.; Gill, D. S.; Adams, R. C.; Holcombe, F. O.; Yu, L. X. Regulatory Considerations of Pharmaceutical Solid Polymorphism in Abbreviated New Drug Applications (ANDAs). *Adv. Drug Deliv. Rev.* **2004**, *56* (3), 397–414. <https://doi.org/10.1016/j.addr.2003.10.011>.
- (17) Cruz-Cabeza, A. J.; Reutzel-Edens, S. M.; Bernstein, J. Facts and Fictions about Polymorphism. *Chem. Soc. Rev.* **2015**, *44* (23), 8619–8635. <https://doi.org/10.1039/c5cs00227c>.
- (18) Brittain, H. G.; Byrn, S. R.; Lee, E. *Polymorphism in Pharmaceutical Solids*, 2nd ed.; Informa Healthcare, Ed.; New York, 2016.
- (19) Purohit, R.; Venugopalan, P. Polymorphism: An Overview. *Resonance* **2009**, 882–893.

- (20) Bernstein, J. *Polymorphism in Molecular Crystals*; Claredon Press: Oxford, 2002.
- (21) Hancock, B. C.; Parks, M. What Is the True Solubility Advantage for Amorphous Pharmaceuticals? *Pharm. Res.* **2000**, *17* (4), 397–404. <https://doi.org/10.1023/A:1007516718048>.
- (22) Kobayashi, Y.; Ito, S.; Itai, S.; Yamamoto, K. Physicochemical Properties and Bioavailability of Carbamazepine Polymorphs and Dihydrate. *Int. J. Pharm.* **2000**, *193* (2), 137–146. [https://doi.org/10.1016/S0378-5173\(99\)00315-4](https://doi.org/10.1016/S0378-5173(99)00315-4).
- (23) Cabri, W.; Ghetti, P.; Pozzi, G.; Alpegiani, M. Polymorphisms and Patent, Market, and Legal Battles: Cefdinir Case Study. *Org. Process Res. Dev.* **2007**, *11* (1), 64–72. <https://doi.org/10.1021/op0601060>.
- (24) Babu, N. J.; Nangia, A. Solubility Advantage of Amorphous Drugs and Pharmaceutical Cocrystals. *Cryst. Growth Des.* **2011**, *11* (7), 2662–2679. <https://doi.org/10.1021/cg200492w>.
- (25) Singhal, D.; Curatolo, W. Drug Polymorphism and Dosage Form Design: A Practical Perspective. *Adv. Drug Deliv. Rev.* **2004**, *56* (3), 335–347. <https://doi.org/10.1016/j.addr.2003.10.008>.
- (26) Grzesiak, A. L.; Lang, M.; Kim, K.; Matzger, A. J. Comparison of the Four Anhydrous Polymorphs of Carbamazepine and the Crystal Structure of Form I. *J. Pharm. Sci.* **2003**, *92* (11), 2260–2271. <https://doi.org/10.1002/jps.10455>.
- (27) Bauer, J.; Spanton, S.; Henry, R.; Quick, J.; Dziki, W.; Porter, W.; Morris, J. Ritonavir: An Extraordinary Example of Conformational Polymorphism. *Pharm. Res.* **2001**, *18* (6), 859–866. <https://doi.org/10.1023/A:1011052932607>.
- (28) Nyman, J.; Day, G. M. Static and Lattice Vibrational Energy Differences between Polymorphs. *CrystEngComm* **2015**, *17* (28), 5154–5165. <https://doi.org/10.1039/c5ce00045a>.
- (29) Giron, D. Investigations of Polymorphism and Pseudo-Polymorphism in Pharmaceuticals by Combined Thermoanalytical Techniques. *J. Therm. Anal. Calorim.* **2001**, *64* (1), 37–60. <https://doi.org/10.1023/A:1011572610005>.
- (30) Chemburkar, S. R.; Bauer, J.; Deming, K.; Spiwek, H.; Patel, K.; Morris, J.; Henry, R.; Spanton, S.; Dziki, W.; Porter, W.; Quick, J.; Bauer, P.; Donaubaue, J.; Narayanan, B. A.; Soldani, M.; Riley, D.; McFarland, K. Dealing with the Impact of Ritonavir Polymorphs on the Late Stages of Bulk Drug Process Development. *Org. Process Res. Dev.* **2000**, *4* (5), 413–417. <https://doi.org/10.1021/op000023y>.
- (31) Rodríguez-Spong, B.; Price, C. P.; Jayasankar, A.; Matzger, A. J.; Rodríguez-Hornedo, N. General Principles of Pharmaceutical Solid Polymorphism: A Supramolecular Perspective. *Adv. Drug Deliv. Rev.* **2004**, *56* (3), 241–274. <https://doi.org/10.1016/j.addr.2003.10.005>.
- (32) Miyazaki, T.; Sivaprakasam, K.; Tantry, J.; Suryanarayanan, R. Physical Characterization of Dibasic Calcium Phosphate Dihydrate and Anhydrate. *J. Pharm. Sci.* **2009**, *98* (3), 905–916. <https://doi.org/DOI.10.1002/jps.21443>.
- (33) Duggirala, N. K.; Perry, M. L.; Almarsson, Ö.; Zaworotko, M. J. Pharmaceutical Cocrystals: Along the Path to Improved Medicines. *Chem. Commun.* **2016**, *52* (4), 640–655. <https://doi.org/10.1039/c5cc08216a>.
- (34) FDA The United States Food and Drug Administration. Regulatory Classification of Pharmaceutical Cocrystals, Guidance for Industry. 2018.
- (35) Porter, W. W.; Elie, S. C.; Matzger, A. J. Polymorphism in Carbamazepine Cocrystals. *Cryst. Growth Des.* **2008**, *8* (1), 14–16. <https://doi.org/10.1021/cg701022e>.
- (36) Karimi-Jafari, M.; Padrela, L.; Walker, G. M.; Croker, D. M. Creating Cocrystals: A Review of Pharmaceutical Cocrystal Preparation Routes and Applications. *Cryst. Growth Des.* **2018**, *18* (10), 6370–6387. <https://doi.org/10.1021/acs.cgd.8b00933>.
- (37) Badorc, A.; Frehel, D. Dextrorotatory Enantiomer of Alpha-(4,5,6,7-Tetrahydrothieno[3,2-c]Pyrid-5-Yl)(2-Chlorophenyl)Methyl Acetate, Process for Its Preparation and Pharmaceutical Compositions Containing It EP0281459 A1, 1988.

- (38) Guerrieri, P.; Rumondor, A. C. F.; Li, T.; Taylor, L. S. Analysis of Relationships Between Solid-State Properties, Counterion, and Developability of Pharmaceutical Salts. *AAPS PharmaSciTech* **2010**, *11* (3), 1212–1222. <https://doi.org/10.1208/s12249-010-9499-4>.
- (39) Pikal, M. J.; Lukes, A. L.; Lang, J. E. Thermal Decomposition of Amorphous  $\beta$ -Lactam Antibacterials. *J. Pharm. Sci.* **1977**, *66* (9), 1312–1316. <https://doi.org/10.1002/jps.2600660927>.
- (40) Byrn, S. R. *Solid-State Chemistry of Drugs*; Academic Press, Ed.; New York, 1982.
- (41) Mullins, J. D.; Macek, T. J. Some Pharmaceutical Properties of Novobiocin. *J. Am. Pharm. Assoc. (Scientific ed.)* **1960**, *49* (4), 245–248. <https://doi.org/10.1002/jps.3030490417>.
- (42) Fukuoka, E.; Makita, M.; Nakamura, Y. Glassy State of Pharmaceuticals. V. Relaxation during Cooling and Heating of Glass by Differential Scanning Calorimetry. *Chem. Pharm. Bull.* **1991**, *39* (8), 2087–2090.
- (43) Bergese, P.; Colombo, I.; Gervasoni, D.; Depero, L. E. Assessment of the X-Ray Diffraction-Absorption Method for Quantitative Analysis of Largely Amorphous Pharmaceutical Composites. *J. Appl. Crystallogr.* **2003**, *36* (1), 74–79. <https://doi.org/10.1107/S002188980201926X>.
- (44) Hancock, B. C.; Zografi, G. Characteristics and Significance of the Amorphous State in Pharmaceutical Systems. *J. Pharm. Sci.* **1997**, *86* (1), 1. <https://doi.org/10.1021/js9601896>.

## CHAPTER 2

### COCRYSTAL SCREENING OF ALLANTOIN

#### 1 INTRODUCTION

##### 1.1 Allantoin

Allantoin (CAS No. 97-59-6) or 2,5-dioxo-4-imidazolidinyl urea (Figure 1) is 5-membered azaheterocycles compound with urea as substituent in position 4<sup>th</sup> and chiral center in the same position.

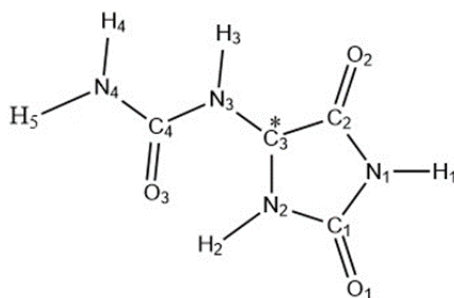


**Figure 1. Allantoin structure**

Allantoin is white, odourless, tasteless, and non-staining powder. Allantoin is amphoteric molecule, soluble in hot water, slightly soluble in cold water, glycerine, and propylene glycol, even less soluble in alcohol and practically insoluble in non-polar solvents. It can be extracted from some plants, as such as callus of *Coffea Arabica* plant, leaves and apical shoots of the *Mertensia maritima* plant, or it can be synthesized from carbonyl compounds, urea and azaheterocycles. <sup>1</sup>

In the 1960s, numerous relevant studies have been conducted on the dependency on pH of hydrolysis and racemization mechanisms of allantoin. Vogels et al. have demonstrated the instability of allantoin in alkaline media, where it hydrolyses to urea and glyoxylic acid, while in ordinary conditions it is stable. <sup>2</sup> In addition to the reactions of hydrolysis and racemization, allantoin can react with phenol, in the presence of heterogeneous catalysts such as mineral acids supported onto solid zeolite, producing ortho/para-hydroxyphenyl hydantoin. <sup>3</sup> Allantoin can highlight chemo and electrochemiluminescence phenomena decomposing and releasing a cyanide radical that react with lucigenin in an alkaline medium. <sup>4</sup> By reacting allantoin with glutaraldehyde and formaldehyde, many bactericides can be synthesized through condensation reactions. <sup>1</sup>

Allantoin has a chiral center in 4<sup>th</sup> position and it exists as a racemic mixture of stereoisomers (R) and (S). The conversion between the two allantoin enantiomers is catalysed by the enzyme allantoin racemase. Allantoin can racemize via two mechanisms S<sub>E</sub>1 and S<sub>E</sub>2 which involve a carbanion as an intermediate stabilized by tautomerization. Another possible racemization process can happen via S<sub>N</sub>2 like mechanism through the intramolecular attack of primary amide nitrogen at carbonyl carbon (C2 in Figure 1) and the formation of a symmetrical bicyclic intermediate. <sup>5</sup> Intramolecular racemization proceeds more rapidly in allantoin in anionic form than in neutral form.

Allantoin is a product of purine and protein metabolism. Back in 1838 it has been shown that allantoin results from oxidation of uric acid, which is a component of metabolism of the purine nitrogenous bases, adenine and guanine, of DNA and RNA. In animals, uric acid is metabolized through various steps mediated by several enzymes including the enzyme urate-oxidase. This enzyme catalyses the decomposition of urate, the uric acid anion physiologically prevalent, into (S)-allantoin. On the other hand, humans have deficiencies in urate-oxidase, consequently they cannot decompose urate in (S)-allantoin, therefore high level of urate can cause significant disorders such as gout. <sup>6</sup> Studies revealed the presence of allantoin and uric acid in the urine of mammals, in some plants and, in small quantities, also in human urine and amniotic fluid. Shestopalov et al. support the significance of allantoin in the forming placenta and its synthesis in embryonic tissues. <sup>7</sup>

The conformational study of allantoin neutral form points out the presence of four conformers of allantoin differing in the dihedral angles and in the bond lengths. <sup>5</sup> The two most stable conformers are characterized by a trans amide bond in the acylurea chain and are referred to as trans-1 and trans-2, the latter is the lowest

energy one. The other two conformers adopt a cis amide bond, and they are referred to as cis-1 and cis-2, the latter cis-2 is characterized "scorpion" conformation with the ureic group above the imidazole ring and a torsion angle of  $21^\circ$  (Figure 2). Using the Boltzmann statistic and the computed conformer energies, the equilibrium population is estimated to be 98.3/1.2/0.4/0.1% (trans-2/trans-1/cis-2/cis-1) at room temperature.<sup>8</sup> Concerning the allantoin in anionic form, in that case the most stable conformer is cis-1. Furthermore, it is observed new possible conformation named cis-3. The different conformations adopted by allantoin in neutral and acid form provide an explanation for the observed dependence on pH of racemization.<sup>5</sup>

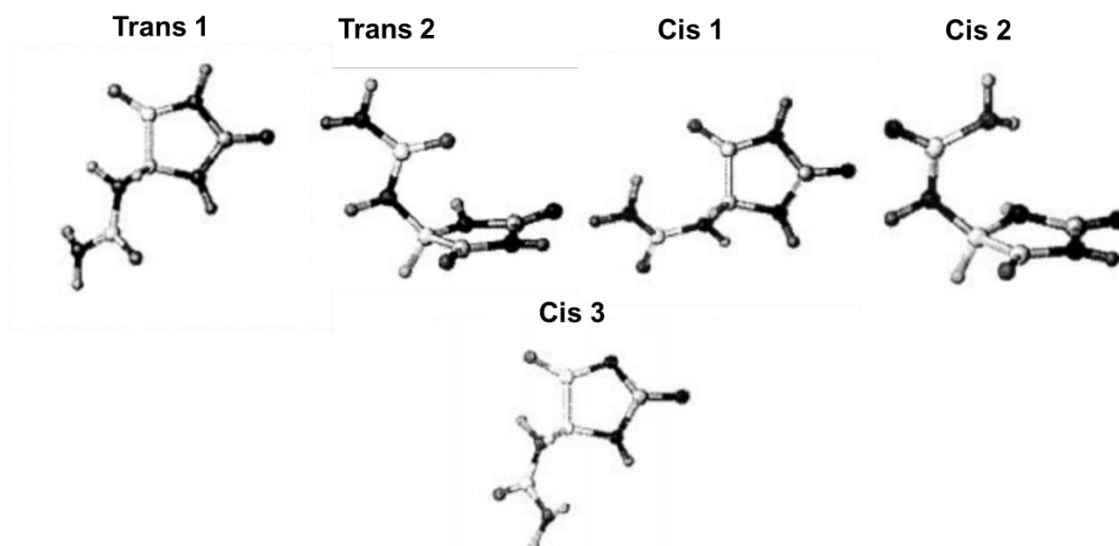


**Figure 2. Allantoin conformers in neutral form on the top and Cis-3 anionic allantoin conformer. Kahn, K.; Tipton, P. A. Kinetics and Mechanism of Allantoin Racemization. *Bioorg. Chem.* 2000, 28 (2), 62–72. <https://doi.org/10.1006/bioo.2000.1162>**

To date, only the crystalline form of RS-allantoin is known registered in CSD with the refcode ALATIN. The monoclinic crystal structure has space group  $P2_1/c$  and following parameters  $a = 8.024 \text{ \AA}$ ,  $b = 5.153 \text{ \AA}$ ,  $c = 14.797 \text{ \AA}$ ,  $\alpha = \gamma = 90^\circ$ ,  $\beta = 93.02^\circ$  with a molecule in the asymmetric unit with a conformation very similar to the trans-2 conformer.<sup>9</sup>

The presence of five hydrogen bond donor sites and three carbonyl oxygens as hydrogen bond acceptors, suggests that the structure is characterized by a complex hydrogen bond network. All hydrogen bonds observed in the crystal structure, are inter-molecular and are summarized in Table 1. Each allantoin molecule forms five hydrogen bonds which correspond to the five hydrogens linked to nitrogen of heterocycle and urea substitute (a and b in Figure 3). Figure 3c shows the crystalline packaging of RS-allantoin, it is worth noting that the hydrogen bond interactions between the urea groups form a sort of channel along the b axis.

**Table 1. Hydrogen bond length calculated by Mercury software**

Hydrogen bond donor	Hydrogen bond acceptor	Length (Å)
N4	O2	3.006 (1)
N2	O1	2.828 (1)
N3	O3	2.912 (1)
N1	O3	2.925 (1)

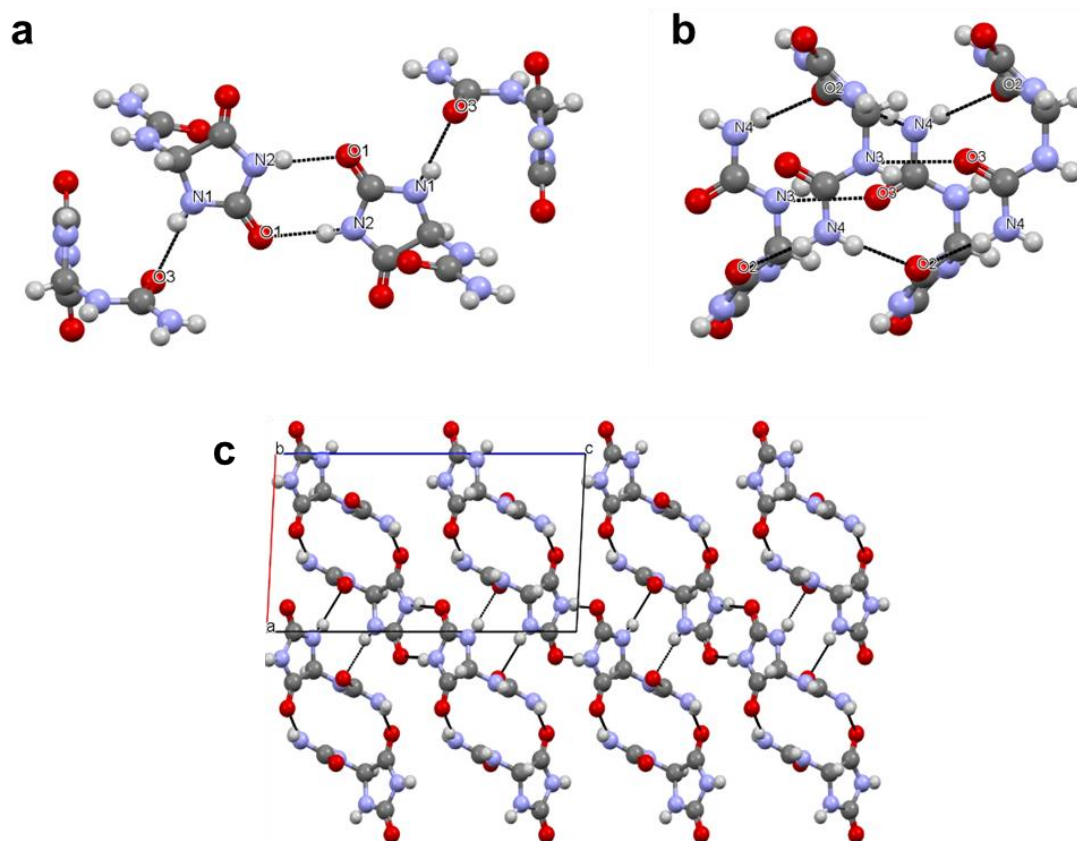


**Figure 3. Hydrogen bonds involving heterocycle N atoms a) and urea N atoms b). Picture c) shows crystalline packing seen along axis b**

Allantoin has biological, pharmaceutical, and cosmetic interest. Relevance of the study of this molecule resurfaces around 2000 when Gus'kov et al. have shown that allantoin is an important marker of oxidative stress and it reduces the genotoxic effect of ultraviolet radiation.<sup>10</sup> Furthermore, allantoin has biological effect comparable to that of vitamin C explained also by their similarity in antioxidant properties and hydrolysis reactions.<sup>11</sup>

Allantoin has been used as a drug for treatment of rheumatoid arthritis, myocardial infarction, some tumours, and its use in cosmetics is increasingly growing. Furthermore, allantoin can be used in agriculture as plant growth regulator, fertilizing, component of veterinary antiseptic and as a reagent in the synthesis of DL-5-(4-hydroxyphenyl) hydantoin, precursor in the enzymatic synthesis of D-(4-hydroxyphenyl) glycine.<sup>7</sup> Allantoin is widely used in cosmetic products, it is used in more than 1300 cosmetic products in concentrations up to 2% for its keratolytic, moisturizing, soothing and anti-irritating effect on the skin; it promotes the renewal of epidermal cells and accelerates the healing of wounds, cuts and scars.<sup>1,12</sup> Furthermore, allantoin stimulates and increases the synthesis of pro-collagen, a precursor of collagen.<sup>1</sup> These properties and beneficial effects of allantoin make it a suitable molecule for any personal care application. It is fully compatible with most cosmetic ingredients and with anionic, cationic, and non-ionic systems. Its use greatly increases the performance of each cosmetic preparation, even in small quantities (used up to 2%). It provides relief and smooth and healthy appearance to the skin.<sup>13</sup> Allantoin is very effective in the dry state or in suspension but it has a limited solubility in water and alcohol, a saturated aqueous solution contains only 0.6% of allantoin. For this reason, allantoin has been associated with several molecules, to improve its solubility and effects. Several patents, mainly of 1970s, claim the use of allantoin alone or linked to organic and inorganic molecules, as such as complexes and salts.<sup>13,14</sup> Some patents claim the production of complexes of allantoin with metals such as aluminium, zinc and silver used in the medical field.<sup>15,16</sup> Patent US3932627 claims the formation of non-thrombogenic and anti-microbial complex formed by silver heparin and allantoin, it combines the antimicrobial properties of silver with the anticoagulant properties of heparin and the capacity of allantoin to form a long-lasting coating in polymeric implants used in heart and vascular surgery to replace defective or diseased valves and arteries.<sup>17</sup>

Among the compounds of allantoin with organic molecules, the most studied and used in the cosmetic field are compounds with galacturonic acid, glycyrrhetic acid, polygalacturonic acid, ascorbic acid, panthenol and biotin. Safety of ascorbic acid, biotin, glycyrrhetic acid and panthenol has already been evaluated and demonstrated by the Expert Group on the Evaluation of Cosmetic Ingredients (CIR), while galacturonic and polygalacturonic acid are sugars, major components of pectin which has been designated by the US Food and Drug Administration (FDA) as a safe food additive.<sup>13</sup> Generally, these patents declare increasing in stability and solubility of the allantoin. Following, some allantoin derivatives presented by these patents are reported. Allantoin ascorbate (CAS No. 57448-83-6) is a yellowish-white powder that is soluble in water.<sup>18</sup> Biotin allantoin (CAS No. 4492-73-3) is a complex soluble 8% in cold water and very soluble in hot water, containing  $57.1 \pm 4\%$  of biotin and  $42.9 \pm 4\%$  of allantoin.<sup>19</sup> Allantoin panthenol is water-soluble white powder.<sup>20</sup> Allantoin with galacturonic acid (CAS No. 5119-24-4) is soluble from 3 to 5% by weight, it is constituted by  $41.6 \pm 4\%$  of allantoin and  $58.4 \pm 4\%$  of  $\alpha$ -D-galacturonic acid. Allantoin with polygalacturonic acid (CAS No. 29659-38-9) is a yellowish-white powder that forms a gel in solutions of sodium citrate. Allantoin with glycyrrhetic acid (CAS No. 4572-09-2) in molar ratio 1:1, 1:2 or 1:3 is a yellowish-white powder with an acrid odour soluble in propylene glycol and alcohol but not in water, the complex contains  $30 \pm 2\%$  of allantoin and  $70 \pm 2\%$  of glycyrrhetic acid.<sup>13</sup> Additionally, patent of complexes of allantoin and urocanic acid, glycine and p-aminobenzoic acid have been issued.<sup>21-24</sup>

Nowadays, Akema fine chemicals is a leading European producer of allantoin offering a wide range of allantoin derivatives and preservatives for personal care. The main products are Allantoin, Alphanta, Alcloxa, Aldioxa (CAS No. 5579-81-7), Allantoin calcium pantothenate, Algycera (CAS No. 4572-09-2), and Almeth.

Alphanta is an allantoin and panthenol derivative with anti-inflammatory, soothing, healing, and moisturizing properties. It is suitable in cosmetic products, for hair care, for oral hygiene and for sun screening.

Alcloxa and Aldioxa are aluminium salts of allantoin that occur as a white powder and combine the astringent and antimicrobial properties of aluminium with the anti-irritant, soothing and healing properties of allantoin.

Particularly, Aldioxa is not soluble in water and alcohol, it is stable in a pH range of 3-8 and on heating up to 80°C. It is a product that can be incorporated into creams and powders for specific applications including antiperspirants (0.2-1%), products for children (0.2-0.3%), anti-acne products (1-2%), products for oral hygiene (0.1-2%).<sup>25</sup> Allantoin calcium pantothenate is a complex of allantoin and calcium pantothenate with protective, anti-irritant, soothing and moisturizing properties. It is soluble in water and glycerine, slightly soluble in propylene glycol and insoluble in oils. It can be used safely as an anti-irritant, wound healing, and conditioning agent. It can be incorporated at 0.2-2% in most formulations, especially in sprays, tonics, gels, lotions, creams and powders.<sup>26</sup> Algycera is allantoin complex with glycyrrhetic acid that maximizes the effectiveness of the individual components, it helps normalize the stratum corneum and stimulates the healing of damaged skin.

Given the low solubility in most solvents, it is applied in solid form as a lotion, cream, paste or powder.<sup>25</sup> Almeth (Allantoin Acetyl Methionine) is a white powder that synergically combines the protective effect of the skin of allantoin with the stimulating effect of the metabolism and donor sulphur of acetyl methionine. The complex is soluble in water up to 1%, it is not soluble in alcohol and oils. It finds application in the cosmetic, dermatological and hair care fields.<sup>25</sup>

Nevertheless, the patent presents the salt of allantoin but the allantoin lacks of a clear protonation site. Additionally, the term 'complex' underlines the chemical association of two or more species linked by intermolecular interactions. In some cases, this definition is inaccurate because the term complex in the chemical field only indicates metal complexes formed by a transition metal coordinated with a set of ions or molecules. The nature of these compounds reported in these patents is unclear. Recently, Puszyńska-Tuszkano et al. have demonstrated the existence of complexes of silver and allantoin.<sup>27</sup> Nevertheless, the solid-state and the real composition of all the complexes of allantoin submitted by the patents mentioned above are not fully characterized. Moreover, in case of the complex of allantoin with panthenol or other organic molecule the term co-crystal should be more appropriate.

## 1.2 Cocrystals

Co-crystal is a stoichiometric multi-component crystal composed by neutral molecular species that exist in the solid state under environmental conditions.<sup>28,29</sup>

The formation of cocrystals is mainly based on the supramolecular synthons, transferable connectors that can be used to bind molecules with non-covalent interactions such as hydrogen bonds, halogen bonds,  $\pi$ -stacking interactions. In the last 30 years, many synthons have been discovered, which can be classified into two macro-groups: supramolecular homo-synthons, which are composed of identical and complementary functional groups; and supramolecular hetero-synthons composed of distinct but complementary functional groups.<sup>30</sup> Corpinot and Bučar report some examples of supramolecular homo-synthons and supramolecular hetero-synthons shown in Figure 4.

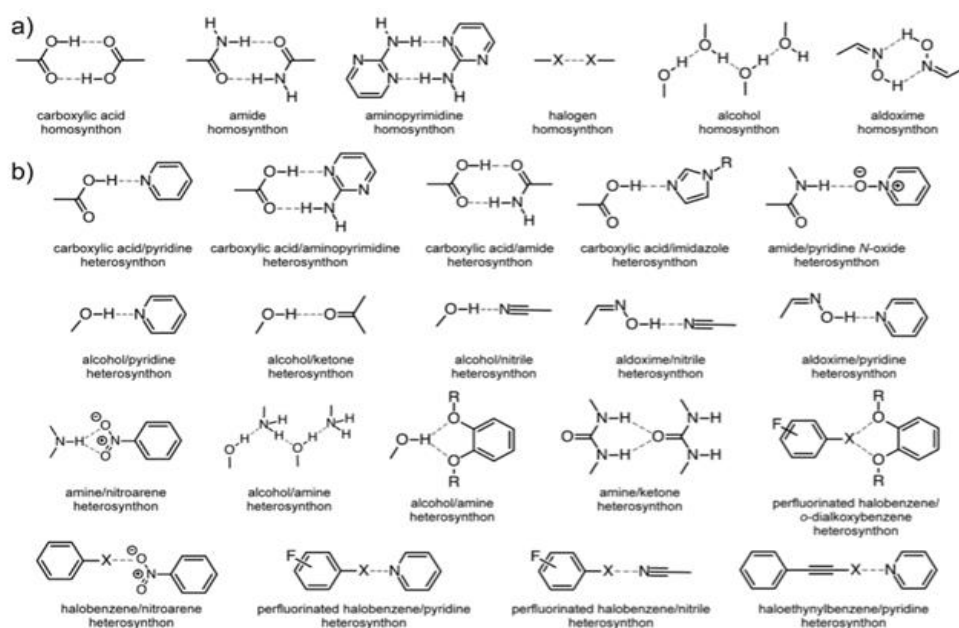


**Figure 4. Common homo-synthons supramolecular (a) and supramolecular hetero-synthons (b) (R = H, alkyl; X = Br, I). Corpinot and Bučar (2019)**

Numerous crystallographic studies have demonstrated the preferential formation of heteromeric synthons compared to the formation of homomeric interactions.<sup>31–35</sup> Generally, synthons are hydrogen bond donors or acceptors, and their formation is fundamental in the formation of co-crystal. Although, the presence of numerous donor and acceptor hydrogen bond functional groups does not ensure the formation of a cocrystal, it is essential to consider the complementarity and the strength of the possible interactions to design the cocrystal.<sup>36</sup> In case of multiple interactions between the molecules with different and competing synthons, the design of the cocrystal must consider the hierarchy of synthons, i.e., which of the possible synthons are formed at the expense of the others, based on their strength as bond acceptors or donors.

Cocrystal formation is promoted between molecules similar in shape and polarity as demonstrated by analysis of cocrystals in the Cocrystal Data Set, a database of co-crystals that contains 974 structures formed by 1949 molecules. Hence, to predict the Cocrystal formation it is important to have descriptors for shape and polarity. The polarity is described by the dipole moment and the ratio of total N and O atoms to the non-hydrogen atoms (FNO). While the shape is defined by two parameters:  $D_{S/L}$  and  $D_{M/L}$ , which are ratio of short (S) medium (M) with long (L) axes of rectangular box enclosing molecule. If these values are similar in the two cofomers, the formation of co-crystal between them will be feasible. Hence, to design co-crystals, it is necessary to understand supramolecular synthons to select suitable cofomers able to create molecular interactions, and to increase the chances of success is recommended to consider the shape and size of the cofomers.<sup>37</sup>

### 1.3 CSD modules

The Cambridge Structural Database (CSD) is the leading crystallographic bibliographic, chemical, and numerical database of X-ray and neutron diffraction studies of organic and organometallic molecules. It was created in 1965 by the Cambridge Crystallographic Data Center (CCDC), whose main purpose is to promote chemistry especially crystallography for the public benefit. Originally the number of crystalline structures was limited and the database was a paper document circulated to the scientific community through a series of volumes called *Molecular Structures and Dimension*.<sup>38</sup>

The evolution of technology, as such as the advances in data collection and structure solution techniques, and the introduction of the standard crystallographic file (CIF) have led to exponential increase in the number of crystal structures reported in the CSD database (Figure 5).<sup>39</sup>

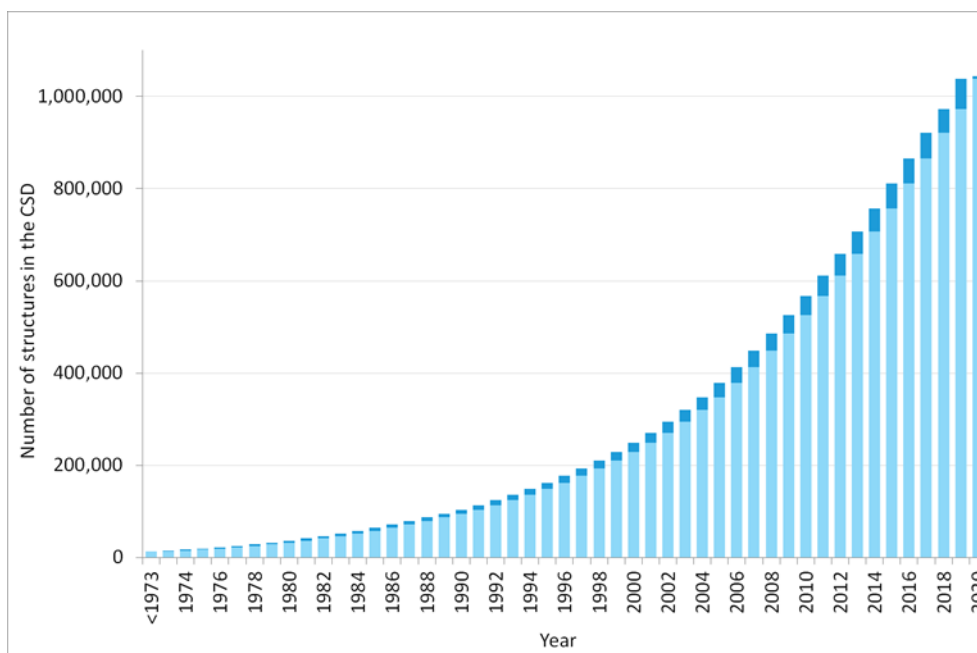


**Figure 5. Increasing of number of structures published per year in the CSD since 1972**

From the paper file to nowadays, the CSD expanded greatly to contain more than one million crystalline structures. The main quality of the CSD is the possibility to browse it for free online via the WebCSD. Additionally, it can be easily consulted via Conquest, a paid software.

In the CSD, each structure is encoded by a specific identification REFCODE of six alphabetic letters, which refer to a specific chemical compound, and 2 numbers, which trace further determinations of the same structure.

The information contained within the CSD can be classified into three different groups that describe the dimensionality of the content: 1D (bibliographic information), 2D (chemical connectivity), 3D (molecular and crystalline structure).

The CCDC supplies other software and programs of crystallographic interest. Currently, these software are available: Mercury, Mogul, Hermes, Isostar, Dash, Gold, enCIFer and CSD Python.

Mercury was created in 2002. It is useful and high-quality tool for visualization and investigation of crystalline structures.

The main functions of this software include:

- Reading various file formats of crystalline structures;
- Viewing in 3D and motion options;
- Displaying and measure display distances, angles and torsion angles involving atoms, centroids and planes;
- Visualization of elements of symmetry, axes of crystalline cells and crystal in any direction;
- Localization and visualization of intermolecular and/or intramolecular hydrogen bonds.

Over the years, the growing interest from both academics and industrial companies, as such as pharmaceutical and cosmetic industries, in Crystal Engineering has prompted the development of more and more tools and modules within Mercury such as CSD-Community, CSD-System, CSD-Materials and CSD-Discovery.<sup>40</sup>

Between these modules, CSD-Materials is extremely helpful tool to understand and to design materials. Specifically, it allows to predict molecular geometry, intermolecular interactions, and crystal packing. Among the applications of CSD-Materials, it includes the ability to engineer new compositions, as such as co-crystals through searching for suitable packing patterns and the study of similarity between crystal structures.

CSD Conformer Generator is a module of CSD-Materials that performs conformational analysis of the target molecule based on CSD data and 3D molecular structure including all hydrogen atoms. It can minimize molecular conformations and generate different conformer subsets according to conformer similarity.<sup>41,42</sup> A molecule can adopt different conformation, therefore performing conformational analysis of the target molecule is important because of the target molecule conformer can vary in co-crystals with different cofomers. CSD Conformer Generator identifies the most probable conformers of target molecule and it can generate subsets with the different conformers based on data provided by the CSD.

Other useful application of CSD-Materials is the evaluation of preferred inter- and intra-molecular interactions through Hydrogen Bond Propensities module which determines the propensity of the molecule to form hydrogen bonds. Hydrogen Bond Propensities leads the evaluation of the presence of polymorphism for the target molecule through a statistical analysis of the hydrogen bond models. Statistical model calculates the probabilities of the formation of hydrogen bonds between each possible combination of donor or acceptor functional groups of given target molecule using the information of the CSD on the frequency of involving of functional group in hydrogen bond. Furthermore, the method reports the coordination number, that is number of hydrogen bonds that donor or acceptor can form simultaneously. Coordination depends on the dual capacity of an atom to be donor and acceptor and on the chemical environment. The determination of coordination number is based on the number of observed non-covalent interatomic contacts involving an H atom below a specified distance and angle threshold. The propensity and coordination numbers are plotted in Hydrogen bond combination plot that displays the potential polymorphs of a given compound. It is mainly used to understand which of all polymorphic forms is more stable.<sup>43,44</sup>

Furthermore, the Full Interaction maps (FIM) is a three-dimensional image of the space around the target molecule that indicates the interaction preferences of a molecule in a specific conformation. Especially, it displays the most likely positions of interaction with specific functional groups such as donors and acceptors of hydrogen bonds and hydrophobic groups.

Summarizing, through this tool it is possible to predict the possible hydrogen bonds for a given molecule, evaluate its plausible crystal forms, calculate hydrogen bond propensities for individual donor and acceptor groups and perform a comprehensive hydrogen bond analysis on a set of structures.

Other important tool is Co-Crystal Design, which allows the identification of suitable cofomers to form co-crystal with a certain target molecule with high probability reducing co-crystal screening trials and time.<sup>45</sup> Through Screen by Molecular Complementarity function, this module calculates the probability of two molecules, a target and a conformer, to form co-crystal based on a semiquantitative model for the formation of co-crystals designed by Fábíán.<sup>36</sup> The most significant molecular properties that leads the formation of co-crystals were identified evaluating a wide range of molecular parameters (in total 131) of each component of the co-crystals in the CSD. The statistical analysis of these data reveals the decisive molecular properties for crystallization of two molecules are their size and polarity depicted by the molecular descriptors: dipole moment,  $D_{FNO}$ ,  $D_{S/L}$  and  $D_{M/L}$ . It is important to point out this method is applicable only for neutral multicomponent systems and not for salts.<sup>30</sup>

## 2 AIM

Allantoin has wide interest in cosmetic for its several cosmetic applications. Hence, the study of allantoin is of great interest for the cosmetic industry. Especially, is of particular concern the study of association of this molecule with other compounds with the mainly purpose to improve the features of allantoin particularly its poor solubility in water. In fact, several patent of '60s claim the correlation of allantoin with several other compounds of cosmetic interest as such as biotin, acid, ascorbate, etc.<sup>13,18–20</sup> Literature reports several studies of allantoin and patents that claims improvements of allantoin characteristics as such as solubility thanks to its correlation with other molecules in form of salts and complexes.<sup>14–17,21–24</sup> However, a clear characterization of solid-state of these compounds is missing. Their improved characteristic in solubility and stability suggests an interaction between these compounds that can be attributed to formation of cocrystal or to interaction of the two individual components in solution. The term Co-crystal had not yet been widely realized at the time of the publications and the term “complex” had been used to denote this type of crystal structures.<sup>35</sup> Therefore, the presence of different properties of these compounds compared to the starting reagents does not exclude the formation of co-crystals. Additionally, the presence of urea in the allantoin structure and its propensity to form co-crystals support this hypothesis.<sup>46–49</sup>

Preliminary studies have been conducted by group of prof. Evelina Colacino of the University of Montpellier. In collaboration prof. Evelina Colacino, the study of possible co-crystal of allantoin is experimentally proceeded in PolyCrystalLine laboratories. The first purpose was to understand the real nature Alphanta, a compound of allantoin and panthenol commercialized by Akema.

Furthermore, the study was extended to the screening of allantoin co-crystals especially with cosmetic interest molecules. The chosen cofomers are D-panthenol, Galacturonic Acid Monohydrate, D-Glucuronic Acid, L-Ascorbic Acid, and trans-Ferulic Acid. Nevertheless, the list of cofomers is extended to evaluate major number of compounds. Moreover, the propensity of allantoin to form co-crystal is evaluated using the Mercury CSD-materials module to study the reactivity of allantoin and identify potential cofomers for the formation of co-crystals of allantoin.

## 3 EXPERIMENTAL PROCEDURE

Allantoin has been evaluated using the Mercury's application to study its propensity to form cocrystals, additionally, the formation of cocrystal of allantoin has been experimentally evaluated. The tested cofomers are selected on the basis their cosmetic benefit and the co-crystal design results and are D-panthenol (PAN), Galacturonic acid monohydrate (GAL), D-Glucuronic acid (DGL), L-ascorbic acid (ASC), Trans-ferulic acid (FER), Citric Acid (CIA), DL-Panthenol (DLPAN), L-Lysine (LLYS), L-Tartaric Acid (LTA), Maleic Acid (MEA), Urea and 2,5-Dihydroxybenzoic acid (DHB).

All the experiments have been performed in PolyCrystalLine laboratories, the following co-crystallization method were tested: evaporations at 60°C (EvHT), cold precipitation, slurry, melting and experiments of mechanochemistry such as grinding and kneading. Grinding and kneading experiments were conducted using Retsch MM 200 grinder. All the products were analysed by X-ray diffraction via Rikagu miniflex, the settings are reported in appendix A. Thermal methods, especially scanning calorimetric analysis (DSC), on the other hand are useful for analysing mixtures composed with the two potential components of the co-crystal to evaluate the possible formation of cocrystal by melting. The presence of endothermic peak associated with the eutectic fusion immediately followed by an exothermic peak due to the crystallization can indicate the formation of the co-crystal. The lack of exothermic crystallization peak indicates that co-crystallization has not occurred.

### 3.1 Reagent and Standards

Allantoin and the cofomer of cosmetic interest D-panthenol, Galacturonic Acid Monohydrate, D-Glucuronic Acid, L-Ascorbic Acid and trans-Ferulic Acid were supplied by Evelina Colacino group. DL-panthenol was provided by Alfa Aesar (Kandel, Germany). Other cofomers: citric acid, L-lysine, L-tartaric acid, DL-Malic acid, Malonic acid, Maleic acid and 2,5-Dihydroxybenzoic acid were provided by Sigma-Aldrich (Saint Louis, MO, USA).

## 3.2 Application CSD modules

### 3.2.1 CSD Conformer Generator

Analysis of the feasible conformers of allantoin has been performed using the Mercury's tool CSD Conformer Generator and the structure of allantoin ALATIN. Maximum of ten conformations were considered.<sup>50</sup> Figure 6 reports the four conformers of allantoin obtained by the analysis of CSD Conformer Generator. The results evidenced the presence of four possible conformers trans-1 (a), trans-2 (b), cis-1 (c) and cis-2 (d) compatible with the literature data for allantoin in neutral form.

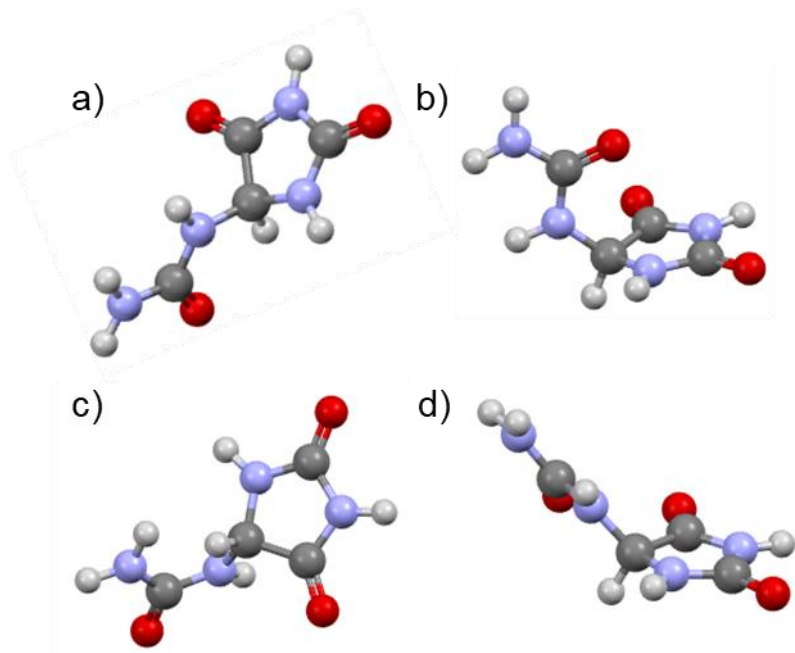
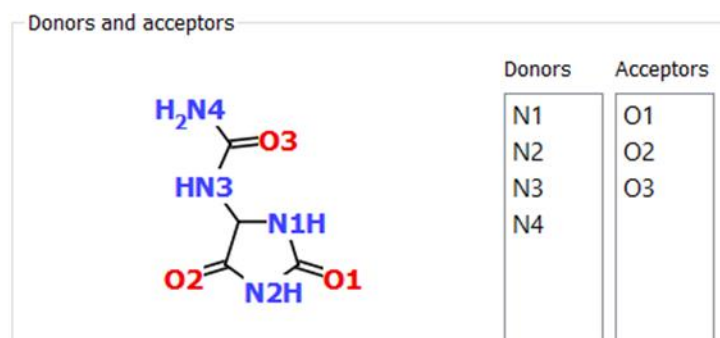


Figure 6. Conformers of allantoin by CSD Conformer Generator: a) trans-1 b) trans-2 c) cis-1 d) cis-2

### 3.2.2 Hydrogen Bond Propensities

The Hydrogen Bond propensities tool of Mercury has been used to evaluate the propensity of allantoin to form hydrogen bond. This tool evaluates the hydrogen bonds formed by the target molecule in its known crystalline structures. In case of different polymorphs, the comparison of the hydrogen bond strength can be used to rank the stability of the polymorphs. In case of allantoin, only one crystal form is known. However, the study of the feasible hydrogen bond is useful to evaluate the possible interaction of the molecule even with another molecule. The functional groups of allantoin were classified in donor and acceptor of hydrogen bond and they were classified considering their propensity to form hydrogen bond in existing crystal structures. Figure 7 displays the functional groups classified by the software Mercury in donors and acceptors of hydrogen bond highlighted in blue and red, respectively. All the nitrogen of both ureic groups, the substituent in position 4<sup>th</sup> and in azaheterocycle were classified as donors, while all the carbonyl oxygens were classified as acceptors of hydrogen bond.



**Figure 7. Determination of donors and acceptors functional groups of allantoin**

The software analyses how many times the functional groups described above form hydrogen bonds in the structures deposited in the database (Figure 8).

Category	Label	# True	# False
Donor(s)	atom_1(2)_of_cyclic_NH_urea (matches N1,N2)	349	149
	atom_1_of_T3NH1_amide (matches N3)	149	141
	atom_1_of_saturated_ring_amide_2 (matches N2)	7	14
	atom_2_of_T3NH1_amide (matches N4)	291	93
Acceptor(s)	atom_3_of_T3NH1_amide (matches O3)	284	157
	atom_3_of_cyclic_NH_urea (matches O1)	208	105
	atom_3_of_saturated_ring_amide_2 (matches O1,O2)	187	72

**Figure 8. Hydrogen bond analysis of functional groups**

The statistical data about the probability of the allantoin's functional groups to form hydrogen bond were used to evaluate the likelihood of hydrogen bond formation of allantoin.

The software Mercury performed a regression analysis using the statistics program R. The software outcomes the hydrogen bond propensity calculation and reported the propensity scores table for both inter- and intramolecular hydrogen bond, and coordination scores table. The first reports donor-acceptor pairs sorted by their propensity to form hydrogen bond. Figure 9 and Figure 10 report the intermolecular and intramolecular hydrogen bond propensity scores table of allantoin, respectively.

The coordination scores table shows the individual atom likelihood to form a hydrogen bond considering the surrounding environment. Figure 11 reports the Hydrogen bond coordination scores table. The table shows calculated likelihoods for allowed coordination numbers for each donor and acceptor computed using CSD derived models. The coordination model evidenced which donors and acceptors of the molecule is likely to coordinate one or more times and which hydrogen bonds can occur simultaneously or mutually exclusive. Values are coloured green or red to indicate optimal or sub-optimal scores, respectively. Green highlighting indicates a maximum likelihood is observed. Red highlighting indicates there is a more likely alternative coordination number for that atom. Higher coordination value indicates increasing hydrogen bond capacity.<sup>44</sup> The most probable intermolecular hydrogen bond is between the urea nitrogen N4 and the carbonyl oxygen O2 in the azaheterocycle with a propensity value of 0.78 corresponding to the 78% probability of formation. The term 'observed' indicates the hydrogen bond has been observed in the crystal structure ALATIN. The nitrogen N4 shows as the most probable coordination number of 2 (Figure 11), in fact it forms two hydrogen bonds with O2 of two different allantoin molecules. As the same way the oxygen O3 showed the most probable coordination number of 2 (Figure 11) and it bind both nitrogen N1 and N3. Considering the coordination scores, the observed hydrogen bonds of ALATIN are the most probable. Specifically, the most probable bond is N4-O2 with 78% of propensity and coordination number of N4 of 2. These atoms are no longer available for forming another bond. Hence, any interactions with these atoms can be excluded despite their high propensity score. This explains how the bond N3-O3 with lowest propensity score of 39% is observed in ALATIN. In fact, N3 shows lowest propensity scores, probably due to its steric density of 40.62 (Figure 9), and it cannot be connected with O2 and O1 already involved in other hydrogen bonds with N4 and N2. Having O3 a coordination number of 2, it can be involved in another hydrogen bond with N3.

It is worth noting that although higher propensity score of 69% of the intra-molecular interaction N1-O3 than the inter-molecular interaction (58%), the last one is observed in ALATIN. This indicates the formation of hydrogen bonds is based on overall energy minimization and consideration on single interaction can be misleading.

Donor	Acceptor	Competition	Donor steric density	Acceptor steric density	Donor aromaticity	Acceptor aromaticity	Propensity	Lower bound	Upper bound	Frequency	Observed Inter-?
N4 of T3NH1_amide	O2 of saturated_ring_amide_2	2.75	28.67	34.63	0.27	0.27	0.78	0.63	0.87	37.5	observed
N2 of cyclic_NH_urea	O2 of saturated_ring_amide_2	3.67	34.64	34.63	0.27	0.27	0.73	0.61	0.82	17.8	
N1 of cyclic_NH_urea	O2 of saturated_ring_amide_2	3.67	38.88	34.63	0.27	0.27	0.72	0.60	0.82	27.0	
N4 of T3NH1_amide	O1 of cyclic_NH_urea	2.75	28.67	29.97	0.27	0.27	0.70	0.56	0.81	71.4	
N2 of cyclic_NH_urea	O1 of cyclic_NH_urea	3.67	34.64	29.97	0.27	0.27	0.65	0.55	0.73	26.6	observed
N4 of T3NH1_amide	O3 of T3NH1_amide	2.75	28.67	30.92	0.27	0.27	0.64	0.49	0.77	50.7	
N1 of cyclic_NH_urea	O1 of cyclic_NH_urea	3.67	38.88	29.97	0.27	0.27	0.64	0.54	0.73	25.3	
N2 of cyclic_NH_urea	O3 of T3NH1_amide	3.67	34.64	30.92	0.27	0.27	0.58	0.44	0.71	42.9	
N1 of cyclic_NH_urea	O3 of T3NH1_amide	3.67	38.88	30.92	0.27	0.27	0.58	0.43	0.71	28.6	observed
N3 of T3NH1_amide	O2 of saturated_ring_amide_2	3.67	40.62	34.63	0.27	0.27	0.55	0.38	0.71	37.5	
N3 of T3NH1_amide	O1 of cyclic_NH_urea	3.67	40.62	29.97	0.27	0.27	0.46	0.32	0.60	42.9	
N3 of T3NH1_amide	O3 of T3NH1_amide	3.67	40.62	30.92	0.27	0.27	0.39	0.26	0.54	38.8	observed

Figure 9. Predicted intermolecular hydrogen bond propensity scores table

Donor	Acceptor	Donor sybyl atom type	Acceptor sybyl atom type	DA Pair constrained connectivity	DA Pair path string	Donor count	Propensity	Lower bound	Upper bound	Observed Intra-?
N1	O3	N.am	O.2	0	0	5	0.69	0.69	0.69	

Figure 10. Predicted intramolecular hydrogen bond propensity scores table

Atom (D/A)	= 0	= 1	= 2	= 3
N1 of cyclic_NH_urea (d)	0.00661533	0.930737	0.0626481	0
N2 of cyclic_NH_urea (d)	0.00631716	0.90971	0.0839728	0
N3 of T3NH1_amide (d)	0.0264016	0.973598	0	0
N4 of T3NH1_amide (d)	0.00142286	0.0967107	0.736836	0.16503
O1 of cyclic_NH_urea (a)	0.0257654	0.454177	0.508888	0.0111697
O2 of cyclic_amide (a)	0.0539818	0.622582	0.298459	0.0249769
O3 of T3NH1_amide (a)	0.0250294	0.30873	0.419807	0.246434

Figure 11. Hydrogen bond coordination scores table

Figure 12 represents the possible hydrogen bond combinations for the system. Each data point in the graphic is a possible structure with unique hydrogen bonding. The horizontal axis is the average propensity for hydrogen bonds in the structure labelled as Mean H-Bond Propensity, while the vertical axis represents the average coordination probability for the atoms in the structure labelled as Mean H- Bond Coordination. The coordination axis is inverted to reflect that more stable structures more negative energies relative to a zero baseline. The magenta point represents the observed ALATIN crystal form.

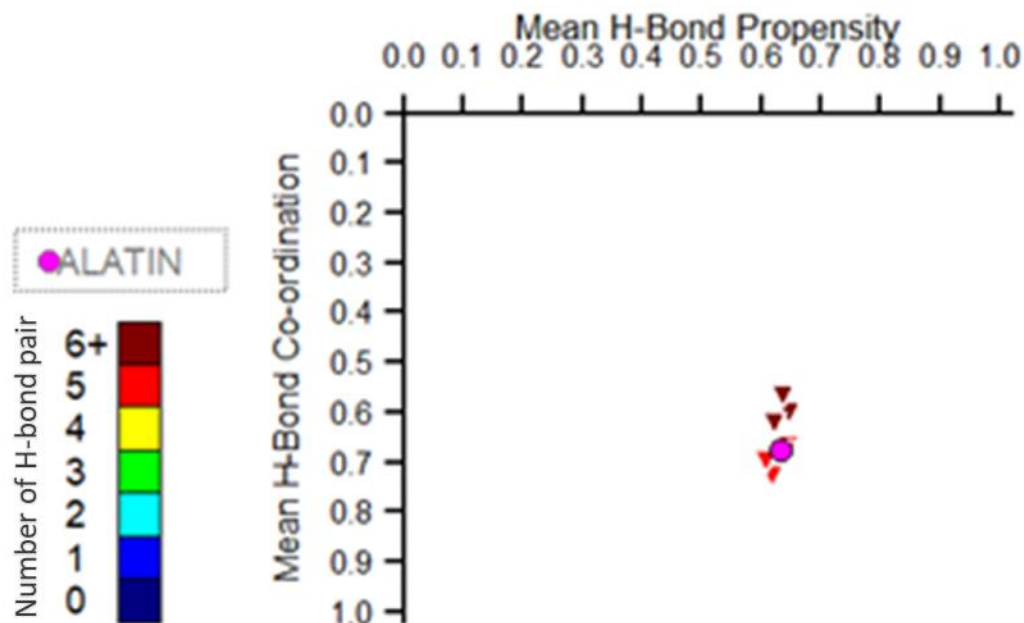


Figure 12. Hydrogen bond combination plot

Full Interaction Maps is a tool that calculates regions around the molecule (maps) where chemical probe groups are likely to be found. The calculation procedure first identifies distinct functional groups in the allantoin, and then finds relevant interaction data in IsoStar (module of the CSD). Next it pulls together the group-based interaction data and takes into account the environmental effects of combinative factors and steric exclusion to create a full 3D picture of molecular interaction preferences.

It represents in red those areas where there is a high probability of locating a hydrogen bond acceptor, in blue those where a donor is more likely to be located, and those in orange indicate hydrophobic preferences. The red and blue area shown in Figure 13 correspond to the presence of donors (nitrogen) and acceptors (carbonyl oxygen) groups of allantoin, which contribute to locate acceptors and donors of hydrogen bond, respectively. It worth noting that no orange area is observed, allantoin is not able to interact with hydrophobic groups. Cofomers with hydrophobic groups are bad candidates to form cocrystal with allantoin.

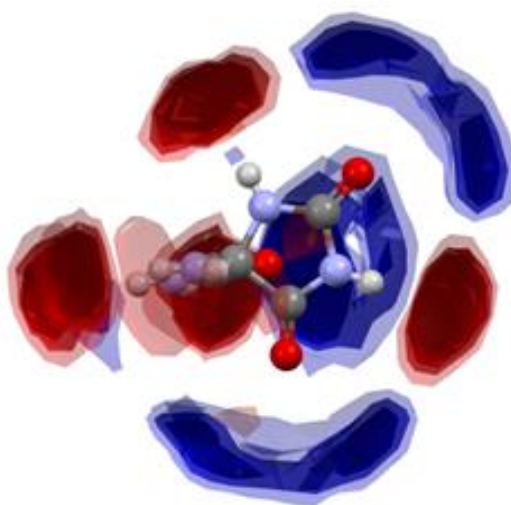


Figure 13. FIM of allantoin

### 3.2.3 Co-Crystal Design

The Co-Crystal Design was useful tool to identify possible cofomers for generation of co-crystal of allantoin. For the analysis all the conformers of allantoin determined by CSD Conformer Generator were considered, labelled by the software ALATIN\_00001, ALATIN\_00002, ALATIN\_00003, ALATIN\_00004. The cofomers molecules were selected by the library of the software. Table 2 reports the results of the elaboration reporting the total hit rate in percentage and the compatibility for each allantoin conformer. Hit rate of 100% indicates high probability for relevant cofomer to generate a cocrystal with allantoin.<sup>50</sup>

Table 2. Co-Crystal Design results

Coformer	Hit Rate %	ALATIN_00 001	ALATIN_00 002	ALATIN_00 003	ALATIN_00 004
(+)-camphoric_acid	0	FAIL	FAIL	FAIL	FAIL
(-)-camphorsulfonic_acid	0	FAIL	FAIL	FAIL	FAIL
1-hydroxyethylidene-1,1-diphosphonic_acid	100	PASS	PASS	PASS	PASS
2-amino-5-methylbenzoic_acid	0	FAIL	FAIL	FAIL	FAIL
3-methylpyridine	0	FAIL	FAIL	FAIL	FAIL
4-acetamidobenzoic_acid	0	FAIL	FAIL	FAIL	FAIL
4-aminobenzoic_acid	0	FAIL	FAIL	FAIL	FAIL
4-hydroxybenzoic_acid	0	FAIL	FAIL	FAIL	FAIL
D-alanine	100	PASS	PASS	PASS	PASS
D-glucuronic_acid	100	PASS	PASS	PASS	PASS
D-panthenol	100	PASS	PASS	PASS	PASS
EDTA	100	PASS	PASS	PASS	PASS
L-arginine	100	PASS	PASS	PASS	PASS
L-aspartic_acid	100	PASS	PASS	PASS	PASS
L-aspartic_acid_z	0	FAIL	FAIL	FAIL	FAIL
L-glutamic_acid	100	PASS	PASS	PASS	PASS
L-glutamic_acid_z	0	FAIL	FAIL	FAIL	FAIL
L-glutamine	100	PASS	PASS	PASS	PASS
L-glutathione	100	PASS	PASS	PASS	PASS
L-lactic_acid	75	PASS	PASS	FAIL	PASS
L-leucine	0	FAIL	FAIL	FAIL	FAIL
L-mandelic_acid	0	FAIL	FAIL	FAIL	FAIL
L-methionine	0	FAIL	FAIL	FAIL	FAIL
L-phenylalanine	0	FAIL	FAIL	FAIL	FAIL
L-proline	100	PASS	PASS	PASS	PASS
L-serine	100	PASS	PASS	PASS	PASS
L-tartaric_acid	100	PASS	PASS	PASS	PASS
L-tryptophan	0	FAIL	FAIL	FAIL	FAIL
L-tyrosine	0	FAIL	FAIL	FAIL	FAIL
N-ethylacetamide	0	FAIL	FAIL	FAIL	FAIL
acesulfame	75	PASS	PASS	FAIL	PASS
acetic_acid	100	PASS	PASS	PASS	PASS
acetophenone_oxime	0	FAIL	FAIL	FAIL	FAIL
acetylenedicarboxylic_acid	100	PASS	PASS	PASS	PASS

Coformer	Hit Rate %	ALATIN_00 001	ALATIN_00 002	ALATIN_00 003	ALATIN_00 004
adipic_acid	75	FAIL	PASS	PASS	PASS
alitame	0	FAIL	FAIL	FAIL	FAIL
apigenin	0	FAIL	FAIL	FAIL	FAIL
azelaic_acid	0	FAIL	FAIL	FAIL	FAIL
benzoic_acid	0	FAIL	FAIL	FAIL	FAIL
biotin	0	FAIL	FAIL	FAIL	FAIL
caprolactam	0	FAIL	FAIL	FAIL	FAIL
capsaicin	0	FAIL	FAIL	FAIL	FAIL
cholic_acid	0	FAIL	FAIL	FAIL	FAIL
citric_acid	100	PASS	PASS	PASS	PASS
ethylparaben	0	FAIL	FAIL	FAIL	FAIL
folic_acid	50	FAIL	PASS	PASS	FAIL
fumaric_acid	75	FAIL	PASS	PASS	PASS
gentisic_acid	100	PASS	PASS	PASS	PASS
glutaric_acid	100	PASS	PASS	PASS	PASS
glycine	100	PASS	PASS	PASS	PASS
glycolic_acid	100	PASS	PASS	PASS	PASS
hesperetin	0	FAIL	FAIL	FAIL	FAIL
hippuric_acid	0	FAIL	FAIL	FAIL	FAIL
hydrocinnamic_acid	0	FAIL	FAIL	FAIL	FAIL
imidazole	100	PASS	PASS	PASS	PASS
isonicotinamide	0	FAIL	FAIL	FAIL	FAIL
ketoglutaric_acid	100	PASS	PASS	PASS	PASS
lactobionic_acid	0	FAIL	FAIL	FAIL	FAIL
lactose	100	PASS	PASS	PASS	PASS
maleic_acid	100	PASS	PASS	PASS	PASS
malic_acid	100	PASS	PASS	PASS	PASS
malonic_acid	100	PASS	PASS	PASS	PASS
maltitol	100	PASS	PASS	PASS	PASS
mannitol	100	PASS	PASS	PASS	PASS
methanesulfonic_acid	0	FAIL	FAIL	FAIL	FAIL
methylparaben	0	FAIL	FAIL	FAIL	FAIL
monobutyryn	100	PASS	PASS	PASS	PASS
nicotinamide	0	FAIL	FAIL	FAIL	FAIL
oxalic_acid	100	PASS	PASS	PASS	PASS
pamoic_acid	0	FAIL	FAIL	FAIL	FAIL
phthalamide	0	FAIL	FAIL	FAIL	FAIL
pimelic_acid	75	FAIL	PASS	PASS	PASS
piperazine	0	FAIL	FAIL	FAIL	FAIL
propylparaben	0	FAIL	FAIL	FAIL	FAIL
pyrazine	0	FAIL	FAIL	FAIL	FAIL
riboflavin	100	PASS	PASS	PASS	PASS
saccharin	0	FAIL	FAIL	FAIL	FAIL
sorbic_acid	0	FAIL	FAIL	FAIL	FAIL

Coformer	Hit Rate %	ALATIN_00 001	ALATIN_00 002	ALATIN_00 003	ALATIN_00 004
suberic_acid	0	FAIL	FAIL	FAIL	FAIL
succinic_acid	100	PASS	PASS	PASS	PASS
t-butylamine	0	FAIL	FAIL	FAIL	FAIL
t-butylhydroxyanisole	0	FAIL	FAIL	FAIL	FAIL
theophylline	100	PASS	PASS	PASS	PASS
thymidine	100	PASS	PASS	PASS	PASS
triphenylacetic_acid	0	FAIL	FAIL	FAIL	FAIL
urea	100	PASS	PASS	PASS	PASS
valerolactam	0	FAIL	FAIL	FAIL	FAIL
xanthine	75	FAIL	PASS	PASS	PASS

Successively, the Co-Crystal Design evaluation was repeated considering as cofomers the molecules of cosmetic interest and correlated with allantoin in the patents. Table 3 evidenced that allantoin has a high compatibility rate with all molecules except trans-ferulic acid.

Generally, the results evidenced the high potential of allantoin to form cocrystals with a lot of molecules, as observed in Table 2. Specifically, Table 3 results revealed allantoin should form co-crystals with cofomers reported in the patents and of cosmetic interest.

The formation of co-crystal has been experimentally evaluated through several technique extending the list of cofomers listed in Table 3 with molecules such as DL-Panthenol, Malonic Acid, DL -Malic Acid, and Urea. These molecules were compatible with allantoin as reported in Table 3. Trans-ferulic acid is also considered in the study because of it is molecule of high cosmetic interest.

**Table 3. Co-Crystal Design results considering the cofomers of cosmetic interest and reported in patents**

Coformer	Hit Rate %	ALATIN_000 01	ALATIN_000 02	ALATIN_000 03	ALATIN_000 04
D-glucuronic_acid	100	PASS	PASS	PASS	PASS
citric_acid	100	PASS	PASS	PASS	PASS
maleic_acid	100	PASS	PASS	PASS	PASS
L-tartaric_acid	100	PASS	PASS	PASS	PASS
D-Panthenol	100	PASS	PASS	PASS	PASS
trans-ferulic acid	0	FAIL	FAIL	FAIL	FAIL
L-Lysine	100	PASS	PASS	PASS	PASS
2,5-Dihydroxybenzoic Acid	100	PASS	PASS	PASS	PASS
L-Ascorbic Acid	100	PASS	PASS	PASS	PASS
D-galacturonic acid	100	PASS	PASS	PASS	PASS

### 3.3 Characterization of Allantoin

Allantoin was characterized performing X-Ray powder diffraction (XRPD) and differential scanning calorimetric analysis (DSC). Additionally, solubility test of allantoin was performed.

The experimental pattern (ALL-SM) is comparable to the calculated pattern of racemic DL-allantoin (ALATIN) (Figure 14).

Allantoin thermograms showed an endothermic peak at approx. 235°C relative to melting followed by degradation (Figure 15).

Allantoin solubility test was carried out by weighting 50 mg of allantoin and successively adding of solvent and stirring the suspension after each addition. At the concentration of 10 mg/mL, allantoin results soluble only in N-dimethylformamide (DMF). Hence, it is considered it is sparingly soluble in DMF. The experiments were also repeated in hot conditions (50° C) and showed that allantoin is soluble in hot water and in N, N-dimethylformamide (DMF). Allantoin is sparingly soluble in hot water. It was considered not soluble in the other tested solvents: ethanol, methanol, acetone, acetonitrile, dichloromethane, ethyl acetate and toluene.

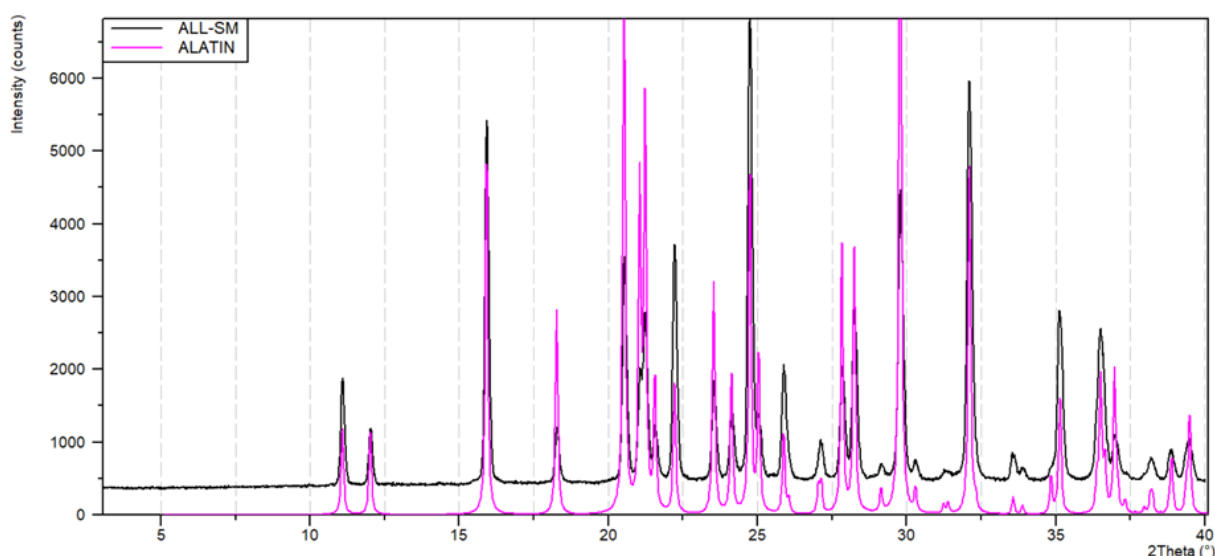


Figure 14. XRPD pattern comparison between experimental pattern of allantoin (black line) and calculated pattern of DL-allantoin (magenta line)

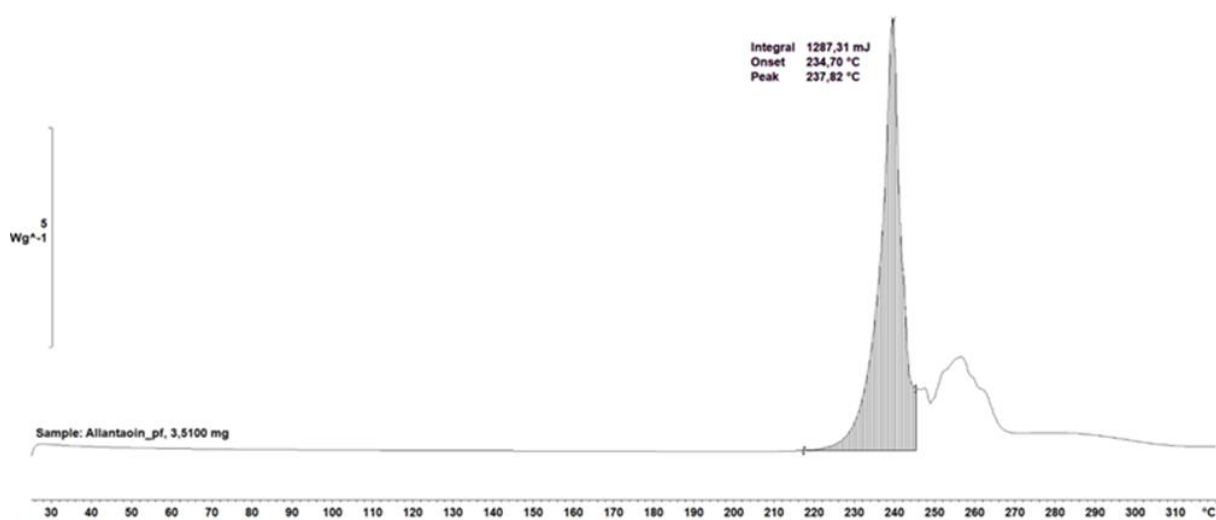


Figure 15. The DSC of allantoin in the range 25-320°C, heating rate of 10K/min in N<sub>2</sub> flow

### 3.4 Characterization of Alphanta

Alphanta is an Akema Chemicals product based on allantoin and panthenol.

The XRPD pattern and the DSC thermogram of alphanta were compared with the starting material DL-allantoin, DL-panthenol and D-panthenol. D-panthenol is a viscous and transparent liquid with amorphous XRPD pattern. While DL-panthenol is white and crystalline solid with melting point at 67°C (see appendix C). The XRPD pattern of alphanta shows all the crystalline reflection of DL-panthenol and of DL-allantoin (Figure 16) resulting a physical mixture of the starting material DL-allantoin and DL-panthenol. This is confirmed by DSC analysis which shows an endothermic peak at 67° C attributable to melting of DL-Panthenol. Clearly peak of allantoin melting is not recognizable, but broad endothermic signal is observed in correspondence of allantoin melting (Figure 17). Probably allantoin is dissolved in the melted DL-Panthenol.

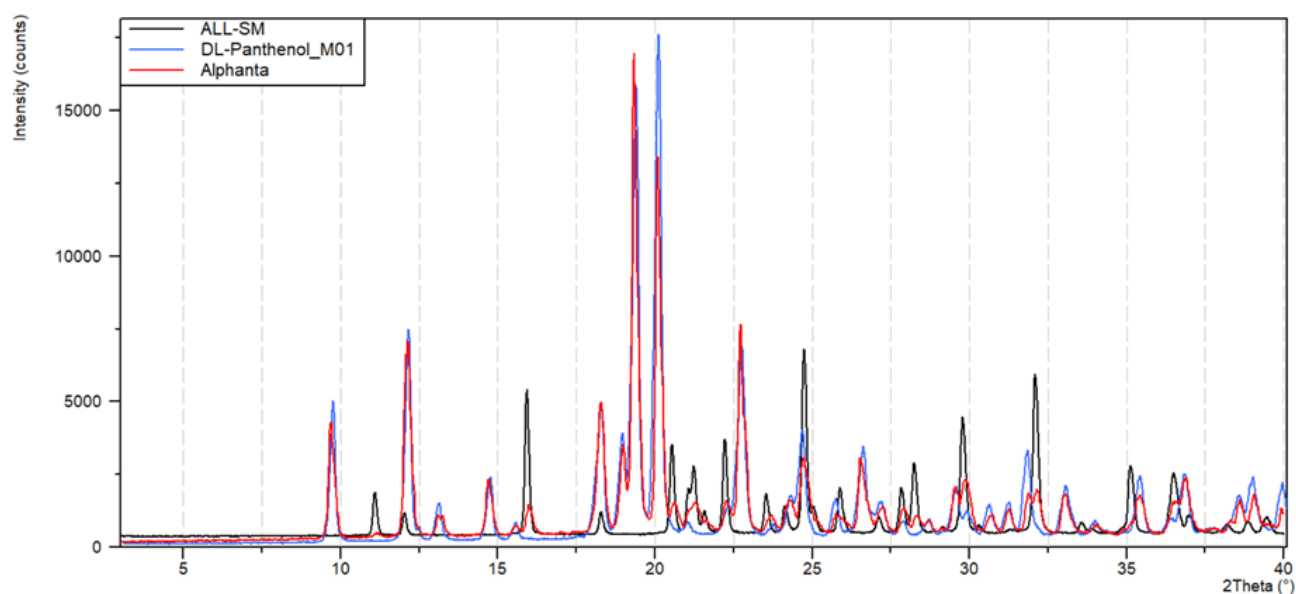


Figure 16. XRPD pattern comparison between alphanta (red line), allantoin (black line) and DL-panthenol (blue line)

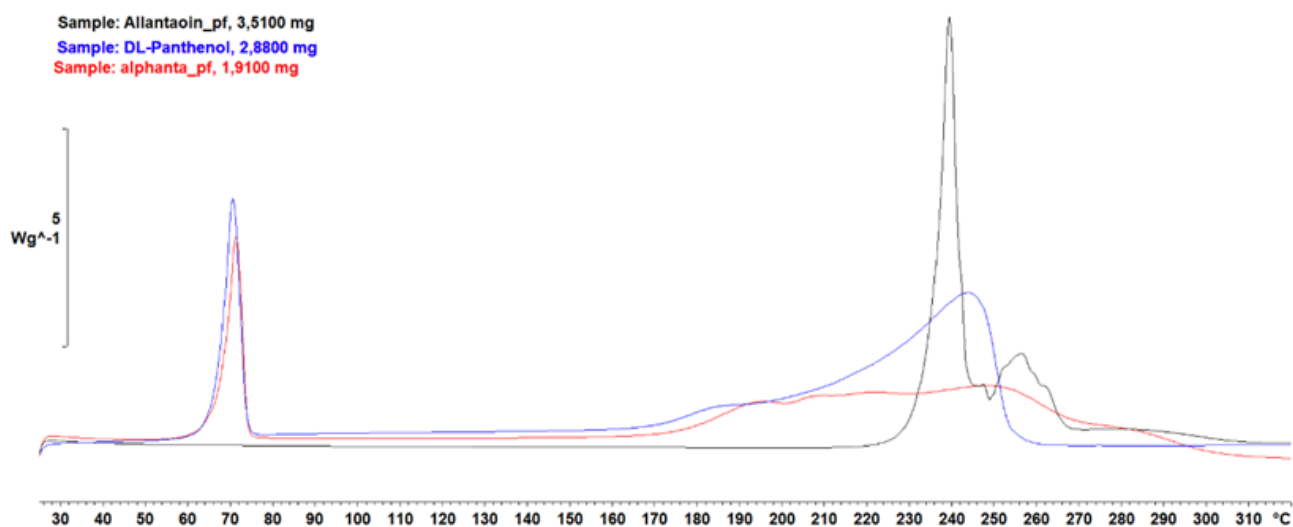


Figure 17. DSC thermogram comparison between alphanta (red line), allantoin (black line) and DL-panthenol (blue line)

### 3.5 Solubility and pH

Several patent of complexes of allantoin, for instance with ascorbic acid, claim the major solubility of this compound compared with the solubility of the pure allantoin. It is unclear whether this better solubility of allantoin is due to interaction of these molecule in solution or by formation of new compound. Therefore, the solubility of allantoin in presence of ascorbic acid was evaluated. Ascorbic acid is a diprotic acid ( $pK_{a1} = 4.08$  and  $pK_{a2} = 10.85$ ) but only the first dissociation will be considered in the following calculations. The initial pH of the aqueous solution used experimentally with ascorbic acid (55.7 mg/mL) is 2.31 (pH calculated for this concentration is 2.29). Two additions of 50 mg of allantoin are made to this solution; after the first addition (5.31 mg/mL) allantoin dissolved while after the second addition of allantoin (10.23 mg/mL) to the solution allantoin was not soluble. The same experiment at the same concentration of allantoin in water was performed in absence of ascorbic acid in the solution, allantoin has been not soluble at the concentration of 5 mg/mL, while it has dissolved in presence of ascorbic acid.

This confirms that solubility of allantoin is promoted in presence of ascorbic acid, but it was not clear if it is due to the acid pH of the solution due to ascorbic acid or to the formation of a complex of the compounds.

### 3.6 EvHT (evaporation at 60°C)

High temperature evaporation experiments were performed in water because of it is the only solvent except DCF in which allantoin is soluble.

50 mg of Allantoin was dissolved in 2 mL of H<sub>2</sub>O by heating. An equivalent of the cofomer was then added, in the case of L-lysine it was added in two equivalents. Solutions were heat at temperature of 60°C until completely evaporation of solvent. Ferulic acid requires different preparation because of it is not soluble in water, but it is soluble in ethanol. Two different solutions were prepared, one with allantoin in water and the latter was prepared dissolving an equivalent of ferulic acid in 1 mL of ethanol. The two solutions were merged and evaporated at 60°C.

The obtained precipitated were analysed by XRPD and the patterns were compared with those of the starting materials: allantoin (ALL-SM) and cofomer.

The diffractograms of the experiments with ascorbic and trans-ferulic acid as cofomers have shown characteristic peaks of both allantoin and conformers, suggesting the formation of physical mixture of these components (see Appendix B). While the XRPD pattern of experiments with D-panthenol, galacturonic acid, and glucoronic acid have shown only the characteristic peaks of allantoin (see Appendix B). The absence of cofomers' signals suggests it has precipitated in amorphous form. It is worth noting that the product obtained by evaporation of allantoin and L-lysine has shown mainly amorphous XRPD pattern with some weak peaks not ascribable neither to allantoin nor to L-lysine hemihydrate used as reagents or toto the monohydrate form of L-lysine (see Figure 18).<sup>51</sup> These peaks could indicate a new phase, but the sample is mainly amorphous, and it is difficult to evaluate a real formation of new form.

Table 4 summarizes obtained results.

Table 4. Results of evaporation experiments

EXPERIMENT	RESULTS	APPENDIX B
<b>ALL-LLYS</b>	Mainly amorphous pattern + small peaks (main peak at $9.0^{\circ}2\theta$ )	Figure 28
<b>ALL-ASC</b>	XRPD pattern ASC+ALL	Figure 29
<b>ALL-DGL</b>	XRPD pattern Allantoin	Figure 30
<b>ALL-GAL</b>	XRPD pattern Allantoin	Figure 31
<b>ALL-PAN</b>	XRPD pattern Allantoin	Figure 32
<b>ALL-FER</b>	XRPD pattern FER+ALL	Figure 33

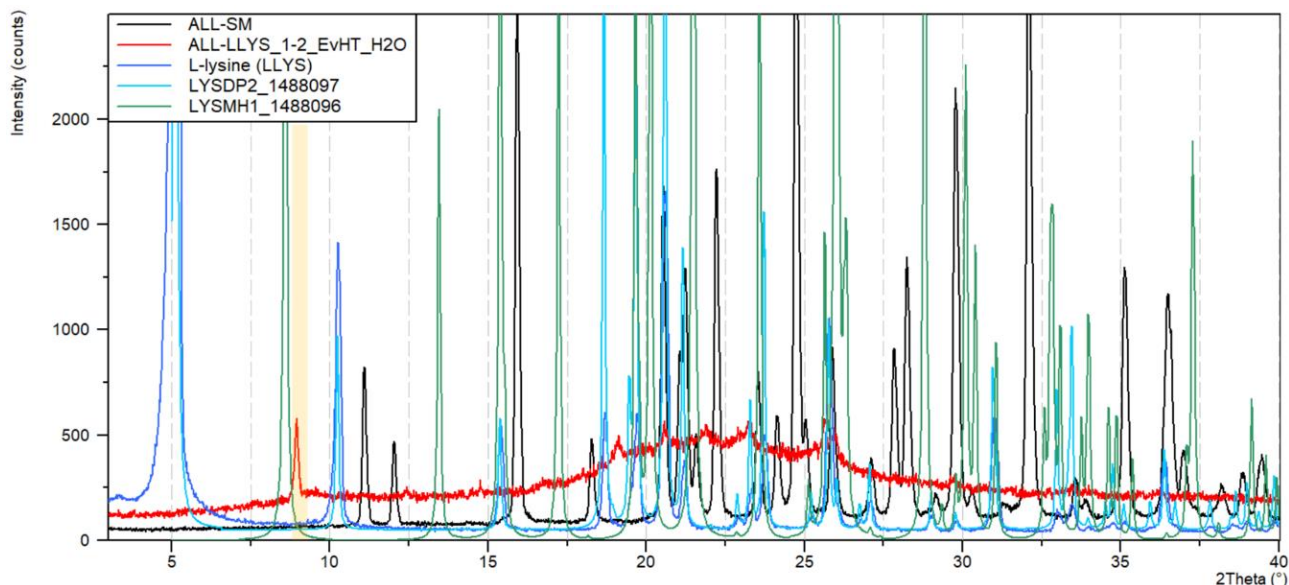


**Figure 18.** XRPD pattern comparison between starting materials allantoin (black line), L-lysine (blue line), EvHT product resulted by allantoin and L-lysine (red line) and the calculated pattern of hemihydrate L-lysine LYSDP2 (cyan line) and monohydrate L-lysine LYSMH1 (green line). Mainly additional peaks were highlighted in yellow.

### 3.7 Precipitation at low temperature

50 mg of Allantoin was dissolved in 2 mL of H<sub>2</sub>O by heating at 50°C. An equivalent of the coformer was then added and dissolved. Ferulic acid requires different preparation because of it is not soluble in water, in this case two different solutions were prepared and merged, one with allantoin in water as aforementioned and the latter was prepared dissolving an equivalent of ferulic acid in 1 mL of ethanol. Precipitation was promoted placing the solutions at 5-8°C in refrigerator.

The precipitates were filtered and analysed by X-ray diffraction. The XRPD pattern were compared with those of the starting compounds.

The XRPD pattern of experiment with allantoin and D-panthenol as starting material has shown only the characteristic peaks of allantoin (see Appendix B), it could be due to lack of precipitation of the conformer or its precipitation in amorphous form.

The diffractograms of allantoin and trans-ferulic acid has suggested the formation of a physical mixture of these compounds (see Appendix B).

The products resulted by experiments performed with ascorbic acid, D-glucuronic acid, and galacturonic acid have shown XRPD pattern characteristic of allantoin plus some small additional peaks. In Figure 19, Figure 20 and Figure 21 the peaks ascribable to conformer are highlighted in green, while the additional peaks not ascribable neither to allantoin nor conformer are highlighted in yellow. The product resulted by precipitation with ascorbic acid (Figure 19) showed three additional peaks at approx.  $2\theta = 10.0$ ,  $20.1$  and  $20.8^\circ$ .

The product resulted by precipitation with galacturonic acid (Figure 20) showed several additional peaks at approx.  $2\theta = 6.1$ ,  $10.1$ ,  $14.4$ ,  $20.1$ ,  $28.9$ ,  $32.9$ ,  $37.7^\circ$ . The peaks at  $14.5$  and  $32.9^\circ 2\theta$  correspond to the peak of galacturonic acid, while the other peaks were not ascribable to galacturonic acid.

The product resulted by precipitation with glucuronic acid (Figure 21) showed one additional peak at approx.  $2\theta = 20.1^\circ$  corresponded to the main peak of glucuronic acid.

In all the cases discussed above the new peaks showed very low intensity, and all the different XRPD patterns have the common peaks at  $10.0$  and  $20.1^\circ 2\theta$  which suggests the formation of another form probably of allantoin rather than formation of cocrystals. Additionally, observation of mainly allantoin pattern and lack of conformer's peaks suggest the failed precipitation of coformer.

Table 5 summarizes obtained results.

Table 5. Results of precipitation experiments

EXPERIMENT	RESULTS	APPENDIX B
ALL-DGL	XRPD pattern Allantoin + some peaks	Figure 34
ALL-FER	XRPD pattern FER+ALL	Figure 35
ALL-GAL	XRPD pattern Allantoin + some peaks	Figure 36
ALL-PAN	XRPD pattern Allantoin	Figure 37
ALL-ASC	XRPD pattern Allantoin + some peaks	Figure 38

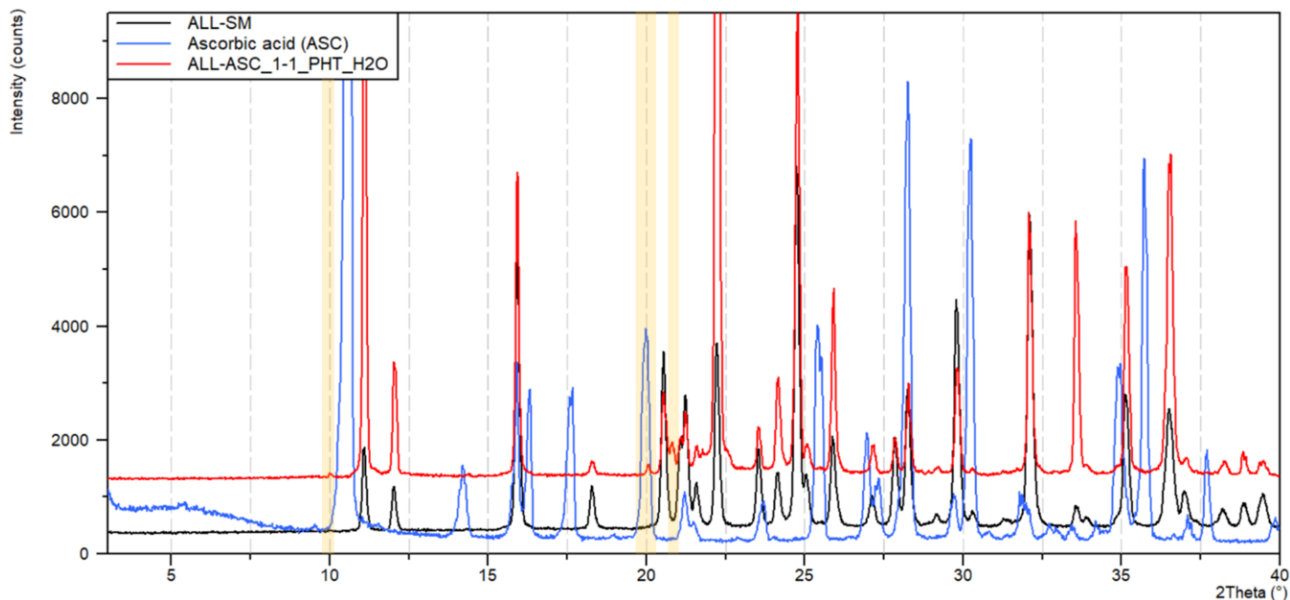


Figure 19. XRPD pattern comparison between starting materials allantoin (black line), ascorbic acid (blue line) and precipitation product resulted by allantoin and ascorbic acid (red line). Additional peaks were highlighted in yellow.

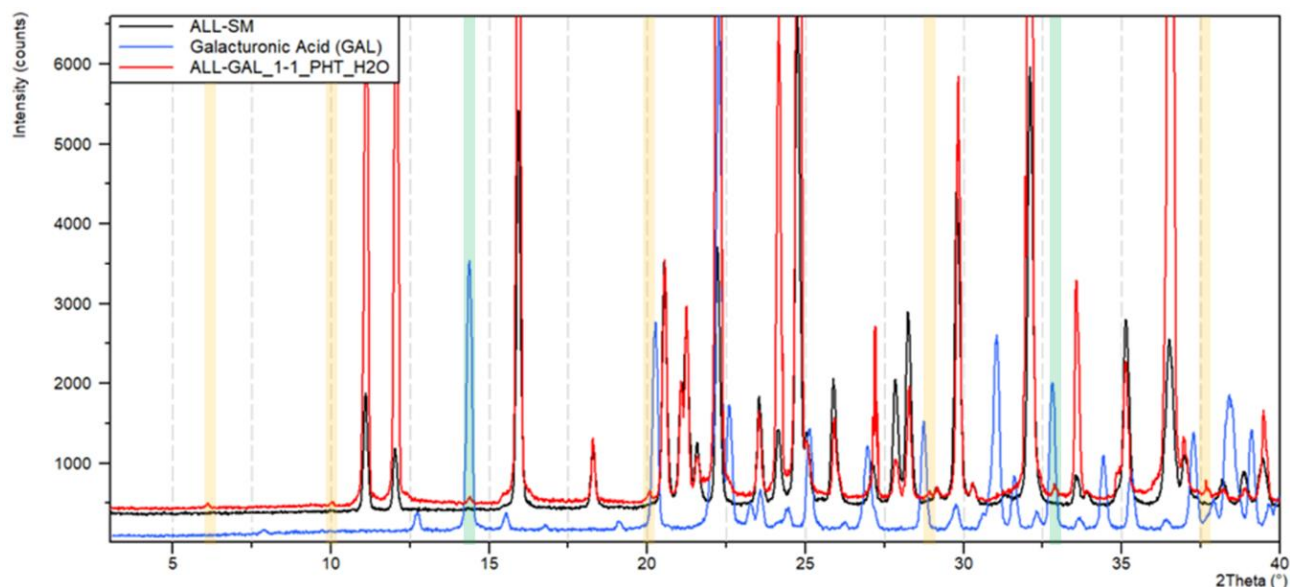


Figure 20. XRPD pattern comparison between starting materials allantoin (black line), galacturonic acid (blue line) and precipitation product resulted by allantoin and galacturonic acid (red line). Additional peaks were highlighted in yellow, while the peaks ascribable to galacturonic acid were highlighted in green.

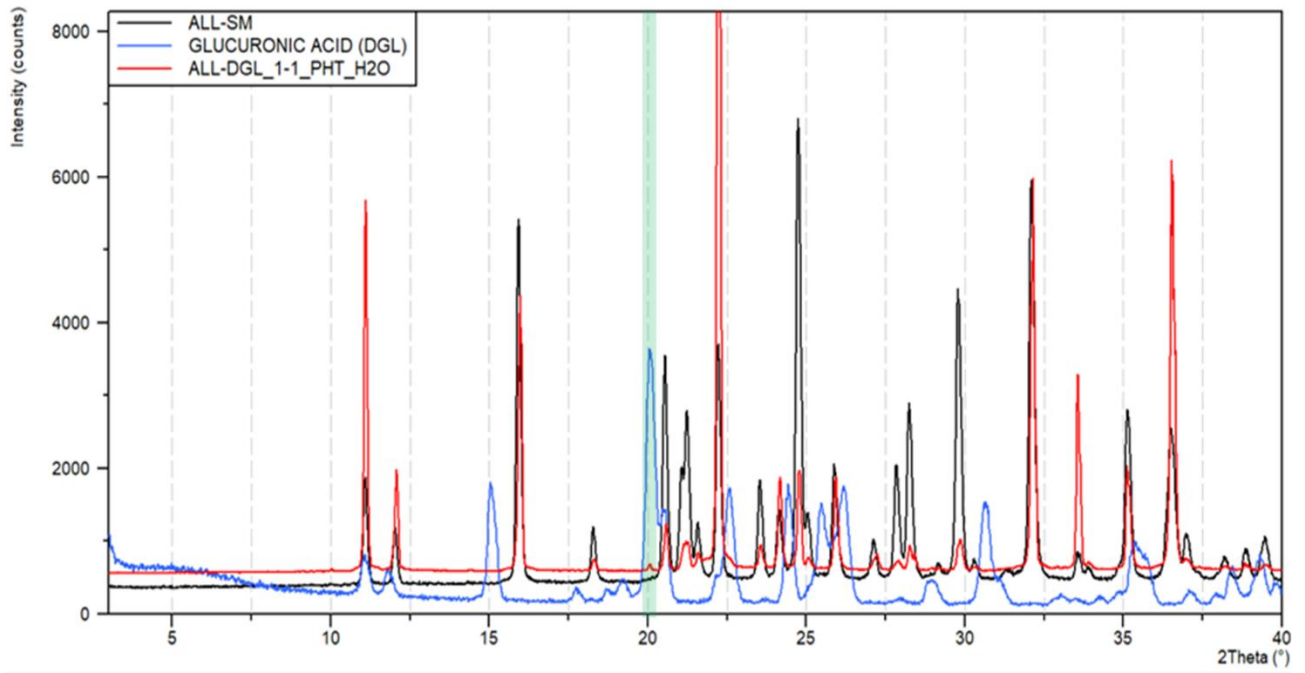


Figure 21. XRPD pattern comparison between starting materials allantoin (black line), glucuronic acid (blue line) and precipitation product resulted by allantoin and glucuronic acid (red line). The peak ascribable to glucuronic acid was highlighted in green.

### 3.8 Slurry

50 mg of allantoin are suspended in 2 mL of solvent and coformer was added to this suspension in ratio 1:2 between allantoin and coformer, respectively. Two set of suspensions are prepared with water and ethanol as a solvent. After 4 days under stirring, the suspension is taken, filtered with filter paper and the solid phase is analysed by X-ray diffraction. The diffractograms obtained were characteristic of the mixture of the reagents or of only allantoin

This is probably because the saturation conditions of the coformer are not reached.

The product resulted by slurry in ethanol of allantoin and L-tartaric acid (Figure 22) showed an additional peak at approx.  $19.8^{\circ}2\theta$  not ascribable to allantoin and L-tartaric acid. Nevertheless, determination of this unique peak is difficult.

Table 6 summarizes obtained results.

**Table 6. Results of slurry experiments**

EXPERIMENT	SOLVENT	RESULTS	APPENDIX B
ALL-ASC	water	XRPD pattern Allantoin	Figure 39
	ethanol	XRPD pattern ASC+ALL	Figure 40
ALL-CIA	water	XRPD pattern Allantoin	Figure 41
	ethanol	XRPD pattern Allantoin	Figure 42
ALL-DGL	water	XRPD pattern Allantoin	Figure 43
	ethanol	XRPD pattern DGL+ALL	Figure 44
ALL-DLPAN	water	XRPD pattern Allantoin	Figure 45
	ethanol	XRPD pattern Allantoin	Figure 46
ALL-FER	water	XRPD pattern FER+ALL	Figure 47
	ethanol	XRPD pattern Allantoin + trace of FER	Figure 48
ALL-GAL	water	XRPD pattern Allantoin	Figure 49
	ethanol	XRPD pattern GAL+ALL	Figure 50
ALL-LTA	water	XRPD pattern Allantoin + trace of LTA	Figure 51
	ethanol	XRPD pattern Allantoin + peak at $19.8^{\circ}2\theta$	Figure 52
ALL-PAN	water	XRPD pattern Allantoin	Figure 53
	ethanol	XRPD pattern Allantoin	Figure 54

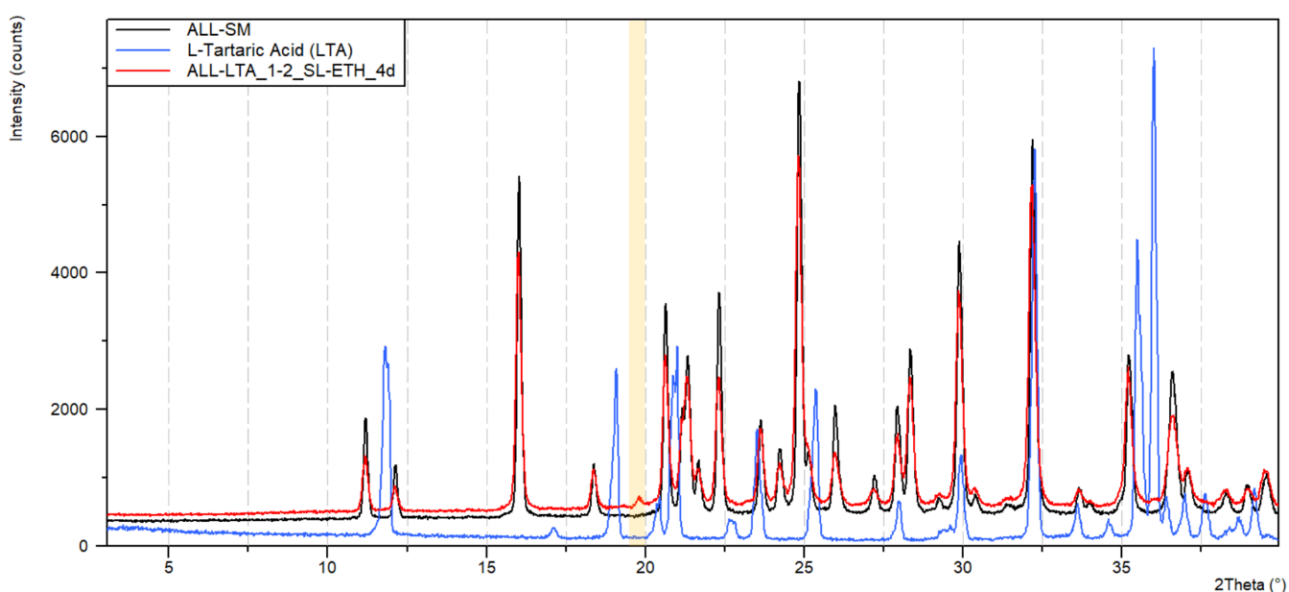


**Figure 22. XRPD comparison between starting materials allantoin (black line), L-tartaric acid (blue line) and slurry product resulted by allantoin and L-tartaric acid in ethanol (red line). Additional peaks were highlighted in yellow.**

### 3.9 Grinding

Allantoin and cofomer were placed in steel jar with two steel balls to promote the grinding. Ball milling was carried out at 30 Hz for 15 minutes.

The compound obtained is recovered and analysed by X-ray diffraction and compared with the starting materials' pattern. The diffractograms obtained are all characteristic of the mixture of reagents except for the one obtained with D-Panthenol, in which only the allantoin peaks are identified, the cofomer was amorphous. Table 7 summarizes obtained results.

**Table 7. Results of grinding experiments**

EXPERIMENT	RESULTS	APPENDIX B
<b>ALL+DLPAN</b>	XRPD pattern DLPAN+ALL	Figure 55
<b>ALL+PAN</b>	XRPD pattern Allantoin	Figure 56
<b>ALL+UREA</b>	XRPD pattern UREA+ALL	Figure 57

### 3.10 Kneading

Allantoin, cofomer and 20  $\mu$ L of H<sub>2</sub>O are placed in steel jar with two small steel balls, which promote grinding. Different ratios of allantoin and cofomer are tested, for example 1:1 or 1:2. Grinding was carried out at 30 Hz for 15 or 30 minutes.

All diffractograms were characteristic of the mixture of the starting materials except for experiments with DL-panthenol in the ratio 1:1 in which only the allantoin was observed

At initial assessment, the product obtained with citric acid (ratio 1:1) showed the presence of a new phase. Further evaluation revealed that the observed additional peaks were ascribable to citric acid monohydrate (CITARC) (Figure 23).<sup>52</sup> Increasing the amount of cofomer in ratio 1:2 allantoin and citric acid it was observed in XRPD pattern peaks of both anhydrous and monohydrate citric acid (Figure 24). The presence of water in kneading promotes the conversion of anhydrous citric acid to monohydrate.

Table 8 summarizes obtained results.

**Table 8. Results of kneading experiments**

EXPERIMENT	RATIO Allantoin:Cofomer	RESULTS	APPENDIX B
<b>ALL-ASC</b>	Ratio 1:2	XRPD pattern ASC+ALL	Figure 58
<b>ALL-CIA</b>	Ratio 1:1	XRPD pattern monohydrate CIA+ALL	Figure 59
	Ratio 1:2	XRPD pattern monohydrate CIA+ anhydrous CIA+ALL	Figure 60
<b>ALL+DGL</b>	Ratio 1:2	XRPD pattern DGL+ALL	Figure 61
<b>ALL+DHB</b>	Ratio 1:2	XRPD pattern DHB+ALL	Figure 62
<b>ALL+DLPAN</b>	Ratio 1:1	XRPD pattern Allantoin (broad peaks)	Figure 63
	Ratio 1:2	XRPD pattern DLPAN+ALL	Figure 64
<b>ALL+FER</b>	Ratio 1:2	XRPD pattern FER+ALL	Figure 65
<b>ALL+GAL</b>	Ratio 1:2	XRPD pattern GAL+ALL	Figure 66
<b>ALL+LLYS</b>	Ratio 1:2	XRPD pattern LYS+ALL	Figure 67
<b>ALL+PAN</b>	Ratio 1:2	XRPD pattern Allantoin	Figure 68
<b>ALL+MEA</b>	Ratio 1:2	XRPD pattern MEA+ALL	Figure 69

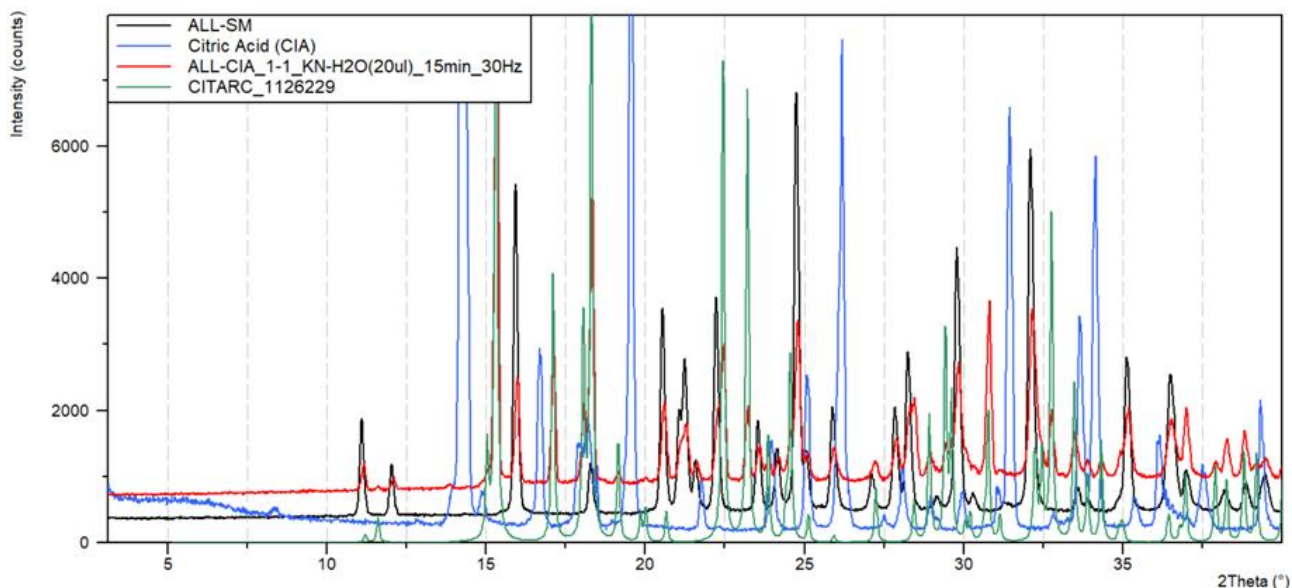


**Figure 23.** XRPD comparison between starting materials allantoin (black line), citric acid (blue line), product resulted by kneading of allantoin and citric acid in ratio 1:1 (red line) and monohydrate citric acid (CITARC, green line) by CSD

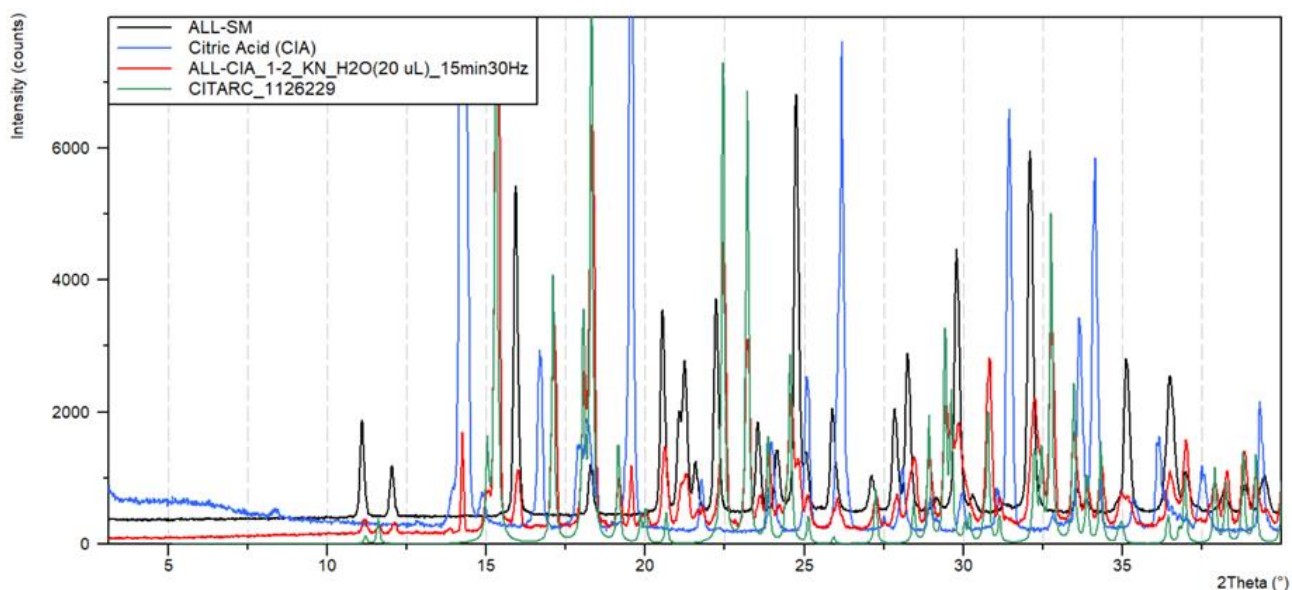


**Figure 24.** XRPD comparison between starting materials allantoin (black line), citric acid (blue line), product resulted by kneading of allantoin and citric acid in ratio 1:2 (red line) and monohydrate citric acid (CITARC, green line) by CSD

### 3.11 Thermal characterization of mixtures

The possibility to obtain cocrystal by melting was evaluated by thermal analysis of the mixtures of allantoin with the conformer. Compounds which soluble in liquid but insoluble in solid can form eutectic mixtures. The mixtures were evaluated through DSC analysis and the formation of eutectic mixture is indicated by presence of endothermic peak associated with the eutectic melting, at temperature lower than the melting temperature of starting material, immediately followed by an exothermic peak due to the crystallization that indicate the formation of cocrystal.

Considering that allantoin begins to decompose subsequently after melting at around 235°C. It would be a significant result to be able to form a eutectic mixture between allantoin and one of the cofomers.

Solid mixtures were prepared by mixing with mortar and pestle cofomers as trans ferulic acid, L-ascorbic acid, and urea in molar ratio 1:1 with allantoin. The presence of eutectic mixtures is evaluated by performing DSC analysis with a heating rate of 10° C/min in flow of N<sub>2</sub>.

The mixture of allantoin and ferulic acid shows an endothermic peak compatible to the melting of ferulic acid at 172°C and a second endothermic peak at approx. 235°C ascribable to the melting and degradation of allantoin (Figure 25).

On the contrary, DSC thermogram of mixture of allantoin and ascorbic acid in the ratio 1:1 showed an endothermic peak at approx. 180°C and successively exothermic peak at temperature lower than the melting of ascorbic acid at 192°C and allantoin at approx. 235°C (Figure 26). It worth noting that the exothermic peak, subsequent to endothermic peak at approx. 182°C could be due to the crystallization of the co-crystal.

In the case of the mixture of allantoin and urea in the ratio 1: 1 was observed a melting at a lower temperature (125°C) than the melting points of the single species, but there are no exothermic peaks that may suggest the formation of co-crystals (Figure 27).

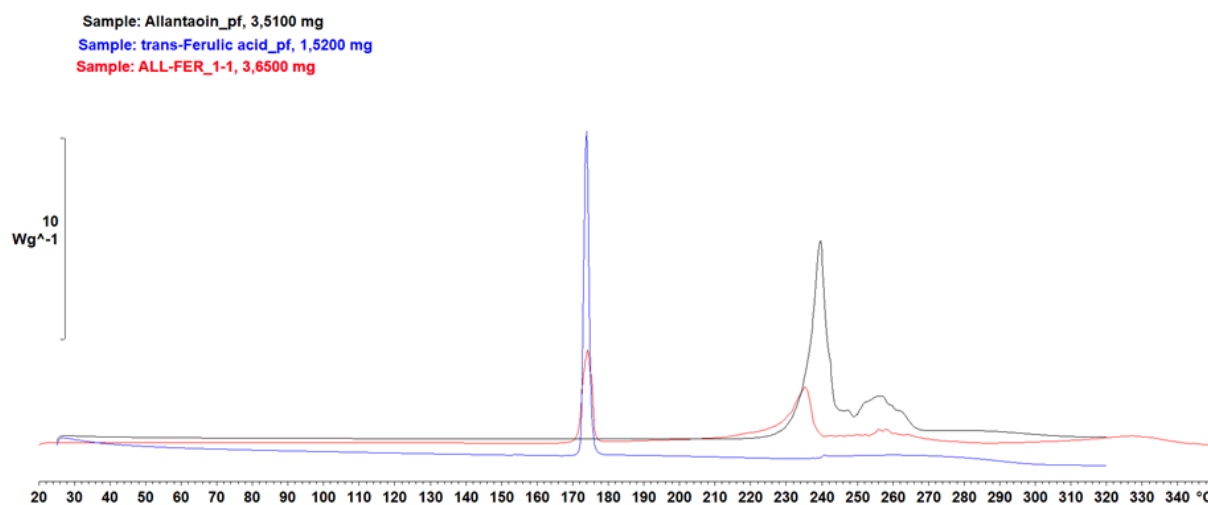


Figure 25. DSC thermogram comparison between starting materials allantoin (black line), trans-ferulic acid (blue line) and their mixture 1:1 (red line)

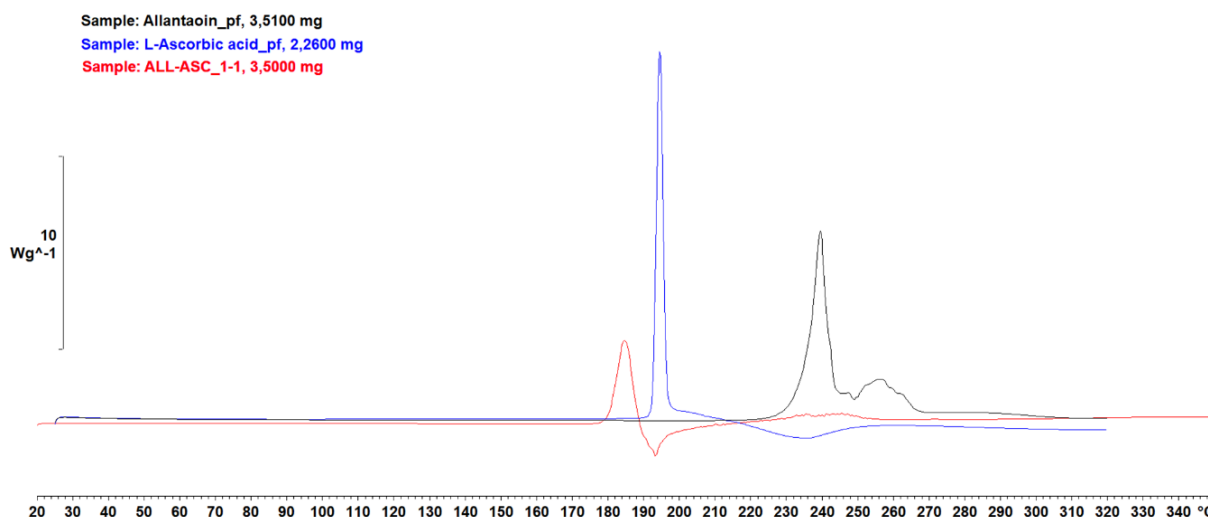


Figure 26. DSC thermogram comparison between starting materials allantoin (black line), ascorbic acid (blue line) and their mixture 1:1 (red line)

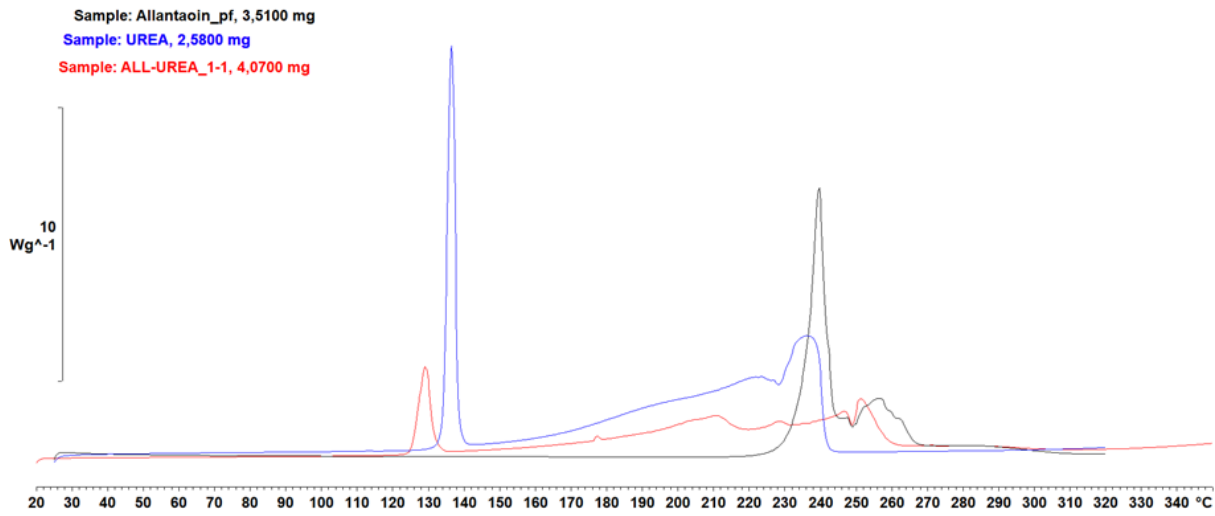


Figure 27. DSC thermogram comparison between starting materials allantoin (black line), urea (blue line) and their mixture 1:1 (red line)

## 4 CONCLUSION

Allantoin has extremely interest in cosmetic due to its wide benefits. In fact, it is used in products as such as skin cream, sunscreen, oral care products and healing products. It has been associated with several molecules to form “complexes”, such as ascorbic acid, biotin, panthenol, galacturonic acid etc. These complexes have been studied mainly in the 60s and 70s of the last century. Improving properties, especially solubility, of these complexes compared to the reagents have been claimed in some patent of 60s and 70s.<sup>14,18-23</sup> Additionally, preparation of allantoin with other compounds are commercialized, for example Alphanta sold by Akema, which consists of allantoin and panthenol, but the solid state of these compounds has not clearly reported.

Dissolution of allantoin was evaluated in different conditions, in water and in an acid solution with ascorbic acid. The results suggest allantoin solubility dependence on the pH of the solution and it is more soluble in acid solution. This indicates that improving solubility of allantoin claimed in the patent may not be due to formation of cocrystal.

At the first stage allantoin was studied by CSD-Materials module present within Mercury to identify its molecular reactive sites, to select suitable cofomers and to evaluate the propensity of allantoin to form cocrystal. The evaluation of possible conformers of allantoin by CSD-Materials agrees with the conformations reported in the literature. Allantoin has four conformers in the neutral form, and in the unique known crystalline structure of RS-allantoin it has a conformation very similar to the trans-2 conformer and forms five inter-molecular hydrogen bonds. The results obtained through CSD-Materials suggest propensity of allantoin to form inter-molecular hydrogen bonds compared to intra-molecular interaction. The Co-crystal design application executes statistical analysis considering correlations of similarity, shape, and polarity of the molecules to identify possible cofomers for generation of co-crystal of target molecule. Allantoin has shown strong compatibility with several molecules, particularly with all molecules of cosmetic interest selected as potential cofomers, except trans-ferulic acid.

Experimentally, different crystallization techniques were used to obtain co-crystals, evaporation at 60°C, precipitation at low temperature, slurry in ethanol and water, grinding, kneading, and melting of the mixtures. The X-Ray diffractograms of the powders obtained do not show significantly different pattern compared to the reagent ones. Several tiny peaks have been detected in the powder obtained by precipitation with ascorbic acid, galacturonic acid and glucuronic acid. The low intensity of the signals and the absence of cofomer's peaks suggest the lack of precipitation of cofomer. For these reasons it was excluded the presence of cocrystal. Probably, it is due to partial formation of new form of allantoin or possible contamination. Furthermore, in product obtained by evaporation with L-lysine has shown mainly amorphous pattern with some small peaks not ascribable neither to allantoin nor to L-lysine hemihydrate and monohydrate forms. However, the sample was mainly amorphous, so it is difficult to study the possible new form.

Moreover, the DSC analysis of the mixtures evidenced the possible formation of cocrystal with ascorbic acid suggested by exothermic peak of crystallization after a melting endothermic peak. Further studies could be carried out on this system to verify the real presence of cocrystal.

In conclusion, experimental results disagree with the statistical analysis of CSD-Materials application. Potentially with its numerous hydrogen bonding sites and small dimension allantoin could form cocrystal with several molecules. However, the unique known crystalline form of DL-allantoin has been shown extremely stable and not available to make interaction with other molecules. Nevertheless, the results obtained with evaporation of L-lysine and the mixture with ascorbic acid should be deepened.

## 5 APPENDIX A

### X-Ray Powder Diffraction (XRPD)

Instrument type: Rigaku MiniFlex600

Application SW: Miniflex Guidance

### Measurement Details

Measurement type: Single scan

Sample mode: Reflection

#### Scan

Scan range: 3.000 – 40.000 ° (2 $\theta$ )

Step size: 0.01 ° (2 $\theta$ )

Speed: 10.0 °/min (2 $\theta$ )

Scan mode: Continuous

#### Used wavelength

Intended wavelength type: K $\alpha$ 1

K $\alpha$ 1: 1.540598 Å

K $\alpha$ 2: 1.544426 Å

K $\alpha$ 2/K $\alpha$ 1 intensity ratio: 0.50

K $\alpha$ : 1.541874 Å

K $\alpha$ : 1.392250 Å

### Instrument Details

#### X-Ray Generator

Tube output voltage: 40 kV

Tube output: 15 mA

High-voltage generation method: High-frequency Cockcroft-Walton method

Stability: Within  $\pm 0.05\%$  for both the tube voltage and tube current, with reference to  $\pm 10\%$  of input power variation

#### X-ray tube

Name: Toshiba Analix type A-26L

Anode material: Cu

Maximum output: 0.60 kW

Focus size: 1 x 10 mm

#### K $\beta$ Filter

Name: Ni-filter

Thickness (mm): 0.015

Material: Ni

#### Goniometer (Angle measuring device)

Type: Vertical  $\theta/2\theta$

Goniometer radius: 150 mm

Scanning axis:  $\theta/2\theta$  linked

2 $\theta$  scanning range: +2 ° to +140 °

$\theta/2\theta$  axis minimum step angle: 0.005 ° (2 $\theta$ )

Position speed: 500 °/min (2 $\theta$ )

Scanning speed: 0.01 to 100 °/min

Datum angle: 2 $\theta$  = 10 °

X-ray take-off angle: 6 ° (fixed)

## Chapter 2

### Slit

DS: 1.25 °

IHS: 10.0 mm

SS: none (open)

RS: none (open)

Incident side Soller slit: 2.5 °

Receiving side Soller slit: 2.5 °

### Detector

Name: D/teX Ultra High-speed 1D Detector

Detection element: 1D semiconductor element

Window material: Be

Effective window size: 13 mm (H) x 20 mm (W)

Dimensions: 80 mm (L)

## 6 APPENDIX B

### 6.1 EvHT results

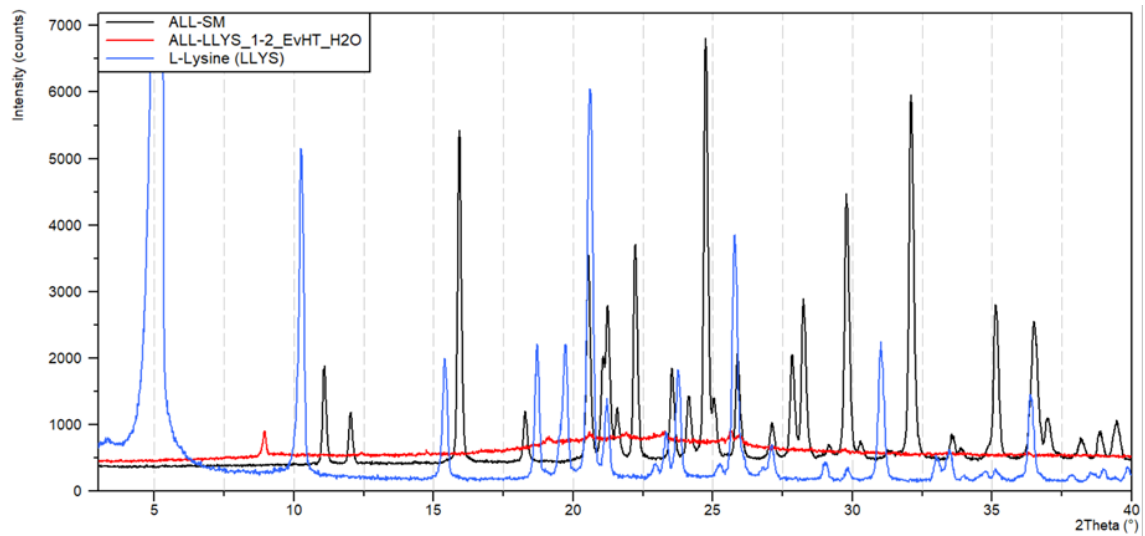


Figure 28. XRPD comparison between starting materials allantoin (black line), L-lysine (blue line) and EvHT product resulted by allantoin and L-lysine (red line)

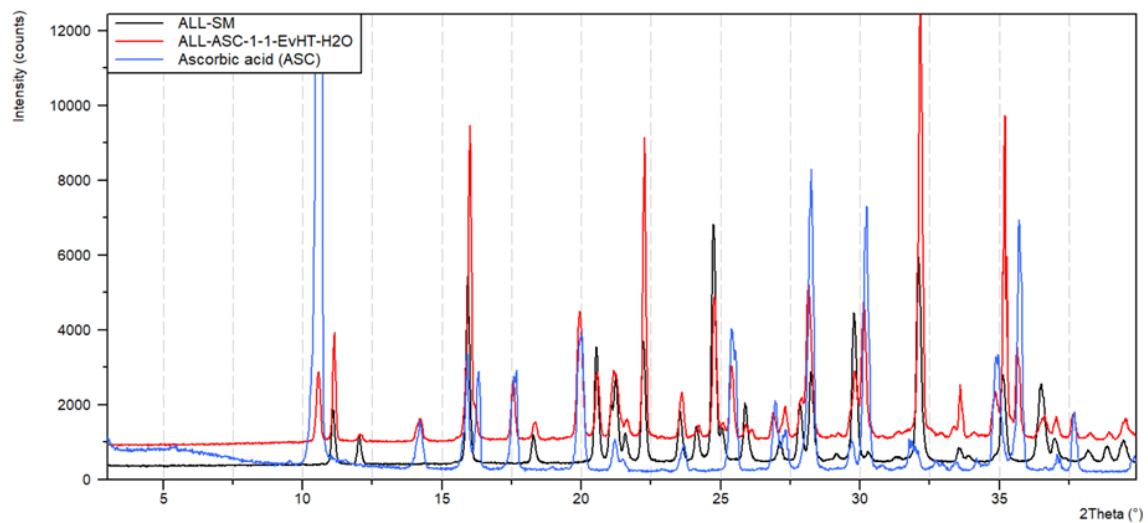


Figure 29. XRPD comparison between starting materials allantoin (black line), ascorbic acid (blue line) and EvHT product resulted by allantoin and ascorbic acid (red line)

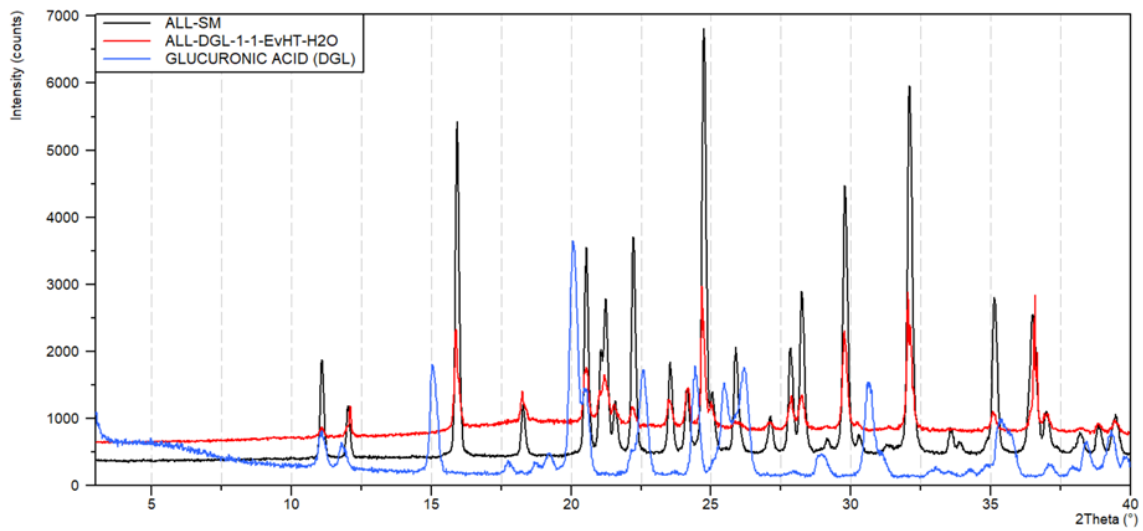


Figure 30. XRPD comparison between starting materials allantoin (black line), D-glucuronic acid (blue line) and EvHT product resulted by allantoin and D-glucuronic acid (red line)

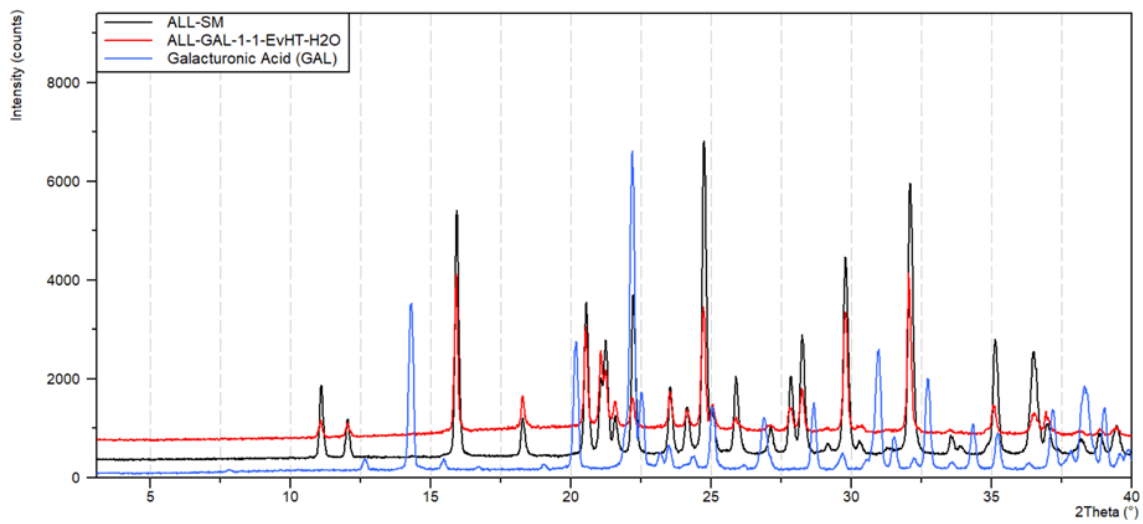


Figure 31. XRPD comparison between starting materials allantoin (black line), galacturonic acid (blue line) and EvHT product resulted by allantoin and galacturonic acid (red line)

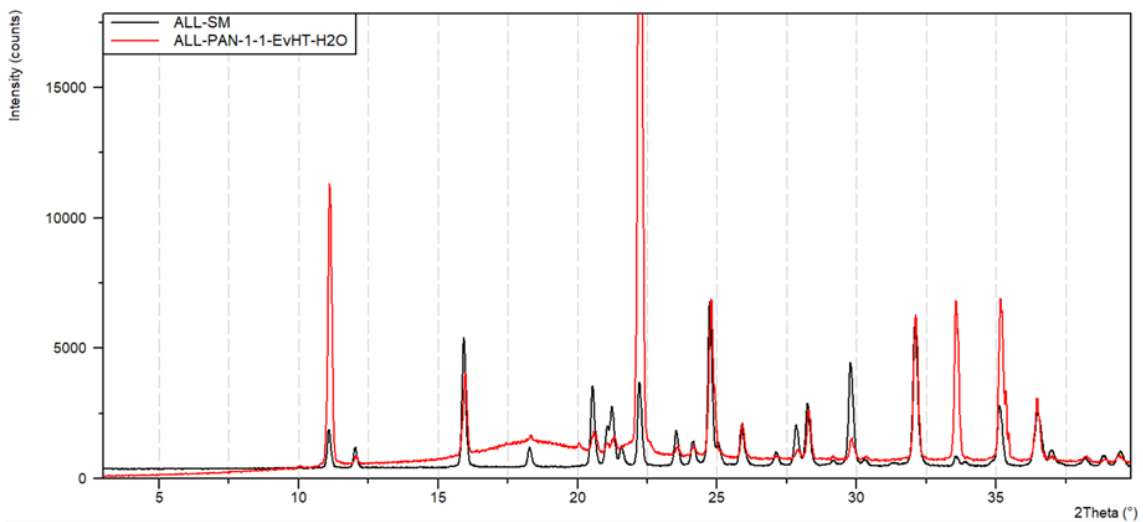


Figure 32. XRPD comparison between starting materials allantoin (black line), D-panthenol (blue line) and EvHT product resulted by allantoin and D-panthenol (red line)

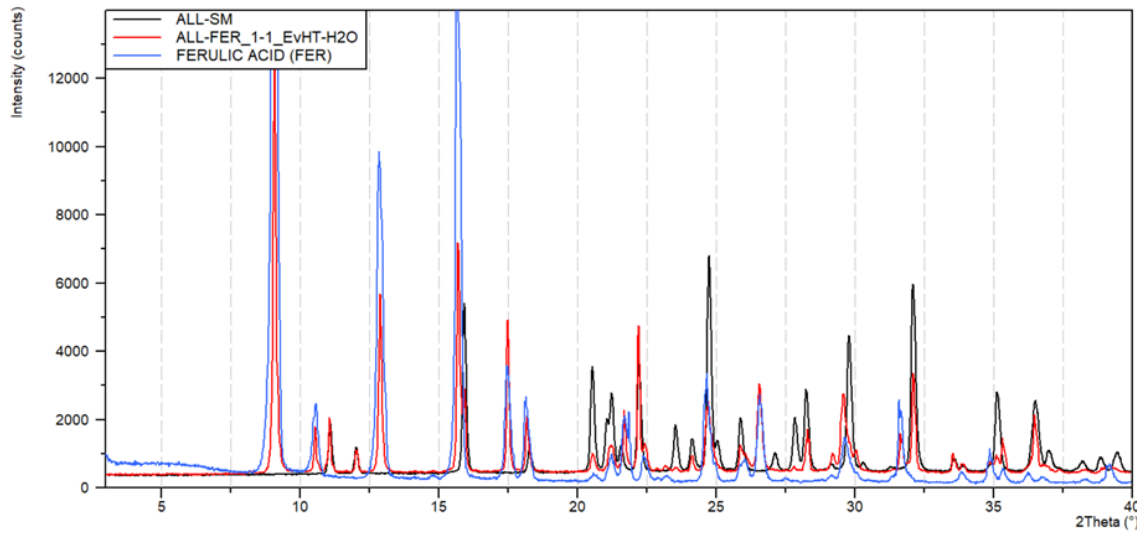


Figure 33. XRPD comparison between starting materials allantoin (black line), trans-ferulic acid (blue line) and EvHT product resulted by allantoin and trans-ferulic acid (red line)

## 6.2 Precipitation results

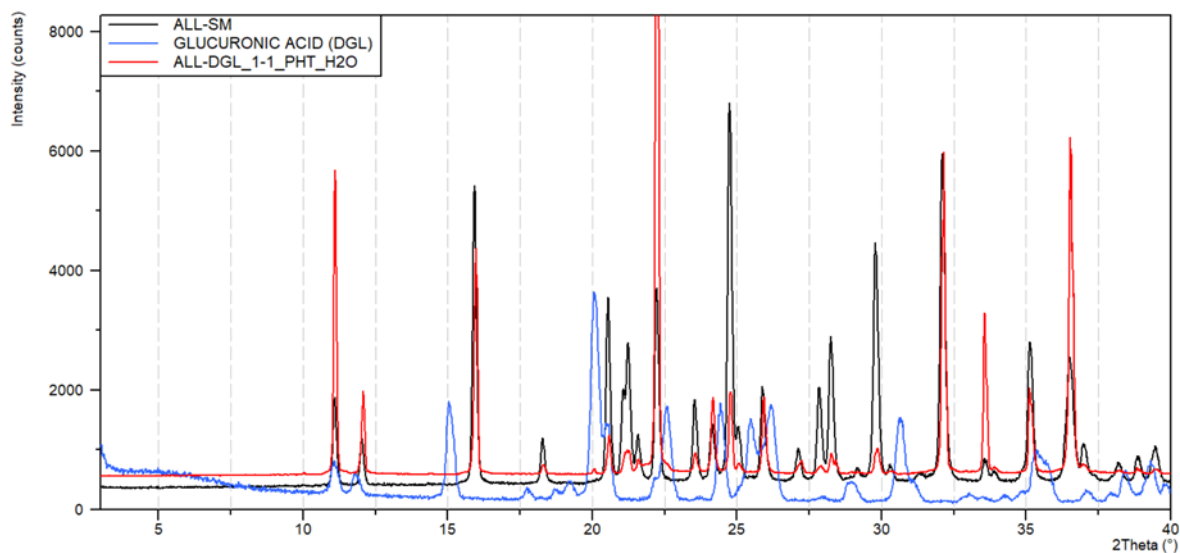


Figure 34. XRPD pattern comparison between starting materials allantoin (black line), glucuronic acid (blue line) and precipitation product resulted by allantoin and glucuronic acid (red line)

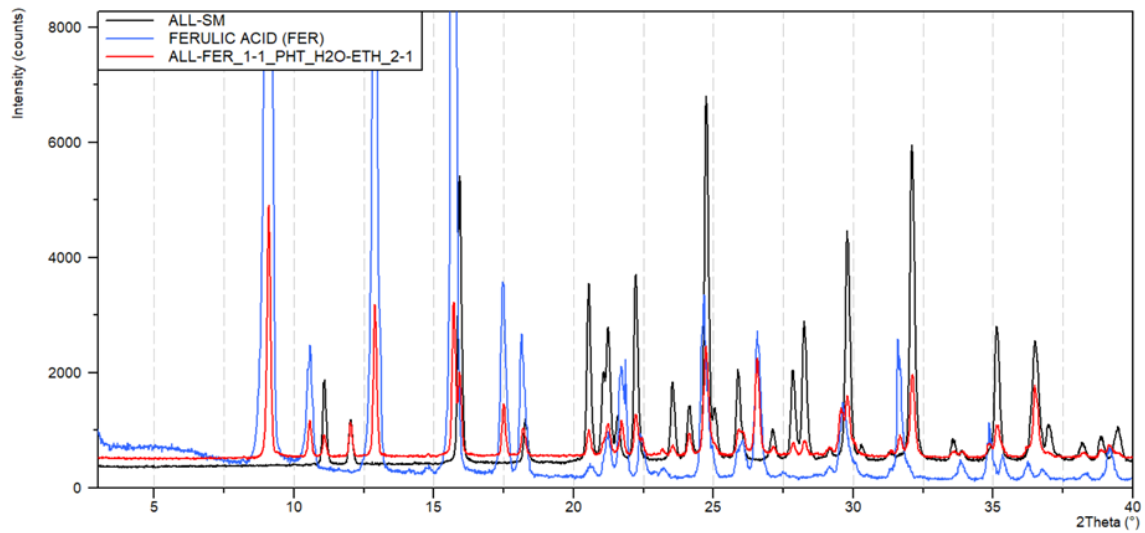


Figure 35. XRPD pattern comparison between starting materials allantoin (black line), trans-ferulic acid (blue line) and precipitation product resulted by allantoin and trans-ferulic acid (red line)

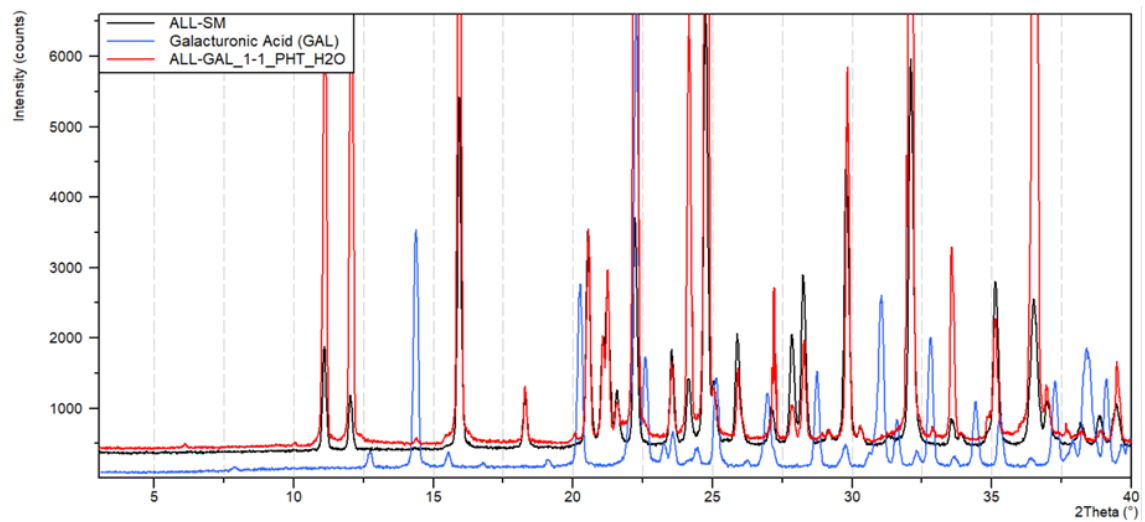


Figure 36. XRPD pattern comparison between starting materials allantoin (black line), galacturonic acid (blue line) and precipitation product resulted by allantoin and galacturonic acid (red line)

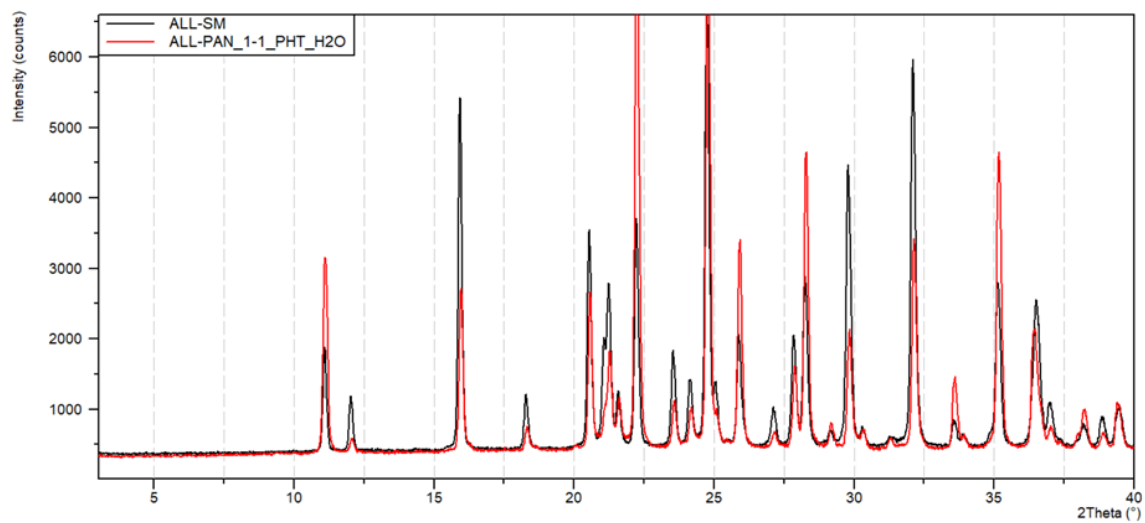


Figure 37. XRPD pattern comparison between starting materials allantoin (black line), D-panthenol (blue line) and precipitation product resulted by allantoin and D-panthenol (red line)

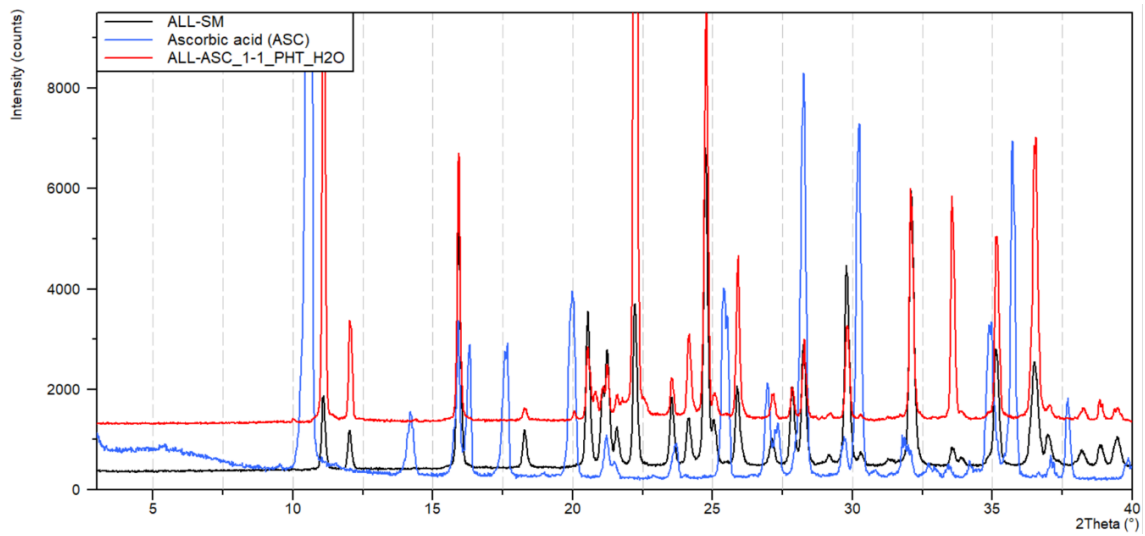


Figure 38. XRPD pattern comparison between starting materials allantoin (black line), ascorbic acid (blue line) and precipitation product resulted by allantoin and ascorbic acid (red line)

### 6.3 Slurry

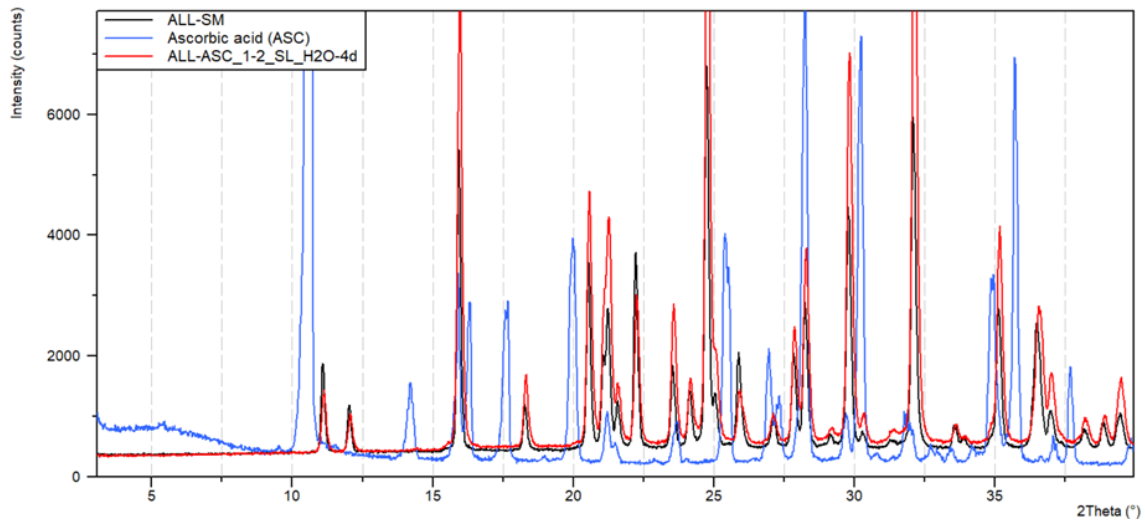
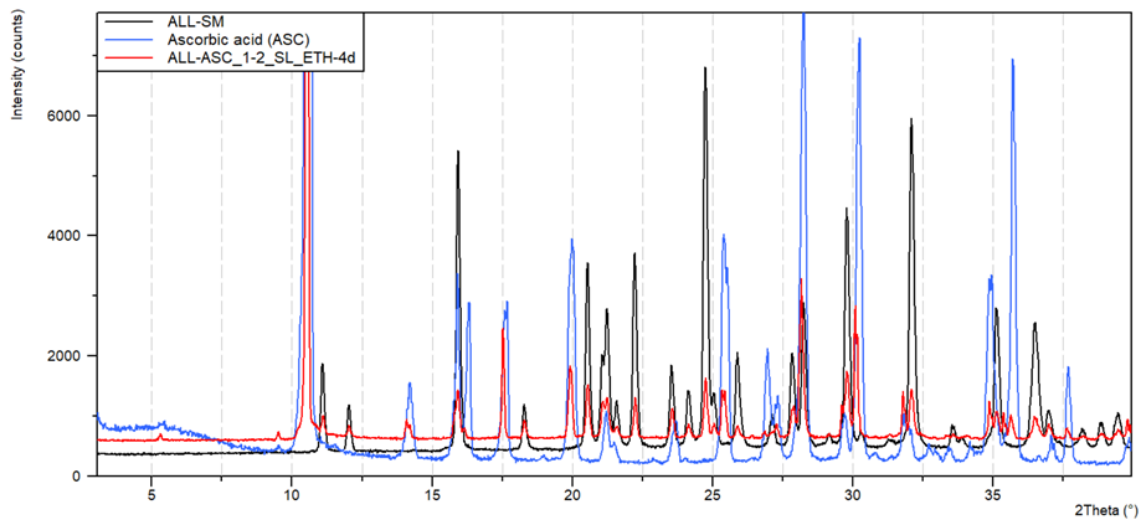
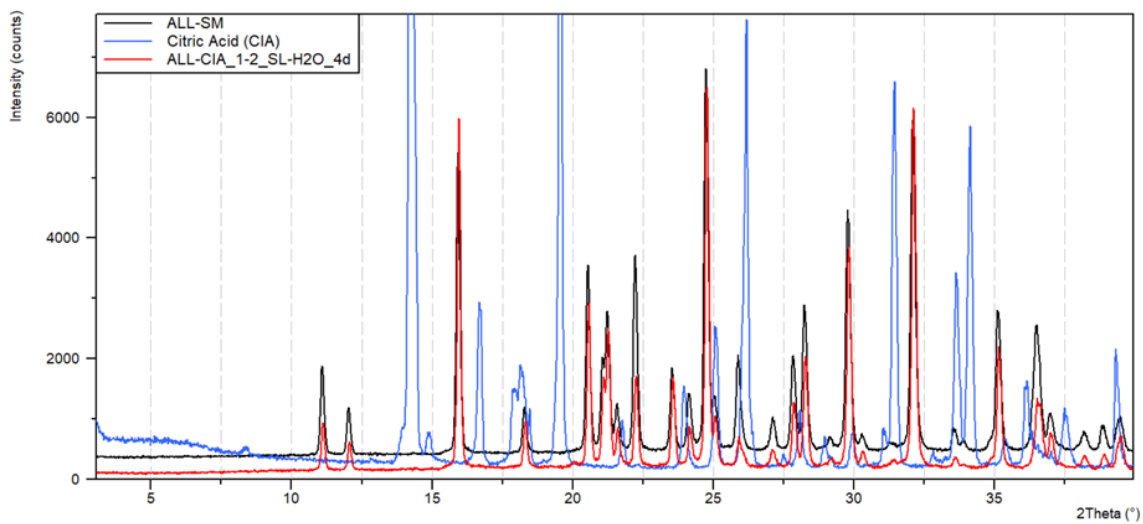


Figure 39. XRPD comparison between starting materials allantoin (black line), ascorbic acid (blue line) and slurry product resulted by allantoin and ascorbic acid in water (red line)



**Figure 40. XRPD comparison between starting materials allantoin (black line), ascorbic acid (blue line) and slurry product resulted by allantoin and ascorbic acid in ethanol (red line)**



**Figure 41. XRPD comparison between starting materials allantoin (black line), citric acid (blue line) and slurry product resulted by allantoin and citric acid in water (red line)**

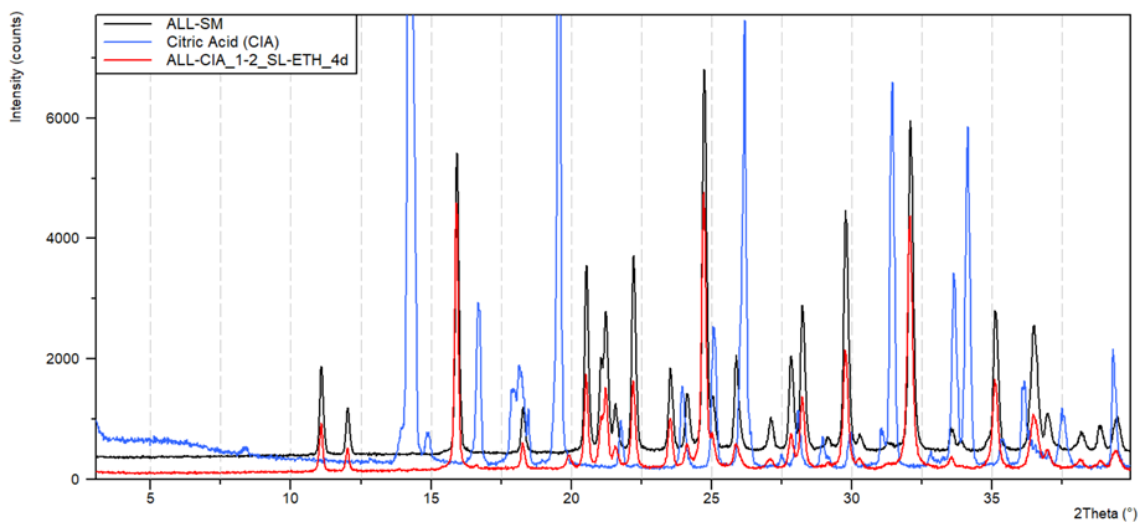


**Figure 42. XRPD comparison between starting materials allantoin (black line), citric acid (blue line) and slurry product resulted by allantoin and citric acid in ethanol (red line)**

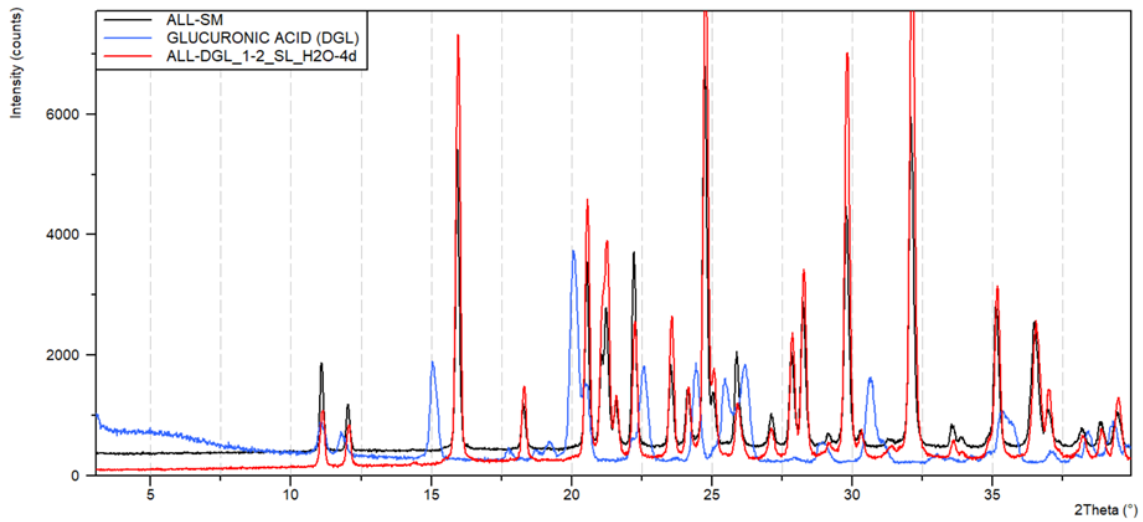


**Figure 43. XRPD comparison between starting materials allantoin (black line), glucuronic acid (blue line) and slurry product resulted by allantoin and glucuronic acid in water (red line)**

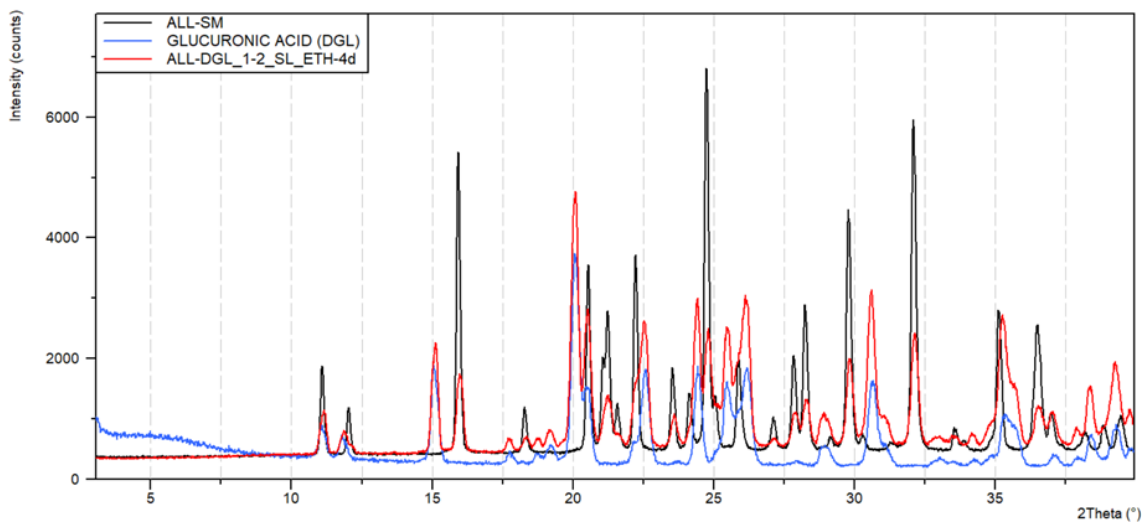


**Figure 44. XRPD comparison between starting materials allantoin (black line), glucuronic acid (blue line) and slurry product resulted by allantoin and glucuronic acid in ethanol (red line)**

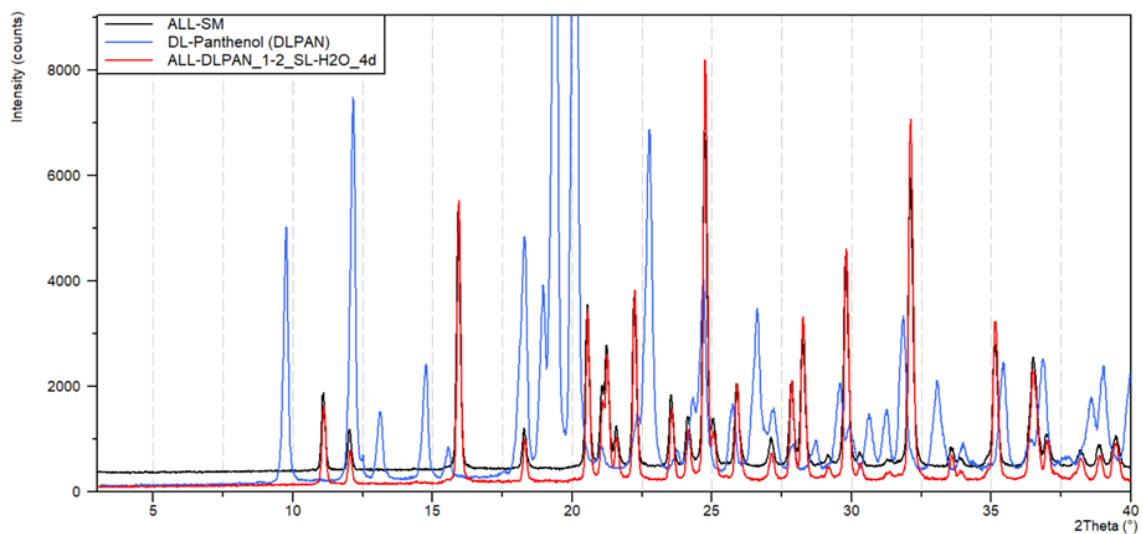


**Figure 45. XRPD comparison between starting materials allantoin (black line), DL-panthenol (blue line) and slurry product resulted by allantoin and DL-panthenol in water (red line)**

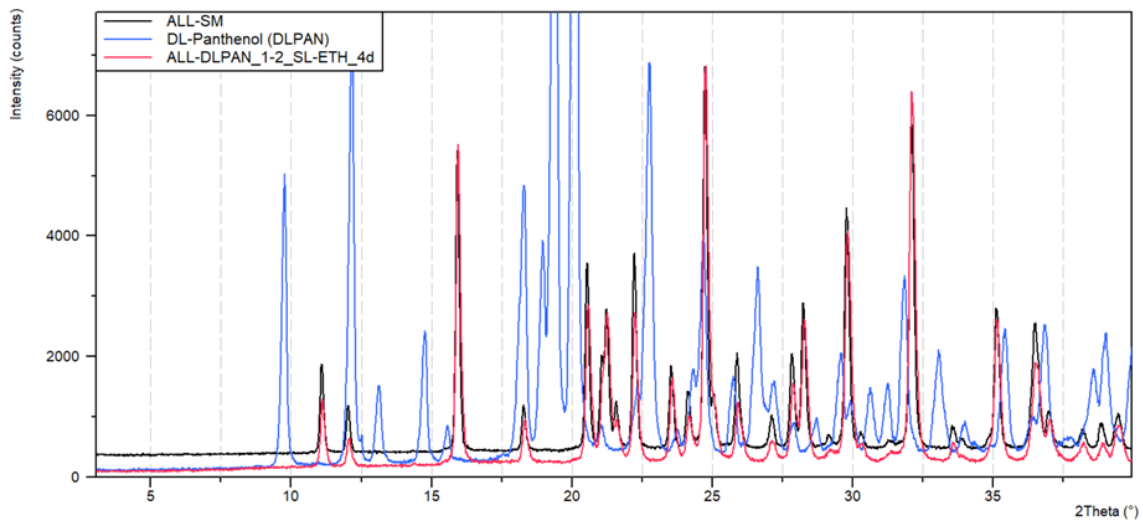


Figure 46. XRPD comparison between starting materials allantoin (black line), DL-panthenol (blue line) and slurry product resulted by allantoin and DL-panthenol in ethanol (red line)

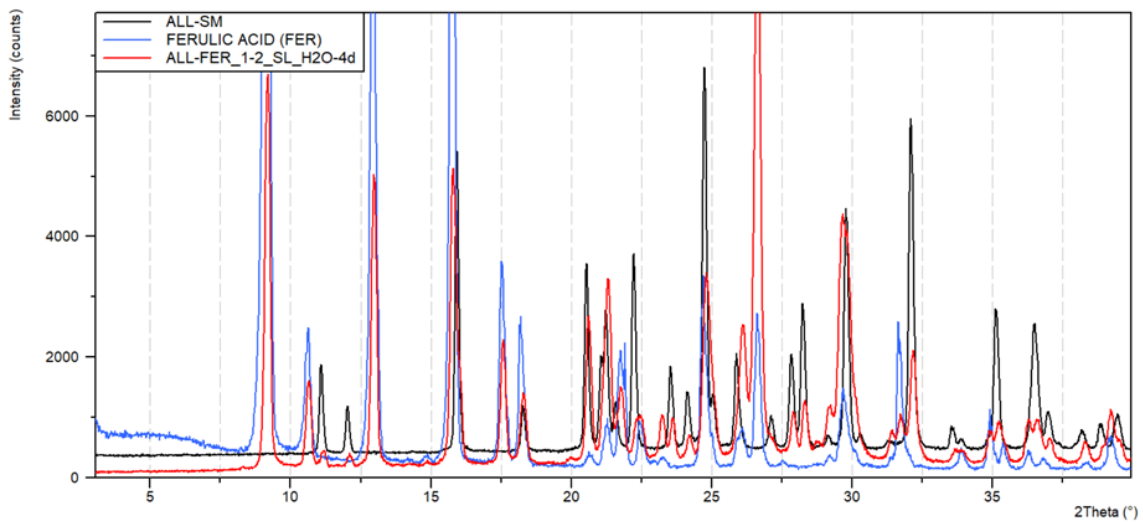


Figure 47. XRPD comparison between starting materials allantoin (black line), trans-ferulic acid (blue line) and slurry product resulted by allantoin and trans-ferulic acid in water (red line)

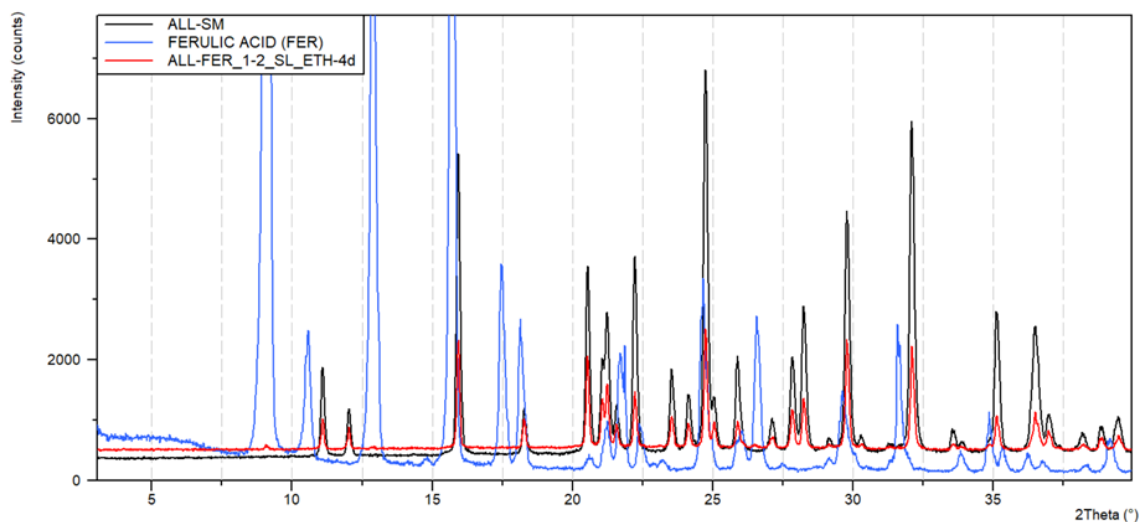


Figure 48. XRPD comparison between starting materials allantoin (black line), trans-ferulic acid (blue line) and slurry product resulted by allantoin and trans-ferulic acid in ethanol (red line)

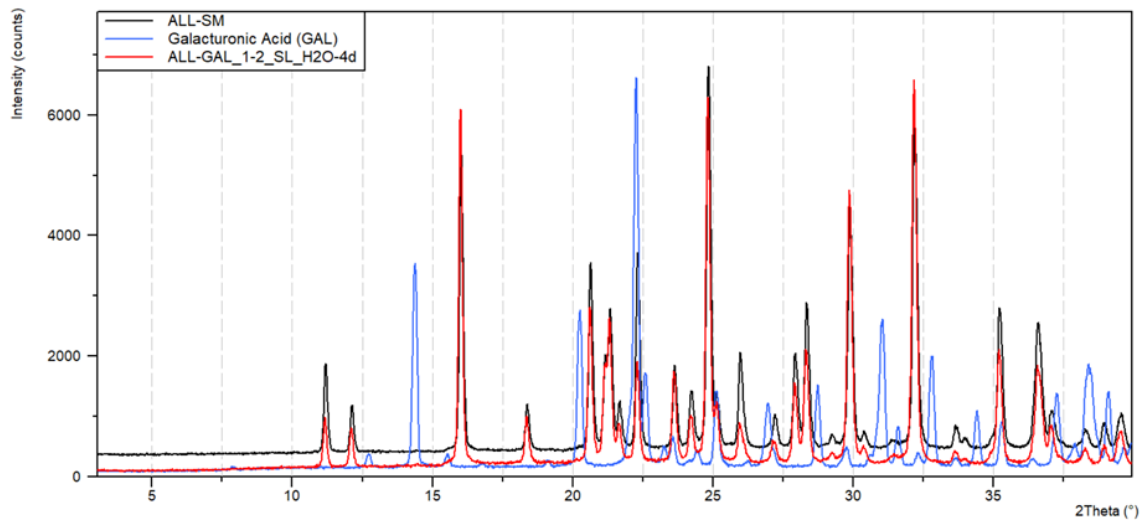


Figure 49. XRPD comparison between starting materials allantoin (black line), galacturonic acid (blue line) and slurry product resulted by allantoin and galacturonic acid in water (red line)

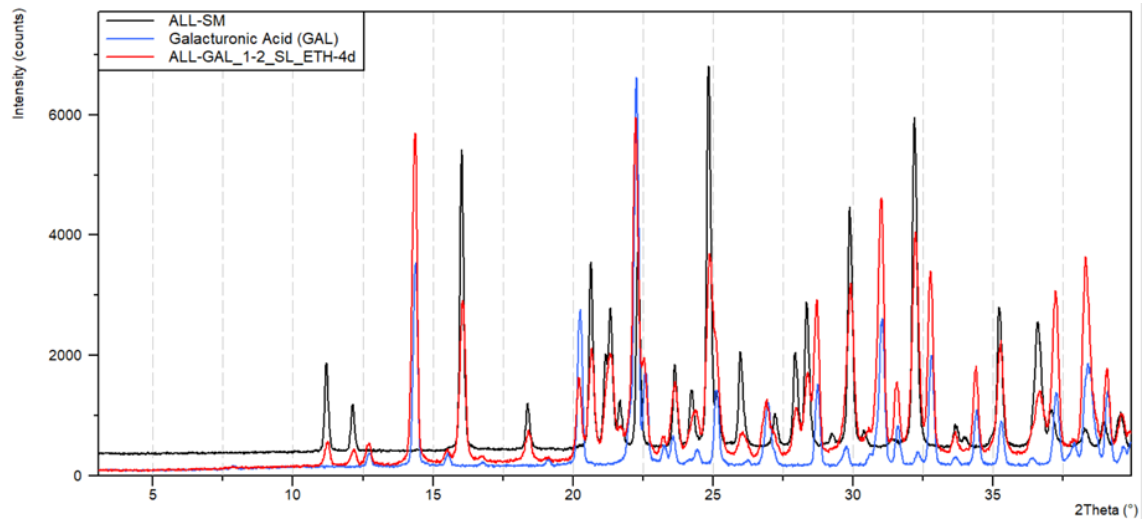


Figure 50. XRPD comparison between starting materials allantoin (black line), galacturonic acid (blue line) and slurry product resulted by allantoin and galacturonic acid in ethanol (red line)

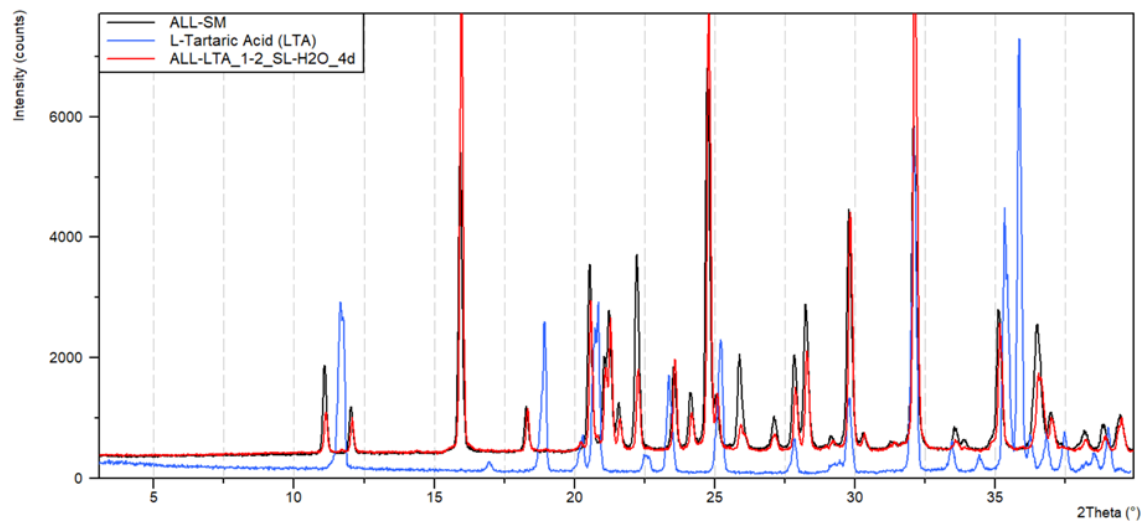


Figure 51. XRPD comparison between starting materials allantoin (black line), L-tartaric acid (blue line) and slurry product resulted by allantoin and L-tartaric acid in water (red line)

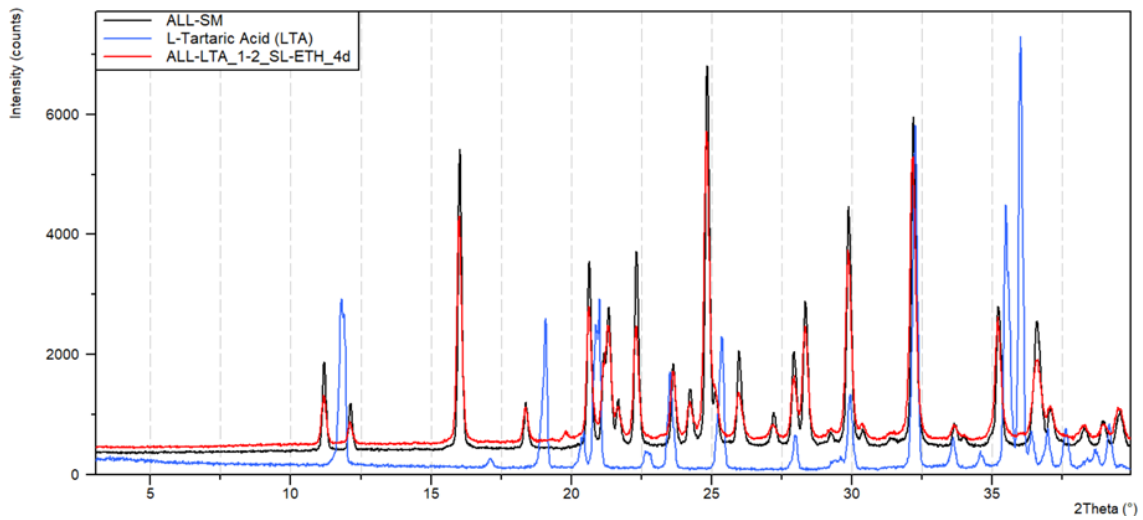


Figure 52. XRPD comparison between starting materials allantoin (black line), L-tartaric acid (blue line) and slurry product resulted by allantoin and L-tartaric acid in ethanol (red line)

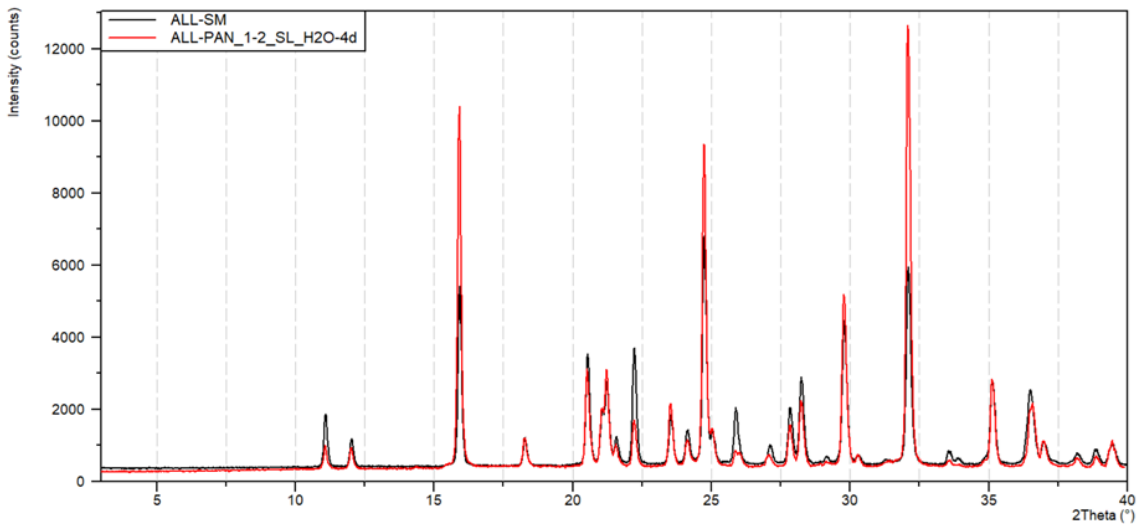


Figure 53. XRPD comparison between starting materials allantoin (black line), D-panthenol (blue line) and slurry product resulted by allantoin and D-panthenol in water (red line)

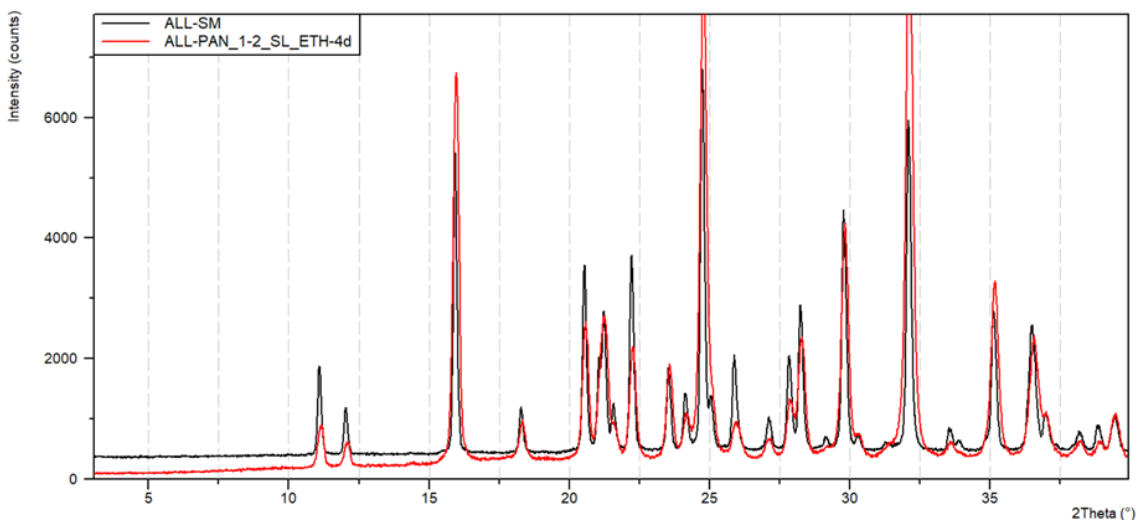
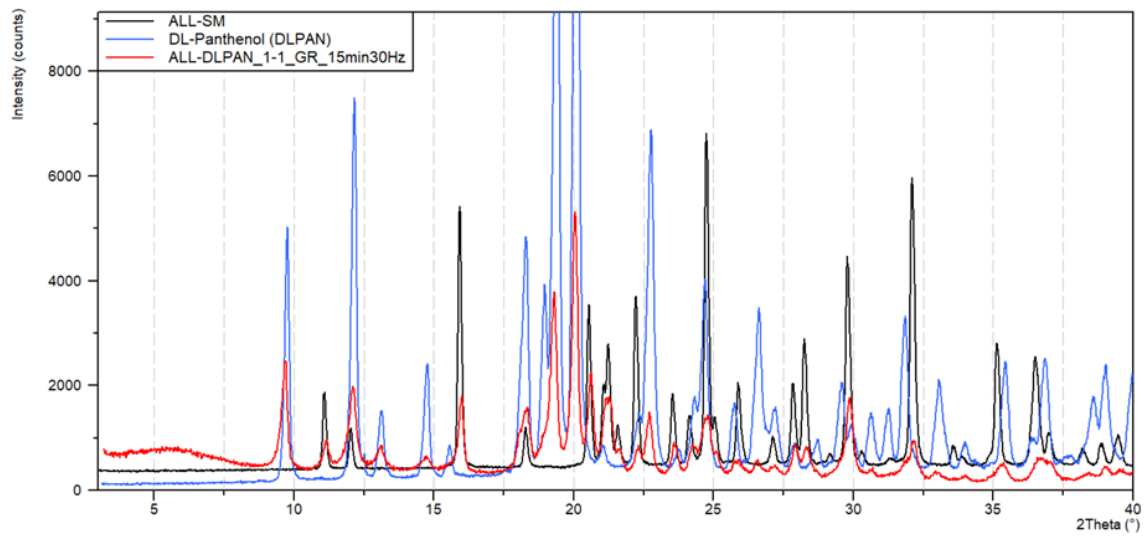
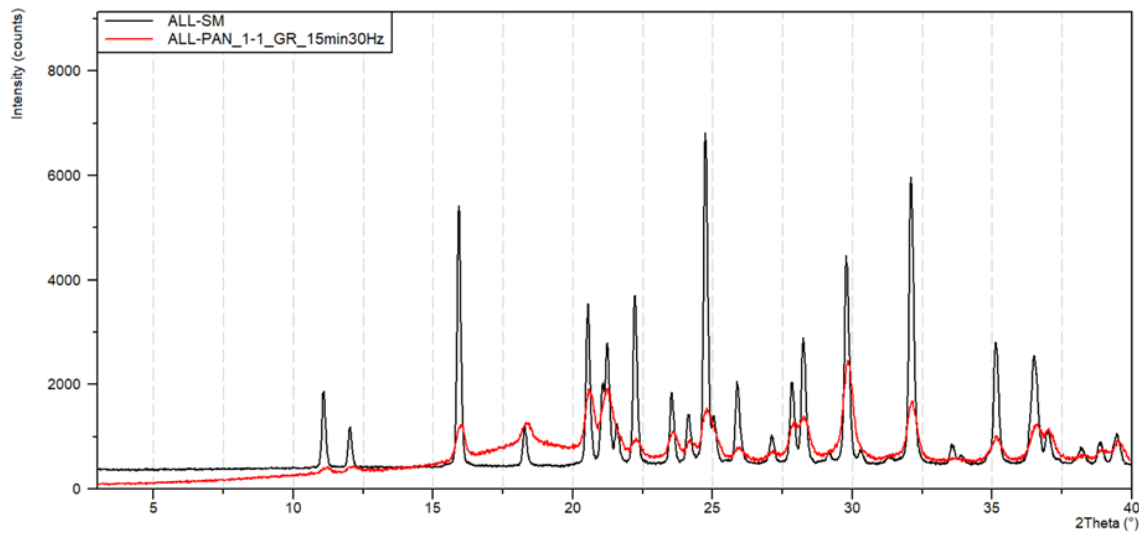


Figure 54. XRPD comparison between starting materials allantoin (black line), D-panthenol (blue line) and slurry product resulted by allantoin and D-panthenol in ethanol (red line)

## 6.4 Grinding



**Figure 55.** XRPD comparison between starting materials allantoin (black line), DL-panthenol (blue line) and product resulted by grinding of allantoin and DL-panthenol (red line)



**Figure 56.** XRPD comparison between starting materials allantoin (black line), D-panthenol (blue line) and product resulted by grinding of allantoin and D-panthenol (red line)

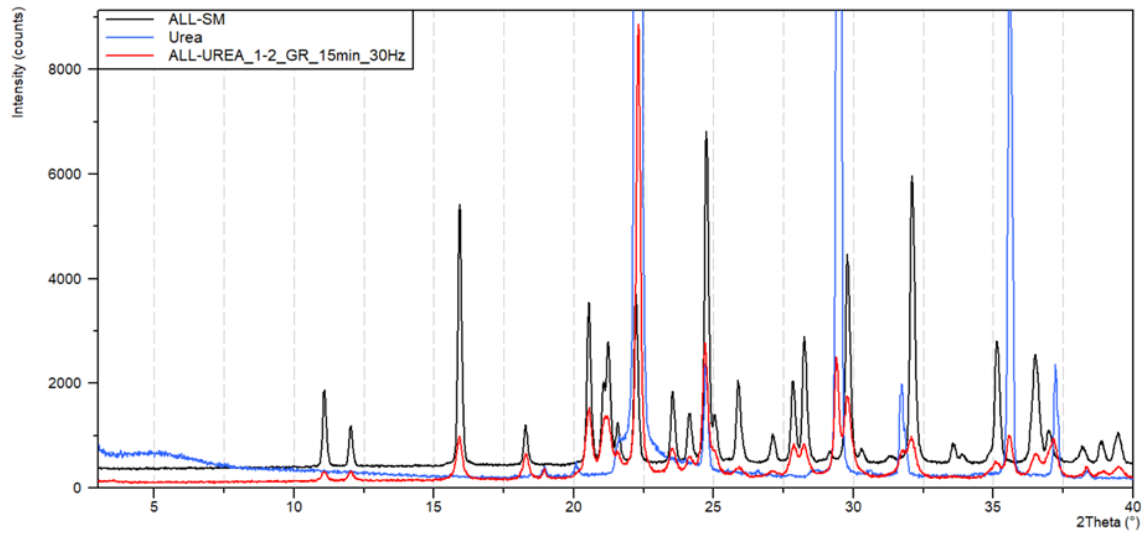


Figure 57. XRPD comparison between starting materials allantoin (black line), urea (blue line) and product resulted by grinding of allantoin and urea (red line)

## 6.5 Kneading

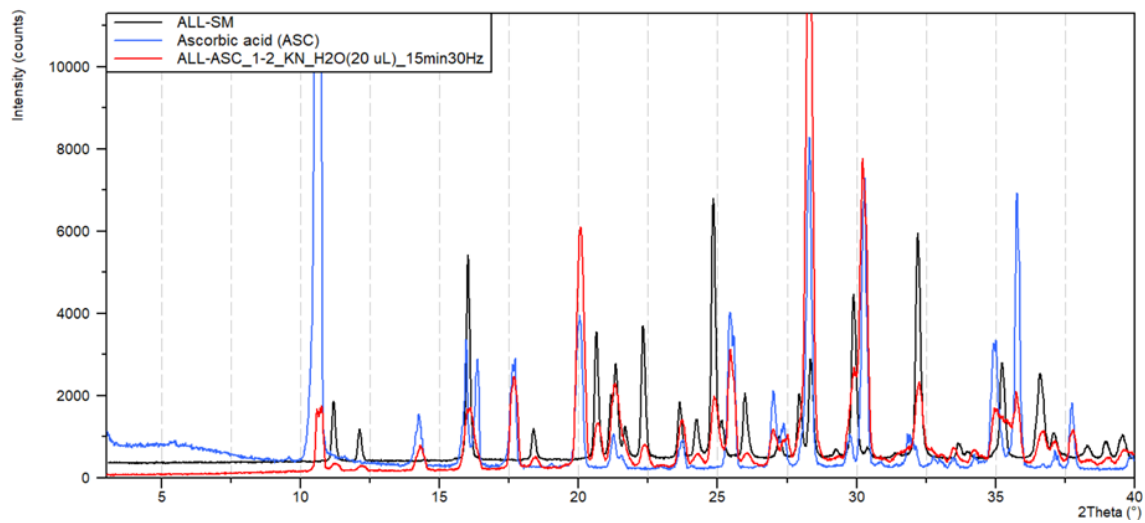


Figure 58. XRPD comparison between starting materials allantoin (black line), ascorbic acid (blue line) and product resulted by kneading of allantoin and ascorbic acid in ratio 1:2 (red line)

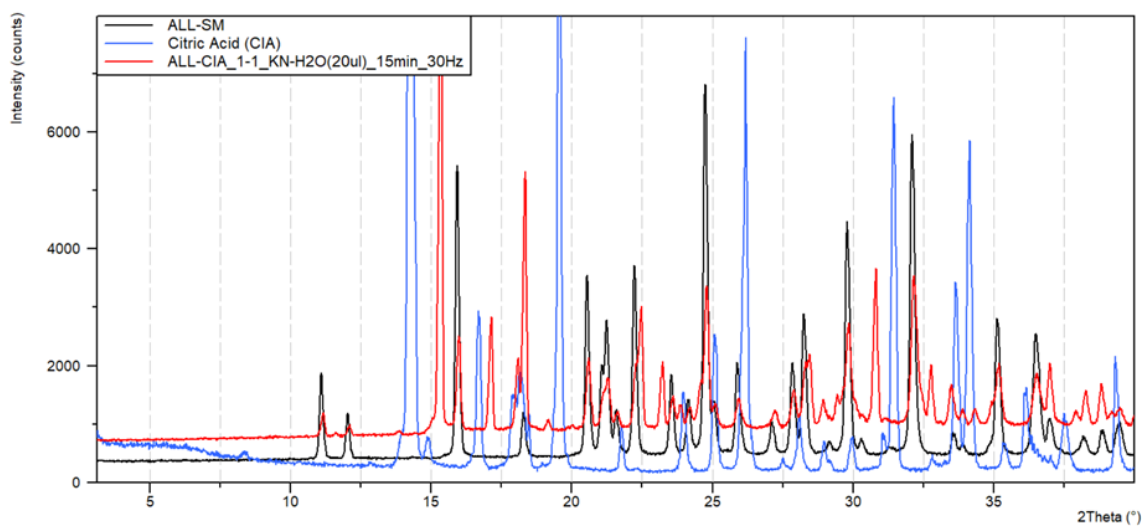


Figure 59. XRPD comparison between starting materials allantoin (black line), citric acid (blue line) and product resulted by kneading of allantoin and citric acid in ratio 1:1 (red line)

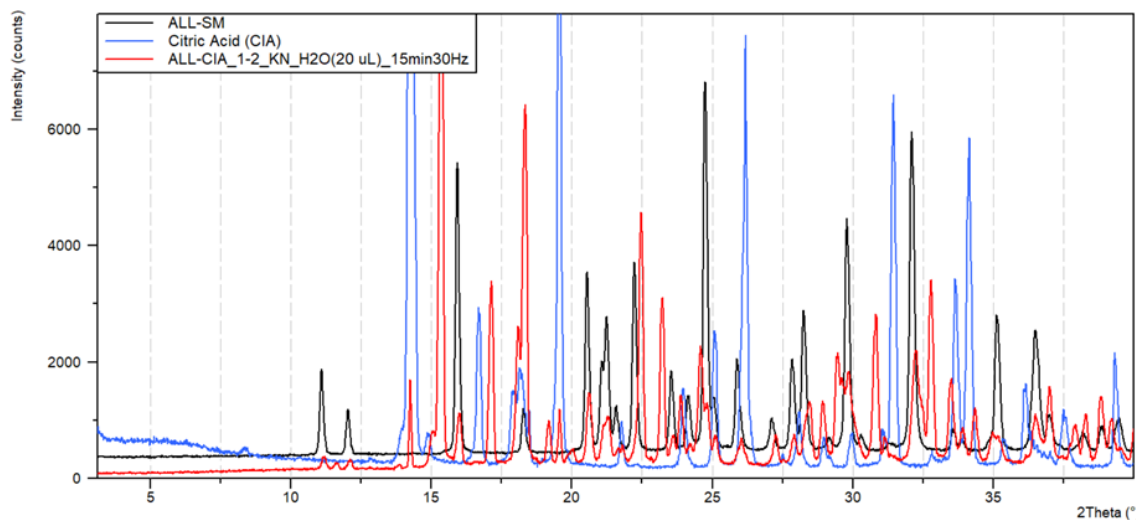


Figure 60. XRPD comparison between starting materials allantoin (black line), citric acid (blue line) and product resulted by kneading of allantoin and citric acid in ratio 1:2 (red line)

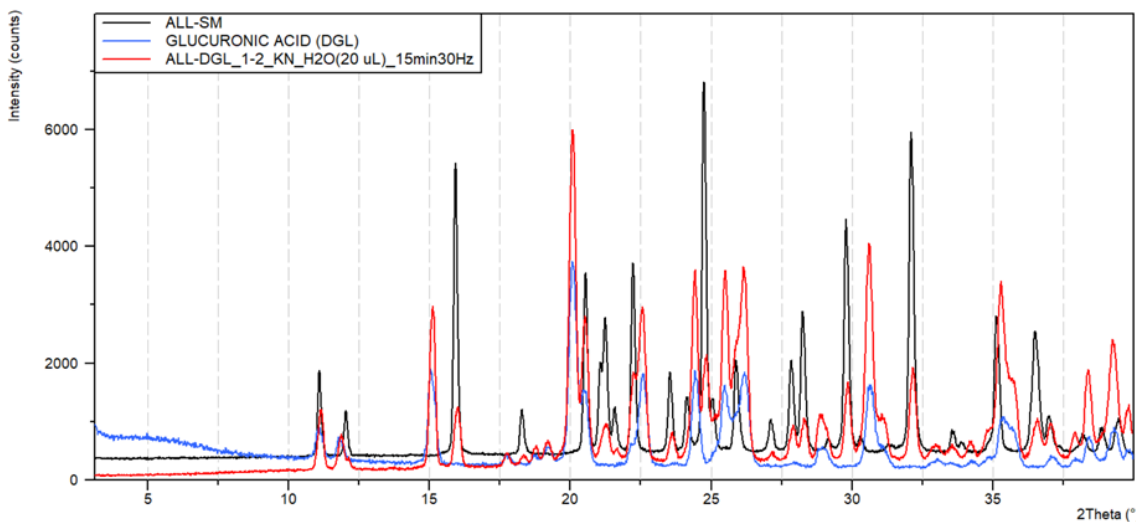


Figure 61. XRPD comparison between starting materials allantoin (black line), glucuronic acid (blue line) and product resulted by kneading of allantoin and glucuronic acid in ratio 1:2 (red line)

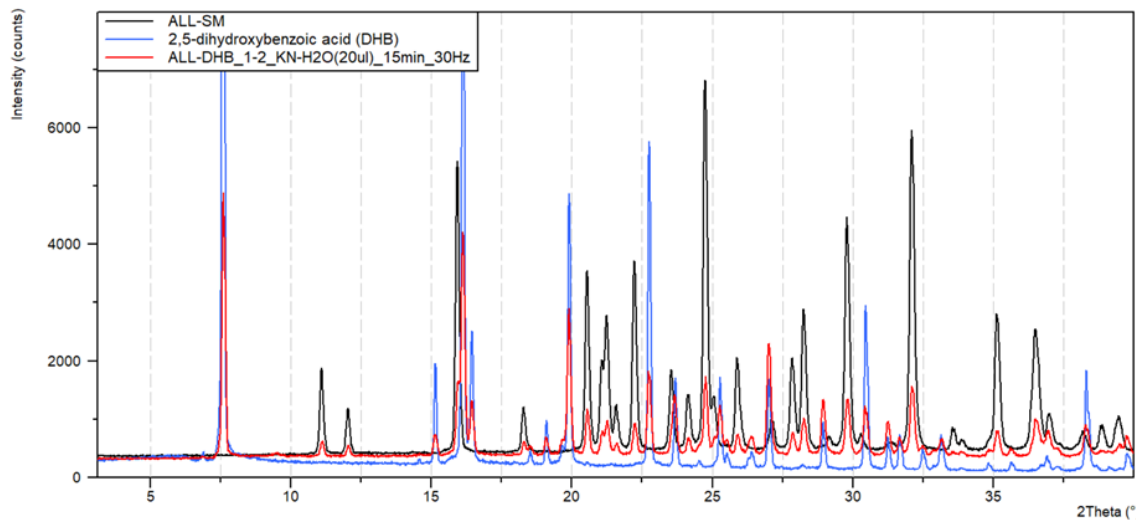


Figure 62. XRPD comparison between starting materials allantoin (black line), 2,5-dihydroxybenzoic acid (blue line) and product resulted by kneading of allantoin and 2,5-dihydroxybenzoic acid in ratio 1:2 (red line)

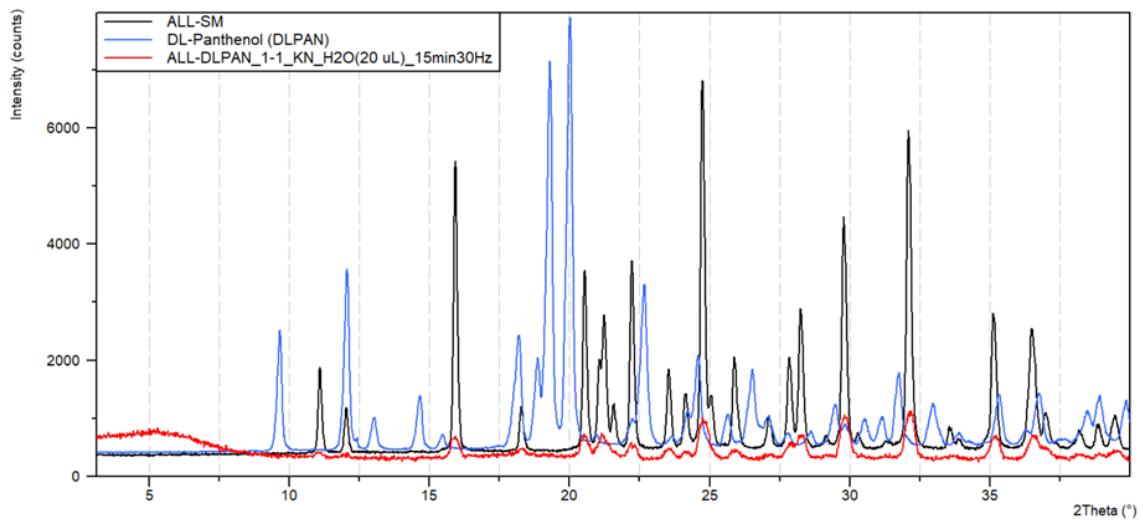


Figure 63. XRPD comparison between starting materials allantoin (black line), DL-panthenol (blue line) and product resulted by kneading of allantoin and DL-panthenol in ratio 1:1 (red line)

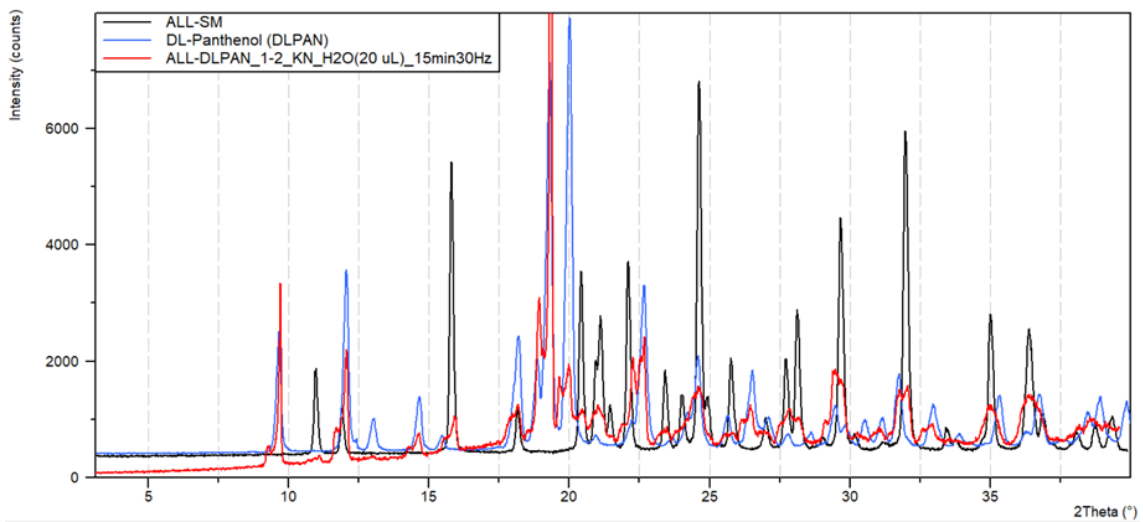


Figure 64. XRPD comparison between starting materials allantoin (black line), DL-panthenol (blue line) and product resulted by kneading of allantoin and DL-panthenol in ratio 1:2 (red line)

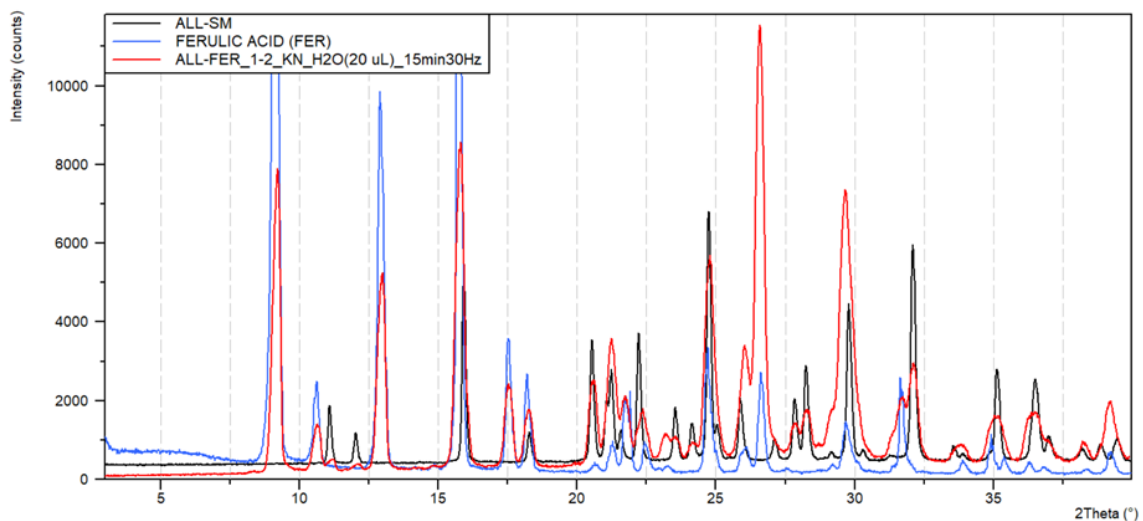


Figure 65. XRPD comparison between starting materials allantoin (black line), trans-ferulic acid (blue line) and product resulted by kneading of allantoin and trans-ferulic acid in ratio 1:2 (red line)

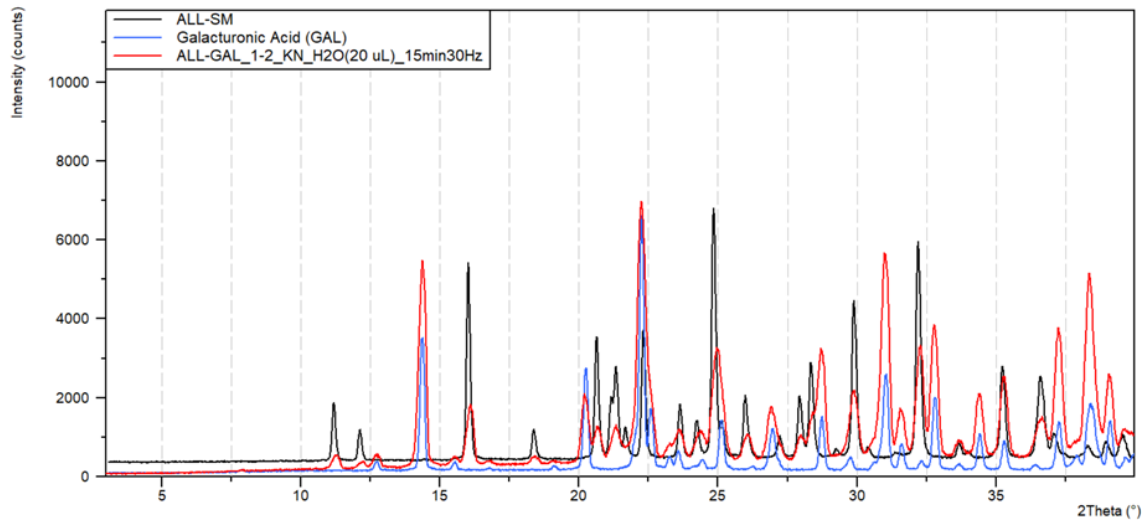


Figure 66. XRPD comparison between starting materials allantoin (black line), galacturonic acid (blue line) and product resulted by kneading of allantoin and galacturonic acid in ratio 1:2 (red line)

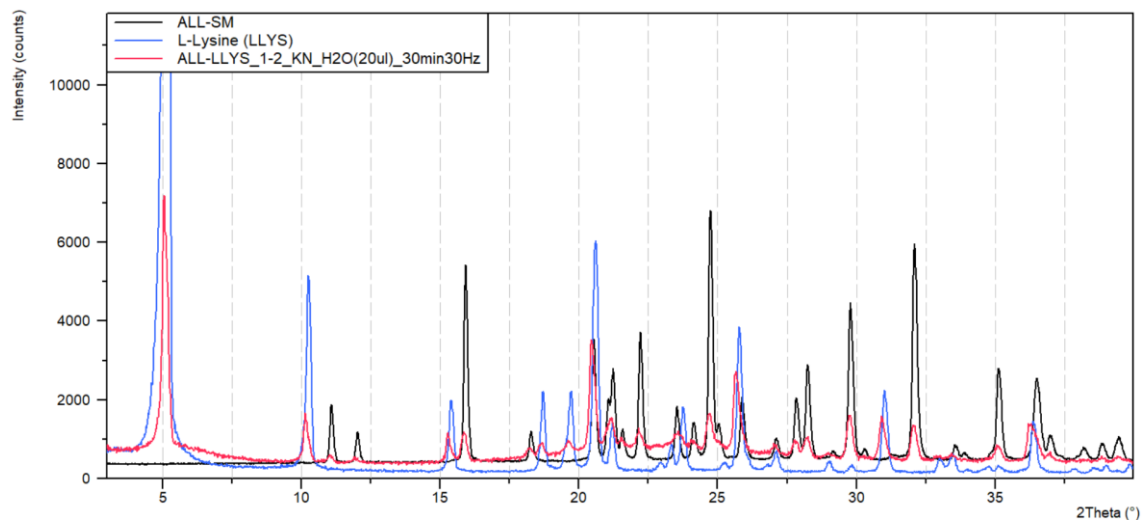


Figure 67. XRPD comparison between starting materials allantoin (black line), L-lysine (blue line) and product resulted by kneading of allantoin and L-lysine in ratio 1:2 (red line)

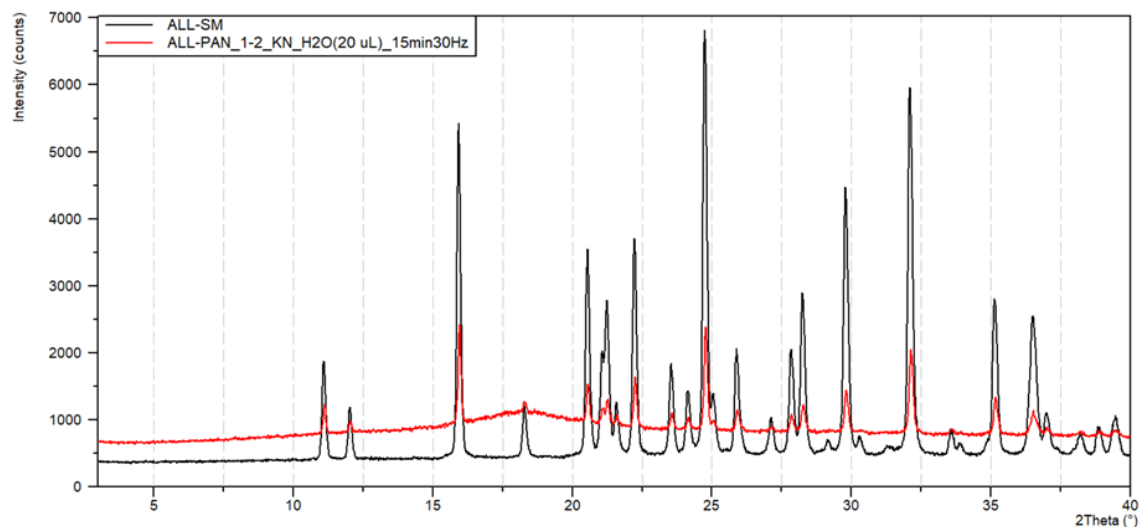
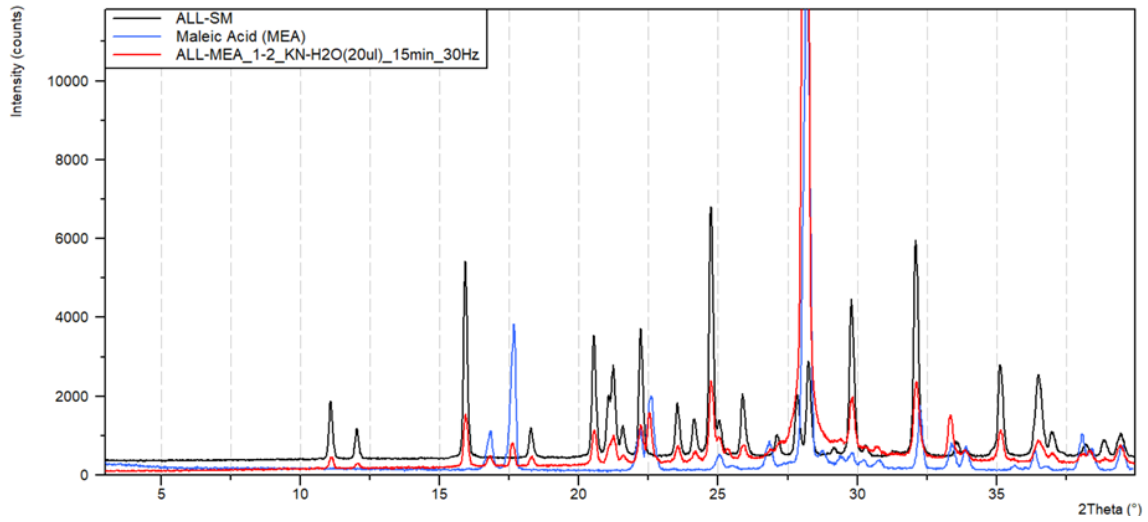


Figure 68. XRPD comparison between starting materials allantoin (black line), D-panthenol (blue line) and product resulted by kneading of allantoin and D-panthenol in ratio 1:2 (red line)



**Figure 69. XRPD comparison between starting materials allantoin (black line), maleic acid (blue line) and product resulted by kneading of allantoin and maleic acid in ratio 1:2 (red line)**

7 APPENDIX C

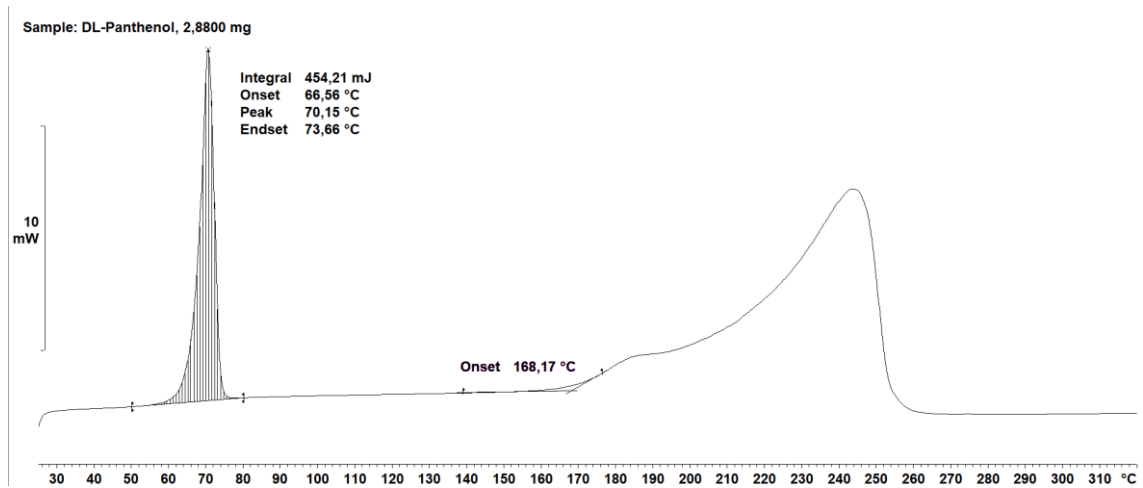


Figure 70. DSC thermogram of DL-panthenol

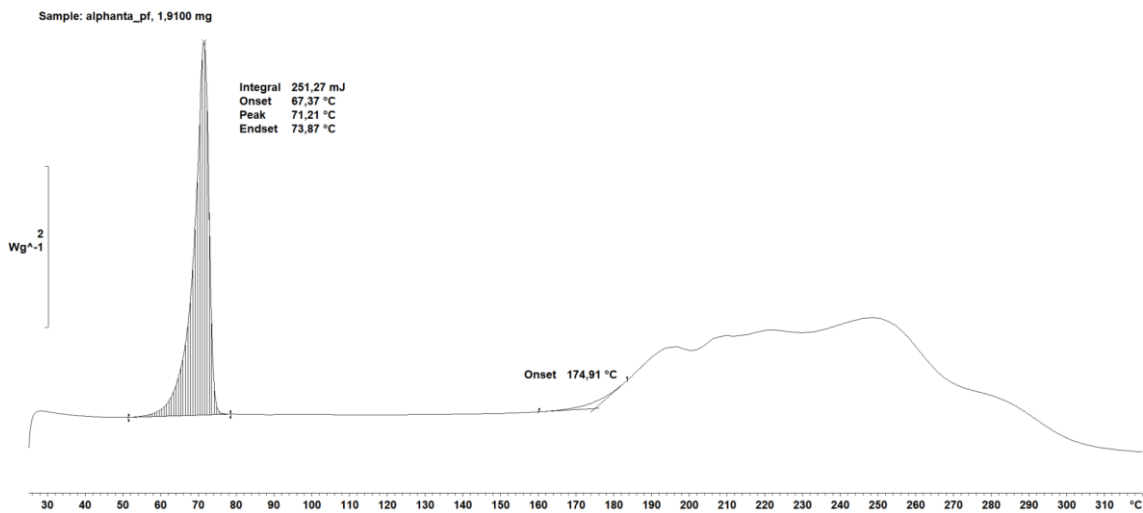


Figure 71. DSC thermogram of Alphanta

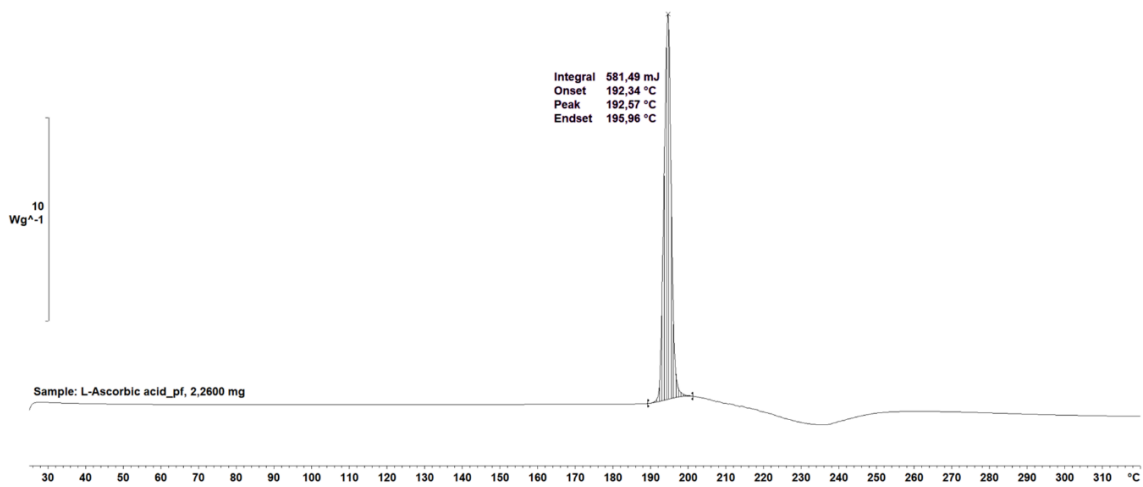


Figure 72. DSC thermogram of ascorbic acid

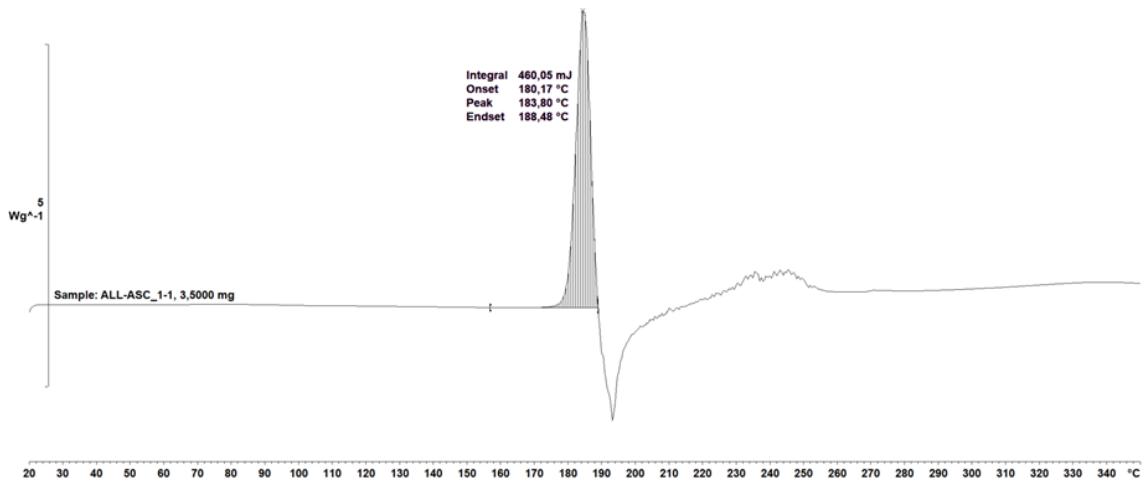


Figure 73. DSC thermogram of mixture 1:1 allantoin and ascorbic acid

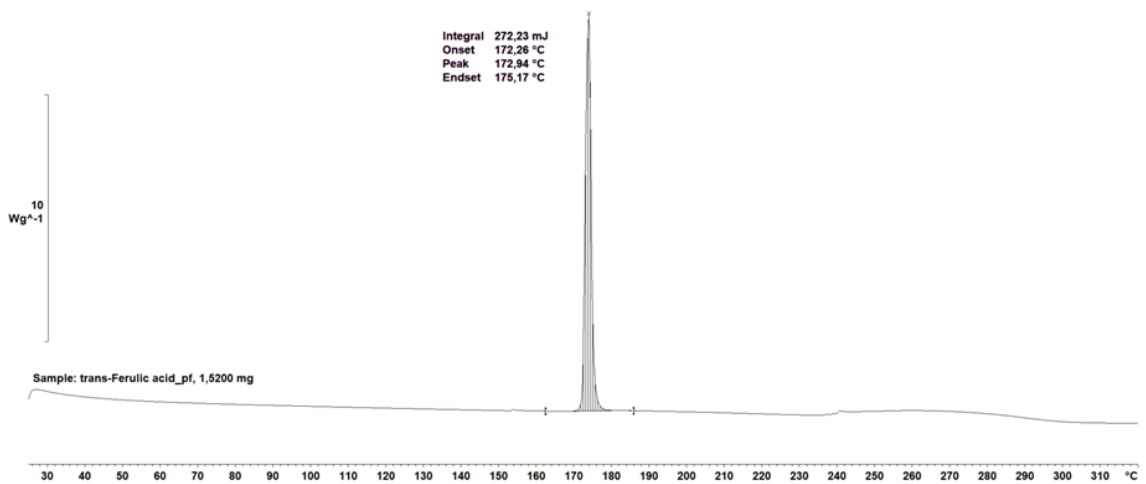


Figure 74. DSC thermogram of trans-ferulic acid

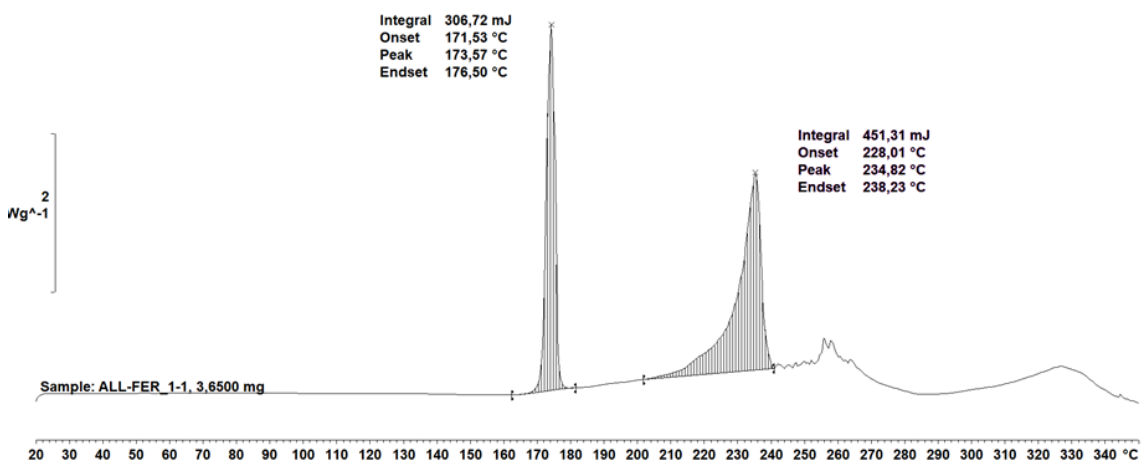


Figure 75. DSC thermogram of mixture 1:1 allantoin and trans-ferulic acid

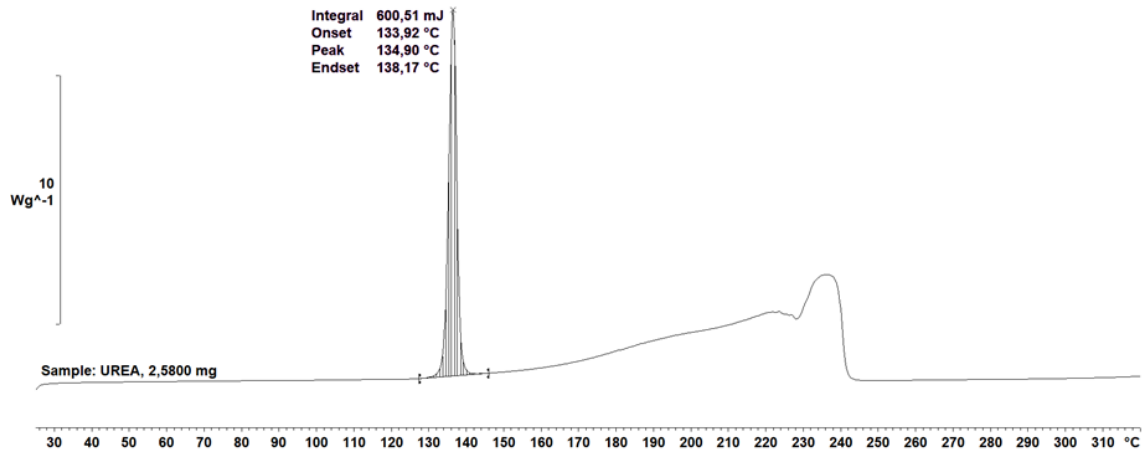


Figure 76. DSC thermogram of urea

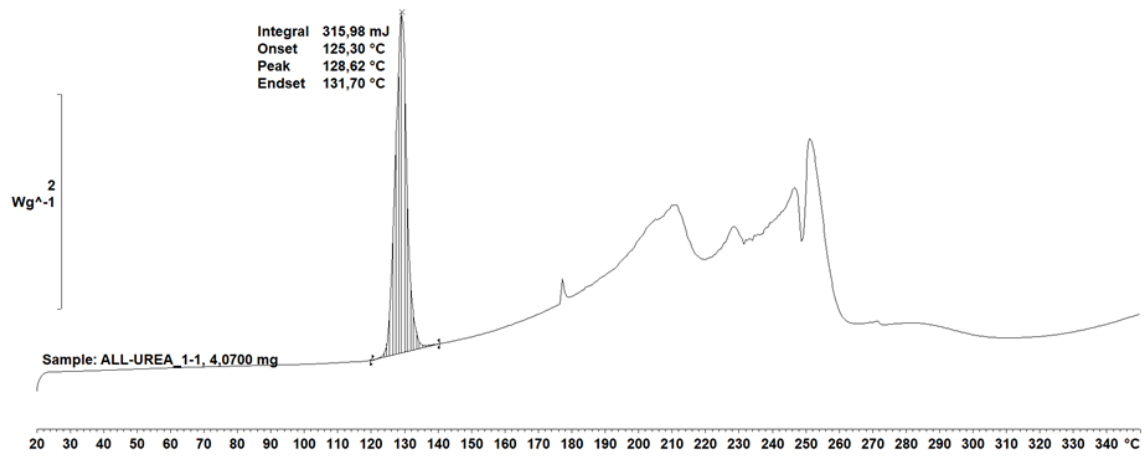


Figure 77. DSC thermogram of mixture 1:1 allantoin and urea

## 8 REFERENCES

- (1) Bakibaev, A. A.; Il'yasov, S. G.; Tatarenko, O. V.; Tuguldurova, V. P.; Zorin, A. O.; Malkov, V. S.; Kasyanova, A. S. Allantoin: Synthesis and Chemical Properties. *Bull. Karaganda Univ. "Chemistry" Ser.* **2020**, *97* (1), 7–21. <https://doi.org/10.31489/2020ch1/7-21>.
- (2) Vogels, G. D.; De Windt, F. E.; Bassie, W. Hydrolysis and Racemization of Allantoin. *Recl. Des Trav. Chim. Des Pays-Bas* **1969**, *88*, 940–950. <https://doi.org/10.1002/recl.19690880807>.
- (3) Cativiela, C.; Fraile, J. M.; García, J. I.; Lázaro, B.; Mayoral, J. A.; Pallarés, A. Heterogeneous Catalysis in the Synthesis and Reactivity of Allantoin. *Green Chem.* **2003**, *5* (2), 275–277. <https://doi.org/10.1039/b212376b>.
- (4) Saqib, M.; Lou, B.; Halawa, M. I.; Kitte, S. A.; Liu, Z.; Xu, G. Chemiluminescence of Lucigenin-Allantoin and Its Application for the Detection of Allantoin. *Anal. Chem.* **2017**, *89* (3), 1863–1869. <https://doi.org/10.1021/acs.analchem.6b04271>.
- (5) Kahn, K.; Tipton, P. A. Kinetics and Mechanism of Allantoin Racemization. *Bioorg. Chem.* **2000**, *28* (2), 62–72. <https://doi.org/10.1006/bioo.2000.1162>.
- (6) Tipton, P. a. Urate to Allantoin , Specifically ( S ) -Allantoin. *Nat. Chem. Biol.* **2006**, *2* (3), 124–125.
- (7) Shestopalov, A. V.; Shkurat, T. P.; Mikashinovich, Z. I.; Kryzhanovskaya, I. O.; Bogacheva, M. A.; Lomteva, S. V.; Prokof'ev, V. N.; Gus'kov, E. P. Biological Functions of Allantoin. *Biol. Bull.* **2006**, *33* (5), 437–440. <https://doi.org/10.1134/S1062359006050037>.
- (8) Kuş, N.; Bayari, S. H.; Fausto, R. Thermal Decomposition of Allantoin as Probed by Matrix Isolation FTIR Spectroscopy. *Tetrahedron* **2009**, *65* (47), 9719–9727. <https://doi.org/10.1016/j.tet.2009.09.088>.
- (9) Mootz, D. The Crystal Structure of DL-Allantoin. *Acta Crystallogr.* **1965**, *19* (5), 726–734. <https://doi.org/10.1107/S0365110X65004280>.
- (10) Gus'kov, E. P.; Kletskii, M. E.; Kornienko, I. V.; Olekhovich, L. P.; Chistyakov, V. A.; Shkurat, T. P.; Prokof'ev, V. N.; Zhdanov, Y. A. Allantoin as a Free-Radical Scavenger. *Dokl. Biochem. Biophys.* **2002**, *383* (3), 105–107. <https://doi.org/10.1023/a:1015331601169>.
- (11) Gus'kov, E. P.; Prokof'ev, V. N.; Kletskii, M. E.; Kornienko, I. V.; Gapurenko, O. A.; Olekhovich, L. P.; Chistyakov, V. A.; Shestopalov, A. V.; Sazykina, M. A.; Markeev, A. V.; Shkurat, T. P.; Malkhos'yan, S. R.; Zhdanov, Y. A. Allantoin as a Vitamin. *Dokl. Biochem. Biophys.* **2004**, *398* (1–6), 320–326. <https://doi.org/10.1023/B:DOBI.0000046649.11374.8d>.
- (12) Araújo, L. U.; Grabe-Guimarães, A.; Mosqueira, V. C. F.; Carneiro, C. M.; Silva-Barcellos, N. M. Profile of Wound Healing Process Induced by Allantoin1. *Acta Cir. Bras.* **2010**, *25* (5), 460–466. <https://doi.org/10.1590/S0102-86502010000500014>.
- (13) Becker, L. C.; Bergfeld, W. F.; Belsito, D. V.; Klaassen, C. D.; Marks, J. G.; Shank, R. C.; Slaga, T. J.; Snyder, P. W.; Andersen, F. A. Final Report of the Safety Assessment of Allantoin and Its Related Complexes. *Int. J. Toxicol.* **2010**, *29* (3\_suppl), 84S–97S. <https://doi.org/10.1177/1091581810362805>.
- (14) Lubowe, I. I. Allantoin Salt US Patent US3107252, 1963.
- (15) Margraf, H. W. Silver Zinc Allantoin Complex US Patent US3856805, 1974.
- (16) Klippel, A. P.; Margraf, H. W. Ant-Microbial Compositions Utilizing Allantoin Compounds and Complexes US3830908, 1974.
- (17) Margraf, H. W. Silver Heparin Allantoin Complex US Patent US3932627, 1976.
- (18) Mecca, S. B. Allantoin Ascorbic Acid Complex US Patent US3898243, 1975.
- (19) Lubowe, I. I. Allantoin Biotin Compositions US Patent US3290324, 1966.
- (20) Lubowe, I. I. Allantoin-Pantothenate Compounds US Patent US3275643, 1966.

- (21) Mecca, S. B. Allantoin Glycine Complex US Patent US3927021, 1975.
- (22) Mecca, S. B. Medicinal or Cosmetic Composition Containing Allantoin Glycinate US Patent US3970756, 1976.
- (23) Lubowe, I. I. Allantoin P-Aminobenzoic Acid Complexes US Patent US3305557, 1967.
- (24) Mecca, S. B. Allantoin Urocanic Acid Complexes US Patent US4181804, 1980.
- (25) Akema <https://www.akema.it/products/allantoin-and-derivatives/>.
- (26) Bährle-Rapp, M.; Bährle-Rapp, M. Allantoin Calcium Pantothenate. *Springer Lex. Kosmet. und Körperpfl.* **2007**, 21–21. [https://doi.org/10.1007/978-3-540-71095-0\\_336](https://doi.org/10.1007/978-3-540-71095-0_336).
- (27) Puszyńska-Tuszkano, M.; Grabowski, T.; Daszkiewicz, M.; Wietrzyk, J.; Filip, B.; Maciejewska, G.; Cieślak-Golonka, M. Silver(I) Complexes with Hydantoins and Allantoin: Synthesis, Crystal and Molecular Structure, Cytotoxicity and Pharmacokinetics. *J. Inorg. Biochem.* **2011**, 105 (1), 17–22. <https://doi.org/10.1016/j.jinorgbio.2010.09.013>.
- (28) Zukerman-Schpector, J.; Tiekink, E. R. T. What Is a Co-Crystal? *Zeitschrift für Krist.* **2008**, 223 (3), 233–234. <https://doi.org/10.1524/zkri.2008.0021>.
- (29) Aakeröy, C. B.; Salmon, D. J. Building Co-Crystals with Molecular Sense and Supramolecular Sensibility. *CrystEngComm* **2005**, 7 (72), 439–448. <https://doi.org/10.1039/b505883j>.
- (30) Corpinot, M. K.; Bučar, D. K. A Practical Guide to the Design of Molecular Crystals. *Cryst. Growth Des.* **2019**, 19 (2), 1426–1453. <https://doi.org/10.1021/acs.cgd.8b00972>.
- (31) He, G.; Chow, P. S.; Tan, R. B. H. Predicting Multicomponent Crystal Formation: The Interplay between Homomeric and Heteromeric Interactions. *Cryst. Growth Des.* **2009**, 9 (10), 4529–4532. <https://doi.org/10.1021/cg900538g>.
- (32) He, G.; Jacob, C.; Guo, L.; Chow, P. S.; Tan, R. B. H. Screening for Cocrystallization Tendency: The Role of Intermolecular Interactions. *J. Phys. Chem. B* **2008**, 112 (32), 9890–9895. <https://doi.org/10.1021/jp803019m>.
- (33) Lemmerer, A.; Bernstein, J. The Co-Crystal of Two GRAS Substances: (Citric Acid)-(Nicotinamide). Formation of Four Hydrogen Bonding Heterosynthons in One Co-Crystal. *CrystEngComm* **2010**, 12 (7), 2029–2033. <https://doi.org/10.1039/b927422g>.
- (34) Childs, S. L.; Zaworotko, M. J. The Reemergence of Cocrystals: The Crystal Clear Writing Is on the Wall Introduction to Virtual Special Issue on Pharmaceutical Cocrystals. *Cryst. Growth Des.* **2009**, 9 (10), 4208–4211. <https://doi.org/10.1021/cg901002y>.
- (35) Patrick Stahly, G. A Survey of Cocrystals Reported Prior to 2000. *Cryst. Growth Des.* **2009**, 9 (10), 4212–4229. <https://doi.org/10.1021/cg900873t>.
- (36) Fábíán, L. Cambridge Structural Database Analysis of Molecular Complementarity in Cocrystals. *Cryst. Growth Des.* **2009**, 9 (3), 1436–1443. <https://doi.org/10.1021/cg800861m>.
- (37) Karki, S.; Frić, T.; Fábíán, L.; Jones, W. New Solid Forms of Artemisinin Obtained through Cocrystallisation. *CrystEngComm* **2010**, 12 (12), 4038–4041. <https://doi.org/10.1039/c0ce00428f>.
- (38) Allen, F. H.; Hoy, V. J. The Cambridge Structural Database (CSD). *Int. Tables Crystallogr.* **2006**, 663–668. <https://doi.org/10.1107/97809553602060000720>.
- (39) Allen, F. H. Research Papers The Cambridge Structural Database: A Quarter of a Million Crystal Structures and Rising Research Papers. *Acta Cryst.* **2002**, B58, 380–388.
- (40) Release, C. Mercury User Guide and Tutorials 2016 CSDS Release. **2016**, No. 800579.
- (41) Taylor, R.; Cole, J.; Korb, O.; McCabe, P. Knowledge-Based Libraries for Predicting the Geometric Preferences of Druglike Molecules. **2014**. <https://doi.org/10.1021/ci500358p>.

- (42) Cole, J. C.; Korb, O.; McCabe, P.; Read, M. G.; Taylor, R. Knowledge-Based Conformer Generation Using the Cambridge Structural Database. *J. Chem. Inf. Model.* **2018**, *58* (3), 615–629. <https://doi.org/10.1021/acs.jcim.7b00697>.
- (43) Wood, P. A.; Olsson, T. S. G.; Cole, J. C.; Cottrell, S. J.; Feeder, N.; Galek, P. T. A.; Groom, C. R.; Pidcock, E. Evaluation of Molecular Crystal Structures Using Full Interaction Maps. *CrystEngComm* **2013**, *15* (1), 65–72. <https://doi.org/10.1039/c2ce25849h>.
- (44) Galek, P. T. A.; Allen, F. H.; Fábrián, L.; Feeder, N. Knowledge-Based H-Bond Prediction to Aid Experimental Polymorph Screening. *CrystEngComm* **2009**, *11* (12), 2634–2639. <https://doi.org/10.1039/b910882c>.
- (45) Macrae, C. F.; Bruno, I. J.; Chisholm, J. A.; Edgington, P. R.; McCabe, P.; Pidcock, E.; Rodriguez-Monge, L.; Taylor, R.; Van De Streek, J.; Wood, P. A. Mercury CSD 2.0 - New Features for the Visualization and Investigation of Crystal Structures. *J. Appl. Crystallogr.* **2008**, *41* (2), 466–470. <https://doi.org/10.1107/S0021889807067908>.
- (46) Jeeva, S.; Muthu, S.; Thomas, R.; Raajaraman, B. R.; Mani, G.; Vinitha, G. Co-Crystals of Urea and Hexanedioic Acid with Third-Order Nonlinear Properties: An Experimental and Theoretical Enquiry. *J. Mol. Struct.* **2020**, *1202*, 127237. <https://doi.org/10.1016/j.molstruc.2019.127237>.
- (47) Khan, E.; Shukla, A.; Jadav, N.; Telford, R.; Ayala, A. P.; Tandon, P.; Vangala, V. R. Study of Molecular Structure, Chemical Reactivity and H-Bonding Interactions in the Cocrystal of Nitrofurantoin with Urea. *New J. Chem.* **2017**, *41* (19), 11069–11078. <https://doi.org/10.1039/c7nj01345k>.
- (48) Powell, K. A.; Bartolini, G.; Wittering, K. E.; Saleemi, A. N.; Wilson, C. C.; Rielly, C. D.; Nagy, Z. K. Toward Continuous Crystallization of Urea-Barbituric Acid: A Polymorphic Co-Crystal System. *Cryst. Growth Des.* **2015**, *15* (10), 4821–4836. <https://doi.org/10.1021/acs.cgd.5b00599>.
- (49) Alhalaweh, A.; George, S.; Boström, D.; Velaga, S. P. 1:1 and 2:1 Urea-Succinic Acid Cocrystals: Structural Diversity, Solution Chemistry, and Thermodynamic Stability. *Cryst. Growth Des.* **2010**, *10* (11), 4847–4855. <https://doi.org/10.1021/cg100823p>.
- (50) Screening, C. K. C.; Release, C. S. D. Knowledge-Based Co-Crystal Design. **2020**, 1–9.
- (51) Williams, P. A.; Hughes, C. E.; Martin, J.; Courvoisier, E.; Buanz, A. B. M.; Gaisford, S.; Harris, K. D. M. Understanding the Solid-State Hydration Behavior of a Common Amino Acid: Identification, Structural Characterization, and Hydration/Dehydration Processes of New Hydrate Phases of L-Lysine. *J. Phys. Chem. C* **2016**, *120* (17), 9385–9392. <https://doi.org/10.1021/acs.jpcc.5b12420>.
- (52) Rammohan, A.; Kaduk, J. A. Crystal Structures of Alkali Metal (Group 1) Citrate Salts. *Acta Crystallogr. Sect. B Struct. Sci. Cryst. Eng. Mater.* **2018**, *74* (2), 239–252. <https://doi.org/10.1107/S2052520618002330>.

## CHAPTER 3

### EVALUATION OF ERRORS AND ABERRATIONS AFFECTING THE ANALYSIS BY X-RAY POWDER DIFFRACTION

#### 1 INTRODUCTION

##### 1.1 X-ray powder diffraction (XRPD)

X-Ray diffraction (XRD) is the main analytical technique used to study crystalline phases of solid samples. X-Ray diffraction results from interaction between electromagnetic radiation and matter. Each electron of sample is secondary diffusing center of X-Ray with the same  $\lambda$  of incident beam. The wavelength  $\lambda$  of X-Ray is in the range 0.1-100 Å. In crystalline samples, the diffraction of the X-Ray occurs when the interatomic distances of crystalline structure are comparable to the  $\lambda$  of the radiation. This is explained by the Bragg's law:

$$n\lambda = 2d \sin \theta$$

where  $n$  is the diffraction order,  $\lambda$  the wavelength of the incident radiation,  $d$  is the distance between parallel reticular planes, and  $\theta$  is the angle between the incident rays and diffraction planes.

The angle of Bragg  $\theta$  is determined experimentally as the half of the angle between the direction of the incident ray and of the reflected ray. The diffraction phenomenon occurs only when the adjacent lattice planes of the same family  $hkl$  reflects the incident beam with constructive interference, that is when the difference between the optical path (AB+BC in Figure 1) is a multiple of  $\lambda$ <sup>1-3</sup>.

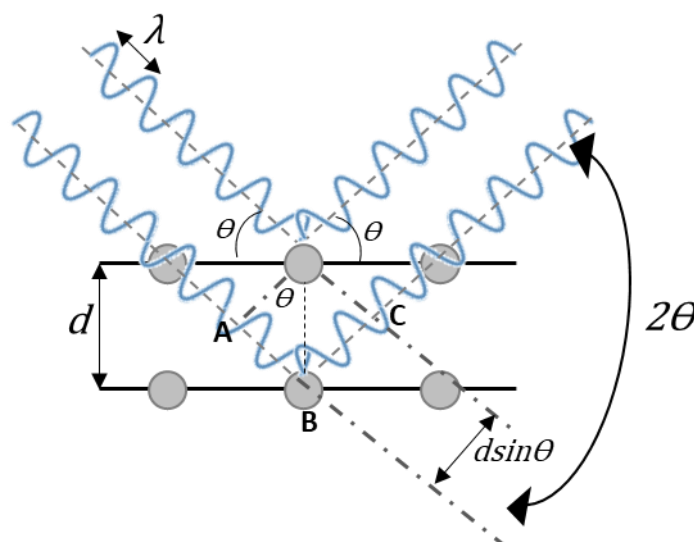
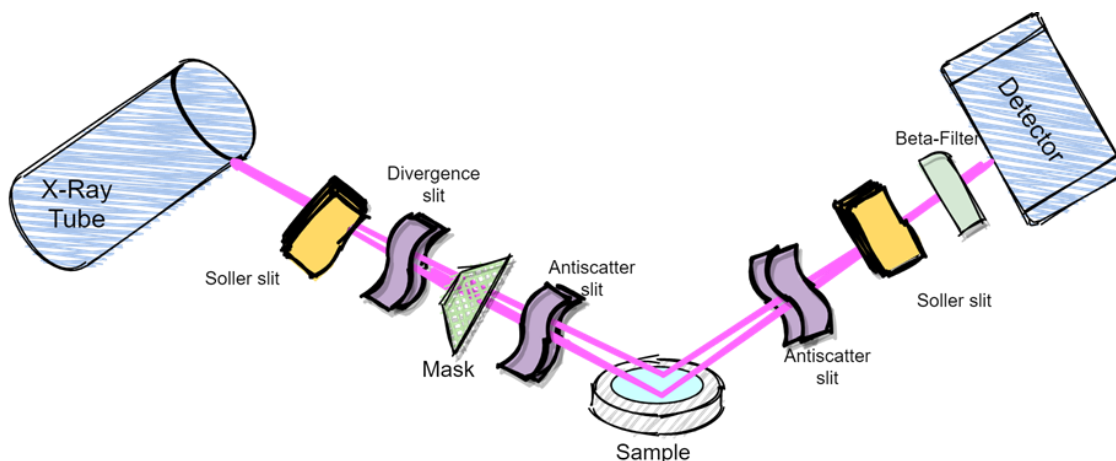


Figure 1. Bragg's law

The X-Ray diffraction is a fundamental physical property of the crystalline phase. The experimental pattern obtained from the analysis show the intensities of the diffraction peaks (count or count/second) as a function of the angular position  $2\theta$ . The diffraction pattern is a fingerprint of each crystalline phase and it is useful for the unique identification of the phase and for complete interpretation of crystalline structure such as position of atoms and molecule in the space. Through diffraction patterns comparison, it is possible to highlight the different phases present in the sample (position of the peaks), their concentration (height or area of the peaks), the amorphous content (trend and area subtended to the background) and the size/deformation of the crystals (width and shape of peaks).<sup>2</sup>

The most common X-Ray diffractometer is in Bragg-Brentano or parafocusing reflection geometry in  $\theta/\theta$  mode in which the sample is kept fixed, while the X-ray tube and the detector rotate respectively at a speed of –

$\theta^\circ/\text{min}$  and  $+\theta^\circ/\text{min}$ . (Figure 2). This geometry, also called para-focusing, allows to use a flat sample holder, which is very easy to prepare. <sup>4</sup>



**Figure 2. Bragg-Brentano geometry**

The diffractometer is constituted by the source of X-Ray beam, X-Ray tube mainly with a Cu anode, a series of optical components (Figure 2), and the detector.

The divergence slit minimizes the equatorial divergence of the incident beam preventing the beam overflow phenomenon that is over-illumination of sample (Figure 3). While the anti-scatter slit limits the scatter contribution due to the air. Smaller divergence and anti-scatter slits reduce the irradiated sample and intensity of reflections accordingly. Additionally, the over-illumination of the sample is demarcated by the mask. It limits the width of the beam and it is chosen considering the type of sample holder. The soller slits are placed in both incident and diffracted beam. These optical components limit the axial divergence collimating the axial component of the X-ray beam. Left side of Figure 4 shows the axial divergence effect not collimated by soller slit, one of two rays shown illuminates center of the sample plane, while the second ray set at the same divergence angle hits the sample at its edge with smaller Bragg angle due to axial divergence. Right side of Figure 4 shows the effect of collimation of the soller slits. <sup>1,5</sup>

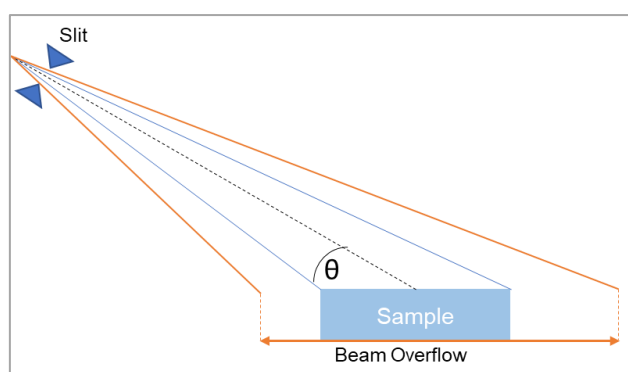


**Figure 3. Beam overflow**

The width of the anti-scatter slit in the diffracted beam depends on the diffractometer and the type of detector. In single point detector usually has the same width of the anti-scatter slit in the incident beam. When linear detectors are present, which collect several degrees at the same time, the anti-scatter slit is chosen in accordance with the collection window of the detector. This slit has the task to assure just reflected beam and no air scatter reaches the detector. The radiation produced in the source includes higher energy X-rays such as  $K\alpha_1$ ,  $K\alpha_2$  and lower energy radiation  $K\beta$  which can be easily removed by the Beta-filter, for the Cu radiation is a Nickel thin foil <sup>1</sup>.

The X-Ray powder diffraction (XRPD) is the mainly technique for the study of the solid state. One of the main advantages is its ease of use. The samples can be easily mounted and analysed with minimal operator intervention. Additionally, it is a non-destructive technique, since the sample can be studied without the need to be dissolved or destroyed. However, there are disadvantages in the use of XRPD due to its inaccuracy in the determination of quantities in non-homogeneous samples, in the size of crystallites, and the inability to detect trace phases.<sup>6</sup>

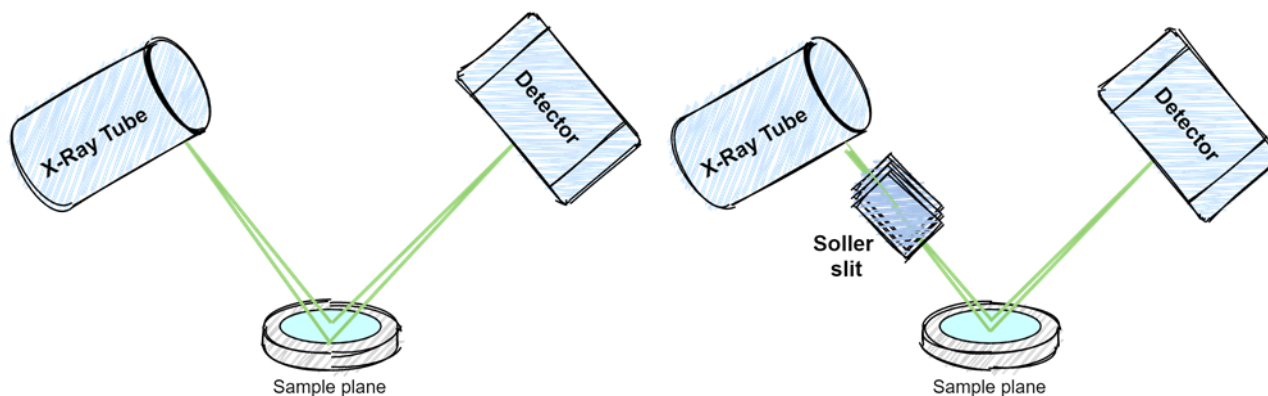


Figure 4. Axial divergence and collimation with soller slits

## 1.2 XRPD errors

It is essential to be aware of all the sources of errors to be able to minimize them and to perform good quality analysis. The errors on X-Ray analysis can be divided in accidental and systematic errors which can be due to the instrument and to sample and its preparation (Table 1). The main causes of accidental errors or instrumental aberrations include statistic of counting, stability of generator and of X-Ray tube and instrumental errors, while systematic errors include errors due to the sample, involving elemental interactions, as such as absorption or transparency, presence of defect and or strain, particle size, crystal size, surface, etc. The systematic errors due to instrumental can be controlled and avoid with suitable constructive solution and correct set of the instrument.<sup>7</sup>

Table 1. Type of error

Accidental errors or instrumental aberrations	<ul style="list-style-type: none"> <li>• statistic of counting</li> <li>• stability of generator and of X-Ray tube</li> <li>• instrumental errors</li> </ul>
Systematic errors	<ul style="list-style-type: none"> <li>• nature of the sample</li> <li>• instrumental errors</li> </ul>

The accuracy of any analysis depends on both systematic and accidental errors, establish the entity of the individual errors is important to have control over each of them.<sup>7</sup>

Concerning the accidental errors, the counting time, and the power of generator impact especially in the intensity of the measure. Depending on the purpose of the analysis, phase identification, quantitative analysis or lattice parameters determination, different level of signal to noise ratio are required and consequently different counting time and instrument configuration are chosen.<sup>8</sup> The instrumental aberration due to the slits' configuration will be discussed later. The systematic errors include error due to the nature of the sample and its preparation, and to geometry of the diffractometer and sample holder. Accidental and systematic errors affect the quality of the diffraction pattern, which is constituted by different element as described by the function:

$$y(2\theta_i) = \sum_p (S_p \sum_{(hkl)_p} (|F_{calc}((hkl)_p)|^2 \phi_{(hkl)_p}(2\theta_i - 2\theta_{(hkl)_p}) \text{Corr}_{(hkl)_p}(2\theta_i))) + Bkg(2\theta_i)$$

Where  $S_p$  is the scale factor, which is a correction constitutes by flexible exponential function chosen and combined according to the needs of the experiment.  $|F_{calc}((hkl)_p)|^2$  represents the peak intensity,  $\phi_{(hkl)_p}(2\theta_i - 2\theta_{(hkl)_p})$  describes the peak profile,  $Corr_{(hkl)_p}(2\theta_i)$  indicates the peak position, and  $Bkg(2\theta_i)$  represents the background intensity not related to the sample. Following, all the variables that impact these elements of the diffraction pattern and the quality of the analysis are summarized (Table 2) and examined. Other aspect that can impact the results of the analysis is the preparation of the sample, of course. Different pre-treatment of the sample, e.g., grinding of the powder, the choice of suitable sample holder and the preparation of the sample by operator are important aspect to consider.

**Table 2 Cause of error**

<b>Sample preparation</b>	<ul style="list-style-type: none"> <li>• Choice of suitable sample holder (sample holder scattering)</li> <li>• Sample particle size and homogeneity</li> <li>• Random orientation of crystallites in space</li> <li>• Sample surface (amount, smooth, flat, and horizontal)</li> <li>• Sample thickness</li> </ul>
<b>Peak position</b>	<ul style="list-style-type: none"> <li>• Unit cell</li> <li>• Wavelength <math>\lambda</math></li> <li>• Misalignment of the mechanical part (zero shift)</li> <li>• Vertical displacement of the sample surface</li> <li>• Sample transparency</li> </ul>
<b>Peak intensity</b>	<ul style="list-style-type: none"> <li>• Incident radiation intensity</li> <li>• Symmetry</li> <li>• Crystalline structure</li> <li>• Preferred orientation</li> <li>• X-ray absorption</li> <li>• Lorentz-polarization factor</li> <li>• Anomalous scattering</li> </ul>
<b>Peak profile</b>	<ul style="list-style-type: none"> <li>• Slit</li> <li>• Soller (peak asymmetry)</li> <li>• Crystallites size</li> <li>• Crystallites strain</li> <li>• Reticular defects</li> </ul>
<b>Background</b>	<ul style="list-style-type: none"> <li>• Lorentz-polarization factor</li> <li>• Air scattering</li> <li>• Sample holder scattering</li> <li>• Anomalous scattering</li> <li>• Amorphous scattering</li> <li>• Sample fluorescence</li> </ul>

### 1.2.1 Sample preparation

Sample preparation is extremely important for XRD analysis because several annoying effects can be introduced with an incorrect sample preparation that can severely affect the result. Some shrewdness can limit systematic errors in the analysis and improve its accuracy and reliability.

Suitable representative sampling of the bulk is the first condition to correctly analyse sample in all the analytical techniques. Moreover, the sample stability should be granted during the sample preparation and analysis.

In X-Ray powder diffraction the random orientation of the crystallites in the space is extremely important to avoid the preferred orientation phenomenon, which occurs when there is a strong tendency for the crystallites to be oriented in one direction, for instance in case of needles or plate. The preferred orientation affects the intensity of the peaks which are no more proportional to the amount of crystalline phase, avoiding the possibility

to run quantitative analysis.<sup>10</sup> Generally, in diffractometer with para-focusing geometry with flat sample, the sample preparation occurs using top-loading sample holder that can induce preferred orientation. This phenomenon can be minimize using different sample holder, as such as back-loading or side-loading. Otherwise, grinding of sample and reduction of the particle size promote random position of the particle during the sample preparation. At last, measurements in transmission mode with detector equipped with focusing mirror and rotating capillary, usually reduce the preferential orientation.<sup>4</sup>

To ensure optimal statistical homogeneity, another important factor is the particle size of the sample, on which it depends the number of particles analyzed on equal sample holder size. Considering a sample with diameter  $D = 10$  mm, thickness  $h = 0.1$  mm and ideal spherical particle with equal size and diameter =  $d$ , the number  $N$  of compactable particles in that volume is given by the following formula.

$$N = 1.1108 \frac{D^2 h}{d^3}$$

It appears that to ensure optimal statistics (particles analysed  $> 10^6$ ), particles should have a diameter  $d < 20$   $\mu\text{m}$ .<sup>2</sup> Crystallites must be small and uniform. Grainy sample with presence of small number of larger crystallites “rocks in dust” impacts the intensity and shape of the peaks, hence it is important in that case grinding the sample to reduce the crystallites and to uniform it.<sup>4</sup> Moreover, one deduces through this formula that the thickness of sample is equally relevant for amount of analysed sample and even for its absorption. Generally, the sample is irradiated by X radiation in the first fraction of mm beyond the surface, however this depends on the presence of high absorption elements in the sample. The sample must be sufficiently thick to limit the loss of photons which are neither absorbed nor diffracted due to the transparency of the sample.<sup>2</sup> Furthermore, it is important to ensure that the primary beam irradiates the sample without exceeding its size hitting the sample holder and causing the phenomenon of sample holder scattering. The portion of the sample analysed depends on the deviation of the primary radius (Divergence slit), the goniometer radius, the Bragg angle (range of analysis) and the length of the sample.<sup>2</sup>

Eventually, for a correct preparation of the sample the surface of the powder should be perfectly smooth (surface porosity  $< 10$   $\mu\text{m}$ ), flat and horizontal, in particular with highly absorbent samples.

### 1.2.2 Peak position

The detection of correct peak position and intensity is fundamental. In fact, the USP chapter <941> reports that the qualitative method by XRPD is usually based on the visual comparison of sample XRPD pattern to the experimental or calculated pattern of a reference material. Another criterion for the qualitative comparison between reference material and an unknown sample is to list the d-spacings or  $2\theta$ -diffraction angles and their normalized intensities [ $I_{\text{norm}}$ ] that represent the crystallographic fingerprint of the material. The tolerance range in the  $2\theta$ -diffraction angles between specimen and reference of the same crystal form is  $\pm 0.2^\circ 2\theta$ , except for hydrates and solvates, for which the tolerance can be greater than  $0.2^\circ 2\theta$ .<sup>8</sup>

The  $\theta$  value is measured as described by the formula below:

$$\theta_m = \theta_{d(hkl)} + \theta_o + \theta_p + \theta_{abs}$$

Where:

**Table 3. Peak position determination factors**

Parameter	Description
$\theta_{d(hkl)}$ <b>d(hkl) plane</b>	It depends on the spacing between the parallel set of lattice planes with Miller index <i>hkl</i> .
$\theta_o$ <b>Offset error</b>	It is due to: <ul style="list-style-type: none"> <li>• <b>Misalignment</b> of the mechanical part;</li> <li>• <b>Specimen displacement</b></li> </ul>
$\theta_p$ <b>Individual peak error</b>	It is different for each peak and depends on: <ul style="list-style-type: none"> <li>• the height of the peak,</li> <li>• the standard deviation,</li> <li>• the intensity of the background,</li> <li>• the time needed to acquire the profile,</li> <li>• the total integrated signal,</li> <li>• the number of points in the peak.</li> </ul>
$\theta_{abs}$ <b>Absorption error</b>	It depends on the nature of the atoms, especially, in organic material, which are non-absorbing and are affected by transparency

The X-ray diffraction phenomenon is resulted by an incident X-Ray beam scattered with constructive interference in the same direction of reflection one by crystalline lattice planes with Miller index *hkl*. This is described by Bragg's law, reported previously.

Therefore, the peak position  $\theta$  depends on spacing between the parallel set of lattice planes with Miller index *hkl* and the  $\lambda$ . The  $\lambda$  is determined by the anode (Cu, Cr, Mo, W). Generally, the copper radiation ( $\lambda = 1.54056 \text{ \AA}$ ) is used. As reported the peak position  $\theta$  depends on the lattice distance *d* of the crystalline, hence any variation occurred in the planar distance, for example due to thermal expansion, causes a shift of the peaks. On the other hand, the precise and accurate determination of the peak position gives insight in the cell parameters and structure.

The correct determination of  $\theta_{d(hkl)}$  of the reflection can be affected by several errors, reported in Table 3, among including offset errors due to misalignment and specimen displacement.

Misalignment of the mechanical part can be overcome by monitoring the diffractometer performance and alignment of the diffractometer by the calibration check using a certificate standard as silicon powder.

Hence, the main source of offset error ( $\theta_o$ ), is the specimen displacement that can be due to:

- Sample preparation;
- Sample holder.

The sample and the mounting of the specimen in a suitable holder are critical steps in many analytical methods, particularly for X-Ray Powder Diffraction analysis. The sample preparation and the different sample holder can affect the measurement causing a shift of the peaks. The sample surface that is offset by *D* with focal plane causes systematic errors in the peak position that are very difficult to avoid entirely (Figure 5). Typically, an offset *D* = 15  $\mu\text{m}$  causes a horizontal shift of the order of  $+0.01^\circ 2\theta$  at low angles. The delta shift is function of  $\theta$ , but the peaks translation will be in the same direction for all the peaks. <sup>8</sup>

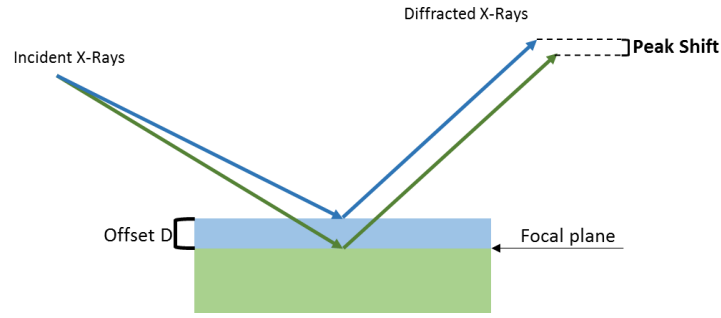


**Figure 5 Specimen displacement**

Moreover, the relevance of correct evaluation of the appropriate data treatment is pointed out to obtain the best peak profile and accurate peak positions extrapolation by function, which is usually based on Gaussian and Lorentzian functions and different combination of them. The use of different function can affect the  $\theta$  position. Indeed, good description of the diffractogram is obtained when the calculated pattern fits with the experimental one.

Lastly, the absorption error can be minimize the contribution of the plate using zero-background-plates constituted by silicon or quartz. <sup>2</sup>

### 1.2.3 Peak intensity

The diffracted intensity is proportional to the incident radiation intensity, which is related to the instrumental parameters, as such as divergence slit and soller that determine the divergence of the incident beam and thus the portion of the irradiated sample.

$$I_{hkl} \sim I_0$$

As summarized in Table 2, the peak intensity depends on several factors as described by the function:

$$I_{hkl} = K_e * K_{hkl} * \frac{1}{2} * \frac{1}{\mu}$$

Where  $K_e$  is the experimental constant constituted by  $\frac{I_0 \lambda^3}{(32\pi)(\frac{l_s}{R})r_e^2}$  wherein  $I_0$  = incident radiation,  $\lambda$  = wavelength,  $l_s$  = width of detector's slits,  $R$  = radius of the goniometer  $r_e = 7.9 \cdot 10^{-26}$  cm is the radius of electron. The  $K_e$  constant expresses influence of the experimental parameters.  $\mu$  is the linear absorption coefficient.  $K_{hkl}$  is the constant of the reflection  $hkl$  described by the function:

$$K_{hkl} = \frac{1}{V_c^2} m_{hkl} |F_{hkl}|^2 Lp_{hkl}$$

$K_{hkl}$  expresses the relation of the diffracted intensity with the volume of the unit cell ( $V_c$ ), the reflection multiplicity factor ( $m_{hkl}$ ), that considers the number of symmetry-equivalent reflections contributing to the single observed peak, the structure factor ( $F_{hkl}$ ), the Lorentz-polarization ( $Lp_{hkl}$ ). <sup>2,11</sup> Furthermore, the background intensity ( $Bkg(2\theta_i)$ ) due to air scattering, fluorescence, etc. <sup>8</sup>, is added to the diffracted intensity, and the function can be rewrote as:

$$I_{hkl} = \left( K_e * K_{hkl} * \frac{1}{2} * \frac{1}{\mu} \right) + Bkg(2\theta_i)$$

The Lorentz-polarization factors (Lp) is known trigonometric factor, resulted by the product of the Lorentz and polarization factors, that corrects the intensities of the x-ray diffraction spectra.

The Lorentz factor (or kinetic factor) depends on the instrument geometry and the method of recording and it considers the angular scanning rate  $\omega$ .

$$\text{Lorentz factor } (L) = \frac{1}{\sin^2\theta \cos\theta}$$

While the polarization factor depends only on the reciprocal lattice coordinate and it is unrelated to method of recording. It considers the polarization induced by a possible monochromator.

$$\text{Polarization factor } (p) = \frac{1 + \cos^2 2\theta}{2}$$

The structure factor  $F_{hkl}$  represents the wave diffracted by the unit cell relative to the  $hkl$  reflection. The structure factor formula is reported below <sup>12,13</sup>.

$$F_{hkl} = \sum_{j=1}^N f_j e^{2\pi i(hu_j + kv_j + lw_j)}$$

Where  $N$  represents the total number of atoms in the unit cell,  $f_j$  is the atomic scattering factor of  $j^{\text{th}}$  atom and  $u_j, v_j, w_j$  are the fractional coordinates of the  $j^{\text{th}}$  atom position in the unit cell. The intensity of the  $hkl$  reflection is proportional to the square of the structure factor. Therefore, the intensity is related to the indices  $hkl$ , and to the nature ( $f_j$ ) and the disposition ( $u_j, v_j, w_j$ ) of atoms in the unit cell, that means it depend on the crystalline structure and symmetry of the sample. <sup>12</sup>

Additionally, the intensity is proportional to the X-Ray absorption, already mentioned above. The X-Ray incident radiation  $I_0$  encounter the sample of thickness  $x$  and it is partly transmitted and partly absorbed causing a decrease in intensity  $I$  of an X-Ray beam proportional to distance travelled  $x$  and density ( $\rho$ ) of the sample.

$$I_x = I_0 e^{-\left(\frac{\mu}{\rho}\right)\rho x}$$

Where  $\mu$  is the linear absorption coefficient proportional to the density ( $\rho$ ).  $\mu/\rho$  is called Mass absorption coefficient (MAC), it is constant of the material and independent of physical state. Hence, crystalline or amorphous material with the same elemental composition and density are characterized by the same MAC.<sup>12</sup> The phenomenon of the preferred orientation of the crystallites, already introduced in the previous sections, causes a distortion of relative intensity inducing inaccuracy of quantitative data.

Additionally, the occurrence of extra-reflections apparently attributable to the sample, can sometimes cause complications in the interpretation of X-ray diffractogram. These reflections may derive from the anode of the X-Ray tube, by detector effects and abnormal reflections by the crystalline sample. It is an uncommon effect, although the anomalous scattering is difficult to recognize. A way to identify the presence of abnormal scattering is to analyse a "blank" to exclude signals due to the anode or detector. <sup>7</sup>

### 1.2.4 Peak profile

Theoretically, ideal powder diffraction pattern is characterized by narrow, symmetrical, positioned peaks. As already pointed out, several variables affect the diffraction pattern. Particularly, the symmetry of the peak is influenced by two mainly reasons: instrumental effects and real sample.

The instruments and the experimental setup affect the peak profile. The diffraction reflections are broadened by several aberrations inherent in the geometry of the instrument, such as slits. <sup>14</sup> As demonstrated by Riello et al. different instruments gives different asymmetry effect. <sup>15</sup> Another important aberration due to experiment setup is the axial divergence, that causes peak asymmetry, also effects in position, and width of the reflections especially at angle  $< 40^\circ 2\theta$ . <sup>16</sup> The axial divergence is due to the X-Ray beam divergence in the perpendicular direction along the axis of the goniometer which generates the asymmetry of the peaks, particularly evident at low angles. The asymmetry can be reduced by using Soller slits which better collimates the X-Ray beam but

unfortunately reduce the intensity of the incident radiation, so narrower Soller slits diminish the asymmetry and the intensity of the peaks.<sup>14-16</sup>

The instrumental contribution can be modelled by measuring NIST standard as Si.

The real sample is characterized by crystal size, domain size, stress, strain all factors that contribute on the final peak profile. Peak broadening and asymmetry indicate crystalline smallness and micro-stress, chemical heterogeneity, long-range internal stress, anisotropic crystalline shape, strain, size, and shape of crystallites. The peak width is expressed by the full width at half maximum (FWHM). The FWHM describes the width of a peak at half height. For the determination of the FWHM is crucial a good description of the baseline. If the baseline of the peak is ambiguous, for instance due to peak overlap, is difficult to establish where exactly half of the height is.<sup>17-20</sup>

The diffraction peak profile is described using a combination of Gauss and Lorentz functions, as Voigt function, that is a convolution of Gauss and Lorentz function and Pseudo-Voigt function, that is a weighted sum of Gauss and Lorentz function. The latter is easier to handle and represent a very good approximation to Voigt functions. Another function for the peak profile description is the Pearson-VII function. All the mentioned functions have in common symmetric, and lack of defined cut-off. The variables used in the determination of the best fitting profile can give information on the crystal size, defects etc.

Another difficult aspect in the description of the peak profile is the peak overlapping. Especially in organic compound, which are characterized by medium size cell and low symmetry, the peak overlap is elevate at high angle, therefore it is preferred to describe peak at low angle, although they are affected by instrumental aberrations. Nevertheless, good experimental setup should be used to minimize the aberration due to the instrument.

### 1.2.5 Background

As mentioned above, an accurate determination of background is essential for the subsequent accurate determination of all the parameters of diffraction pattern, as such as the peak height, the integrated intensity, the integral breadth. The background contributes to the intensity of the diffraction pattern and it is mainly generated by the scattering of the air and can be reduced by using monochromatic rays of a suitable wavelength and by removing air from the space between the sample and the detector.<sup>21</sup> Nevertheless, this is not the only source of background error and an appreciable error remains. Other contribution to the background can be the fluorescence scattering, Compton scattering, anomalous scattering, sample holder scattering, temperature diffuse scattering due to certain types of structural defects, and Lorentz-Polarization factor. Some of these have been previously discussed. Concerning the sample holder, the choice of suitable sample holder, and also experimental setup (slits) linked to the starting point is essential to avoid the sample holder scattering because the beam could hit it and origins to a signal not due to the sample. Other times the sample can contribute itself to an incorrect scattering, as in the case of fluorescence scattering. All the atoms of the crystal are bombarded by X-Ray radiation and themselves become a source of fluorescent radiation. If this radiation has enough energy to reach the detector it will have a background count increment. The magnitude of this background accretion depends on the diffusion power of the crystal, on the effectiveness of the detector and on the actuation due to the optical path distance between crystal and detector.<sup>7</sup> Additionally, presence of amorphous phase in the sample can affected the baseline of the pattern. In case of amorphous sample or sample containing an amorphous phase determination of the background is challenging due to the amorphous halo. Moreover, the determination of the background is arbitrary and subjective to operator. There are several ways to describe the background, as such as manually, using the peak finding of the software, using different function, for example polynomial of Chebishev.

## 2 AIM

The purpose is to experimentally evaluate the effects of systematic (instrumental aberration) and accidental error of X-Ray diffraction technique. Trust of own measure is essential. Understand the causes of which impacts the quality of the measure is crucial to sort the error out and improve the quality of the measure. Therefore, some experimental example of the effect of systematic errors and accidental errors are performed to point out the importance of the suitable experimental setup, sample preparation and sample holder choice.

## 3 EXPERIMENTAL PROCEDURE

For the experiments has been used PANalytical X'Pert PRO diffractometer with Bragg-Brentano geometry, Cu-K $\alpha$  radiation ( $\lambda = 1.54 \text{ \AA}$ ) and X'Celerator as detector.

### 3.1 Instrumental aberrations

As already noted, the most interesting characteristics in a diffraction pattern are the position of the peaks, determined by the size and symmetry of the unit cell, their intensity, influenced by the size of the crystals and by the geometry and setting of the instrument

The components of the diffractometer that most influence the quality and shape of the reflections are divergence, anti-scattering, and soller slits. The divergence of the primary beam is determined by the incident slits, while the diffracted beam is limited by the slits placed in front of the detector. The incident slit system determines the surface portion of the irradiated sample and affects the intensity and shape of the peaks, while the diffracted slit system influences the resolution of the reflections. Furthermore, the slits placed between the source and the sample have the function of limiting the primary beam to optimize the surface irradiated by the radiation avoid the beam overflow phenomenon and the irradiation of the sample holder.

Following are reported the results of the experimental performed changing the divergence slit (FDS) and correspondent incident antiscatter slit (FAS) and diffracted antiscatter slit, soller slits, and different sample holders.

The same sample has been analysed with different sample holder: PANalytical top loading 9430 018 13321 (a), PANalytical sample holder for non-standard sample and low angle analysis 9430 018 12001 (b), and PANalytical back loading sample holder 9430 018 11161 (c) (Figure 6).

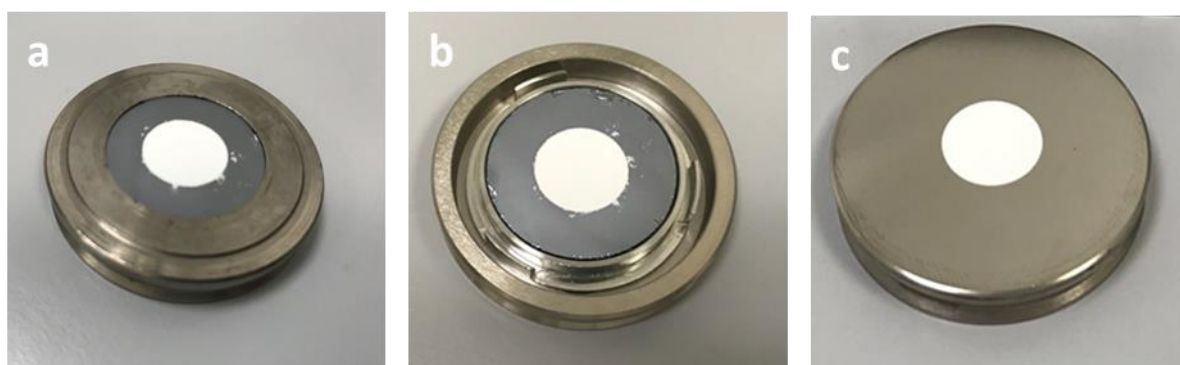
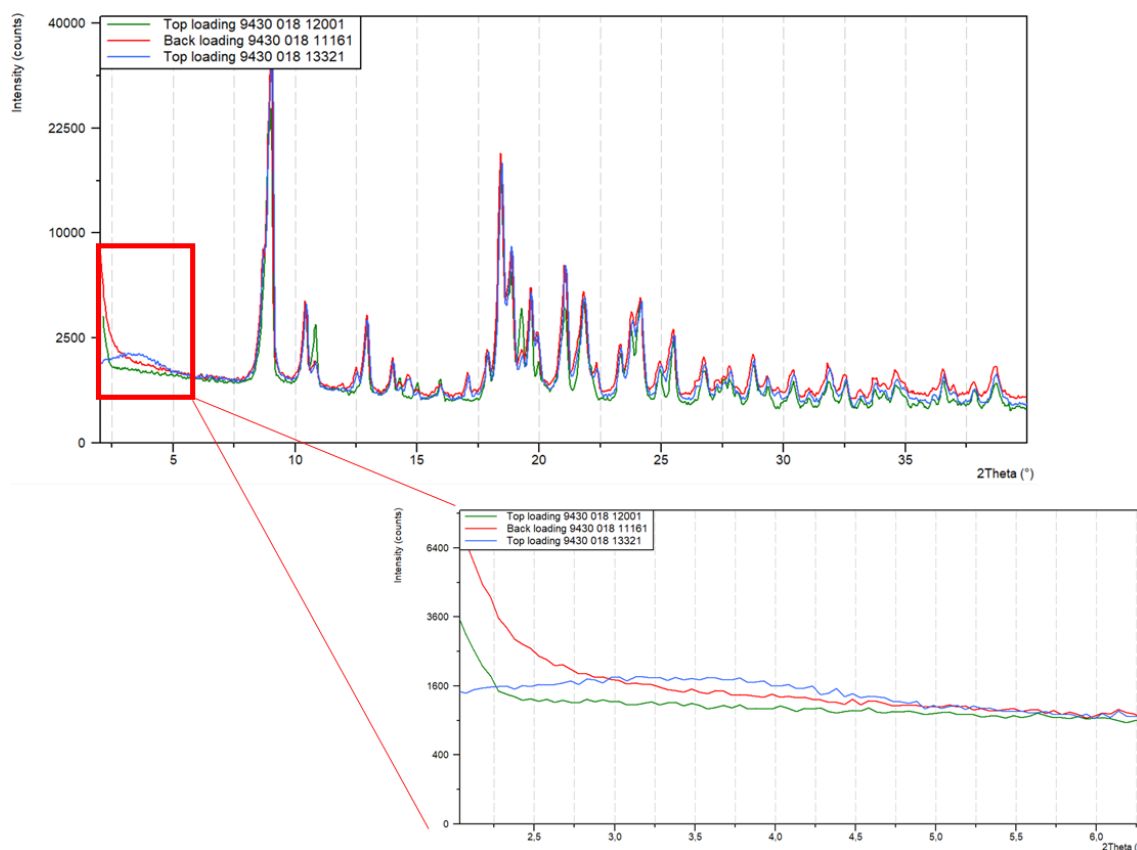


Figure 6. Sample holders: a) PANalytical top loading 9430 018 13321, b) PANalytical for non-standard sample 9430 018 12001 c) PANalytical back loading 9430 018 11161



**Figure 7. Example of effects of sample holder: XRPD pattern comparison of sample analyzed with PANalytical top loading 9430 018 13321 (blue line), PANalytical sample holder for non-standard sample and low angle analysis 9430 018 12001 (green line) and PANalytical back loading sample holder 9430 018 11161 (red line). The bottom image shows the magnification at low angle (range 2-6°2 $\theta$ )**

All the measurements have been detected with the same experimental setup: FDS 1/16°, FAS 1/8°, diffracted antiscatter slit 5.0 mm e soller 0.04 rad. Observing the pattern at low angle in Figure 7, the measurement obtained using the top loading 9430 018 13321 (blue line) shows little hump due to the irradiation of the sample holder. This sample holder is not suitable for analysis at low angle, while the other sample holder 9430 018 12001 (green line) and 9430 018 11161 (red line) are appropriate for analysis starting at low angle. In fact, the patterns obtained using these sample holders does not showed signal ascribable to the sample holder scattering but just signal due to the primary beam at the beginning of the pattern. The choice of the suitable sample holder is fundamental in case of sample with reflection at low angle. Indeed, this signal cannot be detected using the wrong sample holder because the sample holder scattering could cover the sample signal.

Figure 8 shows the XRPD pattern comparison of sample analysed with different experimental set up: FDS 1/4° - FAS 1/2° and FDS 1/16° - FAS 1/8°, the mask and the diffracted antiscatter slit was fixed at 15 mm and 5.0 mm, respectively. FDS equal and lower 1/2° requests diffracted antiscatter slit of 5.0 mm.

Observing the measurements at low angle ( $2\theta < 4$ ), the primary beam is observed in the set up FDS 1/4° - FAS 1/2°. Indeed, analysis at extremely low angle needs lower slits to avoid the detection of primary beam and sample holder scattering. Concerning the reflections, using narrower slits (FDS 1/16° - FAS 1/8°, red line) the intensity is significantly reduced due to lower quantity of irradiated sample. Although, the FWHM does not undergo substantial changes (FDS 1/4° - FAS 1/2°: 0.241 and FDS 1/16° - FAS 1/8°: 0.247).

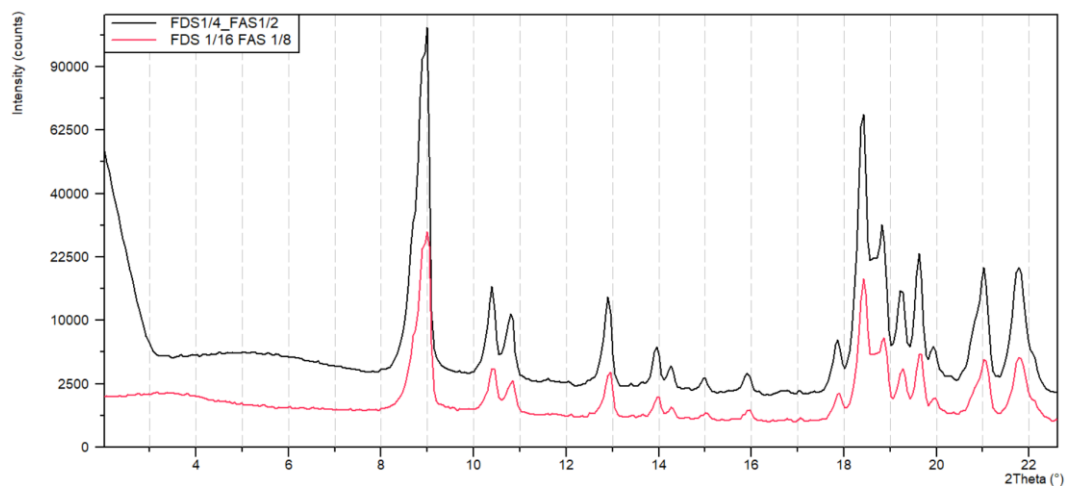


**Figure 8. Example of effects of instrument set up: XRPD pattern comparison of sample analyzed with different slit setup: FDS 1/4° - FAS 1/2° and FDS 1/16° – FAS 1/8°**

The soller slits are placed before and after the sample to limit the axial divergence of the primary and secondary beams. As shown in Figure 9, using Sollers with a smaller angular aperture (red line) remarkable reduction of intensity was obtained with gain in resolution and symmetry of peaks.

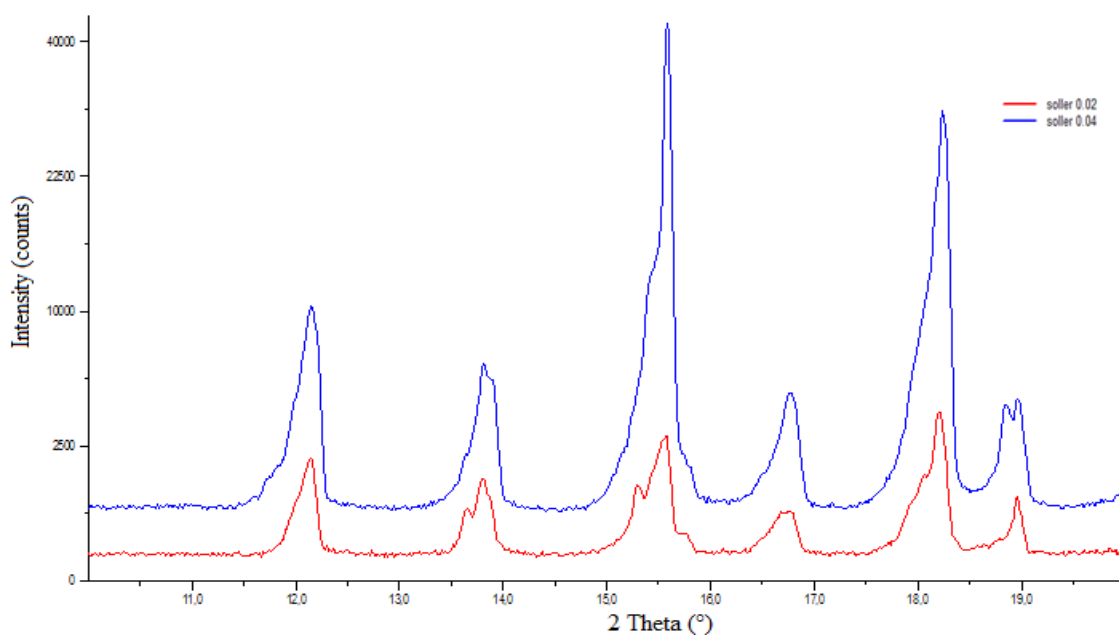


**Figure 9. Example of effects of instrument set up: XRPD pattern comparison of sample analyzed with different soller slit: 0.04 rad. (blue line) and 0.02 rad. (red line)**

The counting time is another important parameter to collect accurate diffractograms. Figure 10 reports the comparison between the same sample analysed with different time (seconds) per step. The sample contains low percentage of crystalline phase, the increasing in time per step allows the detection of the small crystalline peaks thanks to significant improvement in signal to noise ratio. The peaks are not detected with collection time of 120 and 300 sec, blue and red line, respectively. Increasing the collection time to 1000 seconds per step the peaks of the crystalline phase are detected (green line).

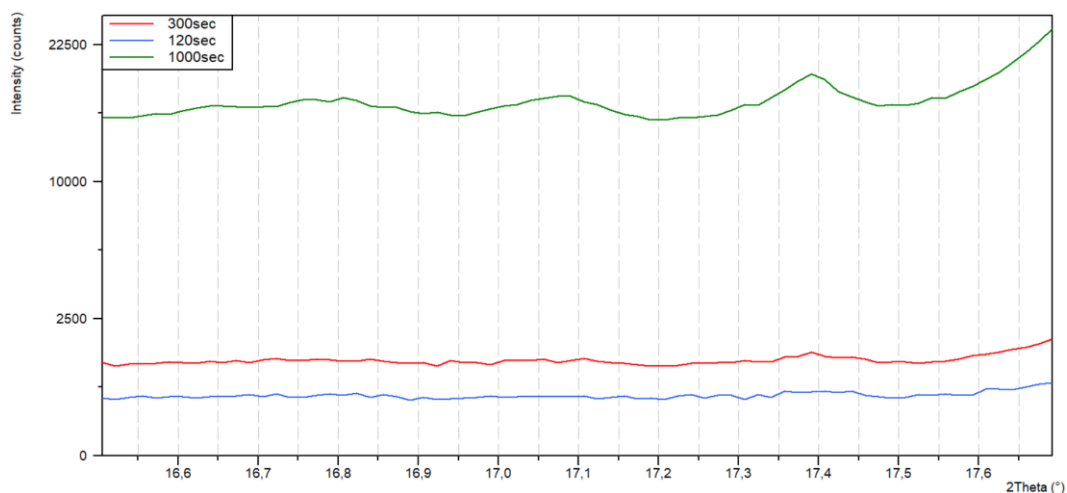


**Figure 10. Example of effects of time of analysis: XRPD pattern comparison of sample analyzed with different counting time: 120 sec (blue line), 300 sec (red line) and 1000 sec (green line)**

Further important parameters to consider especially during the quantitative evaluation is the stability of the generator and the X-Ray tube, that affected the intensity of the reflection as shown in Figure 11. The silicon standard has been analysed with different setup of generator power to simulate the decay of the natural lamp, fundamental factor to consider during quantitative method development because it significantly affects the intensity of the signal.

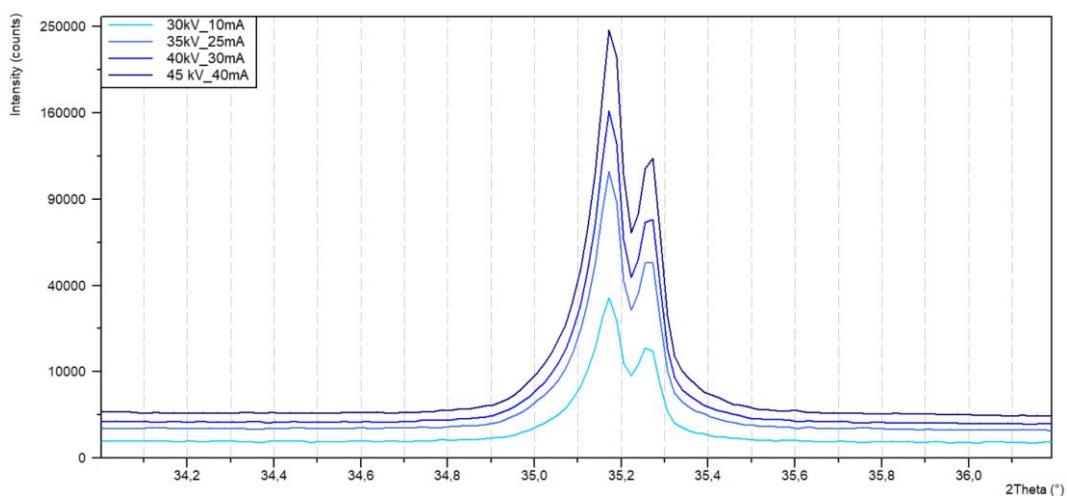


**Figure 11. Example of effects of lamp decay: XRPD pattern comparison of silicon standard analysed using different setup of generator power**

### 3.2 Systematic errors

Many diffractometric systematic errors can be directly related to sample preparation. The ideal sample is constituted by large number of randomly oriented crystals with respect to the incident beam in a homogeneous powder. Therefore, to improve homogeneity, grainy samples should be ground to obtain fine powder which usually helps to minimize preferential orientation and avoid the presence of rocks. Additionally, the amount of sample placed on the sample holder and the fill of the sample holder are fundamental.

Figure 12 shows the effects of grainy sample (green line) compared to the same sample after grinding (red line). It is impressive how the XRPD patterns are different, to the untrained eye these XRPD patterns can appear of different polymorphs due to the wide variations in peak intensity, shape, and profile. Compared with the calculated pattern of the form (Figure 13, black line) can better evaluate the influence of bigger grain in the

sample over XRPD pattern intensity and profile. It is worth noting that ground sample's XRPD pattern is comparable to the calculated one, while the presence of grain in the not treated sample (green line) extremely impact the measure. The XRPD pattern of grainy sample shows altered intensity of the reflections due to preferred orientation phenomenon and it worth noting the presence of double signal in some peaks and the difference in shape and profile of the peaks, especially in the peak in position  $15^{\circ}2\theta$ .

This example evidences the grinding process can be essential to obtain solid measurement especially in case of grainy and orientated samples.

Grinding process can resolved the preferred orientation effect also in case of fine powdery samples that do not show bigger grain. Figure 14 showed the comparison of calculated XRPD pattern (black line) and XRPD patterns before (blue line) and after grinding (red line) of powdery sample that presents preferred orientation. It is worth noting the difference of peak intensity between sample before and after grinding, ground sample shows relative intensity of the peaks comparable to the calculated pattern. Differently than grainy sample, this sample shows alteration exclusively in intensity of the peaks and not in shape and profile, in fact no double peaks are detected.

Nevertheless, some sample are not stable to grinding process. In fact, as shown in Figure 15, grinding can promote amorphization of the sample indicated by broad and less intense peaks. Furthermore, the grinding process can trigger a transition process between two polymorphs.

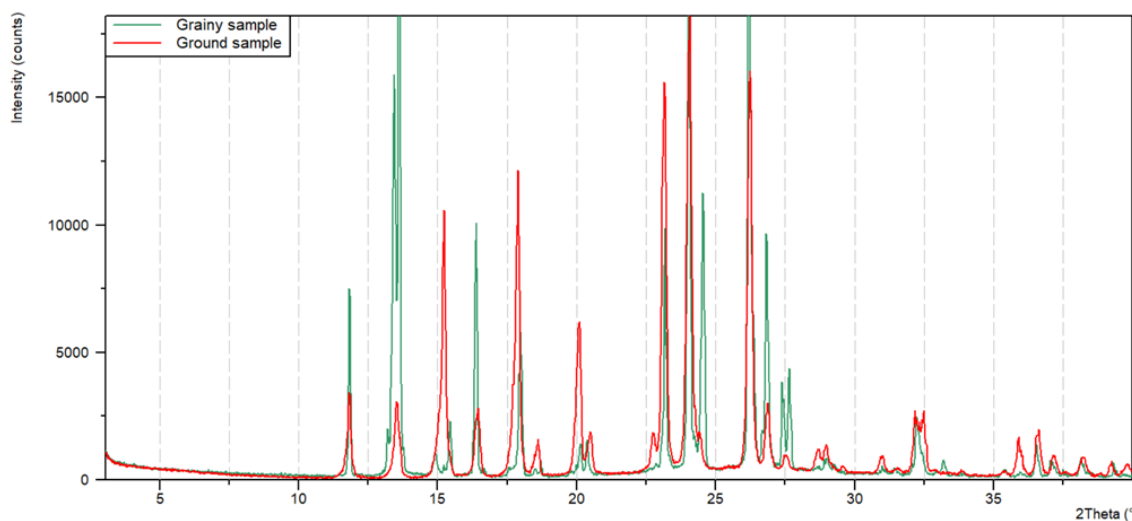


**Figure 12. Example of effects of grainy sample: XRPD pattern comparison between grainy sample before (green line) and after grinding (red line)**

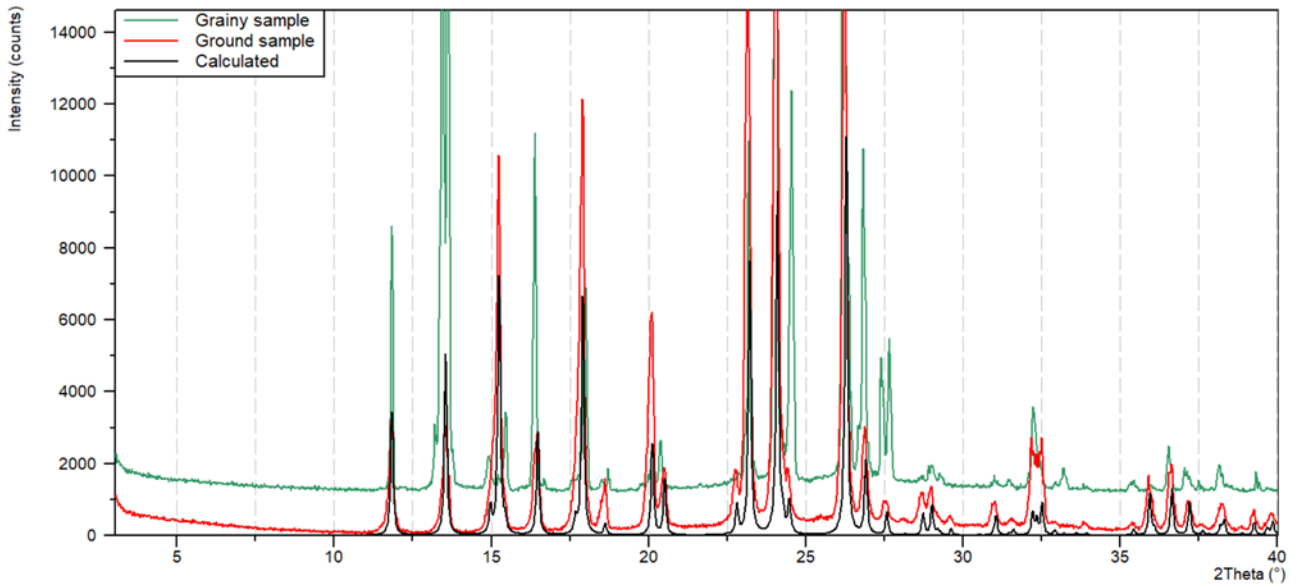


Figure 13. Example of grainy sample: XRPD pattern comparison between grainy sample before (green line) and after grinding (red line) and calculated pattern of the sample (black line)

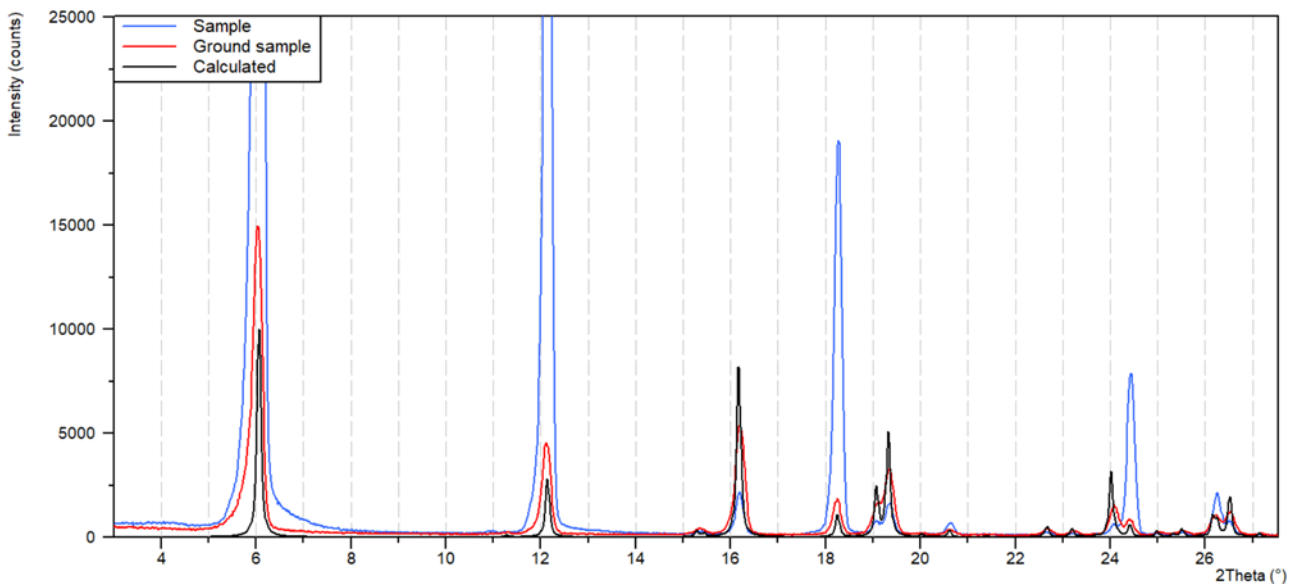
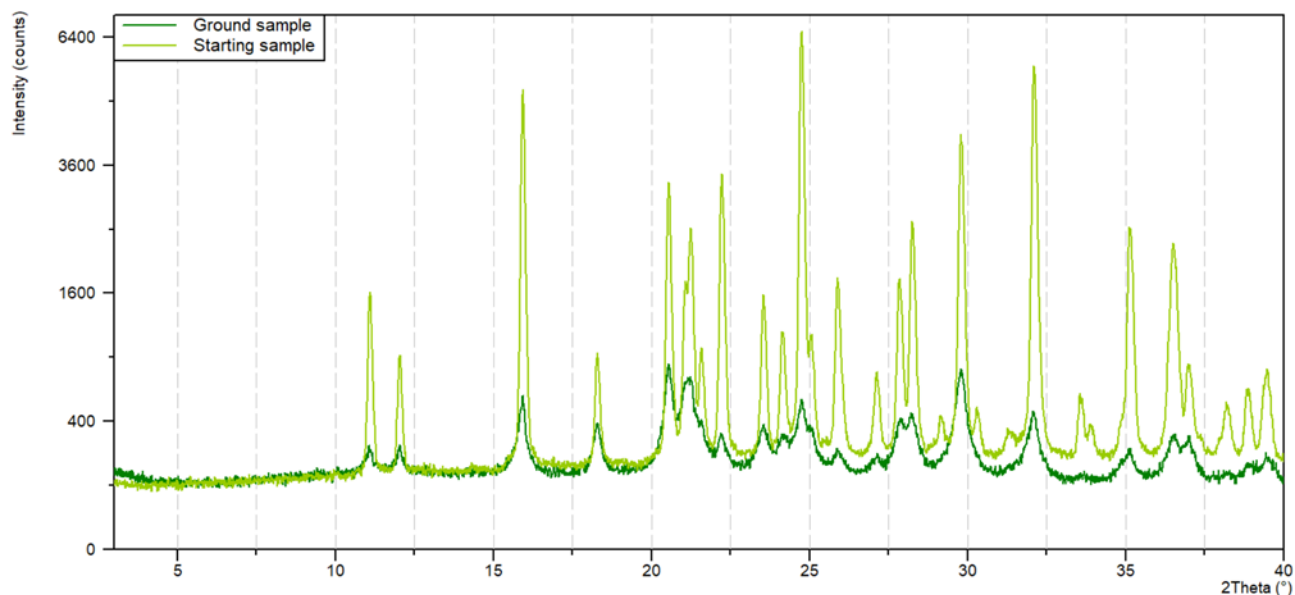


Figure 14. Example of orientated sample: XRPD pattern comparison between orientated sample before (blue line) and after grinding (red line) and calculated pattern of the sample (black line)



**Figure 15. Example of amorphization due to grinding**

Furthermore, preferred orientation phenomenon can be minimized using different sample holder. Sample preparation using top loading sample holder (Figure 16 a) could promote the preferred orientation disposition of the crystalline, as such as needle-like shape, on the sample holder to enhance the signal of mainly expose crystal planes. While side and back loading (Figure 16 b and c, respectively) should promote the random disposition in the space of the crystalline particles and avoid this phenomenon. Figure 16 reports the XRPD pattern of orientated sample prepared in three different sample holder a) top loading (red line), b) side loading (green line) and c) back loading (blue line) to evidence the difference of relative intensity of the reflections. The sample was not ground to evaluate exclusively the different impact of the sample holders. Observing the relative intensity of three patterns it is appreciable that the XRPD pattern collected using side loading sample holder (green line) shows relative intensity comparable between the peaks. Both the XRPD pattern obtained using top (red line) and back loading (blue line) show remarkable effect of preferred orientation evidenced by the higher relative intensity of the first peak, not comparable to the relative intensity of the other peaks.

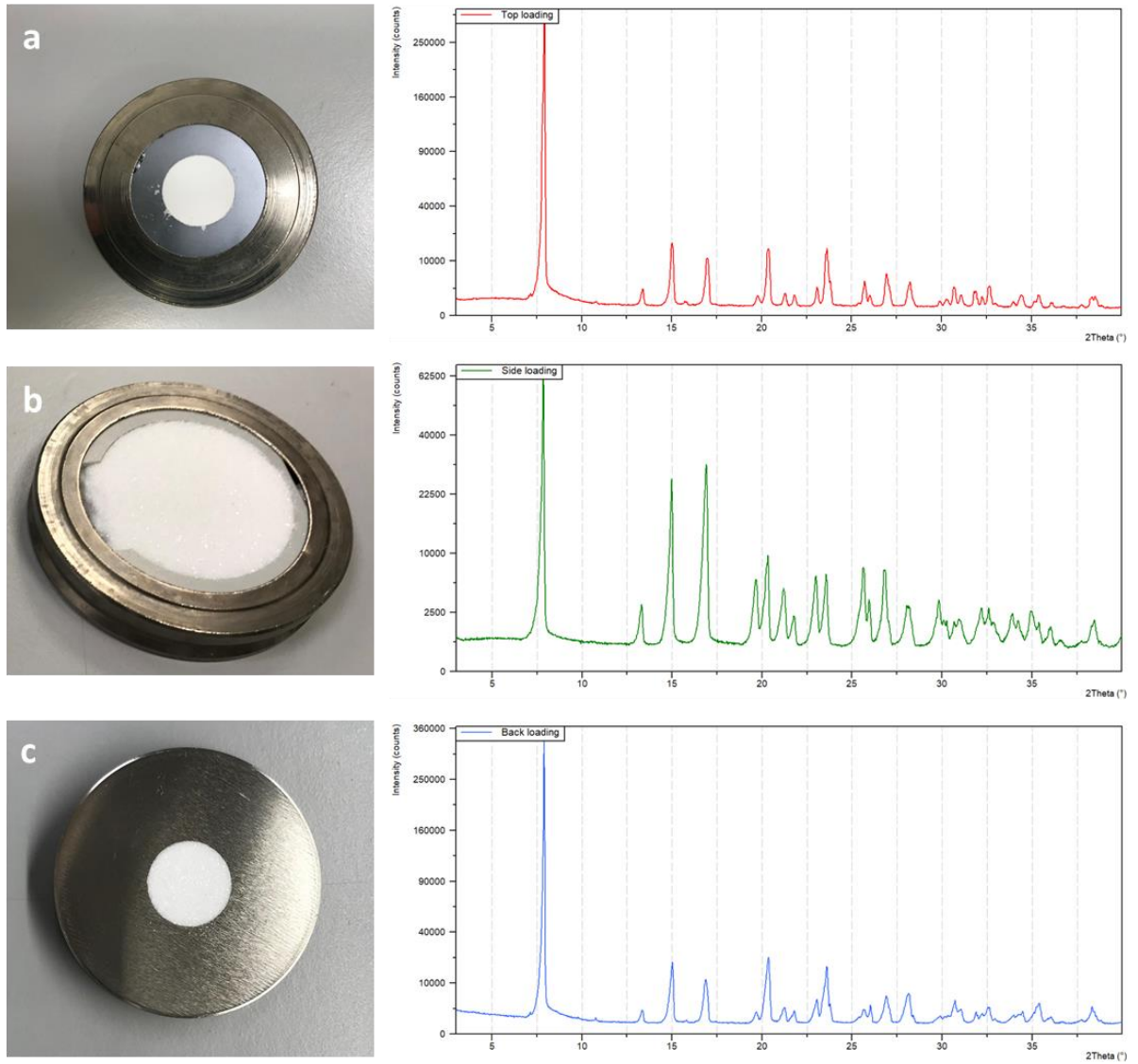
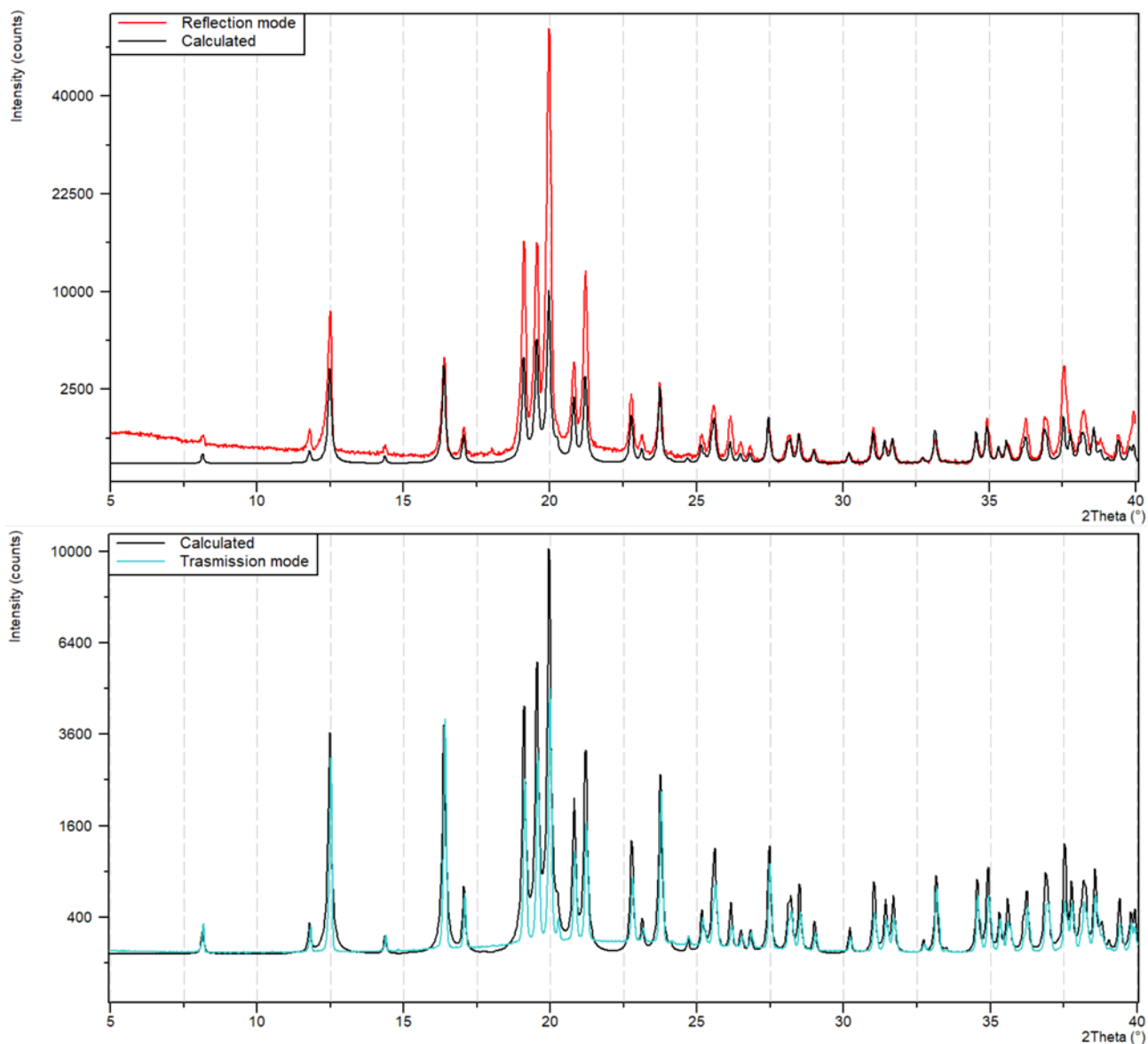


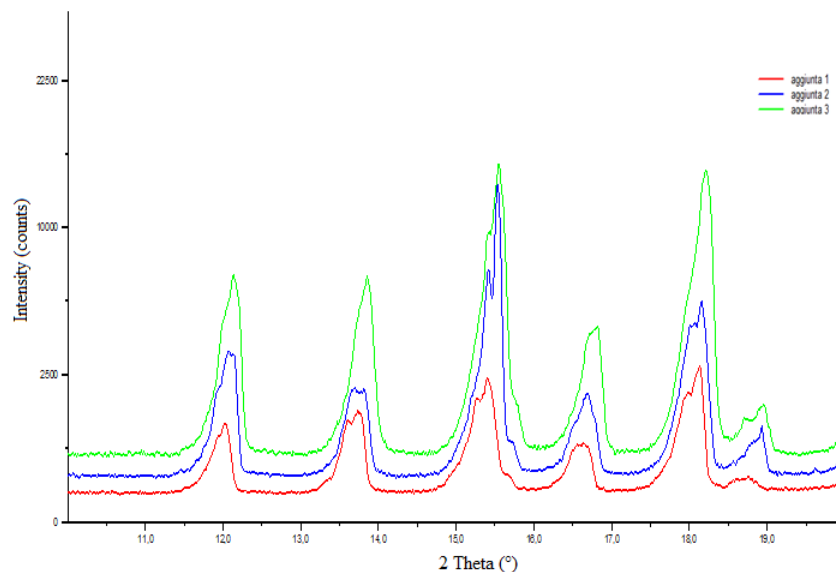
Figure 16. Example of orientated sample prepared with a) top loading (red line), b) side loading (green line) and c) back loading (blue line)

Figure 17 reports the XRPD pattern comparison between sample analysed within a capillary in transmission mode (cyan line) and on top loading sample holder in reflection mode (red line). The measurements are compared with the calculated pattern (black line) to evaluate the relative intensity. The XRPD pattern of the sample analysed in transmission mode shows relative intensity comparable to calculated pattern, while the same sample analysed in reflection mode shows slight preferred orientation phenomenon, especially evident in the highest reflections in the range 18-22°2 $\theta$ .



**Figure 17. Example of orientated sample: XRPD comparison between sample collected in reflection mode (red line), transmission mode (cyan line) and calculated pattern (black line)**

Concerning sample preparation and the amount of analysed sample, the same sample has been analysed with successive addition of powder. Increasing quantities of the sample results in an increase of the intensities and amplitudes of reflections and not negligible shifts in the position of the peaks, due to transparency of the sample (Figure 18).



**Figure 18. XRPD pattern comparison of sample with increasing amount of powder**

#### **4 CONCLUSION**

The X-Ray diffraction is powerful and useful technique for the study of solid-state. It is simple not destructive technique that does not require elaborated sample preparation. Nevertheless, to obtain accurate measurement it is fundamental to not underestimate the importance of the suitable choice of experimental setup, suitable sample holder and appropriate sample preparation. Performing accurate analysis is extremely important for the study of solid-state, especially in case of quantitative analysis. In fact, the preferred orientation phenomenon is the most diffuse effect that alters the relative intensity of peaks compared to the corrected relative intensity of the calculated pattern and especially it may cause errors in the quantification analysis. Nevertheless, this phenomenon can be mitigated with some precautions as such as grinding of the sample, suitable choice of the sample holder and the analysis mode.

## 5 REFERENCES

- (1) Ermrich, M.; Opper, D. *XRD for the Analyst: Getting Acquainted with the Principles*; PANalytical GmbH, 2011.
- (2) Guagliardi, A.; Masciocchi, N. *Analisi Di Materiali Policristallini Mediante Tecniche Di Diffrazione: Atti Della Scuola Di Diffrazione Da Materiali Policristallini: Martina Franca (Ta), Palazzo. 2007.*
- (3) Epp, J. 4 - X-Ray Diffraction (XRD) Techniques for Materials Characterization. In *Materials Characterization Using Nondestructive Evaluation (NDE) Methods*; Hübschen, G., Altpeter, I., Tschuncky, R., Herrmann, H.-G., Eds.; Woodhead Publishing, 2016; pp 81–124. <https://doi.org/https://doi.org/10.1016/B978-0-08-100040-3.00004-3>.
- (4) Whitfield, P. S.; Huq, A.; Kaduk, J. A. Specimen Preparation. In *International Tables for Crystallography Vol. H*; 2019; pp 200–218.
- (5) Ida, T. Formula for the Asymmetric Diffraction Peak Profiles Based on Double Soller Slit Geometry. *Rev. Sci. Instrum.* **1998**, 69 (6), 2268–2272. <https://doi.org/10.1063/1.1148930>.
- (6) Vippagunta, S. R.; Brittain, H. G.; Grant, D. J. W. Crystalline Solids. *Adv. Drug Deliv. Rev.* **2001**, 48 (1), 3–26. [https://doi.org/10.1016/S0169-409X\(01\)00097-7](https://doi.org/10.1016/S0169-409X(01)00097-7).
- (7) Jenkins, R.; De Vries, J. L. *Practical X-Ray Spectrometry*; Macmillan Education UK, 1970. <https://doi.org/10.1007/978-1-349-00055-5>.
- (8) USP-NF Unites States Pharmacopeia and National Formulary. (941) Characterization of Crystalline and Partially Crystalline Solids BY X-Ray Powder Diffraction (XRPD). 2019.
- (9) Otwinowski, Z.; Borek, D.; Majewski, W.; Minor, W. Multiparametric Scaling of Diffraction Intensities. *Acta Crystallogr. Sect. A Found. Crystallogr.* **2003**, 59 (3), 228–234. <https://doi.org/10.1107/S0108767303005488>.
- (10) Campbell Roberts, S. N.; Williams, A. C.; Grimsey, I. M.; Booth, S. W. Quantitative Analysis of Mannitol Polymorphs. X-Ray Powder Diffractometry - Exploring Preferred Orientation Effects. *J. Pharm. Biomed. Anal.* **2002**, 28 (6), 1149–1159. [https://doi.org/10.1016/S0731-7085\(02\)00053-5](https://doi.org/10.1016/S0731-7085(02)00053-5).
- (11) Pickworth Glusker, J.; Trueblood, K. N. *Crystal Structure Analysis: A Primer*; Oxford University Press, Ed.; 2010.
- (12) Waseda, Y.; Matsubara, E.; Shinoda, K. *X-Ray Diffraction Crystallography*; Springer-Verlag, 2011. <https://doi.org/10.1007/978-3-642-16635-8>.
- (13) Buerger, M. J.; Klein, G. E. Correction of X-Ray Diffraction Intensities for Lorentz and Polarization Factors. *J. Appl. Phys.* **1945**, 16 (7), 408–418. <https://doi.org/10.1063/1.1707608>.
- (14) Parrish, W.; Lowitzsch, K. Geometry, Alignment and Angular Calibration of X-Ray Diffractometers. *Am. Mineral.* **1959**, 44.
- (15) Riello, P.; Canton, P.; Fagherazzi, G. A Semi-Empirical Asymmetry Function for X-Ray Diffraction Peak Profiles. *Powder Diffr.* **1995**, 10 (3), 204–206. <https://doi.org/10.1017/S0885715600014779>.
- (16) Finger, L. W.; Cox, D. E.; Jephcoat, A. P. Correction for Powder Diffraction Peak Asymmetry Due to Axial Divergence. *J. Appl. Crystallogr.* **1994**, 27 (pt 6), 892–900. <https://doi.org/10.1107/S0021889894004218>.
- (17) Muhammed Shafi, P.; Chandra Bose, A. Impact of Crystalline Defects and Size on X-Ray Line Broadening: A Phenomenological Approach for Tetragonal SnO<sub>2</sub> Nanocrystals. *AIP Adv.* **2015**, 5 (5). <https://doi.org/10.1063/1.4921452>.
- (18) Ungár, T. Microstructural Parameters from X-Ray Diffraction Peak Broadening. *Scr. Mater.* **2004**, 51 (8 SPEC. ISS.), 777–781. <https://doi.org/10.1016/j.scriptamat.2004.05.007>.
- (19) Balzar, D.; Audebrand, N.; Daymond, M. R.; Fitch, A.; Hewat, A.; Langford, J. I.; Le Bail, A.; Louër, D.; Masson, O.; McCowan, C. N.; Popa, N. C.; Stephens, P. W.; Toby, B. H. Size-Strain Line-Broadening

Analysis of the Ceria Round-Robin Sample. *J. Appl. Crystallogr.* **2004**, 37 (6), 911–924. <https://doi.org/10.1107/S0021889804022551>.

- (20) Mittemeijer, E. J.; Welzel, U. The “State of the Art” of the Diffraction Analysis of Crystallite Size and Lattice Strain. *Zeitschrift fur Krist.* **2008**, 223 (9), 552–560. <https://doi.org/10.1524/zkri.2008.1213>.
- (21) Mitra, G. B.; Misra, N. K. Background Errors in X-Ray Diffraction Parameters. *Br. J. Appl. Phys.* **1966**, 17 (10), 1319–1328. <https://doi.org/10.1088/0508-3443/17/10/310>.

# CHAPTER 4

## UNIVARIATE QUANTITATIVE METHODS BY X-RAY POWDER DIFFRACTION

### 1 INTRODUCTION

The importance of the different properties of different solid forms, especially in pharmaceutical fields, is well established. The pharmaceutical companies spend energy and resources to identify the best API crystal form for the final formulation of the drug product. Metastable forms can be preferred than the thermodynamically stable polymorph because of their more solubility and dissolution rate. However, the possible transition to the thermodynamically stable form, which can be triggered by several variables such as humidity, temperature, and the presence of impurities, requires special attention when studying the stability of the crystalline form over time. In fact, the stability of the selected polymorphs must be guaranteed during and after the manufacturing process.<sup>1</sup>

Frequently, the qualitative identification of the form is not adequate alone and the quantitative determination is usually needed to assure that the transition is limited within the acceptable level and it does not compromise the product performance. The qualitative and quantitative method used to check the API crystal form in the bulk and in the product should be validated. The pharmaceutical companies need to develop, validate, and execute the qualitative and quantitative control in GMP (Good Manufacturing Practice) quality system. Nevertheless, there is not a guideline that reports indication and acceptance criteria for the validation of quantitative method for the determination of polymorphs. Frequently, the pharmaceutical companies refer to the ICH Q2 R(1) guideline for the validation of HPLC methods. The guideline ICH Q2 (R1) points out that the main purpose of validation of an analytical method is to demonstrate that the procedure is suitable for its intent.<sup>2</sup>

Several techniques are suitable for development of quantitative evaluation of solid state as well as for the characterization of polymorphs, such as IR, Raman, NMR, and especially X-Ray Powder Diffraction (XRPD). USP indicates the use of X-Ray Diffraction technique for the solid state qualitative and quantitative analysis.<sup>3</sup>

#### 1.1 Quantitative analysis in X-Ray Powder diffraction

The XRPD is widely used for qualitative analysis of crystal form (identification) and quantitative analysis of mixtures of crystalline polymorphs and for determination of crystallinity degree (amorphous and crystalline form quantification).

The hypothesis of a quantitative use of the technique dates back to the discovery of the technique by Max von Laue in 1912.<sup>4</sup> In 1919 Hull affirmed the potential use of the technique for quantitative analysis demonstrating that the data obtained with a mixture is a superimposed sum of data of the pure components, in position and intensity of the lines quantitatively.<sup>5</sup> It was not until 1948 with Klug and Alexander that the first theoretical treatment about quantitative analysis by X-Ray Powder Diffraction has been developed<sup>6</sup> and from then the quantitative analysis has advanced.

The basic equation relating the intensity of the reflections to the composition of the sample is

$$I_{(hkl)\alpha} = \frac{K x_{\alpha}}{\rho_{\alpha} [x_{\alpha} (\mu_{\alpha}^* - \mu_M^*) + \mu_M^*]}$$

Where  $I_{(hkl)\alpha}$  is the intensity of the hkl reflection of the component  $\alpha$ , K is a constant which depends on the instrument, as such as slit size and goniometer radius, and on the sample,  $x_{\alpha}$  is the weight fraction of the component  $\alpha$ ,  $\rho_{\alpha}$  is its density,  $\mu_{\alpha}^*$  and  $\mu_M^*$  are the coefficient of mass absorption of the component  $\alpha$  and the mixture, respectively.<sup>4</sup>

The value of the coefficient of mass absorption of the mixture  $\mu_M^*$  is given by the weighted mean of the value of coefficient of mass absorption of all the components of the mixture, and it is generally unknown. Theoretically, its value can be experimentally obtained because the K value can be obtained by measure of the pure reference.<sup>7</sup> Predominantly, the quantitative methods have the objective to determine or eliminate the contribution of  $\mu_M^*$ .<sup>4</sup>

The mass absorption coefficient of the analyte  $\alpha$  and the mixture coincides ( $\mu_{\alpha}^* = \mu_M^*$ ) in mixture of polymorphs of the same substance. In this case, the concentration  $x_{\alpha}$  is directly proportional to the intensity. In case of  $\mu_{\alpha}^* \neq \mu_M^*$  the correlation between concentration and intensity deviates from the linearity. This deviation from linearity is severe in case of inorganic compounds, which are characterized by high and very different mass absorption coefficient, whereas organic compounds have relatively low and narrowed range of mass absorption coefficient that does not severely affect the linearity. <sup>1,6</sup>

The formula reveals that the quantitative phase analysis is based on the integrated intensity of a reflection of the phase  $\alpha$ , although the quantitative phase analysis can be based also on the peak height or area of several reflections or on the full pattern. <sup>1,3,4</sup>

The main difficulties encountered in solid state quantitative method development are related to the sample preparation. The accuracy and precision of the method are affected by the characteristic of the sample, particularly by the homogeneity of all phases, particle size distribution in each phase, and to matrix effects. The inhomogeneity of the mixtures and samples is a common issue of the solid state analysis that extremely affect the quantitative method by XRPD and other techniques, often the problem is minimized reducing the particle size of the sample. <sup>8-10</sup> Furthermore, the reduction of particle size by grinding minimizes the preferred orientation phenomenon that affect the quantitative analysis, and sufficiently small particle size should make negligible the micro absorption effect. <sup>6</sup> Nevertheless, in case of organic compound the grinding of the powders can potentially promote the phase transition or amorphization. It is of particular concern because it irretrievably affects the quantitative analysis. For this reason, the quantification of organic metastable compounds and amorphous phase is extremely problematic because of the preparation of the standard mixtures is affected by the instability of the reference. <sup>1</sup>

Additionally, it is very important to ensure that the samples and the standards have the same particle size distribution. It is common that the samples are different than the standard mixtures artificially prepared with the products commercially available. <sup>11</sup>

The guidelines do not give acceptance criteria values for the development and validation of quantitative method in solid state. USP reports that the determination of amounts of crystalline phases as small as 10% can be achieved in favourable cases. <sup>3</sup>

Two approaches of quantitative method can be distinguished, the methods based upon on one reflection, namely traditional methods, or based on the whole pattern. The traditional methods are based on the highest single peak its area or less common the intensity of the reflection is plotted versus the concentration to determine the linear correlation with graphical and mathematical interpolation. <sup>12,13</sup> It is worth noting that the intensity is more sensible than the area to the nature of the sample i.e., different crystal size generates different intensity but not different area of the peak. <sup>11</sup> The traditional methods can be divided into absolute methods, based on the intensity of the pure phase, and relative, based on the ratio between the intensity of the pure phase and e.g., internal standard. <sup>4</sup> The absolute method is based on the ratio between intensity of  $\alpha$  phase in the mixture ( $I_{(hkl)\alpha}$ ) and in pure phase  $\alpha$  ( $I_{(hkl)\alpha}^0$ ) analysed at the same experimental condition. <sup>14,15</sup> This method gives reproducible results in case polymorphs where  $\mu_{\alpha}^* = \mu_M^*$ , otherwise the  $\mu_M^*$  should be determined to avoid deviation form the linearity and nonsense results.

$$\frac{I_{(hkl)\alpha}}{I_{(hkl)\alpha}^0} = \left(\frac{\mu_{\alpha}^*}{\mu_M^*}\right)x_{\alpha}$$

The method with the internal standard is based on the ratio of the intensity of the analyte  $\alpha$  and the internal standard ( $\beta$ ) both in the mixture, therefore the  $\mu_M^*$  is the same for both the phases and it is cancelled in the final equation

$$\frac{I_{(hkl)\alpha}}{I_{(hkl)\beta}} = K * x_{\alpha}/x_{\beta}$$

The proportional constant (K) between  $\frac{I_{(hkl)\alpha}}{I_{(hkl)\beta}}$  versus  $x_{\alpha}$  can be determined analysing standard mixtures with known fraction of  $x_{\alpha}/x_{\beta}$ . Successively, the  $x_{\alpha}$  of the sample is quantified adding known amount of  $\beta$  phase. <sup>7,16</sup> The compound used as internal standard should show low number of peaks and not overlapped with the peak

of the phase  $\alpha$ . It is recommended to use compound with similar mass absorption coefficient of the phase  $\alpha$ , to avoid micro absorption problem.<sup>4,17</sup> This approach is used by the method Reference Intensity Ratio (RIR) developed by Woolf and Visser, who indicates as internal standard the corundum.<sup>18</sup> The method is based on the ratio of the integrated intensity of the highest peak of the phase  $\alpha$  and the highest peak of corundum ( $hkl = 113$ ) in a mixture 50:50 w/w of phase  $\alpha$  and corundum.<sup>19,20</sup>

$$x_{\alpha} = \frac{I_{(hkl)\alpha}}{I_{113cor}} * x_{cor} / RIR_{\alpha,cor}$$

The RIR value of several crystalline phases are tabulated in database Powder Diffraction File (PDF) of ICDD. It is worth noting that the RIR method is considered as semiquantitative. It can be improved by using RIR values determined with the own instrument with the target samples.<sup>4</sup> Nevertheless, addition of internal standard may affect the analysis when the internal standard is not homogeneously mixed into the sample.<sup>17</sup> Alternatively, method based on external standard can be used. This method avoids the inhomogeneity problem potentially encountered in internal standard method and the different absorption between sample and standard does not affected the analysis.<sup>17</sup> Furthermore, the external standard method has the advantages that the sample are not spiked and contaminated by the standard and the standard is not consumed and can be measured several times, and the sample and standard are measured separately avoiding the interference and overlapping of the peaks.<sup>21</sup>

The internal or external standard application is useful to normalize the signal and eliminate the variation due to the fluctuation of the X-Ray source that affect the intensity of the peaks.

This method is used also in the case of amorphous and crystalline mixture because the scattered intensity by a compound, within the same measurement range, it is the same independently of its amorphous or crystalline state, because the number of electron has not changed. Chen et al. have demonstrated the application of the normalization of the signal of amorphous-crystalline samples with the integrated intensity of the 100% crystalline or amorphous reference.<sup>22</sup> Based on this assumption, other method normalizes the signal relating the integrated intensity of individual peak of the diffractogram to the total intensity of the sample's diffractogram. An example will be reported in this chapter.

Generally, the normalization of the signal contributes to minimize the variations due to the instrument fluctuation, although the large contribution of the measurement variation due to the inhomogeneity of the mixture and its sample still affects the results. Any quantitative method requires homogeneous mixing of calibration data set, it is extremely challenging for solid mixtures.<sup>22</sup>

The methods based on the whole pattern typically require more knowledge about the phases in the mixture than the traditional methods, except multivariate chemometric methods as such as Partial Least Squares (PLS). Through the data obtained by the single region or multiple regions of the pattern of a calibration set, ideally with wide source of sample variation, PLS constructs a predictive model for the determination of the samples based on the correlation of intensity and composition of the calibration set.<sup>23,24</sup>

Differently, other whole pattern methods such as Whole Powder-Pattern Decomposition (WPPD) and Rietveld methods require more information about the composition of the mixture and the crystalline structure of the individual phases. Generally, these methods are based to the achievement of best fit between the pure phases data and the experimental pattern and determination of the scale factor of individual phases. The intensity of the pattern ( $Y$ ) at step  $i$  can be described by the background ( $B$ ) function, the profile function ( $P$ ) and the scale factor ( $S$ ).

$$Y(2\theta_i) = B(2\theta_i) + \sum_{k=1}^N S_k \sum_j I_{jk} P(2\theta_i)_{jk}$$

$N$  is the number of components in the mixture,  $I_{jk}$  is the integrated intensity of the  $j^{\text{th}}$  reflection of the  $k$  phase. Different background and profile functions to describe the diffraction pattern are available.<sup>25</sup> The WPPD method applies the least-square refinement decomposing separately the diffraction patterns of the individual components of the mixture into peak profiles and background function to reach the best description. The scale

factor of the individual component is fixed to 1 ( $S_k^{single} = 1$ ). Successively, the WPPD is executed for the mixture sample and the quantification is occurred determining the scale factor of the integrated intensity of the phase being quantified so that the sum of the scale factors of individual phases in the mixture is equal to unity. The ratio  $S_k/S_k^{single}$  is analogous to the ratio of the individual peak  $I_{(hkl)\alpha}/I_{(hkl)\alpha}^0$ . In case of mixture containing amorphous phase, the scale factor of the amorphous phase can be determined adding a known quantity of a crystalline standard (internal standard) <sup>26</sup>

$$S_{amorphous} = 1 - \sum_{k=1}^{N-1} S_k^{crystalline}$$

The WPPD method requires knowledge of the sample composition, chemical composition and mass absorption coefficient of individual phases, and their unit cell parameters. The WPPD method does not require the structural parameters of the individual phases, differently by Rietveld method.

The Rietveld method requires the knowledge of the composition of the multicomponent sample and the structural parameters of each phase involving atomic coordinates essential for the calculation of the structure factor. The Rietveld refinement derives the scale factor of each phase describing the experimental pattern minimizing the difference between the intensity of the experimental pattern and the calculated pattern of the individual phases through the function:

$$Y_{ci} = S_k \sum_{hkl} L_{hkl} |F_{hkl}| P_{Bragg}(2\theta_i - 2\theta_{hkl}) PO_{hkl} A + B$$

Where  $Y_{ci}$  is the intensity calculated at individual point  $i$  in the diffraction pattern,  $L_{hkl}$  involves the Lorentz, polarization, and multiplicity factors,  $F_{hkl}$  is the structure factor of the  $hkl$  Bragg reflection,  $P_{Bragg}$  is the peak profile function,  $PO_{hkl}$  is the preferred orientation function,  $A$  is the absorption factor, and  $B$  represents the background intensity. It worth noting that Rietveld method can correct the preferred orientation phenomenon, although in slight amount. <sup>27</sup> As well as the WPPD method, adding known amount of internal standard in the sample containing amorphous phase its quantification is possible. <sup>28</sup> The Rietveld method is complicated method that requires qualified analyst and the transfer lab-to-lab is problematic and inadvisable. <sup>1</sup>

Concerning the amorphous and crystalline quantification, the USP reports simple method based on the whole pattern that relies on the ratio between the intensity or area of the crystalline part and the total intensity or area of the pattern constituted by the sum of the area of the crystalline and amorphous parts net to the noise. <sup>3,13,29</sup>

## 1.2 Univariate analysis

The univariate analysis is based on the assumption of linear relationship between an independent variable ( $x$ ), e.g., concentration, and a dependent variable ( $y$ ), consisting in measurable instrumental signal as peak intensity or area. This relationship between  $x$  and  $y$  is expressed by the equation:

$$y = a + bx$$

Univariate analysis involves the determination of a regression line which describes the trend between the instrumental signal ( $y$ ) in function of the concentration of the analyte ( $x$ ) and its coefficients  $a$  and  $b$  by the least square method.

The equation of the regression line can be described by:

$$y = a + bx + \varepsilon$$

Where  $\varepsilon$  represents the experimental variability associated to each measure of  $y$ . The least square mathematical process determines the regression line minimizing the summation of the mean quadratic deviations of the ordinates ( $y$ ) of the experimental data with respect to the corresponding ordinates of the points on the curve (back-calculated  $y$ ). This is equivalent to minimizing the quantity:

$$s_{y/x} = \sqrt{\frac{\sum_i^n (y_i - \hat{y}_i)^2}{v}}$$

Where  $y_i$  is the experimental value corresponding to  $i$  value in  $x$ -axis and  $\hat{y}$  denotes the predicted back-calculated value of  $y$  by regression line, and  $v$  is the number of freedom grade.

The quality of the linear correlation between  $y$  and  $x$  is statistically verifiable through the coefficient of correlation  $R$ , that described the goodness of the linear correlation and it is determined by the equation:

$$R = \frac{\sum_i [(x_i - \bar{x})(y_i - \bar{y})]}{\left\{ \left[ \sum_i (x_i - \bar{x})^2 \right] \left[ \sum_i (y_i - \bar{y})^2 \right] \right\}^{1/2}}$$

Where  $x_i$  is the concentration of  $i$ -th value,  $\bar{y}$  and  $\bar{x}$  represent the mean of the  $y$  and  $x$  values. The  $R$  value expresses the quality of the linear correlation, often reported as  $R^2$  which is the coefficient of determination. For both coefficient values can be in the range  $0 < R \leq 1$ , value of 1 denotes a perfect correlation.<sup>30,31</sup>

Once the analytical function of the calibration curve has been determined, it is possible to interpolate the analytical signal to unknown sample.

The regression line method is applicable to the X-Ray Powder Diffraction (XRPD) demonstrated by the equation:

$$I_i = K * X_{ij} / \mu_j$$

Where  $I$  is the intensity of the signal ( $y$ ) of the phase  $i$ ,  $X$  represents the variable  $x_i$  and is the weight fraction of the phase  $i$  in the sample  $j$ ,  $K$  is a constant depending on the nature of the phase, the specific peak, the instrument, and the intensity of the original beam, and  $\mu_j$  represent the average mass absorption coefficient of the sample determined by the sum of mass absorption coefficient of individual  $n$  phases in the sample multiplied by their weight fraction in the sample.<sup>16</sup>

To apply the regression method, it is needed adequate amount of pure analyte to prepare calibration standards for the construction of the calibration curve and evaluate the linear correlation between  $y$  and  $x$  within an interval containing  $x_0$  (unknown concentration to determine). Furthermore, another essential requirement is to individuate a specific signal without overlap with other signals and that depends exclusively on the concentration of the analyte ( $x$ ) and is independent from the matrix.

Deviation from the linearity of the analyte response due to the presence of chemical interferences, is the most frequently encountered problem in case of analysis of complex samples, e.g., pharmaceutical formulation containing several excipients and it is called matrix effect. The correction of the interferences of the matrix can be performed by applying the standard addition method (SAM). This method is applicable when the composition of the matrix is complex, and its nature is not completely known. It is based on addition of increasing known amount of pure analyte to the sample assuming that the interference is the same for both the pure analyte and the one already presents in the sample. The concentration of the analyte  $C_E$  net of spiked pure analyte is extrapolated by the regression line. It is possible to analyse the linear dependence and calculate the value of the concentration of analyte within the sample as following.

$$y = a + bC_E$$

$$C_E = (y - a)/b$$

The  $C_E$  concentration is extrapolated by  $y = 0$ .

$$C_E = a/b$$

Hence, the concentration of the analyte in the matrix can be extrapolated by the ratio between the intercept and the slope of the regression line.<sup>34</sup>

The SAM is a useful calibration method especially in analysis of pharmaceutical formulation including high number of excipients and in which is hard to find a specific peak of analyte, not subjected to overlapping with other matrix's signals. Unfortunately, it is characterized by elevated uncertainty and inaccuracy, which explain why the interpolation method is preferred. The deviation standard of the extrapolated concentration is determined by the equation:<sup>34</sup>

$$s_{x_E} = \frac{s_{y/x}}{b} \sqrt{\frac{1}{n} + \frac{\bar{y}^2}{b^2 \sum_i (x_i - \bar{x})^2}}$$

Another drawback of SAM is the necessary to construct a calibration curve for each unknown sample spiking it with different amount of pure analyte.<sup>32</sup>

To improve accuracy and precision the univariate method are applied in combination with internal standard method.<sup>16,33</sup>

The internal standard method consists in the addition of known quantities of internal standard to the sample. For each standard is detected the signal specific for the analyte  $S_A$  and the signal relating to the internal standard  $S_{IS}$ . The response ( $y$ ) is determined by the ratio between the signal of the analyte and the internal standard  $S_A/S_{IS}$ . In quantitative analysis by XRPD the application of internal standard is extremely useful because it corrects the possible instrumental error, especially the decay of the X-ray tube, that causes decrease of the intensity of the signal over time. The internal standard should have a simple diffraction pattern and with reflections that do not overlap those of the analyte of interest; be chemically stable, and have absorption coefficient similar to the sample. Usually, the used internal standard in X-Ray powder diffraction are stable compounds as alumina, silicon, or zinc oxide.<sup>1</sup>

The goodness of quantification is evaluated by the statistical tools, as such as  $R^2$ , standard deviation  $S_{y/x}$ , relative standard deviation (RSD%) and recovery %. Usually,  $R^2$  value should be higher than 0.99 but in solid-state quantification values higher than 0.9 are accepted. However, excellent  $R^2$  value does not guarantee good prediction of the real value of concentration ( $x$ ), when the standard deviation is high. The standard deviation value estimates the random errors in the  $y$ -direction.

Another measure of spread is the relative standard deviation %, which is given by  $RSD\% = 100 s/x$ , where  $s$  is the deviation and  $x$  is the mean of estimate value of the measured quantity.<sup>34</sup> The RSD% is an expression of the precision and repeatability of the assay. Accepted RSD% values in solid-state analysis are lower than 20%. The Recovery% refers to the difference between the true value and the obtained value calculated by the ratio between the obtained and real values multiplied for 100. The recovery % denotes the accuracy of the method and values close to 100% are desirable.

## 2 AIM

Several quantitative methods by X-Ray Powder Diffraction are available. Nevertheless, in pharmaceutical field the traditional methods are commonly used because the similarities with the quantitative analysis by HPLC, widely used in pharmaceutical companies. The quantitative methods peculiar to the crystallographic field as such as Rietveld, WPPD and RIR are less used because of their difficulties to be implemented in validation method, thus the traditional methods are widely used for the determination of the crystal forms and crystallinity degree.

Following, some examples of quantitative methods developed and evaluated in PolyCrystalLine laboratories are reported. In all cases the methods are tailored on the customer requirements and the name of the compounds are omitted and used name of fantasy. The first is an example of limit test method, the purpose of the limit test method is to determine if the content of the impurity is above or below an established limit of content. The quantitative method evaluates the content of the analyte (polymorphic form) in the range of the calibration curve that can vary according to the necessity of the customer.

The second and third examples regards the quantification of a target crystal phase in a mixture: for example, the unreacted starting material in the co-crystal formation or the presence of an undesired polymorphs.

Amorphous content is of interest for pharmaceutical company due to instability of the amorphous phase, example of amorphous and crystalline quantification will be reported successively in following chapter. Acceptance criteria for solid-state quantitative method are not reported in guidelines, USP reports that the determination of amounts of crystalline phases as small as 10% can be achieved in favourable cases.

In all cases, the quantification method should have the following acceptance criteria: the regression value for the calibration curve needs to higher than  $R^2 > 0.9$  (usually value higher than 0.99 are accepted), The relative standard deviation  $RSD\% \leq 20\%$  and Recovery % within the range 80-120%.

## 3 LIMIT TEST

### 3.1 Aim

The aim is to develop a limit test by X-Ray Powder Diffraction of a polymorph X in the bulk of form Y. The development of quantitative method or limit test is tailored to customer's needs. Generally, limit test is adopted when the determination of low content of the analyte cannot be accurately determined. The manufacturing company is not able to product pure bulk of form Y and traces of form X are detected. The quantification of form X is fundamental for the company to declare its content and to demonstrate that its presence does not impact the quality and performance of the product. Therefore, pure form Y is not available for the construction of calibration curve and it is necessary applied the standard addition method (SAM) to quantify the amount of form X contained in the standard of form Y used for the study.

### 3.2 Experimental procedure

Figure 1 reports the comparison of pure forms X and Y and it is highlighted in yellow the specific peak at  $19.4^\circ 2\theta$  of form X used for the quantification. The pure forms Y was not available in suitable amount to prepare a calibration set. The scale up and production of suitable amount of pure form Y without traces of form X was not achieved, thus the standard addition method was applied.

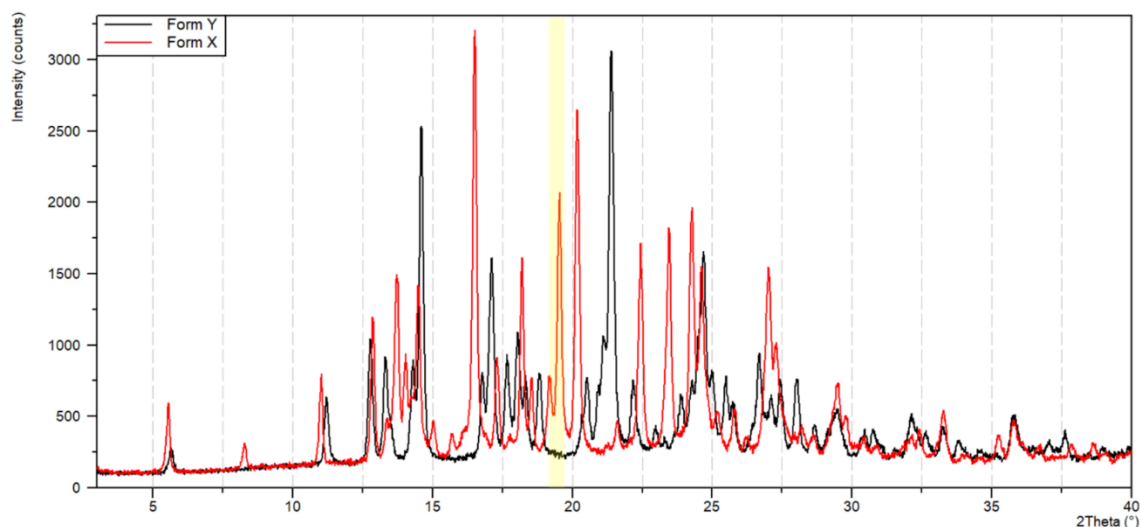


**Figure 1. XRPD pattern comparison of Form X (red) and Form Y (black)**

The measures were performed using PANalytical X'Pert PRO diffractometer in reflection mode and Bragg-Brentano geometry, Cu X-ray tube ( $\lambda = 1.5406$ ) and X'Celerator detector. To minimize the effect of the lamp decay, the signal of the form X was normalized using external standard alumina Standard Reference Material 1976 flat. The calibration standards were prepared by spiking the form Y containing unknown amount of form X with increasing amount of form X in percentage of 2.5, 5, 7.5, 10% w/w.

Three different aliquots of each standards were analysed in the range 17-27°2 $\theta$  to detect the specific peak of form X at 19.4°2 $\theta$ . Daily, one analysis of the external standard alumina was performed to collect the peak at 35.2°2 $\theta$  used for the analysis.

The area of the peak at 19.4°2 $\theta$  of form X and the peak at 35.2°2 $\theta$  of external standard alumina were determined using the software HighScore 4.8. The response (y) of the calibration curve is the ratio between the area of analyte form X and external standard alumina.

$$\text{Ratio} = \frac{\text{Form X peak area at } 19.4^\circ 2\theta}{\text{Al}_2\text{O}_3 \text{ area at } 35.2^\circ 2\theta}$$

Addition standard curve was constructed plotting the ratio between the peak area of form X and that of the alumina versus the % of form X added.

The content of the form X in the standard of form Y was extrapolated from the standard addition curve using the formula:

$$\text{Form X\% extrapolated} = \frac{\text{intercept of the addition curve}}{\text{slope of the addition curve}}$$

The calibration curve was re-calculated considering the content of form X in the standard of form Y, then this calibration was used to quantify form X in other bulk samples of Y.

The limit of detection was evaluated by HighScore software that automatically calculates the S/N using the Signal to noise Algorithm that follows the guideline ICH Q2(R1) definition and uses this simplified formula:

$$S/N = (\text{net maximum intensity}) / (3 * \sqrt{\text{average background intensity}})$$

ICH Q2(R1) reports that the signal-to-noise ratio of 3 is acceptable. The measure is performed by comparing the signal of the standard with the baseline.

Additionally, the robustness of the method was tested. The robustness of an analytical method is the capacity to remain un-affected by small, but deliberate variation in the method parameters. It provides an indication of its reliability during ordinary use. For XRPD, the instrumental parameter that can mainly influence the method performances is the lamp. Indeed, a lamp decay can influence the intensity of the signal of the analyte, reducing the limit of detection capability. The lamp decay was simulated by reduction of the generator voltage

and amperage. The routine analysis was performed with generator settings 40 mA and 45 kV. In this test the generator settings have been modified to simulate lamp decay.

The aim of this assay is to define the acceptance criterion in terms of minimum area of alumina to ensure that the instrument can detect the form X and form Y.

### 3.3 Results

Figure 2 and Table 1 reports the calibration curve and results obtained with standard addition method. Coefficient of correlation met the acceptance criterion of 0.9. The results of SAM evidenced a content of form X of 2.8% with excellently low deviation standard ( $S_E$ ). Figure 3 reports the XRPD pattern comparison of all the aliquots used for the construction of the calibration curve.

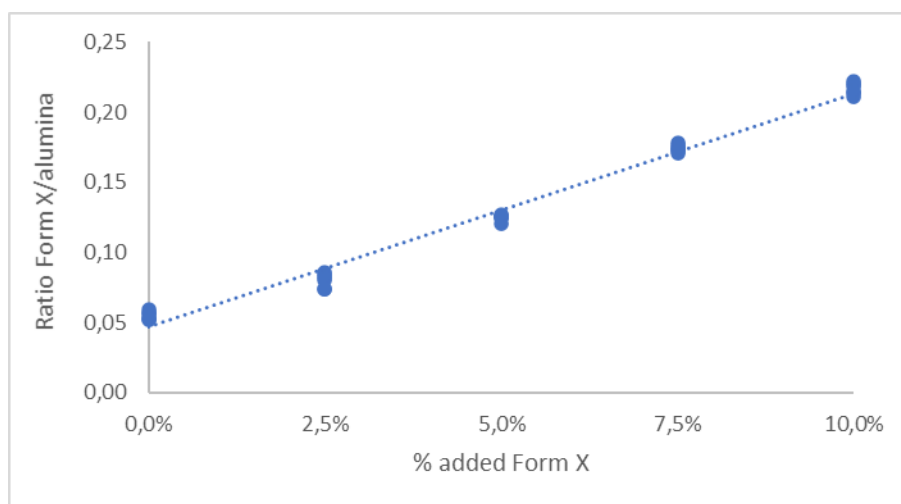


Figure 2. Standard addition calibration curve

Table 1. Results of standard addition calibration curve

	Standard addition method
Slope	1.6682
Intercept	0.0468
$R^2$	0.9867
$S_{y/x}$	7.09E-03
$C_E$	2.8%
$S_E$	1.9E-03

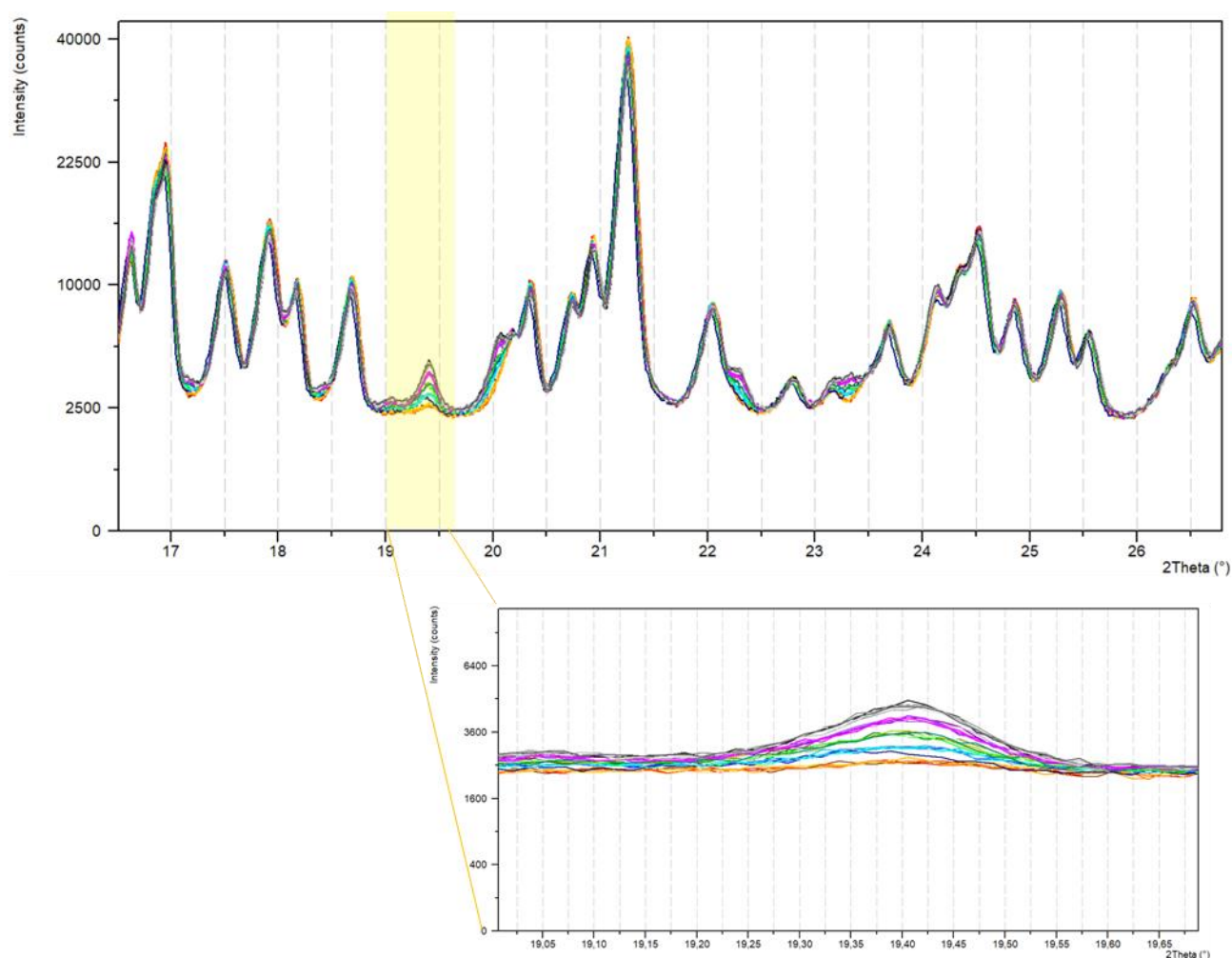


Figure 3. XRPD pattern of the standard mixtures

The content of form X of the standards was recalculated considering the results  $C_E$  obtained with SAM (Table 2).

Table 2. standard re-calculation

<b>Standard</b>	<b>% form X added</b>	<b>Re-calculated % form X</b>	<b>Average of Ratio area Form X/area <math>Al_2O_3</math></b>
<b>STD 0</b>	0%	2.8%	0.06
<b>STD 1</b>	2.5%	5.3%	0.08
<b>STD 2</b>	5.0%	7.8%	0.12
<b>STD 3</b>	7.5%	10.3%	0.17
<b>STD 4</b>	10%	12.8%	0.22

The limit of detection was evaluated to define the value for the limit test. The lamp decay of the instrument can affect the intensity of the signal and the limit of detection decreased over time. For this reason, the value of LOD obtained by HighScore cannot be used for the limit test because of it is not robustness over time, e.g., the LOD of 2.5% is  $>3$  but after time it can decrease at value  $<3$  due to the lamp decay causing an error in the content determination. Hence the limit test is based on the ratio between the area of form X and the alumina than was not affected to the lamp decay. The measurement of the alumina peak was considered a suitability test to determine the intensity of the X-ray beam. The aim was to determine the lowest beam intensity to detect form X in the range 5-10% as requested by the customer. The limit test is evaluated by the ratio of the area of form X and alumina on the assumption that the decay of the lamp affects at the same way the analyte and the external standard. Table 2 reports the average of the ratio for each standard. Robustness assay was evaluated

simulating the lamp decay at different generator settings: 45 kV-40 mA, 40 kV-30 mA, 35 kV-25 mA, 30 kV-10 mA, 15 kV-5 mA.

The STD 0 containing 2.8% of form X showed a LOD value of 3 at 45 kV and 40 mA, settings used for the analysis of measure of calibration curve. The STD1 and STD 3 were measured with the different generator settings. Table 3 reports the minimum values of generator setting and percentage of form X when the characteristic peak of form X achieved the  $S/N > 3$ . The ratio between area of form X and alumina was unchanged at different value of generator power.

Detection of 5% of form X is guarantee up to area of 524 cts, whereas area  $\geq 63$  cts guarantee detection of 10% of form X with suitable signal to noise.

Successively the ratio between the area of peak of form X at  $15.4^\circ 2\theta$  and peak of alumina is calculated. If the ratio is  $\leq 0.17$  the sample contains Form X  $\leq 10\%$ , whereas ratio  $> 0.17$  indicates content of form X  $> 10\%$ .

**Table 3. Robustness assay**

Standard	% Form X	Generator Setting	Area Alumina	Ratio
<b>STD 0</b>	<b>2.8%</b>	45 kV – 40 mA	1025 cts	0.06
<b>STD 1</b>	<b>5.3%</b>	35 kV – 25 mA	524 cts	0.08
<b>STD 3</b>	<b>10.3%</b>	20 kV – 10 mA	63 cts	0.17

### 3.4 Conclusion

Using the standard addition method, a 2.8% of form X was quantified in the bulk of the Y form. Using this value, the quantity of form X in all the standards was established. The limit of detection was evaluated in the different samples with different intensity of the X-ray beam. It was found that the 5% of form X was detectable also with the generator setting at 35 kV and 25 mA which is almost half of the intensity of the normal condition, and 10% of form X is the LOD with the generator setting at 20kV and 10 mA, which are the standby conditions. The results evidenced the robustness for Form X content of the value of the ratio between the area of form X and the area of the alumina over the different intensity of the X-ray beam.

## 4 QUANTITATIVE OF STARTING MATERIAL IN CO-CRYSTAL

### 4.1 Aim

The aim is to develop and validate quantitative method by XRPD for the determination of crystalline form X of molecule A in the bulk powder of the cocrystal formed by A and the conformer B.

### 4.2 Experimental procedure

Figure 4 reports the comparison of form X and cocrystal. The peak at  $2\theta = 7.9^\circ$  of form X was used for quantification.

The form X and cocrystal have extremely similar mass absorption coefficient  $5.4$  and  $5.5 \text{ cm}^2\text{g}^{-1}$ , respectively.

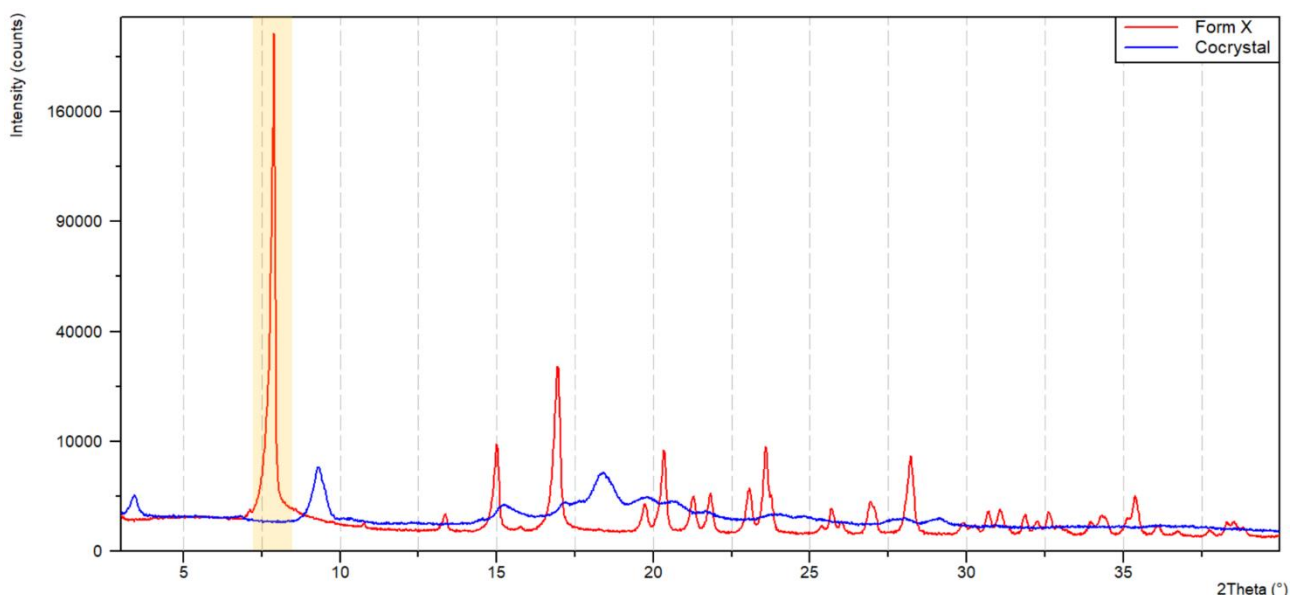


Figure 4. XRPD pattern comparison of Form X and cocrystal

The measures were performed using PANalytical X'Pert PRO diffractometer in reflection mode and Bragg-Brentano geometry, Cu X-ray tube ( $\lambda = 1.5406$ ) and X'Celerator detector. To minimize the effect of the lamp decay, the signal of the form X was normalized using signal of the peak at  $35.2^\circ 2\theta$  of alumina Standard Reference Material 1976 flat.

Seven standard mixtures were prepared with different content of form X respectively 1, 2.5, 5, 7.5, 10, 15, 20% w/w.

Three different aliquots of each standards were analysed in the range  $5-13^\circ 2\theta$  to detect the specific peak of form X at  $2\theta = 7.9^\circ$ . Daily, one analysis of the external standard alumina was performed in the range  $34-36.2^\circ 2\theta$  to collect the peak at  $2\theta = 35.2^\circ$ .

The area (cts) the peak at  $2\theta = 7.9^\circ$  of form X and the peak at  $2\theta = 35.2^\circ$  of external standard alumina were determined using the software HighScore 4.8. The response (y) of the calibration curve is the ratio between the area of analyte form X and external standard alumina.

$$\text{Ratio} = \frac{\text{Form X peak area at } 7.9^\circ 2\theta}{\text{Al}_2\text{O}_3 \text{ area at } 35.2^\circ 2\theta}$$

Calibration curve was constructed plotting the average of the ratio of the three aliquots of each standard versus the % of form X in the standards.

Repeatability, intermediate precision, and accuracy were assessed on the endpoints of the calibration curve as reported by ICH Q2 (R1). Repeatability and accuracy were evaluated on six aliquots of the endpoints of the calibration and the intermediate precision was assessed in two different days.

The limit of detection was evaluated by HighScore software that automatically calculates the S/N using the Signal to noise Algorithm that follows the guideline ICH Q2(R1) definition and uses this simplified formula:

$$S/N = (\text{net maximum intensity}) / (3 * \sqrt{\text{average background intensity}})$$

ICH Q2(R1) reports that the signal-to-noise ratio of 3 is acceptable for LOD, whereas is 10 for the LOQ. The measure is performed by comparing the signal of the standard with the baseline.

### 4.3 Results

The calibration curve in the range 1-20% w/w form X showed good  $R^2$  of 0.98, but the recovery % of the standard 1% w/w was ineligible with value of 183%, indicating that the standard 1% has been overestimated to about the double. It is worth noting that the standard 1% w/w showed signal to noise ratio of 6 which is too low for LOQ as reported in the ICH Q2 (R1). The standard 2.5% showed signal to noise higher than 40. Hence, it is suitable for quantification. The calibration curve was recalculated in the range 2.5-20% (see Figure 5) and showed a good linearity with excellent  $R^2$  equal to 0.9905.

Repeatability and accuracy were tested on six aliquots of endpoints standards 2.5% and 20% w/w of form X. Both standards showed excellent repeatability with RSD% of back-calculated % form X below 5% (Table 7 and Table 8). Standard 20% w/w showed mean of recovery % of the six aliquots equal to 96% (Table 6), while standard 2.5% showed value within 125% (Table 7). This value can be acceptable for the lowest points of the curve, although it worth noting the tendency of the curve to overestimate the lowest point at 2.5% and slightly underestimate the second point at 5%, that showed a recovery of the three aliquots of the curve equal to 86% (Table 4). As ICH Q2 (R1) suggests minimum 5 points for the calibration curve, the range was narrowed down to 5-20% w/w (Figure 6) rising the LOQ of form X to 5% w/w. The  $R^2$  value improved and the standard 5% w/w achieved satisfactory repeatability and accuracy results with RSD % of back-calculated % form X of 4% and mean of recovery % of 94% (Table 9).

Table 10 reports the excellent results of repeatability and accuracy of standard 20% w/w.

The intermediate precision was assessed calculating the RSD% of six aliquots of the standards with 5 and 20% w/w analyzed in two different days, three aliquots of day 1 and three aliquots of day 2. Both standards showed excellent RSD% of recovery % back-calculated % form X equal to 4% (Table 11 and Table 12).

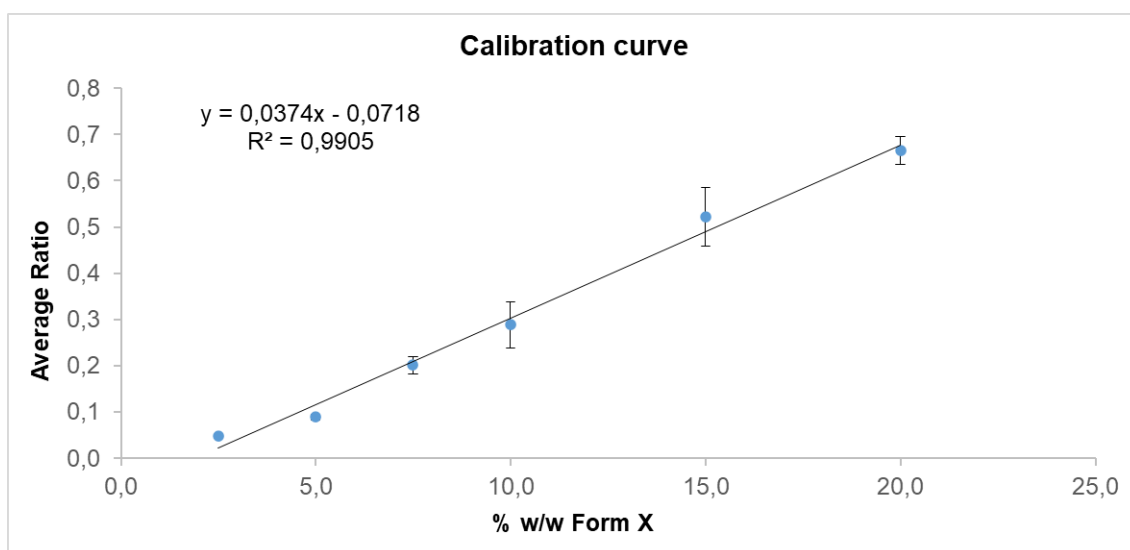


Figure 5. Calibration curve range 2.5-20% w/w form X

Table 4. Calibration data

STANDARD	RATIO		BACK-CALCULATED % FORM X		RECOVERY %
		Mean	Mean	RSD%	Mean
STD 2.5%	0.0508	0.05	3.2	2%	128%
	0.0468				
	0.0461				
STD 5%	0.0928	0.09	4.3	4%	86%
	0.0823				
	0.0926				
STD 7.5%	0.2186	0.20	7.3	7%	97%
	0.2043				
	0.1807				
STD 10%	0.2934	0.29	9.6	14%	96%
	0.3360				
	0.2361				
STD 15%	0.5633	0.52	15.9	11%	106%
	0.5544				
	0.4498				
STD 20%	0.6674	0.66	19.7	4%	98%
	0.6332				
	0.6929				

Table 5. Repeatability and accuracy STD 2.5%

Standard	Ratio	Back-Calculated % Form X	Recovery%
STD 2.5%-.M01	0.04	3.1	124%
STD 2.5%-.M02	0.04	3.0	121%
STD 2.5%-.M03	0.04	2.9	116%
STD 2.5%-.M04	0.04	3.0	120%
STD 2.5%-.M05	0.05	3.3	131%
STD 2.5%-.M06	0.05	3.2	127%
<b>MEAN</b>		<b>3.1</b>	<b>123%</b>
<b>SD</b>		<b>0.1</b>	<b>5%</b>
<b>RSD%</b>		<b>5%</b>	<b>4%</b>

Table 6. Repeatability and accuracy STD 20%

Standard	Ratio	Back-Calculated % Form X	Recovery%
STD 20%-.M01	0.62	18.5	92
STD 20%-.M02	0.64	19.0	95
STD 20%-.M03	0.68	20.1	101
STD 20%-.M04	0.67	19.8	99
STD 20%-.M05	0.65	19.3	96
STD 20%-.M06	0.63	18.8	94
<b>MEAN</b>		<b>19.3</b>	<b>96%</b>
<b>SD</b>		<b>0.6</b>	<b>3%</b>
<b>RSD%</b>		<b>3%</b>	<b>3%</b>

**Table 7. Repeatability and accuracy STD 2.5%**

Standard	Ratio	Back-Calculated % Form X	Recovery%
STD 2.5%-.M01	0.04	3.1	124%
STD 2.5%-.M02	0.04	3.0	121%
STD 2.5%-.M03	0.04	2.9	116%
STD 2.5%-.M04	0.04	3.0	120%
STD 2.5%-.M05	0.05	3.3	131%
STD 2.5%-.M06	0.05	3.2	127%
<b>MEAN</b>		<b>3.1</b>	<b>123%</b>
<b>SD</b>		<b>0.1</b>	<b>5%</b>
<b>RSD%</b>		<b>5%</b>	<b>4%</b>

**Table 8. Repeatability and accuracy STD 20%**

Standard	Ratio	Back-Calculated % Form X	Recovery%
STD 20%-.M01	0.62	18.5	92
STD 20%-.M02	0.64	19.0	95
STD 20%-.M03	0.68	20.1	101
STD 20%-.M04	0.67	19.8	99
STD 20%-.M05	0.65	19.3	96
STD 20%-.M06	0.63	18.8	94
<b>MEAN</b>		<b>19.3</b>	<b>96%</b>
<b>SD</b>		<b>0.6</b>	<b>3%</b>
<b>RSD%</b>		<b>3%</b>	<b>3%</b>

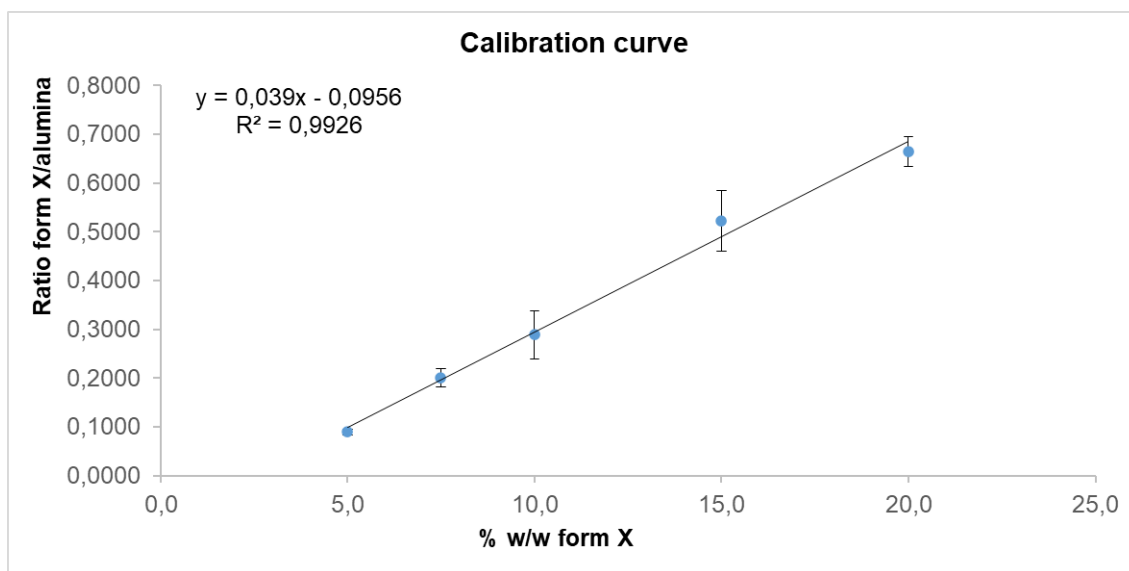


**Figure 6. calibration curve range 5-20% w/w form X**

Table 9. Repeatability and accuracy STD 5%

Standard	Ratio	Back-Calculated % Form X	Recovery%
STD 5%-.M01	0.09	4.82	96%
STD 5%-.M02	0.08	4.56	91%
STD 5%-.M03	0.09	4.82	96%
STD 5%-.M04	0.10	4.95	99%
STD 5%-.M05	0.08	4.48	90%
STD 5%-.M06	0.09	4.66	93%
<b>MEAN</b>		<b>4,72</b>	<b>94%</b>
<b>SD</b>		<b>0,2</b>	<b>4%</b>
<b>RSD%</b>		<b>4%</b>	<b>4%</b>

Table 10. Repeatability and accuracy STD 20%

Standard	Ratio	Back-Calculated % Form X	Recovery%
STD 20%-.M01	0.62	18.3	92
STD 20%-.M02	0.64	18.9	94
STD 20%-.M03	0.68	19.9	99
STD 20%-.M04	0.67	19.6	98
STD 20%-.M05	0.65	19.1	96
STD 20%-.M06	0.63	18.6	93
<b>MEAN</b>		<b>19.1</b>	<b>95%</b>
<b>SD</b>		<b>0.6</b>	<b>3%</b>
<b>RSD%</b>		<b>3%</b>	<b>3%</b>

Table 11. Intermediate precision of STD 5%

Standard	Ratio	Back-Calculated % Form X	Recovery%
STD 5%-.DAY 1	0.09	4.82	96%
STD 5%-.DAY 1	0.08	4.56	91%
STD 5%-.DAY 1	0.09	4.82	96%
STD 5%-.DAY 2	0.10	4.95	99%
STD 5%-.DAY 2	0.08	4.48	90%
STD 5%-.DAY 2	0.09	4.65	93%
<b>MEAN</b>		<b>4,71</b>	<b>94%</b>
<b>SD</b>		<b>0,2</b>	<b>3%</b>
<b>RSD%</b>		<b>4%</b>	<b>4%</b>

Table 12. Intermediate precision of STD 20%

Standard	Ratio	Back-Calculated % Form X	Recovery%
STD 20%-.DAY 1	0.62	18.3	92
STD 20%-.DAY 1	0.64	18.9	94
STD 20%-.DAY 1	0.68	19.9	99
STD 20%-.DAY 2	0.67	19.6	98
STD 20%-.DAY 2	0.63	18.6	93
STD 20%-.DAY 2	0.69	20.1	101
<b>MEAN</b>		<b>19.2</b>	<b>96%</b>
<b>SD</b>		<b>0.7</b>	<b>4%</b>
<b>RSD%</b>		<b>4%</b>	<b>4%</b>

#### **4.4 Conclusion**

The calibration curve in the range 5 to 20% showed the best  $R^2$  value and the best recovery % and it was chosen for the customer. The exclusion of the standard 1 and 2.5% w/w allow to obtain accurate results for the lowest points of the calibration curve. In fact, the recovery % of standard 5% w/w reached the value of 94%, gaining of 8 percentage points (previous value in the range 2.5-20% of 86%). In this case quantification of impurity lower than 5% is not possible, however the LOQ is higher than reported by USP that is 10%.

## 5 QUANTIFICATION OF CRYSTALLINE POLYMORPHS

### 5.1 Aim

The aim is to validate quantitative method by XRPD for the determination of polymorph X of an API within the bulk of the polymorph Y.

The customer has interest to quantify extreme low percentage of the form X in form Y.

The purpose is to evaluate the method based to the response involving the ratio between the area of the specific peak of the Form X and the total area of the full pattern of the mixture as required by the customer. In this case, the normalization of the signal is performed by the total area of the pattern in the whole range 2.5-40°2 $\theta$ . The analysis of the external standard is not necessary.

### 5.2 Experimental procedure

Figure 7 reports the comparison of polymorphs form X and form Y. The peak at 2 $\theta$  = 17.0 °, highlighted in yellow was used for the quantification of form X because no peaks of form Y are present at those values.

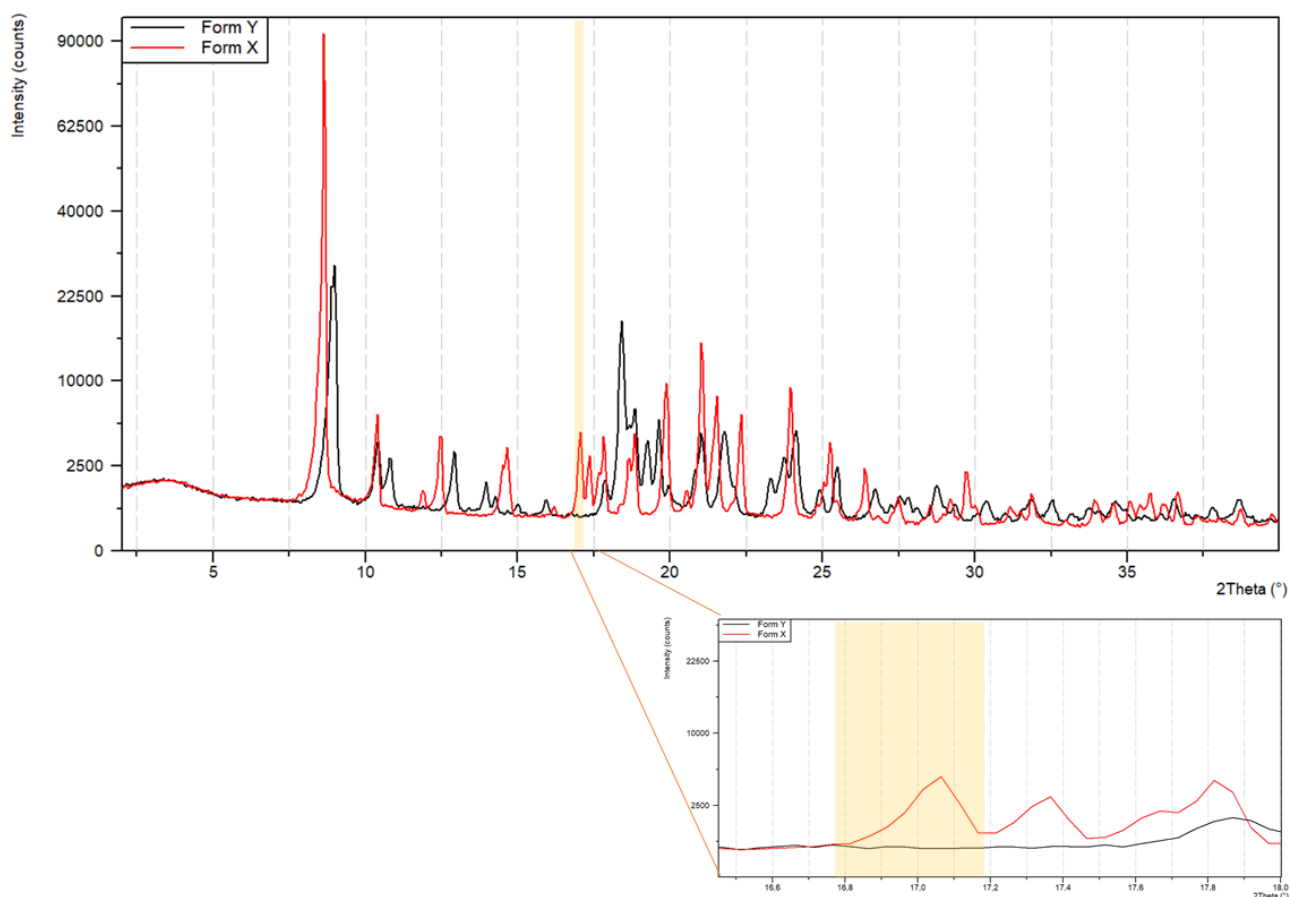


**Figure 7. XRPD pattern comparison of Form X and Form Y**

The measures were performed using PANalytical X'Pert PRO diffractometer in reflection mode and Bragg-Brentano geometry, Cu X-ray tube ( $\lambda = 1.5406$ ) and X'Celerator detector. To minimize the effect of the lamp decay, the signal of the form X was normalized using signal of the whole pattern of the mixtures.

Seven standard mixtures were prepared with different content of form X 0.5, 1, 2, 3, 5, 10, 20% w/w.

Three different aliquots of each standard were analysed in narrow range of 16.5-17.7°2 $\theta$  using slow scan rate to maximize the signal of the specific peak at 17.0°2 $\theta$ , while the full pattern for the normalization was collected in the range 2-40°2 $\theta$  at higher scan rate.

The area (cts) of the peak at 17.0°2θ of form X and the area of the whole pattern were determined using the software HighScore 4.8. The response (y) of the calibration curve is the ratio between the area of analyte form X and whole pattern of the mixture.

$$\text{Ratio} = \frac{\text{Form X peak area at } 17.0^{\circ}2\theta}{\text{Area of total pattern}}$$

Calibration curve was constructed plotting the average of the ratio of the three aliquots of each standard versus the % of form X in the standards.

### 5.3 Results

Seven standard mixtures were prepared and analysed in three different aliquots.

Figure 8 displays the calibration curve with excellent  $R^2$ . Nevertheless, the standard 5% w/w showed high variability probably due to the inhomogeneity of the mixture and the samplings evidenced by the wide values of RSD% but good mean values and excellent recovery %. Considering the excellent mean value and recovery the 5% was not excluded from the calibration curve, its back-calculated value perfectly fit the calibration curve as showed by the recovery % value. For this reason, this exclusion does not significantly improve the calibration as showed in Figure 10.

Nevertheless, the excellent  $R^2$  the calibration curve was not precise and accurate especially for the lowest point of the calibration curve (0.5%). The back-calculated and recovery% of the standards of the calibration curve were used to the assessment of the precision and accuracy of the calibration (Cross-validation). The RSD% of ratio and of back-calculated % of the standards 0.5, and 5% w/w form X showed wide values higher than 20%. Additionally, the recovery of standard 2% w/w form X was lower than 80% (Table 13).

The technique is not able to quantify accurately percentage of 0.5% w/w, thus this data was excluded and the calibration curve was evaluated in the range 1-20% w/w (Figure 9).

The results reported in Table 14 indicate that the method is accurate for all the standards and precise, except for the standard 5% w/w form X due to its inhomogeneity.

The results, especially of standard 5%, evidenced the importance of effective mixing of the standard to obtain good value of precision.

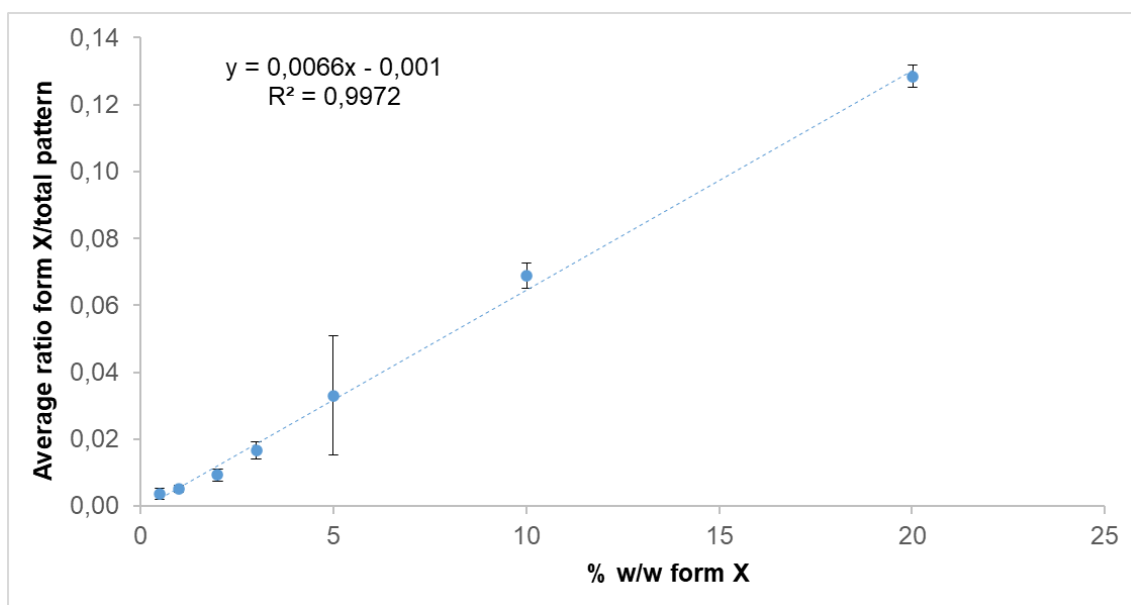


Figure 8. Calibration curve standard range 0.5-20% w/w form X

Table 13. Cross-validation range 0.5-20% w/w form X

STANDARD	RATIO			BACK-CALCULATED % FORM X		RECOVERY %
		Mean	RSD%	Mean	RSD%	Mean
STD 0.5%	0,0019	0,0037	44%	0.7%	34%	144%
	0,0042					
	0,0050					
STD 1%	0,0058	0,0052	18%	0.9%	15%	85%
	0,0056					
	0,0041					
STD 2%	0,0083	0,0094	19%	1.6%	17.5%	79%
	0,0083					
	0,0115					
STD 3%	0,0138	0,0026	15%	2.7%	14%	90%
	0,0182					
	0,0182					
STD 5%	0,0228	0,0331	54%	5.2%	52%	104%
	0,0229					
	0,0536					
STD 10%	0,0711	0,0687	6%	11%	5%	106%
	0,0708					
	0,0644					
STD 20%	0,1291	0,1284	3%	20%	3%	99%
	0,1314					
	0,1248					

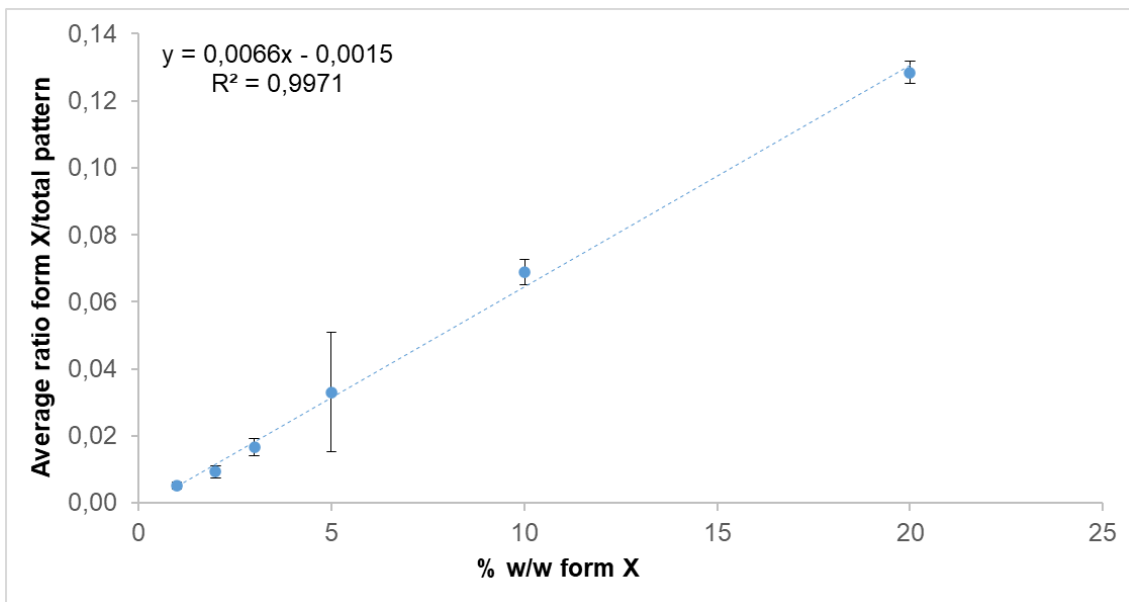


Figure 9. Calibration curve standard range 1-20% w/w form X

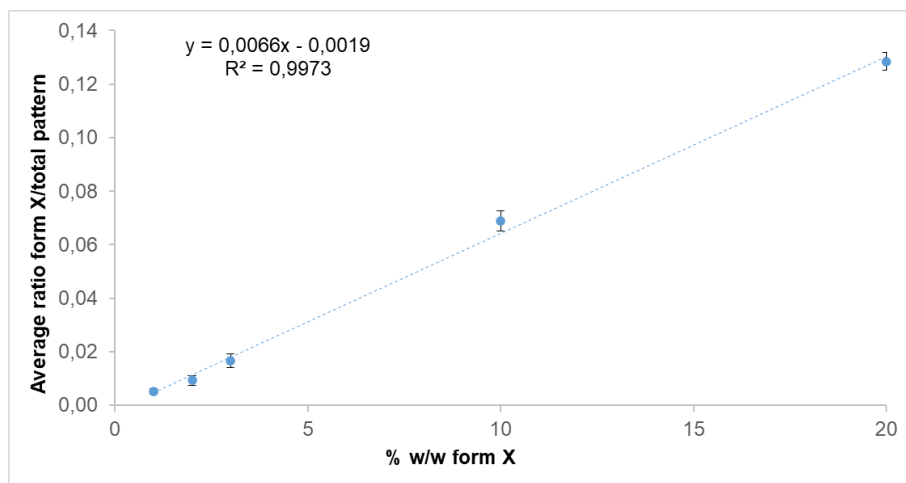


Figure 10. Calibration curve standard range 1-20% w/w form X without standard 5%

Table 14. Cross-validation range 1-20% w/w form X

STANDARD	RATIO			BACK-CALCULATED % FORM X		RECOVERY %
		Mean	RSD%	Mean	RSD%	Mean
STD 1%	0,0058	0,0052	18%	0.9%	14%	102%
	0,0056					
	0,0041					
STD 2%	0,0083	0,0094	19%	1.7%	17%	83%
	0,0083					
	0,0115					
STD 3%	0,0138	0,0026	15%	2.8%	14%	92%
	0,0182					
	0,0182					
STD 5%	0,0228	0,0331	54%	5.2%	51%	105%
	0,0229					
	0,0536					
STD 10%	0,0711	0,0687	6%	11%	5%	107%
	0,0708					
	0,0644					
STD 20%	0,1291	0,1284	3%	20%	3%	98%
	0,1314					
	0,1248					

## 5.4 Conclusion

The range of this method is extremely challenging with respect to the limits of quantification of the technique, trying to quantify a percentage of 0.5% w/w. In fact, the recovery % results for this standard revealed that the X-Ray Powder Diffraction cannot accurately quantify content of 0.5% w/w. Nevertheless, the method showed accurate determination of the standard at 1 and 2%, widely lower than the suggested limit of 10% of the technique reported by the USP.

The data of the standard 5% showed the influence of the inhomogeneity of the mixture. The deviation standard values are huge due to the variability of the signal cause by the sampling of inhomogeneous mixture. In this case, the plotted mean value fit the calibration curve not affecting the results, evidenced by the excellent value of  $R^2$ , and mean of back calculated % and recovery % of the standard 5%.

## 6 REFERENCES

- (1) Stephenson, G. A.; Forbes, R. A.; Reutzel-Edens, S. M. *Characterization of the Solid State: Quantitative Issues*; 2001; Vol. 48. [https://doi.org/10.1016/S0169-409X\(01\)00099-0](https://doi.org/10.1016/S0169-409X(01)00099-0).
- (2) ICH International Conference on Harmonization of Technical Requirements for Registration of Pharmaceuticals for Human use. ICH Q2(R1) Validation of Analytical Procedures: Text and Methodology. 2005. <https://doi.org/10.1590/s1984-82502011000100012>.
- (3) USP-NF United States Pharmacopeia and National Formulary. (941) Characterization of Crystalline and Partially Crystalline Solids BY X-Ray Powder Diffraction (XRPD). 2019.
- (4) Guagliardi, A.; Masciocchi, N. *Analisi Di Materiali Policristallini Mediante Tecniche Di Diffrazione: Atti Della Scuola Di Diffrazione Da Materiali Policristallini: Martina Franca (Ta), Palazzo. 2007.*
- (5) Hull, A. W. A New Method of Chemical Analysis. *J. Am. Chem. Soc.* **1919**, *41* (8), 1168–1175. <https://doi.org/10.1021/ja02229a003>.
- (6) Alexander, L.; Klug, H. P. Basic Aspects of X-Ray Absorption: In Quantitative Diffraction Analysis of Powder Mixtures. *Anal. Chem.* **1948**, *20* (10), 886–889. <https://doi.org/10.1021/ac60022a002>.
- (7) Copeland, L. E.; Bragg, R. H. Quantitative X-Ray Diffraction Analysis. *Anal. Chem.* **1958**, *30* (2), 196–201. <https://doi.org/10.1021/ac60134a011>.
- (8) Nunes, C.; Mahendrasingam, A.; Suryanarayanan, R. Quantification of Crystallinity in Substantially Amorphous Materials by Synchrotron X-Ray Powder Diffractometry. *Pharm. Res.* **2005**, *22* (11), 1942–1953. <https://doi.org/10.1007/s11095-005-7626-9>.
- (9) MacHado, R. C.; Andrade, D. F.; Babos, D. V.; Castro, J. P.; Costa, V. C.; Sperança, M. A.; Garcia, J. A.; Gamela, R. R.; Pereira-Filho, E. R. Solid Sampling: Advantages and Challenges for Chemical Element Determination- A Critical Review. *J. Anal. At. Spectrom.* **2020**, *35* (1), 54–77. <https://doi.org/10.1039/c9ja00306a>.
- (10) Strachan, C. J.; Rades, T.; Gordon, K. C.; Rantanen, J. Raman Spectroscopy for Quantitative Analysis of Pharmaceutical Solids. *J. Pharm. Pharmacol.* **2007**, *59* (2), 179–192. <https://doi.org/10.1211/jpp.59.2.0005>.
- (11) Jenkins, R.; De Vries, J. L. *Practical X-Ray Spectrometry*; Macmillan Education UK, 1970. <https://doi.org/10.1007/978-1-349-00055-5>.
- (12) Tiwari, M.; Chawla, G.; Bansal, A. K. Quantification of Olanzapine Polymorphs Using Powder X-Ray Diffraction Technique. *J. Pharm. Biomed. Anal.* **2007**, *43* (3), 865–872. <https://doi.org/10.1016/j.jpba.2006.08.030>.
- (13) Fix, I.; Steffens, K. J. Quantifying Low Amorphous or Crystalline Amounts of Alpha-Lactose-Monohydrate Using X-Ray Powder Diffraction, near-Infrared Spectroscopy, and Differential Scanning Calorimetry. *Drug Dev. Ind. Pharm.* **2004**, *30* (5), 513–523. <https://doi.org/10.1081/DDC-120037482>.
- (14) Campbell Roberts, S. N.; Williams, A. C.; Grimsey, I. M.; Booth, S. W. Quantitative Analysis of Mannitol Polymorphs. X-Ray Powder Diffractometry - Exploring Preferred Orientation Effects. *J. Pharm. Biomed. Anal.* **2002**, *28* (6), 1149–1159. [https://doi.org/10.1016/S0731-7085\(02\)00053-5](https://doi.org/10.1016/S0731-7085(02)00053-5).
- (15) Ong, J. L.; Farley, D. W.; Norling, B. K. Quantification of Leucite Concentration Using X-Ray Diffraction. *Dent. Mater.* **2000**, *16* (1), 20–25. [https://doi.org/10.1016/S0109-5641\(99\)00079-2](https://doi.org/10.1016/S0109-5641(99)00079-2).
- (16) Monshi, A. Quantitative Phase Analysis in Industrial Research. *Acxri.* 1996, pp 40–46.
- (17) Snellings, R.; Bazzoni, A.; Scrivener, K. The Existence of Amorphous Phase in Portland Cements: Physical Factors Affecting Rietveld Quantitative Phase Analysis. *Cem. Concr. Res.* **2014**, *59*, 139–146. <https://doi.org/10.1016/j.cemconres.2014.03.002>.
- (18) de Woolf, P. M.; Visser, J. W. Absolute Intensities - Outline of a Recommended Practice. *Powder Diffr.* **1988**, *3* (4), 202–204. <https://doi.org/10.1017/S0885715600013488>.

- (19) Davis, B. L.; Kath, R.; Spilde, M. The Reference Intensity Ratio: Its Measurement and Significance. *Powder Diffr.* **1990**, *5* (2), 76–78. <https://doi.org/10.1017/S0885715600015372>.
- (20) Davis, B. L. Quantitative Phase Analysis with Reference Intensity Ratios. In *International Conference of Accuracy in Powder Diffraction II*; 1992.
- (21) Schreyer, M.; Guo, L.; Tjahjono, M.; Garland, M. Three Approaches to Total Quantitative Phase Analysis of Organic Mixtures Using an External Standard. *J. Appl. Crystallogr.* **2011**, *44* (1), 17–24. <https://doi.org/10.1107/S0021889810053082>.
- (22) Chen, X.; Bates, S.; Morris, K. R. Quantifying Amorphous Content of Lactose Using Parallel Beam X-Ray Powder Diffraction and Whole Pattern Fitting. *J. Pharm. Biomed. Anal.* **2001**, *26* (1), 63–72. [https://doi.org/10.1016/S0731-7085\(01\)00346-6](https://doi.org/10.1016/S0731-7085(01)00346-6).
- (23) Moore, M. D.; Cogdill, R. P.; Wildfong, P. L. D. D. Evaluation of Chemometric Algorithms in Quantitative X-Ray Powder Diffraction (XRPD) of Intact Multi-Component Consolidated Samples. *J. Pharm. Biomed. Anal.* **2009**, *49* (3), 619–626. <https://doi.org/10.1016/j.jpba.2008.12.007>.
- (24) Xie, Y.; Tao, W.; Morrison, H.; Chiu, R.; Jona, J.; Fang, J.; Cauchon, N. Quantitative Determination of Solid-State Forms of a Pharmaceutical Development Compound in Drug Substance and Tablets. *Int. J. Pharm.* **2008**, *362* (1–2), 29–36. <https://doi.org/10.1016/j.ijpharm.2008.05.038>.
- (25) Paufler, P. R. A. Young (Ed.). The Rietveld Method. International Union of Crystallography. Oxford University Press 1993. 298 p. Price £ 45.00. ISBN 0–19–855577–6. *Cryst. Res. Technol.* **1995**, *30* (4), 494–494. <https://doi.org/10.1002/crat.2170300412>.
- (26) Toraya, H.; Tsusaka, S. Quantitative Phase Analysis Using the Whole-Powder-Pattern Decomposition Method. I. Solution from Knowledge of Chemical Compositions. *J. Appl. Crystallogr.* **1995**, *28* (4), 392–399. <https://doi.org/10.1107/s0021889894014986>.
- (27) Bish, D. L.; Howard, S. A. Quantitative Phase Analysis Using the Rietveld Method. *J. Appl. Crystallogr.* **1988**, *21* (2), 86–91. <https://doi.org/10.1107/S0021889887009415>.
- (28) Gomes Silva, M.; Santos, V. S.; Fernandes, G. D.; Calligaris, G. A.; Santana, M. H. A. A.; Cardoso, L. P.; Ribeiro, A. P. B. B. Physical Approach for a Quantitative Analysis of the Phytosterols in Free Phytosterol-Oil Blends by X-Ray Rietveld Method. *Food Res. Int.* **2019**, *124* (April), 2–15. <https://doi.org/10.1016/j.foodres.2019.04.006>.
- (29) Madsen, I. C.; Scarlett, N. V. Y. Y.; Kern, A. Description and Survey of Methodologies for the Determination of Amorphous Content via X-Ray Powder Diffraction. *Zeitschrift fur Krist.* **2011**, *226* (12), 944–955. <https://doi.org/10.1524/zkri.2011.1437>.
- (30) Asuero, A. G.; Sayago, A.; González, A. G. The Correlation Coefficient: An Overview. *Crit. Rev. Anal. Chem.* **2006**, *36*, 41–59. <https://doi.org/10.1080/10408340500526766>.
- (31) Rodgers, J. L.; Nicewander, W. A. Thirteen Ways to Look at the Correlation Coefficient. *Am. Stat.* **1988**, *42* (1), 59–66.
- (32) Andersen, J. E. T. The Standard Addition Method Revisited. *TrAC - Trends Anal. Chem.* **2017**, *89*, 21–33. <https://doi.org/10.1016/j.trac.2016.12.013>.
- (33) Burns, D. T.; Walker, M. J. Origins of the Method of Standard Additions and of the Use of an Internal Standard in Quantitative Instrumental Chemical Analyses. *Anal. Bioanal. Chem.* **2019**, 2749–2753. <https://doi.org/10.1007/s00216-019-01754-w>.
- (34) Miller, J. N.; Miller, J. C. *Statistic and Chemometrics for Analytical Chemistry*, 5th ed.; Pearson Prentice Hall, 2005.

## CHAPTER 5

### QUANTIFICATION BY STANDARD ADDITION METHOD IN X-RAY DIFFRACTOMETRY: A COMPARISON OF UNIVARIATE AND MULTIVARIATE ANALYSES

#### 1 INTRODUCTION

##### 1.1 Multivariate analysis

Multivariate analysis is a statistical powerful method capable to analyse wide number of data. In univariate analysis exclusively are involved two variables, independent  $x$  and dependent  $y$ , directly correlated. The determination of the concentration  $x$  involving a single variable  $y$ . Differently to univariate analysis, multivariate analysis involves wide number of experimental data consist of numerous variables  $y$ . For example, the univariate analysis determines the concentration using a single wavelength, while multivariate analysis considers several wavelengths often improving the estimation thanks to the average effect. <sup>1</sup>. In various experimental situations the number of variables can be extremely high and even higher than the number of samples, moreover these variables are often highly correlated. Nevertheless, in a multicomponent sample the multivariate method can determine the concentration of all the components basing on several variables. As for univariate method, multivariate analysis requires a calibration curve based on a training set of mixtures of compounds of known concentration.

The multivariate linear regression model is expressed by the equation:

$$Y_i = \beta_0 + \beta_1 x_i^{(1)} + \beta_2 x_i^{(2)} + \dots + \beta_n x_i^n$$

Where  $Y_i$  is the estimation of the  $i$ -th component of the dependent variable  $y$ ,  $n$  is the number of the independent variables,  $x_i$  indicates the  $i$ -th component of the  $n$ -th variable, and  $\beta$  represents the coefficients. <sup>2</sup>

Several multivariate methods have been developed, of particular importance are the Principal Component Regression (PCR) and Partial Least Square Regression (PLS) models.

The PCR used the PCA (principal component analysis), that is the most popular multivariate statistical technique. It has the scope to reduce the wide number of variables of interest using independent auxiliary variables created by a linear combination of the original ones. The construction of these latent variables has the scope to maximize the information contained in the data and to reduce the number of variables, preserving the accuracy of the data. In this way, reduction of typical noise of real cases, e.g., due to instrumental oscillations, is obtained avoiding possible data interpretation problems. These latent variables are the principal components. The principal components that efficiently highlight and summarize the information from the original huge variables, are used to construct the regression line which is based on the equation <sup>2,3</sup>

$$Y = X * B + E$$

Where  $Y$  is  $n \times q$  matrix,  $X$  is  $n \times p$  matrix,  $B$  is  $p \times q$  matrix, and  $E$  represents the residuals. The  $n$  represent the observations on  $q$  responses  $y$  and  $p$  are the independent or explanatory variables. <sup>4,5</sup>

Both PCR and PLS methods decomposed  $X$  into orthogonal scores  $T$  and loadings  $P$  to overcome the excess of variables (columns) compared to the rows represent the number of objects (samples).

$$X = TP$$

The differences between PCR and PLS methods is that PCR includes information from the vector  $X$ , whereas PLS includes information on both  $X$  and  $Y$ . <sup>4,6</sup> The PLS differs from the PCR because it uses the data set of  $X$  in an active way during statistical analysis, this allows to better balance the information. Scores  $T$  and loadings

P are selected to reach a better description of the covariance between X and Y, while PCR is focus on the variance of X. In this way, for PLS the choice of the main components to be used for the regression is more targeted and effective.<sup>6</sup>

The model constructs a new set of variables, the principal components (PCs) on which to perform a multivariate analysis. These variables are a linear combination of the original ones and identify in the space of the explanatory variable directions of maximum variance between them, also taking into account the correlations with the response variables.<sup>3</sup> PLS organizes the data in number A of latent variables (vectors)  $t_j$  and  $u_j$  linked together by the least squares regressive model:

$$u_i = b_j t_j + e_j \quad j = 1, \dots, A$$

being  $e_j$  the error vector,  $b_j$  the vector of the regression parameter. The regression parameter is estimated by  $\hat{b}_j = (t_j^T t_j)^{-1} t_j^T u_j$ , while the latent variables are computed through unit vector  $w_j$  and  $q_j$  obtained maximizing the covariance between scores  $t_j$  and  $u_j$ .<sup>6,7</sup>

$$t_j = X_j w_j \quad u_j = Y_j q_j$$

The matrices X and Y are described

$$X = \sum_{j=1}^A t_j p_j^T + E \quad Y = \sum_{j=1}^A \hat{u}_j q_j^T + F$$

E and F represents the residuals of X and Y. The procedure stops when there are no more pairs of components in X and Y significantly correlated with each other or when there is no longer any useful information obtainable for the prediction. The number A of optimal PCs is determined by validation, maximizing the coefficient of determination in cross validation ( $R^2$ ) and minimizing the mean square error in prediction (RMSEP).

The vectors  $t_j$ ,  $p_j$ , for  $j = 1, \dots, A$ , respectively constitute the j columns of the matrices of the scores (T), of the loadings (P) of X,  $w_j$  and  $q_j$  are the weight vectors of X and Y, respectively. The first matrix has as elements the coordinates of the objects with respect to the PCs in the space of the explanatory variables, the second represents the relevance of these variables with respect to the PCs and the last two report the coefficients of the combinations of the matrix X and of the matrix Y, from which the components  $t_j$  and  $u_j$  are generated, respectively.<sup>6-8</sup>

After the application of the multivariate analysis the information is used to extract from the analytical signals the information about the analyte of interest. For this purpose, various methods have been proposed, such as Net Analyte Signal (NAS) introduced by Lorber et al. and developed by Ferré et al. and Hemmateenejad et al.<sup>9-11</sup> NAS is based on search for that part of the analytical signal orthogonal (independent), respect to other species in the sample. In statistical processing it can be assumed that the NAS signal increases linearly as the concentration of the analyte under study increases. The NAS technique, combined with the standard addition method (SAM), allows quantification even in the case of not known matrix containing the analyte and different species of interferences.<sup>12</sup>

The calibration matrix Y is constituted by the rows  $s_i$  of the experimental measures, for  $i = 1, n$ , while the matrix X reports the vector of the added concentrations  $c$ . The matrix Y is decomposed in:

$$Y_{rip} = T P^T$$

Subsequently, the signal related to all the species in the sample is determined after the subtraction of the contribution of the k-th analyte under study through:

$$Y -_k = Y_{rip} - \alpha c_k s^T$$

where  $c_k$  is the prediction of the vector  $c$  in the A-dimensional subspace of the PCs and the vector  $s$  is obtained based on the signal of the pure analyte. Respectively,  $c_k$  and  $s$  are a linear combination of the columns and the rows of Y. The  $c_k$  and the scalar  $\alpha$  can be calculated, respectively, through the relations:

$$c_k = Y_{rip} Y_{rip}^+ c \qquad \alpha = 1/s^T Y_{rip}^T c_k$$

To determine the signal relative to the analyte of interest, the orthogonal component of the original signal is compared to the space identified by the interferences present in the sample. For this purpose, the prediction matrix is considered.

$$O = I - Y_{-k} Y_{-k}^+$$

Where  $I$  is the matrix of identity of order  $m \times m$ . The Net Analyte Signal vector  $s_i^*$  is calculated as:

$$s_i^* = O s_i$$

Bro and Andresen propose a modification to the calculation procedure directly considering the results of the PLS analysis and assuming the following as projection matrix:

$$O = b(b^T b)^{-1} b^T$$

where  $b$  is the vector of the regression coefficients of the component PCs. <sup>13</sup> The Net Analyte Signal vector  $s_i^*$  is again calculated with the above equation.

The NAS vector is the part of the spectrum used to make the prediction alone, therefore no information is lost by transforming this vector into its Euclidean norm (e.g., length)  $\|s_i^*\|$ , which constitutes the scalar NAS, often identified in literature simply as NAS. At this point, a pseudo-univariate regressive model of the NAS can be constructed based on the added concentrations:

$$\|s^*\| = bc + a$$

Hence, the concentration of the analyte of interest in the original sample and the relative standard error can be determined through:

$$c_E = \frac{a}{b} \quad e \quad s_E = \frac{s_{y/x}}{b} \sqrt{\frac{1}{n} + \frac{\overline{NAS}^2}{b^2 \sum_{i=1}^n (c_i - \bar{c})^2}}$$

Being  $s_{y/x}$  the root of the mean square error (RMSE),  $\overline{NAS}$  and  $\bar{c}$  are the means of the NAS norm and of the concentration, respectively.

Deep analysis for the calculation of the analyte concentration can be carried out by subsequently adding components in the model, starting from the first PC, performing linear regressions of the NAS on the concentrations each time and, through determining different values of  $c_E$ . Eventually, the number of PCs in the model that optimizes both RMSE and coefficient of determination  $R^2$  is then selected and the corresponding  $c_E$  is extrapolated.

## 2 AIM

This study deals with the solid-state quantitative analysis by X-Ray Powder Diffraction (XRPD) applying the standard addition method and comparing univariate and multivariate analysis in two different scenarios. The first scenario is the quantification of paracetamol form II in tachifludec formulation containing various excipients and paracetamol form I as API. The second scenario consists in amorphous-crystalline quantification of  $\alpha$ -lactose.

The multivariate analysis is performed in collaboration with Laboratory of "Analytical Methodologies" of the "Giacomo Ciamician" Department of Chemistry of the University of Bologna.

In pharmaceutical field the control of the crystal form of the API at any stage of the process, as well as in the final product, is essential. Nevertheless, it is common to obtain drug substance and product containing trace of another form. Frequently, it does not cause a rejection of the drug substance or product because the presence of this "contaminant" does not affect the quality and efficacy of the products. However, the regulatory agencies could require a limit test or quantification of the "contaminant" in the product. In case of impossibility to obtain polymorphic pure drug substance the application of the standard addition method is the solution. In this case, it is necessary the availability of the pure contaminant to spike the sample. Additionally, in case of analysis of formulation containing several excipients, the matrix effect can be overcome.

Here after, The SAM was evaluated applying univariate and multivariate methods, combining the SAM with the NAS in NASSAM multivariate model (NAS + SAM) to quantify the presence of paracetamol form II in the formulation of tachifludec.

The amorphous phase is typically unstable, and it is common to obtain sample mainly amorphous with some trace of crystalline phase. Due to the different properties between amorphous and crystalline phases, such as solubility, the presence of partial crystallization of the API can impact the efficacy of the product. For this reason, the crystalline-amorphous quantification is an important issue. Here after the amorphous-crystalline  $\alpha$ -lactose quantification is evaluated by spiking the crystalline phase and the univariate and multivariate method are compared.

The crystalline-amorphous quantification is extremely troublesome for the instability of amorphous, transition can occur during the mixture preparation. In some cases, to overcome the amorphous instability, instead of the amorphous API, the standard mixtures can be prepared with a "surrogate" amorphous which is a stable organic amorphous phase i.e., hydroxyl propyl methylcellulose (HPMC).

To evaluate the correctness of this procedure the quantification of crystalline  $\alpha$ -lactose monohydrate was determined in two set of standards, one containing amorphous lactose and the second containing hydroxyl propyl methylcellulose (HPMC) as amorphous surrogate. The univariate analysis is tested evaluating the response of different peaks of  $\alpha$ -lactose monohydrate to observing the different response with the differ type of amorphous content. Additionally, the signal of the  $\alpha$ -lactose monohydrate was evaluated with and without the normalization with silicon as internal standard.

### 3 QUANTIFICATION METHODS OF PARACETAMOL FORM II IN TACHIFLUDEC

#### 3.1 Paracetamol polymorphism

Paracetamol, also known as acetaminophen, is a drug substance included in class of non-steroidal anti-inflammatory drugs. It has central and peripheral analgesic and antipyretic action due to inhibition of enzyme cyclo-oxygenase (COX) that yield the prostaglandins. Preventing the production of these important mediator of inflammation, paracetamol is effective for treatment of headaches, fever, and pain even post-operative.<sup>14-17</sup> Paracetamol is included in several pharmaceutical products of pharmaceutical company Angelini (Ancona, Italy), e.g., tachipirina, tachifludec, etc. Its chemical structure is shown in Figure 1.

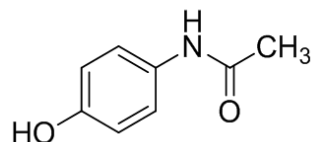


Figure 1. Chemical structure of paracetamol

Paracetamol exists in three different polymorphs, form I and form II and the elusive form III. Form I is the stable polymorph at RT and it is marketed form, although it is not suitable for compression and making tablets. Haisa et al. obtained form I and form II from aqueous solution and slow evaporation from ethanol solution, respectively. They resolve the structures of both forms I and II, reported in CSD as HXACAN01 and HXACAN, respectively.<sup>18,19</sup> Form I and form II share the same hydrogen bond network. Both the structures showed two hydrogen bonds involving the phenolic OH that acts as donor and acceptor respectively with carbonyl group (acceptor) and amide NH (donor). Although, the two forms showed very different structures. Form I crystallizes as monoclinic unit cell with group of symmetry of  $P2_1/a$ . The structure is characterized by fish bone packing with sheet stacked along b axis, causing no sliding surfaces which affect the compressibility of the structure (Figure 2).<sup>20</sup>

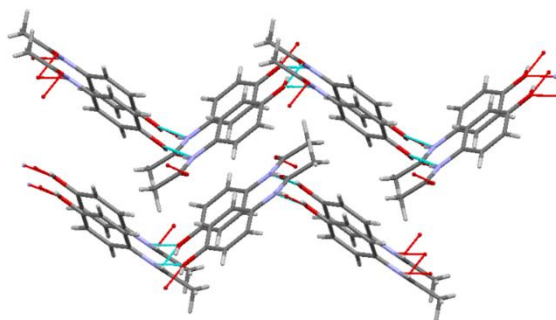


Figure 2. Form I structure along axis c

Form II crystallizes in orthorhombic crystal system and  $Pcab$  space group. It showed sheet-like packing with sheets stacked along the c axis (Figure 3, left side).<sup>18</sup> Form II has well developed sliding surfaces and undergoes plastic deformation, this makes it very suitable for producing tablets.<sup>21</sup> Form I and form II differ also for habit, form I showed hexagonal blocks while form II rectangular ones.<sup>20</sup>

Form I is thermodynamically stable at room temperature and atmospheric pressure, while form II is metastable under environmental conditions. In fact, Form II and form III are metastable polymorph, labelled elusive forms over the years.<sup>22,23</sup> The method of preparation of form II by Haisa et al. was revealed to be not reproducible. Di Martino et al. provided method for production of form II and form III by melting of form I.<sup>24</sup> Form I melts at approx.  $168^\circ\text{C} - 169^\circ\text{C}$ , slowly cooling the molten form I until room temperature it gets a glassy phase, which heating at about  $60^\circ\text{C}$  it converts into form II, that melts at approx.  $157/158^\circ\text{C}$ . The crystallization of the glassy phase around  $60^\circ\text{C}$ , also allows to obtain form III, which completely converts to form II at about  $120^\circ\text{C}$ .<sup>24</sup>

The existence of metastable form III was reported for the first time by Burger about 40 years ago, but it was only in 2002 that Peterson et al. have collected XRPD pattern of paracetamol form III.<sup>25,26</sup> First Perrin et al. have resolved the structure of form III, successively improved by Reiss et al. the structures are deposited in CSD labelled as HXACAN29 and HXACAN40, respectively.<sup>20,27</sup> Reiss et al. confirm the orthorhombic unit cell and Pca21 space group of form III (Figure 3, right side).<sup>20</sup> Form III showed analogies with form II structure, both forms equivalent two-dimensional layers of hydrogen bonded molecules. The two forms differ in hydrogen bonding plane and in the tilt angles between the benzene rings. Moreover, as shown in Figure 3 surprisingly the cell axis of the forms are correlated in perfect ratios, namely  $a(\text{III}) = b(\text{II})$ ,  $c(\text{II}) = 2b(\text{III})$ , and  $c(\text{III}) = 2a(\text{II})$ .<sup>27</sup>

Figure 4 reports the comparison of XRPD pattern of paracetamol form I, II, and III.

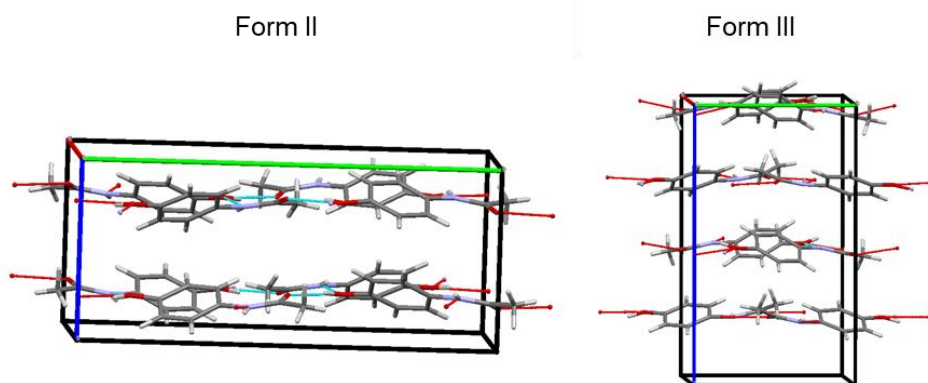


Figure 3. Unit cell and structure of Form II and Form III along axis a

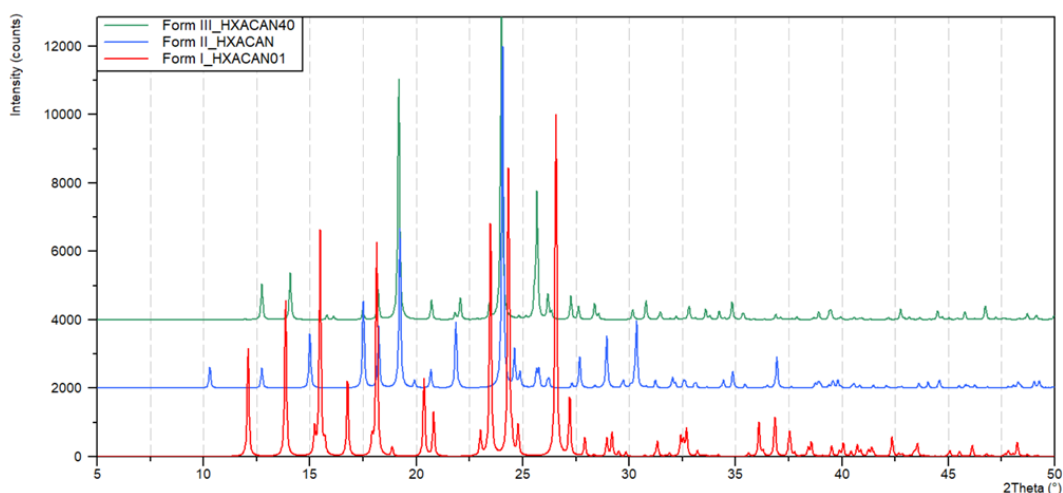


Figure 4. XRPD pattern of paracetamol form I (red line), form II (blue line), and form III (green line)

During their study, Reiss et al. have discovered and solved the structure of another monoclinic polymorph of paracetamol, labelled form III m, obtained by cooling of form III to 100 K (-173°C). The reversible transition from form III-o to form III-m occurred in the range 170-220 K.<sup>20</sup>

Furthermore, Parkin et al. and McGregor et al. report the existence of monohydrate and trihydrate form of paracetamol, respectively.<sup>28,29</sup> The monohydrate form of paracetamol was characterized at the low temperature of 150 K (-123°C) because it is unstable in ambient condition, the quick loss of water in five minutes induces the conversion in stable form I.<sup>28</sup> The trihydrate form of paracetamol has been prepared by McGregor et al. through slow cooling at 0°C in 12 hours of aqueous solution of paracetamol. McGregor et al. have succeeded in characterizing the trihydrate form despite its instability because of it rapidly dehydrates in more stable form. Table 1 reports the crystal data of the known paracetamol forms. Nevertheless, the forms of interest are form I and form II due to instability of the other forms.

Table 1. Crystal data of paracetamol forms

	<i>Form I</i>	<i>Form II</i>	<i>Form III-o</i>	<i>Form III-m</i>	<i>Form Monohydrate</i>	<i>Form Trihydrate</i>
<b>CSD Refcode</b>	HXACAN01 <sup>19</sup>	HXACAN <sup>18</sup>	HXACAN40 <sup>20</sup>	HXACAN39 <sup>20</sup>	HUMJEE <sup>28</sup>	XOMWOL <sup>29</sup>
<b>T (K)</b>	295	295	293	100	150	150
<b>Space Group</b>	<i>P2<sub>1</sub>/a</i>	<i>Pcab</i>	<i>Pca2<sub>1</sub></i>	<i>Pc11</i>	<i>P2<sub>1</sub>/n</i>	<i>Pbca</i>
<b>Unit Cell</b>	<i>Monoclinic</i>	<i>Orthorhombic</i>	<i>Orthorhombic</i>	<i>Monoclinic</i>	<i>Monoclinic</i>	<i>Orthorhombic</i>
<b>a (Å)</b>	12.93(4)	11.805(5)	11.8376(3)	111.7546(3)	4.5039(6)	7.3324(16)
<b>b (Å)</b>	9.40(1)	17.164(2)	8.5688(3)	8.5720(3)	10.5391(14)	12.590(3)
<b>c (Å)</b>	7.10(2)	7.393(2)	14.81837(16)	14.5155(5)	17.048(2)	22.636(6)
<b>α</b>	90°	90°	90°	84.160(14)°	90°	90°
<b>β</b>	115.9(2)°	90°	90°	90°	96.399(3)°	90°
<b>γ</b>	90°	90°	90°	90°	90°	90°
<b>Z (Z')</b>	4	8	8	8	4	8
<b>Volume (Å<sup>3</sup>)</b>	776.272	1497.98	1503.09 (7)	1454.99 (9)	804.18 (19)	20897 (9)

## 3.2 Experimental procedure

### 3.2.1 Characterization of Paracetamol form I

Form I paracetamol was characterized by XRPD and DSC.

Figure 5 shows the comparison between experimental (red line) and calculated (HXACAN01 1178859, black line) XRPD pattern of paracetamol form I. XRPD pattern of paracetamol form I is comparable to the calculated pattern.

The stability of paracetamol form I was evaluated after grinding for 30 minutes at 30 Hz. Figure 6 reports XRPD pattern comparison between paracetamol for I before and after extremely stressful condition of grinding. Ground paracetamol form I XRPD pattern is superimposable to XRPD pattern of Paracetamol form I before grinding. Paracetamol form I is stable to grinding process.

DSC analysis of paracetamol form I was performed at rate of 5K/min in different step. The first heating cycle was performed in the range 25-180°C, after the sample was cooled up to 25°C and successively heating until 180°C.

In the first heating (orange background in Figure 7) the endothermic peak at approx. 169°C with enthalpy of about 183 J/g corresponds to the melting of paracetamol form I. During the cooling cycle (light blue background) no event is observed. In the second heating cycle (second segment with orange background in Figure 7) the exothermic peaks at about 72°C with enthalpy of about -129 J/g is related to crystallization (cold crystallization) of paracetamol in form II and which melts at approx. 157°C correspond with enthalpy of 179 J/g.

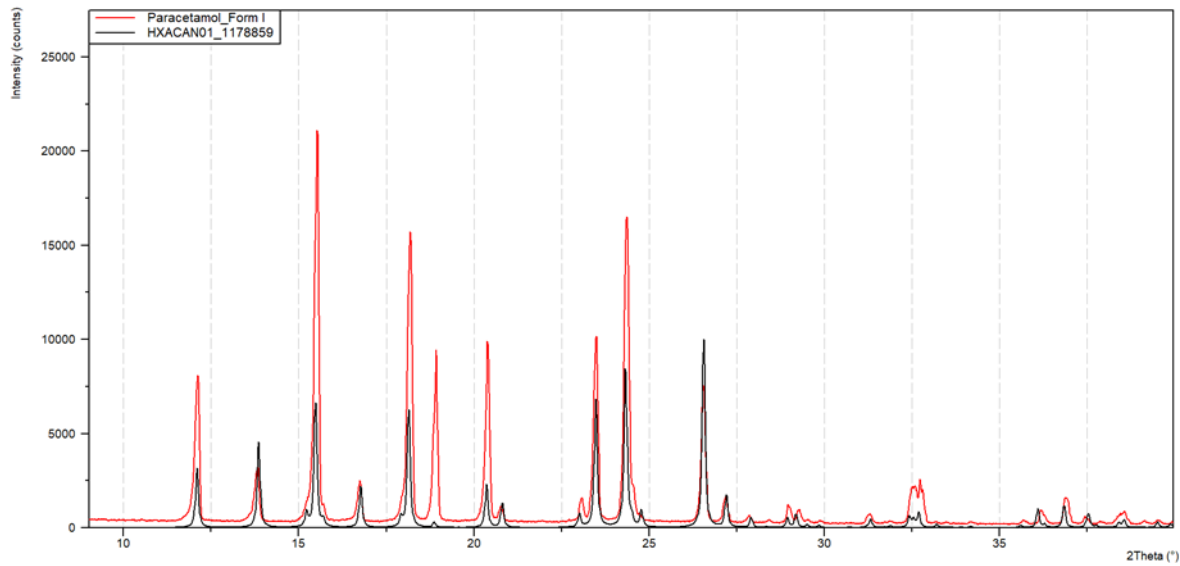


Figure 5. XRPD pattern comparison between experimental (red line) and calculated pattern (HXACAN01 1178859, black line) of paracetamol form I

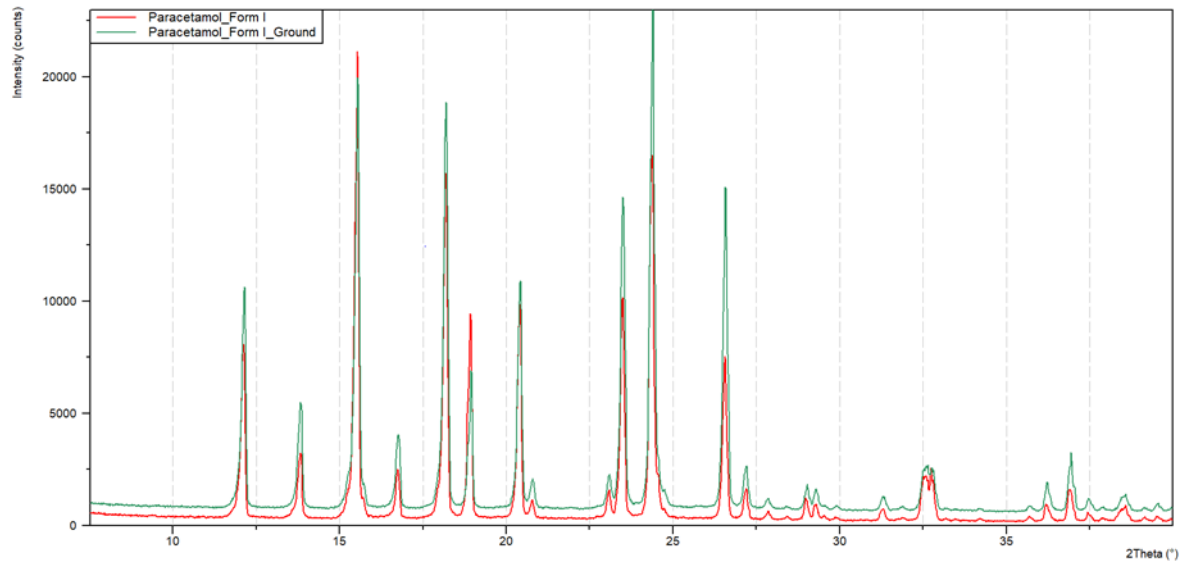


Figure 6. XRPD pattern comparison between paracetamol form I before (red line) and after (green line) grinding for 30 minutes at 30 Hz.

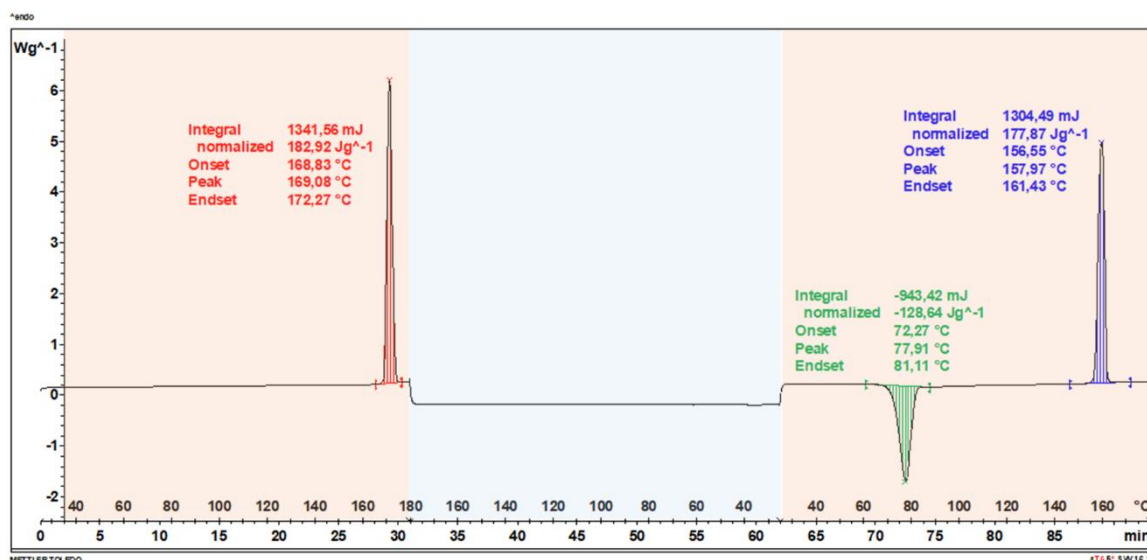


Figure 7. DSC analysis of paracetamol form I: heating cycles (orange background) and cooling cycle (light blue background)

### 3.2.2 Crystallization and characterization of paracetamol form II

Di Martino et al. provide the method for crystallization of paracetamol form II via melting and slow cooling of form I.<sup>24</sup> 2 g of form I in closed glass vial was placed in the oven at temperature of 180°C for 30 minutes to completely melt the form I. Then the oven was turned off and the sample was kept inside the oven for 24 hours to slowly cool at room temperature and to promote the crystallization.

The obtained sample was characterized by XRPD which confirmed the formation of form II (see Figure 8) and no peaks of form I are detected.

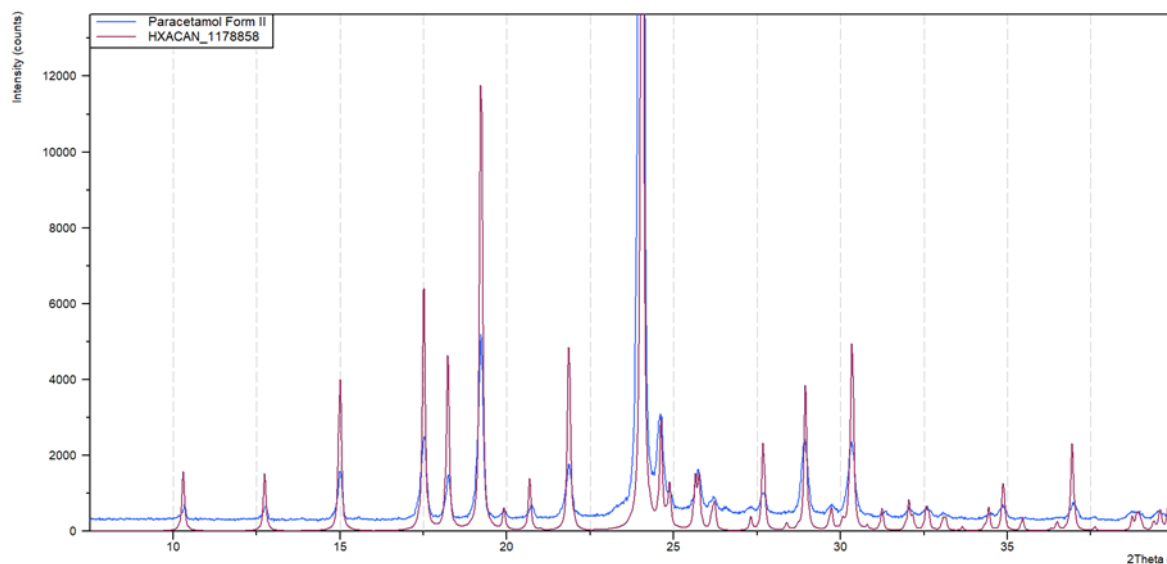
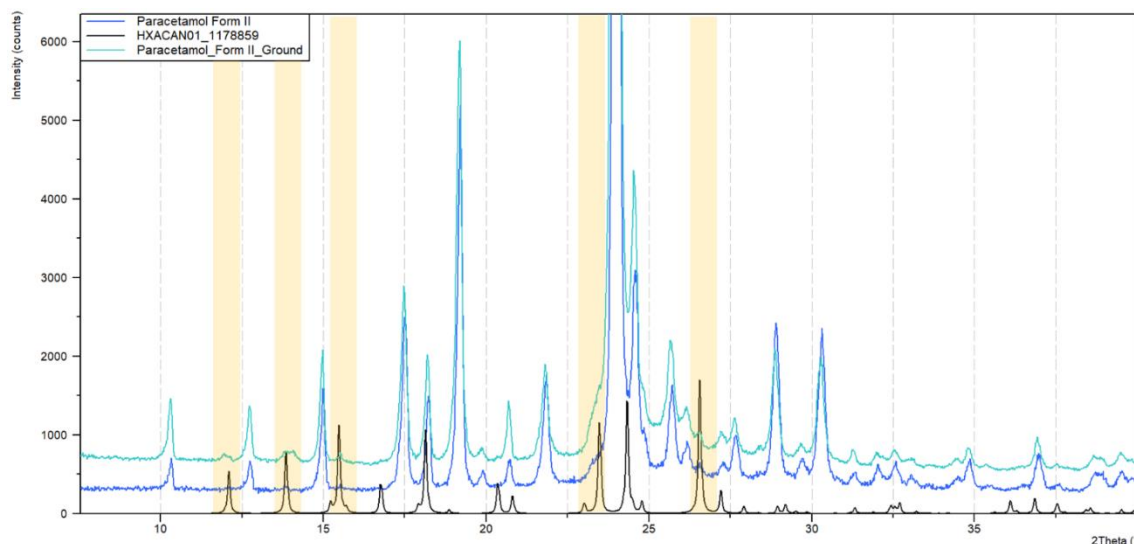


Figure 8. XRPD pattern comparison between experimental (blue line) and calculated pattern (HXACAN 1178858, purple line) of paracetamol form II

Stability of the form II was evaluated by grinding for 30 minutes at 30 Hz. The sample showed some tiny peaks of paracetamol form I (highlighted in yellow in Figure 9) which suggest avoiding stressful condition during the preparation of the standards.



**Figure 9. XRPD pattern comparison between paracetamol form II before (blue line) and after (cyan line) grinding for 30 minutes at 30 Hz and calculated pattern of paracetamol form I (black line)**

### 3.2.3 Specificity assay

Tachifludec is a multicomponent formulation consistent of paracetamol form I and several excipients. Generally, univariate method requires a specific peak of the analyte, which should not overlap with other peaks in the mixture and it should be well separated from the nearby reflections. Furthermore, the peak should have a good relative intensity and not be subject to preferential orientation. Nevertheless, the method of the additional standard is useful in case of matrix effect and a specific peak is not available. Exclusively, the peak at approx.  $15.0^{\circ}2\theta$  of paracetamol form II has all these features and it is used for the construction of the calibration curve. Although, it has not a remarkable intensity, which can affect the limit of detection. The highest peak of paracetamol form II at  $24^{\circ}2\theta$  is not specific but it can be used for construction of calibration curve with the method of addition standard. Figure 10 reports the comparison between tachifludec (black line) and paracetamol form II (blue line), the peak at  $15.0^{\circ}2\theta$  is highlighted in yellow, while the peak at  $24.0^{\circ}2\theta$  is highlighted in green.

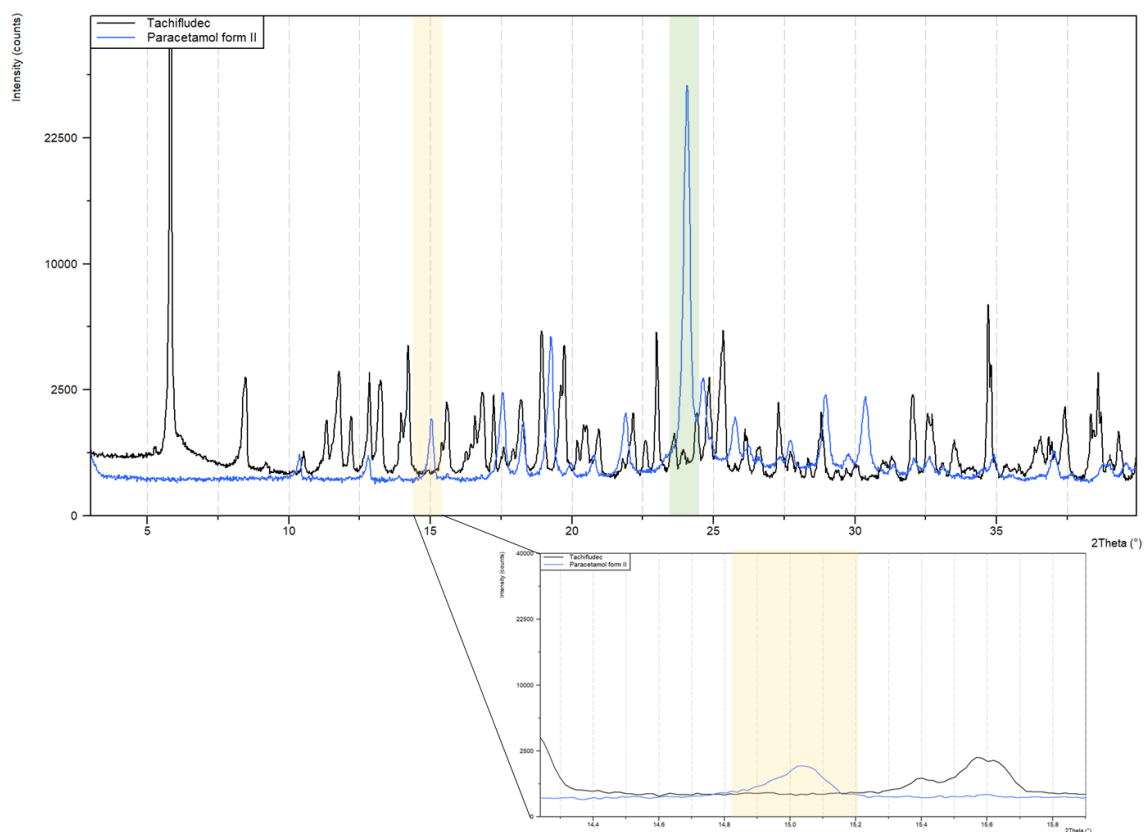


Figure 10. Specificity: XRPD pattern comparison between tachifludec (black line) and paracetamol form II (blue line)

### 3.2.4 Standard mixtures preparation

Tachifludec is a granulated product, hence it was ground using an agata mortar to obtain a fine powder. Successively, six standard mixtures were prepared containing tachifludec and increasing amount of form II. Additionally, the same quantity of silicon equal to about 10% of the total mass was introduced into each mixture (Table 2). The use of silicon as internal standard allows to minimize errors due to sample preparation and instrumental variables, especially in univariate method in which the signal of the analyte was normalized out the signal of the internal standard. Moreover, the presence of silicon, which is a black powder allows a visually evaluation of the efficiency of the mixing of the samples.

The mixing of the standard was performed via the geometric dilution method in a ceramic mortar.

Table 2. Standard preparation with additional standard method

	STD 0	STD 1	STD 2	STD 3	STD 4	STD 5
<b>TACHIFLUDEC</b>	434.66	427.42	397.54	377.06	340.82	319.94
<b>FORM II</b>	10.99	25.11	49.87	74.79	100.04	124.38
<b>SILICON</b>	49.47	50.27	49.75	50.15	49.08	49.41
<b>% FORM II</b>	<b>2%</b>	<b>5%</b>	<b>10%</b>	<b>15%</b>	<b>20%</b>	<b>25%</b>

### 3.2.5 Data analysis

PANalytical X'Pert Pro X-Ray Diffractometer in reflection mode and Bragg-Brentano geometry with Cu source ( $\lambda = 1.5406$ ) and XCellerator detector was used for the collection. Each standard mixture has been analyzed in three different aliquots. The mixtures were analyzed in the range  $3-40^\circ 2\theta$  collecting the whole pattern for the evaluation with the chemometric method. For the construction of the calibration curve via univariate method the mixtures were analysis with two different programs of analysis, one in the range  $14-16^\circ 2\theta$  for the collection of the signal of paracetamol form II and the latter in the range  $55-57^\circ 2\theta$  for the collection of the reflection of silicon. The program settings were summarized in Table 3.

Table 3. Experimental settings

EXPERIMENTAL SETTING			
Incident beam path			
Soller slit (rad)	0.04		
Divergence slit	$\frac{1}{4}$		
Mask	15		
Antiscatter slit	$\frac{1}{2}$		
Filter	None		
Diffracted beam path			
Soller slit	0.04		
Antiscatter slit	5.0		
Measurement Settings	Full range Multivariate analysis	Form II signal Univariate analysis	Silicon signal Univariate analysis
Generator settings	40 kV-40mA	40 kV-40mA	40 kV-40mA
Scan Range ( $^\circ 2\theta$ )	3-40	14.4-16	55-57
Step size ( $^\circ \theta$ )	0.017	0.017	0.017
Time per step (s)	20	300	300
Spinner revolution time (rps)	1	1	1

## 3.3 Data evaluation and results

### 3.3.1 Univariate analysis

Univariate analysis is based on the linear relationship between the signal  $y$  and the concentration of analyte  $x$  graphically displayed in a calibration curve.

In this case the response value  $y$  was the ratio between the area of the paracetamol form II peak at  $2\theta = 15.0^\circ$  and the area of the internal standard silicon at  $2\theta = 56.1^\circ$ .

The area was determined using the software PANalytical HighScore 4.8. The integration of peak at  $15.0^\circ 2\theta$  of paracetamol form II was evaluated in the range  $14.6-15.2^\circ 2\theta$ .

The background and the peak position of paracetamol form II and silicon peaks were determined using the dedicated function of the software. The profile, width, and shape of the peaks were fitted using the Pseudo Voigt function. Table 4 summarized the integration method for peaks of analyte Form II and silicon.

Table 4 Integration method

	Analyte	Internal standard
<b>Clip range</b>	14.6-15.2°2 $\theta$	-
<b>Background</b>	Bending = 2 Granularity = 100 No smoothed data	Bending = 2 Granularity = 100 No smoothed data
<b>Search peak</b>	Minimum significance = 1 Minimum tip width = 0,01 Maximum tip width = 1 Peak base width = 2 Method = Minimum 2nd derivative	Minimum significance = 5 Minimum tip width = 0,01 Maximum tip width = 1 Peak base width = 2 Method = Minimum 2nd derivative
<b>Fitting</b>	FWHM function = Individual FWHM Profile function = Pseudo Voigt Asymmetry type = Split width and shape No shape function	FWHM function = Individual FWHM Profile function = Pseudo Voigt Asymmetry type = Split width and shape Shape function

The ratio between obtained values of area of peak of paracetamol form II at 15.0°2 $\theta$  and the peak of silicon at 56.1°2 $\theta$  was calculated and plotted versus the percentage of paracetamol form II in the mixture. Figure 11 shows peak at 15.0°2 $\theta$  of the standards.

For each standard was calculated the average, standard deviation (SD) and the residual standard deviation (RSD%).

The slope, intercept, coefficient of determination  $R^2$ , deviation of the linear regression ( $S_{y/x}$ ), and limit of detection (LOD) were calculated.

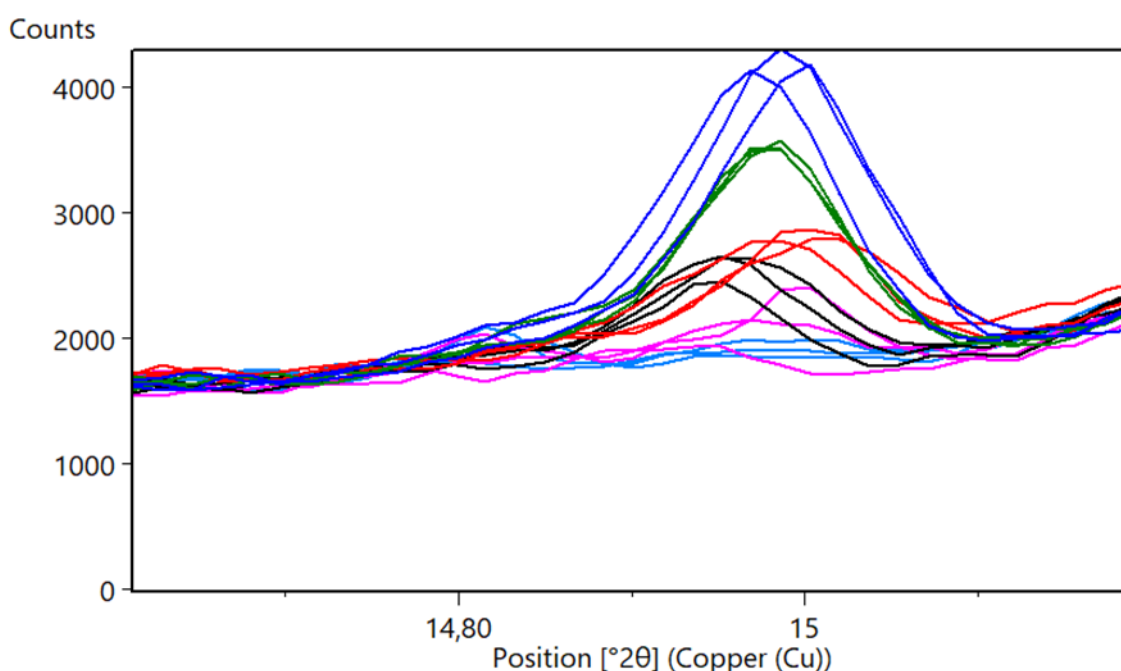


Figure 11. XRPD comparison of signal of peak at 15°2 $\theta$  of the standards: STD 0 (cyan line), STD 1 (magenta lines), STD 2 (black lines) STD 3 (red lines), STD 4 (green line), and STD 5 (blue line)

Figure 12 and Table 5 report the results for the univariate analysis using the signal of peak at 15.0°2 $\theta$ . The signal of peak at 15.0°2 $\theta$  in the standard STD 0 (2% w/w Form II) was not detected, hence it was not used for the construction of the calibration curve.

Table 5. Data of calibration curve via univariate analysis using peak at 15.0°2θ

STANDARD	%w/w Form II	Aliquots	Area Form II	Area Silicon	Ratio	Average Ratio	SD	RSD%
STD 1	5%	M01	27.89	634.04	0.04	0.04	0.02	47%
		M02	21.18	957.65	0.02			
		M03	51.85	838.72	0.06			
STD 2	10%	M01	66.54	783.69	0.08	0.09	0.01	6%
		M02	58.80	624.36	0.09			
		M03	70.49	839.65	0.08			
STD 3	15%	M01	78.68	1048.06	0.08	0.08	0.02	24%
		M02	87.80	881.76	0.10			
		M03	63.97	1035.63	0.06			
STD 4	20%	M01	137.03	929.43	0.15	0.16	0.01	6%
		M02	139.83	854.60	0.16			
		M03	149.74	906.55	0.17			
STD 5	25%	M01	192.99	900.08	0.21	0.20	0.01	7%
		M02	192.63	1036.98	0.19			
		M03	178.31	879.41	0.20			
<b>R<sup>2</sup></b>						<b>0.8679</b>		
<b>SLOPE</b>						<b>0.0078</b>		
<b>INTERCEPT</b>						<b>-0.0026</b>		
<b>S<sub>Y/X</sub></b>						<b>2.30E-02</b>		
<b>LOD</b>						<b>8.89%</b>		

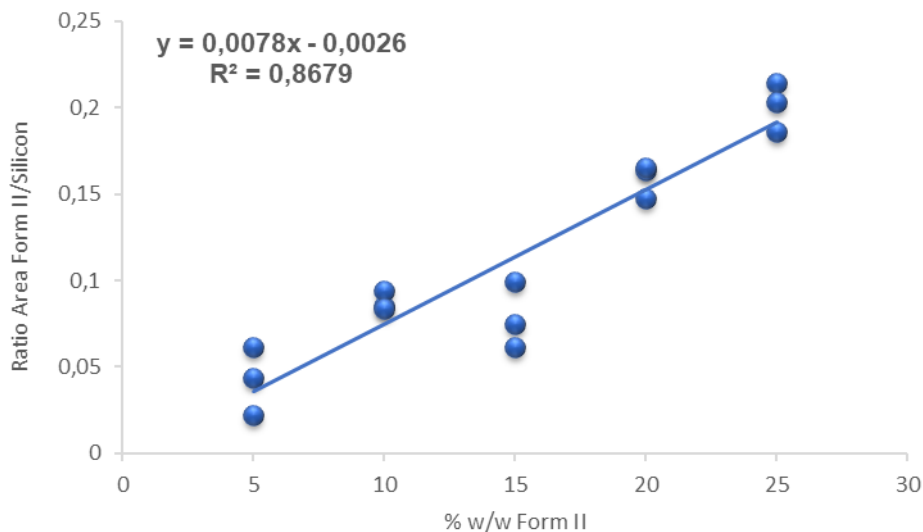


Figure 12. Calibration curve via univariate analysis using peak at 15.0°2θ

The calibration curve showed unsatisfactory coefficient of determination lower than the minimum acceptance value of 0.90. Additionally, the limit of detection, calculated with the formula below, was quite high approximately 9%, higher than the first point in the calibration curve (5%).

$$LOD = 3 * \frac{S_y}{Slope_x}$$

STD 1 (5%) and 3 (15%) are the samples with high RSD % clearly visible in the calibration curve in Figure 12. Moreover, data and calibration curve revealed the inability of the regression to distinguish between the standard STD 2 (10%) and STD 3 (15%) probable because of underestimation of the signal of STD 3.

The results evidenced that the peak at  $15.0^{\circ}2\theta$  is not suitable for the quantification because of its low intensity. In fact, no signal was detected in the STD 0 (2%), and also STD 1 (5%) is below the value of the limit of detection of 9%.

Additionally, some standard such as STD 3 (15%) showed highly variable results probable due to inhomogeneity of the mixture maybe due to partial conversion of form II. Although, energetic mixing was avoided. In conclusion, it is not possible to quantify small quantities of Form II in tachifludec using the univariate method by XRPD.

### 3.3.2 Standard addition method (SAM)

In standard addition method it is not necessary to identify a specific peak of the analyte, therefore the highest peak of form II at  $2\theta = 24.0^{\circ}$  was used for the univariate method, while for the multivariate method was based on the NAS approach.

The STD 0 containing the 2% of form II was considered the unknown sample. Consequently, the other standards were considered as spiked with form II.

#### 3.3.2.1 Univariate analysis

The calibration curve was constructed using as response value  $y$  the ratio between the area of the paracetamol form II peak at  $24.0^{\circ}2\theta$  and the area of the internal standard silicon at  $56.1^{\circ}2\theta$ .

The area the silicon's peak was determined as reported in right column of Table 4. While the area of the peak at  $24.0^{\circ}2\theta$  of form II was determined using the software PANalytical HighScore 4.8 as reported Table 6.

**Table 6 Integration method of peak at  $24.0^{\circ}2\theta$  of form II**

Analyte	
<b>Background</b>	Bending = 0
	Granularity = 100
	No smoothed data
<b>Search peak</b>	Minimum significance = 1
	Minimum tip width = 0,01
	Maximum tip width = 1
	Peak base width = 2
	Method = Minimum 2nd derivative
<b>Fitting</b>	FWHM function = Individual FWHM
	Profile function = Pseudo Voigt
	Asymmetry type = Split width and shape
	Shape function

The ratio between area of peak of paracetamol form II at  $24.0^{\circ}2\theta$  and of the peak of silicon at  $56.1^{\circ}2\theta$  was calculated and plotted versus the percentage of paracetamol form II in the mixture.

For each standard was calculated the average, standard deviation (SD) and the residual standard deviation (RSD%).

The slope, intercept, coefficient of determination  $R^2$ , and deviation of the linear regression ( $S_{y/x}$ ) were calculated.

Figure 13 shows peak at  $24.0^{\circ}2\theta$  of the standards.

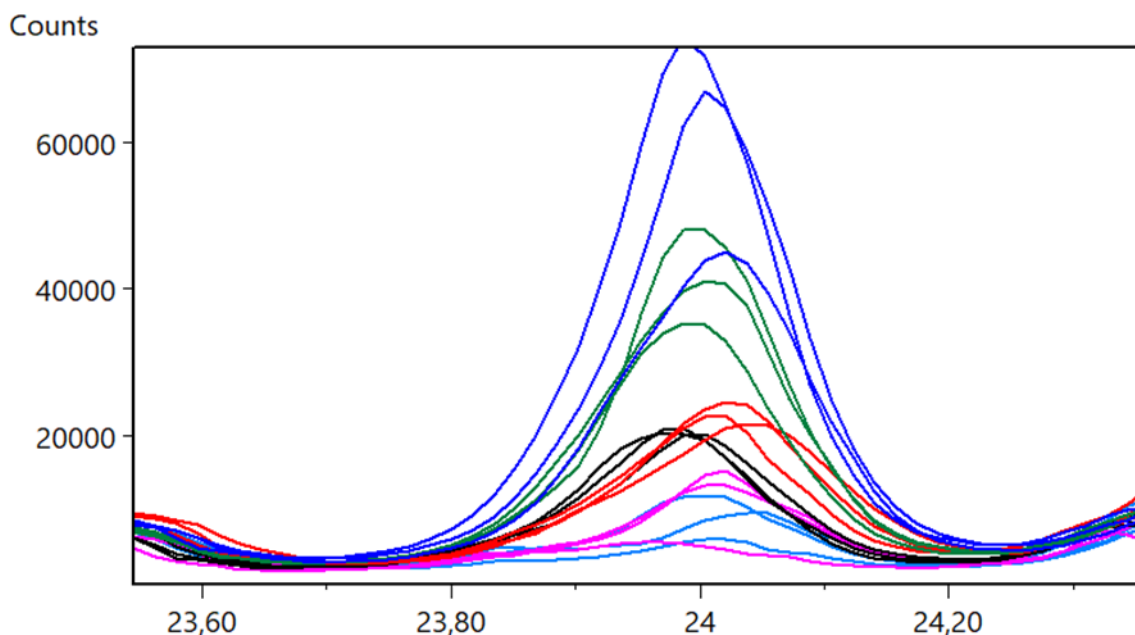


**Figure 13. XRPD comparison of signal of peak at  $24^{\circ}2\theta$  of the standards: STD 0 (cyan line), STD 1 (magenta lines), STD 2 (black lines) STD 3 (red lines), STD 4 (green line), and STD 5 (blue line)**

Figure 14 and Table 7 report the results for the univariate analysis using the signal of peak at  $24.0^{\circ}2\theta$  and the additional standard method. In this case the STD 0 considered with unknown sample and therefore added from II equal to 0% was considered in the construction of calibration curve.

The results evidenced the high value of RSD% for all the standard mixtures, especially for STD 0 and STD 1. Compared to the RSD% obtained in the analysis based on peak at  $15.0^{\circ}2\theta$ , the data of peak at  $24.0^{\circ}2\theta$  showed highly variable results. Observing the average values of the ratio and the calibration curve in Figure 14 it is noticeable the underestimation of the STD 3 and the consequent inability of the regression to distinguish between the standard STD 2 (8%w/w form II) and STD 3 (13% w/w form II). This drastically affected quality of the regression and of coefficient of determination, which value was lower than the acceptance criterion of 0.90. The extrapolated concentration of the unknown sample STD 0 was calculated using the ratio between the intercept and slope of the calibration curve obtaining the value of 1.7%, but the deviation standard ( $S_e$ ) of this value was dramatically high.

Table 7. Data of calibration curve of additional standard method via univariate analysis using peak at 24.0°2θ

STANDARD	%w/w Form II	Aliquots	Area Form II	Area Silicon	Ratio	Average Ratio	SD	RSD%
STD 0	0%	M01	864.81	903.22	0.96	1.00	0.40	40%
		M02	519.14	834.50	0.62			
		M03	1132.26	799.50	1.42			
STD 1	3%	M01	451.34	634.04	0.71	1.37	0.59	43%
		M02	1485.62	957.65	1.55			
		M03	1556.02	838.72	1.86			
STD 2	8%	M01	2657.70	783.69	3.39	3.48	0.55	16%
		M02	2535.08	624.36	4.06			
		M03	2497.09	839.65	2.97			
STD 3	13%	M01	3140.07	1048.06	3.00	3.12	0.46	15%
		M02	3195.22	881.76	3.62			
		M03	2824.70	1035.63	2.73			
STD 4	18%	M01	5651.29	929.43	6.08	6.04	0.82	14%
		M02	5843.11	854.60	6.84			
		M03	4717.49	906.55	5.20			
STD 5	23%	M01	9370.94	900.08	10.41	8.54	1.70	20%
		M02	8411.51	1036.98	8.11			
		M03	6238.80	879.41	7.09			
						<b>R<sup>2</sup></b>	<b>0.8582</b>	
						<b>SLOPE</b>	<b>0.3135</b>	
						<b>INTERCEPT</b>	<b>0.5277</b>	
						<b>S<sub>y/x</sub></b>	<b>1.09E+00</b>	
						<b>C<sub>E</sub></b>	<b>1.7%</b>	
						<b>S<sub>E</sub></b>	<b>3.6</b>	

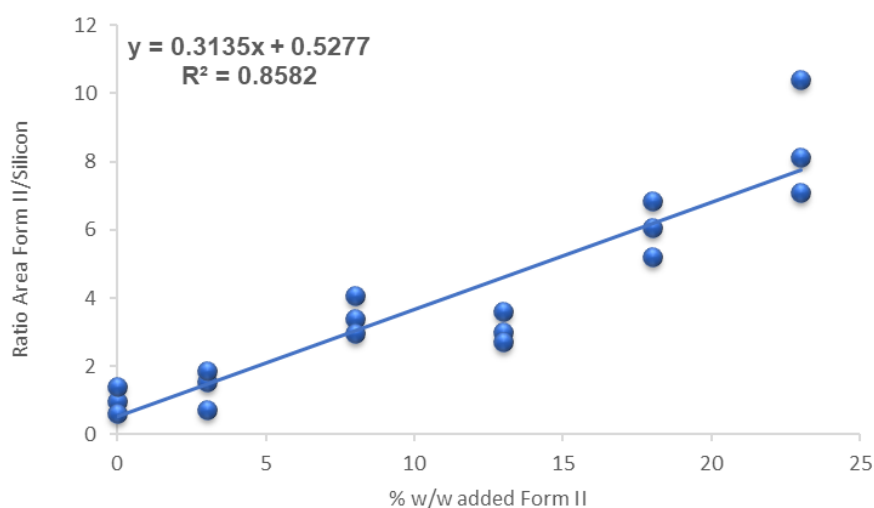


Figure 14. Calibration curve of additional standard method via univariate analysis using peak at 24.0°2θ: six points

Because the underestimation of the STD 3 significantly affects the regression, the calibration curve was recalculated excluding the STD 3. The new calibration curve presents improved  $R^2$  and deviation  $S_{y/x}$  values (see Figure 15 and Table 8). The  $R^2$  reaches and exceeds the value of 0.9, the extrapolated concentration ( $C_E$ ) is 2.2%, but it is still associated with high deviation standard value 3.0%.

Despite the good results of  $C_E$ , the standard mixtures showed significant variability between the three aliquots evidenced by the high RSD% values, probably due to the inhomogeneity of the mixtures. Inhomogeneity of the standard mixtures extremely affect the quality of the regression and it is the main issue of the solid-state quantification.

**Table 8. Results of calibration curve of additional standard method via univariate analysis using peak at 24.0°2 $\theta$ : five points**

$R^2$	<b>0.9198</b>
Slope	<b>0.3235</b>
Intercept	<b>0.7207</b>
$S_{y/x}$	<b>9.00E-01</b>
$C_E$	<b>2.2%</b>
$S_E$	<b>3.0</b>

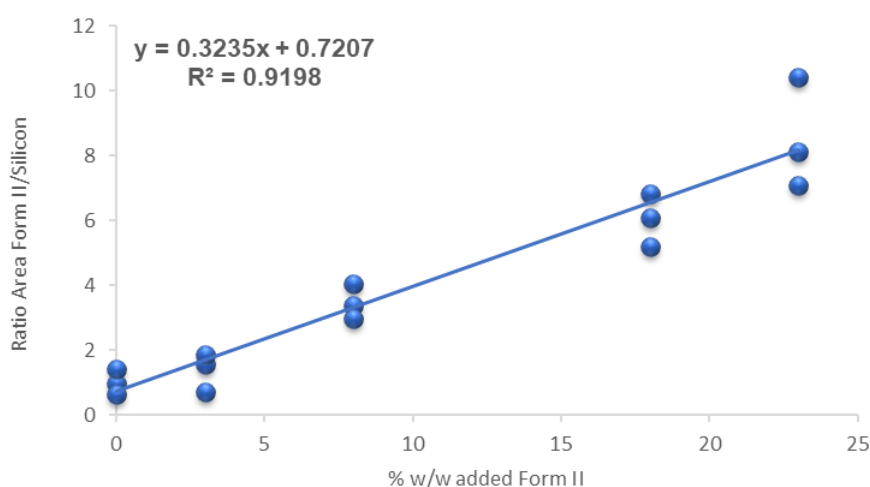


**Figure 15. Calibration curve of additional standard method via univariate analysis using peak at 24.0°2 $\theta$ : five points**

### 3.3.2.2 Multivariate analysis

The addition standard method combined with the multivariate NAS technique allows the quantification of unknown sample bypassing the matrix effect using the signal of the pure analyte and using all the signals of the analyte instead of only one peak giving reliable results based on more data

The NAS technique was applied to the standards of tachifludec and form II. The concentration of STD 0 (2%w/w Form II) was extrapolated by the application of NAS technique using the statistical software R. The descriptive system based on five main components PC was chosen based on the values of  $R^2$  and RMSE.

The value obtained for the coefficient of determination  $R^2$  indicates excellent fit of the linear NAS model to the data.

The analysis with NAS technique reached excellent value of standard deviation of the extrapolated concentration compared to the high values obtained using the univariate analysis. Thus, the NAS results were more precise than the univariate method, however the  $C_E$  is not accurate. Nevertheless, it is worth taking in mind that the matrix effect and the potential shift of the pattern, common in the XRPD technique, could have undermined the reliability of the data. The results in Table 9 and the curve in Figure 16 suggest that multivariate analysis overcomes the problem of the inhomogeneity of mixtures, especially of the STD3 mixture, observing in the univariate analysis.

Table 9. Tachifludec results of additional standard method via NAS technique

$R^2$	0.9993
Slope	256.283
Intercept	330.204
RMSE	1.74E-00
$C_E$	1.3%
$S_E$	1.13E-01%

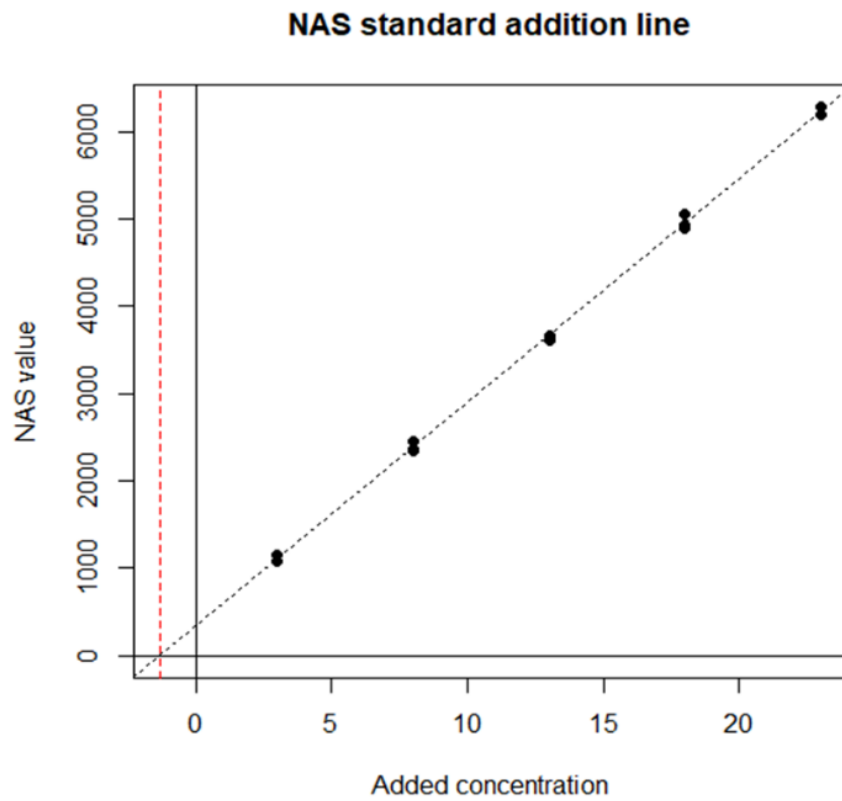


Figure 16. Tachifludec curve of additional standard method via NAS technique

## 4 QUANTIFICATION METHODS OF CRYSTALLINE AND AMORPHOUS LACTOSE

### 4.1 $\alpha$ -lactose polymorphism

Lactose is a natural disaccharide derived from the condensation of galactose and glucose, which form by a  $\beta$ -1,4 glycosidic bond. The  $\alpha$ -lactose and  $\beta$ -lactose refer to the anomeric form of the glucopyranose ring which can be in either  $\alpha$ -pyranose form or the  $\beta$ -pyranose form, whereas the galactose can only have the  $\beta$ -pyranose form. Lactose is extensively used as pharmaceutical excipients especially in tablet and inhalation dosing products. Lactose exists in five different forms, one amorphous form and four crystalline forms. The  $\alpha$ -lactose monohydrate ( $L\alpha H_2O$ ) is the commercially leading form and largely used as excipient. Additionally,  $\alpha$ -lactose exists in two anhydrous forms which differ for the stability and hygroscopicity, stable form is labelled  $L\alpha s$  while unstable  $L\alpha H$ . Whereas  $\beta$ -lactose is just known in one anhydrous form ( $L\beta$ ).<sup>30</sup>

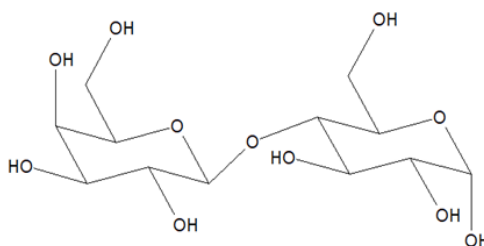


Figure 17. Chemical structure of lactose

Several studies have been conducted on the stability of the lactose polymorphs because it can affect the quality of the pharmaceutical products, especially solubility and compressibility.

The leading form  $\alpha$ -lactose monohydrate is extremely stable and poorly hygroscopic, at 75% RH and 25°C it absorbs just <1%.<sup>31</sup> It is not deliquescent behaviour until 99% RH and it does not undergo to dehydration after 2 hours at 0% RH and 50°C.<sup>32</sup> Dehydration occurs at temperature higher than 140°C, giving a mixture of  $L\alpha s$  and  $L\alpha H$  depending on the temperature.<sup>33</sup> Generally, the other forms of lactose tend to convert in more stable  $L\alpha H_2O$ .  $L\alpha H$  is extremely hygroscopic, it absorb water and crystallize in  $L\alpha H_2O$  already at 10%RH, by heating in the range 120-170°C it converts in more stable anhydrous  $L\alpha s$ .<sup>33,34</sup> Whereas, compared to  $L\alpha H$ ,  $L\alpha s$  and  $L\beta$  irreversibly crystallize in  $L\alpha H_2O$  at higher relative humidity, about 64% and 77% respectively.<sup>34</sup> Amorphous is extremely hygroscopic, it starts to gain water at 30% RH until it crystallizes in  $L\alpha H_2O$  at 50-60% RH. DSC analysis reveals it crystallizes at about 174°C.<sup>35,36</sup> However, because it is widely used as excipient several studies on its stability and quantifications are reported.<sup>36-41</sup>

The crystal data of the polymorphs of lactose are reported in Table 10.

Table 10. Crystal data of lactose forms

	$L\alpha H_2O$	$L\alpha s$	$L\alpha H$	$L\beta$
<b>CSD Refcode</b>	LACTOS01 <sup>42</sup>	EYOCUQ01 <sup>43</sup>	EYOCUQ <sup>44</sup>	BLACTO02 <sup>34</sup>
<b>Space Group</b>	$P2_1$	$P1$	$P2_1$	$P2_1$
<b>Unit Cell</b>	Monoclinic	Triclinic	Monoclinic	Monoclinic
<b>a (Å)</b>	7.815	7.6521(17)	7.7795(2)	4.9325(4)
<b>b (Å)</b>	21.567	19.8637(5)	19.6931(6)	13.2700(11)
<b>c (Å)</b>	4.844	4.98773(13)	4.90643(11)	10.7792(9)
<b><math>\alpha</math></b>	90°	92.0279(10)°	90°	90°
<b><math>\beta</math></b>	106.2°	106.2610(7)°	103.6909(15)°	91.554(4)°
<b><math>\gamma</math></b>	90°	97.1529(8)°	90°	90°
<b>Z (Z')</b>	2	2	2	2
<b>Volume (Å<sup>3</sup>)</b>	784.02	720.178	730.32	705.285

## 4.2 Experimental procedure

### 4.2.1 Characterization of crystalline $\alpha$ -lactose monohydrate

The crystalline  $\alpha$ -lactose monohydrate was ground to tested to stability and to detect eventual transition of the form during the mixing of the standard samples. The starting materials were analysed by X-Ray diffraction with Bragg-Brentano geometry diffractometer PANalytical X'Pert PRO in the range  $3\text{-}40^\circ 2\theta$  with step size of  $0.017^\circ$  and time per step of 20 s.

The crystalline  $\alpha$ -lactose monohydrate was analyzed after grinding in agata mortar and in more stressful condition in grinder Retsch MM 200 for 10 minutes at 30 Hz. Figure 18 reports the comparison between the  $\alpha$ -lactose monohydrate before and after grinding, the XRPD patterns were superimposable indicating that  $\alpha$ -lactose monohydrate is stable to grinding process.

Figure 19 shows the comparison of experimental XRPD pattern of  $\alpha$ -lactose monohydrate (red line) and the calculated pattern LACTOS03 (black line). It is worth noting that the relative intensities the experimental pattern are not comparable the calculated pattern revealing the presence of preferred orientation phenomenon. In fact, the relative intensities of the experimental pattern are comparable to the ones of the calculated pattern considering the plane 011 preferred orientated (green line).

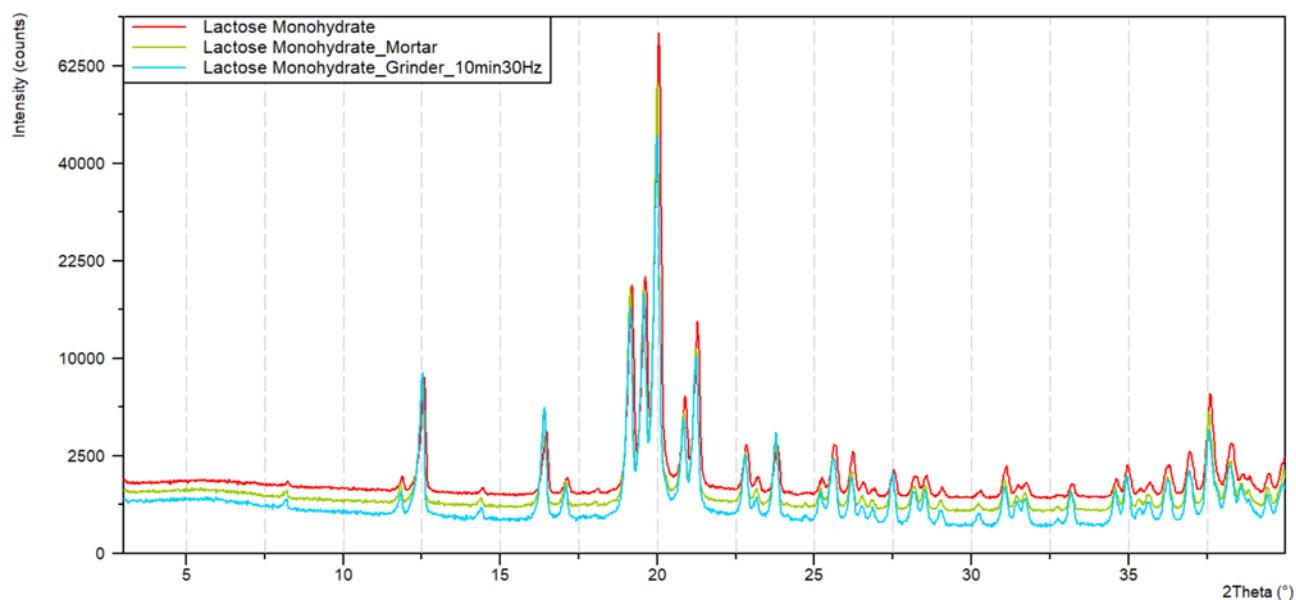


Figure 18. XRPD pattern comparison between  $\alpha$ -lactose monohydrate starting material (red line) and after grinding in agata mortar (light green line) and grinder (light blue line)

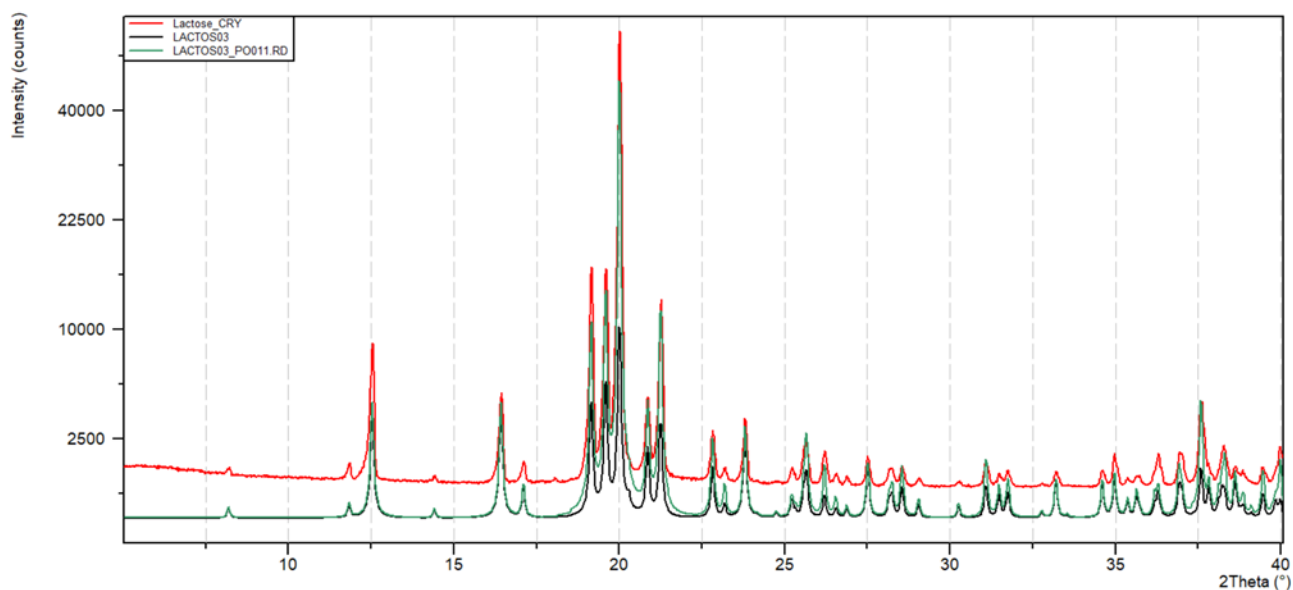


Figure 19. XRPD pattern comparison between  $\alpha$ -lactose monohydrate (red line), calculated pattern LACTOS03 (black line), and the calculated pattern considering plane 011 orientated (green line)

#### 4.2.2 Synthesis and stability of amorphous lactose

The amorphous lactose was produced by Spray drying. Solution 7 mg/L of monohydrate  $\alpha$ -lactose in HPLC water was processed using Büchi Spray Dryer B-290 at following condition: inlet temperature 170°C, aspiration 100%, Nitrogen flow 357 L/min. The solution inlet rate was 5 mL/min and the outlet temperature was 93°C. The obtained lactose was verified by X-Ray powder Diffraction. Amorphous lactose is extremely unstable because it is highly hygroscopic. It tends to absorb water and to convert in monohydrate  $\alpha$ -lactose. Therefore, amorphous lactose was placed in  $P_2O_5$  to avoid its crystallization in the monohydrate form.

The stability of amorphous lactose was evaluated after manually grinding in agata mortar, the results are reported in Figure 20 and revealed the stability of amorphous lactose to grinding.

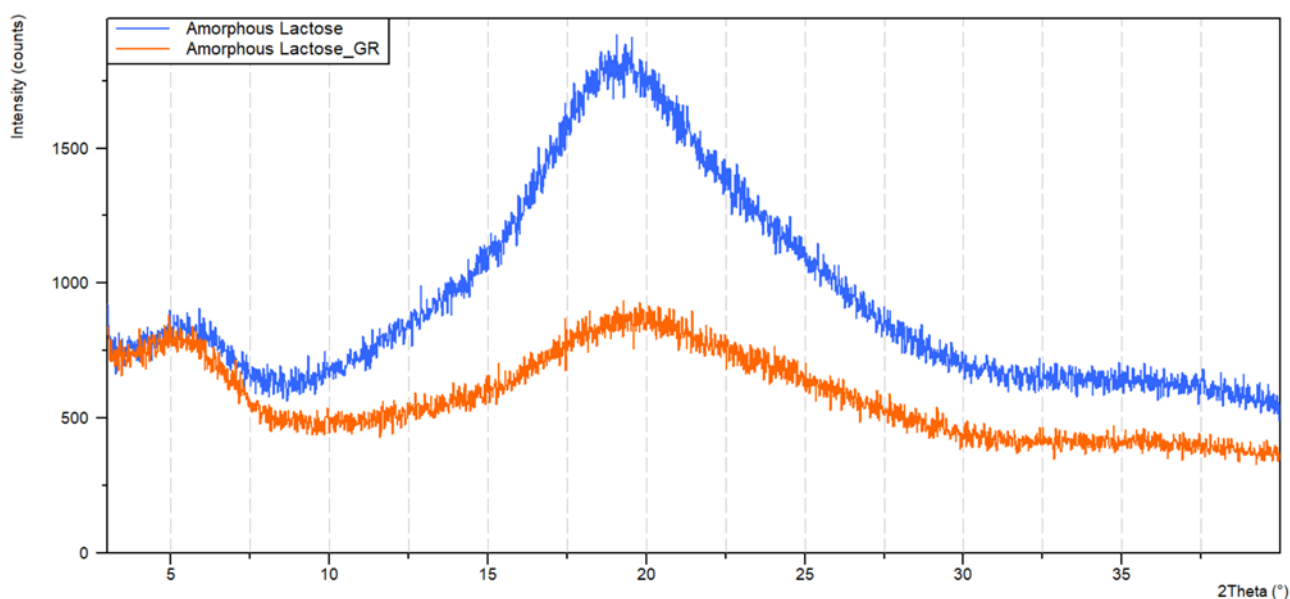


Figure 20. XRPD pattern comparison between amorphous lactose starting material (blue line) and after grinding in agata mortar (orange line)

### 4.2.3 Standard preparation

The starting sample, labelled STD 0 was prepared as a binary mixture of amorphous and crystalline lactose in percentage of 10% w/w.

The bulk STD 0 was spiked with increasing percentage of crystalline  $\alpha$ -lactose monohydrate. Additionally, silicon powder was introduced as internal standard in the mixtures in amount equal to 10% of the total weight.  $\alpha$ -lactose monohydrate and silicon were purchase by Sigma-Aldrich (Saint Louis, MO, USA).

The presence of silicon minimizes errors due to sample preparation and instrumental variables. Moreover, given its black colour, it allows the evaluation of the mixing efficiency of the components to obtain the maximum homogeneity of the mixtures. Table 11 reports the preparation of the standard mixtures.

**Table 11. Standard mixture preparation of amorphous and crystalline  $\alpha$ -lactose**

	STD 0	STD 1	STD 2	STD 3	STD 4
<b>BULK (MG)</b>	300.32	282.49	267.28	239.80	224.95
<b>ADDED CRY LACTOSE (MG)</b>	0.00	15.77	29.57	60.96	75.57
<b>SILICON (MG)</b>	30.73	30.37	30.96	30.26	30.20
<b>ADDED CRY LACTOSE (%)</b>	<b>0%</b>	<b>5%</b>	<b>10%</b>	<b>20%</b>	<b>25%</b>

Effective mixing was achieved through the method of geometric dilutions performed by mildly mixing the components in a ceramic mortar with gradual additions. This step is extremely sensitive because the mutual presence of crystalline and amorphous  $\alpha$ -lactose can promote the crystallization of the amorphous triggered by the seeding of crystalline part. Furthermore, to avoid the transition of the amorphous phase the preparation of the standard was performed in humidity condition below to 40%RH to avoid the absorption of water.

Transition of amorphous was observed in previously prepared standard set in which the amorphous lactose converted in monohydrate  $\alpha$ -lactose probably promoted by excessively energetic mixing and not controlled ambient condition. The transition of amorphous in crystalline form was evidenced by the not gradual intensity of the peaks but the intensity was visually comparable between the mixtures (Figure 21).

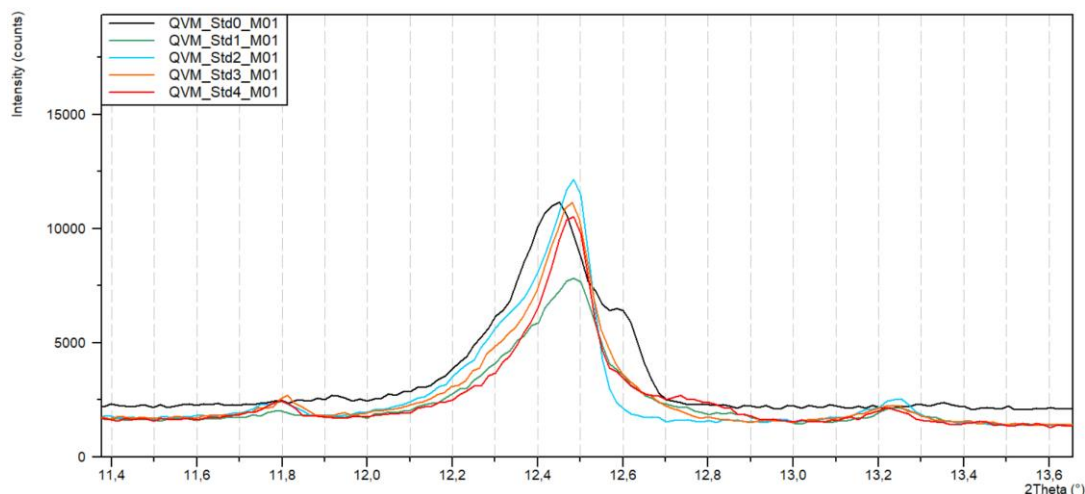


**Figure 21. XRPD comparison of peak approx. at 12.4°2 $\theta$  of the converted set of standards**

#### 4.2.4 Data analysis

Each standard was analysed in three different aliquots (labelled M01, M02, M03) by XRPD in the range 3-40°2 $\theta$  with step size equal to 0.02°, a time per step of 100 s, and generator settings of 40 kV and 40 mA.

The XRPD diffraction patterns of crystalline form constituted of well-defined peaks, while amorphous does not show the phenomenon of diffraction and its pattern results in the diffusion measurements as hump. The quantification of the amorphous content was carried out indirectly, determining the percentage of crystalline. The specificity for the lactose's peaks was not evaluated because no crystalline interferences were presented in the mixture except for silicon that showed the first peak at 28.4°2 $\theta$ .

The internal standard must be evaluated in a range where the analyte has not signal. For this reason, the standard's aliquots were also analysed in the range 55-57°2 $\theta$  to collect the peak at 56.1°2 $\theta$  of silicon. Table 12 summarized the experimental setting used for the collection of analyte and internal standard signal.

**Table 12. Experimental settings**

<b>EXPERIMENTAL SETTING</b>		
<b>Incident beam path</b>		
Soller slit (rad)	0.04	
Divergence slit	¼	
Mask	15	
Antiscatter slit	½	
Filter	None	
<b>Diffracted beam path</b>		
Soller slit	0.04	
Antiscatter slit	5.0	
<b>Measurement Settings</b>	<b>Analyte signal</b>	<b>Internal standardsignal</b>
Generator settings	40 kV-40mA	40 kV-40mA
Scan Range (°2 $\theta$ )	3-40	55-57
Step size (° $\theta$ )	0.017	0.017
Time per step (s)	100	100
Spinner revolution time (rps)	1	1

### 4.3 Data evaluation and results

#### 4.3.1 Univariate analysis

For the univariate linear model, instead of unique peak the area of five peaks at approx. 12.5, 19.1, 19.6, 20.0, and 21.3°2θ of α-lactose monohydrate were used for the construction of the calibration curves. Figure 22 shows the XRPD pattern of the aliquot M01 of the standard mixtures and the peaks chosen for the calibration were highlighted in yellow.

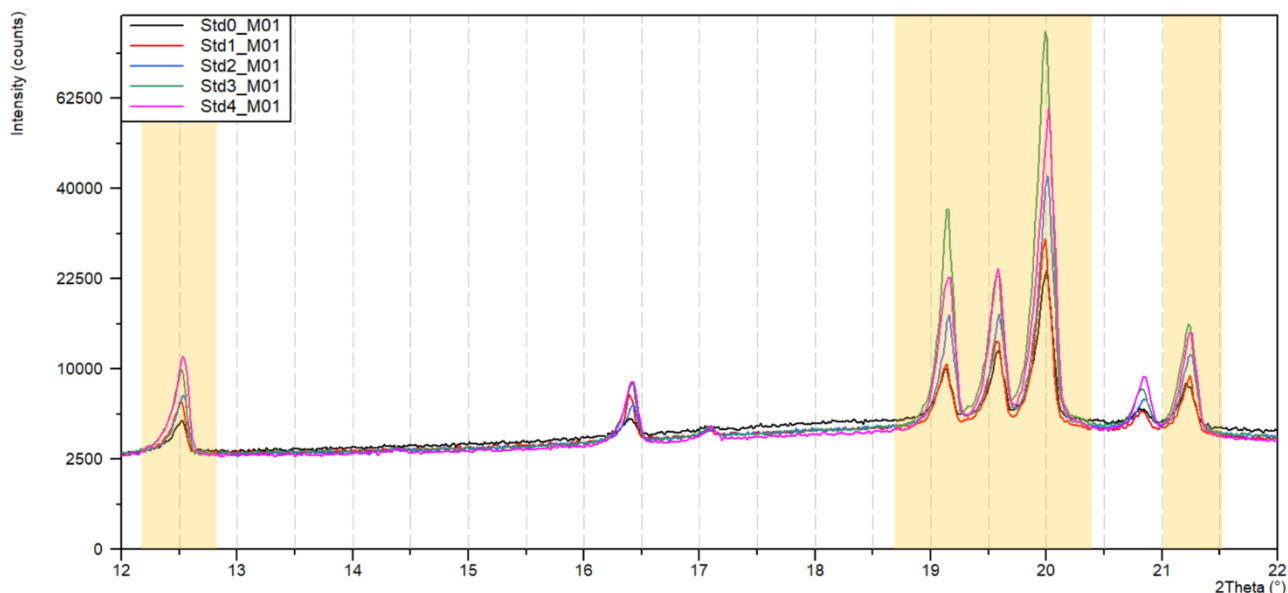


Figure 22. XRPD pattern of standard mixtures with peaks using for the construction of calibration curves highlighted in yellow

Table 13 Integration method

	Analyte	Internal standard
<b>Strip Kα<sub>2</sub></b>	-	Ratio 0.5
<b>Background</b>	Bending = 2 Granularity = 13 No smoothed data	Bending = 0 Granularity = 92 Smoothed data
<b>Search peak</b>	Minimum significance = 1 Minimum tip width = 0,01 Maximum tip width = 1 Peak base width = 2 Method = Minimum 2nd derivative	Minimum significance = 5 Minimum tip width = 0,01 Maximum tip width = 1 Peak base width = 2 Method = Minimum 2nd derivative
<b>Fitting</b>	FWHM function = Individual FWHM Profile function = Pseudo Voigt Asymmetry type = Split width and shape Shape function	FWHM function = Individual FWHM Profile function = Pseudo Voigt Asymmetry type = Split width and shape No shape function

The α-lactose monohydrate peaks' area and the area of the silicon's peak at 56.1°2θ were determined using the HighScore 4.8 software as summarized in Table 13.

For each peak two different calibration curves were plotted One considering as response the area of the α-lactose monohydrate ( Table 14), while in the latter the response was constituted by the ratio between the area of α-lactose monohydrate's peak and area of silicon

The calibration curves based only on the peak shows unsatisfactory value of R<sup>2</sup> for the peaks at 19.1 and 20.0° (see Table 14 On the contrary, the R<sup>2</sup> of calibration with peaks 12.5, 19.6 and 21.3°2θ has good values of R<sup>2</sup>,

higher than acceptance criterion of 0.9, especially the calibration with 12.5°2 $\theta$  peak. Furthermore, it showed excellent value of  $S_{y/x}$ . It is worth mentioning that the  $S_{y/x}$  value is related to the value of the response of the calibration.  $C_E$  values were excellent, especially for the calibration based on 12.5°2 $\theta$  peak (real value 10%). In conclusion, the calibration based on 12.5°2 $\theta$  peak showed the best results in term of  $R^2$ ,  $S_{y/x}$ ,  $C_E$  and related  $S_E$ .

**Table 14. Data of calibration curves from area [cts] of  $\alpha$ -lactose monohydrate's peaks**

STANDARD	% w/w cry	Area [cts] at 12.5°2 $\theta$	Area [cts] at 19.1°2 $\theta$	Area [cts] at 19.6°2 $\theta$	Area [cts] at 20.0°2 $\theta$	Area [cts] at 21.3°2 $\theta$
STD 0 M01	0%	255.20	525.33	664.79	2119.22	447.08
STD 0 M02	0%	260.67	884.51	693.26	2099.61	375.39
STD 0 M03	0%	326.51	558.01	641.42	2013.99	394.02
STD 1 M01	5%	403.87	579.89	847.51	2519.34	521.50
STD 1 M02	5%	355.81	701.06	834.95	2709.98	489.56
STD 1 M03	5%	431.04	845.18	744.85	2714.31	519.56
STD 2 M01	10%	500.72	1130.06	1136.17	3900.12	822.26
STD 2 M02	10%	484.75	1065.52	1221.74	3680.85	838.87
STD 2 M03	10%	500.13	1017.32	954.06	4043.26	704.11
STD 3 M01	20%	747.68	2595.72	1683.37	7850.63	1220.81
STD 3 M02	20%	840.71	1671.28	1628.36	6291.94	1262.82
STD 3 M03	20%	783.60	1357.69	1544.76	4480.49	1091.87
STD 4 M01	25%	946.76	1976.69	1803.84	5984.15	1163.97
STD 4 M02	25%	915.00	1812.35	1599.90	5627.67	1197.73
STD 4 M03	25%	946.36	2281.49	1870.03	6821.83	1160.17
<b>R<sup>2</sup></b>		<b>0.9828</b>	<b>0.7984</b>	<b>0.9582</b>	<b>0.8387</b>	<b>0.9368</b>
<b>SLOPE</b>		<b>26.41</b>	<b>61.23</b>	<b>46.36</b>	<b>182.15</b>	<b>34.38</b>
<b>INTERCEPT</b>		<b>263.02</b>	<b>532.00</b>	<b>634.97</b>	<b>2004.69</b>	<b>401.46</b>
<b>S<sub>y/x</sub></b>		<b>3.48E+01</b>	<b>3.07E+02</b>	<b>9.65E+01</b>	<b>7.96E+02</b>	<b>8.90E+01</b>
<b>C<sub>E</sub></b>		<b>10%</b>	<b>9%</b>	<b>14%</b>	<b>11%</b>	<b>12%</b>
<b>S<sub>E</sub></b>		<b>8.76E-01</b>	<b>3.16E+00</b>	<b>1.58E+00</b>	<b>3.02E+00</b>	<b>1.83E+00</b>

The calibration curves constructed based on the ratio between the area of  $\alpha$ -lactose and silicon are summarized in Table 15. The regression obtained with peak at 19.1 and 20.0° showed unsatisfactory value of  $R^2$ . While the  $R^2$  of calibration with peaks 12.5, 19.6 and 21.3°2 $\theta$  has good values of  $R^2$ , higher than acceptance criterion of 0.9.

The calibration based on 19.6°2 $\theta$  peak showed the best results in term of  $C_E$  and related  $S_E$  and good results of  $R^2$  and  $S_{y/x}$ .

For each peak, the difference between the calibration curves based on area of peaks of  $\alpha$ -lactose monohydrate (orange) and on ratio between  $\alpha$ -lactose monohydrate and silicon signal (blue) as response are graphically displayed in Figure 23.

Both calibration curves, area and ratio, constructed based on peaks 12.5 and 19.6°2 $\theta$  showed comparable trend. It is worth noting that aliquots of STD 3 (20% w/w crystalline) showed high variability in both area and ratio calibration curve of peaks at 19.1 and 20.0°2 $\theta$ . Although, the variability decreased using the ratio of  $\alpha$ -lactose monohydrate area and silicon area as response. The RSD% of the three aliquots of STD 3 improved from 34% to 23% for peak 19.1°2 $\theta$  respectively in area and ratio curves, and from 27% to 15% for the curves of peak at 20.0°2 $\theta$ .

The curves based on the peak at  $2\theta = 21.3^\circ$  showed comparable area and ratio values for STD 3 and STD 4, respectively 20 and 25%w/w crystalline. Hence, these curves cannot accurately discriminate between standard at 20 and 25%w/w crystalline.

The high variability of the peak's area in the standards and the similar values of STD 3 and 4 affected the linear correlation of curves constructed in particular the curves based on peaks at  $19.1$ ,  $20.0$  and  $21.3^\circ 2\theta$  of  $\alpha$ -lactose monohydrate. Contrary, the signal of peaks at  $12.5$  and  $19.6^\circ 2\theta$  of  $\alpha$ -lactose monohydrate reached good value of  $R^2$  and extrapolated concentration.

Nevertheless, it worth pointing out that the RSD% of standards were better for the area curves compared to the ratio curves of peaks  $12.5$  and  $19.6^\circ 2\theta$  (Table 16). The normalization with internal or external standard in X-Ray diffraction quantitative analysis is appropriate to adjust the signal change over time due to the lamp decay. Additionally, the presence of internal standard is beneficial to minimize errors due to sample preparation. In our case the normalization with silicon, did not improve the situation, and the calibration curves based on peak  $12.5$ ,  $19.6$  and  $21.3^\circ 2\theta$ , showed a better linearity without normalization.

Generally, the comparison between the deviation standard of the regression through Test F demonstrated that the method without normalization with silicon is more precise. The test was conducted computing the back calculating of the standard to compare the entity of the deviation standard.

In this case, it would be more favourable the use of daily single measure of external standard, e.g., silicon or alumina.

It is worth noting that the peaks at  $19.1^\circ$  and  $20.0^\circ$  are those which are more affected by the preferential orientation and this could explain the great variability on the peak area

**Table 15. Data of calibration curves from ratio between area of  $\alpha$ -lactose monohydrate and silicon**

STANDARD	% w/w cry	Area [cts] of silicon at $56.1^\circ 2\theta$	Ratio area lactose/silicon at				
			$12.5^\circ 2\theta$	$19.1^\circ 2\theta$	$19.6^\circ 2\theta$	$20^\circ 2\theta$	$21.3^\circ 2\theta$
STD 0 M01	0%	1148.47	0.22	0.46	0.58	1.85	0.39
STD 0 M02	0%	1135.94	0.23	0.78	0.61	1.85	0.33
STD 0 M03	0%	1146.58	0.28	0.49	0.56	1.76	0.34
STD 1 M01	5%	813.92	0.50	0.71	1.04	3.10	0.64
STD 1 M02	5%	1032.32	0.34	0.68	0.81	2.63	0.47
STD 1 M03	5%	927.23	0.46	0.91	0.80	2.93	0.56
STD 2 M01	10%	1247.80	0.40	0.91	0.91	3.13	0.66
STD 2 M02	10%	936.64	0.52	1.14	1.30	3.93	0.90
STD 2 M03	10%	976.75	0.51	1.04	0.98	4.14	0.72
STD 3 M01	20%	983.38	0.76	2.64	1.71	7.98	1.24
STD 3 M02	20%	893.18	0.94	1.87	1.82	7.04	1.41
STD 3 M03	20%	766.85	1.02	1.77	2.01	5.84	1.42
STD 4 M01	25%	999.19	0.95	1.98	1.81	5.99	1.16
STD 4 M02	25%	851.77	1.07	2.13	1.88	6.61	1.41
STD 4 M03	25%	828.77	1.14	2.75	2.26	8.23	1.40
	$R^2$		<b>0.9283</b>	<b>0.8653</b>	<b>0.9245</b>	<b>0.8908</b>	<b>0.9206</b>
	SLOPE		<b>0.03</b>	<b>0.07</b>	<b>0.06</b>	<b>0.22</b>	<b>0.04</b>
	INTERCEPT		<b>0.23</b>	<b>0.45</b>	<b>0.57</b>	<b>1.77</b>	<b>0.36</b>
	$S_{Y/X}$		<b>9.03E-02</b>	<b>2.94E-01</b>	<b>1.67E-01</b>	<b>7.83E-01</b>	<b>1.25E-01</b>
	$C_E$		<b>7%</b>	<b>6%</b>	<b>10%</b>	<b>8%</b>	<b>8%</b>
	$S_E$		<b>1.64E+00</b>	<b>2.22E+00</b>	<b>1.87E+00</b>	<b>2.13E+00</b>	<b>1.82E+00</b>

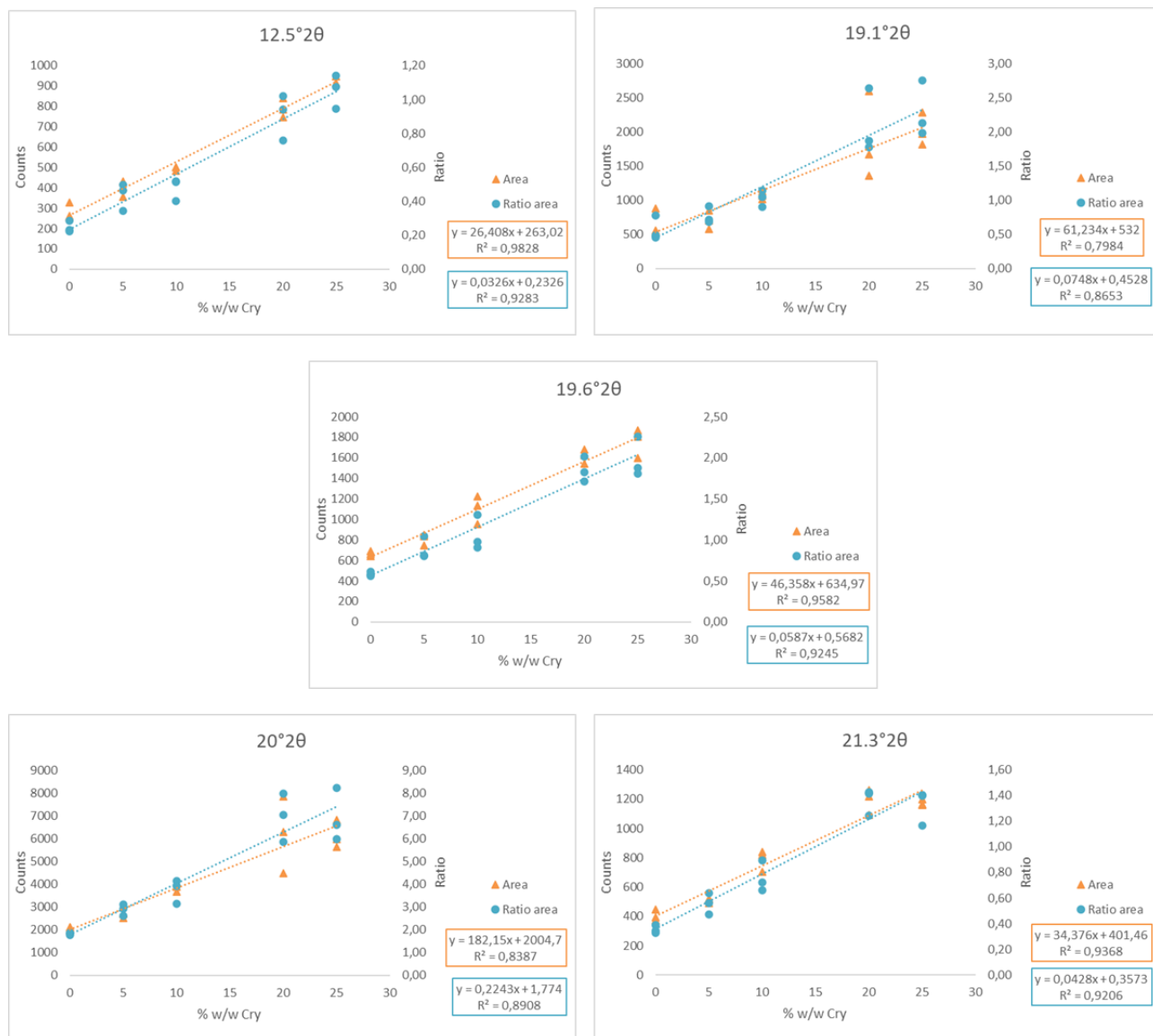


Figure 23. Comparison of the calibration curves obtained with area of peaks of  $\alpha$ -lactose monohydrate (orange) and with ratio between  $\alpha$ -lactose monohydrate and silicon (blue) as response

Table 16. Comparison between RSD% of standards for area and ratio curves obtained with peaks 12.5°2 $\theta$  and 19.6°2 $\theta$

Peak	Curve	STD 0	STD 1	STD 2	STD 3	STD 4
12.5°2 $\theta$	Area	14%	10%	2%	6%	2%
	Ratio	14%	18%	14%	15%	9%
19.6°2 $\theta$	Area	4%	7%	12%	4%	8%
	Ratio	4%	15%	20%	8%	12%

### 4.3.2 Multivariate analysis

The addition standard method combined with the multivariate NAS technique allows the quantification of content of crystalline  $\alpha$ -lactose monohydrate in the bulk based on all the diffractometric data and not only relying on the signal of individual peak.

The NAS technique was applied to determine the concentration of STD 0 (10%w/w crystalline  $\alpha$ -lactose) extrapolated using the statistical software R. The descriptive system based on nine main components PC was chosen based on the  $R^2$  and RMSE values.

The results of the analysis are shown in Figure 24 and Table 17. The value obtained for the coefficient of determination  $R^2$  indicates a very good fit of the linear NAS model to the data. The extrapolated concentration value of 12% is very close to that introduced in the preparation of the initial bulk equal to 10%. Additionally, the deviation of extrapolated concentration  $S_E$  is remarkable low, the method is extremely accurate and precise.

Both univariate and multivariate analysis gave back satisfactory value of concentration of bulk sample, but the multivariate analysis showed excellent  $R^2$  value and especially highly better  $S_E$  value compared to univariate analysis. The possibility to average the analyte signal on the whole pattern allowed to minimize the variability and error due to the preferred orientation.

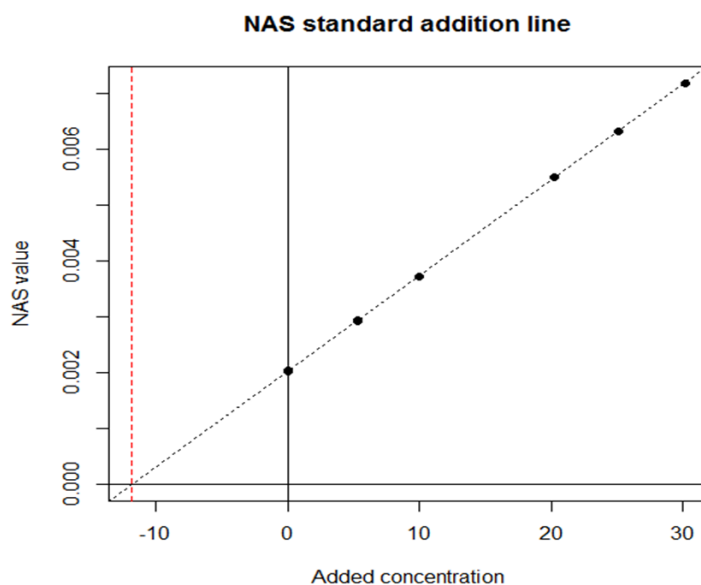


Figure 24. Amorphous-crystalline  $\alpha$ -lactose curve of additional standard method via NAS technique

Table 17. Amorphous-crystalline  $\alpha$ -lactose results of additional standard method via NAS technique

$R^2$	0.9999
Slope	1.71E-04
Intercept	2.03E-03
RMSE	1.13E-00
$C_E$	12%
$S_E$	2.23E-02

## 5 QUANTIFICATION METHOD OF CRYSTALLINE LACTOSE AND HPMC

Generally, amorphous phase is unstable form and in presence of crystalline form, the crystallization can be easily triggered. That is why it is fundamental that the amorphous is stable during all the processes of standard preparation, mixing, and analysis, to guarantee a correct quantification.

Indeed, a set of standards containing crystalline and amorphous  $\alpha$ -lactose monohydrate showed transition of the amorphous phase probably occurred during the standard preparation and observable from the similar intensity of the peaks of theoretically different crystalline concentration standards.

To overcome the crystallization of the amorphous, the quantification of crystallinity of  $\alpha$ -lactose was carried out in standard which contains stable amorphous component to prevent errors in quantification. Hydroxypropyl methyl cellulose (HPMC) was used as amorphous surrogate. HPMC is a semi-synthetic, inert, and viscoelastic polymer used as excipient in several commercial products. The choice of this polymer was motivated by analogous characteristics to real amorphous particularly its MAC (Mass Absorption Coefficient) of 6.49, very similar to those of  $\alpha$ -lactose (7.46). The MAC coefficient is related to the intensity transmitted by a material when interacting with X-rays, its density, and its thickness. Nevertheless, XRPD pattern of HPMC and amorphous  $\alpha$ -lactose looked slightly different, especially at low angles (Figure 25).

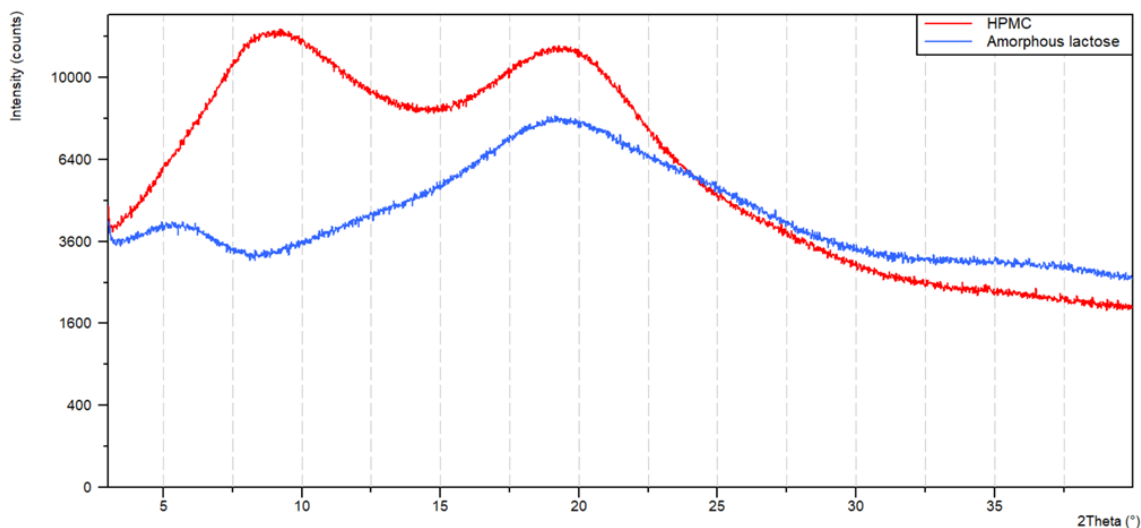


Figure 25. XRPD pattern comparison between HPMC (red line) and amorphous  $\alpha$ -lactose (blue line)

### 5.1 Experimental procedure

#### 5.1.1 Standard preparation

The preparation of the mixtures containing HPMC was carried out using the same procedure for amorphous  $\alpha$ -lactose mixtures.

A bulk, labelled STD 0, constitutes the binary mixture of HPMC and crystalline  $\alpha$ -lactose in percentage of 10% w/w then the sample was spiked with increasing percentage of crystalline  $\alpha$ -lactose monohydrate. HPMC was provided by Acros Organics (Geel, Belgium).

Furthermore, silicon powder was introduced as internal standard in the mixtures in amount equal to 10% of the total weight. Table 18 reports the preparation of the standard mixtures.

The method of geometric dilution was used to mix the components in a ceramic mortar with gradual additions.

**Table 18. Standard mixture preparation of amorphous and crystalline  $\alpha$ -lactose**

	<b>STD 0</b>	<b>STD 1</b>	<b>STD 2</b>	<b>STD 3</b>	<b>STD 4</b>
<b>BULK (MG)</b>	399.50	380.10	359.75	319.49	299.39
<b>ADDED CRY LACTOSE (MG)</b>	0.00	20.25	40.4	80.73	100.71
<b>SILICON (MG)</b>	39.84	40.06	40.03	40.00	40.00
<b>ADDED CRY LACTOSE (%)</b>	<b>0%</b>	<b>5%</b>	<b>10%</b>	<b>20%</b>	<b>25%</b>

### 5.1.2 Data analysis

The analysis of the standard mixtures containing HPMC was carried out using the same procedure for amorphous  $\alpha$ -lactose mixtures.

Each standard was analysed in three aliquots by XRPD in the range 3-40°2 $\theta$  with step size equal to 0.02°, a time per step of 100 s, and generator settings of 40 kV and 40 mA.

Table 12 summarized the experimental setting used for the collection of analyte and internal standard signal.

**Table 19. Experimental settings**

<b>EXPERIMENTAL SETTING</b>		
<b>Incident beam path</b>		
Soller slit (rad)	0.04	
Divergence slit	¼	
Mask	15	
Antiscatter slit	½	
Filter	None	
<b>Diffacted beam path</b>		
Soller slit	0.04	
Antiscatter slit	5.0	
<b>Measurement Settings</b>	<b>Analyte signal</b>	<b>Internal standard signal</b>
Generator settings	40 kV-40mA	40 kV-40mA
Scan Range (°2 $\theta$ )	3-40	55-57
Step size (° $\theta$ )	0.017	0.017
Time per step (s)	100	100
Spinner revolution time (rps)	1	1

## 5.2 Data evaluation and results

### 5.2.1 Univariate analysis

The area of peaks at approx. 12.5, 19.1, 19.6, 20.0, and 21.3°2 $\theta$  of  $\alpha$ -lactose monohydrate were used for the construction of the calibration curves in the univariate model

**Table 20 Integration method**

	Analyte	Internal standard
<b>Strip K<math>\alpha_2</math></b>	-	Ratio 0.4
<b>Background</b>	Bending = 2 Granularity = 10 No smoothed data	Bending = 0 Granularity = 92 Smoothed data
<b>Search peak</b>	Minimum significance = 1 Minimum tip width = 0,01 Maximum tip width = 1 Peak base width = 2 Method = Minimum 2nd derivative	Minimum significance = 10 Minimum tip width = 0,01 Maximum tip width = 1 Peak base width = 2 Method = Minimum 2nd derivative
<b>Fitting</b>	FWHM function = Individual FWHM Profile function = Pseudo Voigt Asymmetry type = Split width and shape No shape function	FWHM function = Individual FWHM Profile function = Pseudo Voigt Asymmetry type = Split width and shape No shape function

The  $\alpha$ -lactose monohydrate peaks' area and the area of the silicon's peak at 56.1°2 $\theta$  were determined using the HighScore 4.8 software as summarized in Table 20.

For each peak two different calibration curves were plotted. One considering as response the area of the  $\alpha$ -lactose monohydrate (Table 21) while in the latter the response was constituted by the ratio between the area of  $\alpha$ -lactose monohydrate's peak and area of silicon( Table 22)

The results in Table 21 show that all the regression showed satisfactory value of  $R^2$ , higher than acceptance criterion of 0.9, except the regression obtained with the area of the peak at 19.1°2 $\theta$ .  $C_E$  values were generally excellent (real value 10%). The best  $S_E$ ,  $R^2$ , and  $S_{y/x}$  was observed for the calibration curve based on peak 21.3°2 $\theta$ , but it showed slight inaccurate value of  $C_E$ .

Table 21. Data of calibration curves from area [cts] of  $\alpha$ -lactose monohydrate's peaks

STANDARD	% w/w cry	Area [cts] at 12.5°2 $\theta$	Area [cts] at 19.1°2 $\theta$	Area [cts] at 19.6°2 $\theta$	Area [cts] at 20.0°2 $\theta$	Area [cts] at 21.3°2 $\theta$
STD 0 M01	0%	289.19	453.46	444.13	1836.53	503.59
STD 0 M02	0%	238.56	574.69	485.39	1598.84	555.77
STD 0 M03	0%	247.17	409.56	692.18	1477.26	430.66
STD 1 M01	5%	468.57	804.89	941.25	2551.66	609.20
STD 1 M02	5%	396.39	672.26	788.66	3126.11	606.18
STD 1 M03	5%	473.69	646.27	689.08	2280.25	597.36
STD 2 M01	10%	563.98	838.02	847.39	3703.76	721.38
STD 2 M02	10%	493.82	909.85	970.85	3562.44	780.81
STD 2 M03	10%	500.92	1084.89	977.69	4831.52	809.24
STD 3 M01	20%	870.54	1106.24	1456.88	5627.89	1155.80
STD 3 M02	20%	1024.13	1493.13	1593.58	6274.77	1110.47
STD 3 M03	20%	801.31	1734.08	1697.08	5564.81	1216.75
STD 4 M01	25%	916.71	1551.47	1531.62	6996.14	1374.12
STD 4 M02	25%	987.86	1581.65	2067.81	6509.41	1478.26
STD 4 M03	25%	996.01	1950.59	1731.03	6720.61	1367.56
<b>R<sup>2</sup></b>		<b>0.9513</b>	<b>0.8947</b>	<b>0.9185</b>	<b>0.9622</b>	<b>0.9738</b>
<b>SLOPE</b>		<b>29.06</b>	<b>48.82</b>	<b>50.61</b>	<b>204.52</b>	<b>36.85</b>
<b>INTERCEPT</b>		<b>269.19</b>	<b>468.27</b>	<b>520.28</b>	<b>1723.26</b>	<b>445.66</b>
<b>S<sub>YX</sub></b>		<b>6.55E+01</b>	<b>1.67E+02</b>	<b>1.50E+02</b>	<b>4.04E+02</b>	<b>6.02E+01</b>
<b>C<sub>E</sub></b>		<b>9%</b>	<b>10%</b>	<b>10%</b>	<b>8%</b>	<b>12%</b>
<b>S<sub>E</sub></b>		<b>1.45E+00</b>	<b>2.24E+00</b>	<b>1.99E+00</b>	<b>1.23E+00</b>	<b>1.17E+00</b>

Table 22 reports the results related to the calibration curves constructed based on the ratio between the area of  $\alpha$ -lactose and silicon. Again, the regression obtained with peak at 19.1 showed unsatisfactory value of  $R^2$ . While the  $R^2$  of the calibration with the other peaks showed good values higher than acceptance criterion of 0.9. Nevertheless, they were worse than the values in Table 21, also in term of  $S_{y/x}$  values. Also, the obtained  $C_E$  were less accurate as highlighted by the higher the  $S_E$  values.

, In Figure 26 the difference between the calibration curves based on area of peaks of  $\alpha$ -lactose monohydrate (red) and on ratio between  $\alpha$ -lactose monohydrate and silicon signal (green) as response are graphically displayed.

Both calibration curves, area and ratio, constructed based on peaks 12.5 and 21.3°2 $\theta$  showed comparable trend.

It is worth noting that all the curves showed comparable response (y value) for STD 3 and STD 4, respectively 20 and 25%w/w crystalline. Hence, accurate discrimination between standard at 20 and 25%w/w crystalline was not possible, except for both calibration curves of peak 21.3°2 $\theta$ .

Even for the  $\alpha$ -lactose-HPMC quantification, the results obtained using the ratio between area of  $\alpha$ -lactose and silicon were lesser satisfactory, as well as for the quantification amorphous-crystalline  $\alpha$ -lactose. Test F carried out on the deviation standard of the back-calculated regressions revealed all the regression based on the area were more precise than the regression with normalization with silicon.

Concerning the response of the different peaks in the two type of quantification, the calibration curve based on the peak at 19.1°2 $\theta$  gave the worst results in both the quantifications while the peak at 12.5°2 $\theta$  had good correlation and results in both the calibration. In the quantification HPMC-crystalline  $\alpha$ -lactose the best results were obtained using the peak at 21.3°2 $\theta$ .

Generally, the determination of crystallinity degree of  $\alpha$ -lactose monohydrate using HPMC as amorphous was successful, HPMC has proven to be valid option in case of unstable amorphous.

Table 22. Data of calibration curves from ratio between area of  $\alpha$ -lactose monohydrate and silicon

STANDARD	% w/w cry	Area [cts] of silicon at 56.1°2 $\theta$	Ratio area lactose/silicon at				
			12.5°2 $\theta$	19.1°2 $\theta$	19.6°2 $\theta$	20°2 $\theta$	21.3°2 $\theta$
STD 0 M01	0%	1120.54	0.26	0.40	0.40	1.64	0.45
STD 0 M02	0%	1314.16	0.18	0.44	0.37	1.22	0.42
STD 0 M03	0%	1052.14	0.23	0.39	0.66	1.40	0.41
STD 1 M01	5%	1189.08	0.39	0.68	0.79	2.15	0.51
STD 1 M02	5%	1092.16	0.36	0.62	0.72	2.86	0.56
STD 1 M03	5%	1218.79	0.39	0.53	0.57	1.87	0.49
STD 2 M01	10%	1178.77	0.48	0.71	0.72	3.14	0.61
STD 2 M02	10%	1320.23	0.37	0.69	0.74	2.70	0.59
STD 2 M03	10%	1303.55	0.38	0.83	0.75	3.71	0.62
STD 3 M01	20%	1109.61	0.78	1.00	1.31	5.07	1.04
STD 3 M02	20%	1141.72	0.90	1.31	1.40	5.50	0.97
STD 3 M03	20%	1056.42	0.76	1.64	1.61	5.27	1.15
STD 4 M01	25%	1031.61	0.89	1.50	1.48	6.78	1.33
STD 4 M02	25%	1249.95	0.79	1.27	1.65	5.21	1.18
STD 4 M03	25%	1255.37	0.79	1.55	1.38	5.35	1.09
	<b>R<sup>2</sup></b>		<b>0.9273</b>	<b>0.8854</b>	<b>0.9012</b>	<b>0.9341</b>	<b>0.9406</b>
	<b>SLOPE</b>		<b>0.03</b>	<b>0.04</b>	<b>0.04</b>	<b>0.18</b>	<b>0.03</b>
	<b>INTERCEPT</b>		<b>0.22</b>	<b>0.38</b>	<b>0.44</b>	<b>1.42</b>	<b>0.37</b>
	<b>S<sub>Y/X</sub></b>		<b>7.15E-02</b>	<b>1.55E-01</b>	<b>1.46E-01</b>	<b>4.79E-01</b>	<b>8.20E-02</b>
	<b>C<sub>E</sub></b>		<b>9%</b>	<b>9%</b>	<b>10%</b>	<b>8%</b>	<b>11%</b>
	<b>S<sub>E</sub></b>		<b>1.76E+00</b>	<b>2.28E+00</b>	<b>2.18E+00</b>	<b>1.61E+00</b>	<b>1.75E+00</b>

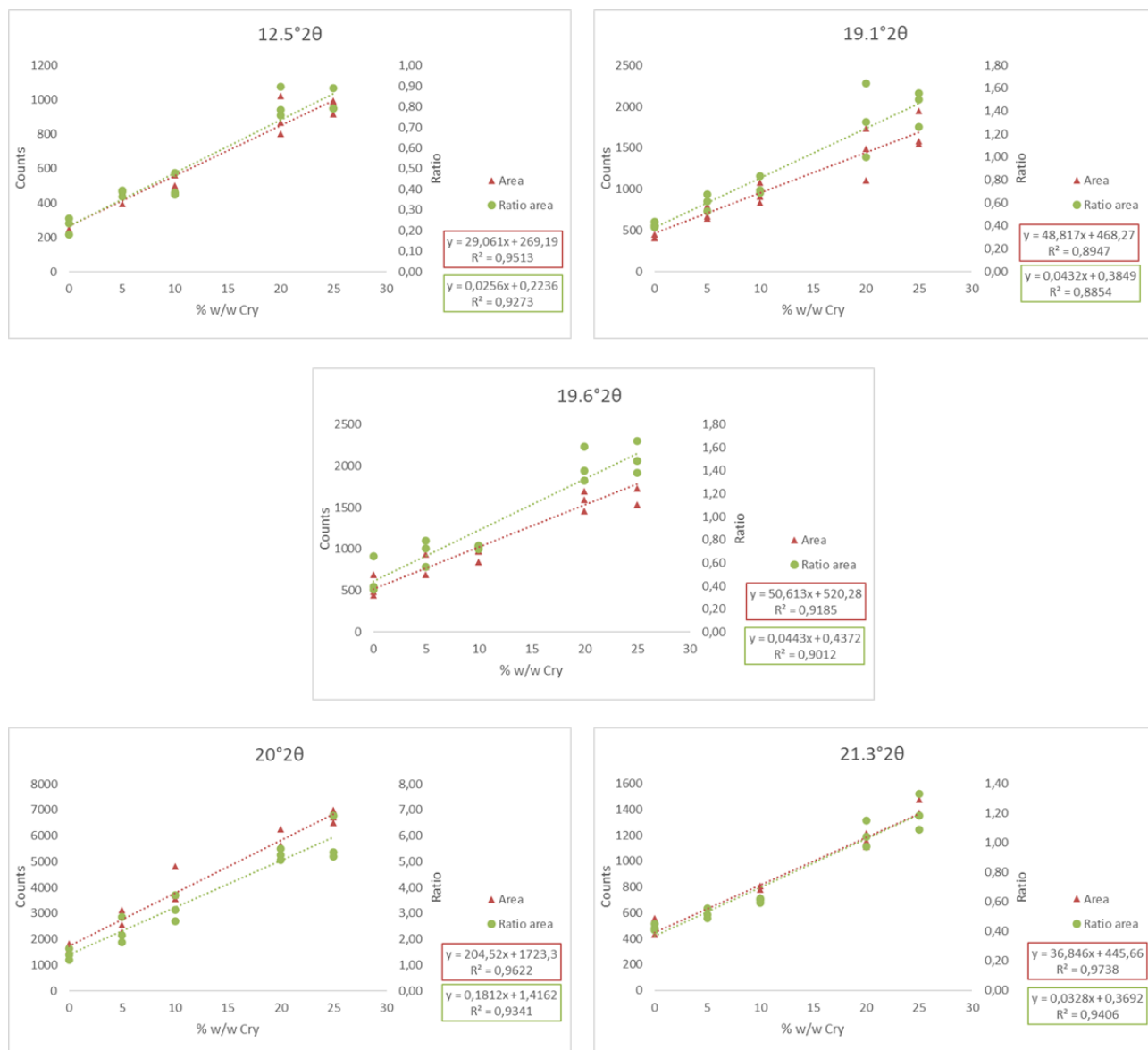


Figure 26. Comparison of the calibration curves obtained with area of peaks of α-lactose monohydrate (red) and with ratio between α-lactose monohydrate and silicon (green) as response

To evaluate the possible use of HPMC for the construction of calibration curve in case of unstable amorphous, the calibration curve based on the integrated area of the peak at 21.3° was used to quantify the crystalline phase of STD3 (20%) made of α-lactose crystalline and amorphous. The interpolated values are reported in Table 23. Satisfactory results were obtained with an average of recovery nearby the 100% and RSD% of the three aliquots less than 20%.

Table 23. Interpolation of STD 3 (20%)

	Back-calculated	Recovery%	Average of recovery%	SD of recovery %	RSD%
STD 20%	21,04	105%	101%	0,12	12%
	22,18	111%			
	17,54	88%			

### 5.2.2 Multivariate analysis

The addition standard method combined with the multivariate NAS technique was evaluated for the quantification of content of crystalline  $\alpha$ -lactose monohydrate in the binary mixtures containing  $\alpha$ -lactose monohydrate and HPMC.

The NAS technique was applied to determine the concentration of STD 0 (10%w/w crystalline  $\alpha$ -lactose) extrapolated using the statistical software R. The descriptive system based on nine main components PC was chosen based on the  $R^2$  and RMSE values.

The results of the analysis are shown in Figure 27 and Table 24. The value obtained for the coefficient of determination  $R^2$  indicates a very good fit of the linear NAS model to the data. The extrapolated concentration value of 9% is very close to that introduced in the preparation of the initial bulk equal to 10%. Additionally, the deviation of extrapolated concentration  $S_E$  is remarkable low, the method is extremely accurate and precise.

Both univariate and multivariate analysis gave back satisfactory value of concentration of bulk sample. Nevertheless, multivariate analysis showed excellent  $R^2$  value and especially highly better  $S_E$  value compared to univariate analysis for both system amorphous-crystalline  $\alpha$ -lactose and HPMC-crystalline  $\alpha$ -lactose. The analyses carried out using both the real amorphous and the surrogate one (HPMC) showed a substantial agreement in the results, particularly by multivariate method.

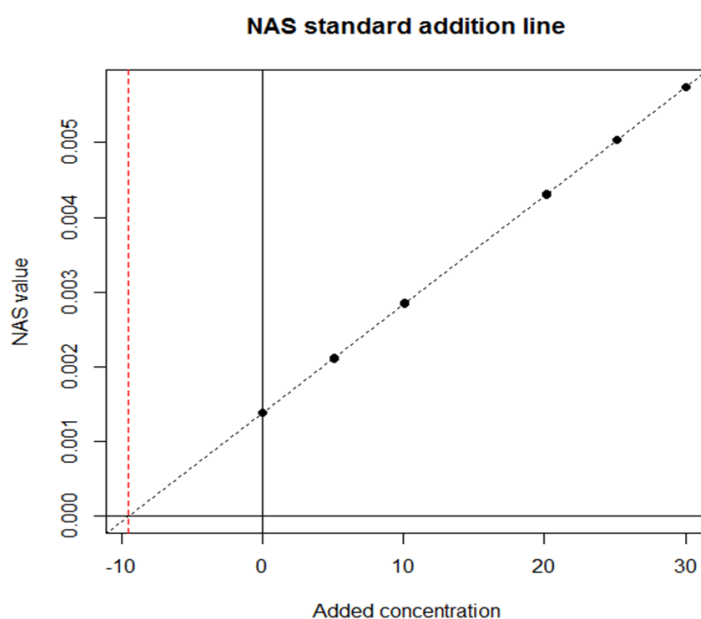


Figure 27. HPMC-crystalline  $\alpha$ -lactose curve of additional standard method via NAS technique

Table 24. HPMC-crystalline  $\alpha$ -lactose results of additional standard method via NAS technique

$R^2$	0.9999
Slope	1.45E-04
Intercept	1.38E-03
RMSE	1.61E-00
$C_E$	9%
$S_E$	2.66E-02

## 6 CONCLUSION

The work aimed to evaluate the potential application of the standard addition method (SAM) in solid-state quantification in two different cases, formulation, and amorphous-crystalline samples. Additionally, the comparison between univariate and multivariate statistical methods was carried out.

In case of analysis of paracetamol form II in tachifludec formulation, the selection of suitably intense specific peak of paracetamol form II was difficult. In fact, the only specific peak, which does not overlap the peaks of the matrix was not enough intense to obtain a satisfactory calibration curve. Hence, the SAM method was applied with univariate analysis based on the most intense peak at  $24.0^{\circ}2\theta$  of paracetamol form II, which gave accurate quantification, but with a high standard deviation.

. The multivariate analysis gave better results than the univariate analysis, especially in term of  $R^2$  and deviation standard of the extrapolated concentration. Probably, the multivariate analysis based on whole pattern can overcome the problem of the variability of the aliquots of the same standard mixtures, that affect the solid-state analysis, especially the univariate analysis based exclusively on one peak.

The determination of the crystalline fraction in the amorphous-crystalline samples was quite challenging.  $\alpha$  - lactose monohydrate is affected by preferential orientation and in the mixtures the relative intensities are not preserved which decrease the precision and accuracy of the quantification.

Even in the case of amorphous-crystalline quantification the multivariate analysis evidenced the best results. Concerning the comparison between real amorphous and HPMC standard sets, slightly different results were observed for the five  $\alpha$ -lactose monohydrate peaks tested. Although, for both the standard set the calibration curves based on peaks  $12.5$  and  $21.3^{\circ}2\theta$  showed satisfactory results with  $R_2$  values within the acceptance criterion of 0.9. It was possible to quantify the crystalline in STD3 of the sample containing amorphous lactose and 20% of  $\alpha$ -lactose monohydrate on the curve of  $21.3^{\circ}2\theta$  peak constructed with HPMC. The obtained back-loading and recovery % are accurate. Hence, the HPMC may be used as surrogate amorphous in construction of calibration curve in case of unstable real amorphous.

Surprisingly, both the curves with real amorphous and HPMC showed worst results normalizing the area of the  $\alpha$ -lactose monohydrate with the internal standard silicon. Increase in deviation standard and decrease of the  $R^2$  was observed with the application of internal standard. Nevertheless, the use of internal standard is useful in X-Ray Powder Diffraction because of the decay of the lamp. The results of samples analysed with calibration curve constructed with normalization are more trustworthy than calibration without normalization because the changes in intensity due to the decay of the lamp over time are considered. Therefore, the minor linearity, accuracy, and precision of the calibration curve are balanced by the trustworthiness of the curve over time.

## 7 REFERENCES

- (1) Brereton, R. G. *Applied Chemiometric for Scientists*; John Wiley & Sons, Ltd, 2007.
- (2) Miller, J. N.; Miller, J. C. *Statistic and Chemometrics for Analytical Chemistry*, 5th ed.; Pearson Prentice Hall, 2005.
- (3) Kurt Varmuza, K.; Filzmoser, P. *Introduction to Multivariate Statistical Analysis in Chemometrics*; Taylor and Francis Ltd, 2009.
- (4) Sekulic, S.; Seasholtz, M. B.; Wang, Z.; Kowalski, B. R.; Lee, S. E.; Holt, B. R. Nonlinear Multivariate Calibration Methods in Analytical Chemistry. *Anal. Chem.* **1993**, *65* (19), 835A-845A. <https://doi.org/10.1021/ac00067a001>.
- (5) Yuan, M.; Ekici, A.; Lu, Z.; Monteiro, R. Dimension Reduction and Coefficient Estimation in Multivariate Linear Regression. *J. R. Stat. Soc. Ser. B Stat. Methodol.* **2007**, *69* (3), 329–346. <https://doi.org/10.1111/j.1467-9868.2007.00591.x>.
- (6) Mevik, B.-H.; Wehrens, R. The PLS Package: Principal Component and Partial Least Squares Regression in R. *J. Stat. Softw.* **2007**, *18* (2).
- (7) Li, B.; Morris, J.; Martin, E. B. Model Selection for Partial Least Squares Regression. *Chemom. Intell. Lab. Syst.* **2002**, *64* (1), 79–89. [https://doi.org/10.1016/S0169-7439\(02\)00051-5](https://doi.org/10.1016/S0169-7439(02)00051-5).
- (8) S. De Jong. SIMPLS: An Alternative Approach to Partial Least Squares Regression. *Chemom. Intell. Lab. Syst.* **1993**, *18*, 251–263.
- (9) Lorber, A.; Fabert, K.; Kowalski, B. R. Net Analyte Signal Calculation in Multivariate Calibration. *Anal. Chem.* **1997**, *69* (8), 1620–1626. <https://doi.org/10.1021/ac960862b>.
- (10) Ferré, J.; Faber, N. M. Net Analyte Signal Calculation for Multivariate Calibration. *Chemom. Intell. Lab. Syst.* **2003**, *69* (1–2), 123–136. [https://doi.org/10.1016/S0169-7439\(03\)00118-7](https://doi.org/10.1016/S0169-7439(03)00118-7).
- (11) Hemmateenejad, B.; Yousefinejad, S. Multivariate Standard Addition Method Solved by Net Analyte Signal Calculation and Rank Annihilation Factor Analysis. *Anal. Bioanal. Chem.* **2009**, *394* (7), 1965–1975. <https://doi.org/10.1007/s00216-009-2870-1>.
- (12) Zappi, A.; Maini, L.; Galimberti, G.; Caliandro, R.; Melucci, D. Quantifying API Polymorphs in Formulations Using X-Ray Powder Diffraction and Multivariate Standard Addition Method Combined with Net Analyte Signal Analysis. *Eur. J. Pharm. Sci.* **2019**, *130* (October 2018), 36–43. <https://doi.org/10.1016/j.ejps.2019.01.014>.
- (13) Bro, R.; Andersen, C. M. Theory of Net Analyte Signal Vectors in Inverse Regression. *J. Chemom.* **2003**, *17* (12), 646–652. <https://doi.org/10.1002/cem.832>.
- (14) Sinatra. Erratum: Efficacy and Safety of Single and Repeated Administration of 1 Gram Intravenous Acetaminophen Injection (Paracetamol) for Pain Management after Major Orthopedic Surgery (Anesthesiology (April 2005) 102 (822-831)). *Anesthesiology* **2005**, *103* (4), 916. <https://doi.org/10.1097/00000542-200510000-00051>.
- (15) Bertolini, A.; Ferrari, A.; Ottani, A.; Guerzoni, S.; Tacchi, R.; Leone, S. Paracetamol: New Vistas of an Old Drug. *CNS Drug Rev.* **2006**, *12* (3–4), 250–275. <https://doi.org/10.1111/j.1527-3458.2006.00250.x>.
- (16) Graham, G. G.; Scott, K. F. Mechanism of Action of Paracetamol. *Am. J. Ther.* **2005**, *12* (1), 46–55. <https://doi.org/10.1097/00045391-200501000-00008>.
- (17) Duggan, S. T.; Scott, L. J. Intravenous Paracetamol (Acetaminophen). *Drugs* **2009**, *69* (1), 101–113. <https://doi.org/10.2165/00003495-200969010-00007>.
- (18) Haisa, B. Y. M.; Kashino, S.; Maeda, H. The Orthorhombic Form Ofp-Hydroxyacetanilide. *Acta Crystallogr. Sect. B Struct. Sci. Cryst. Eng. Mater.* **1974**, *30*, 2510–2512.
- (19) Haisa, B. Y. M.; Kashino, S.; Kawai, R.; Maeda, H. The Monoclinic Form Ofp-Hydroxyacetanilide. *Acta Crystallogr. Sect. B Struct. Sci. Cryst. Eng. Mater.* **1976**, *32*, 1283–1285.
- (20) Reiss, C. A.; Van Mechelen, J. B.; Goubitz, K.; Peschar, R. Reassessment of Paracetamol Orthorhombic Form III and Determination of a Novel Low-Temperature Monoclinic Form III-m from Powder Diffraction Data. *Acta Crystallogr. Sect. C Struct. Chem.* **2018**, *74* (3), 392–399. <https://doi.org/10.1107/S2053229618002619>.
- (21) Di Martino, P.; Guyot-Hermann, A. M.; Conflant, P.; Drache, M.; Guyot, J. C. A New Pure Paracetamol

- for Direct Compression: The Orthorhombic Form. *Int. J. Pharm.* **1996**, *128* (1–2), 1–8. [https://doi.org/10.1016/0378-5173\(95\)04127-3](https://doi.org/10.1016/0378-5173(95)04127-3).
- (22) Burley, J. C.; Duer, M. J.; Stein, R. S.; Vrcelj, R. M. Enforcing Ostwald's Rule of Stages: Isolation of Paracetamol Forms III and II. *Eur. J. Pharm. Sci.* **2007**, *31* (5), 271–276. <https://doi.org/10.1016/j.ejps.2007.04.002>.
- (23) Thomas, L. H.; Wales, C.; Zhao, L.; Wilson, C. C. Paracetamol Form II: An Elusive Polymorph through Facile Multicomponent Crystallization Routes. *Cryst. Growth Des.* **2011**, *11* (5), 1450–1452. <https://doi.org/10.1021/cg2002018>.
- (24) Di Martino, P.; Conflant, P.; Drache, M.; Huvenne, J. P.; Guyot-Hermann, A. M. Preparation and Physical Characterization of Forms II and III of Paracetamol. *J. Therm. Anal.* **1997**, *48* (3), 447–458. <https://doi.org/10.1007/bf01979491>.
- (25) Burger, A. Zur Interpretation von Polymorphie-Untersuchungen. *Acta Pharm. Technol.* **1982**, *28*, 1–20.
- (26) Peterson, M. L.; Morissette, S. L.; McNulty, C.; Goldsweig, A.; Shaw, P.; LeQuesne, M.; Monagle, J.; Encina, N.; Marchionna, J.; Johnson, A.; Gonzalez-Zugasti, J.; Lemmo, A. V.; Ellis, S. J.; Cima, M. J.; Almarsson, Ö. Iterative High-Throughput Polymorphism Studies on Acetaminophen and an Experimentally Derived Structure for Form III. *J. Am. Chem. Soc.* **2002**, *124* (37), 10958–10959. <https://doi.org/10.1021/ja020751w>.
- (27) Perrin, M. A.; Neumann, M. A.; Elmaleh, H.; Zasko, L. Crystal Structure Determination of the Elusive Paracetamol Form III. *Chem. Commun.* **2009**, No. 22, 3181–3183. <https://doi.org/10.1039/b822882e>.
- (28) Parkin, A.; Parsons, S.; Pulham, C. R. Paracetamol Monohydrate at 150 K. *Acta Crystallogr. Sect. E Struct. Reports Online* **2002**, *58* (12), o1345–o1347. <https://doi.org/10.1107/s1600536802019840>.
- (29) McGregor, P. A.; Allan, D. R.; Parsons, S.; Pulham, C. R. Preparation and Crystal Structure of a Trihydrate of Paracetamol. *J. Pharm. Sci.* **2002**, *91* (5), 1308–1311. <https://doi.org/10.1002/jps.10131>.
- (30) Kirk, J. H.; Dann, S. E.; Blatchford, C. G. Lactose: A Definitive Guide to Polymorph Determination. *Int. J. Pharm.* **2007**, *334* (1–2), 103–114. <https://doi.org/10.1016/j.ijpharm.2006.10.026>.
- (31) Listiohadi, Y.; Hourigan, J. A.; Sleight, R. W.; Steele, R. J. Moisture Sorption, Compressibility and Caking of Lactose Polymorphs. *Int. J. Pharm.* **2008**, *359* (1–2), 123–134. <https://doi.org/10.1016/j.ijpharm.2008.03.044>.
- (32) Allan, M. C.; Grush, E.; Mauer, L. J. RH-Temperature Stability Diagram of  $\alpha$ - and  $\beta$ -Anhydrous and Monohydrate Lactose Crystalline Forms. *Food Res. Int.* **2020**, *127* (October 2019), 108717. <https://doi.org/10.1016/j.foodres.2019.108717>.
- (33) Figura, L. O.; Epple, M. Anhydrous  $\alpha$ -Lactose A Study with DSC and TXRD. *J. Therm. Anal.* **1995**, *44* (1), 45–53. <https://doi.org/10.1007/BF02547132>.
- (34) Garnier, S.; Petit, S.; Coquerel, G. Dehydration Mechanism and Crystallisation Behaviour of Lactose. *J. Therm. Anal. Calorim.* **2002**, *68* (2), 489–502. <https://doi.org/10.1023/A:1016087702409>.
- (35) Listiohadi, Y.; Hourigan, J. A.; Sleight, R. W.; Steele, R. J. Thermal Analysis of Amorphous Lactose and  $\sigma$ -Lactose Monohydrate. *Dairy Sci. Technol.* **2009**, *89* (1), 43–67. <https://doi.org/10.1051/dst:2008027>.
- (36) Price, R.; Young, P. M. Visualization of the Crystallization of Lactose from the Amorphous State. *J. Pharm. Sci.* **2004**, *93* (1), 155–164. <https://doi.org/10.1002/jps.10513>.
- (37) Fix, I.; Steffens, K. J. Quantifying Low Amorphous or Crystalline Amounts of Alpha-Lactose-Monohydrate Using X-Ray Powder Diffraction, near-Infrared Spectroscopy, and Differential Scanning Calorimetry. *Drug Dev. Ind. Pharm.* **2004**, *30* (5), 513–523. <https://doi.org/10.1081/DDC-120037482>.
- (38) Lehto, V. P.; Tenho, M.; Vähä-Heikkilä, K.; Harjunen, P.; Päällysaho, M.; Väliisaari, J.; Niemelä, P.; Järvinen, K. The Comparison of Seven Different Methods to Quantify the Amorphous Content of Spray Dried Lactose. *Powder Technol.* **2006**, *167* (2), 85–93. <https://doi.org/10.1016/j.powtec.2006.05.019>.
- (39) Haque, M. K.; Roos, Y. H. Crystallization and X-Ray Diffraction of Crystals Formed in Water-Plasticized Amorphous Spray-Dried and Freeze-Dried Lactose/Protein Mixtures. *J. Food Sci.* **2005**, *70* (5), 347–350. <https://doi.org/10.1111/j.1365-2621.2005.tb09977.x>.
- (40) Thomsen, M. K.; Jespersen, L.; Sjøstrøm, K.; Risbo, J.; Skibsted, L. H. Water Activity - Temperature State Diagram of Amorphous Lactose. *J. Agric. Food Chem.* **2005**, *53* (23), 9182–9185. <https://doi.org/10.1021/jf0508394>.

- (41) Clark, Z.; Paterson, A. H. J.; Joe, R.; Mcleod, J. S. Amorphous Lactose Crystallisation Kinetics. *Int. Dairy J.* **2016**, *56*, 22–28. <https://doi.org/10.1016/j.idairyj.2015.12.012>.
- (42) Beevers, C. A.; Hansen, H. N. The Structure of  $\alpha$ -Lactose Monohydrate. *Acta Crystallogr. Sect. B Struct. Crystallogr. Cryst. Chem.* **1971**, *27* (7), 1323–1325. <https://doi.org/10.1107/s0567740871003947>.
- (43) Platteau, C.; Lefebvre, J.; Affouard, F.; Willart, J. F.; Derollez, P.; Mallet, F. Structure Determination of the Stable Anhydrous Phase of  $\alpha$ -Lactose from X-Ray Powder Diffraction. *Acta Crystallogr. Sect. B Struct. Sci.* **2005**, *61* (2), 185–191. <https://doi.org/10.1107/S0108768105000455>.
- (44) Platteau, C.; Lefebvre, J.; Affouard, F.; Derollez, P. Ab Initio Structure Determination of the Hygroscopic Anhydrous Form of  $\alpha$ -Lactose by Powder X-Ray Diffraction. *Acta Crystallogr. Sect. B Struct. Sci.* **2004**, *60* (4), 453–460. <https://doi.org/10.1107/S0108768104014375>.

## CHAPTER 6

### DIRECT DERIVATION OF THE CRYSTALLINE FRACTION OF HIGHLY POTENT ACTIVE PHARMACEUTICAL INGREDIENTS BY X-RAY POWDER DIFFRACTION

#### 1 INTRODUCTION

Solid drugs are commonly delivered in crystalline forms, including polymorphs, solvates, salts, and cocrystals. However, amorphous forms are attracting considerable interest because of their superior physicochemical and absorption properties.<sup>1,2</sup> The main disadvantage associated with the amorphous form is its tendency to convert into crystalline form because of environmental conditions such as humidity, temperature, or presence of impurities.<sup>3-7</sup>

Determining the crystalline fraction in drugs and formulations is extremely important to pharmaceutical companies because the behavior of an active pharmaceutical ingredient is affected by its form (amorphous or crystalline).<sup>8-10</sup> The quantification of crystalline and amorphous content is an important and difficult task that has been tackled using various techniques.<sup>11-13</sup> The United States Pharmacopeia (USP) reports a method for estimating the amorphous and crystalline fractions of a compound via X-ray powder diffraction (XRPD) in chapter <941>; this is the main method for qualitative and quantitative analyses in case of phase investigation.<sup>14</sup>

The difficulties associated with the usage of XRPD for amorphous quantification can be attributed to the different response of crystalline and amorphous compounds observed in the diffractogram. The crystalline solids can diffract the X-ray beam and generate sharp peaks, whereas the amorphous solids can only scatter the X-ray beam, generating a broad halo in the diffractogram. Thus, the amorphous part is mainly detected from the XRPD pattern via an indirect method. Madsen et al. comprehensively surveyed methods for quantifying amorphous materials via XRPD. They identified the following three main approaches: 1) single-peak intensity analysis, 2) whole-powder-pattern fitting (WPPF), and 3) crystallinity degree estimation.<sup>15</sup> The single-peak intensity analysis method is extensively used because it can be easily performed and requires no particular knowledge of crystallography. This method requires the construction of a calibration curve based on the intensity of a peak or group of peaks, but it can be easily subject to systematic alteration due to, for example, the presence of preferential orientation phenomenon.<sup>16,17</sup> This method is frequently used with an internal or external standard or normalization to eliminate the sample variation and X-ray tube fluctuations.<sup>18</sup>

The whole-powder-pattern fitting method includes the crystal modeling method (Rietveld modeling) and the pattern summation method. Rietveld modeling is an indirect approach based on which the absolute concentration of the crystalline phases can be determined using an internal standard and the amorphous content can be estimated on the basis of the difference between the total and crystalline contents.<sup>19</sup> However, Rietveld modeling requires the crystal structure parameters of all the crystalline phases so it will be useless when the crystal structure of an individual phase will be partially or completely unknown (which is frequently observed). An alternative solution called PONKCS (denoting “partial or no crystal structures”) provides an empirical derivation of the structural information of ZMV (where ZM represents the mass of the contents of the unit cell and V is the unit-cell volume) based on a mixture of phases and a known standard.<sup>20</sup>

The pattern summation method is a direct approach based on which the concentration of the amorphous phase can be estimated from its contribution to the pattern.<sup>15</sup> The degree of crystallinity method reported in USP <941> is based on the ratio of the crystalline intensity to the sum of the crystalline and amorphous intensities minus the constant background.<sup>21,22</sup> However, this method is limited to compounds with the same elemental composition and does not consider the microabsorption problem. Recently, a more sophisticated degree of crystallinity method was developed by Toraya.<sup>23</sup> This new quantification technique, called direct derivation (DD), relies on whole pattern fitting and uses a simple intensity–composition (IC) equation to calculate the weight fractions of crystalline phases in a mixture.

$$w_k = a_k S_k / \sum_{k'=1}^k a_{k'} S_{k'}$$

Where  $a_k$  is the total scattering intensity per chemical formula weight and  $S_k$  is the sum of the observed powder diffraction intensities of each component. For the calculation of  $a_k$  and  $S_k$  and to obtain the weight fraction using the IC equation only the chemical formulas of all the phases in the mixture of known components are required as external input.<sup>23</sup> Similar to the degree of crystallinity method and Rietveld modeling, the DD method is a single-measurement technique; however, it does not require spiking with an internal standard or the crystal structure parameters as Rietveld method. Moreover, it is applicable to multicomponent mixtures because it accounts for mass absorption. Toraya and Omote successfully applied the DD method to the quantitative phase analysis of the mixtures containing an amorphous phase claiming that the total scattering power per molecular formula weight ( $a_k$ ), which depends on the chemical formula and not on the crystallinity, plays a fundamental role with respect to the IC equation.<sup>24</sup> They applied WPPF to the diffraction patterns of the mixtures containing amorphous phase and directly fitted the amorphous halo extracted from the experimental pattern along the crystalline phase model. Toraya and Omote indicated the importance of determining the background of an amorphous component because it was difficult to identify the edge between the background and amorphous halo.<sup>24</sup>

This study evaluates the DD method with respect to the quantification of the crystallinity degree of crystalline–amorphous mixtures of organic compounds, wherein the crystalline part does not exceed 20%. The considered scenarios are observed in real cases. The active pharmaceutical ingredient (API) is a nonstoichiometric hydrated, highly potent compound dispensed in batches of 20 mg. The crystal structure of the API is known, and it refers to the highest degree of water molecule. The crystalline part of the formulation shows a different degree of hydration respect to the known structure, as a result, the position of the peaks in the powder diffractogram do not perfectly match the calculated values.<sup>25</sup>

In case of highly potent API, it must be handled and analyzed under safe conditions within a suitable containment system, hence, prior to the XRPD measurements, highly potent APIs are commonly covered with Kapton® film on the top of the sample holder. Although the Kapton® film is amorphous and transparent to X-ray, it considerably contributes to the background signal.

Therefore, we prepared different mixtures of hydroxypropyl methylcellulose (HPMC) and  $\alpha$ -lactose monohydrate as amorphous and crystalline phases, respectively. The different natures of the amorphous and crystalline parts prevent spontaneous crystallization of the amorphous; further, the slightly different mass absorption coefficients of the two compounds (MAC = 7.58 and 6.49 for  $\alpha$ -lactose monohydrate and HPMC, respectively, under copper radiation) can be corrected by the DD method.

The quantification method was evaluated in three scenarios: a) the unit cell parameters of the target API are available, b) the unit cell parameters are not known but the pure crystalline and pure amorphous reference materials are available and c) only the mixture of amorphous and crystalline material with unknown weight composition is available. Finally, to simulate the measurement of a high potent compound the measurements were collected with the use of the Kapton® film as the containment system and the crystallinity was determined with the scenarios b. The methods, results, analysis, and conclusions are presented in the following sections.

## 2 MATERIAL AND METHODS

### 2.1 Materials

$\alpha$ -lactose monohydrate ( $C_{12}H_{24}O_{12}$ ) and hydroxypropyl methylcellulose (HPMC) were selected as standards because they are stable organic compounds regularly used as excipients in the pharmaceutical industry.  $\alpha$ -lactose monohydrate (purity  $\geq 99\%$ ) was purchased from Sigma-Aldrich (Saint Louis, MO, USA). HPMC, an amorphous polymer with the chemical formula  $C_{56}H_{108}O_{30}$  was purchased from Acros Organics (Geel, Belgium). It is worth noting that in the DD method requires only the chemical formula. <sup>26</sup>

### 2.2 Sample preparation and data collection

The mixing process is affected by the different densities, particle sizes, and morphologies of the powder constituents. The preparation of large quantities of bulk mixtures and sampling for analysis are primary sources of error in solid-state quantification. For this reason, the mixtures were prepared in small amounts and analyzed in their entirety to avoid inaccuracy because of the inhomogeneity of the mixture and its sampling.

Both the standard materials were sifted through a 100- $\mu$ m sieve to improve the particle statistics and powder homogenization before preparing the mixture. Prior to sieving, the particle size of HPMC was vigorously reduced by grinding with an agata mortar and pestle. Samples were prepared with 5% w/w ( $SM_1$ ) and 15% w/w ( $SM_2$ ) crystalline  $\alpha$ -lactose monohydrate, respectively. Three different samples of 50 mg each were prepared for each percentage (see Table 1). The samples were prepared by accurately weighting the powders on a microanalytical balance that records values of up to six decimal figures (Mettler Toledo XPE26DR). The weighted compounds were manually mixed in an agata mortar using the geometric dilution method. The main difficulty associated with solid-state quantification is obtaining homogeneous mixtures.

The mixtures were loaded into a top-loading zero-background silicon sample holder with a recess having a diameter and depth of 15 and 0.2 mm, respectively. All the mixtures and pure compounds were analyzed with a PANalytical X'Pert PRO diffractometer in Bragg–Brentano geometry with Cu  $K\alpha$  radiation (40 kV, 40 mA) and an X'Celerator detector. The operating parameters were a divergence fixed slit of 1/4, a mask of 15 mm, an antiscatter slit of 1/2, a diffracted antiscatter slit of 5.0 mm, and a soller slit of 0.04 rad (for both incident and diffracted radiation). During the measurement, the sample spun at 1 rps to analyze whole sample surface. All the data were collected when  $2\theta = 3.5^\circ$ – $80^\circ$  with a step size of  $0.0167^\circ$  and a scanning speed of  $0.02^\circ/s$ .

Measurements in containment were performed using the Kapton® film. Kapton® is a polyimide film commonly used to isolate highly potent API from the ambient environment. However, its signal is a source of error in quantitative phase analysis. All the standard mixtures were analyzed with and without the Kapton® film to inspect the contribution of Kapton® signal to the measurement. Blank analysis of the empty sample holders with the Kapton® film was performed.

**Table 1 Composition of the prepared mixtures. Readability of the balance  $d = 0.001$  mg.**

	$\alpha$ -lactose monohydrate (mg)	HPMC (mg)	% w/w crystalline $\alpha$ -lactose monohydrate
<b>SM<sub>11</sub></b>	2.59 (4)	47.51 (2)	5.2
<b>SM<sub>12</sub></b>	2.55 (6)	47.49 (6)	5.1
<b>SM<sub>13</sub></b>	2.51 (6)	47.49 (8)	5.0
<b>SM<sub>21</sub></b>	7.51 (4)	42.70 (2)	15.0
<b>SM<sub>22</sub></b>	7.59 (6)	42.44 (6)	15.2
<b>SM<sub>23</sub></b>	7.63 (6)	42.56 (4)	15.2

## 2.3 Data analysis

The XRPD patterns were characterized by a broad halo introduced by the scattering of the amorphous material and well-defined peaks generated by the crystalline part. In this study, we applied the DD method presented by Toraya and Omote.<sup>24</sup> They proved that the commonly used IC equation, which can be used to obtain the weight fractions of the individual phases in a mixture from the sum of their intensities measured over a wide  $2\theta$  range with respect to the chemical composition data, can be extended to quantify amorphous materials with nonperiodic structures.

The DD method is based on the WPPF procedure. The fitting function is a linear combination of subfunctions with different profile models to describe the powder diffraction patterns of the individual phases. Based on the information and knowledge of the single components, three subfunctions were proposed in this study. These subfunctions are necessary to extract the intensities of the different compounds, apply the IC equation, and derive the weight fraction.<sup>27</sup>

The reference material patterns were obtained using three methods. In method *a*, wherein the unit cell parameters of crystalline reference were known, the Pawley method can be applied and the integrated intensities were considered to be adjustable parameters. In method *b*, wherein no structural information was available, the peak positions and intensities can be determined from the X-ray powder patterns of the pure standard reference materials.<sup>20</sup> The pattern can be fitted directly by adjusting the scale parameter, as reported in case of the full-pattern-fitting method by Smith et al.<sup>28</sup> In method *c* (the worst-case scenario), only the mixture of amorphous and crystalline references with unknown weight composition was available and no structural information and pure standard references were available; therefore, the peaks were detected directly based on the mixture.<sup>29</sup>

The organic crystalline compounds are usually characterized by their low symmetry and large cells. Therefore, their peaks often overlap, and their determination is a nontrivial task, especially when the peaks are both weak and overlapped at  $2\theta$  exceeds  $30^\circ$ . The method *a* based on the Pawley method should reduce this problem because the peak positions are determined based on the unit cell parameters.

We applied the DD method to the  $\alpha$ -lactose monohydrate analyzed by methods *a*, *b*, and *c* and compared the results to evaluate the importance of detecting the maximum number of peaks. All the data in this study were elaborated using the Malvern PANalytical HighScore Plus 4.8 software.

### 2.3.1 Common observations in all the methods

In accordance with the proposal of Toraya and Omote, all the samples were analyzed over a wide range ( $2\theta = 3.5^\circ\text{--}80^\circ$ ).<sup>24</sup> Although no  $\alpha$ -lactose monohydrate signals were observed beyond  $60^\circ$ , extending the range to high angles improved the background determination. In quantification analysis by X-Ray diffraction, the background treatment is the most challenging step, especially in case of crystalline-amorphous quantification. In crystalline pattern, the background is determined due to the presence of the peaks, while it is difficult to divide the halo of the amorphous phase from the background generated by air scattering, fluorescence, and equipment. Toraya and Omote suggested that the materials of the same composition analyzed under identical experimental conditions resulted in the same background intensity which can be determined at high angle where the signal is dominated by the instrument contribution.<sup>24</sup> In the USP crystallinity degree quantification method, the background noise is considered constant and described as a flat line.<sup>14,21</sup> The same approach was applied in our study, and the background line was set flat with constant value determined at high angles. Aware of the roughness of the approximation, we were surprised of the goodness of the results, while more elaborated description of the background, which are at the same time more user dependent, gave results less accurate and reproduceable.

The halo of the amorphous reference material was described by four manually added peaks and was individually refined with a pseudo-Voigt function. After inputting the peaks, the background was set as a flat function with a constant value equal to the counts of the experimental pattern at high angles (see SI for details). This model of the amorphous halo was used in methods *a* and *b*.

The % w/w of crystalline  $\alpha$ -lactose monohydrate ( $W_c\%$ ), the relative error percentage ( $E_r\%$ ), the weighted profile residual error ( $R_{wp}$ ), and the chi-square ( $\chi^2$ ) were reported for each mixture. The relative error percentage ( $E_r\%$ ) is calculated as the ratio of the absolute error to the true value (expressed in percentage)

and it is an indication of the accuracy of the method (the lower, the better). The absolute error is the difference between the crystalline fraction determined in the quantification ( $W_c\%$ ) and the known value (true value %w/w in table 1). In solid-state quantification an  $E_r\%$  lower than 20% is considered acceptable. The weighted profile residual error ( $R_{wp}$ ), and the chi-square ( $\chi^2$ ), also called Goodness of fit indicate the fitting quality between the experimental pattern and the calculated one. The  $R_{wp}$  is calculated using a point-by-point weighting factor directly from the square root of the quantity minimized. The  $\chi^2$  is equal to  $(R_{wp}/R_{exp})^2$ , while  $R_{exp}$  is the expected R factor and it is the best possible  $R_{wp}$ .<sup>30</sup> Generally,  $R_{wp}$  value  $< 10\%$  is considered satisfactory, while for  $\chi^2$  values in the range 1-2 are good, but they do not guarantee the accuracy of the model and a careful inspection of the difference plot is recommended.<sup>31</sup>

### 3 RESULTS

#### 3.1 Method a

In method a, the diffraction pattern of the pure crystalline  $\alpha$ -lactose monohydrate reference was refined using a Pawley function. The peak positions were refined with the unit cell information of the crystalline  $\alpha$ -lactose monohydrate LACTOS03 of CCDC and the pseudo-Voigt function for the peak profile.<sup>32</sup> The background was described using a polynomial function. The refinement reached weighted profile R-value  $R_{wp} = 8.04$  (see SI for details).

The refined crystalline and amorphous references were used as the initial pattern to describe the diffraction patterns of the mixtures. The refined background was considered to be flat in all the diffraction patterns to eliminate the instrumental offset. During the first step, the specimen displacement was refined and the scale parameters of the references and quantification approached their actual values in all the SM1 mixtures. However, the difference plot showed several problems in crystalline peak assignment (Figure 1), especially in the SM<sub>2</sub> mixture with high crystalline content. The agreement between the calculated and experimental profiles was improved after Pawley refinement of the crystalline reference, which refined the lattice parameters and the peak profile. Further, each peak shape of the amorphous reference was individually refined. Figure 1 compares the refinements and difference plots after the first and final steps in method a; based on the difference plot, the y-axis entity was observed to considerably decrease in method a (right side, red line) because of the considerably improved peak profile and intensity description. The difference plots were almost flat, and the quantification as well as  $R_{wp}$  are reported in Table 2 (Figure 2).

**Table 2. Results of the SM1 and SM2 mixtures in Method a, showing the %w/w of the crystalline  $\alpha$ -lactose monohydrate ( $W_c$ , %), relative errors  $E_r$  (%), and reliability indices  $R_{wp}$**

	$W_c\%$	$E_r\%$	$R_{wp}$ (%)	$\chi^2$	Figure in SI
<b>SM<sub>11</sub></b>	5.7	10	1.97	1.23	9 b)
<b>SM<sub>12</sub></b>	4.8	6	2.64	1.68	8 b)
<b>SM<sub>13</sub></b>	3.8	24	2.38	1.51	7 b)
<b>SM<sub>21</sub></b>	13.1	13	3.37	2.15	6 b)
<b>SM<sub>22</sub></b>	13.2	13	2.92	1.86	5 b)
<b>SM<sub>23</sub></b>	12.7	16	3.40	2.12	4 b)

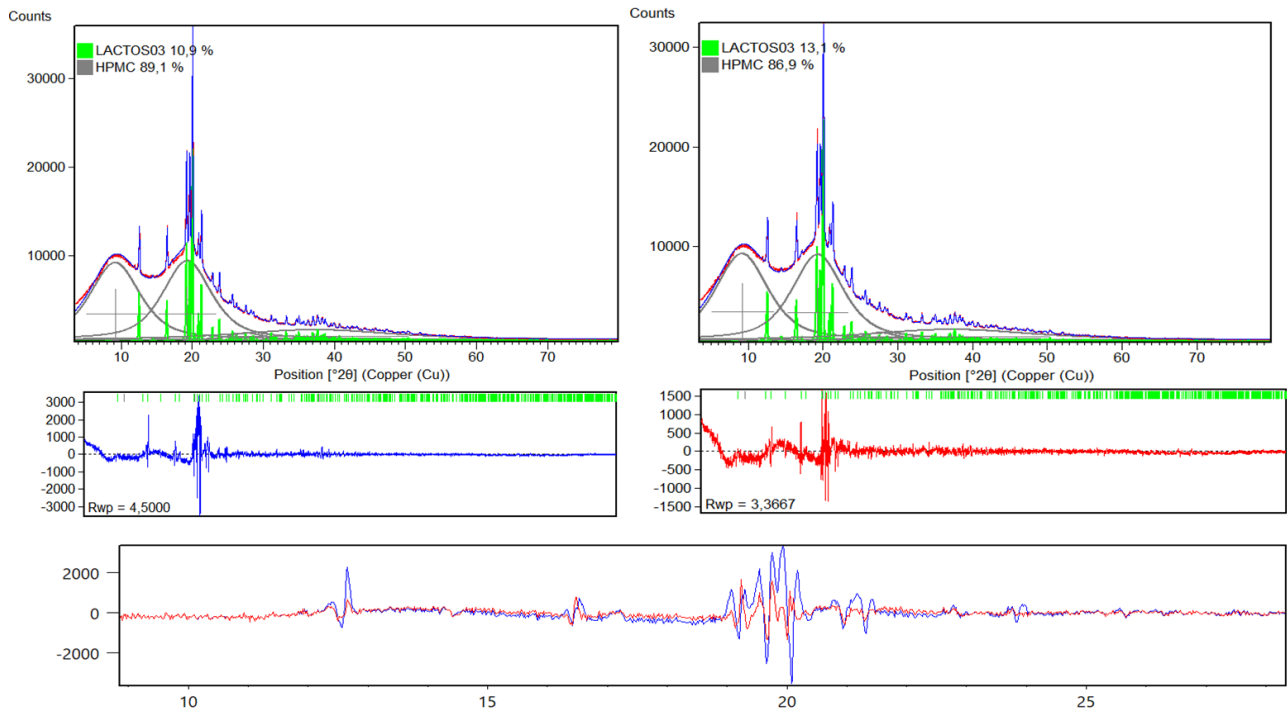


**Figure 1.** Comparison of the refinement results of the diffraction pattern of SM<sub>21</sub> in Method a. Left panels show the signals after refinement and scaling of the SRM patterns (Step 1). Right panels show the signals after Pawley refinement (method a). The bottom panel compares the difference plots in the range  $2\theta = 10^\circ\text{--}30^\circ$  in Step 1 (blue line) and method a (red line).

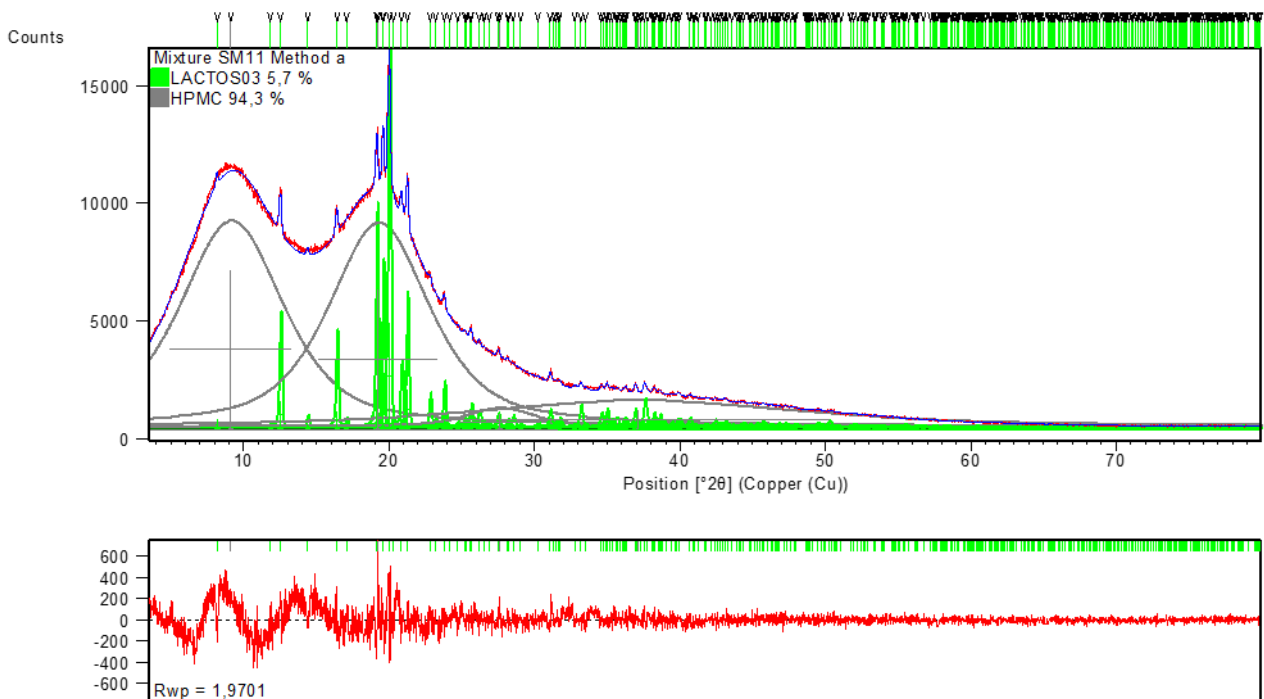


**Figure 2.** Refinement results for the diffraction pattern of SM<sub>11</sub> in Method a. Red and blue patterns are the experimental and calculated patterns, respectively and the gray lines correspond to the peaks used to describe the amorphous signal of HPMC and the green line to the  $\alpha$ -lactose reference. The bottom plot shows the difference between the experimental and calculated intensities, the short lines indicate the peak positions.

### 3.2 Method *b*

In method *b*, the peak positions, profiles, and intensities were determined from the diffraction pattern of the pure crystalline  $\alpha$ -lactose monohydrate reference. The peaks were determined by applying the peak-finding function of the Malvern PANalytical HighScore Plus 4.8 software. The peak positions, profiles, and intensities were refined as a group. The profiles were fitted by a pseudo-Voigt function, and the full-width-at-half-maximum (FWHM) and asymmetry function were determined using the Caglioti formula. The refinement reached  $R_{wp} = 9.74$  (see SI for details). The listed peaks and parameters of the crystalline reference were assumed to constitute the initial pattern to fit the whole pattern of the mixtures ( $SM_{xy}$ ), and the background was described by a flat function. The first step with the  $SM_{xy}$  included refining the profile of the crystalline and amorphous references based on the scale parameter (Figure 3). However, the difference plots were very noisy and the  $R_{wp}$  values were quite high, especially in the  $SM_2$  mixtures. Therefore, a second refinement was performed. Here, the peak set of the crystalline reference was described as a group using the Caglioti formula, but the FWHMs of the amorphous reference were individually refined for each peak. Figure 3 compares the diffraction patterns of the first step and those obtained after final refinement in method *b*. The bottom panel compares the difference plots of step 1 and the final step of method *b*. The crystalline  $\alpha$ -lactose monohydrate and amorphous references' description clearly improved after refinement, as evidenced in the flat difference plot, improved quantification, and low  $R_{wp}$  values (Table 3 and Figure 4).

**Table 3. Results of the SM1 and SM2 mixtures in Method *b*, showing the %w/w of crystalline  $\alpha$ -lactose monohydrate ( $W_c$ , %), relative errors  $E_r$  (%), and reliability indices  $R_{wp}$**

	$W_c$ %	$E_r$ %	$R_{wp}$ (%)	$\chi^2$	Figure in SI
<b>SM<sub>11</sub></b>	5.0	4	2.17	1.29	16 b)
<b>SM<sub>12</sub></b>	4.8	6	2.30	1.39	15 b)
<b>SM<sub>13</sub></b>	5.0	0	2.23	1.35	14 b)
<b>SM<sub>21</sub></b>	13.2	12	2.69	1.63	13 b)
<b>SM<sub>22</sub></b>	13.8	9	2.63	1.60	12 b)
<b>SM<sub>23</sub></b>	13.2	13	2.71	1.61	11 b)

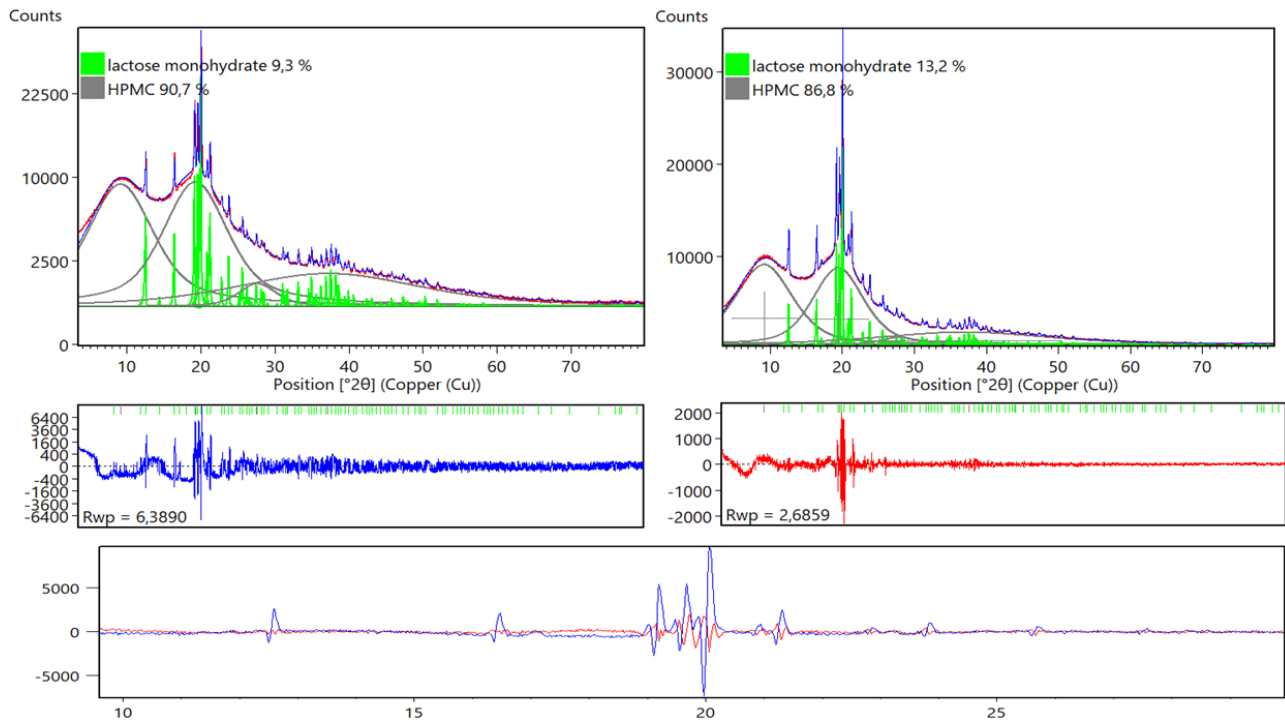


**Figure 3.** Comparison of the refinement results of the diffraction pattern of SM<sub>21</sub> in Method b. Left panels report the signals after refinement and scaling of the patterns (step 1). Right panels report the signals after refinement with the Caglioti function (method b). The bottom panel compares the difference plots in the range  $2\theta = 10^\circ\text{--}30^\circ$  in step 1 (blue line) and at the end of method b (red line).

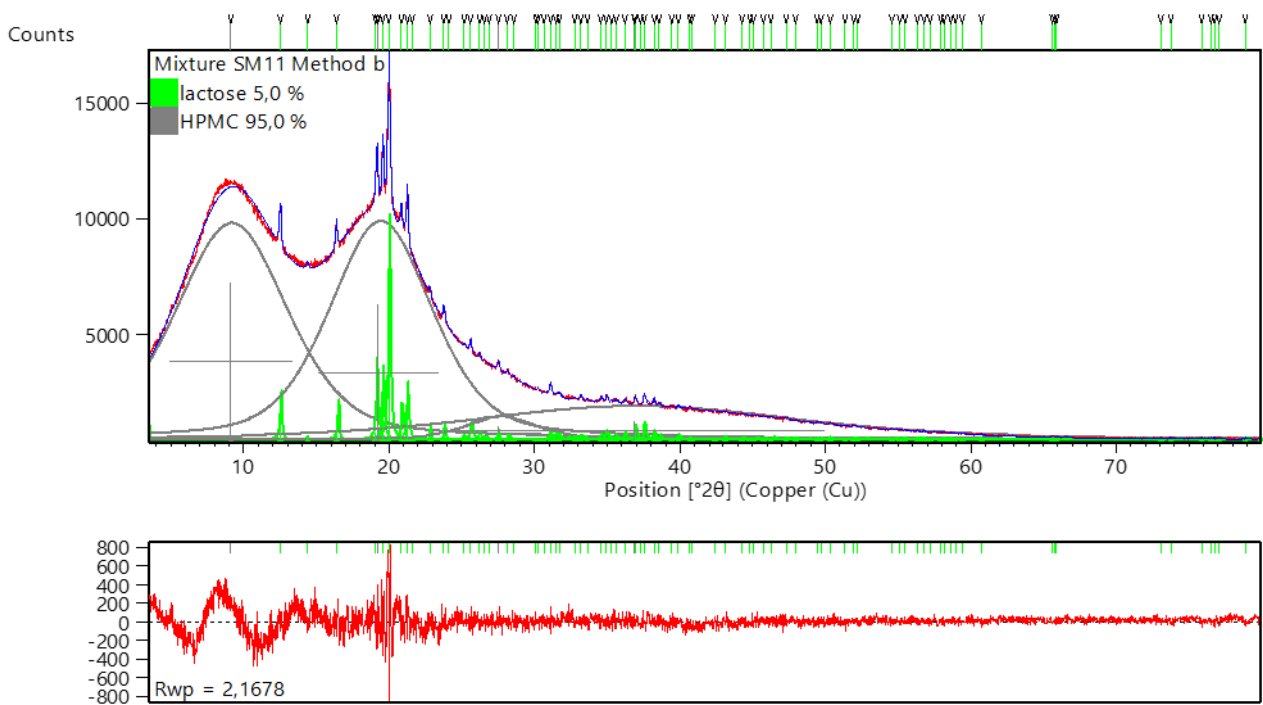


**Figure 4.** Refinement results for the diffraction pattern of SM<sub>11</sub> in method b. Red and blue patterns are the experimental and calculated patterns, respectively and the gray lines correspond to the peaks used to describe the amorphous signal of HPMC and the green line to the  $\alpha$ -lactose reference. The bottom plot shows the difference between the experimental and calculated intensities. The short lines indicate the peak positions.

### 3.3 Method c

We also evaluated the DD method in the absence of pure crystalline and amorphous materials which can be used as references. Although this approach is discouraged in text books, the crystal parameters of the reference materials are often unknown in reality and not always the references are available. The DD method was applied directly to the diffraction patterns of the mixtures. Because the background description critically affected the quantification, initially, the peak set of the  $\alpha$ -lactose monohydrate was determined by the peak-finding function of the software and refined as a group using the Caglioti formula. In this case, the crystalline area is represented only by the peaks with significant signal-to-noise ratios, which can be detected by the peak-finding function. Subsequently, the amorphous hump was described by inserting four peaks and modeling them manually against a flat background. The crystalline and amorphous peaks were scaled and refined with a profile-fitting function (the pseudo-Voigt function) and an asymmetry function (Figure 5). The refinement and quantification values are presented in Table 4.

**Table 4. Results of the SM1 and SM2 mixtures in Method c, showing the %w/w of the crystalline  $\alpha$ -lactose monohydrate ( $W_c$ , %), relative errors  $E_r$  (%), and reliability indices  $R_{wp}$**

	$W_c$ %	$E_r$ %	$R_{wp}$ (%)	$\chi^2$	Figure in SI
<b>SM<sub>11</sub></b>	3.3	37	2.29	1.35	23
<b>SM<sub>12</sub></b>	3.1	39	2.11	1.27	22
<b>SM<sub>13</sub></b>	3.0	40	2.39	1.43	21
<b>SM<sub>21</sub></b>	12.2	19	3.26	1.98	20
<b>SM<sub>22</sub></b>	11.7	23	3.47	2.11	19
<b>SM<sub>23</sub></b>	10.6	30	3.13	1.85	18

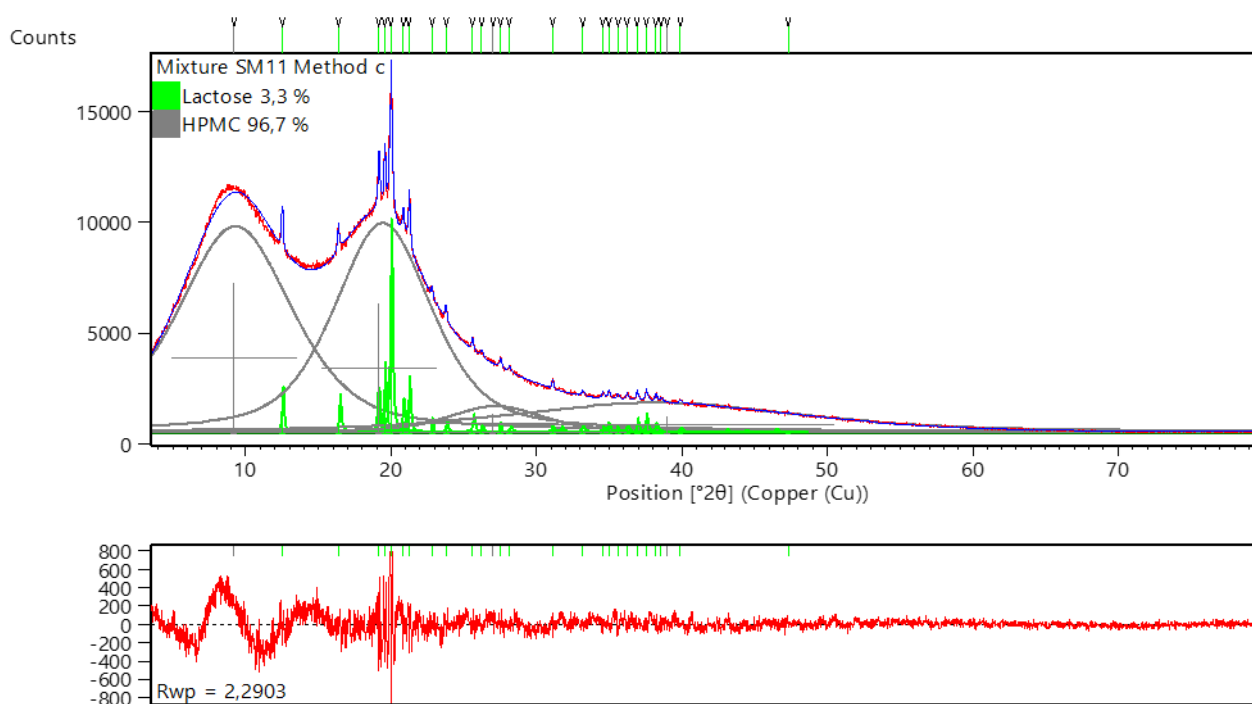


**Figure 5. Diffraction patterns of SM<sub>11</sub> refined with a peak-finding function (method c). Red and blue patterns are the experimental and calculated patterns, respectively and the gray lines correspond to the peaks used to describe the amorphous signal of HPMC and the green line to the  $\alpha$ -lactose reference. The bottom plot shows the difference between the experimental and calculated intensities. The short lines indicate the peak positions.**

### 3.4 Kapton film

An increasing number of pharmaceutical compounds are highly potent APIs. Such materials must be handled safely to prevent their release into the environment and avoid the exposure of the operators. Therefore, they are covered with the Kapton® film during the XRPD analysis. This protective material, which is amorphous, contributes to the background signal and should be removed from the measurements before quantification. As a blank control, an empty sample holder wrapped in Kapton® film was measured under the same experimental conditions, and the blank Kapton® intensities were subtracted from the observed measurements of the mixtures by assuming that the intensities of the Kapton® were identical in all the standard mixtures. Figure 6 shows the diffraction patterns obtained after the subtraction of the Kapton® signals. After this subtraction, the diffraction patterns were elaborated as described for method *b* (subsection 3.2).

The Kapton® film pattern made a large contribution at low angles, necessitating an additional peak in the description of the first hump of the amorphous reference. The added peak improved the agreement between the calculated and observed patterns (Figure 7). The refinement and quantification values are presented in Figure 7 and Table 5.

**Table 5. Results of the SM<sub>1</sub> and SM<sub>2</sub> mixtures covered with the Kapton® film and analyzed by method *b*, showing the %w/w of the crystalline  $\alpha$ -lactose monohydrate ( $W_c$ ), relative errors  $E_r$  (%), and reliability indices  $R_{wp}$**

	$W_c$ %	$E_r$ %	$R_{wp}$ (%)	$\chi^2$	Figure in SI
<b>SM<sub>11</sub></b>	5.4	4	5.22	2.16	30
<b>SM<sub>12</sub></b>	5.1	0	4.59	1.97	29
<b>SM<sub>13</sub></b>	5.9	18	4.63	2.01	28
<b>SM<sub>21</sub></b>	12.9	14	5.88	2.59	27
<b>SM<sub>22</sub></b>	13.3	13	4.78	2.18	26
<b>SM<sub>23</sub></b>	13.0	14	5.01	2.17	25

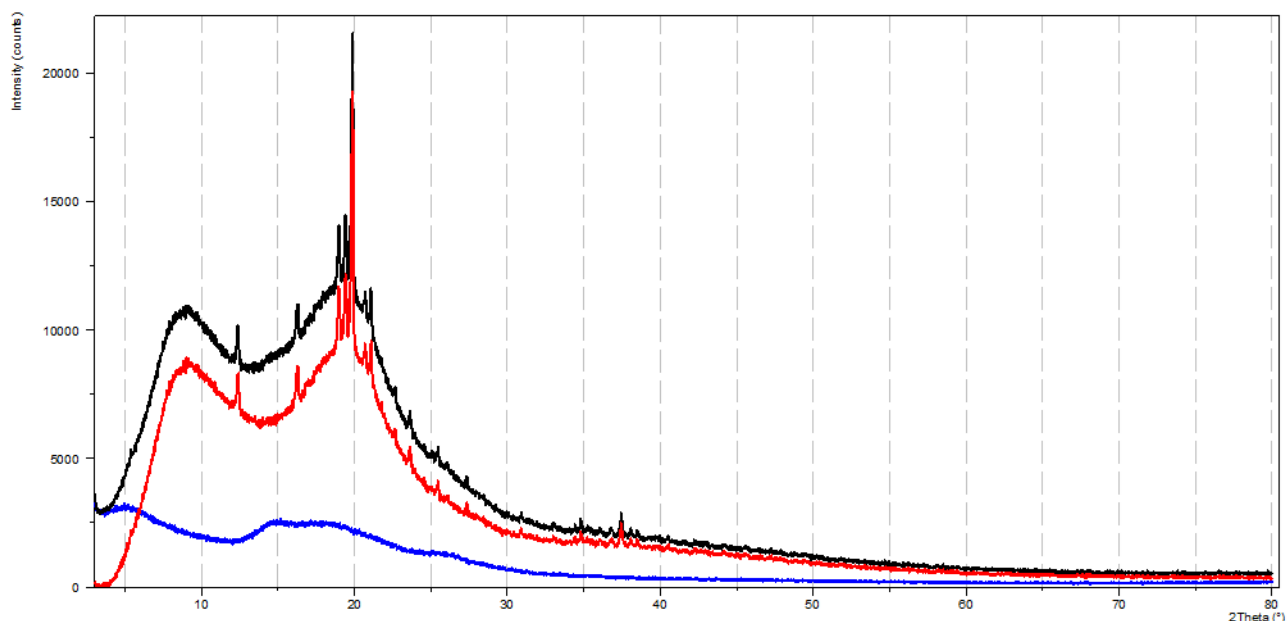


**Figure 6.** Example of the effect of subtracting the Kapton® signal from the signals of the SM11 mixture. The black line and blue line are the patterns collected of the sample SM11 and of the empty sample holder with Kapton® film respectively. The red pattern is obtained by subtracting the blue pattern from the black one.

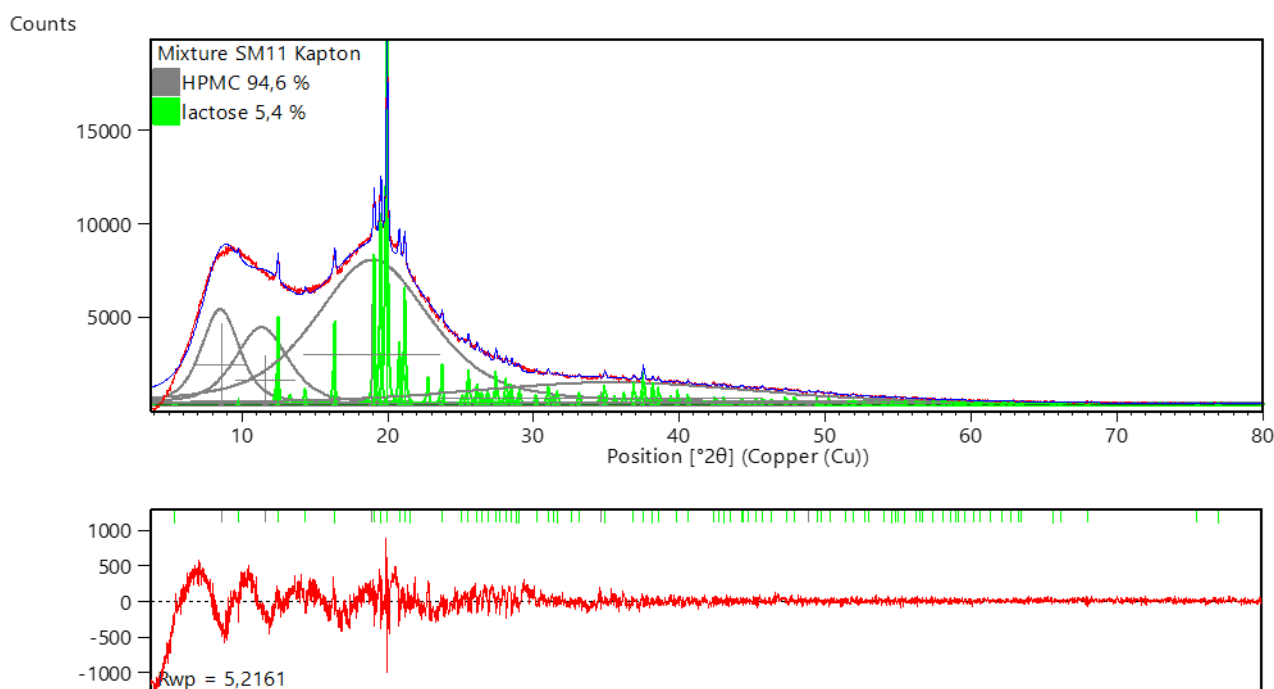


**Figure 7.** Refinement results of the diffraction pattern of the SM<sub>11</sub> mixture with the Kapton® film (method b). The red and blue patterns are the experimental and calculated patterns, respectively and the gray lines correspond to the peaks used to describe the amorphous signal of HPMC and the green line to the  $\alpha$ -lactose reference. The bottom plot shows the difference between the experimental and calculated intensities. The short lines indicate the peak positions.

#### 4 DISCUSSION

Here, we discuss the quantitative and refinement results of method *a* when unit cell parameters of crystalline reference are available and the refinement is based on Pawley function; method *b* when no structural information is known but crystalline and amorphous references are available and can be used to describe the pattern profiles; and method *c*, when no structural information or pure standard references are available. The crystalline percentages  $W_c$ , relative error  $E_r\%$ , reliability indices  $R_{wp}$ , and chi-squared ( $\chi^2$ ) results of the

refinement are reported. Methods *a* and *b* obtained comparable  $W_c$  and  $E_r$ , except in case of SM<sub>13</sub>, where method *a* resulted in a considerably high relative error (out of trend with the remaining SM<sub>1</sub> mixtures). Both the methods achieved excellent  $W_c$  and  $E_r$  values of lower than 20%. When converted into absolute errors, these percentage errors were around one unit in SM<sub>1</sub> and approximately two percentage points in SM<sub>2</sub>. As expected, the results obtained using method *c* showed large errors, with significant underestimation of the crystalline percentages and extremely large relative errors (up to 40%). However, the reliability indices  $R_{wp}$  and the  $\chi^2$  values were similar and achieved satisfactory values in all the refinements. The exceptionally low values of the reliability indices were affected by the large amount of amorphous material, and the  $R_{wp}$  values increases with the increasing of the crystalline percentage. The  $\chi^2$  were always lower than 3 in all the method, except for the method *b* which showed excellent  $\chi^2$  values lower than 2. As indicated by Toby, the goodness of fitting can be optimally assessed by observing the experimental and calculated difference plots, which were almost flat in our study, taking into account the scale of the y-axis of the difference plot, and its relation with the intensity of the diffraction pattern.<sup>31</sup>

Figure 2, Figure 4, and Figure 5 show the diffraction patterns and difference plots of the SM<sub>11</sub> mixture obtained using methods *a*, *b*, and *c*, respectively. The main differences between these methods are the descriptions of the final peaks of the amorphous reference (method *c* versus methods *a* and *b*) and the number of crystalline peaks, which considerably decreased from methods *a* to *c*. The number of crystalline peaks was determined based on the unit cell parameters obtained via method *a*, the peaks detected in the pure crystalline  $\alpha$ -lactose monohydrate reference via method *b*, and the peaks detected in the mixtures via method *c*. In the final case, the crystalline peaks obtained using the peak-finding function were dominated by the limit of detection (LOD) and several peaks were missed. Although the peaks at high angles could be barely detected, they significantly contributed to the quantification. When the SM<sub>11</sub> pattern refined by method *a* was clipped to the range of  $2\theta = 3.5^\circ$ – $40^\circ$  (Figure 8), to eliminate the contribution of high angles peaks, the crystalline percentage decreased from 5.7% to 3.3%, equal to that obtained using method *c*.

Collecting the powder patterns obtained up to  $2\theta = 80^\circ$  is important not only for defining the background contribution, which severely affected the quantification, but also for considering the crystalline contribution at high angles when the reference crystalline material was known. The spinning of the sample guarantees the irradiation of the all sample also at high angle, consequently the representativity of the sample.

The error percentages of the samples wrapped in the Kapton® film (Table 5) were similar to those obtained in case of the same samples using method *b* but were more variable. In case of SM<sub>1</sub>, the percentage errors were at most 18% and  $R_{wp}$  and  $\chi^2$  were comparable to those of the remaining refinements.

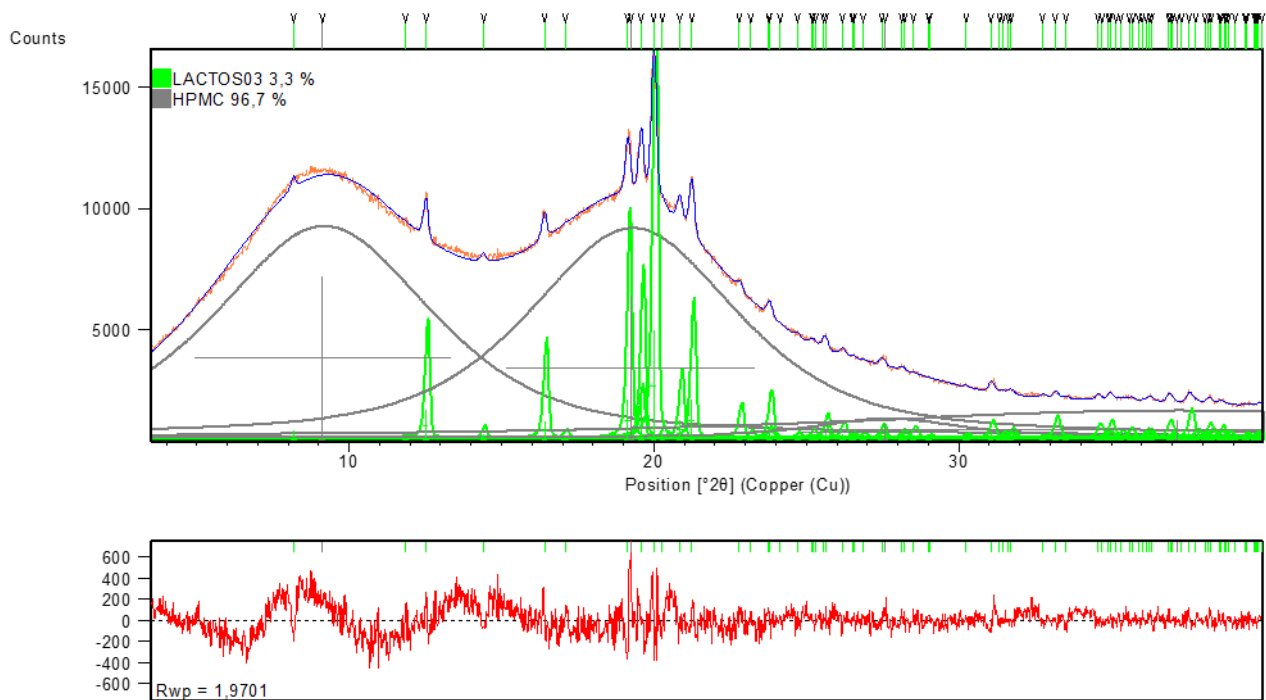


**Figure 8.** Refinement results of the diffraction pattern in the range  $2\theta = 3.5^\circ\text{--}40^\circ$  of SM<sub>11</sub> in method a. The red and blue patterns are the experimental and calculated patterns, respectively and the gray lines correspond to the peaks used to describe the amorphous signal of HPMC and the green line to the  $\alpha$ -lactose reference. The bottom plot shows the difference between the experimental and calculated intensities. The short lines indicate the peak positions.

## 5 CONCLUSIONS

The IC formula is a powerful equation based on which the weight fraction of the individual phases in a mixture can be determined using only the chemical formulas of the mixture's constituents. The formula requires two input parameters: the sum  $S_k$  of the observed powder diffraction intensities of each component measured over a wide  $2\theta$  range and the parameter  $a_k$  representing the total scattering power per chemical formula weight. Toraya and Omote indicated that the IC formula can be used to quantify the amorphous materials in mixtures because the scattering power obtained from unit composition is dependent on the number of electrons in its atoms, regardless of whether the atom assemblage is ordered.<sup>24,33</sup>

The DD method for crystalline degree determination is extremely advantageous respect to other common quantification method. It does not require the use of internal standard, which is compulsory for Rietveld and univariate methods. The addition of internal standard is challenging in case of small amount of material and the errors due to the weighting, mixing procedures can deeply affect the results. In case of high potent compounds, the difficulties of these operations are enhanced due to the safety protocols. Additionally, the DD method avoids construction of calibration curve, impossible in case of lack of reference materials.

In this study, the DD method was applied to the quantification of an amorphous–crystalline binary mixture of organic materials. The quantification of crystalline materials in amorphous matrices is gaining interest and is always difficult.<sup>34</sup> The difficulties are exacerbated by the lack of information, such as crystal structures or standard reference materials, low amount of materials, or the presence of high potent API, which have to be handled and analyzed under safe conditions within a suitable containment system.

We evaluated the DD method in mixtures containing low percentages of crystalline  $\alpha$ -lactose monohydrate (5 and 15% w/w) in amorphous HPMC under different scenarios. Three refinement methods were tested: method *a* (unit cell parameters available), method *b* (unit cell parameters are not available but the pure crystalline and pure amorphous references are available), and method *c* (no structural information and references available). Method *b* was also applied to mixtures contained within the Kapton® film.

Based on the results of these different procedures, the importance of determining the crystalline reflections can be understood. The limited number of peaks in the mixtures observed using method *c* resulted in the low area of the crystalline reference and considerable underestimation of the crystalline weight fraction. As expected, the usage of standard reference materials improved the accuracy of the results. No large differences were observed between the results of methods *a* and *b*, although describing the peaks based on the cell parameters offers distinct advantages. For instance, the task of adding the peaks becomes easier, and Pawley refinement can reveal crystalline impurities. Further, the differences of the crystalline profile from that of the standard reference can be tracked in nonstoichiometrically hydrated mixtures.

The powder pattern must be collected up to a high angle to properly describe the background. The background was described by a flat line in agreement with the degree of crystallinity method of USP.<sup>21</sup>

The DD method was also applied to the mixtures contained within the Kapton® film. The film signal was eliminated by subtracting the blank measure of the film from the measured diffractogram. The obtained diffractograms were studied using method *b*. Despite the difficulty in describing the diffractograms at low angles, accurate crystalline weight percentage results were obtained. The subtraction of the Kapton® film signal to remove the matrix effect is an outstandingly effective approach for evaluating potent compounds that must be contained for safety and environmental purposes.

## 6 REFERENCES

- (1) Babu, N. J.; Nangia, A. Solubility Advantage of Amorphous Drugs and Pharmaceutical Cocrystals. *Cryst. Growth Des.* **2011**, *11* (7), 2662–2679. <https://doi.org/10.1021/cg200492w>.
- (2) Hancock, B. C.; Zografi, G. Characteristics and Significance of the Amorphous State in Pharmaceutical Systems. *J. Pharm. Sci.* **1997**, *86* (1), 1. <https://doi.org/10.1021/js9601896>.
- (3) Chieng, N.; Rades, T.; Saville, D. Formation and Physical Stability of the Amorphous Phase of Ranitidine Hydrochloride Polymorphs Prepared by Cryo-Milling. *Eur. J. Pharm. Biopharm.* **2008**, *68* (3), 771–780. <https://doi.org/10.1016/j.ejpb.2007.09.001>.
- (4) Clark, Z.; Paterson, A. H. J.; Joe, R.; Mcleod, J. S. Amorphous Lactose Crystallisation Kinetics. *Int. Dairy J.* **2016**, *56*, 22–28. <https://doi.org/10.1016/j.idairyj.2015.12.012>.
- (5) Laitinen, R.; Löbmann, K.; Strachan, C. J.; Grohgan, H.; Rades, T.; Löbmann, K.; Strachan, C. J.; Grohgan, H.; Rades, T. Emerging Trends in the Stabilization of Amorphous Drugs. *Int. J. Pharm.* **2013**, *453* (1), 65–79. <https://doi.org/10.1016/j.ijpharm.2012.04.066>.
- (6) Ma, X.; Williams, R. O. Characterization of Amorphous Solid Dispersions: An Update. *J. Drug Deliv. Sci. Technol.* **2019**, *50* (January), 113–124. <https://doi.org/10.1016/j.jddst.2019.01.017>.
- (7) Yu, L. *Amorphous Pharmaceutical Solids: Preparation, Characterization and Stabilization*; Elsevier, 2001; Vol. 48. [https://doi.org/10.1016/S0169-409X\(01\)00098-9](https://doi.org/10.1016/S0169-409X(01)00098-9).
- (8) FDA The United States Food and Drug Administration. Guidance for Industry. ANDAs: Pharmaceutical Solid Polymorphism. Chemistry, Manufacturing and Controls Information. *Journal of Generic Medicines*. 2007.
- (9) ICH International Conference on Harmonization of Technical Requirements for Registration of Pharmaceuticals for Human use. Specifications: Test Procedures and Acceptance Criteria for New Drug Substances and New Drug Products: Chemical Substances. 2000.
- (10) Singhal, D.; Curatolo, W. Drug Polymorphism and Dosage Form Design: A Practical Perspective. *Adv. Drug Deliv. Rev.* **2004**, *56* (3), 335–347. <https://doi.org/10.1016/j.addr.2003.10.008>.
- (11) Lehto, V. P.; Tenho, M.; Vähä-Heikkilä, K.; Harjunen, P.; Päällysaho, M.; Väliisaari, J.; Niemelä, P.; Järvinen, K. The Comparison of Seven Different Methods to Quantify the Amorphous Content of Spray Dried Lactose. *Powder Technol.* **2006**, *167* (2), 85–93. <https://doi.org/10.1016/j.powtec.2006.05.019>.
- (12) Shah, B.; Kakumanu, V. K.; Bansal, A. K. Analytical Techniques for Quantification of Amorphous/Crystalline Phases in Pharmaceutical Solids. *J. Pharm. Sci.* **2006**, *95* (8), 1641–1665. <https://doi.org/https://doi.org/10.1002/jps.20644>.
- (13) Xie, Y.; Tao, W.; Morrison, H.; Chiu, R.; Jona, J.; Fang, J.; Cauchon, N. Quantitative Determination of Solid-State Forms of a Pharmaceutical Development Compound in Drug Substance and Tablets. *Int. J. Pharm.* **2008**, *362* (1–2), 29–36. <https://doi.org/10.1016/j.ijpharm.2008.05.038>.
- (14) USP-NF Unites States Pharmacopeia and National Formulary. (941) Characterization of Crystalline and Partially Crystalline Solids BY X-Ray Powder Diffraction (XRPD). 2019.
- (15) Madsen, I. C.; Scarlett, N. V. Y. Y.; Kern, A. Description and Survey of Methodologies for the Determination of Amorphous Content via X-Ray Powder Diffraction. *Zeitschrift fur Krist.* **2011**, *226* (12), 944–955. <https://doi.org/10.1524/zkri.2011.1437>.
- (16) Ong, J. L.; Farley, D. W.; Norling, B. K. Quantification of Leucite Concentration Using X-Ray Diffraction. *Dent. Mater.* **2000**, *16* (1), 20–25. [https://doi.org/10.1016/S0109-5641\(99\)00079-2](https://doi.org/10.1016/S0109-5641(99)00079-2).
- (17) Tiwari, M.; Chawla, G.; Bansal, A. K. Quantification of Olanzapine Polymorphs Using Powder X-Ray Diffraction Technique. *J. Pharm. Biomed. Anal.* **2007**, *43* (3), 865–872. <https://doi.org/10.1016/j.jpba.2006.08.030>.
- (18) Chen, X.; Bates, S.; Morris, K. R. Quantifying Amorphous Content of Lactose Using Parallel Beam X-Ray Powder Diffraction and Whole Pattern Fitting. *J. Pharm. Biomed. Anal.* **2001**, *26* (1), 63–72. [https://doi.org/10.1016/S0731-7085\(01\)00346-6](https://doi.org/10.1016/S0731-7085(01)00346-6).

- (19) Bish, D. L.; Howard, S. A. Quantitative Phase Analysis Using the Rietveld Method. *J. Appl. Crystallogr.* **1988**, *21* (2), 86–91. <https://doi.org/10.1107/S0021889887009415>.
- (20) Scarlett, N. V. Y.; Madsen, I. C. Quantification of Phases with Partial or No Known Crystal Structures. *Powder Diffr.* **2006**, *21* (4), 278–284. <https://doi.org/10.1154/1.2362855>.
- (21) Fix, I.; Steffens, K. J. Quantifying Low Amorphous or Crystalline Amounts of Alpha-Lactose-Monohydrate Using X-Ray Powder Diffraction, near-Infrared Spectroscopy, and Differential Scanning Calorimetry. *Drug Dev. Ind. Pharm.* **2004**, *30* (5), 513–523. <https://doi.org/10.1081/DDC-120037482>.
- (22) Nakai, Y.; Fukuoka, E.; Nakajima, S.-I.; Morita, M. Physicochemical Properties of Crystalline Lactose. I. Estimation of the Degree of Crystallinity and the Disorder Parameter by an X-Ray Diffraction Method. *Chem. Pharm. Bull.* **1982**, *30*, 1811–1818. <https://doi.org/https://doi.org/10.1248/cpb.30.1811>.
- (23) Toraya, H. A New Method for Quantitative Phase Analysis Using X-Ray Powder Diffraction: Direct Derivation of Weight Fractions from Observed Integrated Intensities and Chemical Compositions of Individual Phases. *J. Appl. Crystallogr.* **2016**, *49* (5), 1508–1516. <https://doi.org/10.1107/S1600576716010451>.
- (24) Toraya, H.; Omote, K. Quantitative Phase Analysis of Amorphous Components in Mixtures by Using the Directderivation Method. *J. Appl. Crystallogr.* **2019**, *52*, 13–22. <https://doi.org/10.1107/S1600576718016394>.
- (25) Braga, D.; Grepioni, F.; Chelazzi, L.; Campana, M.; Confortini, D.; Viscomi, G. C. The Structure-Property Relationship of Four Crystal Forms of Rifaximin. *CrystEngComm* **2012**, *14* (20), 6404–6411. <https://doi.org/10.1039/c2ce25920f>.
- (26) Toraya, H. Quantitative Phase Analysis Using Observed Integrated Intensities and Chemical Composition Data of Individual Crystalline Phases: Quantification of Materials with Indefinite Chemical Compositions. *J. Appl. Crystallogr.* **2017**, *50* (3), 820–829. <https://doi.org/10.1107/S1600576717005052>.
- (27) Toraya, H. Direct Derivation (DD) of Weight Fractions of Individual Crystalline Phases from Observed Intensities and Chemical Composition Data: Incorporation of the DD Method into the Whole-Powder-Pattern Fitting Procedure. *J. Appl. Crystallogr.* **2018**, *51* (2), 446–455. <https://doi.org/10.1107/S1600576718001474>.
- (28) Smith, D. K.; Johnson, G. G.; Scheible, A.; Wims, A. M.; Johnson, J. L.; Ullmann, G. Quantitative X-Ray Powder Diffraction Method Using the Full Diffraction Pattern. *Powder Diffr.* **1987**, *2* (2), 73–77. <https://doi.org/10.1017/S0885715600012409>.
- (29) Toraya, H.; Tsusaka, S. Quantitative Phase Analysis Using the Whole-Powder-Pattern Decomposition Method. I. Solution from Knowledge of Chemical Compositions. *J. Appl. Crystallogr.* **1995**, *28* (4), 392–399. <https://doi.org/10.1107/s0021889894014986>.
- (30) Yuan, H.; Bish, D. L. Automated Fitting of X-Ray Powder Diffraction Patterns from Interstratified Phyllosilicates. *Clays Clay Miner.* **2010**, *58* (6), 727–742. <https://doi.org/10.1346/CCMN.2010.0580601>.
- (31) Toby, B. H. R Factors in Rietveld Analysis: How Good Is Good Enough? . *Powder Diffr.* **2006**, *21* (1), 67–70. <https://doi.org/10.1154/1.2179804>.
- (32) Noordik, J. H.; Beurskens, P. T.; Bennema, P. Crystal Structure, Polarity and Morphology of 4-O-β-D-Galactopyranosyl-α-D-Glucopyranose Mono-Hydrate (α-Lactose Monohydrate): A Redetermination. *Zeitschrift für Krist. - Cryst. Mater.* **1984**, *168*, 59–65.
- (33) Warren, J. L. Further Considerations on the Symmetry Properties of the Normal Vibrations of a Crystal. *Rev. Mod. Phys.* **1968**, *40* (1), 38–76. <https://doi.org/10.1103/RevModPhys.40.38>.
- (34) London, UNiversity College. Allied Health Professions, Dentistry, N. and P. Impact Case Study: Developing Methods to Measure and Quantify Amorphous Content in Micronised Particles, Leading to Improved Manufacture and Performance of Inhaled Drug Delivery Devices. *REF2014*. 2014. <https://doi.org/https://www.ref.ac.uk/>.

## 7 SUPPLEMENTARY DATA

### 7.1 The intensity–composition (IC) equation

$$w_k = a_k S_k / \sum_{k'=1}^k a_{k'} S_{k'}$$

Where

$$S_k = \sum_{j=1}^{N_k} I_{jk} G_{jk}$$

$$a_k = M_k / \sum_{i=1}^{N_k^A} n_{ik}^2$$

$I_{jk}$  = integrated intensity of  $j^{\text{th}}$  reflection of  $K^{\text{th}}$  component in a  $K$ -component mixture

$$G_{jk} = 2 \sin \theta_{jk} \sin 2\theta_{jk} / (1 + \cos^2 2\theta_{jk})$$

$M_k$  = molecular weight

$N_k^A$  = number of atoms in the chemical formula unit

$n_{ik}$  = number of electrons belonging to  $i^{\text{th}}$  atom of the chemical formula

Toraya, H., 2016. A new method for quantitative phase analysis using X-ray powder diffraction: Direct derivation of weight fractions from observed integrated intensities and chemical compositions of individual phases. *J. Appl. Cryst.* 49, 1508–1516. <https://doi.org/10.1107/S1600576716010451>

### 7.2 Instrument and measure settings

Instrumental Settings	
Equipment	PANalytical X'Pert Pro X-Ray Diffractometer
Anode	Cu
Mode	Reflection
Detector	XCelerator
Sample holder	Top loading Silicon Zero background plate
Incident beam path	
Soller slit (rad)	0.04
Divergence slit	Fixed 1/4°
Mask	Fixed 15mm
Antiscatter slit	Fixed 1/2°
Filter	None
Diffracted beam path	
Soller slit	0.04
Antiscatter slit	5.0mm
Filter	Nickel
Measurement Settings	
Scan axis	Gonio
Scan properties	Continuous
Generator settings	40 kV, 40 mA
Scan Range (°θ)	3,5 - 80
Step size (°θ)	0.0167
Time per step (s)	100
Spinner revolution time (rps)	1

## 7.3 Integration methods

	Method a		Method b		Method c	
<b>Crystalline reference</b>	<ul style="list-style-type: none"> <li>• Pawley function Refinement (LACTOS03):               <ul style="list-style-type: none"> <li>○ FWHMs function: Caglioti</li> <li>○ Profile function: Pseudo Voigt</li> <li>○ Asymmetry function: Split width and shape</li> </ul> </li> </ul>		<ul style="list-style-type: none"> <li>• Peak finding function</li> <li>• Profile fit refinement:               <ul style="list-style-type: none"> <li>○ FWHMs function: Caglioti</li> <li>○ Profile function: Pseudo Voigt</li> <li>○ Asymmetry function: Split width and shape</li> </ul> </li> </ul>		Not available	
<b>Amorphous reference</b>	<ul style="list-style-type: none"> <li>• Manually add four peaks</li> <li>• Profile fit refinement:               <ul style="list-style-type: none"> <li>○ FWHMs function: Individual FWHMs</li> <li>○ Profile function: Pseudo Voigt</li> <li>○ Asymmetry function: No asymmetry Function</li> </ul> </li> </ul>		<ul style="list-style-type: none"> <li>• Manually add four peaks</li> <li>• Profile fit refinement:               <ul style="list-style-type: none"> <li>○ FWHMs function: Individual FWHMs</li> <li>○ Profile function: Pseudo Voigt</li> <li>○ Asymmetry function: No asymmetry Function</li> </ul> </li> </ul>		Not available	
<b>Mixtures</b>	<i>Crystalline reference</i>	<i>Amorphous reference</i>	<i>Crystalline reference</i>	<i>Amorphous reference</i>	<i>Crystalline reference</i>	<i>Amorphous reference</i>
<b>Step 1</b>	<ul style="list-style-type: none"> <li>• Scale parameters</li> <li>• Specimen displacement</li> </ul>	<ul style="list-style-type: none"> <li>• Scale parameters</li> </ul>	<ul style="list-style-type: none"> <li>• Scale parameters</li> </ul>	<ul style="list-style-type: none"> <li>• Scale parameters</li> </ul>	<ul style="list-style-type: none"> <li>• Peak finding function</li> <li>• Profile fit refinement</li> </ul>	<ul style="list-style-type: none"> <li>• Manually add and modelling four peaks</li> </ul>
<b>Final</b>	<ul style="list-style-type: none"> <li>• Pawley function refinement:               <ul style="list-style-type: none"> <li>○ FWHMs function: Caglioti</li> <li>○ Profile function: Pseudo Voigt</li> <li>○ Asymmetry function: Split width and shape</li> </ul> </li> </ul>	<ul style="list-style-type: none"> <li>• Profile fit refinement:               <ul style="list-style-type: none"> <li>○ FWHMs function: Individual FWHMs</li> <li>○ Profile function: Pseudo Voigt</li> <li>○ Asymmetry function: No asymmetry Function</li> <li>○ Shape function</li> </ul> </li> </ul>	<ul style="list-style-type: none"> <li>• Profile fit refinement:               <ul style="list-style-type: none"> <li>○ FWHMs function: Caglioti</li> <li>○ Profile function: Pseudo Voigt</li> <li>○ Asymmetry function: Split width and shape</li> </ul> </li> </ul>	<ul style="list-style-type: none"> <li>• Profile fit refinement:               <ul style="list-style-type: none"> <li>○ FWHMs function: Individual FWHMs</li> <li>○ Profile function: Pseudo Voigt</li> <li>○ Asymmetry function: No asymmetry Function</li> <li>○ Shape function</li> </ul> </li> </ul>	<ul style="list-style-type: none"> <li>• Profile fit refinement:               <ul style="list-style-type: none"> <li>○ FWHMs function: Caglioti</li> <li>○ Profile function: Pseudo Voigt</li> <li>○ Asymmetry function: Split width and shape</li> </ul> </li> </ul>	<ul style="list-style-type: none"> <li>• Profile fit refinement:               <ul style="list-style-type: none"> <li>○ FWHMs function: Individual FWHMs</li> <li>○ Profile function: Pseudo Voigt</li> <li>○ Asymmetry function: No asymmetry Function</li> <li>○ Shape function</li> </ul> </li> </ul>

## 7.4 Standard reference material

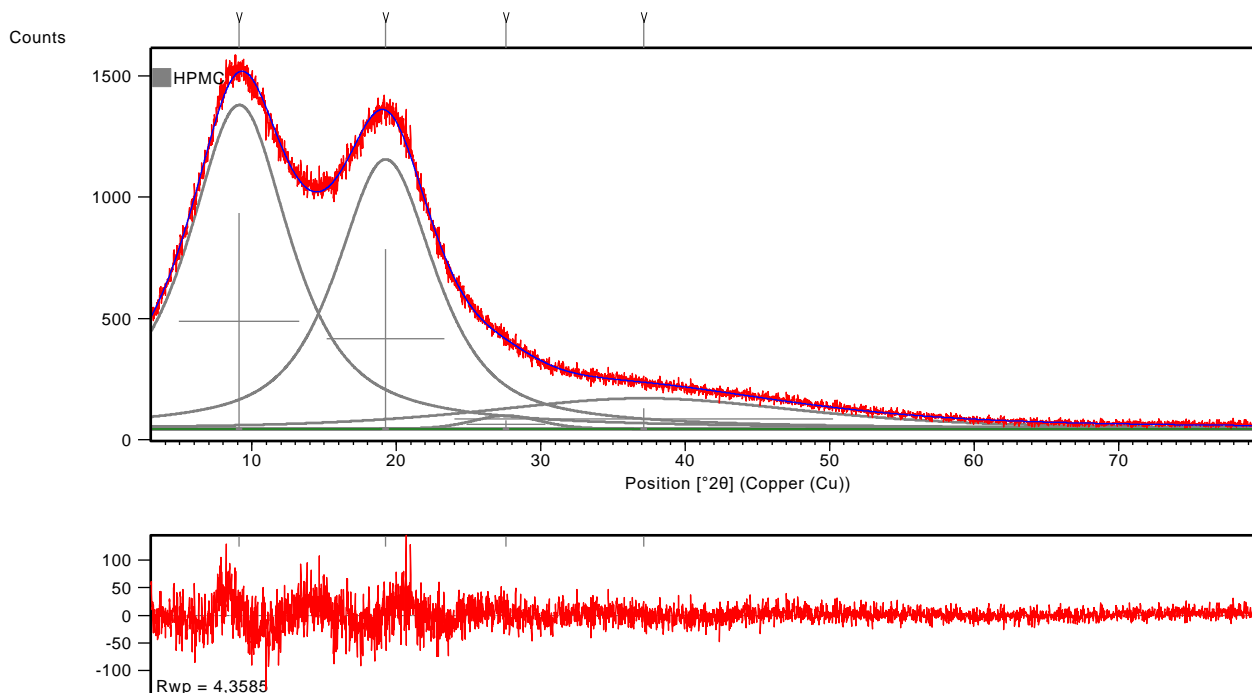


**Figure 1.** Refinement results for the diffraction pattern of HPMC. Red and blue patterns are the experimental and calculated patterns, respectively. The bottom plot shows their difference. The grey lines indicate the peak positions and area of HPMC. The chi-square is 0.91.

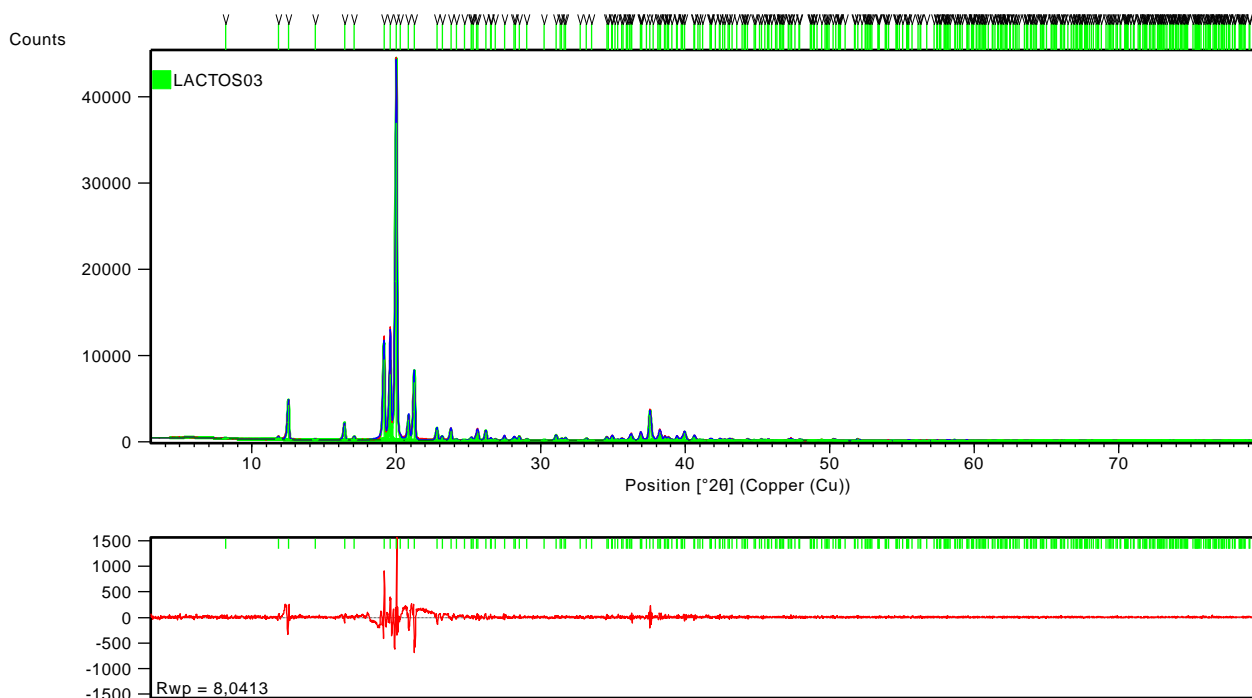


**Figure 2.** Refinement results for the diffraction pattern of  $\alpha$ -lactose monohydrate in Method a. Red and blue patterns are the experimental and calculated patterns, respectively. The bottom plot shows their difference. The green lines indicate the peak positions area of  $\alpha$ -lactose monohydrate. The chi-square is 1.78.

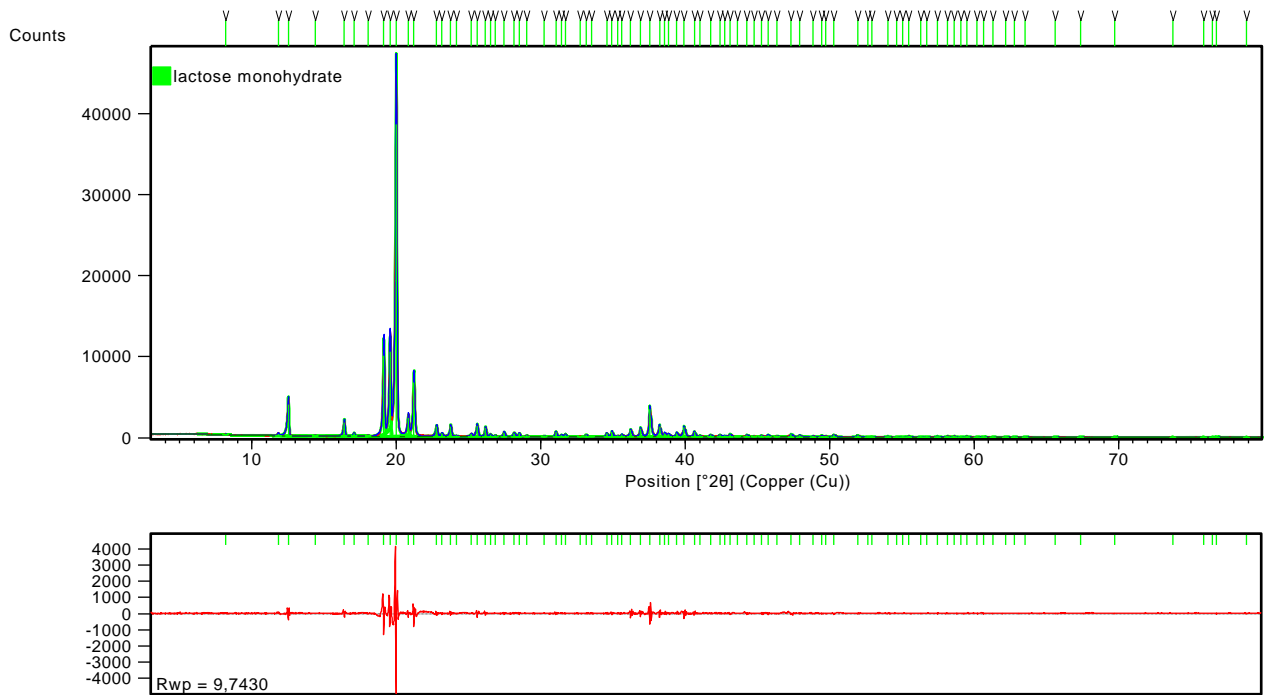
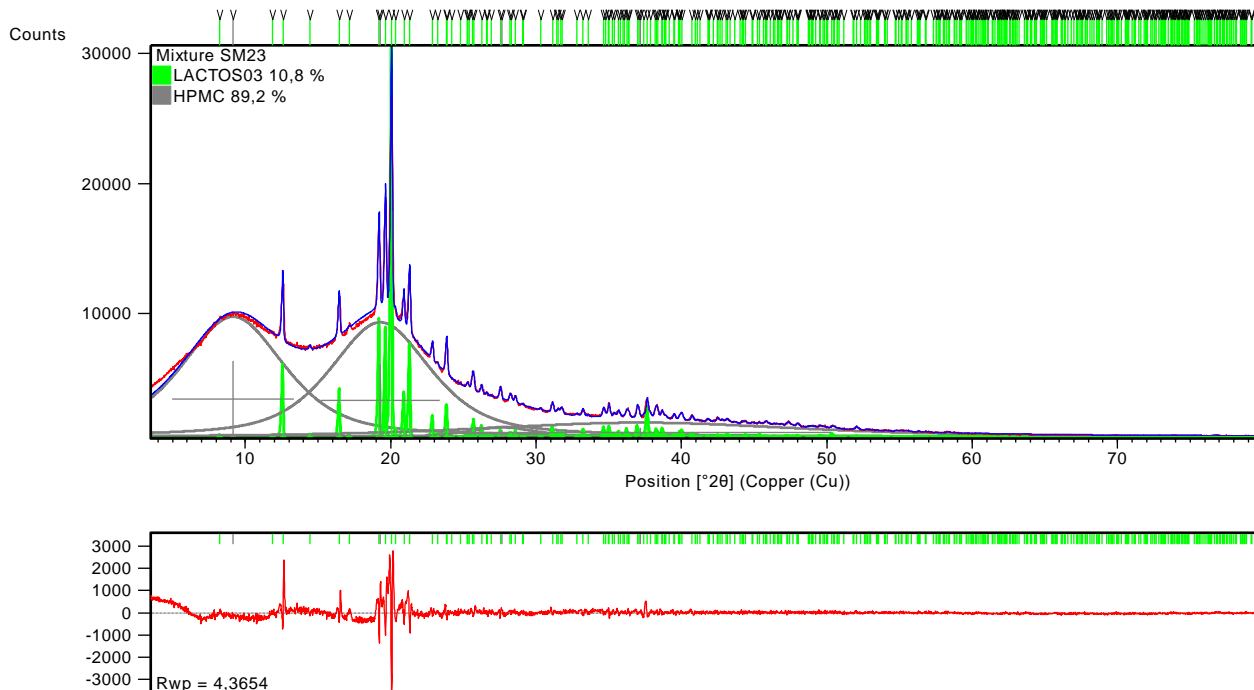


**Figure 3.** Refinement results for the diffraction pattern of  $\alpha$ -lactose monohydrate in Method b. Red and blue patterns are the experimental and calculated patterns, respectively. The bottom plot shows their difference. The green lines indicate the peak positions and area of  $\alpha$ -lactose monohydrate. The chi-square is 2.12.

## 7.5 Method a

- Mixture SM23 Method a

a)



b)

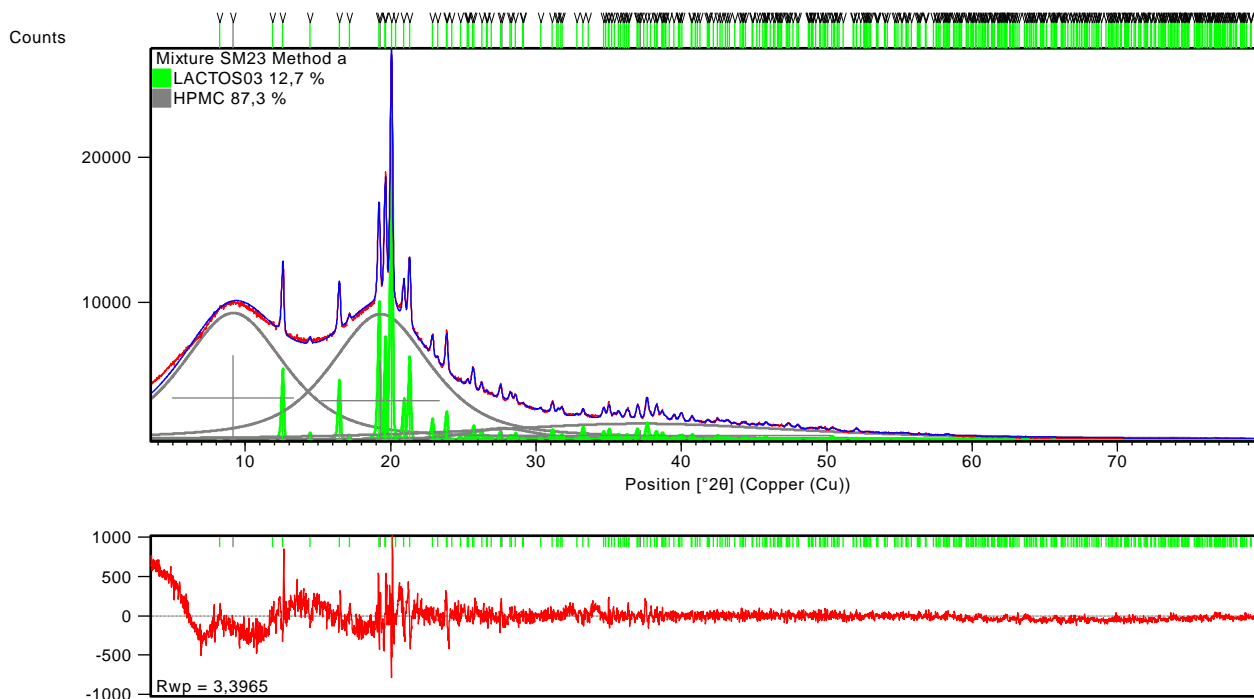
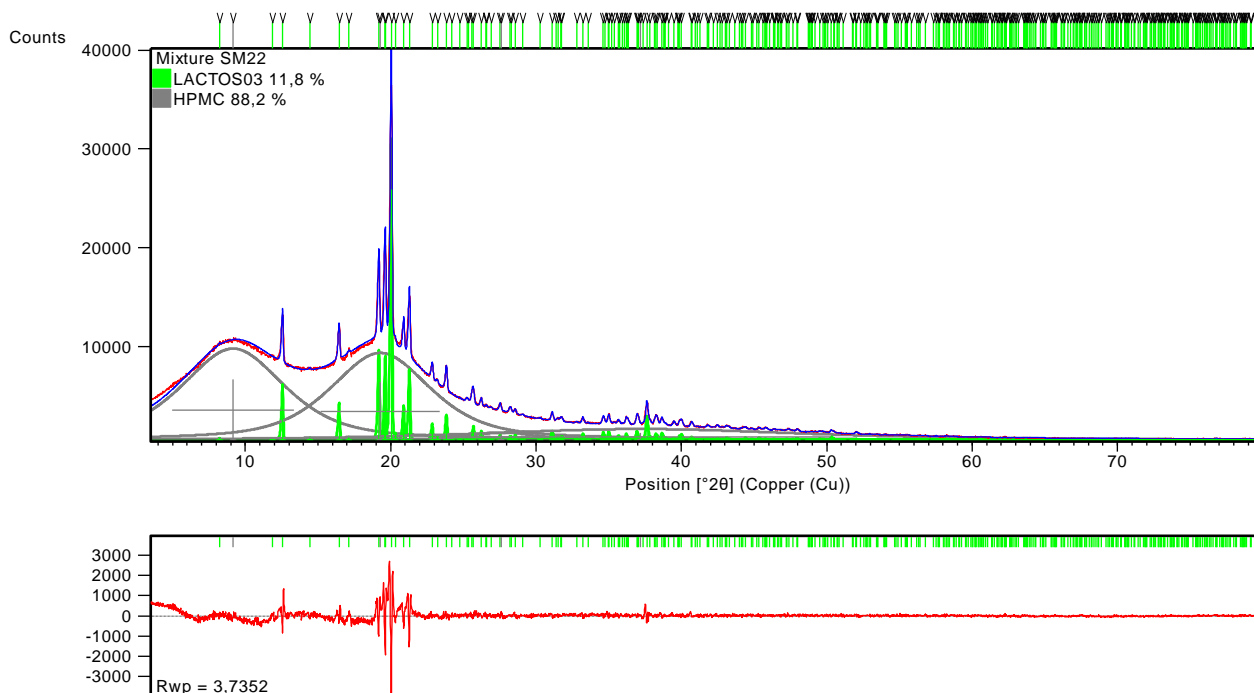


**Figure 4. Refinement results for the diffraction pattern of SM<sub>23</sub> in Method a: picture a) shows the signals after refinement and scaling of the SRM patterns (Step 1) and picture b) shows the results after final Pawley refinement. The chi-square is 2.72 and 2.12, respectively. Red and blue patterns are the experimental and calculated patterns. The bottom plot shows their difference. The grey and green lines indicate the peak positions and area of HPMC and  $\alpha$ -lactose monohydrate, respectively.**

- Mixture SM22 Method a

a)



b)

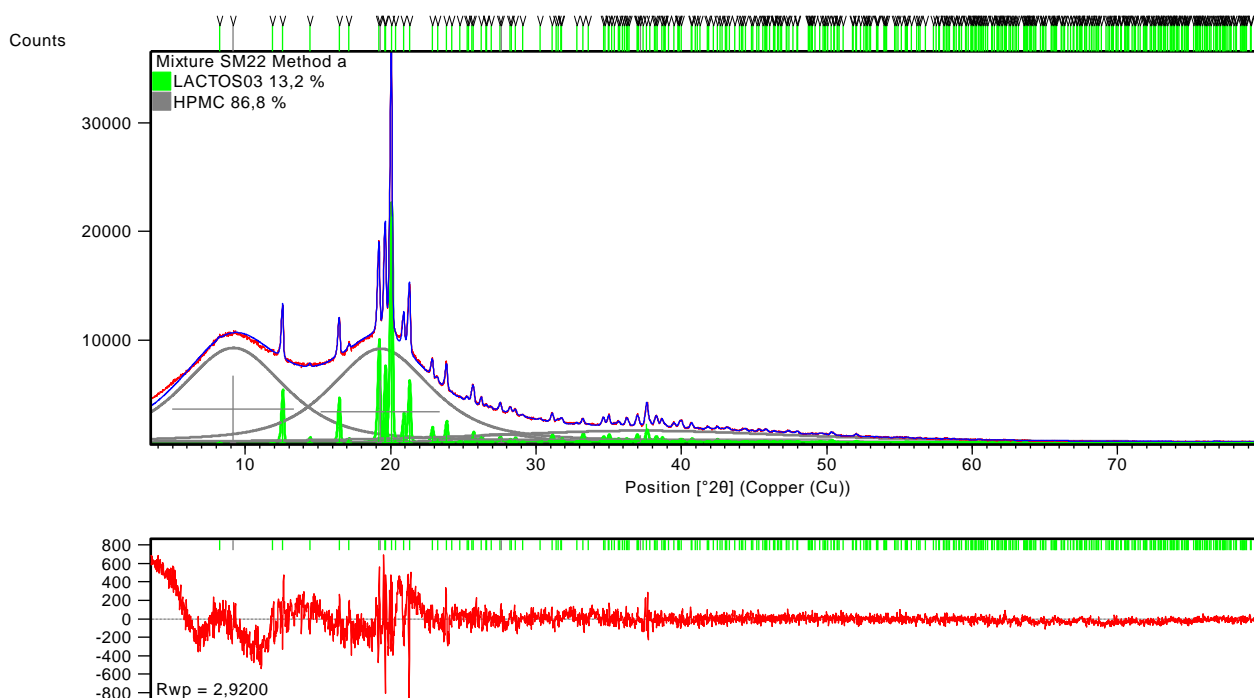
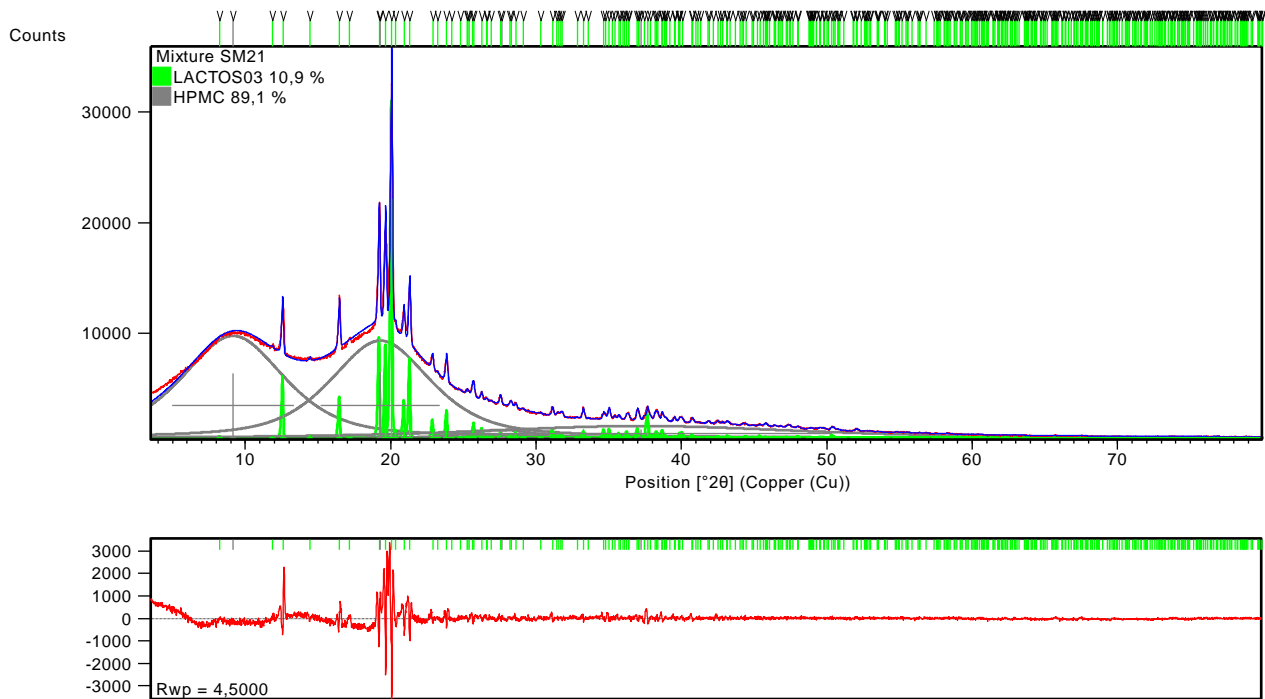


**Figure 5. Refinement results for the diffraction pattern of SM<sub>22</sub> in Method a: picture a) shows the signals after refinement and scaling of the SRM patterns (Step 1) and picture b) shows the results after final Pawley refinement. The chi-square is 2.38 and 1.86, respectively. Red and blue patterns are the experimental and calculated patterns. The bottom plot shows their difference. The grey and green lines indicate the peak positions and area of HPMC and  $\alpha$ -lactose monohydrate, respectively.**

- Mixture SM21 Method a

a)



b)

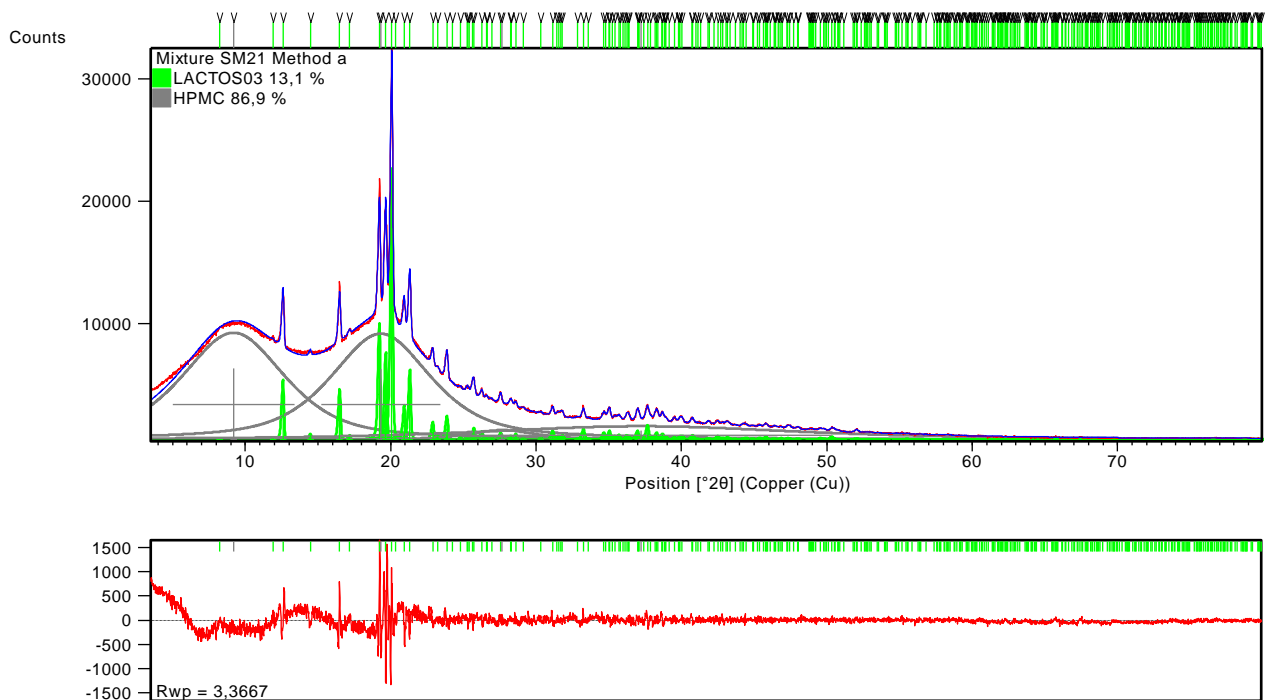
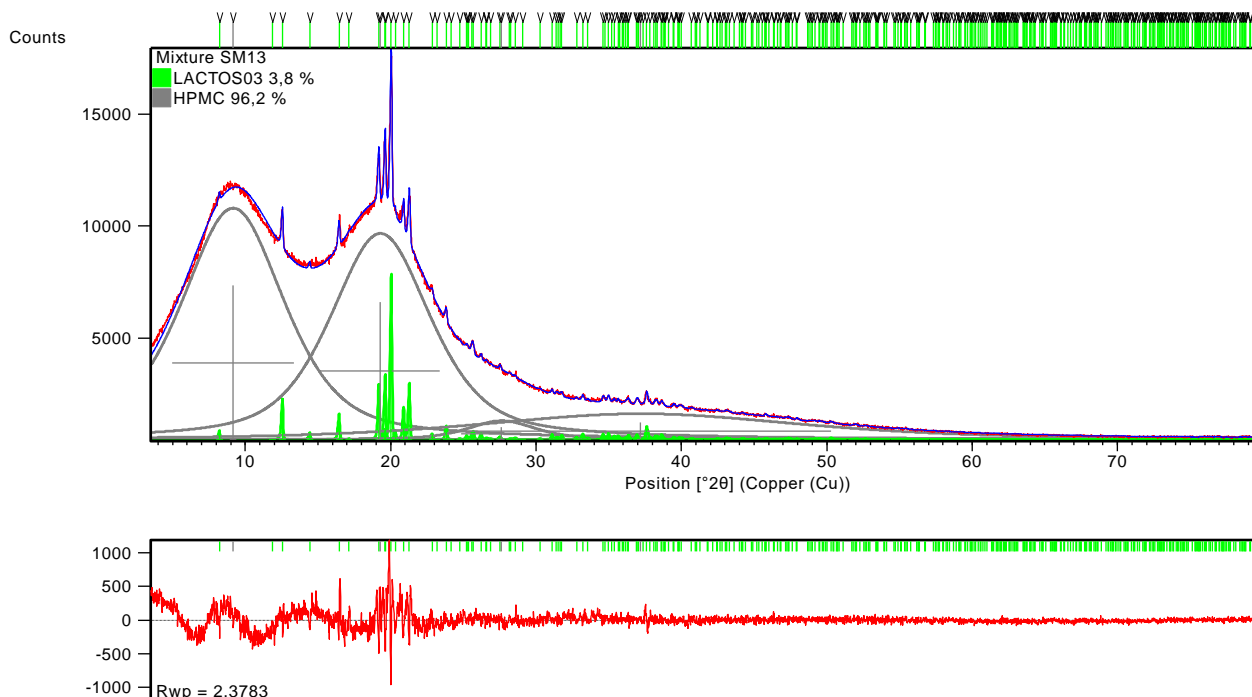


**Figure 6.** Refinement results for the diffraction pattern of SM<sub>21</sub> in Method a: picture a) shows the signals after refinement and scaling of the SRM patterns (Step 1) and picture b) shows the results after final Pawley refinement. The chi-square is 2.87 and 2.15, respectively. Red and blue patterns are the experimental and calculated patterns. The bottom plot shows their difference. The grey and green lines indicate the peak positions and area of HPMC and  $\alpha$ -lactose monohydrate, respectively.

- Mixture SM13 Method a

a)



b)

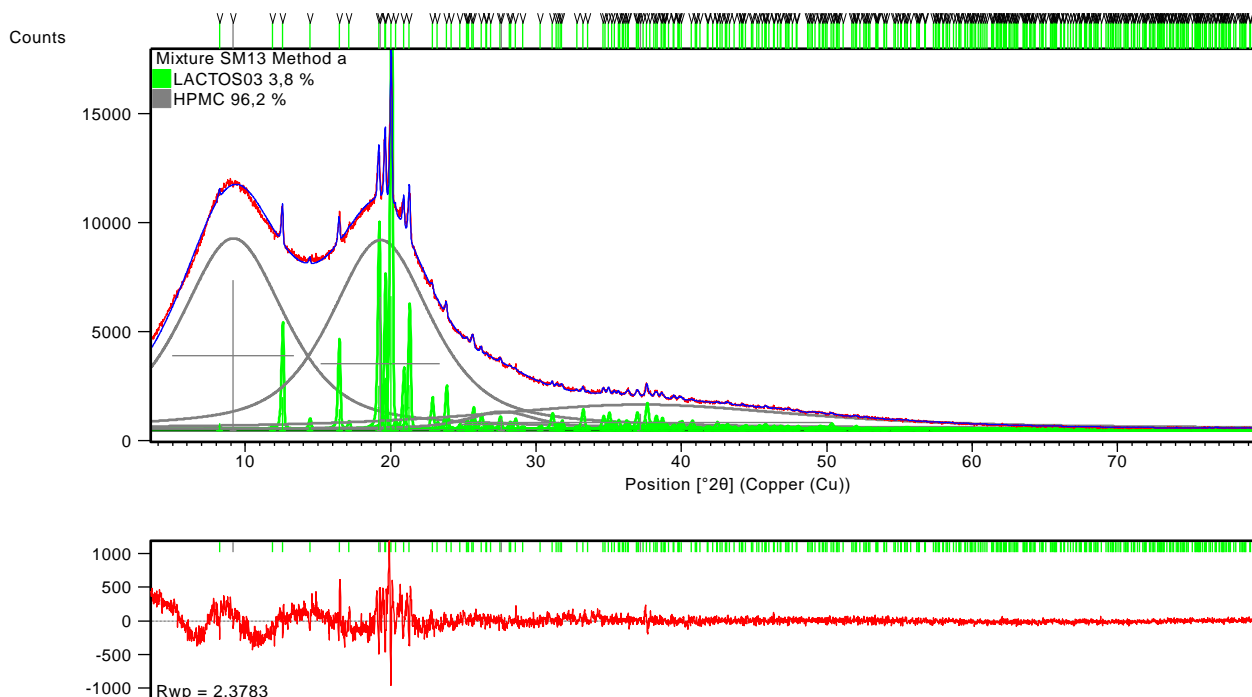
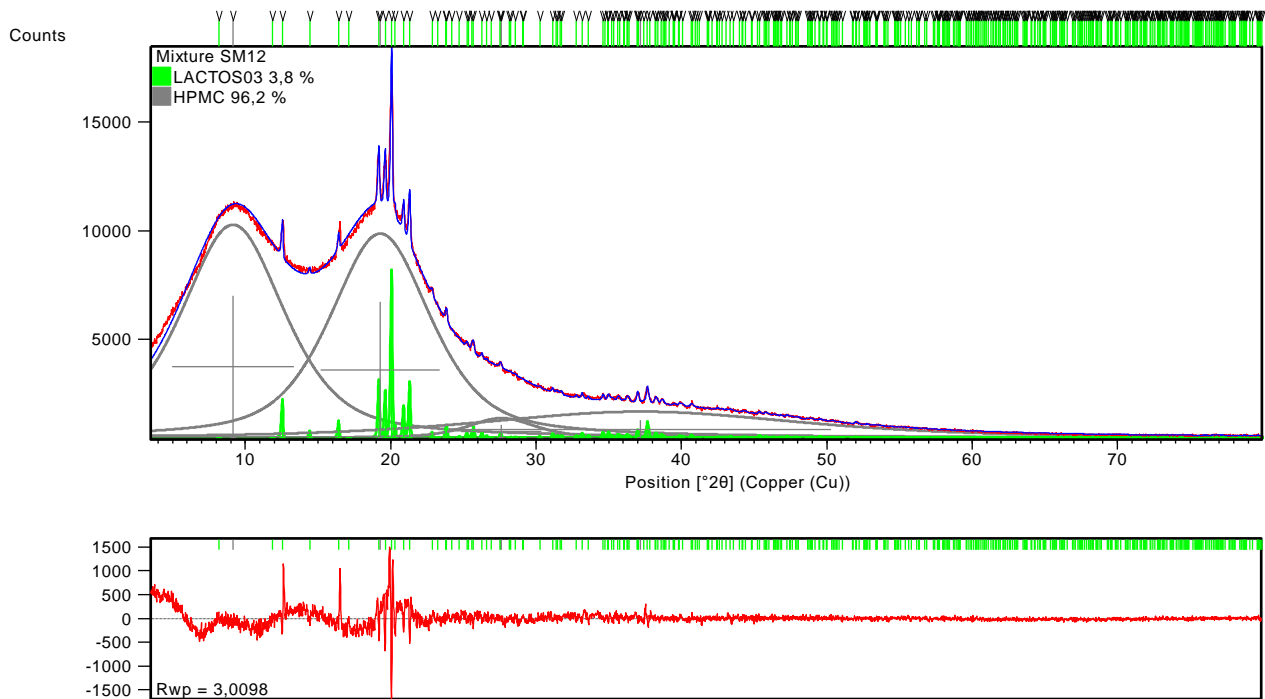


**Figure 7.** Refinement results for the diffraction pattern of SM<sub>13</sub> in Method a: picture a) shows the signals after refinement and scaling of the SRM patterns (Step 1) and picture b) shows the results after final Pawley refinement. The chi-square is 1.51 and 1.51, respectively. Red and blue patterns are the experimental and calculated patterns. The bottom plot shows their difference. The grey and green lines indicate the peak positions and area of HPMC and  $\alpha$ -lactose monohydrate, respectively.

- Mixture SM12 Method a

a)



b)

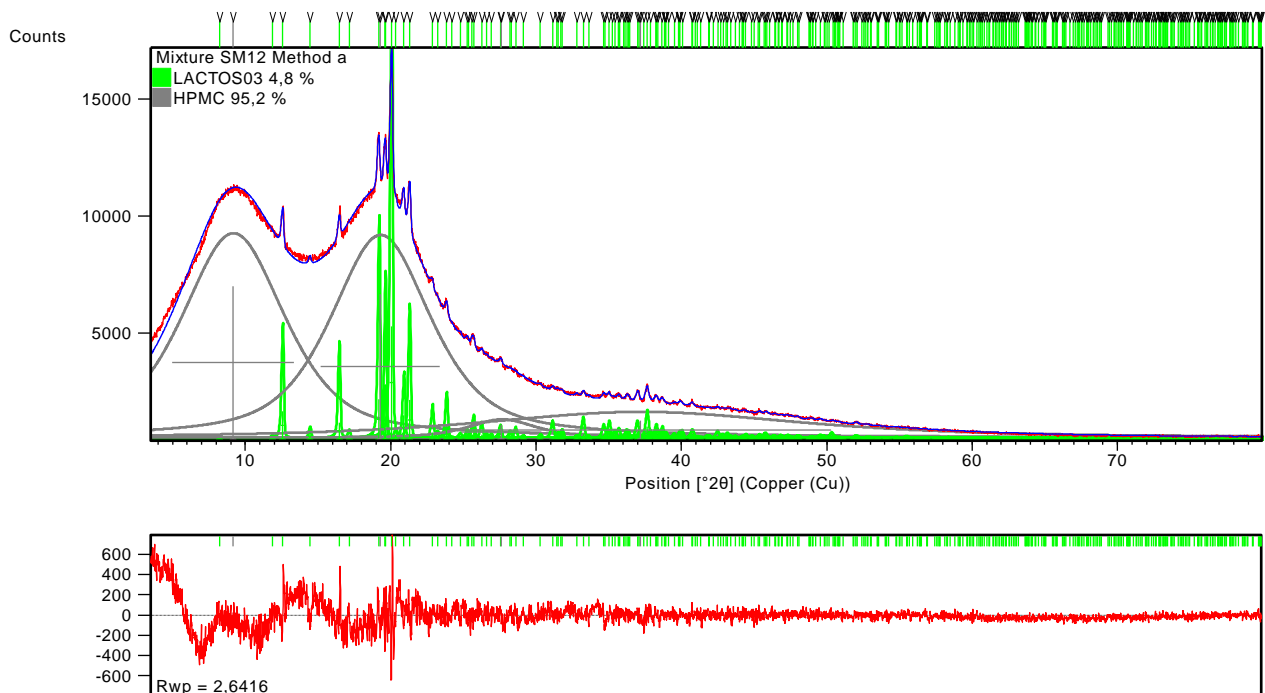
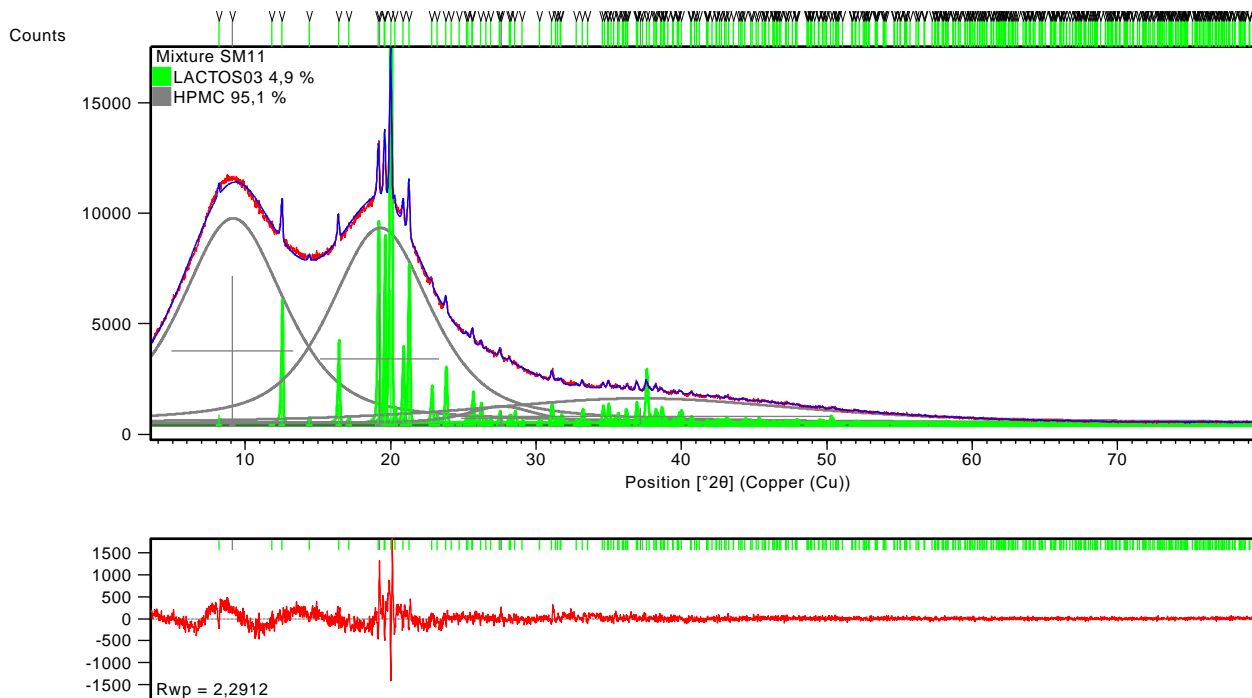


**Figure 8.** Refinement results for the diffraction pattern of SM<sub>12</sub> in Method a: picture a) shows the signals after refinement and scaling of the SRM patterns (Step 1) and picture b) shows the results after final Pawley refinement. The chi-square is 1.91 and 1.68, respectively. Red and blue patterns are the experimental and calculated patterns. The bottom plot shows their difference. The grey and green lines indicate the peak positions and area of HPMC and  $\alpha$ -lactose monohydrate, respectively.

- Mixture SM11 Method a

a)



b)

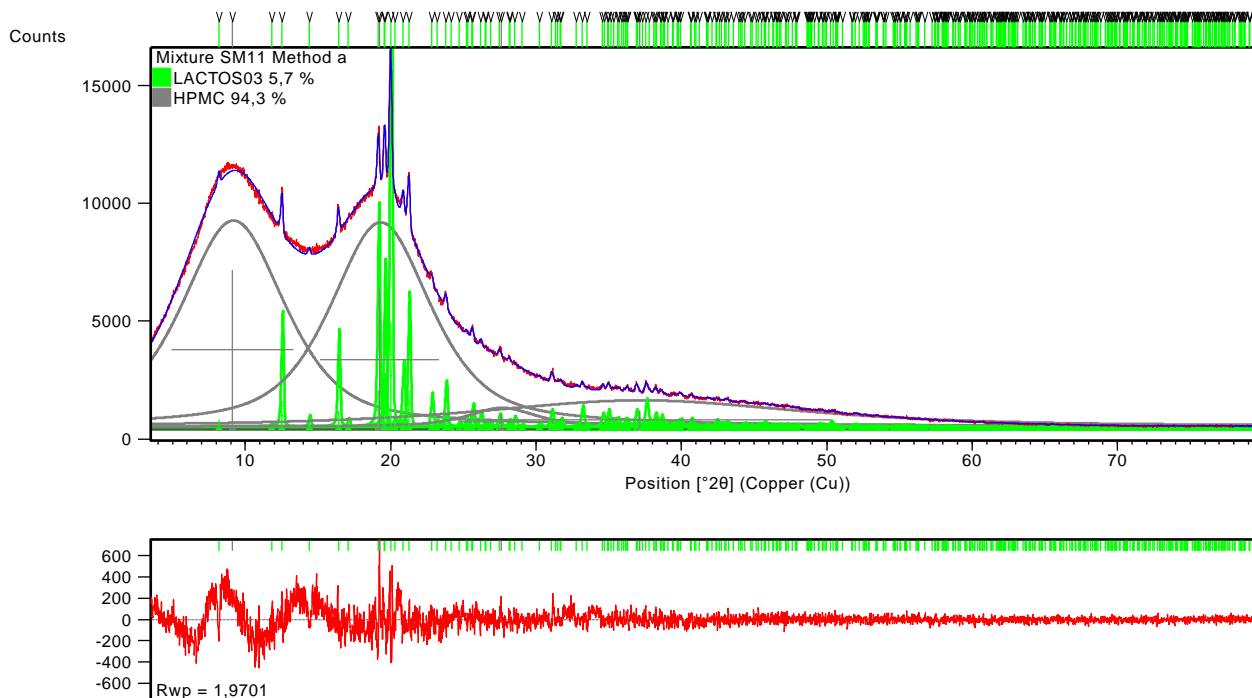


**Figure 9. Refinement results for the diffraction pattern of SM<sub>11</sub> in Method a: picture a) shows the signals after refinement and scaling of the SRM patterns (Step 1) and picture b) shows the results after final Pawley refinement. The chi-square is 1.43 and 1.23, respectively. Red and blue patterns are the experimental and calculated patterns. The bottom plot shows their difference. The grey and green lines indicate the peak positions and area of HPMC and  $\alpha$ -lactose monohydrate, respectively.**

- Mixture SM11 clipped at  $40^\circ 2\theta$  Method a

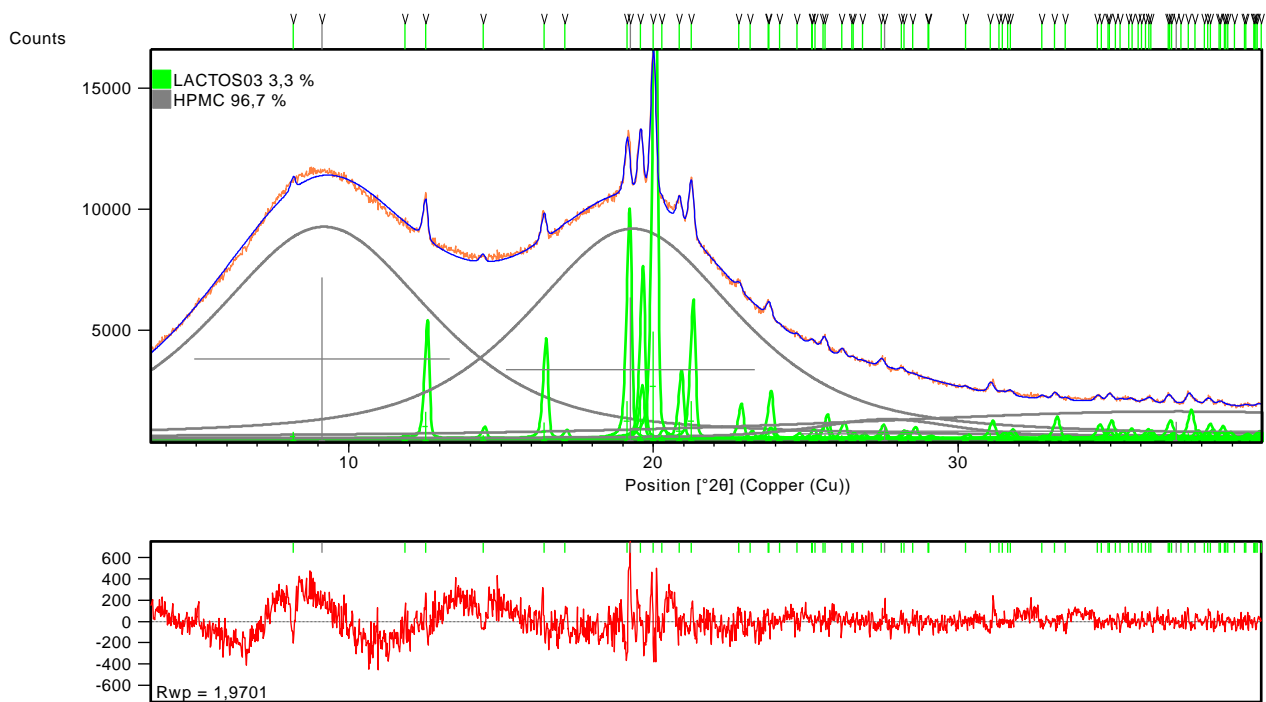
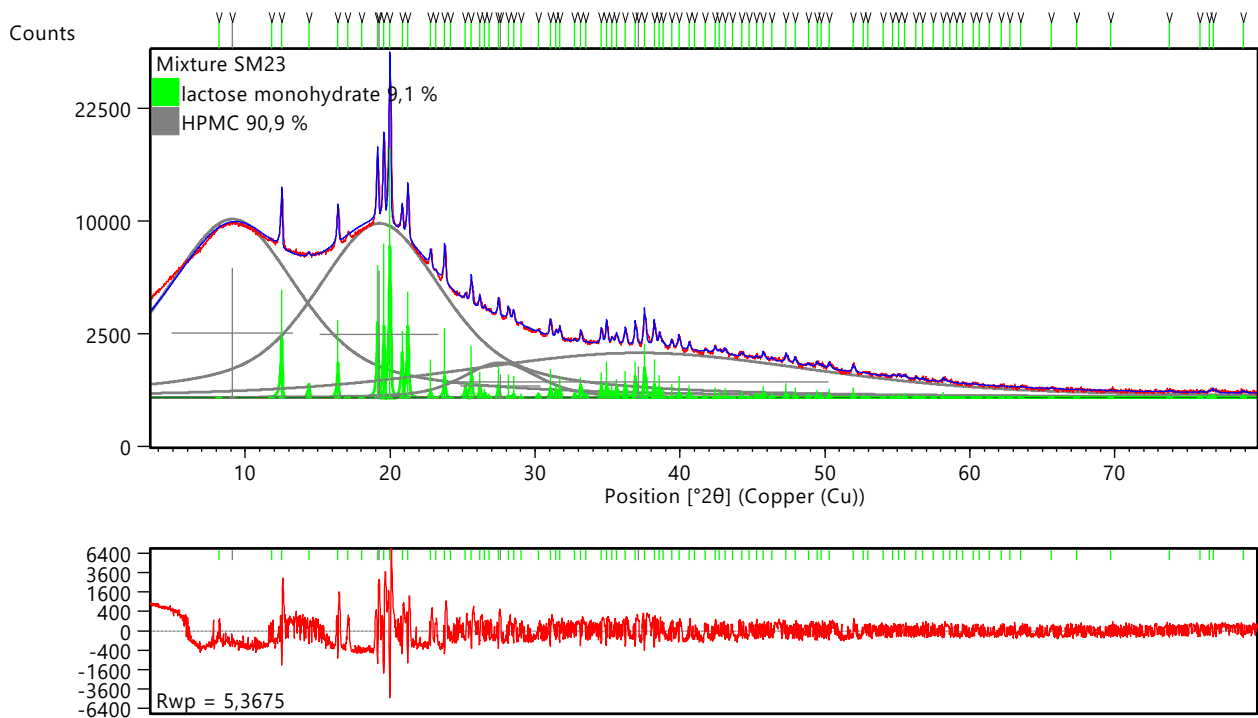


**Figure 10.** Refinement results for the diffraction pattern of SM<sub>11</sub> clipped at  $40^\circ 2\theta$  in Method a. Red and blue patterns are the experimental and calculated patterns, respectively. The bottom plot shows their difference. The grey and green lines indicate the peak positions and area of HPMC and  $\alpha$ -lactose monohydrate, respectively. The chi-square is 1.23.

## 7.6 Method b

- Mixture SM23 Method b

a)



b)

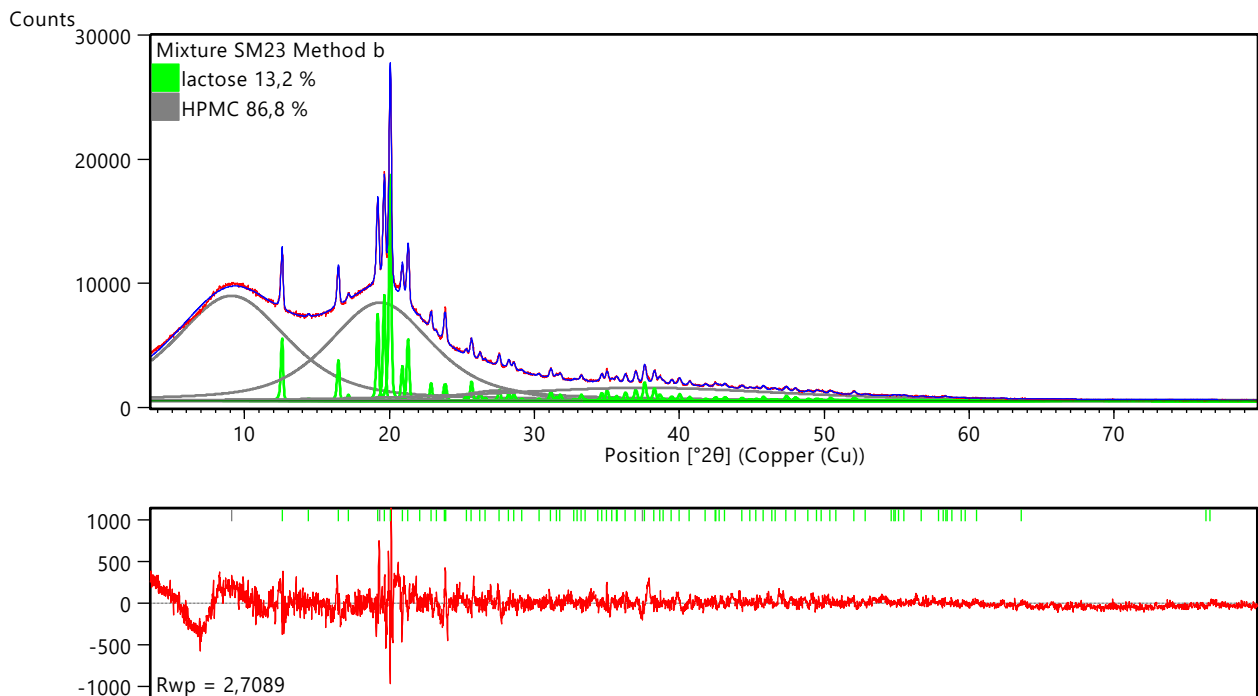
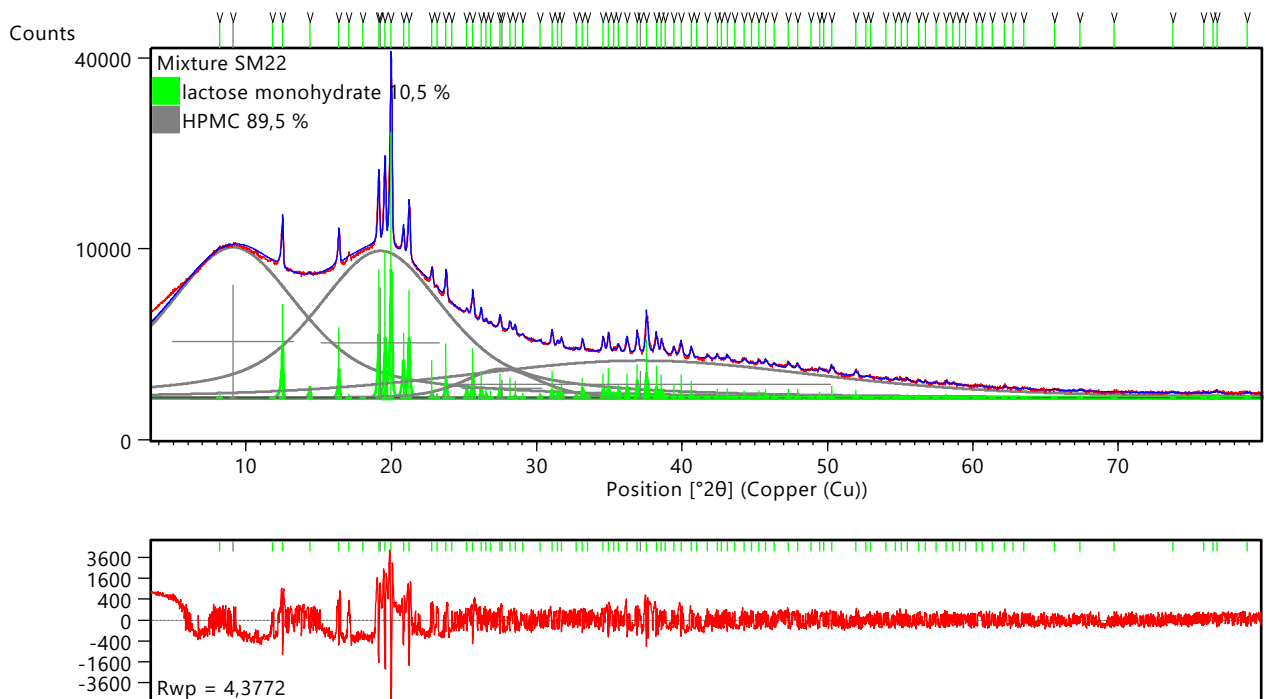


**Figure 11. Refinement results for the diffraction pattern of SM<sub>23</sub> in Method a: picture a) shows the signals after scaling of the SRM patterns (Step 1) and picture b) shows the results after final refinement. The chi-square is 3.18 and 1.61, respectively. Red and blue patterns are the experimental and calculated patterns. The bottom plot shows their difference. The grey and green lines indicate the peak positions and area of HPMC and  $\alpha$ -lactose monohydrate, respectively.**

- Mixture SM22 Method b

a)



b)

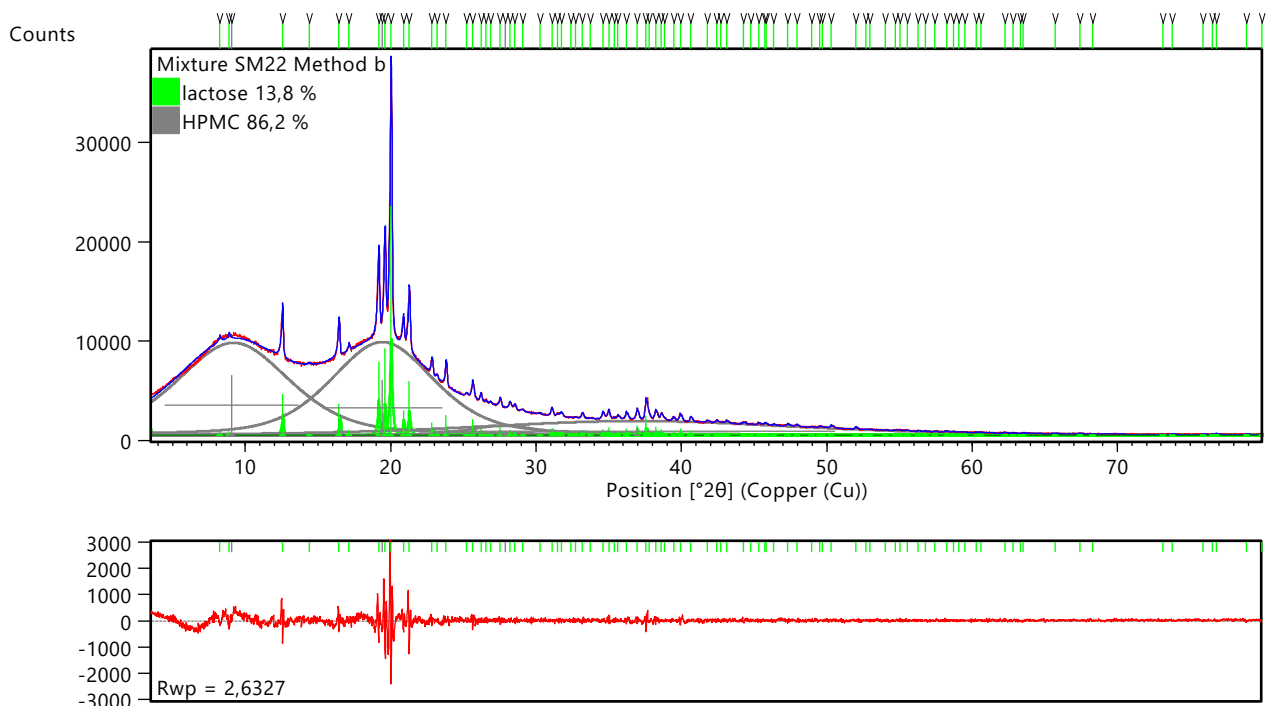
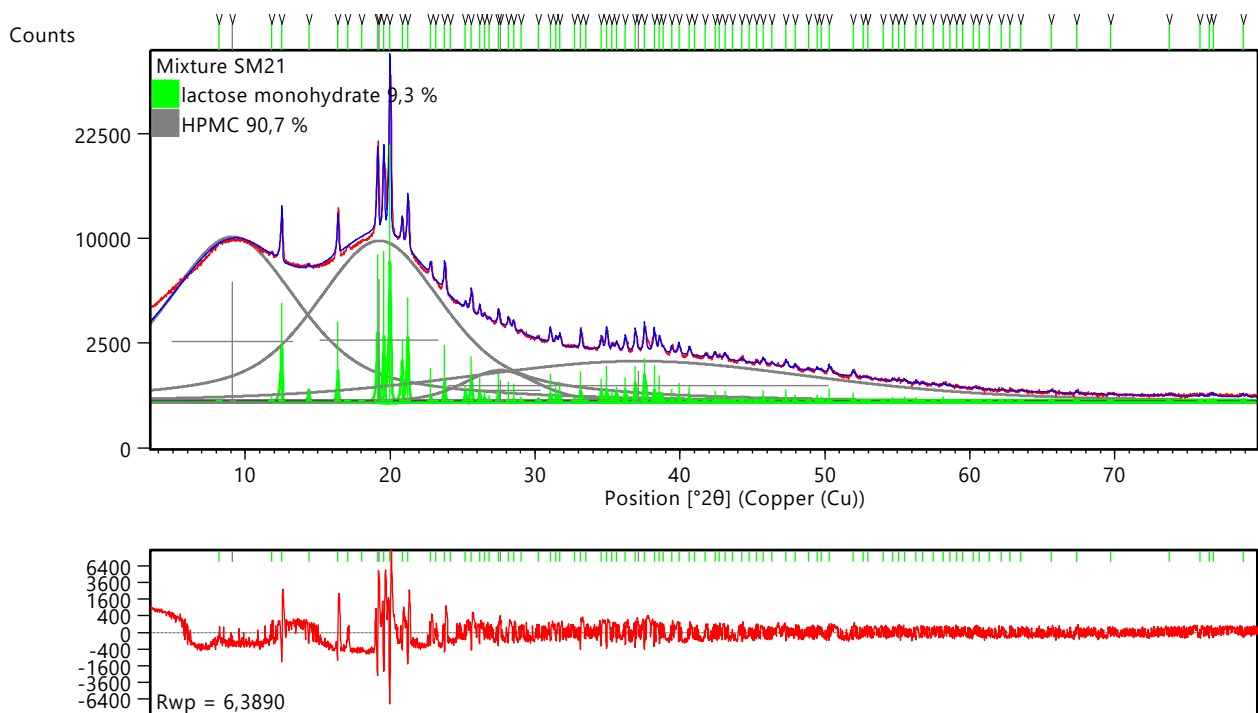


**Figure 12. Refinement results for the diffraction pattern of SM<sub>22</sub> in Method a: picture a) shows the signals after scaling of the SRM patterns (Step 1) and picture b) shows the results after final refinement. The chi-square is 2.66 and 1.60, respectively. Red and blue patterns are the experimental and calculated patterns. The bottom plot shows their difference. The grey and green lines indicate the peak positions and area of HPMC and  $\alpha$ -lactose monohydrate, respectively.**

- Mixture SM21 Method b

a)



b)

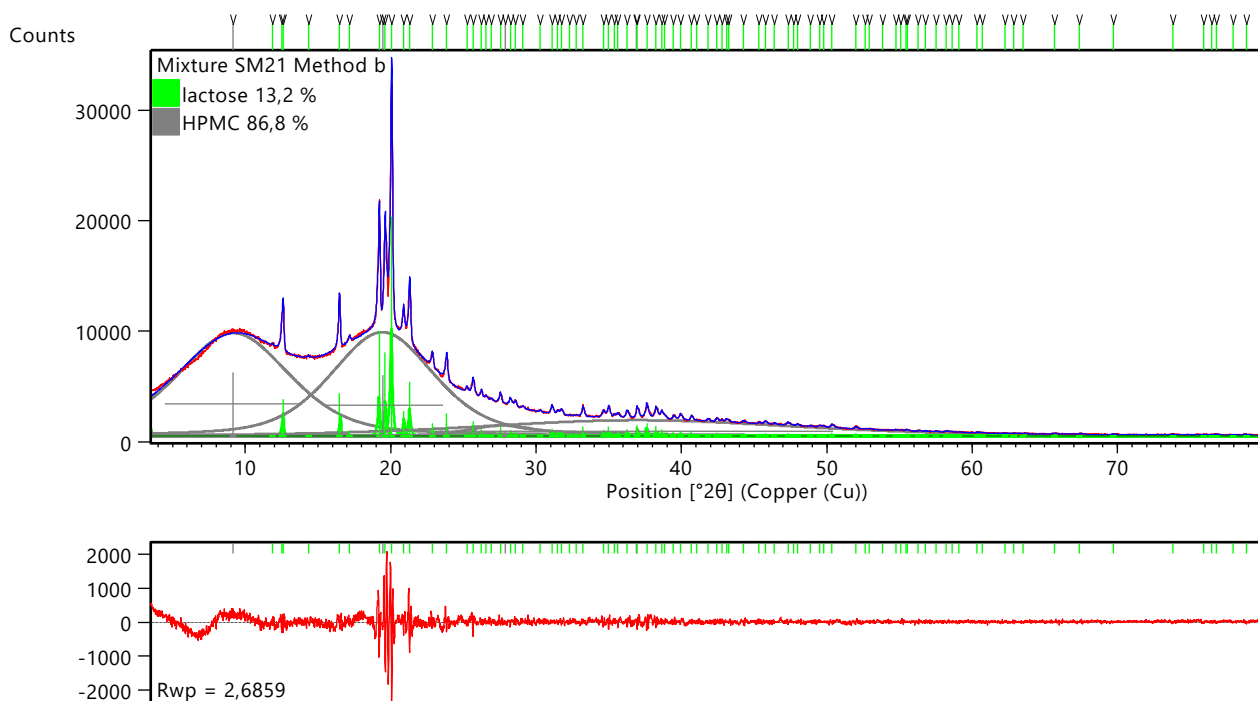
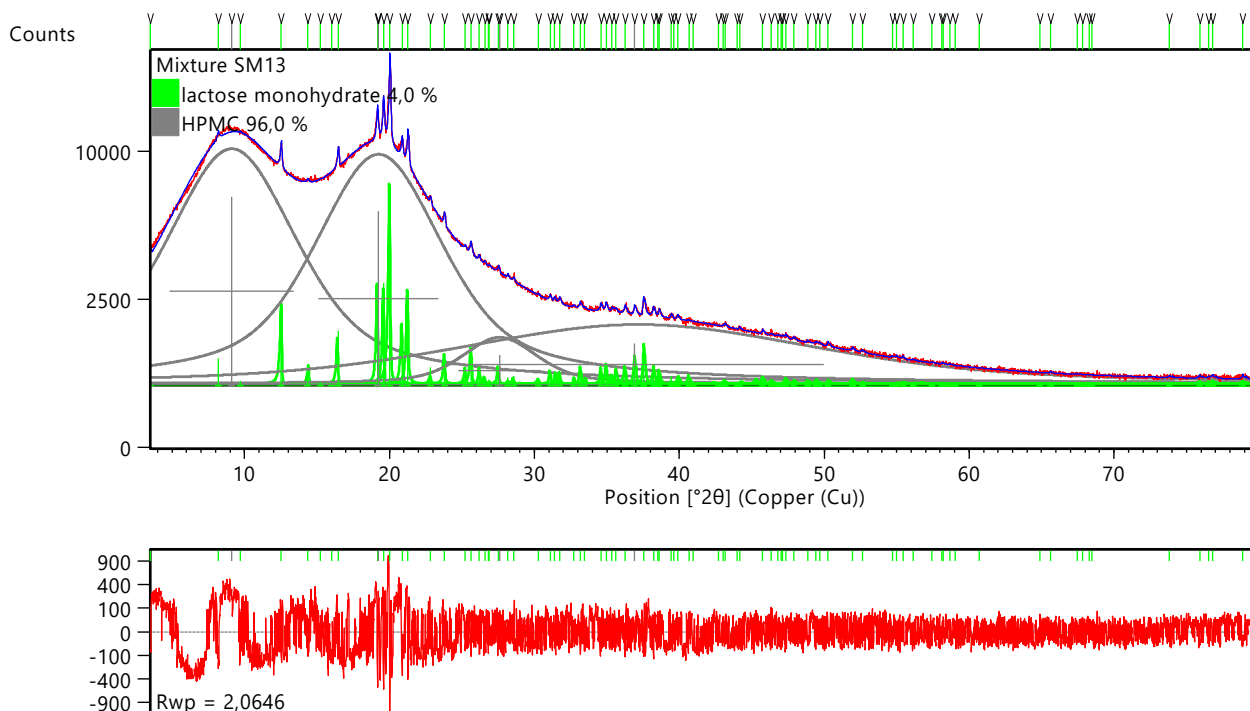


**Figure 13. Refinement results for the diffraction pattern of SM<sub>21</sub> in Method a: picture a) shows the signals after scaling of the SRM patterns (Step 1) and picture b) shows the results after final refinement. The chi-square is 3.88 and 1.63, respectively. Red and blue patterns are the experimental and calculated patterns. The bottom plot shows their difference. The grey and green lines indicate the peak positions and area of HPMC and  $\alpha$ -lactose monohydrate, respectively.**

- Mixture SM13 Method b

a)



b)

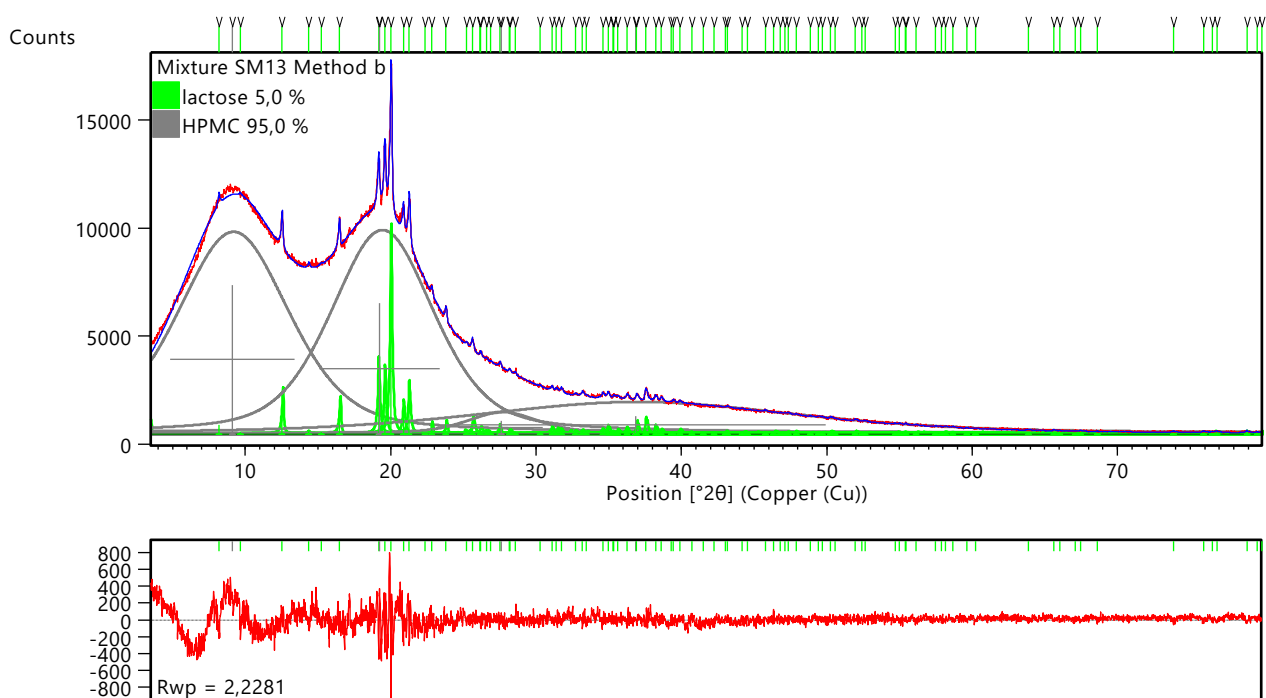
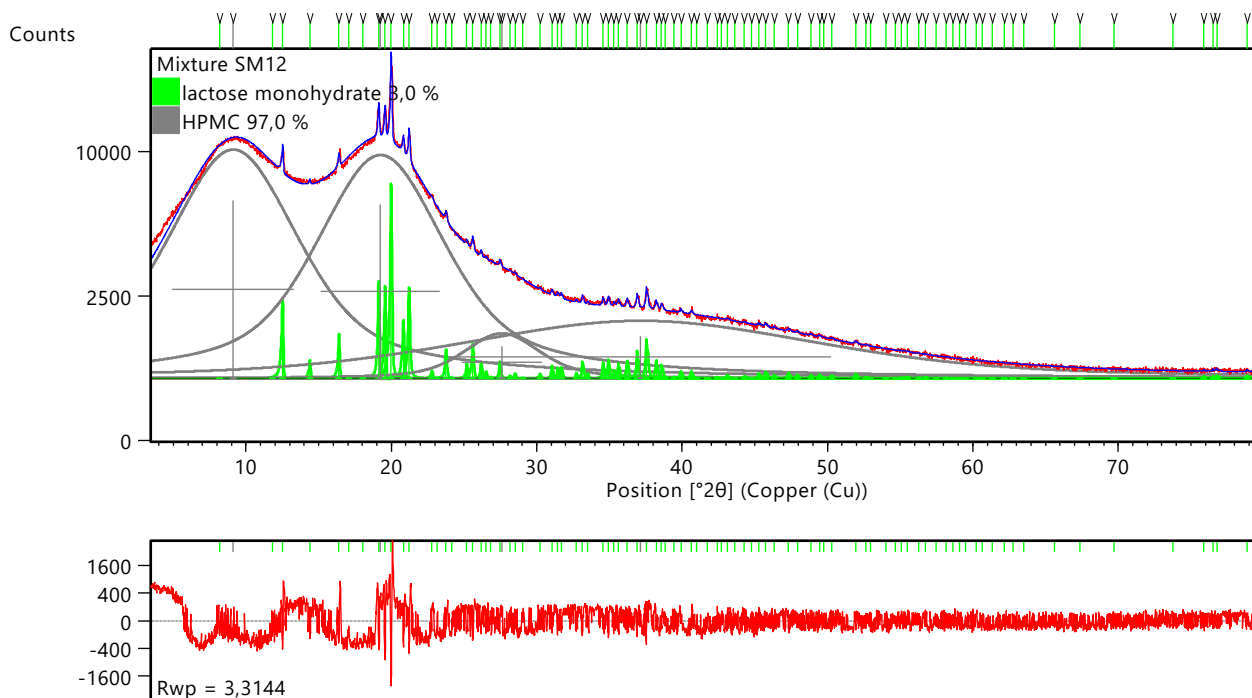


**Figure 14.** Refinement results for the diffraction pattern of SM<sub>13</sub> in Method a: picture a) shows the signals after scaling of the SRM patterns (Step 1) and picture b) shows the results after final refinement. The chi-square is 1.25 and 1.35, respectively. Red and blue patterns are the experimental and calculated patterns. The bottom plot shows their difference. The grey and green lines indicate the peak positions and area of HPMC and  $\alpha$ -lactose monohydrate, respectively.

- Mixture SM12 Method b

a)



b)

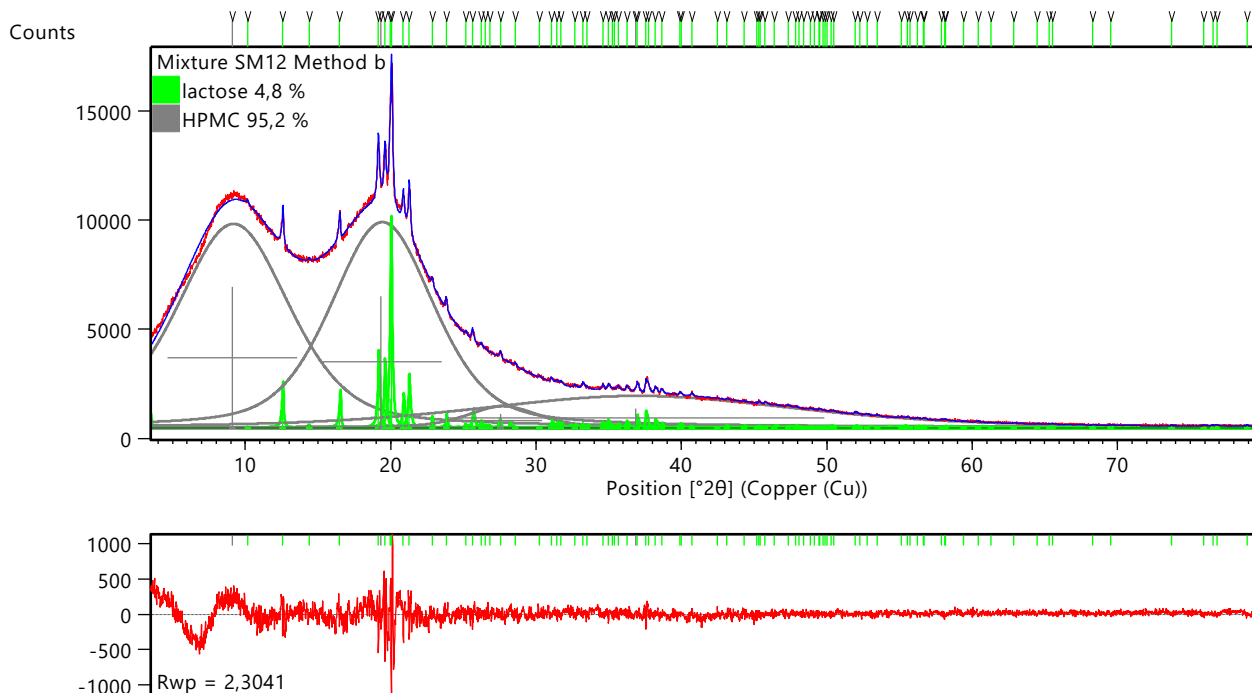
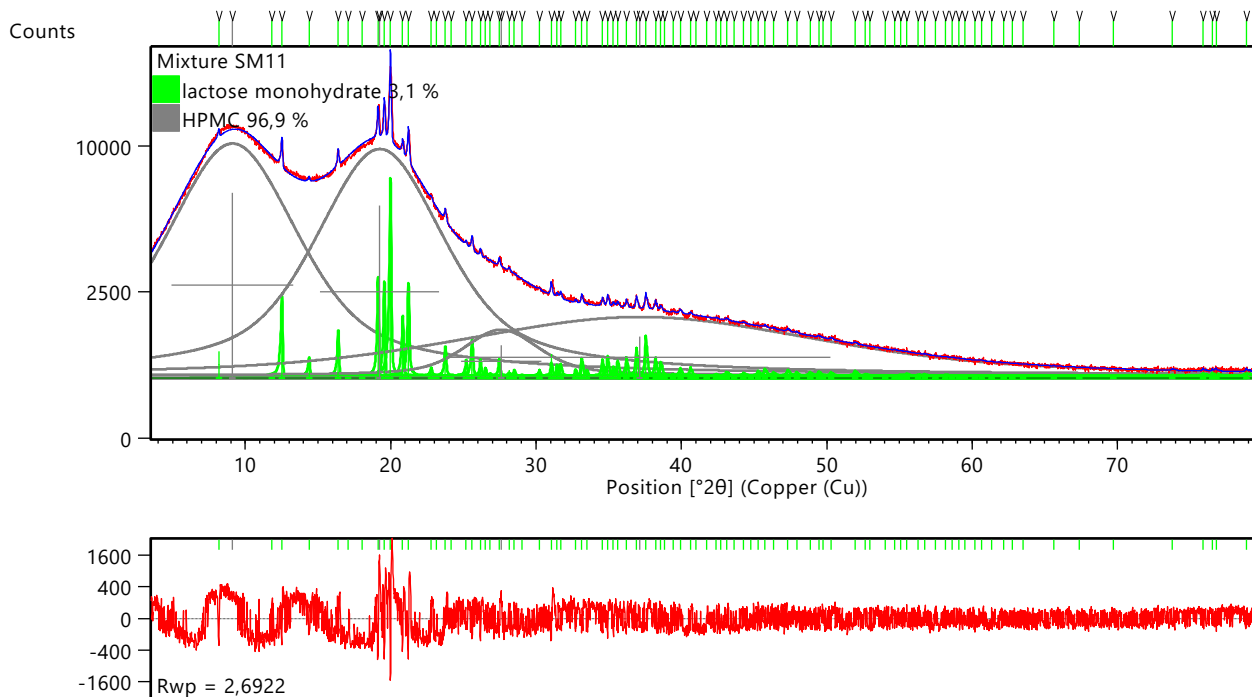


Figure 15. Refinement results for the diffraction pattern of SM<sub>12</sub> in Method a: picture a) shows the signals after scaling of the SRM patterns (Step 1) and picture b) shows the results after final refinement. The chi-square is 2.01 and 1.39, respectively. Red and blue patterns are the experimental and calculated patterns. The bottom plot shows their difference. The grey and green lines indicate the peak positions and area of HPMC and  $\alpha$ -lactose monohydrate, respectively.

- Mixture SM11 Method b

a)



b)

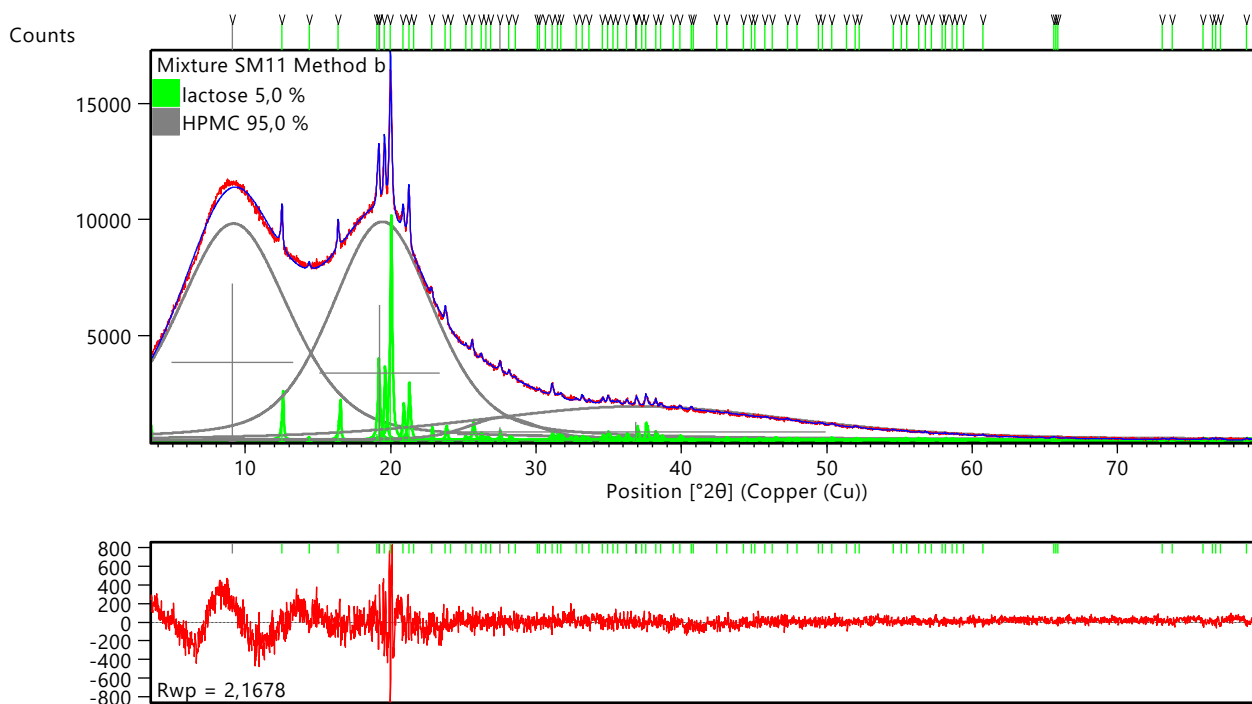


**Figure 16. Refinement results for the diffraction pattern of SM<sub>11</sub> in Method a: picture a) shows the signals after scaling of the SRM patterns (Step 1) and picture b) shows the results after final refinement. The chi-square is 1.60 and 1.29, respectively. Red and blue patterns are the experimental and calculated patterns. The bottom plot shows their difference. The grey and green lines indicate the peak positions and area of HPMC and α-lactose monohydrate, respectively.**

- Mixture SM11 clipped at  $40^\circ 2\theta$  Method b

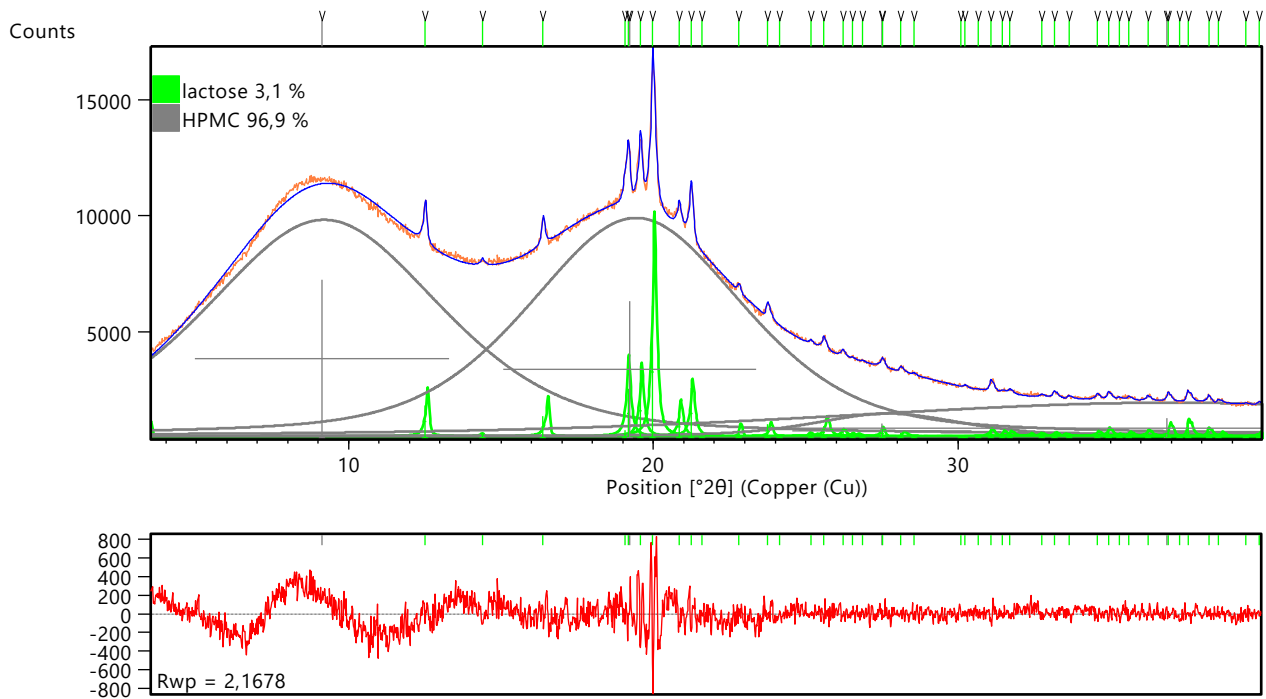


**Figure 17.** Refinement results for the diffraction pattern of SM<sub>11</sub> clipped at  $40^\circ 2\theta$  in Method b. Red and blue patterns are the experimental and calculated patterns, respectively. The bottom plot shows their difference. The grey and green lines indicate the peak positions and area of HPMC and  $\alpha$ -lactose monohydrate, respectively. The chi-square is 1.29.

## 7.7 Method c

- Mixture SM23 Method c

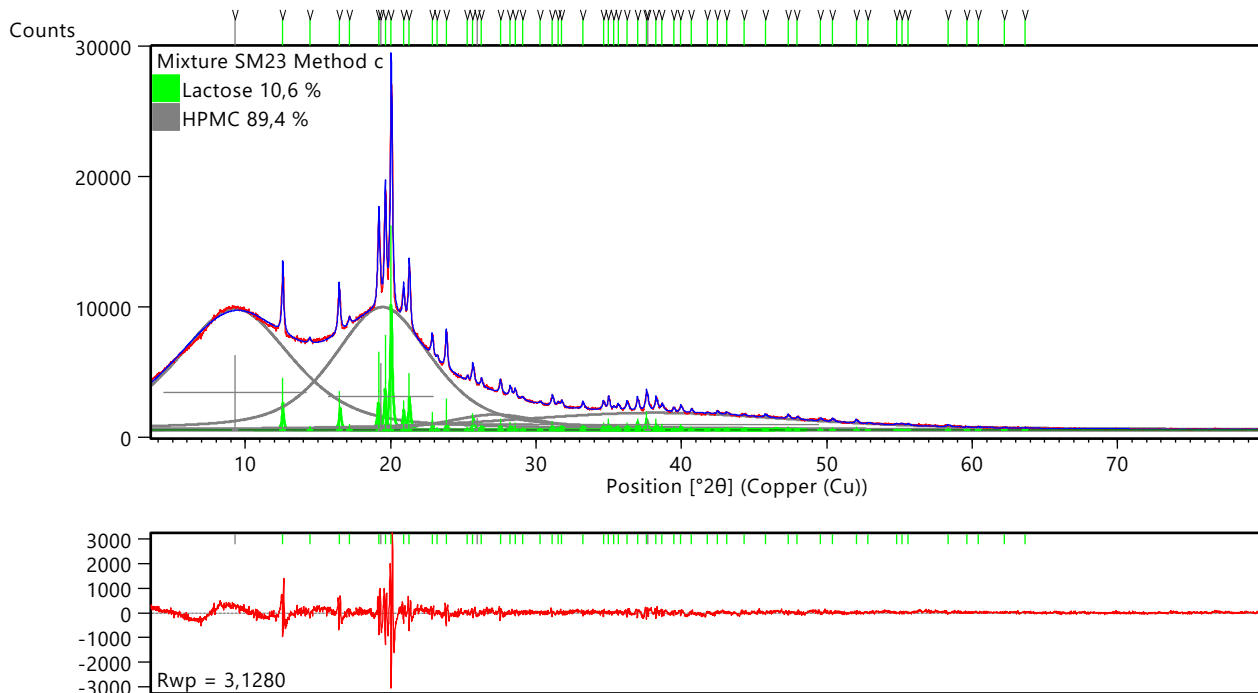


Figure 18. Refinement results for the diffraction pattern of SM<sub>23</sub> in Method c. The chi-square is 1.85. The red and blue patterns are the experimental and calculated patterns. The bottom plot shows their difference. The grey and green lines indicate the peak positions and area of HPMC and  $\alpha$ -lactose monohydrate, respectively.

- Mixture SM22 Method c

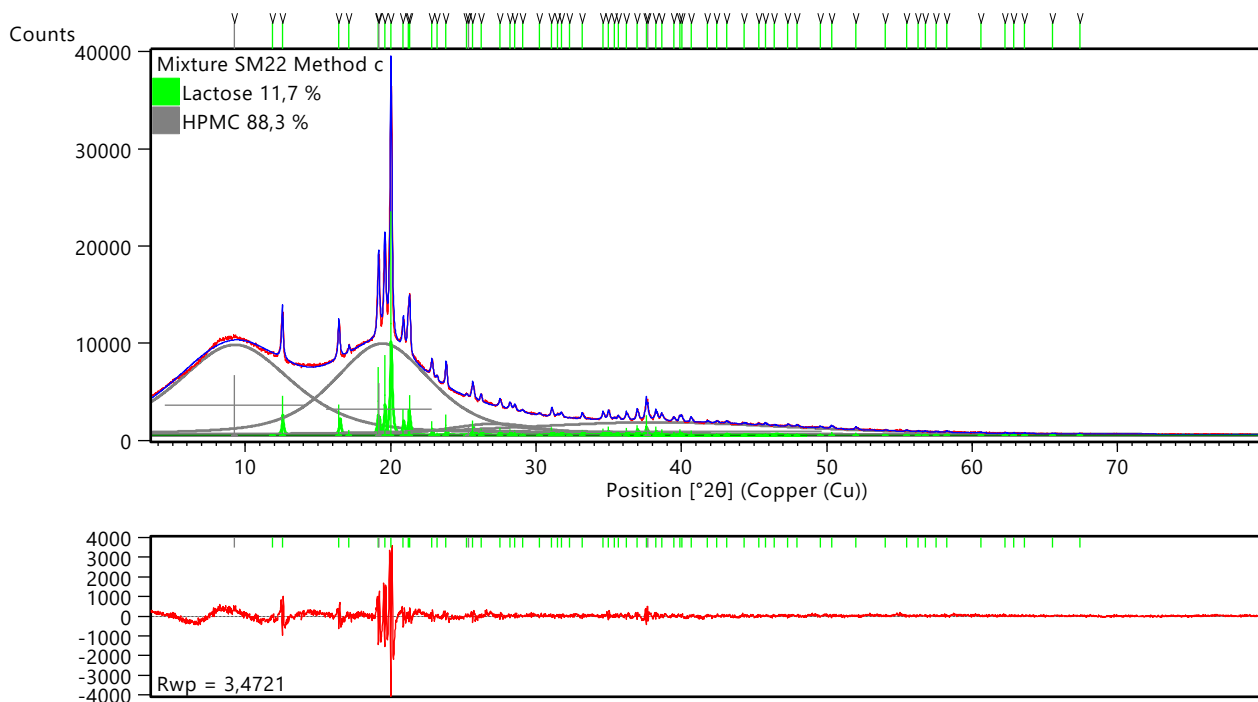


Figure 19. Refinement results for the diffraction pattern of SM<sub>22</sub> in Method c. The chi-square is 2.11. The red and blue patterns are the experimental and calculated patterns. The bottom plot shows their difference. The grey and green lines indicate the peak positions and area of HPMC and  $\alpha$ -lactose monohydrate, respectively.

- Mixture SM21 Method c

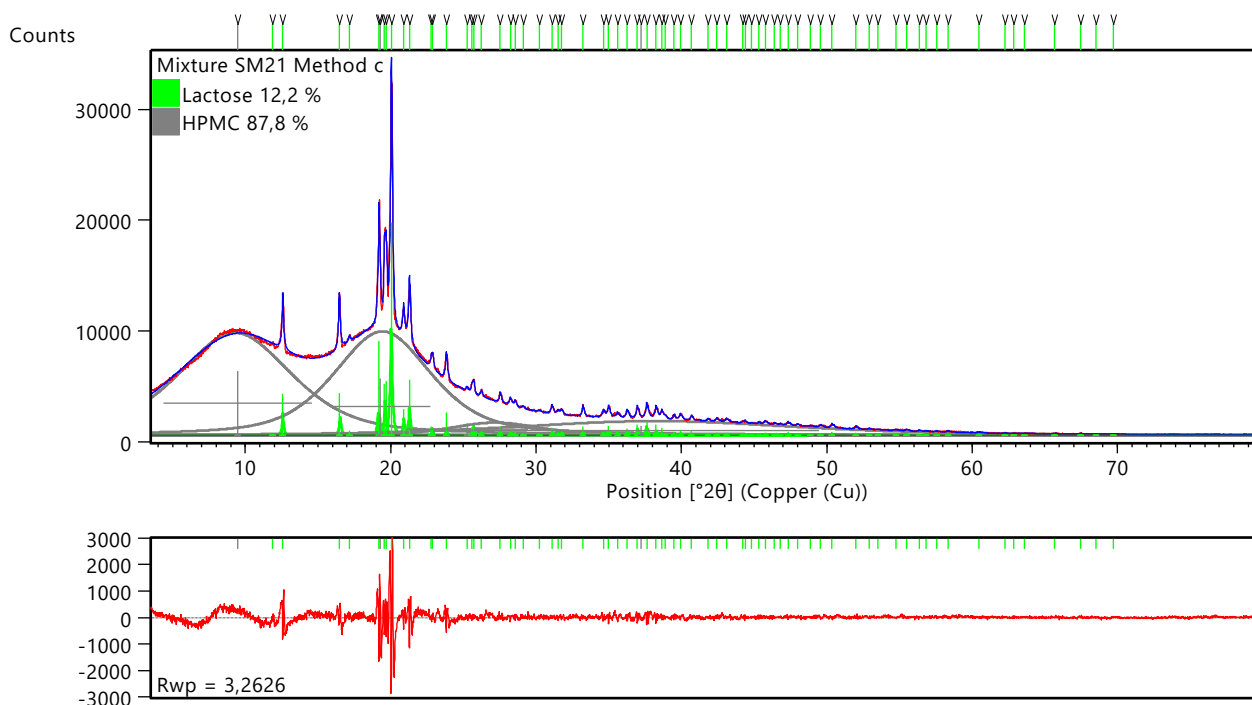


Figure 20. Refinement results for the diffraction pattern of SM<sub>21</sub> in Method c. The chi-square is 1.98. The red and blue patterns are the experimental and calculated patterns. The bottom plot shows their difference. The grey and green lines indicate the peak positions and area of HPMC and  $\alpha$ -lactose monohydrate, respectively.

- Mixture SM13 Method c

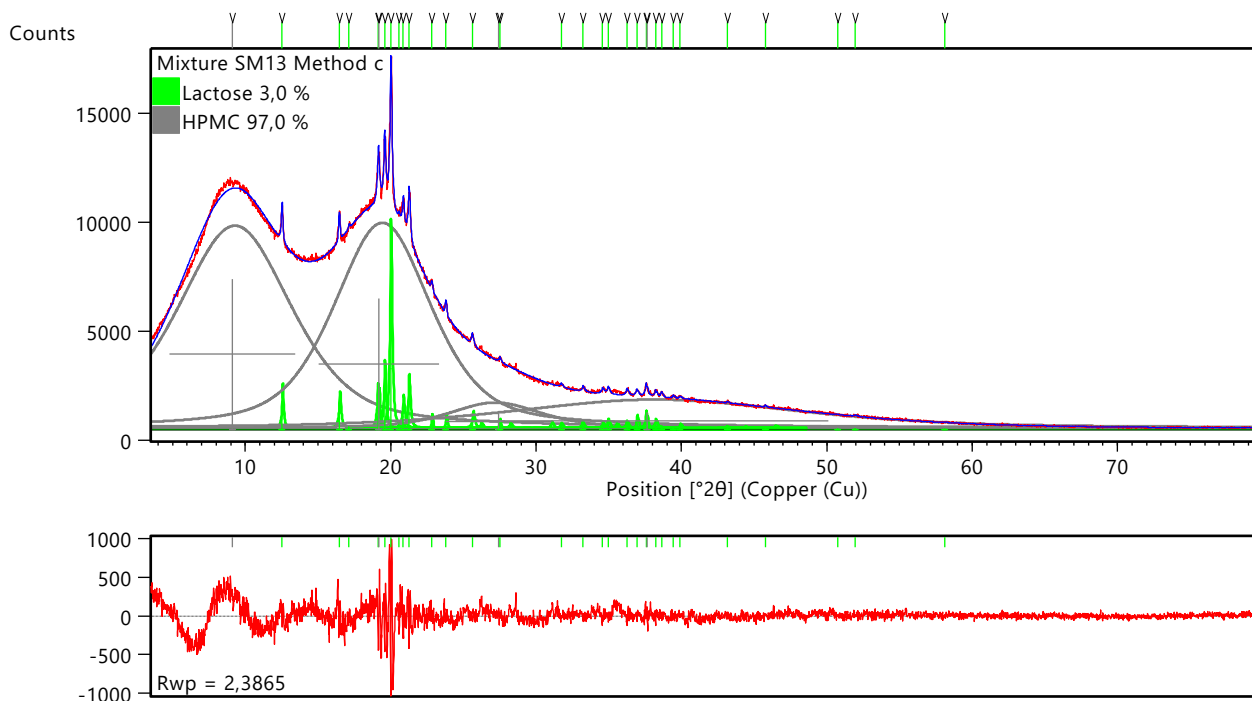


Figure 21. Refinement results for the diffraction pattern of SM<sub>13</sub> in Method c. The chi-square is 1.43. The red and blue patterns are the experimental and calculated patterns. The bottom plot shows their difference. The grey and green lines indicate the peak positions and area of HPMC and  $\alpha$ -lactose monohydrate, respectively.

- Mixture SM12 Method c

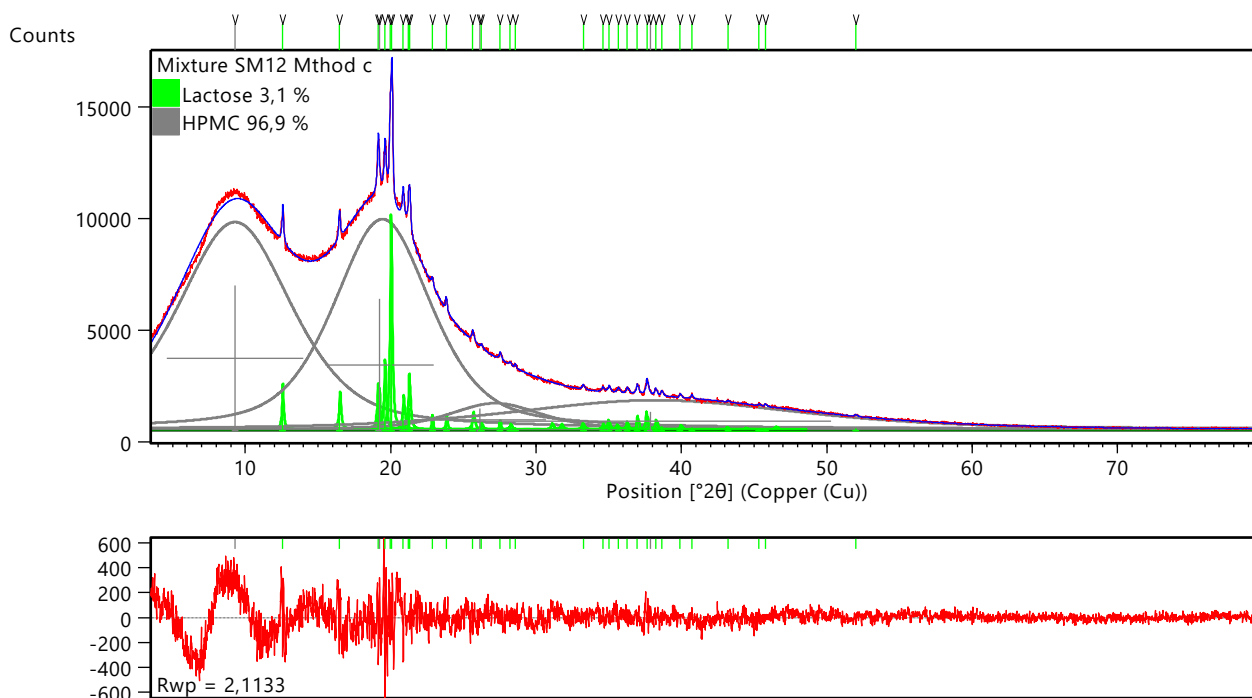


Figure 22. Refinement results for the diffraction pattern of SM<sub>12</sub> in Method c. The chi-square is 1.27. The red and blue patterns are the experimental and calculated patterns. The bottom plot shows their difference. The grey and green lines indicate the peak positions and area of HPMC and  $\alpha$ -lactose monohydrate, respectively.

- Mixture SM11 Method c

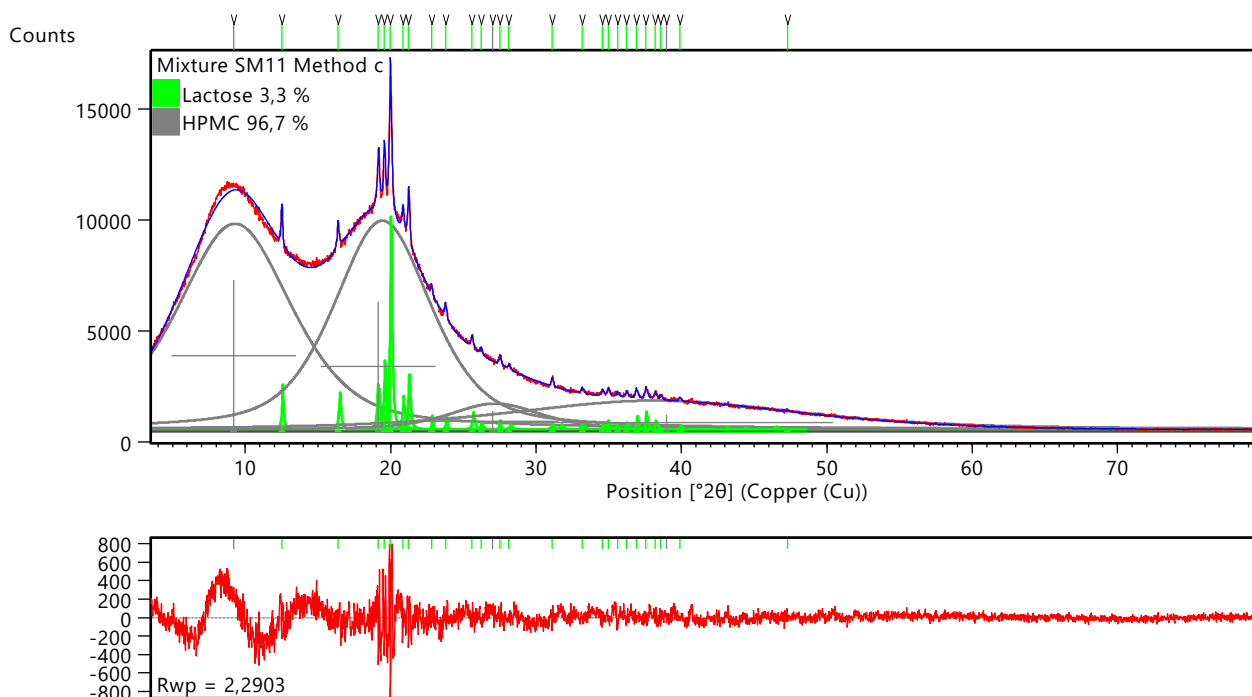
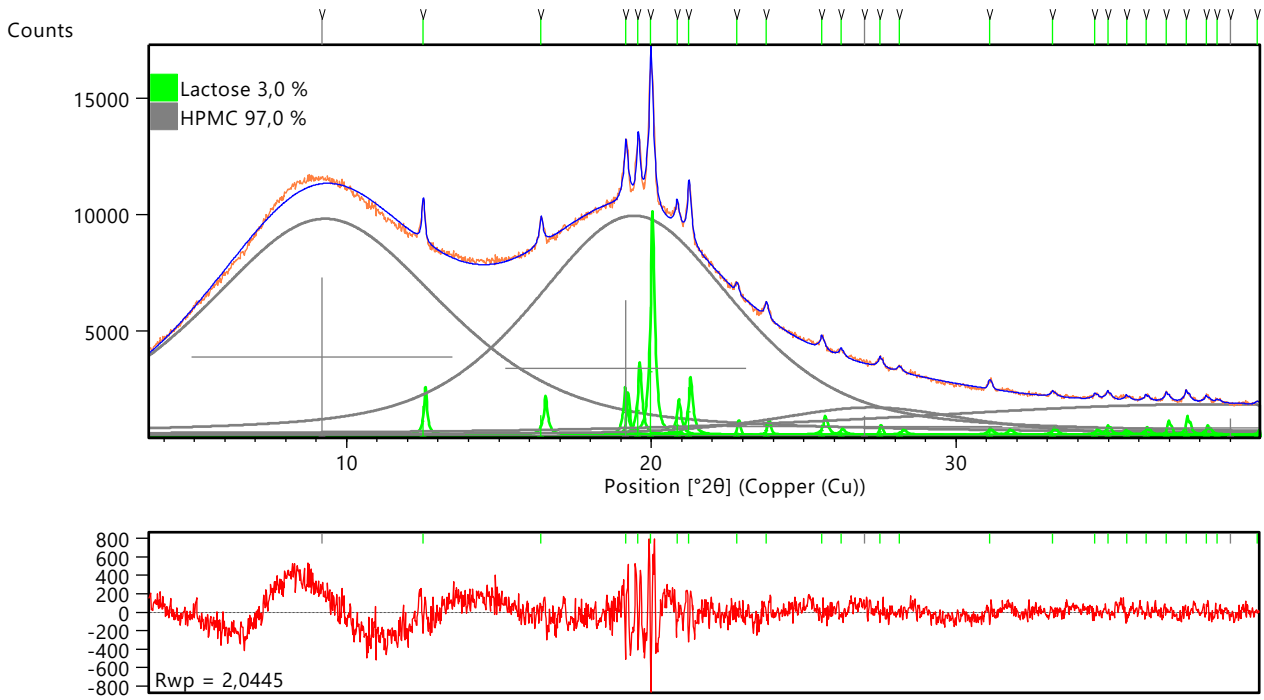


Figure 23. Refinement results for the diffraction pattern of SM<sub>11</sub> in Method c. The chi-square is 1.35. The red and blue patterns are the experimental and calculated patterns. The bottom plot shows their difference. The grey and green lines indicate the peak positions and area of HPMC and  $\alpha$ -lactose monohydrate, respectively.

- Mixture SM11 clipped at  $40^\circ 2\theta$  Method c



**Figure 24.** Refinement results for the diffraction pattern of SM<sub>11</sub> clipped at  $40^\circ 2\theta$  in Method c. The chi-square is 1.63. The red and blue patterns are the experimental and calculated patterns. The bottom plot shows their difference. The grey and green lines indicate the peak positions and area of HPMC and  $\alpha$ -lactose monohydrate, respectively.

## 7.8 Method b - Kapton

- Mixture SM23 Kapton Method b

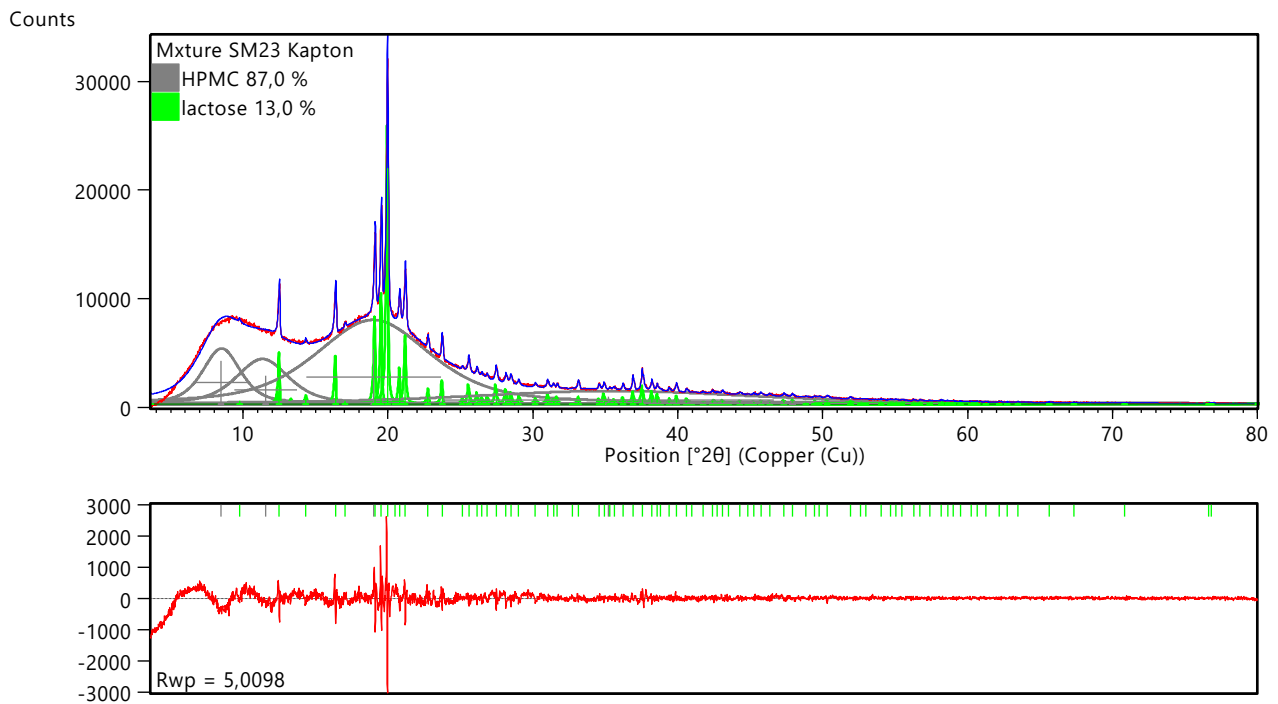


**Figure 25.** Refinement results of the diffraction pattern of the SM<sub>23</sub> mixture with the Kapton® film (method b). The chi-square is 2.17. The red and blue patterns are the experimental and calculated patterns. The bottom plot shows their difference. The grey and green lines indicate the peak positions and area of HPMC and  $\alpha$ -lactose monohydrate, respectively.

- Mixture SM22 Kapton Method b

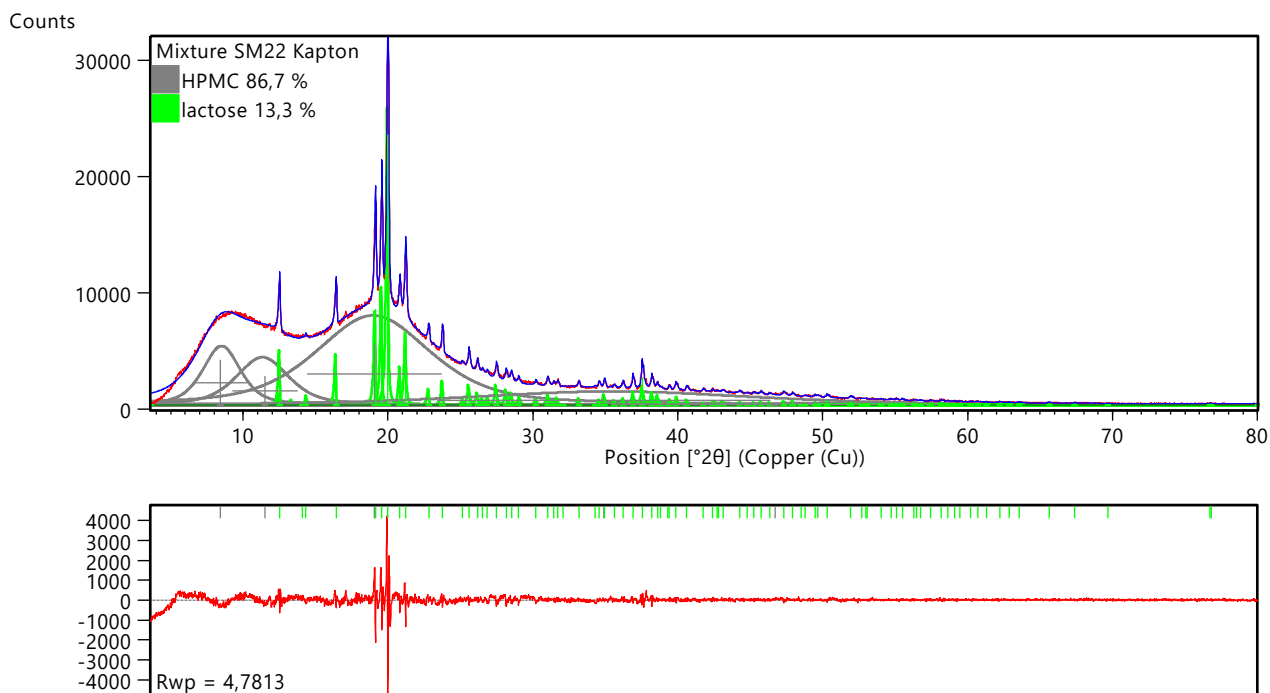


**Figure 26.** Refinement results of the diffraction pattern of the SM<sub>22</sub> mixture with the Kapton® film (method b). The chi-square is 2.18. The red and blue patterns are the experimental and calculated patterns. The bottom plot shows their difference. The grey and green lines indicate the peak positions and area of HPMC and α-lactose monohydrate, respectively.

- Mixture SM21 Kapton Method b

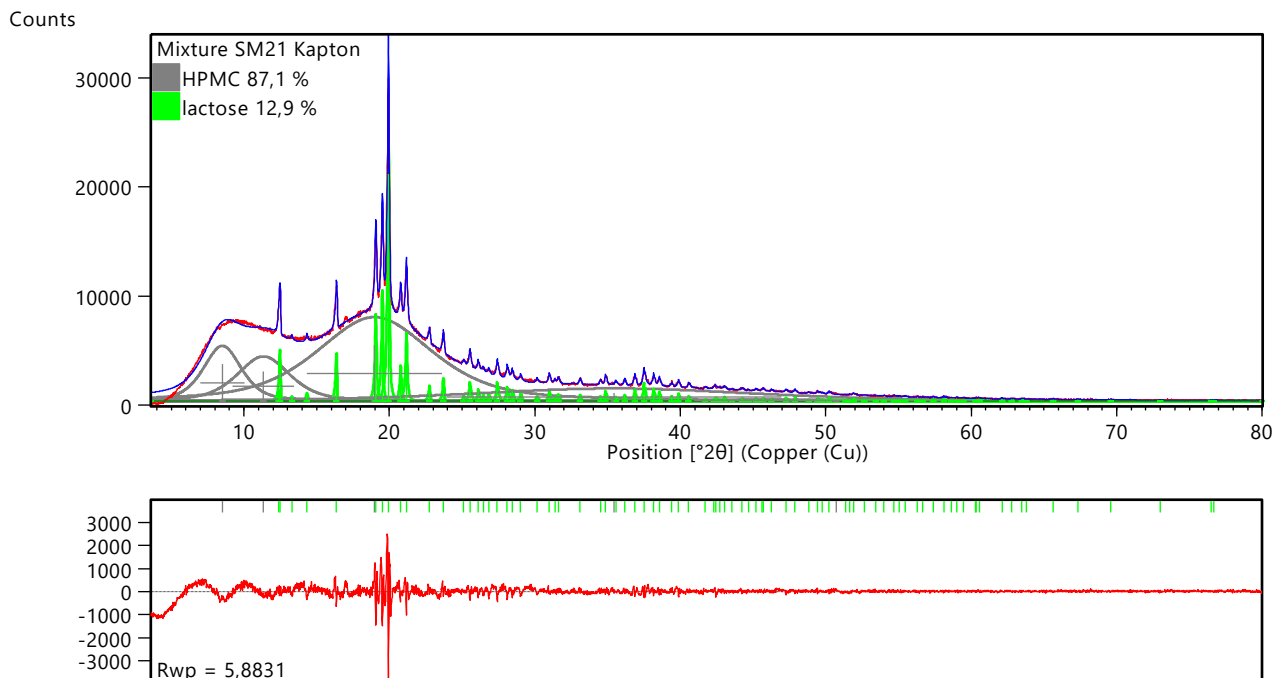


**Figure 27.** Refinement results of the diffraction pattern of the SM<sub>21</sub> mixture with the Kapton® film (method b). The chi-square is 2.59. The red and blue patterns are the experimental and calculated patterns. The bottom plot shows their difference. The grey and green lines indicate the peak positions and area of HPMC and α-lactose monohydrate, respectively.

- Mixture SM13 Kapton Method b

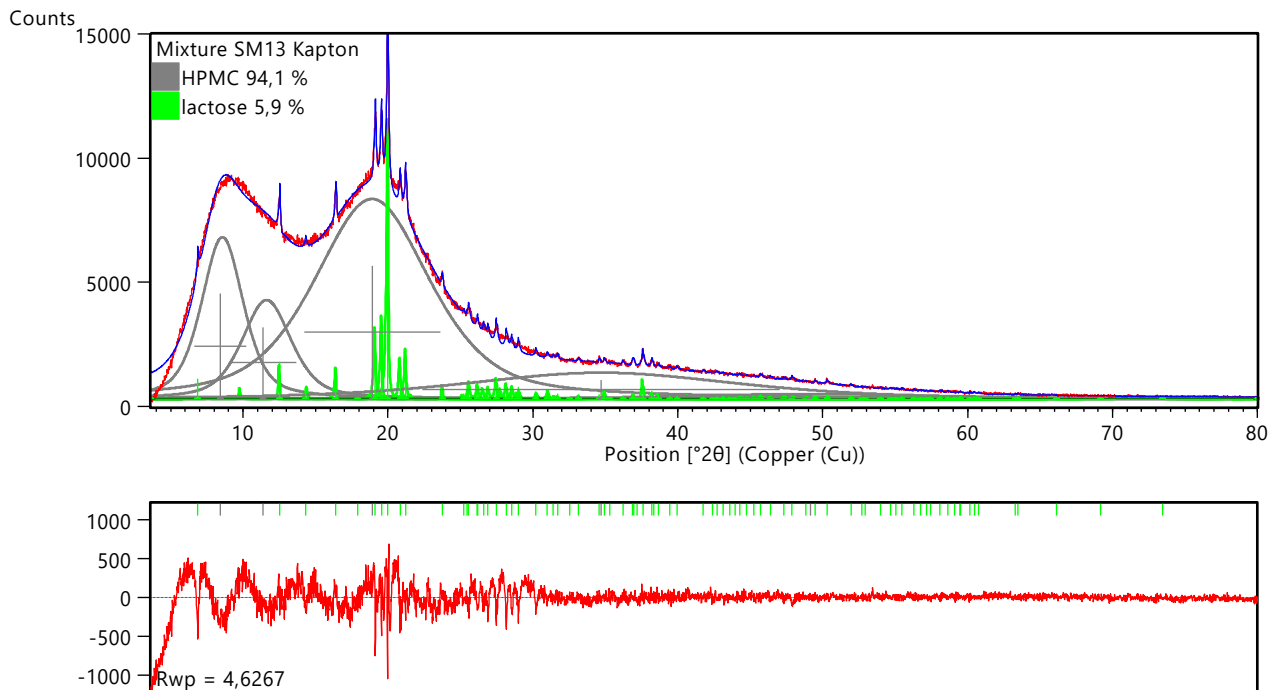


**Figure 28.** Refinement results of the diffraction pattern of the SM<sub>13</sub> mixture with the Kapton® film (method b). The chi-square is 2.01. The red and blue patterns are the experimental and calculated patterns. The bottom plot shows their difference. The grey and green lines indicate the peak positions and area of HPMC and  $\alpha$ -lactose monohydrate, respectively.

- Mixture SM12 Kapton Method b

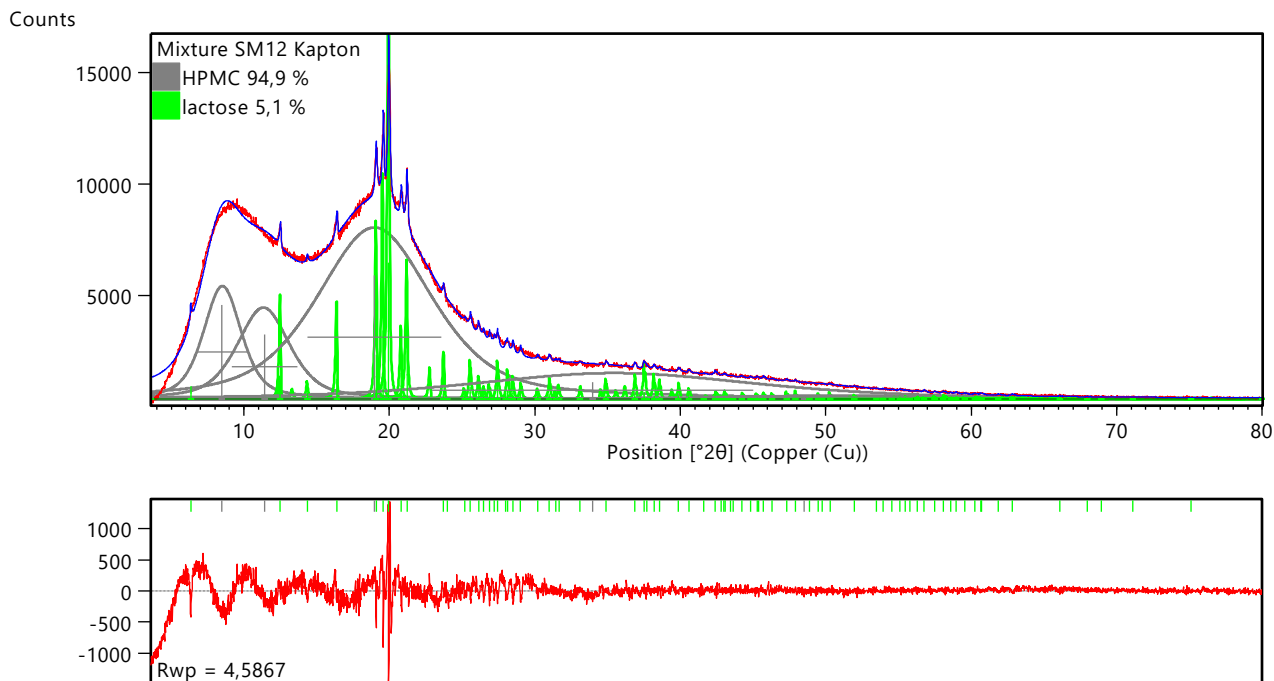


**Figure 29.** Refinement results of the diffraction pattern of the SM<sub>12</sub> mixture with the Kapton® film (method b). The chi-square is 1.97. The red and blue patterns are the experimental and calculated patterns. The bottom plot shows their difference. The grey and green lines indicate the peak positions and area of HPMC and  $\alpha$ -lactose monohydrate, respectively.

- Mixture SM11 Kapton Method b

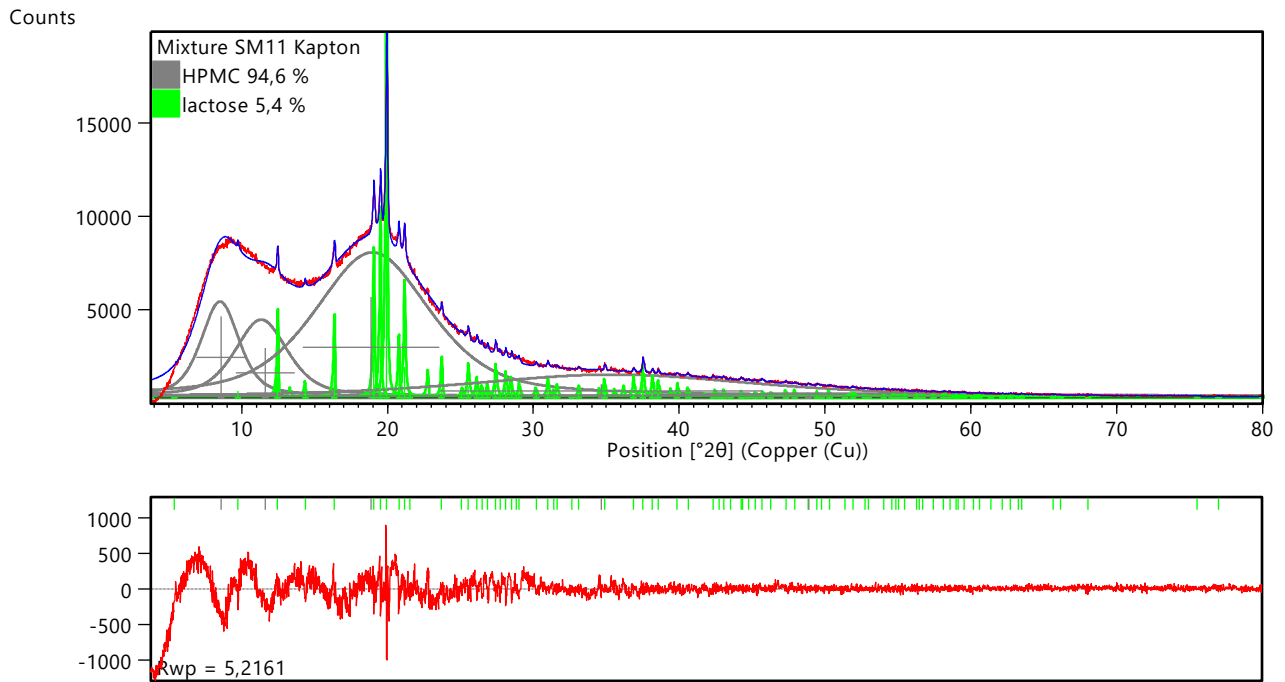


**Figure 30. Refinement results of the diffraction pattern of the SM<sub>11</sub> mixture with the Kapton® film (method b). The chi-square is 2.16. The red and blue patterns are the experimental and calculated patterns. The bottom plot shows their difference. The grey and green lines indicate the peak positions and area of HPMC and α-lactose monohydrate, respectively.**

## CHAPTER 7

### DIRECT DERIVATION OF THE CRYSTALLINE FRACTION OF FORMULATION DEPOSITED ONTO DRUG COATED BALLOON BY X-RAY POWDER DIFFRACTION

#### 1 INTRODUCTION

##### 1.1 Drug-coated balloon catheter

Cardiovascular diseases are the first cause of death globally. In 2016, 17.9 million people died from cardiovascular diseases, equivalent to 31% of all global deaths, a number that is expected to grow to more than 23.6 million by 2030.<sup>1</sup> Cardiovascular diseases include several disorders of the heart and blood vessels as such as coronary heart disease, cerebrovascular disease, peripheral arterial disease, rheumatic heart disease, congenital heart disease and deep vein thrombosis and pulmonary embolism.<sup>1</sup>

Peripheral arterial disease (PAD) is noncoronary arterial syndromes affecting the arterial beds causing alteration of structure and function of the arteries, it can process in stenosis and aneurysm of the noncoronary arterial circulation and develop in coronary artery disease and cerebrovascular disease with the risk of cardiovascular ischemic events. PAD may arise in any blood vessel, commonly it appears in legs.<sup>1,2</sup> Worldwide PAD affects 35.54% of adult population.

Coronary artery disease (CAD), also called Coronary heart disease (CHD) or ischemic heart disease, is caused by atherosclerosis which partially or, in the most severe cases, totally blocks coronary artery caused by plaque of cholesterol and other substances in the wall's arteries that supply blood to heart.<sup>3</sup> American Heart Association acknowledges that heart diseases (including Coronary Heart Disease, hypertension, and stroke) are the first cause of death in the USA. From 2006 to 2016 the annual death rate attributable to coronary heart disease declined 31.8%, however risk factors remain alarmingly high.<sup>1</sup> Risk factors of PAD and CAD are smoking, physical inactivity, nutrition, obesity, cholesterol diabetes and high blood pressure. The reduction of incidence of heart diseases is to be awarded to the prevention of risk factors and treatments as such as percutaneous transluminal angioplasty (PTA) and percutaneous coronary interventions (PCI).<sup>1</sup>

In the years, several studies and technological progresses have been done in the treatment of PAD and CAD through PCI. Coronary angioplasty was introduced by Grüntzig in 1977, who is considered the father of the percutaneous transluminal coronary angioplasty (PTCA). PTCA is a nonsurgical method for arterial revascularization based on dilatation of stenotic artery by inflation of balloon catheter system introduced by systematic artery under local anaesthesia.<sup>4,5</sup> PTCA had showed some shortcomings abrupt vessel occlusion, dissection and restenosis.<sup>6</sup> Restenosis is inflammation response to injury that causes elastic recoil, mural thrombosis formation, neointimal proliferation and chronic arterial changes.<sup>7</sup> In 1986 the first patients affected by restenosis after PTCA were treated by implantation of bare metal stents (BMS), hollow cylinders metal stretched opened by inflating of balloon catheter. Comparing to the PTCA, BMS had showed better long-term success (85-90%). Although the most common cause of failure of treatment with BMS is local inflammation and successively restenosis (20-25%). Additionally, other drawbacks of BMS were the difficulties to place it at correct side in tortuous vessel and possible mechanical stent deformity and strut fractures. In 2001 the BMS evolves into drug eluting stent (DES), it was developed to overcome the problem of restenosis encountered with BMS.<sup>8</sup> DES is metal scaffolding device coated with single or multiple bioactive ingredients. The localized and controlled release of drug has numerous advantages as such as the delivery in the precise site of the lesion, achievement of high local tissue concentration of active agents and minimal systematic concentration with constrained systematic side effects and toxicity.<sup>9</sup> DES improved the long-term success below 90% and decreased the insurgence of in-stent restenosis at 7-15%.<sup>10</sup> Different therapeutic drug mechanism of action against restenosis process has been picked out: immunosuppressive, antiproliferative, anti-inflammatory and antithrombotic. The drugs deposited onto DES should have the specific characteristics: wide therapeutic window, both local and systematic safe profile and it should reach the therapeutic concentration. Literature reports several active pharmaceutical ingredients that can be used in DES: rapamycin (sirolimus), paclitaxel, tacrolimus, everolimus, zotarolimus, biolimus, dexamethasone, tranilast, batimastat, mycophenolic acid,

actinomycin D, estrogen, cyclosporin, angiopeptin, C-myc antisense and nitric oxide.<sup>7,9</sup> The adhesion onto metallic stent surface was an obstacle for most drugs, which needed a biocompatible polymeric coating as carrier. Nevertheless, the permanent device implantation and the polymeric coating can induce foreign body reaction, inflammation and thrombosis.<sup>10–12</sup> Furthermore the rigid structure of the stent did not allowed the implantation in particularly location as such as small vessel and vessel bifurcations and sometimes in the margins of the device it was observed an incomplete suppression of neointimal hyperplasia.<sup>13,14</sup> Stent increases rigidity of the vessel affecting its compliance and it is not suitable for small vessel because it has reduced already narrowed lumen with its physical footprint. Moreover, the presence of stent may be problematic in case of necessity of subsequent surgeries.<sup>15</sup> These drawbacks have been overcome by the latest developed technique: the drug coated balloon (DCB). Drug coated balloon combines two therapeutic effects: mechanic action, due to the dilation of the balloon, and pharmacological bioactivity due to the release of drugs triggered by the inflation of the balloon. The first multicenter clinical trial of this new technology dates back to 2003 of PACCOATH-ISR, which has taken out the several advantages of DCB.<sup>16</sup> In fact, the DCB does not require the implantation of stent eliminating the inflammatory response due to the permanent foreign scaffold in the vessel and DCB is placeable in location not reachable by DES, for instance in small and tortuous vessel and vessel bifurcation. Nowadays, DCB is the treatment of choice of in-stent restenosis, in de novo coronary diseases in challenging side for DES.<sup>10,17</sup> Moreover, DCB is indicated for the treatment of peripheral artery disease, even de novo femoropopliteal and below to knee disease and it can be a valid alternative for the treatment of de novo coronary diseases.<sup>13,18–21</sup> DCB releases therapeutic dose of active agents directly in the target with brief time of exposure and high drug surface area present to wall vessel.<sup>16,22</sup> Indeed, the recommended time of inflection is not higher than 60 seconds. Even with this short time of contact between vascular muscle cells and lipophilic agents, DCB achieves inhibition of proliferation of such cells for long period thank to the drug retention by tissue for prolonged time.<sup>6,23</sup> Among the many advantages of DCB there is also the short-term of dual antiplatelet therapy of few months following DCB treatment, while after DES implantation dual antiplatelet therapy is recommended for 6 to 12 months.<sup>18,24,25</sup> The first line drug for DCB has been the anti-proliferative taxane paclitaxel, though DCB coated with other drugs have been emerging, as such as zotarolimus, sirolimus, everolimus, biolimus A9, dexamethasone, tranilast and nuclear factor-kappa B oligodeoxynucleotides.<sup>26–30</sup> In DCB the release of the drug is not controlled, but the transfer of the active agent in the tissue is influenced by the coating characteristic. Hence the active ingredient, the excipients and the manufacturing process is extremely important and impactful for the drug release and the success of the therapy<sup>22</sup>. The excipients must be compatible with the active ingredients, able to generate a homogeneous coating, enhance the adherence of the drug during the handling and the release of the drug to the vessel upon balloon dilatation.<sup>23</sup> Scheller et al. estimate paclitaxel DCB loses 6% of the dose during the transit and about 80% of the drug is released during inflation.<sup>14</sup> Additionally, Afari & Granada pointed the impact of coating crystallinity out.<sup>22</sup> For paclitaxel DCB, they observed that amorphous coating has better uniformity and less particulate formulation but steeper decrease of tissue levels and lower long term tissue retention than crystalline coatings which, instead, reach higher tissue level and biological efficacy.<sup>22</sup> These studies highlight the importance of the study of the polymorphism and crystallinity degree of the formulation to achieve efficacy product, consequently it requests a control of the manufacturing process.

## 1.2 Drug polymorphism

As pointed out by Afari & Granada the polymorphism and the crystallinity degree of the drug coated onto the balloon catheter impact the tissue transfer and consequently affect the efficacy of the therapy.<sup>22</sup> Hence, the control of the manufacturing process from which depends the final characteristic of the formulation, is extremely important.

Polymorphism refers to the ability of a certain compound to exist in different crystallographic structures, resulting from different packing arrangements of its molecules in the crystal structure. While the term polymorphism is restricted to compound with have the same chemical formula in pharmaceutical industries the attention is focused also in the presence of hydrates and solvates which are regulated in the same way.<sup>31–33</sup> Crystal forms are of particular importance in the pharmaceutical industry, as many APIs receive regulatory approval only for a single crystal form or polymorph. Furthermore, polymorphism in drugs can affect such physicochemical properties as dissolution rate, solubility, bioavailability and manufacturability.<sup>34</sup>

In this study we evaluated the crystal forms and crystallinity degree of the formulation coated onto a balloon catheter. This work was conducted in collaboration with the manufacturing company of the device. For business and conflict of interest the manufacturing company, the device commercial name, the active ingredient and the formulation ingredients cannot be revealed. For this reason, the references consulted will not be cited.

The API is a huge molecule with molecular mass higher than 800 u.m.a.. Studies associate the formation of particular crystallinity grade of API with the polarity of the solvent used in the evaporation process. Especially, higher polarity index and lower viscosity of organic solvents achieve API with higher crystallinity degree, whereas amorphous API is obtained using non-polar solvents with polarity index lower than 4.00.

The Cambridge Structure Database (CSD) reports six structures of the API, of which five are solvates and one is anhydrous. Table 1 and Figure 1 report the structure information and the XRPD patterns comparison. The structure coordinates and the calculated XRPD pattern of Form 6 are not available.

**Table 1. API structures reported in the Cambridge Structure Database (CSD)**

	Solvent	Space group	Cell length (Å)	Cell angle (°)	Cell volume (Å <sup>3</sup> )
<b>Form 1</b>	N-methyl-2-pyrrolidone acetonitrile solvate trihydrate	P 2 <sub>1</sub> 2 <sub>1</sub> 2 <sub>1</sub> Orthorhombic	a 9.541(1) b 28.456(4) c 37.238(5)	α 90 β 90 γ 90	10110.1
<b>Form 2</b>	dimethylformamide solvate monohydrate	P 2 <sub>1</sub> 2 <sub>1</sub> 2 <sub>1</sub> Orthorhombic	a 9.512(1) b 27.787(4) c 34.788(5)	α 90 β 90 γ 90	9194.81
<b>Form 3</b>	dihydrate	P 2 <sub>1</sub> 2 <sub>1</sub> 2 <sub>1</sub> Orthorhombic	a 9.512(1) b 28.064(6) c 33.08(2)	α 90 β 90 γ 90	8830.53
<b>Form 4</b>	hemihydrate	P 2 <sub>1</sub> 2 <sub>1</sub> 2 <sub>1</sub> Orthorhombic	a 9.68905(17) b 28.0760(4) c 33.6166(8)	α 90 β 90 γ 90	9144.72
<b>Form 5</b>	anhydrous	P 2 <sub>1</sub> 2 <sub>1</sub> 2 <sub>1</sub> Orthorhombic	a 9.6530(3) b 28.1196(8) c 33.5378(14)	α 90 β 90 γ 90	9103.45
<b>Form 6</b>	dioxane solvate hydrate	P 2 <sub>1</sub> Monoclinic	a 9.661(1) b 28.275(3) c 19.839(2)	α 90 β 99.730(4) γ 90	5341.36

Hydrate and the anhydrous forms show very similar XRPD patterns, in fact the crystalline structure of the forms is resembling. The core of the molecule maintains basic conformation in all the hydrated and anhydrous forms and the packing is almost unchanged between the forms. Nevertheless, hydrated and anhydrous forms show some difference in intermolecular hydrogen bonding network, which is affected by the presence of water in the system. In the anhydrous form the two API molecules in the asymmetric unit are connected by one hydrogen bond. While the hydrated forms showed the same hydrogen bonding network with two more intermolecular bonds between the API molecules, the water molecules are not directly involved in the hydrogen bonds. This different interaction between the molecules affect the physical properties, especially the solubility. In fact, the literature reports major solubility in water for the anhydrous form.

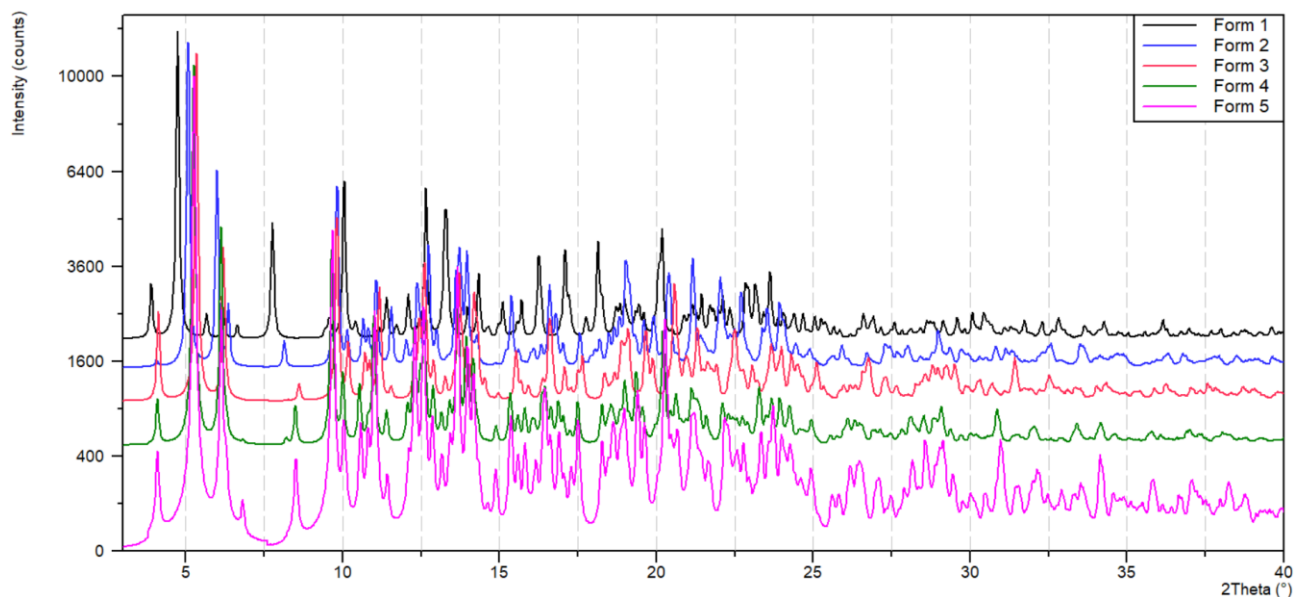
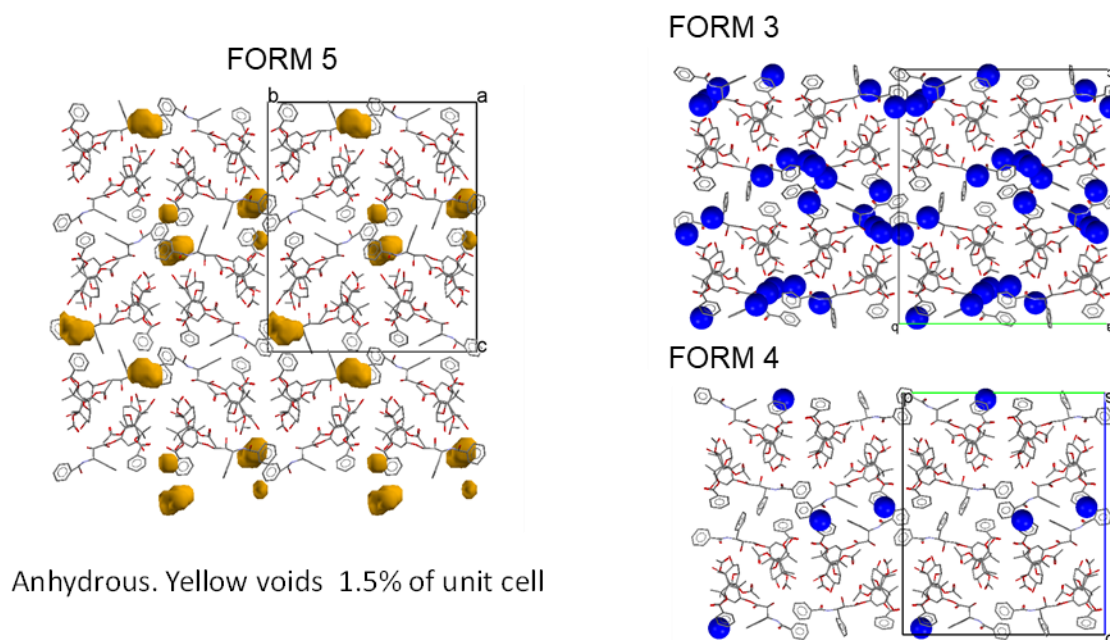


Figure 1 XRPD comparison of the calculated patterns of API by the CSD

Figure 2 shows the crystal structures of the hydrated forms and anhydrous form. The blue spots represent the water molecule in the structure. Hemihydrate Form 4 and dihydrate Form 3 share the position of one water molecule. The yellow spots in anhydrous Form 5 represent the void in the structure, which amounts to 1.5% of unit cell. In conclusion the API structures are characterized by cavities between the drug molecules which are filled up by solvent without substantial changing in packing arrangement. This behaviour is typical of non-stoichiometric hydrates, whose structure can allocate a variable number of water molecules with only small structural change. The absolute determination of the amount of solvent can be challenging also in the single crystal structure because usually their position is highly disordered into the cavities between the API molecules. Figure 3 reports the structure representation of N-methyl-2-pyrrolidone acetonitrile solvate trihydrate (Form 1) dimethylformamide solvate monohydrate (Form 2), dihydrate form (Form 3) and hemihydrate form (Form 4). The structures are isostructural: the molecules are almost in the same positions. Moreover, the cell parameters of all the structures are very similar as reported in Table 1, it suggests the capability of the API to incorporate different solvent molecules in the structures without significant structure changes. Additionally, the literature points out the similarity between the unit cell parameters of dihydrate Form 3 and dioxane hydrate Form 6 (structure coordinates not available).

Solvate solids are common in pharmaceutical compounds, especially hydrates, it is estimated one third of pharmaceutical active ingredients can arrange in hydrated crystalline. Based on their structure, hydrates can be classified in three different classes. Class 1 is constituted by isolated hydrates in which water molecules interact exclusively with drug molecule without interaction between other molecule of water. Contrarily, in class 2 category water molecules are contiguous into channels through crystalline structure. Hydrates included in class 3 contain metal ion coordinated with water molecules. Class 2 hydrates can be differentiated in stoichiometric and non-stoichiometric.<sup>33</sup> Stoichiometric hydrates have peculiar crystal structure clearly distinct from other phases and they have a definite content of water at defined relative humidity. Contrarily, non-stoichiometric solvates has not a well-defined content of solvent but they have continuously variable composition and their crystal structure is stable in a wide range of solvent content.<sup>35,36</sup> Especially non-stoichiometric behaviour is observed in large and rugged shaped molecules that cannot pack closely and present voids and channels in the structure in which the solvent molecules can locate. In literature is commonly reported example of non-stoichiometric hydrates, e.g. rifaximin<sup>37,38</sup>, moreover the structure can host not exclusively water molecules but also different solvents. The amount of solvent's molecules in the structure depends on several factors as such as the partial pressure of the solvent in the environment, the temperature, and relative humidity.<sup>39</sup> The peculiarity of non-stoichiometric compounds is the absence of significant changes in the crystal structure in response to variation in solvent content, except for some anisotropic distortion due to accommodation or loss of solvent molecules. Hence, the structure is retained with different solvent content, and the alteration of solvent content has a moderate effect on the cell axes dimensions and therefore on the

position of the diffraction peaks. Non-stoichiometric compounds with different solvent content usually show some small difference in X-Ray diffraction patterns, as such as variation of intensity of specific peaks and shifts in the peak position.<sup>37</sup> Additionally, the presence of water and solvent molecules within the lattice impacts solubility, dissolution rate, stability, and bioavailability of pharmaceutical compounds due to the packing arrangement and the intermolecular interactions in a crystal structure.<sup>40</sup> In the crystal structure of stoichiometric solvates, the solvent has stabilizing role of the crystal packing. When no clear hydrogen bonding is present in the crystal, the molecules are weakly bound and appear to be disordered, as such the compound shows a non-stoichiometric behaviour. In non-stoichiometric solvates the free water can interact with other components, compromising the stability and performance of formulated products.<sup>36</sup> Additionally, the loss of solvent lets voids in crystal structure that can reduce chemical or physical stability, besides the original solvent to minimize the void space the compound can take up other solvents.<sup>41</sup>



**Figure 2 Structure of anhydrous form (Form 5), dihydrate form (Form 3) and hemihydrate form (Form 4)**

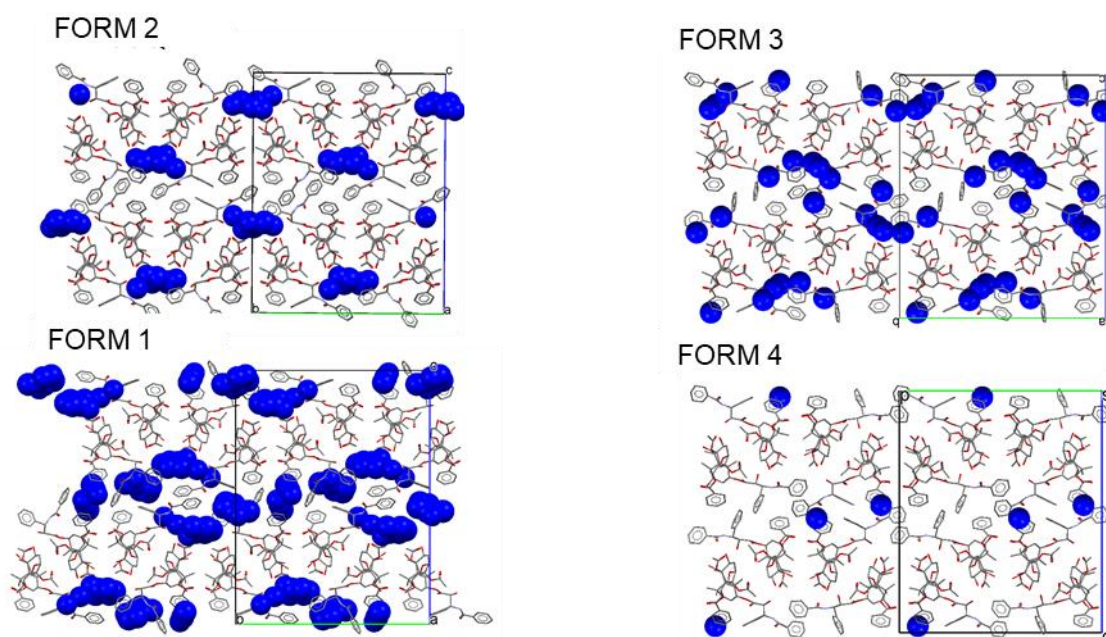


**Figure 3 Structure of N-methyl-2-pyrrolidone acetonitrile solvate trihydrate (Form 1) dimethylformamide solvate monohydrate (Form 2), dihydrate form (Form 3) and hemihydrate form (Form 4)**

## 2 AIM

The aim of this work is the quantification of the crystallinity degree by X-Ray powder Diffraction of formulation coated on Drug Coated Balloon. For business and conflict of interest the active ingredient and excipients of the formulation cannot be revealed. The manufacturing company is concerned to determine the crystallinity degree of its formulation since studies have revealed more bioactivity and efficacy than the competitor's products attributed to differences in grade of crystallinity of the various formulations.

DCB is a complex sample that present several difficulties. First, it is a formulation including excipients that contribute to sample signal. DCB devices are very expensive, each DCB carries tiny amount of powder, therefore available quantity of sample is exiguous for the collection. Hence, the use of internal standard is not possible because weight and mixture errors in such small amount of powder can remarkably affect the quantification. Moreover, suitable amounts of crystalline and amorphous API references are not available wherefore the preparation of set of standard mixtures and construction of calibration curve is not feasible. Additionally, it is important to point out the difference between the mixtures of standard references and the real formulation which undergoes a production process. Indeed, the manufacturing process impacts on several features as such as morphology, particle size, content of solvent and crystallinity degree, important elements in solid-state quantitative analysis which make the standard mixtures not representative of the DCB formulation samples. Furthermore, the API is classified as highly potent due to its activity and its side effects. Hence, it is necessary to enclosure the powder for environment and operator safety with system as Kapton® film or sealed glass capillary. Both Kapton® and glass capillary give amorphous contribution, which is necessary to consider in the quantitative analysis and elaboration of the data.

Thereby the impossibility to use an internal standard, the low amount of sample and the lack of reference standards exclude the quantification by many of common amorphous-crystalline quantitative methods, as such as univariate and multivariate methods, RIR and Rietveld. Three methods were pinpointed as suitable for the quantification of this project: Direct Derivation Quant Method (DDQM), US Pharmacopeia (USP) method and Autoscale.

Autoscale method is very simple method that scale the patterns of references with the sample. It is evaluated for its simplicity and execution speed, despite the pattern of DCB sample and references are not perfectly superimposable.

USP method is semi-quantitative and comparative method reported in the Unit State Pharmacopeia. USP recommends this method for crystallinity degree quantification of compound with the same elementary composition. Nevertheless, USP method is evaluated for DCB formulation because API and excipient have similar mass absorption coefficient (MAC).

DDQM is a new quantitative method, it is similar but more sophisticated than USP method. It is based on the Intensity-composition (IC) equation which takes in consideration the chemical formula and consequently the electronic density and mass absorption coefficient of the phases in the mixture. Additionally, the references' patterns can be described by the cell parameters.

Accuracy and precision of quantitative method could not be evaluated due to impossibility of construction of calibration curve with DCB samples. Therefore, the three described methods are applied on standard mixtures of  $\alpha$ -lactose monohydrate (crystalline part) and HPMC (amorphous part). The standards are prepared to simulate the DBC in crystallinity fraction and measurement conditions (i.e., small amount of material and amorphous signal due to the sample holder), which allowed us to define the best way to describe the background signal (capillary or Kapton®) for each method and finally to choose the more appropriate method for the determination of crystallinity in the real case.

### 3 EXPERIMENTAL PROCEDURE

#### 3.1 Lactose – HPMC

##### 3.1.1 Material

$\alpha$ -lactose monohydrate ( $C_{12}H_{24}O_{12}$ ) and hydroxypropyl methylcellulose (HPMC) were chosen as respectively crystalline and amorphous standards because they are stable organic compounds regularly used as excipients in the pharmaceutical industry.

$\alpha$ -lactose monohydrate (purity  $\geq 99\%$ ) was from Sigma-Aldrich (Saint Louis, MO, USA). Hydroxypropyl methylcellulose was acquire from Acros Organics (Geel, Belgium).

##### 3.1.2 Sample preparation and Data collection

Three mixtures containing  $\alpha$ -lactose monohydrate and HPMC were prepared with content percentage of  $\alpha$ -lactose monohydrate equal to 25%w/w, 50% w/w and 75%w/w by accurately weighting with micro-analytical Balance Mettler Toledo XPE26DR (6 decimal figures, Table 2). The standard mixtures have been blended in an agata mortar following the method of the geometric additions to reach homogeneous mixture. The mainly issue of the preparation of solid-state sample is the achievement of homogeneous mixtures, indeed different density, particle size and morphology of the powders impact the mixing and the inhomogeneity of the powdered standards may deeply affect the outcome of the quantitative method. To minimize the error due to the sampling, the mixtures have been prepared in small amount 50 mg and all the powder was measured at once.

The standard mixtures and the pure reference standards of  $\alpha$ -lactose monohydrate and HPMC, relevant respectively of 100% and 0% of crystalline content, have been analysed by X-Ray diffraction in transmission mode in Hilgenberg borosilicate glass 3.3 capillary diameter 0.5 mm and wall thickness = 0.01 mm. The patterns were collected on Panalytical X'Pert Pro equipped with a focusing Mirror and a Pixcel detector in the range  $3-60^\circ 2\theta$ . The samples have been analyzed in the same point six time, 30 minutes for single analysis. The diffraction pattern of empty capillary has been collected in the same condition. The mean of the six data has been calculated by HighScore software to improve the signal to noise ratio of the measurements.

**Table 2 Standard mixture of  $\alpha$  lactose monohydrate and HPMC**

	STD 25% w/w	STD 50% w/w	STD 75% w/w
<b>HPMC (mg)</b>	37.614 mg	25.412 mg	12.602 mg
<b>Monohydrate <math>\alpha</math> lactose (mg)</b>	12.642 mg	25.848 mg	37.696 mg
<b>% crystalline <math>\alpha</math> lactose</b>	<b>25% w/w</b>	<b>50% w/w</b>	<b>75% w/w</b>

##### 3.1.3 Crystallinity determination: USP Method

The crystallinity degree of  $\alpha$ -lactose monohydrate reference (100% crystalline) and standard mixtures was calculated using the USP method.

The USP method require the determination of three areas: A due to the crystalline sample, B due the scattering of the amorphous powder and C is the background, due to the air scattering, sample holder etc.

The C area was described by the pattern of the empty capillary. The amorphous was determined by the function "determine background" in Highscore Plus while the crystalline contribution is represented by the area of sharp peaks (area A). Hence, the three areas (A, B and C) were determined as following:

- A XRPD pattern of samples
- B background calculated using HighScore
  - Granularity 5
  - Bending 0
  - Use smoothed input data
- C empty capillary pattern

The intensity of the samples, the background lines and the capillary measure were elaborated using Excel software calculating the three areas and the crystalline percentage. Table 3 and Figure 4, Figure 5, Figure 6 and Figure 7 report the results obtaining with USP method. The crystalline lactose reference considered as 100% crystalline showed a crystallinity degree of 66%. To reach the actual crystalline percentage (100%) a correction factor of 1.51 was applied. The same value of correction factor was applied to the % crystalline of all the standard mixtures (see Table 3). It was observed general underestimation of the corrected % crystalline of the standard mixtures with negative absolute error of 4% for all the standards. Recovery % values were satisfactory, well as for the 25%w/w standard, which showed the lowest recovery % of 85%, even so in the acceptable range 80-120%. However, it is important to point out that the USP method is a comparative method.

**Table 3  $\alpha$ -Lactose-HPMC: USP method results**

Actual % crystalline	Back calculated % crystalline	Recovery%	Correction factor	% crystalline corrected	Recovery%
100	66	66%	1.51	100	100%
75	47	62%		71	94%
50	31	61%		46	92%
25	14	56%		21	85%

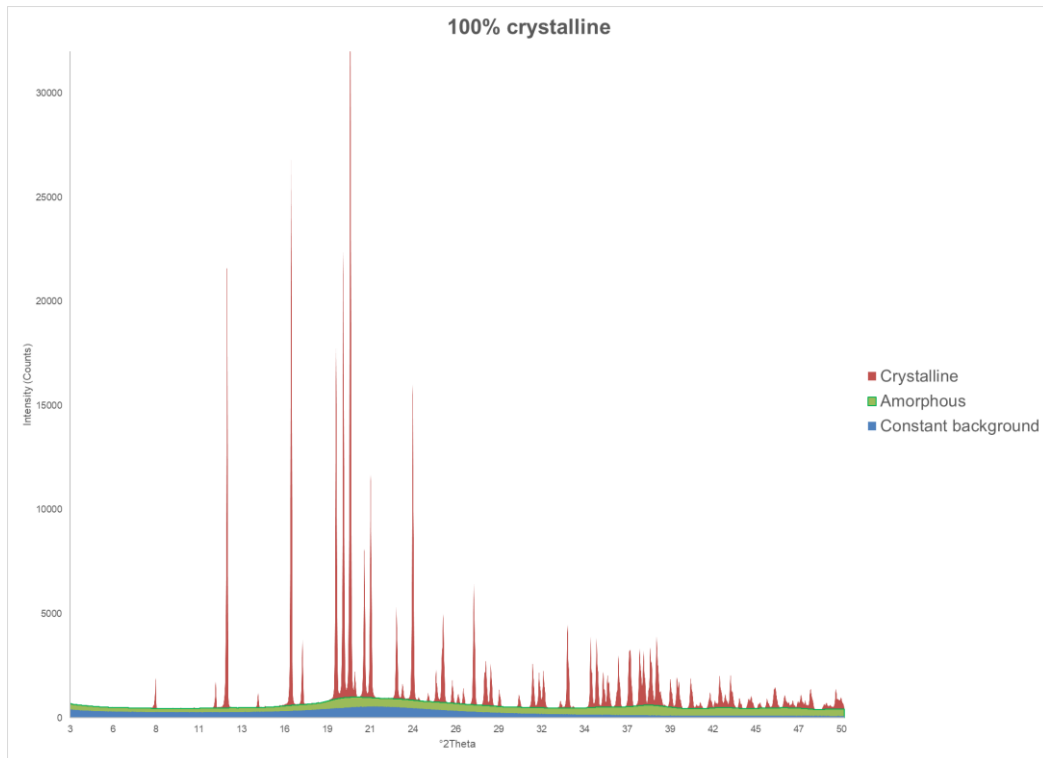


**Figure 4 USP method results of  $\alpha$  lactose monohydrate (100% crystalline) with blank capillary as constant background (blue area). The red and green area represent respectively the crystalline and amorphous area.**

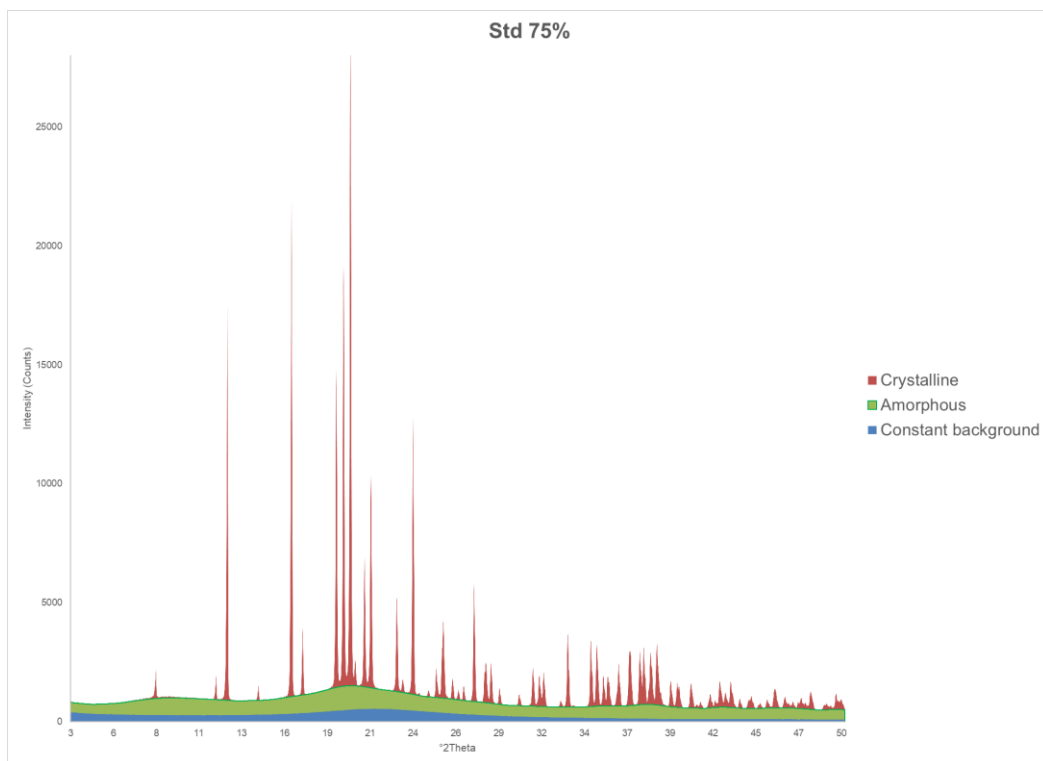


**Figure 5 USP method results of Std 75% w/w of  $\alpha$  lactose monohydrate with blank capillary as constant background (blue area). The red and green area represent respectively the crystalline and amorphous area.**

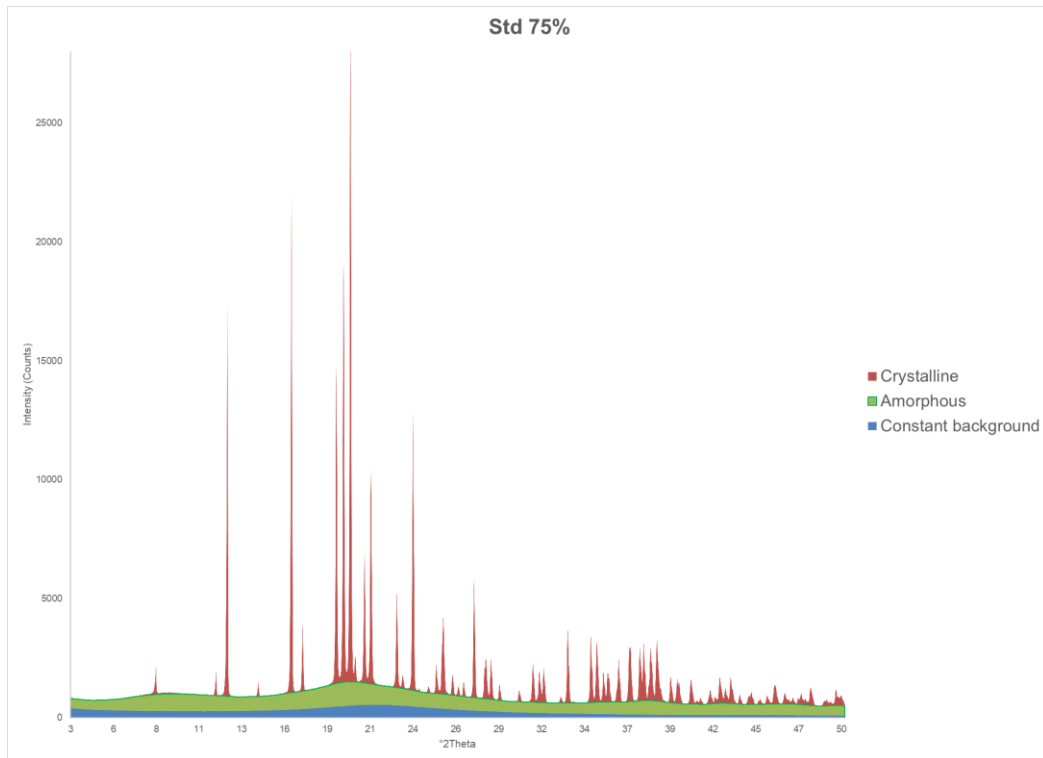


Figure 6 USP method results of Std 50% w/w of  $\alpha$  lactose monohydrate with blank capillary as constant background (blue area). The red and green area represent respectively the crystalline and amorphous area.

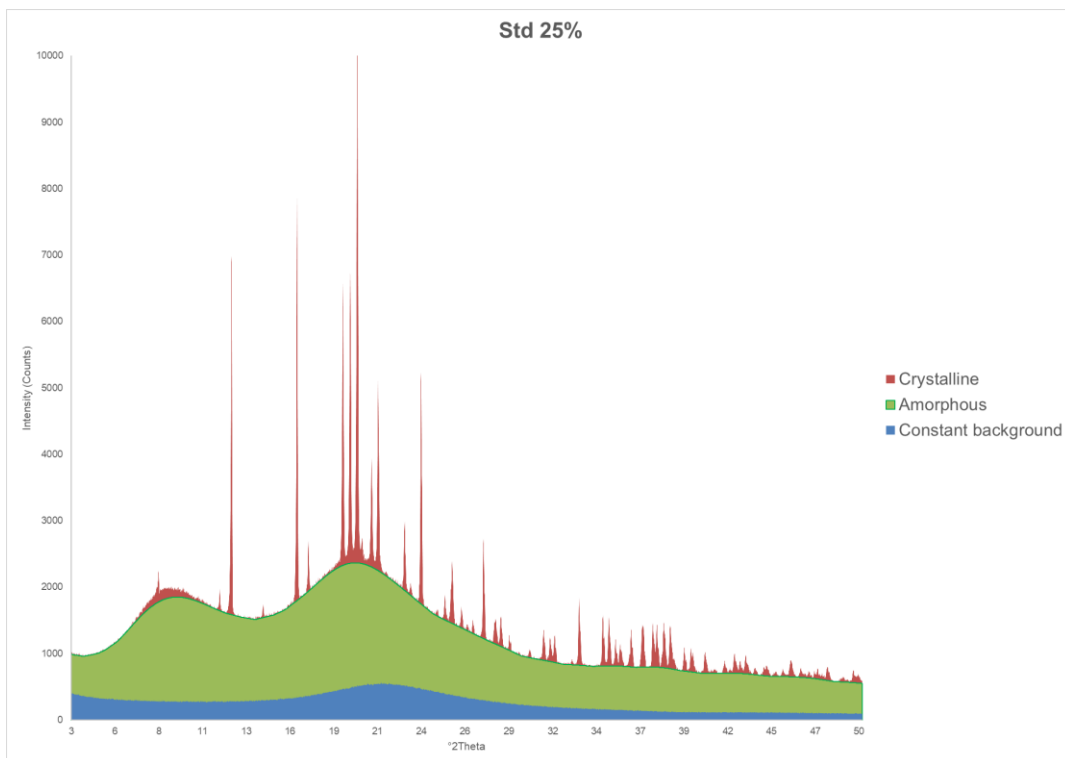


Figure 7 USP method results of Std 25% w/w of  $\alpha$  lactose monohydrate with blank capillary as constant background (blue area). The red and green area represent respectively the crystalline and amorphous area.

### 3.1.4 DDQM

The method DDQM is a new quantification method developed by Toraya and available by HighScore.<sup>42</sup> It is based on the Intensity-composition (IC) equation that can determinate the weight fraction of the individual phases in a mixture using few input as such as the chemical formulas of the mixture's constituents,  $S_k$  sum of the observed powder diffraction intensities of each component, and  $a_k$  the total scattering intensity per chemical formula weight.

$$w_k = a_k S_k / \sum_{k'=1}^k a_{k'} S_{k'}$$

It requires the chemical formula of the phases and good description of experimental pattern to determine  $S_k$  and  $a_k$ .

$$S_k = \sum_{j=1}^{N_k} I_{jk} G_{jk}$$

$$a_k = M_k / \sum_{i=1}^{N_k^A} n_{ik}^2$$

Where  $I_{jk}$  is the integrated intensity of  $j^{\text{th}}$  reflection of  $K^{\text{th}}$  component in a  $K$ -component mixture,  $M_k$  is the molecular weight,  $N_k^A$  is the number of atoms in the chemical formula unit,  $n_{ik}$  is the number of electrons belonging to  $i^{\text{th}}$  atom of the chemical formula and  $G_{jk}$  is given by the formula below<sup>43</sup>.

$$G_{jk} = 2 \sin \theta_{jk} \sin 2\theta_{jk} / (1 + \cos^2 2\theta_{jk})$$

Firstly, the capillary blank pattern was subtracted to patterns of references and standards to eliminate the contribution of the scattering of the sample holder, air and instrument.

Then, the peaks of the pure crystalline  $\alpha$ -lactose monohydrate were defined by a Pawley refinement. The cell parameters were retrieved by CSD<sup>44</sup> (LACTOS03):

Space Group Number: P21 (4)

Crystal System: Monoclinic (beta)

a [Å]: 7.937

b [Å]: 21.568

c [Å]: 4.815

$\alpha$  [°]: 90

$\beta$  [°]: 109.77

$\gamma$  [°]: 90

Volume [Å<sup>3</sup>]: 778.521

The profile was refined using pseudo Voigt function as profile fit function, Caglioti formula for the FWHM and the background was maintained flat at 0 cps. The refinement reached the value of  $R_{wp}=10.8$ , the deviation between calculated and experimental patterns was observed mainly in the description of peak intensity (Figure 8). The determination of the peak list based on the cell parameters allow to detect also low intensity peaks, which can be missed by the "search peaks" procedure.

The description of the amorphous hump was done by manually adding five peaks (Figure 9). The peaks' profile was refined individually using the pseudo Voigt function and individual FWHMs function. The background was automatically set flat at 1.4 cps by HighScore and it was not changed during the fitting. The refinement reached the value of  $R_{wp}=2.7$ , good description of the amorphous pattern was achieved.

The modelled pattern of crystalline and amorphous phases were used to fit the mixtures (see Figure 10, Figure 11, Figure 12 and Figure 13).

Red and blue line patterns represent experimental and calculated patterns, respectively. The plot in the bottom shows the difference between the experimental and calculated intensities. The area of crystalline peaks is represented by the green area, while area of amorphous is represented by the blue area.

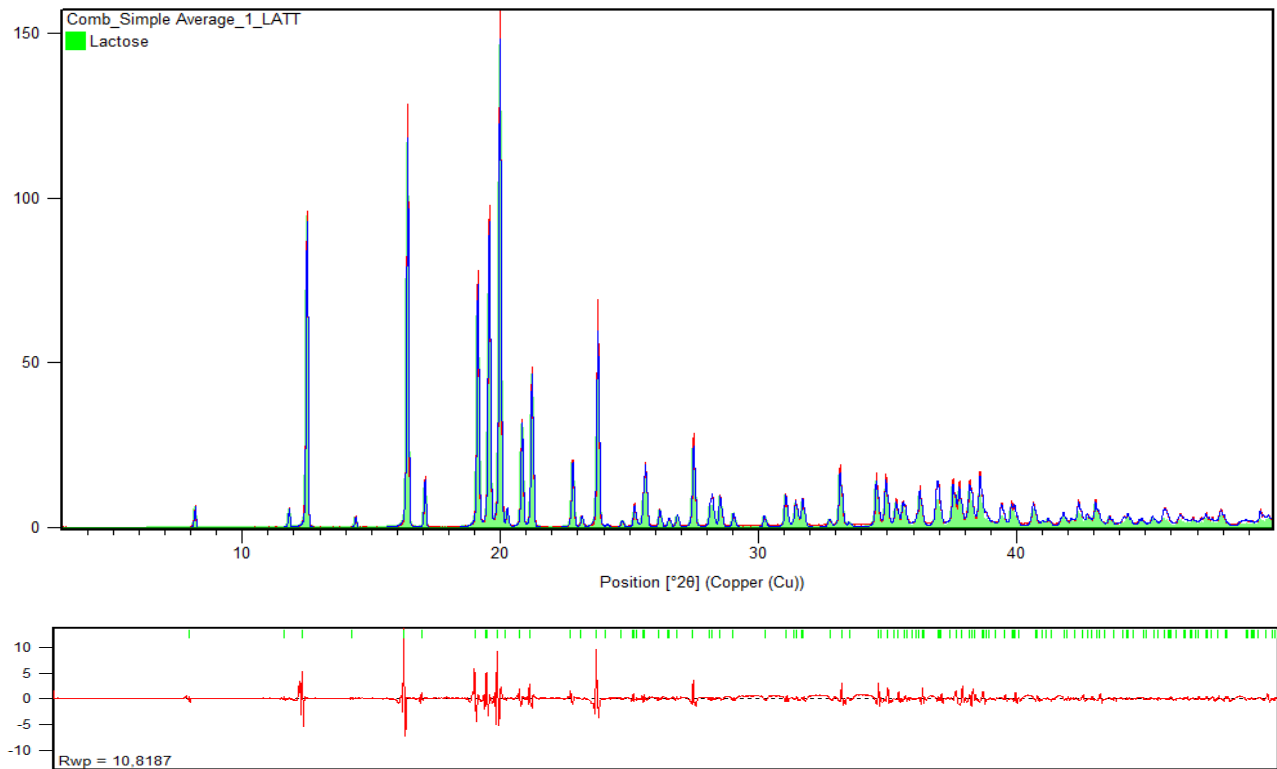


**Figure 8. Pawley refinement result of crystalline reference  $\alpha$  lactose monohydrate. Red and blue line patterns represent experimental and calculated patterns, respectively. The plot in the bottom shows the difference between the experimental and calculated intensities. Green area represents the crystalline peaks area.**

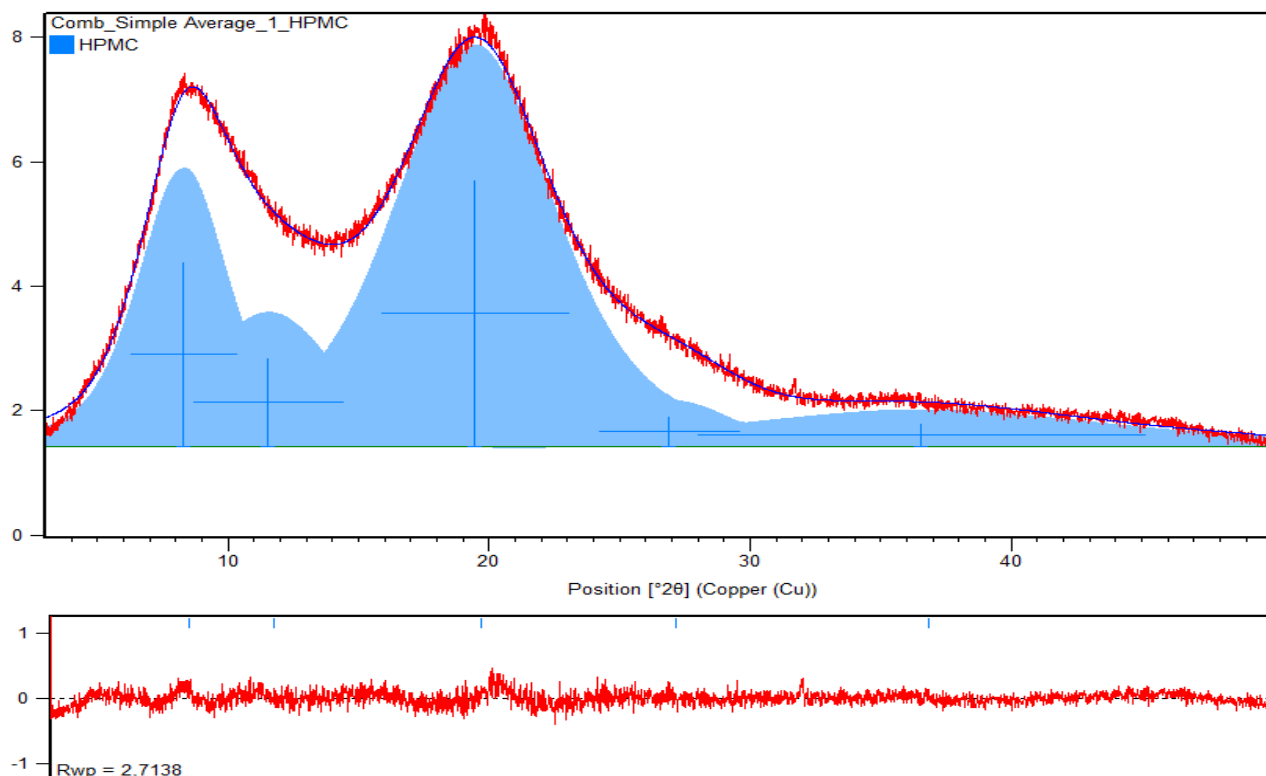


**Figure 9.** Refinement result of amorphous reference HPMC. Red and blue line patterns represent experimental and calculated patterns, respectively. The plot in the bottom shows the difference between the experimental and calculated intensities. Blue area represents the amorphous area.

Initially, the reference phases were scaled to describe the pattern of the mixture, then to improve the fitting, the crystalline peaks were refined as a group using Caglioti and pseudo Voigt function as profile function, while amorphous bands were individually refined using individual FWHMs and pseudo Voigt function as profile function. The background was refined using polynomial function with two coefficients.

It is worth noting that the peak profile of the crystalline references usually shows a lower FWHM than the crystalline part in the mixtures.

Observing the results reported in table below, underestimation of the crystalline % was noticed especially for standard with high content of crystalline phase. These results may be due to poor description of the background. Nevertheless, the method obtained satisfactory results with recovery % > 91% (see Table 4).

**Table 4.**  $\alpha$ -Lactose-HPMC: DDQM results

Actual % crystalline	Backcalculated % crystalline	Recovery%	R <sub>wp</sub> (%)
25	25	100%	3.1
50	48	96%	4.5
75	70	93%	6.1
100	91	91%	8.6

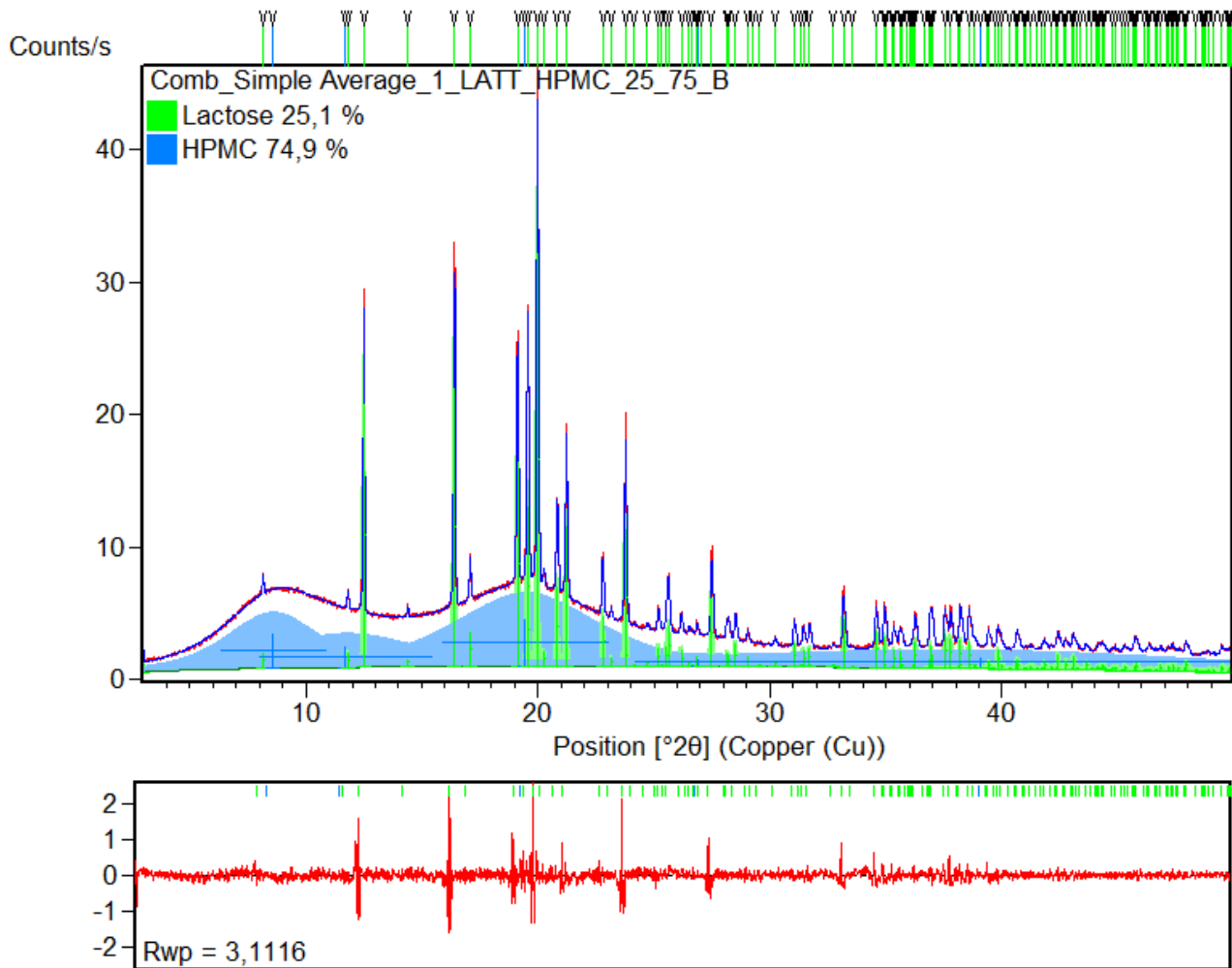


Figure 10. Refinement of Std 25% w/w of  $\alpha$  lactose monohydrate. Red and blue line patterns represent experimental and calculated patterns, respectively. The plot in the bottom shows the difference between the experimental and calculated intensities. The area of the crystalline and amorphous peaks is represented respectively by the green area and blue area. The short lines correspond to peak positions.

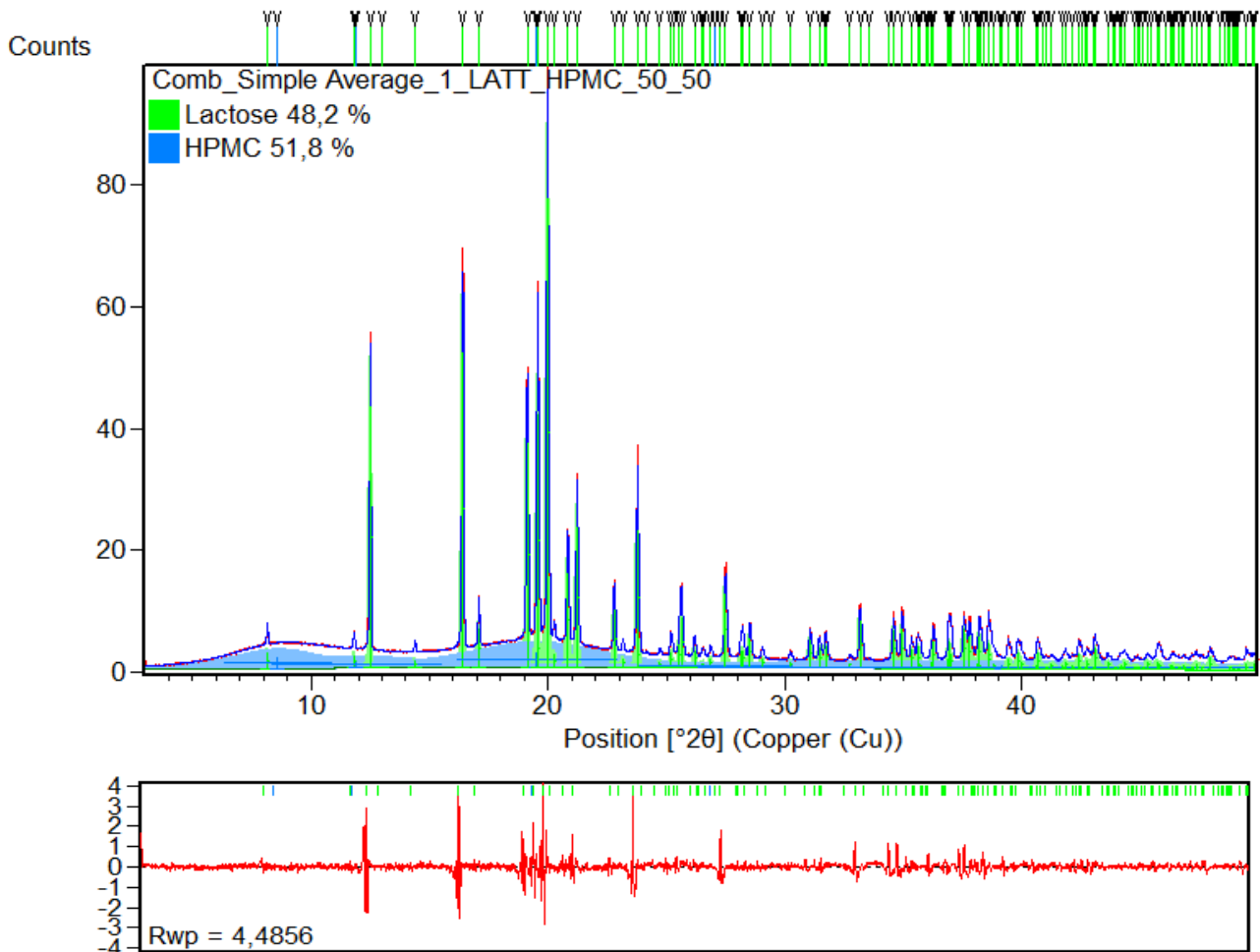


Figure 11. Refinement of Std 50% w/w of  $\alpha$  lactose monohydrate. Red and blue line patterns represent experimental and calculated patterns, respectively. The plot in the bottom shows the difference between the experimental and calculated intensities. The area of the crystalline and amorphous peaks is represented respectively by the green area and blue area. The short lines correspond to peak positions.

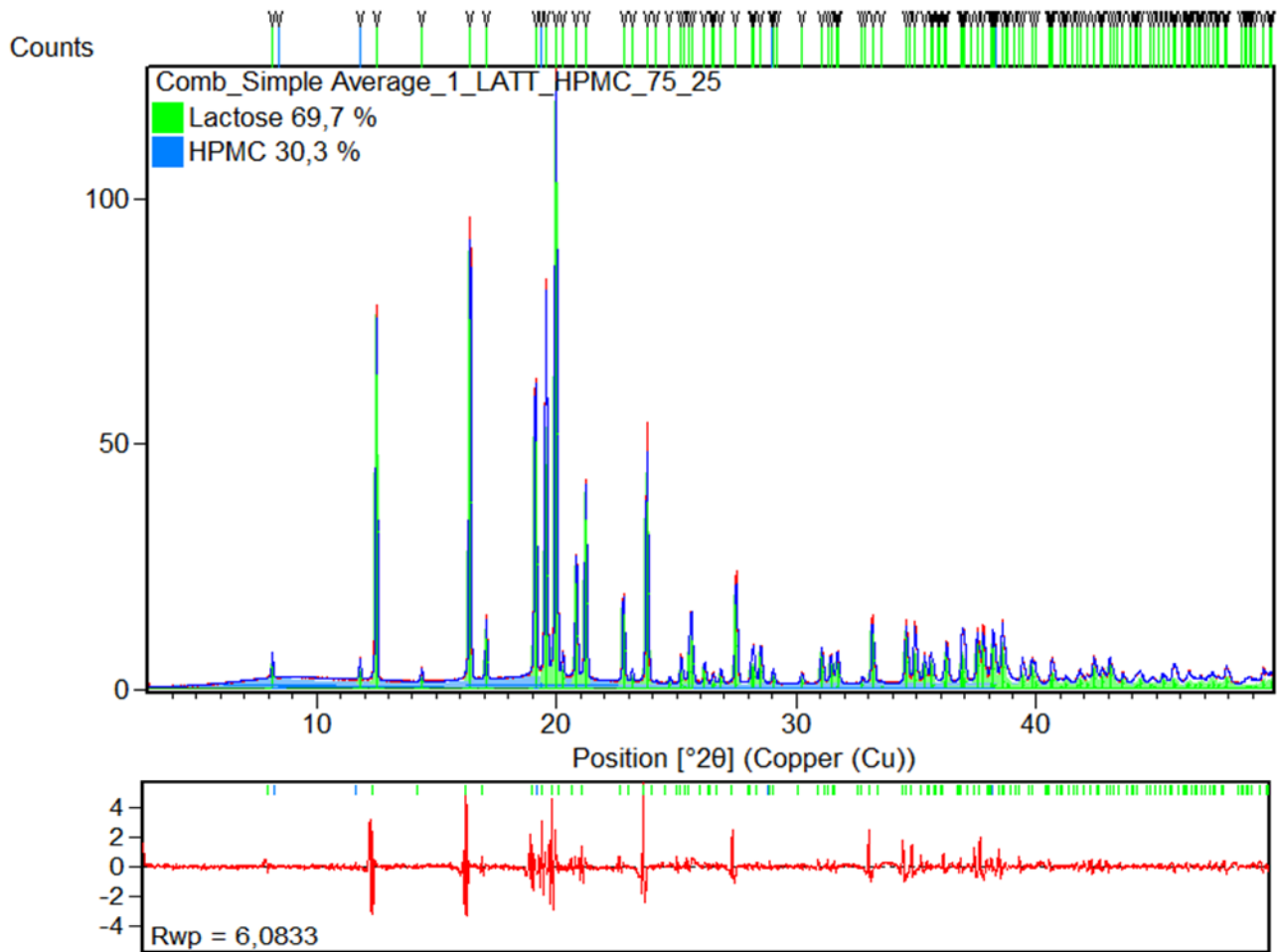
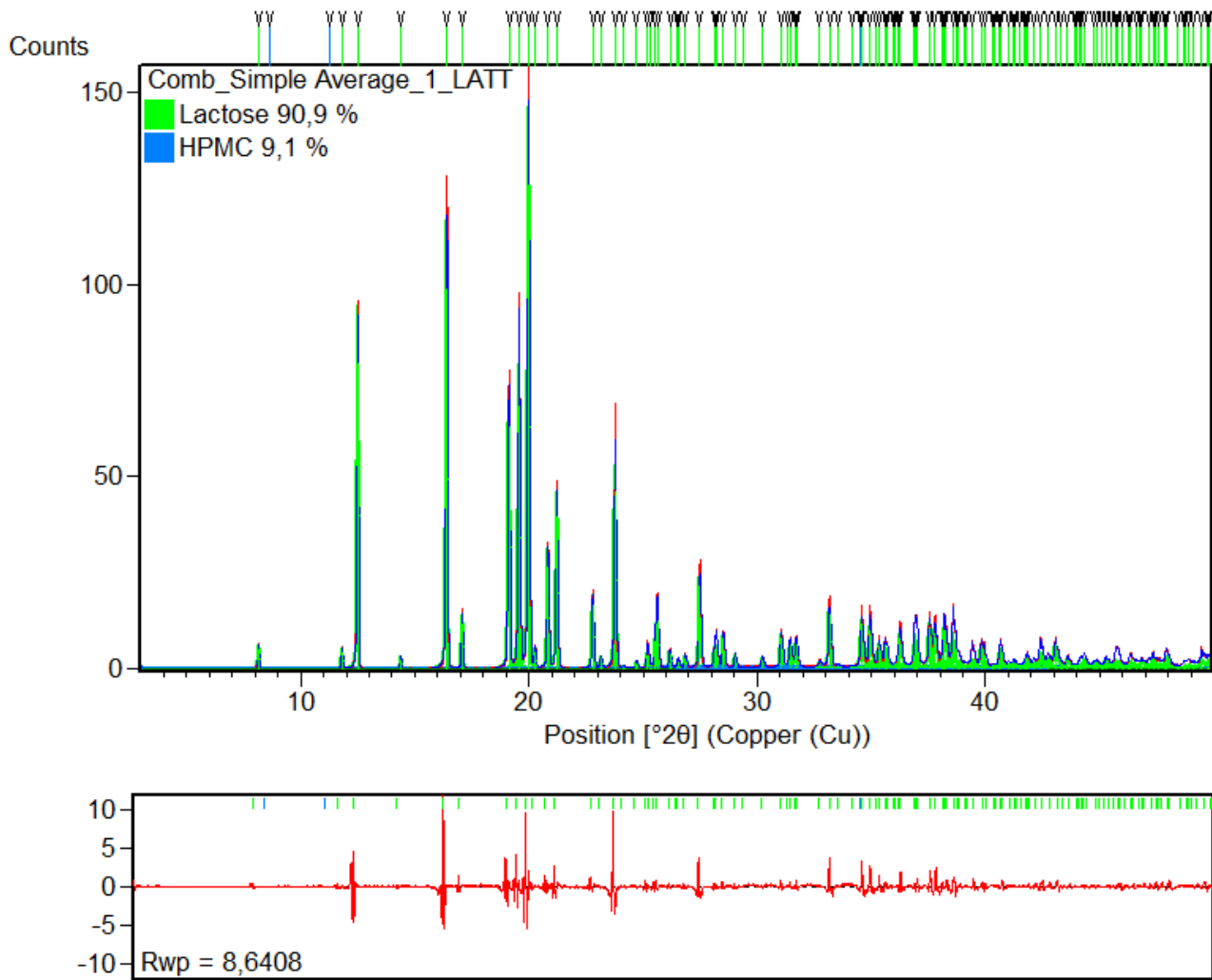


Figure 12. Refinement of Std 75% w/w of  $\alpha$  lactose monohydrate. Red and blue line patterns represent experimental and calculated patterns, respectively. The plot in the bottom shows the difference between the experimental and calculated intensities. The area of the crystalline and amorphous peaks is represented respectively by the green area and blue area. The short lines correspond to peak positions.



**Figure 13. Refinement of Std 100% w/w of  $\alpha$  lactose monohydrate. Red and blue line patterns represent experimental and calculated patterns, respectively. The plot in the bottom shows the difference between the experimental and calculated intensities. The area of the crystalline and amorphous peaks is represented respectively by the green area and blue area. The short lines correspond to peak positions.**

### 3.1.5 Autoscale

The autoscale method is a simple and fast semi-quantitative method available in HighScore software and it requires reference patterns to compare with the sample. The pure references of monohydrate  $\alpha$ -lactose and HPMC were analyzed and used as standard for autoscale quantification. Obviously for this method the reference 100% crystalline was not evaluated and compared with itself.

The autoscale analysis gives back excellent recovery % values and good  $R_{wp}$  values, except for the 25% w/w standard, which showed recovery % of 84%, even so within the acceptable range 80-120% (see Table 5). Despite the good  $R_{wp}$  values, the difference graph showed a weak description of intensity of crystalline peaks in particular for the amorphous phase (see Figure 14, Figure 15 and Figure 16). Probably the over- and under-estimation of the amorphous humps cancel the error, on the other hand the crystalline pattern is slightly affected by preferential orientation, which is mitigated in the mixtures, and prevents an exact match in the intensity of the crystalline part. Nevertheless, this method seems to work better in presence of high percentage of crystalline part.

**Table 5.  $\alpha$ -Lactose-HPMC: Autoscale results**

Actual % crystalline	Backcalculated % crystalline	Recovery%	$R_{wp}$ (%)
25	21	84	3.73
50	49	98	3.25
75	72	96	3.38

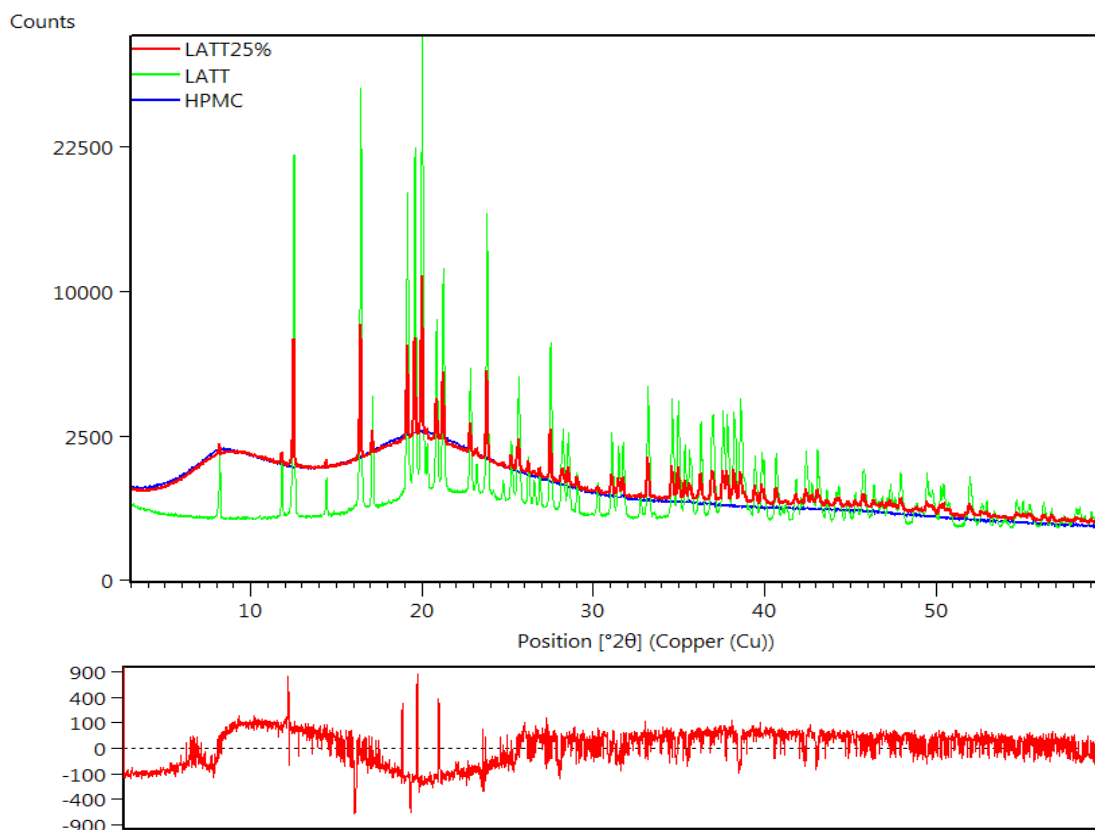


**Figure 14. Autoscale result of Std 25% w/w of  $\alpha$  lactose monohydrate. The image in the top shows the XRPD pattern comparison between the Std 25% w/w in red, amorphous HPMC (blue line), and crystalline  $\alpha$  lactose monohydrate (green line) references. In the bottom the difference plot resulting from the autoscale evaluation.**

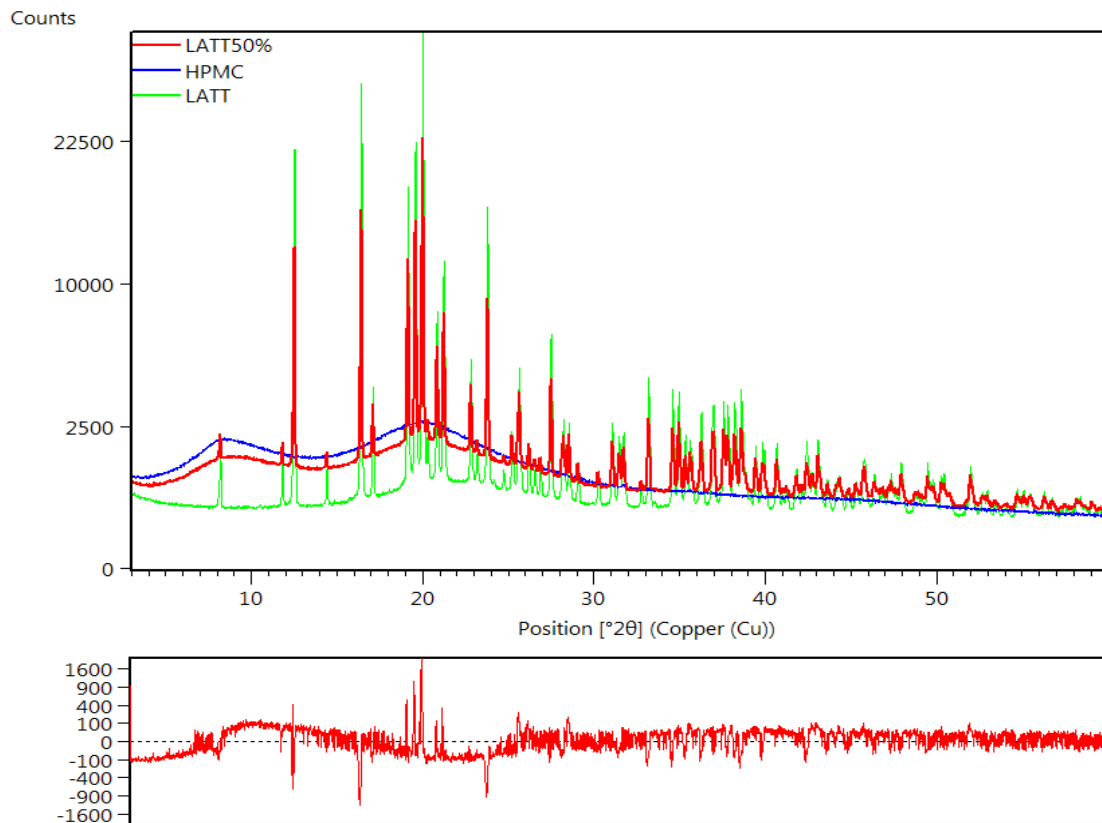


Figure 15. Autoscale result of Std 50% w/w of  $\alpha$  lactose monohydrate. The image in the top shows the XRPD pattern comparison between the Std 50% w/w in red, amorphous HPMC (blue line), and crystalline  $\alpha$  lactose monohydrate (green line) references. In the bottom the difference plot resulting from the autoscale evaluation.

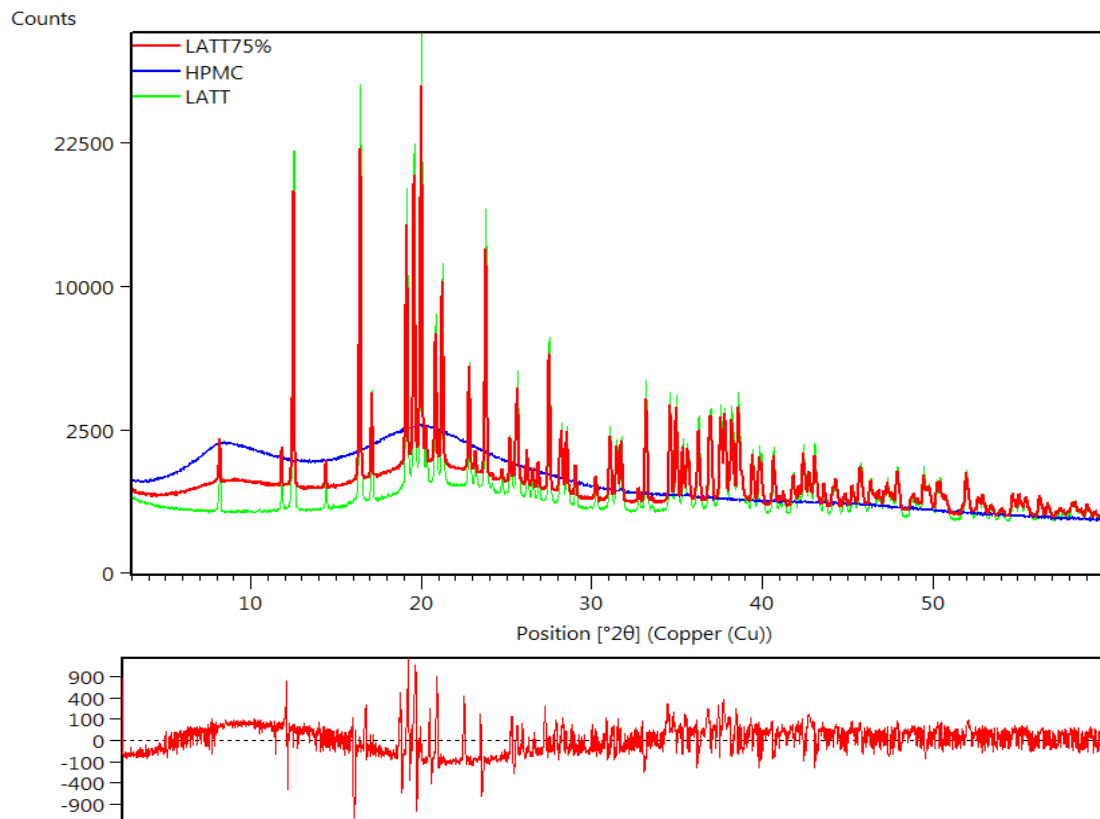


Figure 16. Autoscale result of Std 75% w/w of  $\alpha$  lactose monohydrate. The image in the top shows the XRPD pattern comparison between the Std 75% w/w in red, amorphous HPMC (blue line), and crystalline  $\alpha$  lactose monohydrate (green line) references. In the bottom the difference plot resulting from the autoscale evaluation.

## 3.2 Drug Coated Balloon

### 3.2.1 Material

The manufacturing company of the drug-coated balloon catheter identity cannot be disclosed. The manufacturing company supplied the starting material and three balloon catheters with different batches labelled Test02, Test03 and Test04. The balloon catheter Test02 had swollen diameter of 5 mm, while the Test03 and Test04 had swollen diameter of 6 mm. The three devices diverged as well as for the length of the balloon catheter: Test02 and Test03 were 60mm long, whereas the Test04 was 200 mm long.

The API is classified as High Potent, it is OEB 4 (control exposure to the range of  $1\mu\text{g}/\text{m}^3$  to  $< 10\mu\text{g}/\text{m}^3$ ) and it is suspected of causing genetic defects (H341) and it may damage fertility and unborn child (H360FD). For safety reason the HPAPI was processed always in a confined environment.

In the PolycrystalLine S.p.A. laboratories the pure crystalline and amorphous references of the API have been isolated. The amorphous reference has been obtained by evaporation at low pressure at  $40^\circ\text{C}$  of saturated solution in dichloromethane of anhydrous starting material. The crystalline reference has been isolated by slurry with two different experimental conditions labelled with EXP01 and EXP03:

- EXP01: slurry in water HPLC grade at the concentration of 37.5 mg/mL for three days at temperature condition variable in the range  $10\text{-}50^\circ\text{C}$ .
- EXP03: slurry in water HPLC grade at the concentration of 10 mg/mL for three days at room temperature.

The samples have been analysed by X-Ray diffraction in transmission mode in Hilgenberg borosilicate glass 3.3 capillary diameter  $\varnothing=0.5$  mm and wall thickness=0.01 mm. The patterns were collected on Panalytical X'Pert Pro equipped with a focusing Mirror and a Pixcel detector in the range  $3\text{-}50^\circ 2\theta$ .

It is worth noting that the powder is fluffy and sticky hence the preparation of the capillary is very challenging. It was possible to fill the capillary for about 1-1.5 cm with difficulties and the powder packing is not homogeneous.

The crystalline references showed a crystalline pattern ascribable to the hemihydrate crystalline form retrieved from the CSD (Figure 18). No significant differences for the position and relative intensities of the peaks have been observed. Nevertheless, the crystalline\_EXP03 showed lower intensity and signal to noise ratio. It was probably due to the lower amount of material present in the capillary, indeed the contribution of the capillary profile (grey line) appeared clear in all the patterns (Figure 17).

The crystalline powder obtained by EXP01 was considered as the 100% crystalline reference. The XRPD pattern of EXP01 is comparable to the calculated pattern of hemihydrate form of the API. Nevertheless, it is worth to point out that in solid state quantification the 100% crystalline reference might be not achievable because of not-negligible number of defects are expected to be present in the structure.

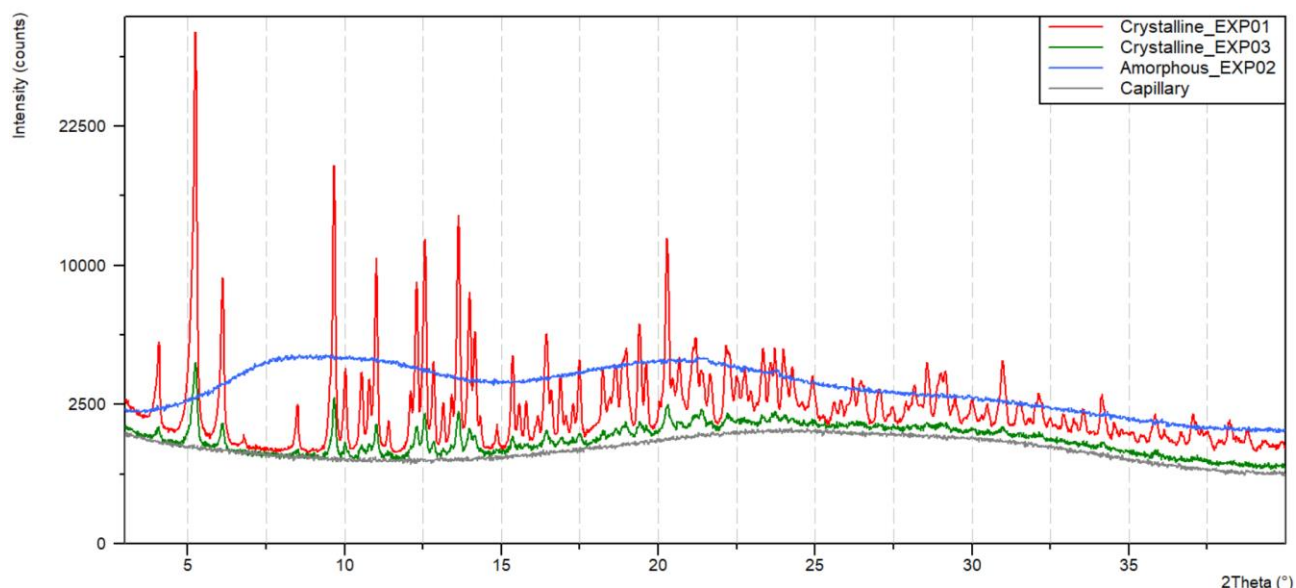


Figure 17. XRPD pattern comparison between crystalline references EXP01 (red line), EXP03 (green line), amorphous reference (blue line) and empty glass capillary (grey line)

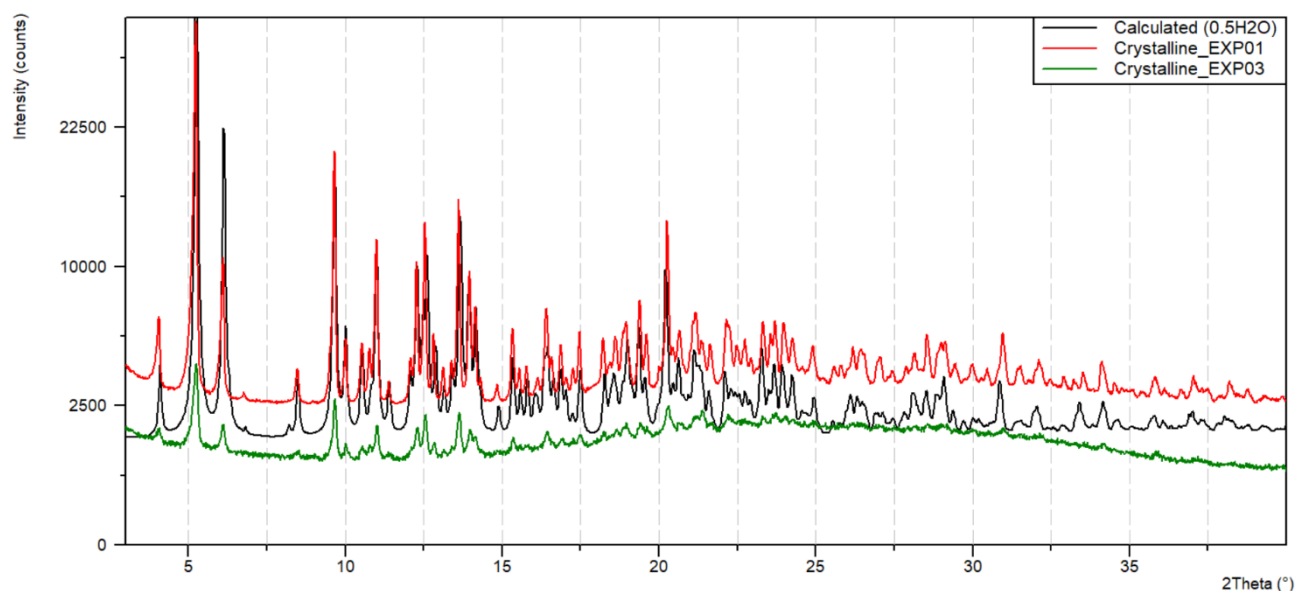


Figure 18. XRPD pattern comparison between crystalline references EXP01 (red line), EXP03 (green line) and calculated pattern from CSD of hemihydrate form

### 3.2.2 Technique selection

The balloon catheter holds  $3.5 \mu\text{g}/\text{mm}^2$ , indeed the diminished amount of the drug was one of the challenging of the quantitative method development. Further issue was the requirement of powder isolation due to the high potency of the drug. Therefore, the choice of the analytical technique and the analysis settings were relevant and preliminary test were performed to optimize the instrumental and measurement condition. The powder pattern was collected with different diffractometers with different set-ups to select the more effective option:

- Micro-diffractometer (UNIFI)
- Transmission diffractometer (UNIBO)
  - Soller 0.04 rad.
  - Soller 0.02 rad.

In collaboration with the University of Firenze chemistry department “Ugo Schiff” Structural Crystallography (UNIFI-CRIST), the DCB sample Test 02 was analysed using micro-diffractometer Bruker D8 Venture equipped with  $\mu$ S 3.0 micro focus X-ray source (Cu and Mo) and PHOTON III detector. The pattern was collected with Cu radiation and spot of the X-ray focus in the range of 100  $\mu$ m.

Three different patterns in three different point of the sample were collected using the micro-diffractometer in the range 4-36°2 $\theta$ . The three XRPD patterns were comparable, denoting the homogeneity of the sample (Figure 19).

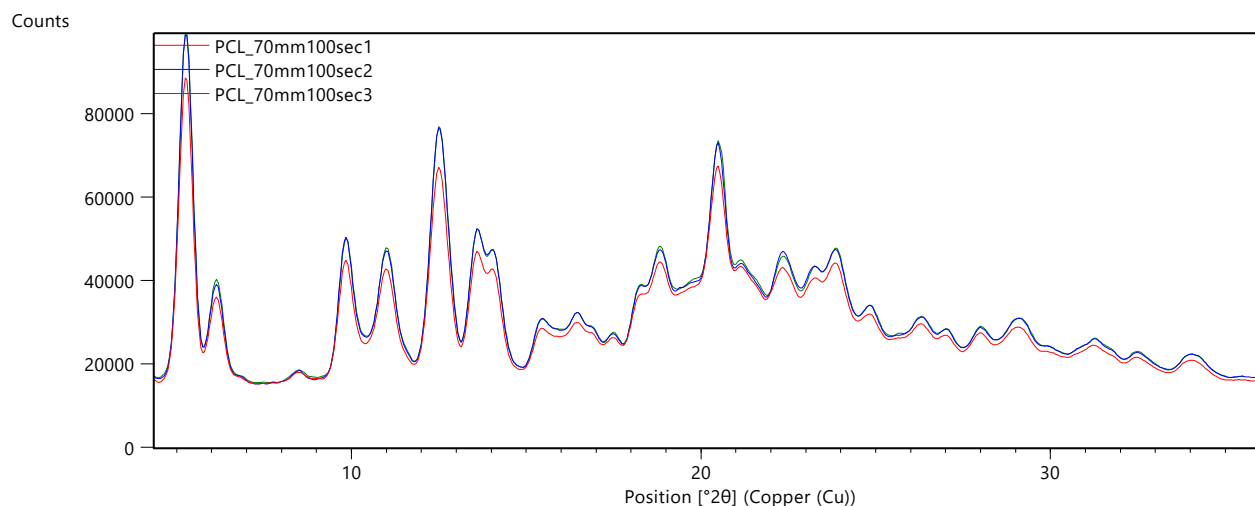


**Figure 19. XRPD pattern comparison between three different area of the drug powder capillary collected by UNIFI-CRIST**

At University of Bologna chemistry department “Giacomo Ciamician”, the powder patterns of all samples were collected with PANalytical X’pert Pro in transmission geometry equipped with a focusing Mirror and a Pixel detector. Measurements in the range 3-40°2 $\theta$  with both soller 0.02 rad. and soller 0.04 rad were performed. As expected, the pattern collected with soller 0.02 rad. showed less instrumental aberration and better resolved peaks (Figure 20). The pattern UNIBO\_soller004 was scaled to appreciate the resolution difference of the two measurements settings.

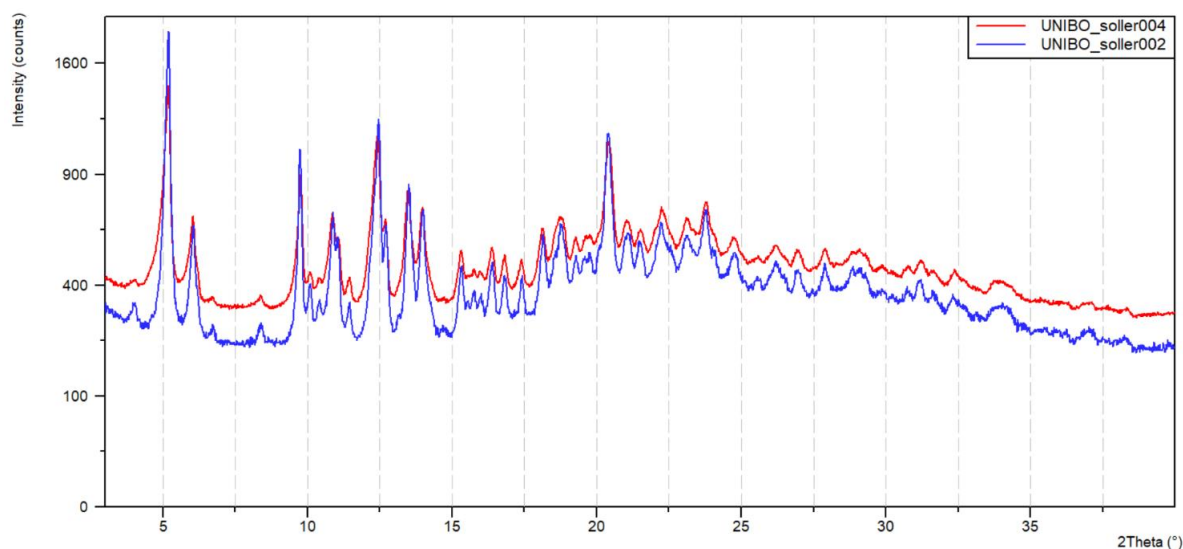


**Figure 20. XRPD pattern comparison of the drug powder capillary collected by UNIBO with soller 0.04 rad (red line) and soller 0.02 rad. (blue line)**

The XRPD patterns collected with micro-diffractometer at UNIFI-CRIST and with transmission diffractometer and soller 0.02 rad. at UNIBO were compared. The patterns collected at UNIFI are characterized by a wide

FWHM due to instrumental aberration, while the patterns collected at UNIBO showed a remarkable resolution. Moreover, the X-ray beam irradiate a larger amount of sample increasing the representativeness of the measure (Figure 21). Additionally, the UNIBO analysis required less time for the results release. Therefore, the UNIBO transmission set up was chosen to analyse the samples for the significantly higher resolution, better statistic and representativity due to the amount of analysed sample and faster analysis procedure.

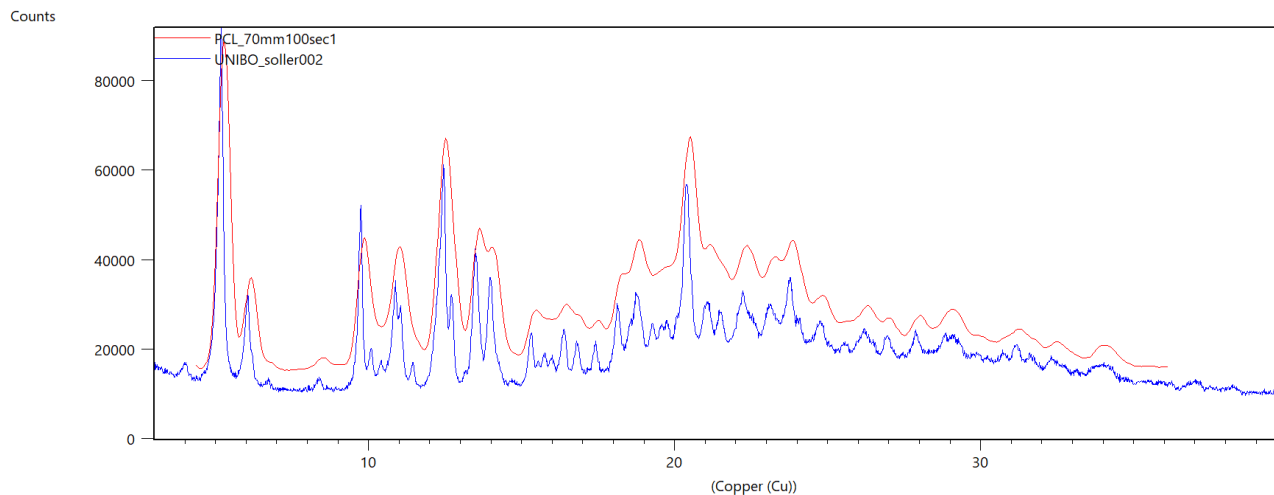


**Figure 21. XRPD pattern comparison between UNIFI-micro (red line) and UNIBO-transmission with soller 0.02 rad. (blue line)**

### 3.2.3 Sample preparation and Data collection

During the manufacturing process of the drug coated balloon, the drug has been stored above inflated balloon. Successively, the balloon coated by the drug has been deflated and folded. To recover all the drug onto the balloon, it was inflated using water until pressure 10 bar as such all the surface of the balloon was exposed. The thin layer of powder deposited onto the balloon was gently scratched using a spatula avoiding the breaking of the balloon and water spill. It is possible to recover about 10 mg of powder.

The glass capillary for the X-ray measurements was filled with the recovered powder.

All the balloon samples (Test 02, Test 03, and Test 04) and the crystalline and amorphous references were analysed into glass capillary by X-Ray diffraction in transmission mode with generator 40 kV and 40 mA in the range  $3-50^{\circ}2\theta$  with step size  $0.0131^{\circ}$  and counting time 130 seconds. The pattern was collected four times to increase the signal to background ratio. Additionally, an empty capillary was measured in the same condition to describe the background.

For all the data treatment the PANalytical HighScore 4.8 software was used.

The DCB formulation contains a low amount of an excipient, that cannot be revealed. Nevertheless, any peak of the excipient was not detected in the XRPD pattern of the DCB sample Test 02, Test 03 and Test 04 (see Figure 22), probably because the excipient is in very small amount or it is amorphous. Therefore, the contribution of the excipient was disregarded.

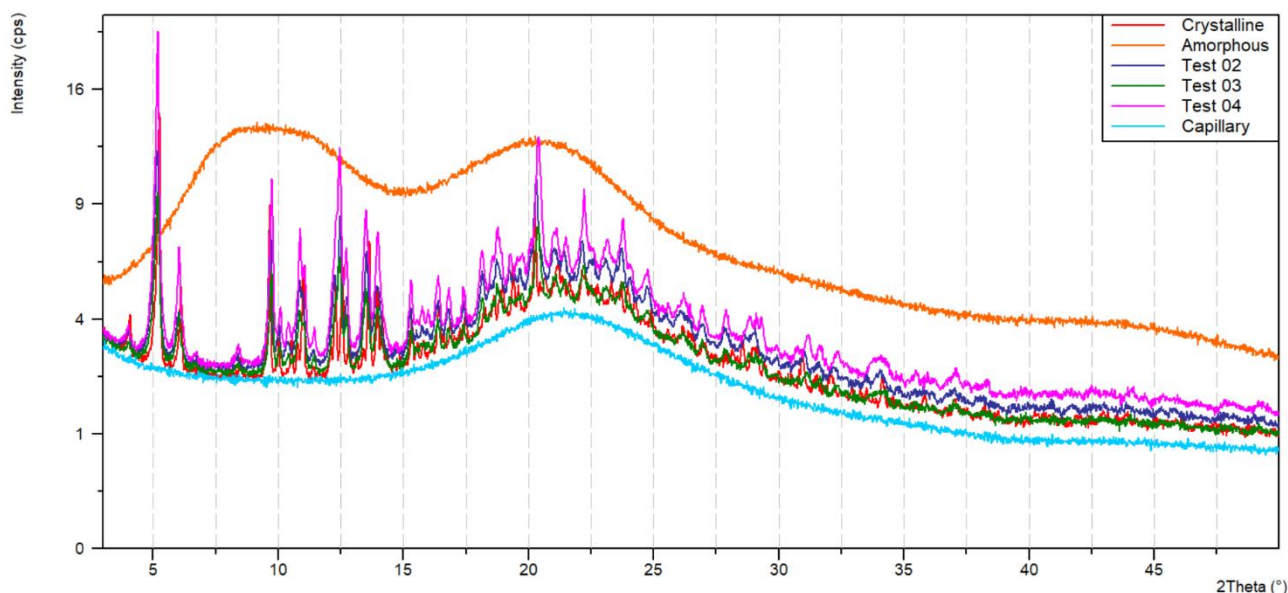
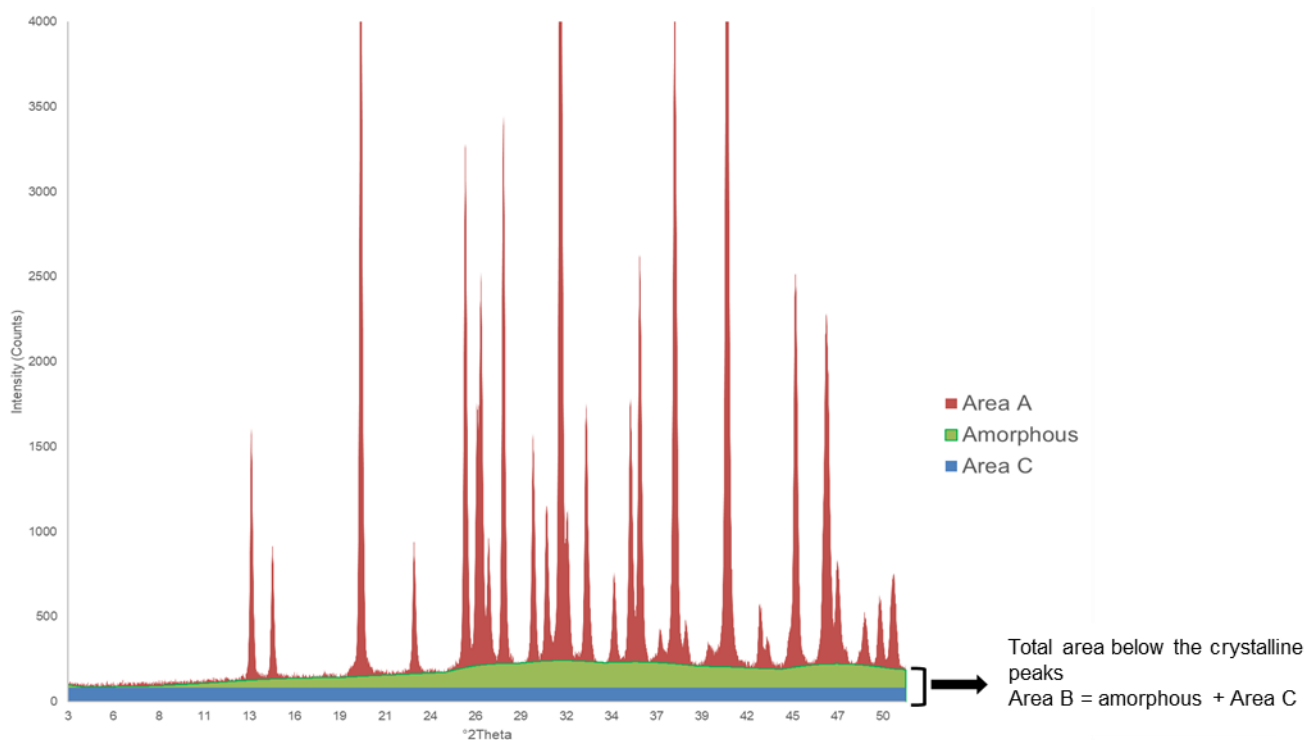


Figure 22. Comparison between the mean XRPD pattern of the samples Test 02 (blue line), Test 03 (green line), Test 04 (pink line), blank analysis of glass capillary (cyan line) and references amorphous (orange line) and crystalline (red line)

### 3.2.4 Crystallinity determination: USP method

The crystallinity degree of crystalline API (100% crystalline) and the DCB samples was calculated using the USP method.

As described before, this method requires the identification of the three different areas in the X-ray pattern: the background area (C in Figure 23) which is due to scattering of the air, instrument and sample holder, the Crystalline area (A) which is due to the crystalline phase present in the sample, normally is the area of the visible peaks, and the area due to the amorphous phase which is the between zone A and C.



**Figure 23. Example of USP method: graphical illustration of area A, B and C**

The identification of the three areas labelled as crystalline area (A), total area below the crystalline peaks (B) and background area (C) was delimited as following:

- A XRPD pattern of samples
- B Background calculated using HighScore as following:
  - Granularity 12
  - Bending 0
  - Use smoothed input data
- C Empty capillary measure

Figure 25, Figure 26, Figure 27 and Figure 28 reports the area determination for crystalline reference and DCB samples. The crystalline area A was composed by the area of the crystalline peaks (red area) and it was delimited by the experimental XRPD pattern line (red line) and the background line (green line). All the area below the background line (green line) was identified as area B, which comprised the signal due to the amorphous component (green area) and background area (blue area). The background area (C) was included in the area B and it was identified with the area below the capillary blank pattern (blue area), it represents the signal due to capillary and instrument scattering (air scattering, fluorescence, equipment etc). The crystalline degree is calculated with the following formula:

$$\% \text{ crystallinity} = 100 * \frac{A}{(A + B - C)}$$

In Figure 24 it can be noticed that crystalline reference pattern followed the contour of the capillary, indeed the crystalline reference did not show an amorphous contribute and it can be considered 100% crystalline.

Nevertheless, applying the area determination described above, the crystalline reference crystallinity degree resulted to be 54.39%, considerably lower than the expected value, therefore it was necessary to apply a correction factor of 1.84 to reach the 100% of crystallinity degree in the crystalline reference. Supposing that the entity of the underestimation error was constant, the % crystalline of the DCB samples was calculated applying the correction factor. The corrected crystalline %, all the DCB samples showed high crystallinity degree, especially the sample Test 03 with 97%, regardless the samples Test 02 and Test 04 showed crystallinity degree higher than 80% (see Table 6).

The results obtained reported only and indication and are comparative to the crystalline reference considering it 100% crystalline. It is important to point out that the USP method is a comparative method. Regrettably, in absence of a known sample of drug-coated balloon is unattainable to determine the accuracy of the results.

The general underestimation of crystallinity is due to difficulties to distinguish in the amorphous hump the contribution of due to the instrument and capillary and the ones attributable to the amorphous content. Especially at high angle, the determination of the background line by HighScore, is placed at the bases of the peaks, which does not reflect the real situation. In fact, at high angle there is the overlap of several peaks, hence the base line should be lower.

**Table 6. USP method results of crystalline reference and DCB samples Test 02, Test 03 and Test 04**

Sample	% crystalline	Correction factor	% crystalline corrected
Crystalline	54.39		100
Test 02	43.83	*1.84	81
Test 03	52.80		97
Test 04	44.71		82

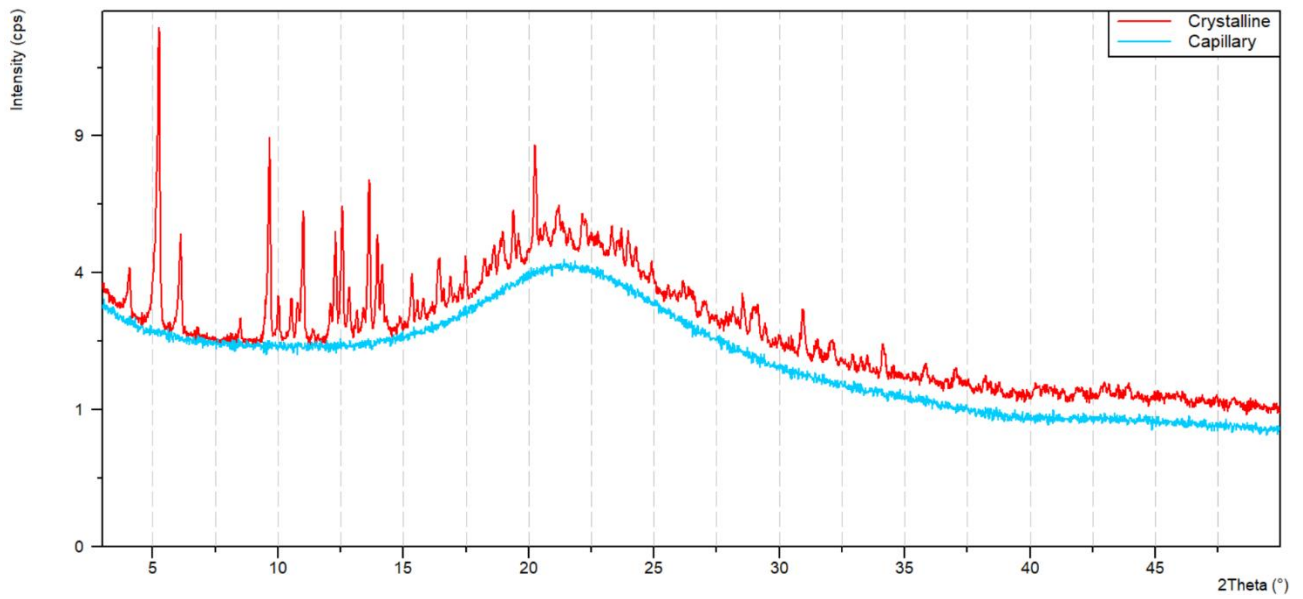


Figure 24. XRPD pattern comparison between crystalline reference (red line) and blank glass capillary (cyan line)

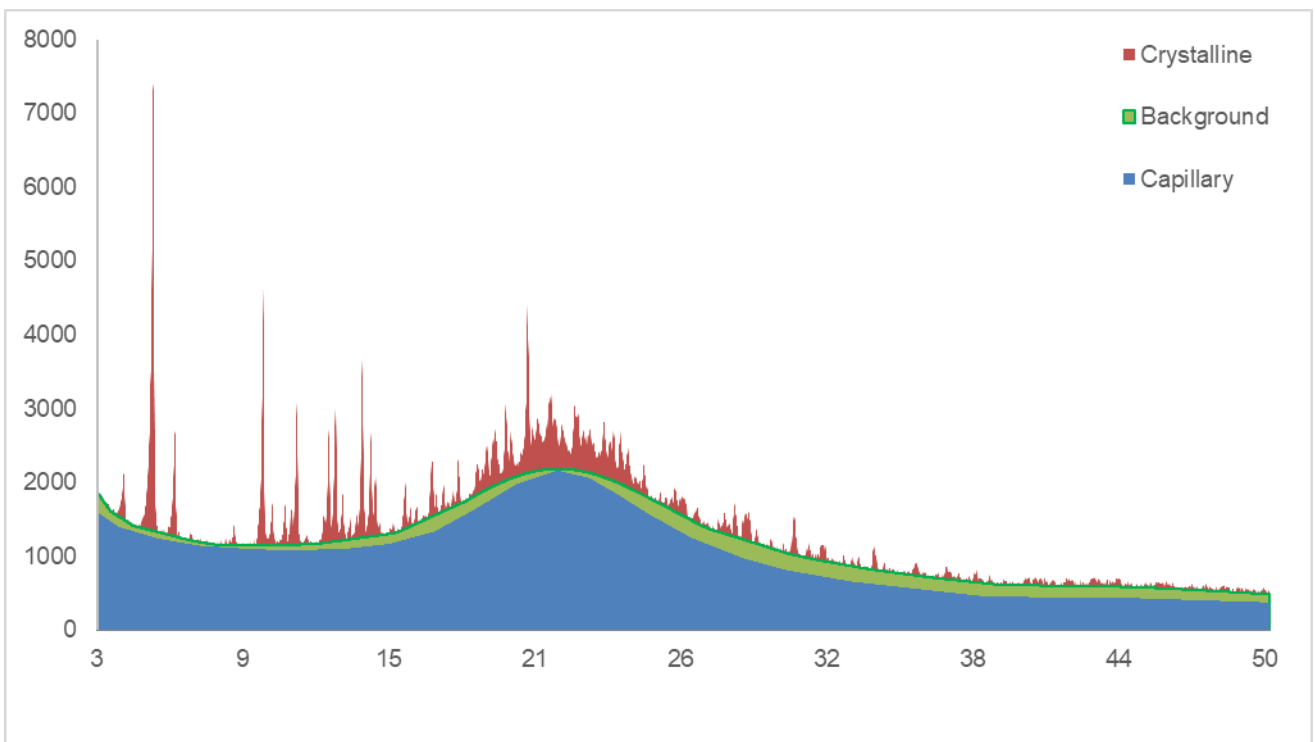


Figure 25. USP method results of crystalline reference with blank capillary as constant background (blue area). The red and green area represent respectively the crystalline and amorphous area.

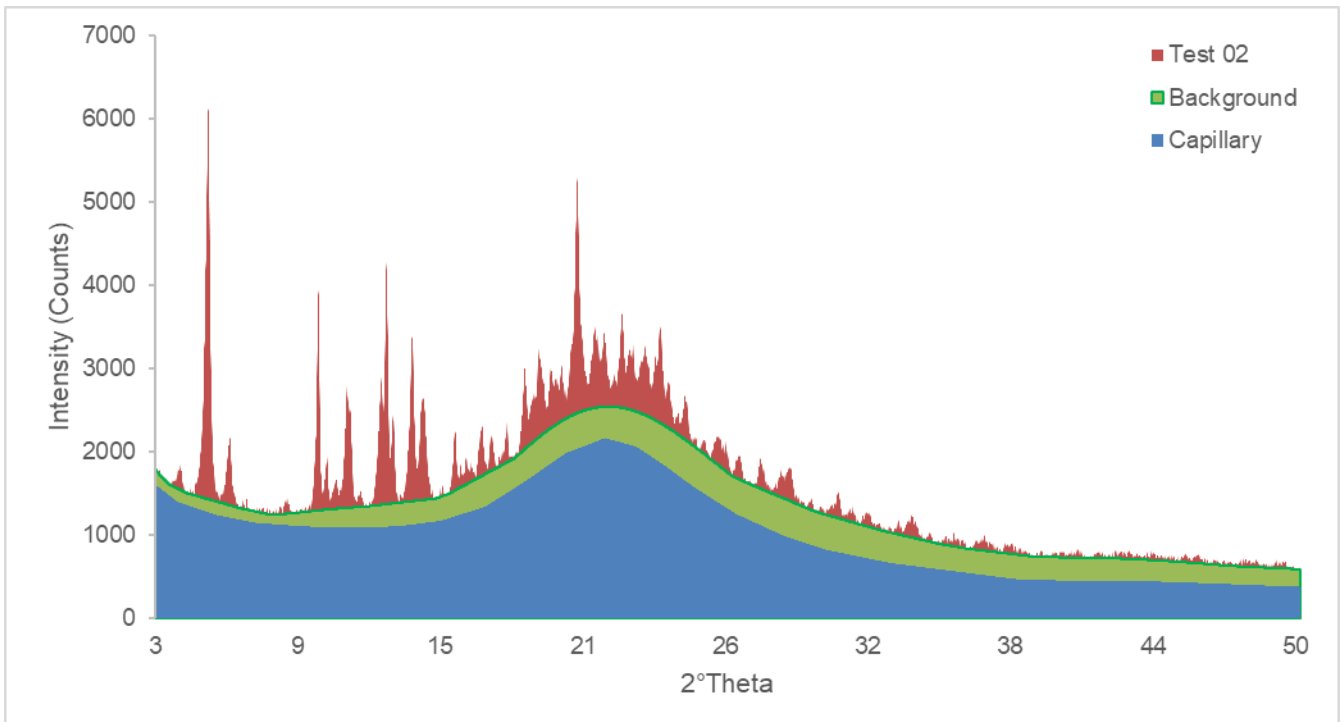


Figure 26. USP method results of DCB sample Test 02 with blank capillary as constant background (blue area). The red and green area represent respectively the crystalline and amorphous area.

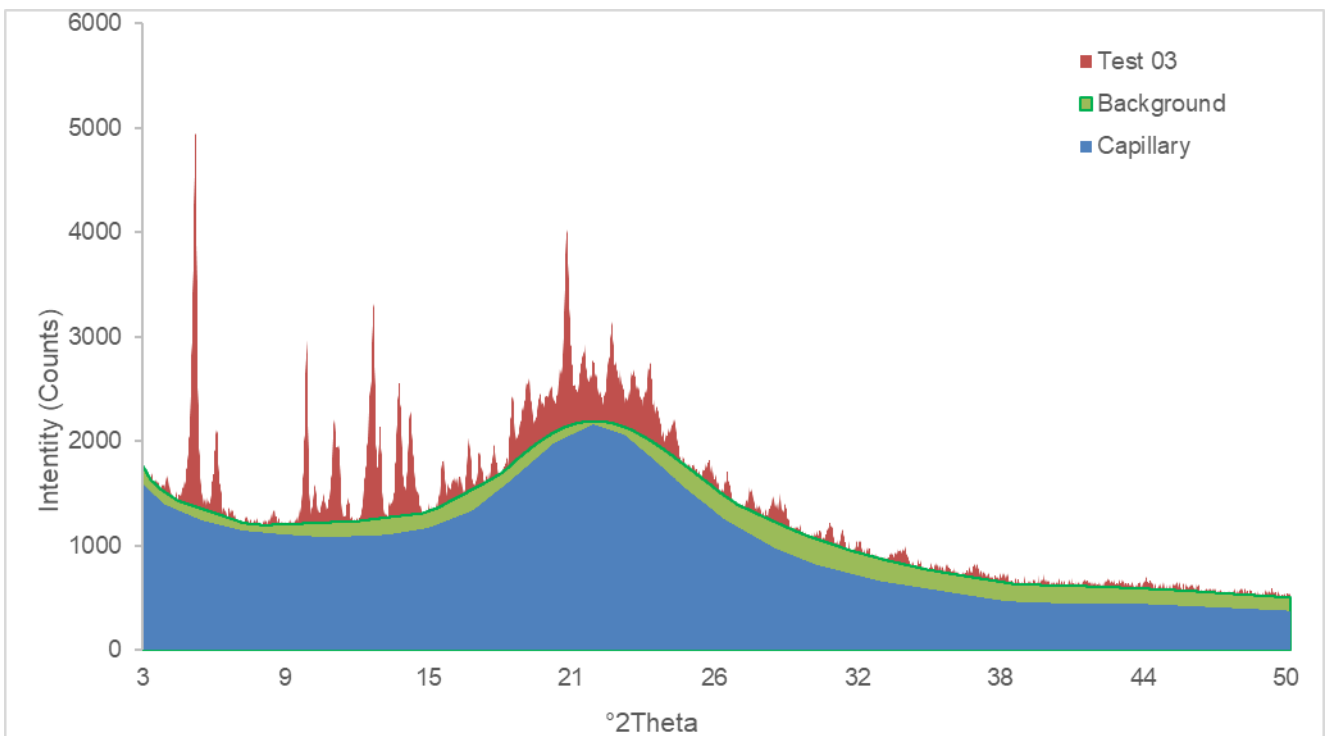


Figure 27. USP method results of DCB sample Test 03 with blank capillary as constant background (blue area). The red and green area represent respectively the crystalline and amorphous area.

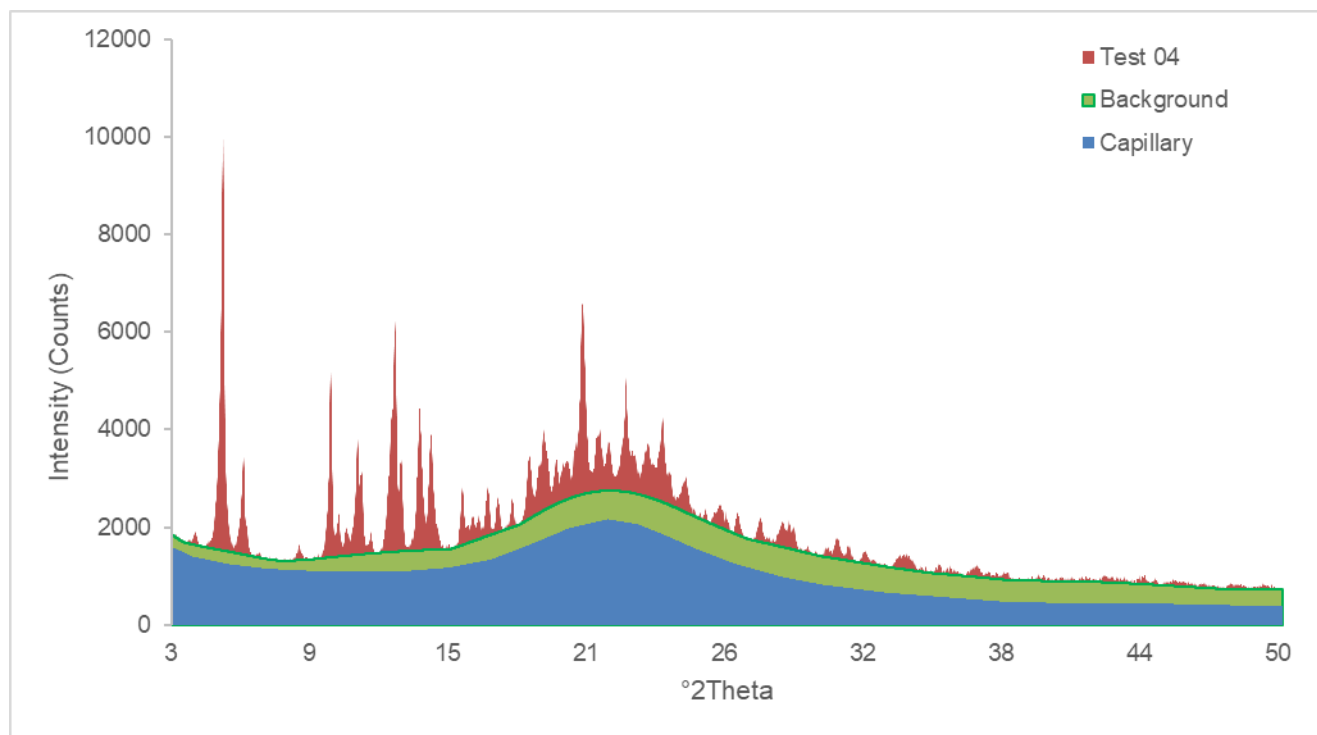


Figure 28. USP method results of DCB sample Test 04 with blank capillary as constant background (blue area). The red and green area represent respectively the crystalline and amorphous area.

### 3.2.5 DDQM

The application of the DDQM method with the lactose-HPMC system was useful to obtain indication of the best approach to follow for the measurements of the challenging DCB samples.

The raw patterns were analysed as following:

1. Mean of the measurements (4 scans)
2. Subtract of the capillary
3. Define the reference phases
4. Fit the samples using the reference phases

The samples were evaluated in the range 3-35°2θ. The signal of the glass capillary was subtracted in order to eliminate the signal due to the sample holder, air scattering and instrumental contribution.

The availability of pure reference patterns and of crystallographic structure for the crystalline phase was notably useful for the quantification method. Concerning the crystalline phase, the peak positions were determined on the basis of the cell parameters. This approach was preferred to the utilization of the function “search peaks”, which detected only the visible peaks and did not recognize the presence of overlapped peaks at high angle.

The crystalline reference pattern was refined using the Pawley function starting with the unit cell parameters related to the crystalline form in the DCB samples:

Space Group Number: P212121 (19)

Crystal System: Orthorhombic

a [Å]: 9.689

b [Å]: 28.076

c [Å]: 33.617

alpha [°]: 90

beta [°]: 90

gamma [°]: 90

Volume [Å<sup>3</sup>]: 9144.72

The profile was refined using pseudo Voigt function as profile fit function and Caglioti formula for the FWHM. The  $a$ ,  $b$ ,  $c$  [Å] values were refined and the background was refined using polynomial function with two coefficients. The refinement reached the value of  $R_{wp}=17.7$ . The achieved  $R_{wp}$  was high, although observing the difference plot (in the bottom of Figure 29) satisfactory description of the pattern was achieved in terms of peak position and profile, the deviation was observed merely for the intensity of the most intense peaks. The amorphous reference was described by manually adding three peaks and modelling them to simulate the experimental pattern. After that, the profile of the peaks was refined individually using the pseudo Voigt function and individual FWHMs function. The background was set flat at 0 cps (see Figure 30). The refinement reached the value of  $R_{wp}=2.6$ , good description of the amorphous pattern was achieved.

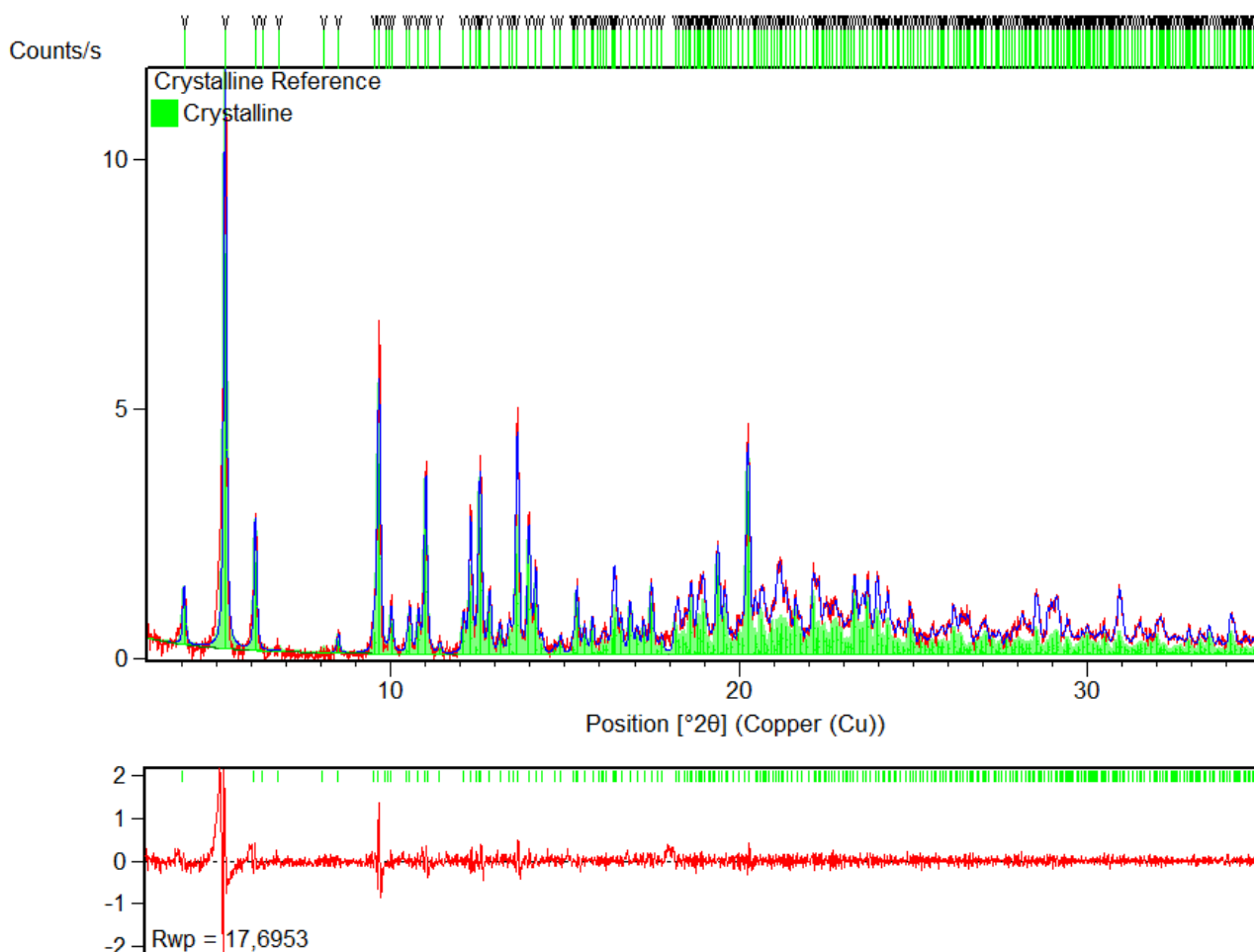


**Figure 29.** Refinement result for the diffraction pattern of crystalline reference. Red and blue line patterns represent experimental and calculated patterns, respectively. The plot in the bottom shows the difference between the experimental and calculated intensities. The peak positions are represented by the short lines in the top, while the area of the crystalline peaks is represented by the green area.

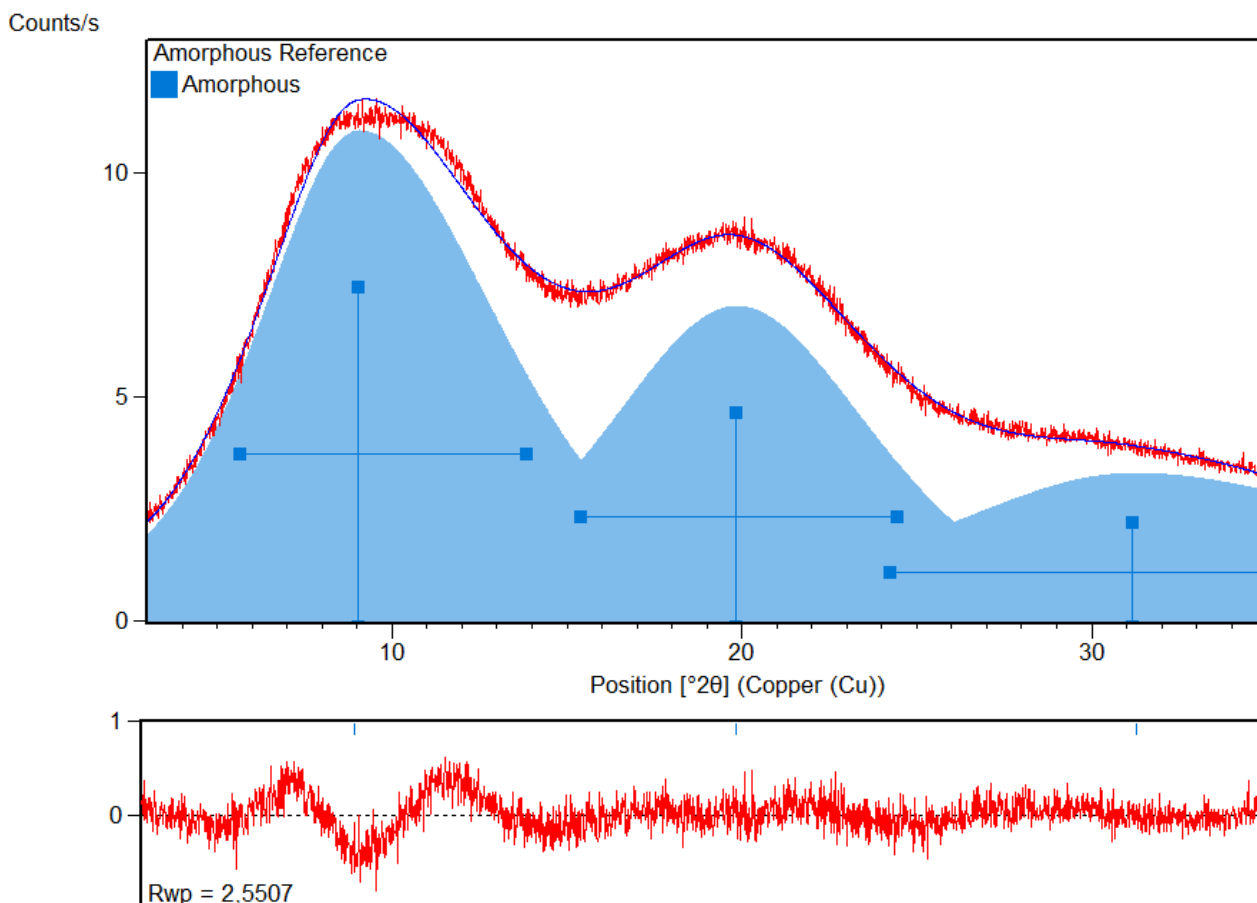


**Figure 30. Refinement result for the diffraction pattern of amorphous reference. Red and blue line patterns represent experimental and calculated patterns, respectively. The plot in the bottom shows the difference between the experimental and calculated intensities. The peak positions are represented by the short lines in the top, while the area of the crystalline peaks is represented by the blue area.**

The DCB samples were evaluated based on the refinement achieved for the crystalline and amorphous references. The cell and peak profile parameters refined against the reference were used as starting point in for the DCB samples. The comparison of the crystalline reference patterns with the DBC test pattern highlight some peak shift which suggest a slightly different cell parameters, which is not surprising, considering the nature of the molecule and its tendency to absorb small molecule as water and solvent (Figure 31). The Pawley refinement was applied to the DBC samples to evaluate potential small variations of cell parameters occur during the manufacturing process. The crystalline phase was refinement using Caglioti function and pseudo Voigt function as profile function and size and strain function was applied to consider the change of the profile compared to reference due to the manufacturing process of the DCB.

The amorphous phase was refined using individual FWHMs and pseudo Voigt function as profile function. No size and strain functions were applied as we were facing to amorphous phase without crystalline order and defined structure. The background was refinement using polynomial function with two coefficients.

Table 7 reports the comparison between the cell parameters of the DCB samples and the crystalline API reference after Pawley fit. All the samples showed cell parameters slightly different compared to the crystalline reference. The observed increase of the cell volume in the samples was probably ascribable to the nature of the molecule, which is inclined to absorb water molecules or small solvent molecules. The absorption of solvent that can happen during the manufacturing process because of the deposition of the API occurs by solvent evaporation.

Table 7. Refined unit cell parameter comparison

Cell parameters	Crystalline Reference after Pawley refinement	Crystalline reference after DDQM evaluation	Test 02 after DDQM evaluation	Test 03 after DDQM evaluation	Test 04 after DDQM evaluation
<b>a [Å]</b>	9.676	9.657	9.624	9.637	9.658
<b>b [Å]</b>	28.146	28.124	28.285	28.260	28.225
<b>c [Å]</b>	33.664	33.520	33.929	33.855	33.839
<b>Volume [Å<sup>3</sup>]</b>	9167.788	9103.814	9236.183	9219.658	9224.372

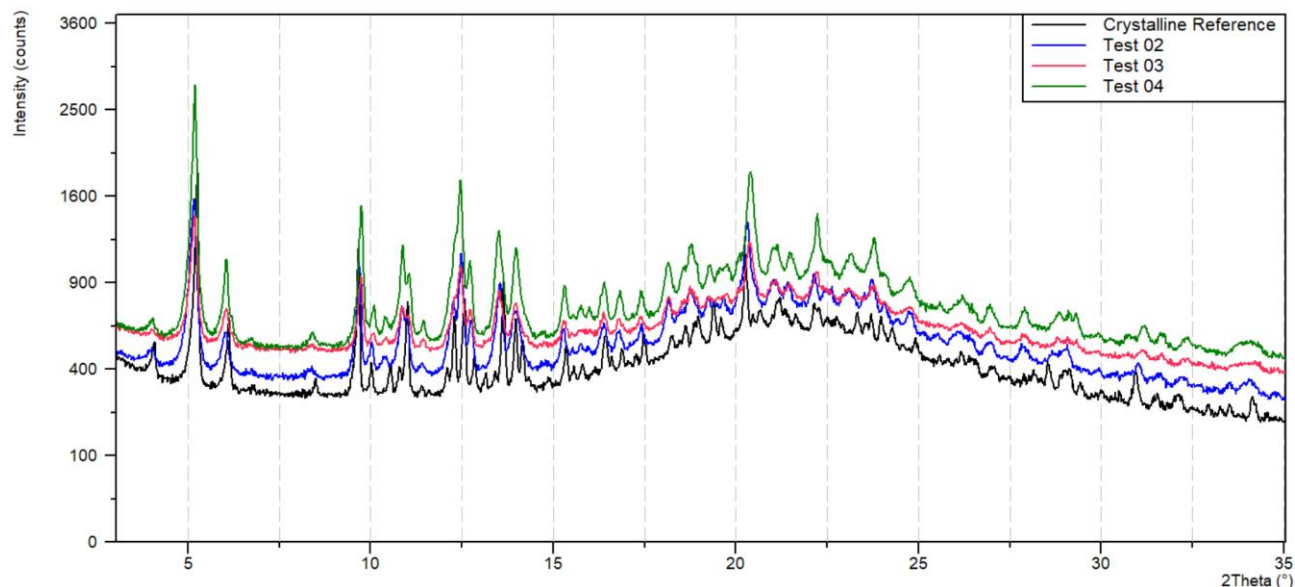


Figure 31. XRPD patterns comparison between crystalline reference (black line) and DCB samples: Test 02 (blue line), Test 03 (red line) and Test 04 (green line)

Figure 32, Figure 33, Figure 34 and Figure 35 show the crystalline determination by DDQM in crystalline reference and DCB samples Test 02, Test 03 and Test 04, respectively.

The green area represents the crystalline area, while the blue one represents the amorphous area.

Even the crystalline reference was refined as described above, it was used as control sample to have indication of the potency and accuracy of the method. The refinement of the crystalline reference gave back excellent results with crystallinity degree of 99.6%. Otherwise, it showed wide  $R_{wp}$  value of approx. 21% due to bad description of the intensity of the highest peaks (Figure 32). Nevertheless, the result obtained for the crystalline reference were really encouraging.

The results for the DCB samples were comparable for samples Test 02 and Test 04, which showed crystallinity degree approx. 60% and  $R_{wp}$  value about 8%. The sample Test 03 showed higher crystallinity degree 70% and also  $R_{wp} = 10\%$ . Nevertheless, the difference plot was satisfactory for all the samples (see Table 8).

Table 8. DDQM results of crystalline reference and DCB samples Test 02, Test 03 and Test 04

Sample	% crystalline	$R_{wp}$
<b>Crystalline reference</b>	100%	20.90
<b>Test 02</b>	59%	8.41
<b>Test 03</b>	71%	10.15
<b>Test 04</b>	60%	8.07

Counts/s

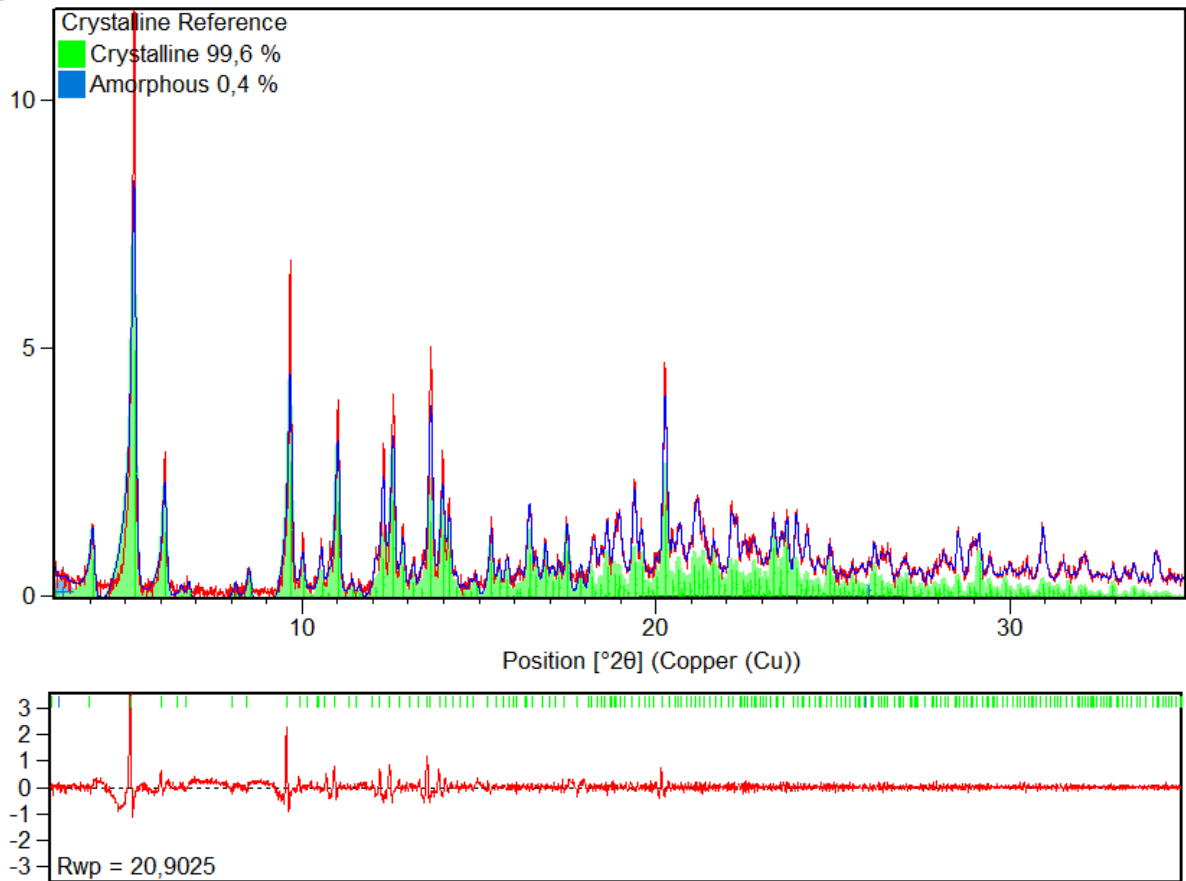


**Figure 32.** Refinement result for the diffraction pattern of crystalline reference. Red and blue line patterns represent experimental and calculated patterns, respectively. The plot in the bottom shows the difference between the experimental and calculated intensities. The peak positions are represented by the short lines in the top, while the area of the crystalline and amorphous peaks are represented respectively by the green area and blue area.

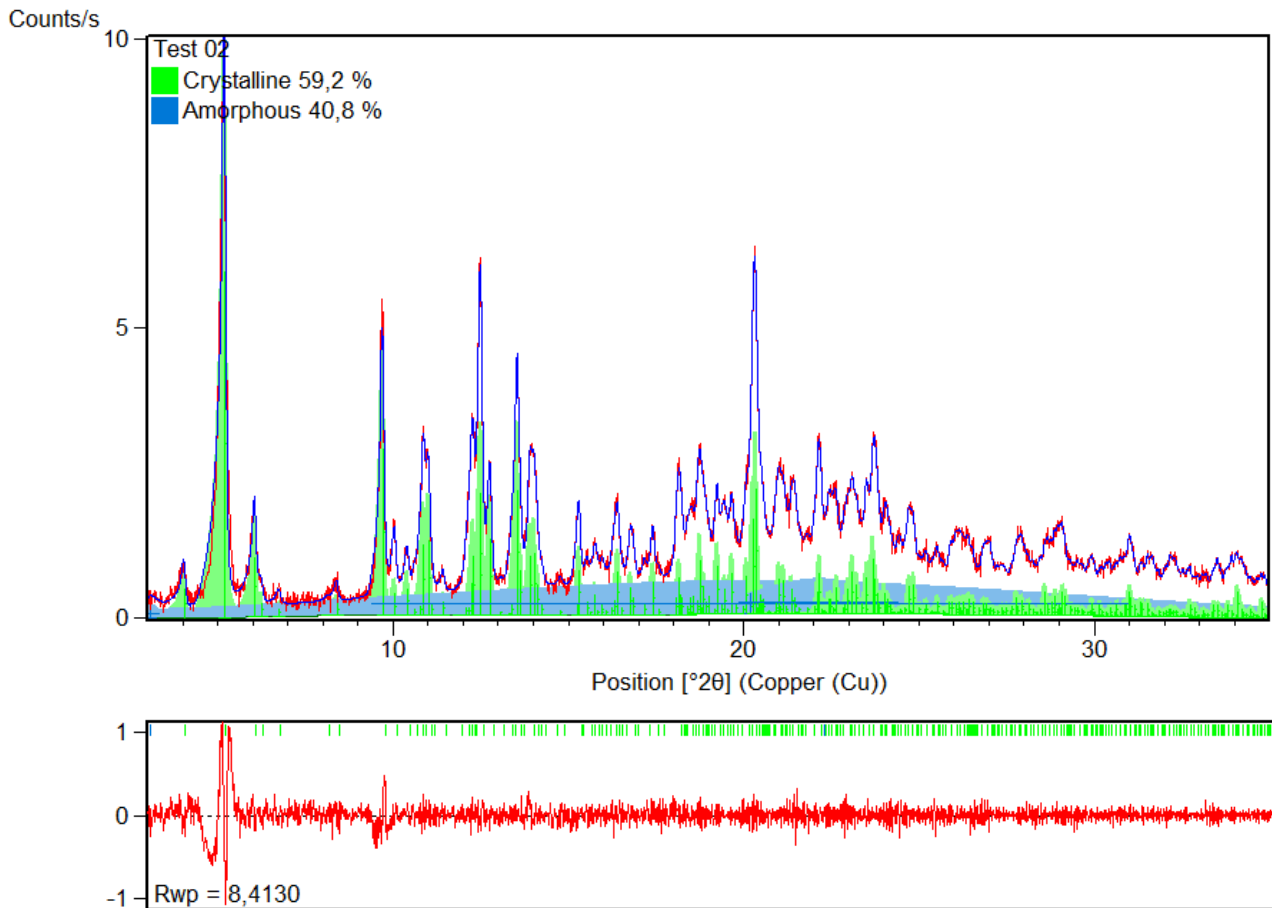


**Figure 33.** Refinement result for the diffraction pattern of DCB sample Test 02. Red and blue line patterns represent experimental and calculated patterns, respectively. The plot in the bottom shows the difference between the experimental and calculated intensities. The peak positions are represented by the short lines in the top, while the area of the crystalline and amorphous peaks is represented respectively by the green area and blue area.

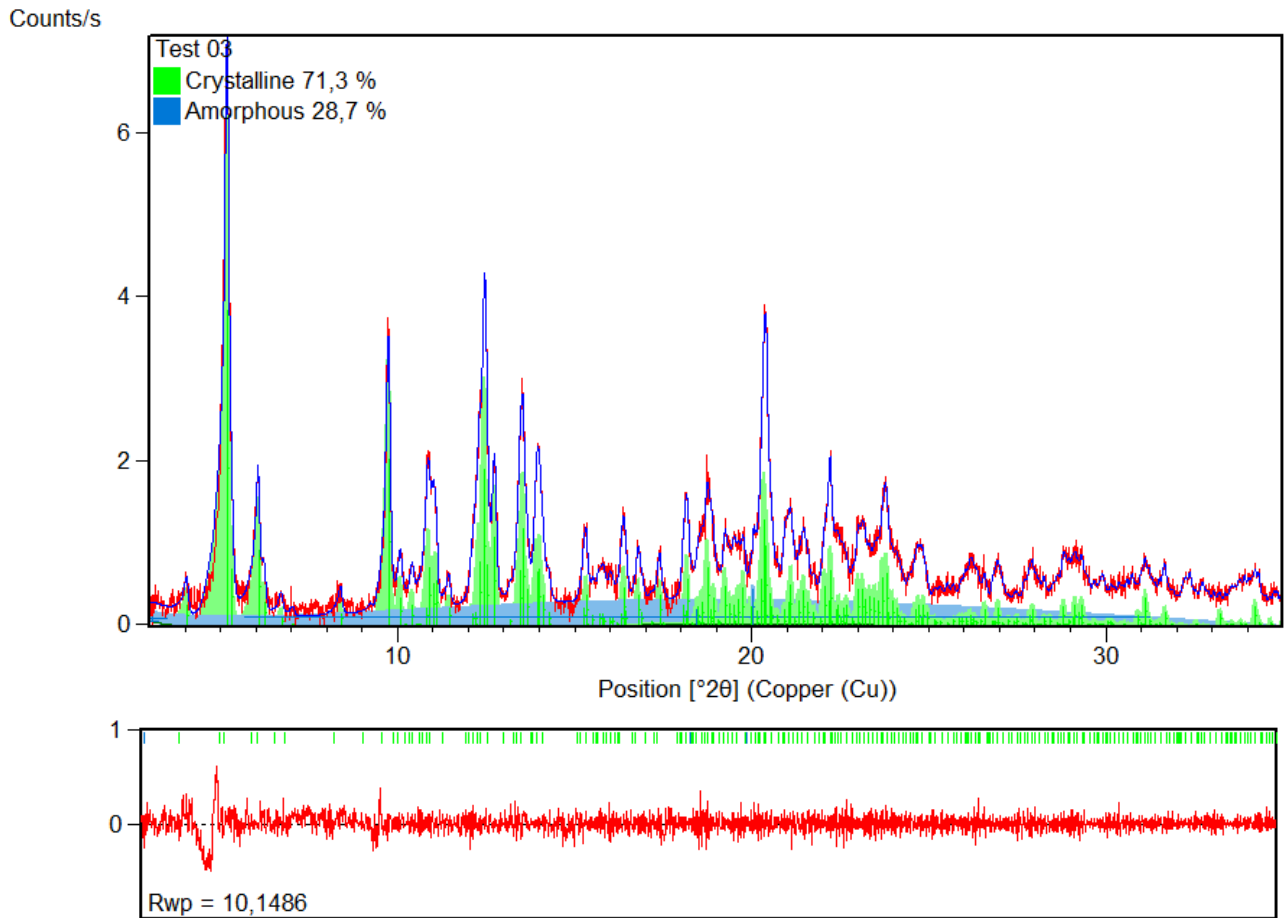
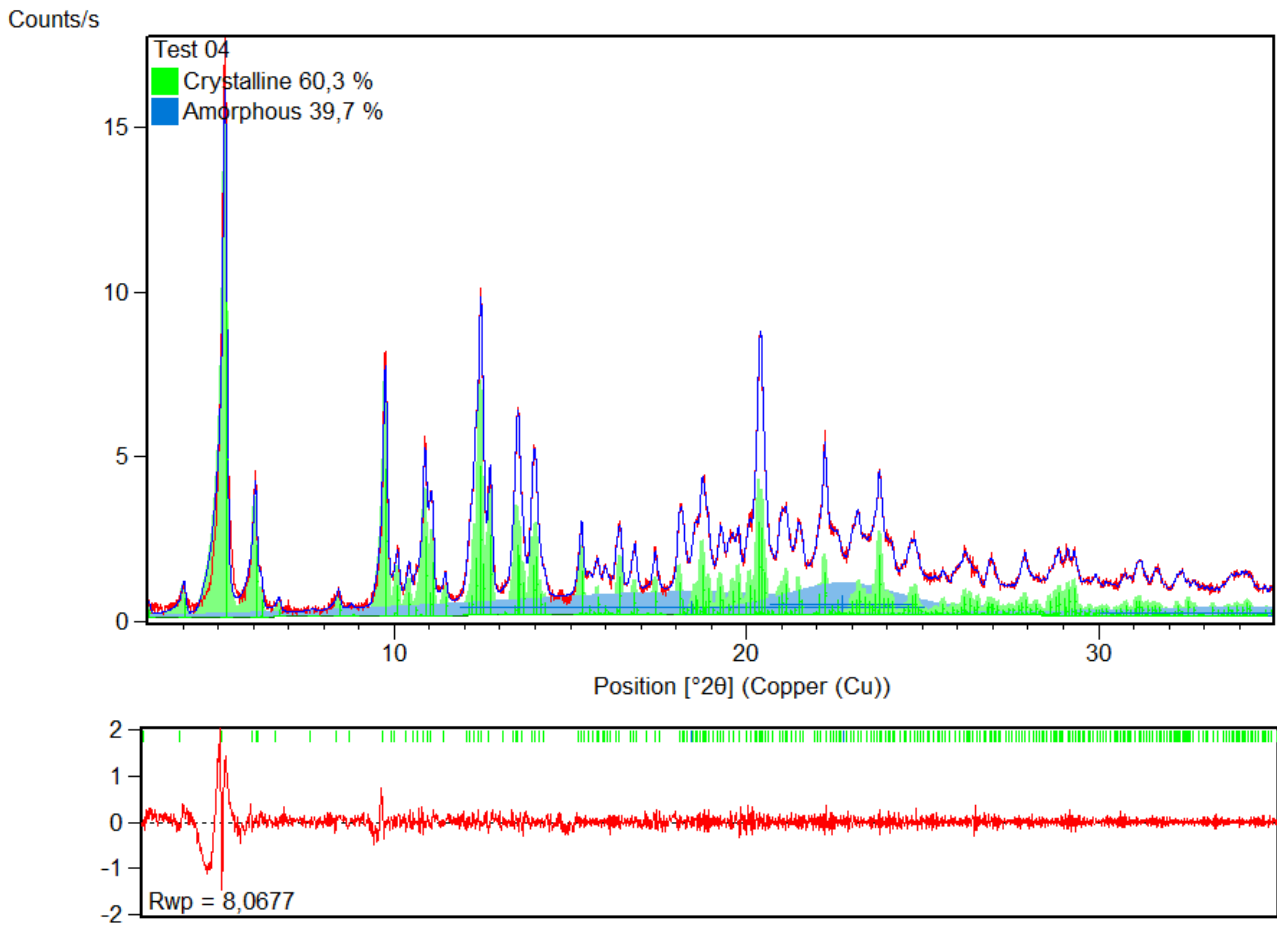


Figure 34. Refinement result for the diffraction pattern of DCB sample Test 03. Red and blue line patterns represent experimental and calculated patterns, respectively. The plot in the bottom shows the difference between the experimental and calculated intensities. The peak positions are represented by the short lines in the top, while the area of the crystalline and amorphous peaks is represented respectively by the green area and blue area.



**Figure 35.** Refinement result for the diffraction pattern of DCB sample Test 04. Red and blue line patterns represent experimental and calculated patterns, respectively. The plot in the bottom shows the difference between the experimental and calculated intensities. The peak positions are represented by the short lines in the top, while the area of the crystalline and amorphous peaks is represented respectively by the green area and blue area.

### 3.2.6 Autoscale

The pure references of crystalline and amorphous API were used as standard for autoscale quantification. All samples were analysed into glass capillary, on the assumption that the entity of the capillary signal is constant, the samples and the standards patterns were evaluated without the subtraction of the blank capillary measure. The autoscale is very quick and simply method. Nevertheless, it is important point out that it does not consider the difference in peak positions and profile due to the different cell parameters of the sample.

Table 9 and Figure 36, Figure 37 and Figure 38 report the results obtained for the DCB samples. The autoscale method detected that all the sample were highly crystalline with the  $R_{wp}$  values in the range of 8-13%. However, observing the difference plot, the mismatch of the peak positions between the reference pattern and the DCB samples was not negligible.

**Table 9. Autoscale results of DCB samples Test 02, Test 03 and Test 04**

Sample	% crystalline	$R_{wp}$
Test 02	100	9.38
Test 03	97	8.43
Test 04	99	13.35

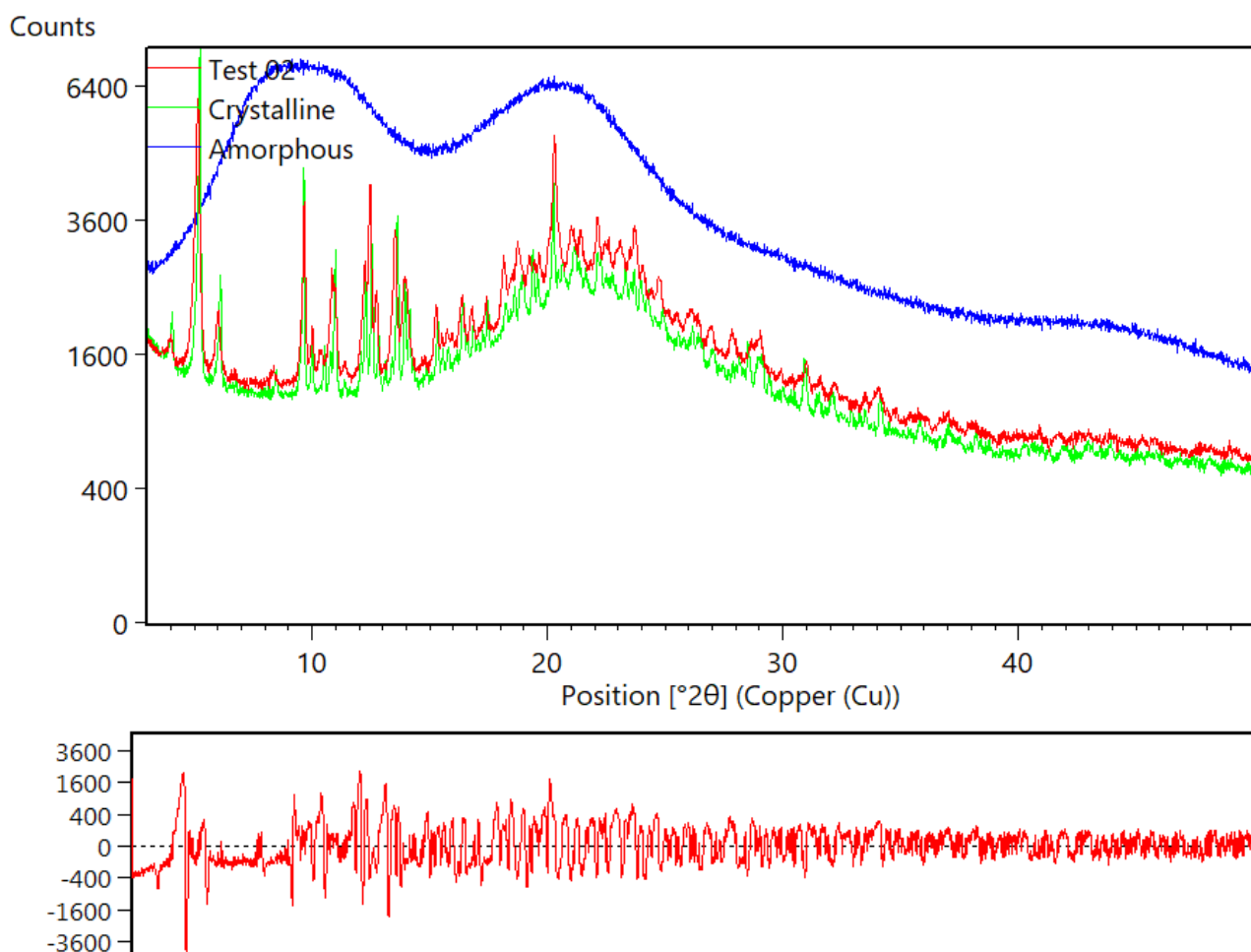


**Figure 36. Autoscale result of DCB sample Test 02. The image in the top shows the XRPD pattern comparison between the DCB sample in red and the amorphous (blue line) and crystalline (green line) references. In the bottom the difference plot resulting from the autoscale evaluation.**

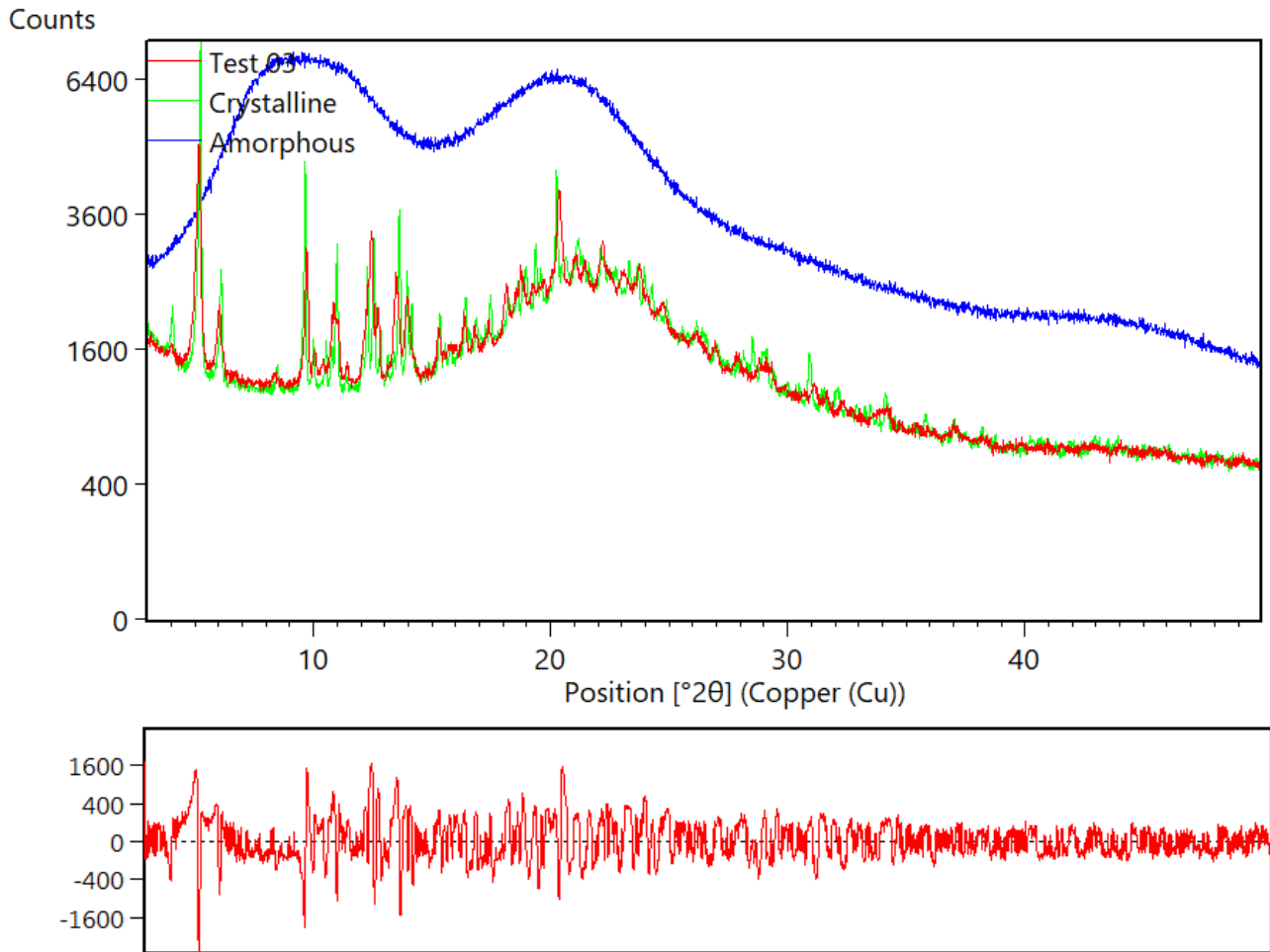


**Figure 37. Autoscale result of DCB sample Test 03. The image in the top shows the XRPD pattern comparison between the DCB sample in red and the amorphous (blue line) and crystalline (green line) references. In the bottom the difference plot resulting from the autoscale evaluation.**

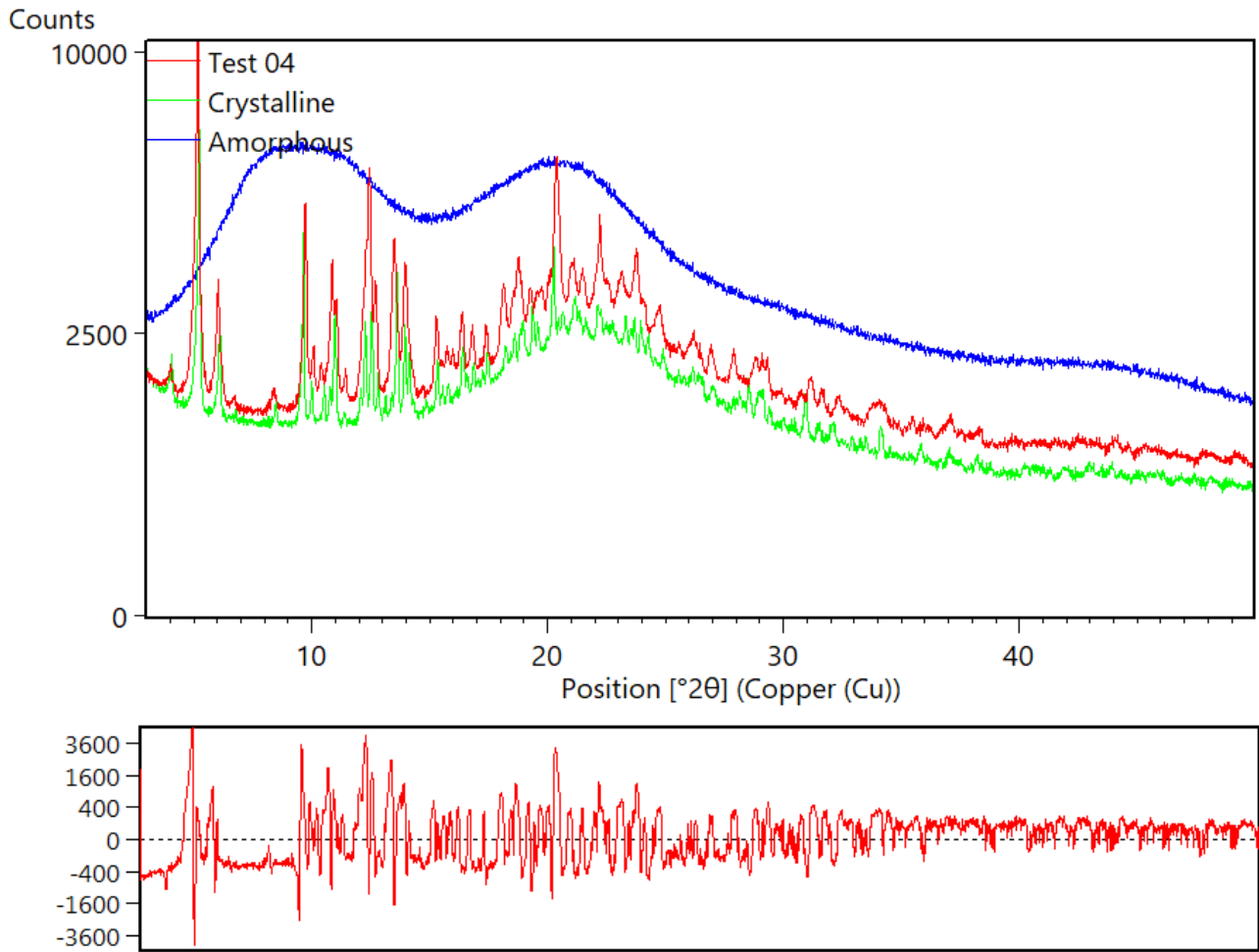


**Figure 38.** Autoscale result of DCB sample Test 04. The image in the top shows the XRPD pattern comparison between the DCB sample in red and the amorphous (blue line) and crystalline (green line) references. In the bottom the difference plot resulting from the autoscale evaluation.

## 4 CONCLUSION

The aim of this work was to determine the grade of crystallinity of formulation coated on Drug Coated Balloon by X-Ray powder Diffraction. The samples are challenging under different aspects: it is a High Potent classified OEB 4, only small amount of sample is available (around 10-15 mg), the reference and DBC patterns are slightly different due to different cell parameters.

Many of the most common amorphous-crystalline quantitative methods, as such as RIR, PONKS, Rietveld and univariate method, cannot be applied. In fact, the lack of suitable amount of reference standard does not allow to prepare suitable standard mixtures for the quantification. Additionally, the poor amount of formulation does not allow to add correct amount of internal standard to the DCB samples.

Three methods were pinpointed as suitable for the quantification of this problematic type of sample: USP method, DDQM and Autoscale.

First, the three methods were evaluated by means of standard mixtures of  $\alpha$ -lactose monohydrate (crystalline part) and HPMC (amorphous part), simulating the condition of the DCB samples like the analysis in confined condition (analysis in glass capillary), percentage of crystalline and amorphous phases.

In the case of the USP method, the evaluation of the crystalline part gave good results only after the application of a correction factor which was determined on the 100% crystalline. On account of this, USP method can be utilized with at least a known sample or when the 100% of crystalline is available as reference standard. In this case, the capillary signal was considered as constant background (area C).

The DDQM compares the area of the involved phases correlated with molecular weight and number of atoms. Hence, it can be applied with mixture of compound with different elemental composition. Additionally, DDQM is particularly interesting when the crystallographic parameters of the phase are known, the crystalline part can be described based on the crystalline structure parameters. The use of Pawley function allowed a better description of the crystalline phase thanks to good definition of the crystalline peaks. The capillary signal was subtracted by the sample measurement to evaluate exclusively the signal ascribable to the sample.

The autoscale method is very simple method that requires purely two reference standards: in our case 100% crystalline and 100% amorphous. Nevertheless, it is less reliable when the crystalline phase slightly changed in the mixture. Although the  $R_{wp}$  values were low, the difference plots were very noisy, the results were due to the sum of positive and negative errors. For all the methods the results of crystallinity degree obtained for  $\alpha$ -lactose monohydrate and HPMC mixtures are comparable and satisfactory.

The studies on the  $\alpha$ -lactose-HPMC mixtures allowed us to optimize the data treatment and the background correction to apply in the DCB samples.

The three DCB samples (Test 02, Test 03 and Test 04), present more difficulties respect to the standard mixture of  $\alpha$ -lactose-HPMC: 1) the amount of powder for each sample is around 10-15mg so the filling of the capillary is a crucial step. Moreover, the powder did not properly pack inside the capillary, hence the amount of powder irradiated is quite variable; 2) the presence of an excipient, which has not been detected in the powder, so it was supposed to contribute to the amorphous hump; 3) the nature of API itself because it has non-stoichiometric hydrate behaviour, so the crystal structure can slightly change from sample to sample. In particular it was not possible to obtain the reference sample 100% crystalline with peak in the same position as in the DCB samples.

Visually, the samples Test 02, Test 03 and Test 04 were very similar in intensity and peak shape and they slightly differed from the crystalline API, which was characterized by sharper peaks and shifted in positions, in particular, at high angle.

The three quantitative methods gave back different results on the crystalline %. Concerning the autoscale method, all DCB samples showed crystallinity degree comparable to the crystalline reference however this method was not considered suitable method because the difference plot was very noisy due to the mismatch of the crystalline peak positions in the reference and the samples, that suggests unreliability of the results.

USP method gave a crystallinity around the 81%-97%, while the DDQM gave a crystallinity between 59%-71%. The results of USP method and DDQM method are not comparable between them but they are consistent inside the method. Both methods agree to determine the sample Test 03 as the most crystalline sample and the other sample Test 02 and Test 04 with a comparable crystallinity degree. Unfortunately, it is impossible to estimate the accuracy of each method because of lack of known DCB sample. The only available known sample determined with both the methods is the assume 100% crystalline reference standard, which did not undergo manufacturing process. Nevertheless, the methods differed substantially in the determination of the

percentage of the crystalline reference. In fact, for USP method needs a correction factor to reach the value of 100%. The reference was used to determine the value of this correction factor to determine crystallinity degree of the DCB sample on the assumption that there is a linear correlation. Differently, in DDQM method the reference 100% crystalline was firstly used to determine the crystalline phase. Successively, the crystalline API pattern was quantified as the same way of the other DCB sample given back excellent result of 100% crystalline without application of correction factor. Furthermore, DDQM sample allowed the application of Pawley function. Hence, it was possible to calculate the unit cell parameters of the DCB samples. Considering the nature of API molecule, which has non-stoichiometric behaviour, it allows to supervise modification in the unit cell due to the manufacturing process. In fact, the Test 02, Test 03, and Test 04 showed unit cell parameters slightly different than the reference, especially with larger volume of the cell, indicating a modification in solvent content during the manufacturing process.

In conclusion, considering the three quantitative methods evaluated, the DDQM is considered the best method to estimate the crystallinity degree of formulation onto DCB because of the directly determination without application of a correct factor and of the possible application of Pawley function and hence determination of the changing in unit cell parameter after manufacturing.

## 5 REFERENCES

- (1) Benjamin, E. J.; Muntner, P.; Alonso, A.; Bittencourt, M. S.; Callaway, C. W.; Carson, A. P.; Chamberlain, A. M.; Chang, A. R.; Cheng, S.; Das, S. R.; Delling, F. N.; Djousse, L.; Elkind, M. S. V.; Ferguson, J. F.; Fornage, M.; Jordan, L. C.; Khan, S. S.; Kissela, B. M.; Knutson, K. L.; Kwan, T. W.; Lackland, D. T.; Lewis, T. T.; Lichtman, J. H.; Longenecker, C. T.; Loop, M. S.; Lutsey, P. L.; Martin, S. S.; Matsushita, K.; Moran, A. E.; Mussolino, M. E.; O'Flaherty, M.; Pandey, A.; Perak, A. M.; Rosamond, W. D.; Roth, G. A.; Sampson, U. K. A.; Satou, G. M.; Schroeder, E. B.; Shah, S. H.; Spartano, N. L.; Stokes, A.; Tirschwell, D. L.; Tsao, C. W.; Turakhia, M. P.; VanWagner, L. B.; Wilkins, J. T.; Wong, S. S.; Virani, S. S. Heart Disease and Stroke Statistics-2019 Update: A Report From the American Heart Association. *Circulation* **2019**, *139* (10), e56–e528. <https://doi.org/10.1161/CIR.0000000000000659>.
- (2) Hirsch, A. T.; Haskal, Z. J.; Hertzner, N. R.; Bakal, C. W.; Creager, M. A.; Halperin, J. L.; Hiratzka, L. F.; Murphy, W. R. C.; Olin, J. W.; Puschett, J. B.; Rosenfield, K. A.; Sacks, D.; Stanley, J. C.; Taylor, L. M.; White, C. J.; White, J.; White, R. A.; Antman, E. M.; Smith, S. C.; Adams, C. D.; Anderson, J. L.; Faxon, D. P.; Fuster, V.; Gibbons, R. J.; Hunt, S. A.; Jacobs, A. K.; Nishimura, R.; Ornato, J. P.; Page, R. L.; Riegel, B. ACC/AHA 2005 Practice Guidelines for the Management of Patients with Peripheral Arterial Disease (Lower Extremity, Renal, Mesenteric, and Abdominal Aortic). *Circulation* **2006**, *113* (11), e463–e654. <https://doi.org/10.1161/Circulationaha.106.174526>.
- (3) Centers for Disease Control and Prevention. Heart Disease: Coronary Artery Disease (CAD) [https://www.cdc.gov/heartdisease/coronary\\_ad.htm](https://www.cdc.gov/heartdisease/coronary_ad.htm).
- (4) Grüntzig, A. R.; Senning, Å.; Siegenthaler, W. E. Nonoperative Dilatation of Coronary-Artery Stenosis: Percutaneous Transluminal Coronary Angioplasty. *N. Engl. J. Med.* **1979**, *301* (2), 61–68. <https://doi.org/10.1056/NEJM197907123010201>.
- (5) Smith, J.; Dove, J. T.; Jacobs, A. K.; Kennedy, J. W.; Kereiakes, D.; Kern, M. J.; Kuntz, R. E.; Popma, J. J.; Schaff, H. V.; Williams, D. O.; Gibbons, R. J.; Alpert, J. P.; Eagle, K. A.; Faxon, D. P.; Fuster, V.; Gardner, T. J.; Gregoratos, G.; Russell, R. O.; Smith, J. ACC/AHA Guidelines for Percutaneous Coronary Intervention. *Circulation* **2001**, *103* (24), 3019–3041. <https://doi.org/10.1161/01.cir.103.24.3019>.
- (6) Unverdorben, M.; Kleber, F. X.; Heuer, H.; Figulla, H. R.; Vallbracht, C.; Leschke, M.; Cremers, B.; Hardt, S.; Buerke, M.; Ackermann, H.; Boxberger, M.; Degenhardt, R.; Scheller, B. Treatment of Small Coronary Arteries with a Paclitaxel-Coated Balloon Catheter. *Clin. Res. Cardiol.* **2010**, *99* (3), 165–174. <https://doi.org/10.1007/s00392-009-0101-6>.
- (7) García-García, H. M.; Vaina, S.; Tsuchida, K.; Serruys, P. W. Drug-Eluting Stents. *Arch. Cardiol. Mex.* **2006**, *76* (3), 297–319.
- (8) Finci, L. The Coronary Stent Story. *Srce i krvni Sudov.* **2014**, *33* (1), 1–7. <https://doi.org/10.5937/siks1401001f>.
- (9) Burt, H. M.; Hunter, W. L. Drug-Eluting Stents: A Multidisciplinary Success Story. *Adv. Drug Deliv. Rev.* **2006**, *58* (3), 350–357. <https://doi.org/10.1016/j.addr.2006.01.014>.
- (10) Nakazawa, G.; Finn, A. V.; Virmani, R. Vascular Pathology of Drug-Eluting Stents. *Herz Kardiovaskuläre Erkrankungen* **2007**, *32* (4), 274–280. <https://doi.org/10.1007/s00059-007-2997-9>.
- (11) Hezi-Yamit, A.; Sullivan, C.; Wong, J.; David, L.; Chen, M.; Cheng, P.; Shumaker, D.; Wilcox, J. N.; Udipi, K. Impact of Polymer Hydrophilicity on Biocompatibility: Implication for DES Polymer Design. *J. Biomed. Mater. Res.* **2009**, *90A* (1), 133–141. <https://doi.org/10.1002/jbm.a.32057>.
- (12) Schwartz, R. S.; Murphy, J. G.; Edwards, W. D.; Camrud, A. R.; Vlietstra, R. E.; Holmes, D. R. Restenosis after Balloon Angioplasty. A Practical Proliferative Model in Porcine Coronary Arteries. *Circulation* **1990**, *82* (6), 2190–2200. <https://doi.org/10.1161/01.CIR.82.6.2190>.
- (13) Byrne, R. A.; Joner, M.; Alfonso, F.; Kastrati, A. Drug-Coated Balloon Therapy in Coronary and Peripheral Artery Disease. *Nat. Rev. Cardiol.* **2014**, *11* (1), 13–23. <https://doi.org/10.1038/nrcardio.2013.165>.
- (14) Scheller, B.; Speck, U.; Abramjuk, C.; Bernhardt, U.; Böhm, M.; Nickenig, G. Paclitaxel Balloon Coating,

- a Novel Method for Prevention and Therapy of Restenosis. *Circulation* **2004**, *110* (7), 810–814. <https://doi.org/https://doi.org/10.1161/01.CIR.0000138929.71660.E0>.
- (15) Cortese, B.; Di Palma, G.; Nerla, R.; Micari, A. Nuove Tecnologie e Applicazioni per Il Pallone Medicato Nel 2017. *G. Ital. Cardiol.* **2017**, *18* (2), 22S–30S. <https://doi.org/10.1714/2657.27245>.
  - (16) Scheller, B.; Hehrlein, C.; Bocksch, W.; Rutsch, W.; Haghi, D.; Dietz, U.; Böhm, M.; Speck, U. Two Year Follow-up after Treatment of Coronary in-Stent Restenosis with a Paclitaxel-Coated Balloon Catheter. *Clin. Res. Cardiol.* **2008**, *97* (10), 773–781. <https://doi.org/10.1007/s00392-008-0682-5>.
  - (17) Stella, P. R.; Belkacemi, A.; Dubois, C.; Nathoe, H.; Dens, J.; Naber, C.; Adriaenssens, T.; Van Belle, E.; Doevendans, P.; Agostoni, P. A Multicenter Randomized Comparison of Drug-Eluting Balloon plus Bare-Metal Stent versus Bare-Metal Stent versus Drug-Eluting Stent in Bifurcation Lesions Treated with a Single-Stenting Technique. *Catheter. Cardiovasc. Interv.* **2012**, *80* (7), 1138–1146. <https://doi.org/10.1002/ccd.23499>.
  - (18) Wöhrle, J. Drug-Coated Balloons for Coronary and Peripheral Interventional Procedures. *Curr. Cardiol. Rep.* **2012**, *14* (5), 635–641. <https://doi.org/10.1007/s11886-012-0290-x>.
  - (19) Jackson, D.; Tong, D.; Layland, J. A Review of the Coronary Applications of the Drug Coated Balloon. *Int. J. Cardiol.* **2017**, *226*, 77–86. <https://doi.org/10.1016/j.ijcard.2016.09.045>.
  - (20) Waksman, R.; Serra, A.; Loh, J. P.; Malik, F. T. N.; Torguson, R.; Stahnke, S.; Von Strandmann, R. P.; Rodriguez, A. E. Drug-Coated Balloons for de Novo Coronary Lesions: Results from the Valentines II Trial. *EuroIntervention* **2013**, *9* (5), 613–619. <https://doi.org/10.4244/EIJV9I5A98>.
  - (21) Ang, H.; Lin, J.; Huang, Y. Y.; Chong, T. T.; Cassese, S.; Joner, M.; Foin, N. Drug-Coated Balloons: Technologies and Clinical Applications. *Curr. Pharm. Des.* **2018**, *24* (4), 381–396. <https://doi.org/10.2174/1381612824666171227221305>.
  - (22) Afari, M. E.; Granada, J. F. Mechanisms of Action in Drug- Coated Balloons. *Endovasc. Today* **2012**, 53–58.
  - (23) Klein, A. J. P.; Feldman, D. N. The Era of Drug-Coated Balloons: Are All Created Equal?\*. *JACC Cardiovasc. Interv.* **2018**, *11* (23), 2365–2367. <https://doi.org/10.1016/j.jcin.2018.10.001>.
  - (24) Scheller, B.; Clever, Y. P.; Kelsch, B.; Hehrlein, C.; Bocksch, W.; Rutsch, W.; Haghi, D.; Dietz, U.; Speck, U.; Böhm, M.; Cremers, B. Long-Term Follow-up after Treatment of Coronary in-Stent Restenosis with a Paclitaxel-Coated Balloon Catheter. *JACC Cardiovasc. Interv.* **2012**, *5* (3), 323–330. <https://doi.org/10.1016/j.jcin.2012.01.008>.
  - (25) Cortese, B.; Berti, S.; Biondi-Zoccai, G.; Colombo, A.; Limbruno, U.; Bedogni, F.; Cremonesi, A.; Silva, P. L.; Sgueglia, G. A. Drug-Coated Balloon Treatment of Coronary Artery Disease: A Position Paper of the Italian Society of Interventional Cardiology. *Catheter. Cardiovasc. Interv.* **2014**, *83* (3), 427–435. <https://doi.org/10.1002/ccd.25149>.
  - (26) Stankus, J.; Trollsasa, M.; Hossainy, S.; Zhang, L. Drug Coated Balloon Catheter and Pharmacokinetic Profile. WO 2010/147805 A2, 2010.
  - (27) Kangas, S. Drug Coated Balloon with Transferable Coating. WO 2012/039884 A1, 2012.
  - (28) Cremers, B.; Toner, J. L.; Schwartz, L. B.; Von Oepen, R.; Speck, U.; Kaufels, N.; Clever, Y. P.; Mahnkopf, D.; Böhm, M.; Scheller, B. Inhibition of Neointimal Hyperplasia with a Novel Zotarolimus Coated Balloon Catheter. *Clin. Res. Cardiol.* **2012**, *101* (6), 469–476. <https://doi.org/10.1007/s00392-012-0415-7>.
  - (29) Lemos, P. A.; Farooq, V.; Takimura, C. K.; Gutierrez, P. S.; Virmani, R.; Kolodgie, F.; Christians, U.; Kharlamov, A.; Doshi, M.; Sojitra, P.; Van Beusekom, H. M. M.; Serruys, P. W. Emerging Technologies: Polymer-Free Phospholipid Encapsulated Sirolimus Nanocarriers for the Controlled Release of Drug from a Stent-plus-Balloon or a Stand-Alone Balloon Catheter. *EuroIntervention* **2013**, *9* (1), 148–156. <https://doi.org/10.4244/EIJV9I1A21>.
  - (30) Miyake, T.; Ihara, S.; Miyake, T.; Tsukada, Y.; Watanabe, H.; Matsuda, H.; Kiguchi, H.; Tsujimoto, H.; Nakagami, H.; Morishita, R. Prevention of Neointimal Formation after Angioplasty Using Nuclear

- Factor-KB Decoy Oligodeoxynucleotide-Coated Balloon Catheter in Rabbit Model. *Circ. Cardiovasc. Interv.* **2014**, *7* (6), 787–796. <https://doi.org/10.1161/CIRCINTERVENTIONS.114.001522>.
- (31) Sharma, A.; Mishra, R.; Poonam, T. Polymorphism in Pharmaceutical Compounds. In *Advancements and Futuristic Trends in Material Science*; 2011; pp 39–47.
- (32) Haleblian, J.; McCrone, W. Pharmaceutical Applications of Polymorphism. *J. Pharm. Sci.* **1969**, *58* (8), 911–929. <https://doi.org/10.1002/jps.2600580802>.
- (33) Vippagunta, S. R.; Brittain, H. G.; Grant, D. J. W. Crystalline Solids. *Adv. Drug Deliv. Rev.* **2001**, *48*, 3–26.
- (34) Brittain, H. G. Polymorphism and Solvatomorphism 2005. *J. Pharm. Sci.* **2007**, *96* (4), 705–728. <https://doi.org/10.1002/jps.20772>.
- (35) Hilfiker, R.; Von Raumer, M. *Polymorphism: In the Pharmaceutical Industry*; Wiley-VCH Verlag GmbH & Co. KGaA: Weinheim, Germany, 2006.
- (36) Brittain, H. G.; Byrn, S. R.; Lee, E. *Polymorphism in Pharmaceutical Solids*, 2nd ed.; Informa Healthcare USA, I., Ed.; New York, 2016.
- (37) Braga, D.; Grepioni, F.; Chelazzi, L.; Campana, M.; Confortini, D.; Viscomi, G. C. The Structure-Property Relationship of Four Crystal Forms of Rifaximin. *CrystEngComm* **2012**, *14* (20), 6404–6411. <https://doi.org/10.1039/c2ce25920f>.
- (38) Viscomi, G. C.; Campana, M.; Barbanti, M.; Grepioni, F.; Polito, M.; Confortini, D.; Rosini, G.; Righi, P.; Cannata, V.; Braga, D. Crystal Forms of Rifaximin and Their Effect on Pharmaceutical Properties. *CrystEngComm* **2008**, *10* (8), 1074–1081. <https://doi.org/10.1039/b717887e>.
- (39) Braun, D. E.; Griesser, U. J. Stoichiometric and Nonstoichiometric Hydrates of Brucine. *Cryst. Growth Des.* **2016**, *16* (10), 6111–6121. <https://doi.org/10.1021/acs.cgd.6b01231>.
- (40) Khankari, R. K.; Grant, D. J. W. Pharmaceutical Hydrates. *Thermochim. Acta* **1995**, *248* (C), 61–79. [https://doi.org/10.1016/0040-6031\(94\)01952-D](https://doi.org/10.1016/0040-6031(94)01952-D).
- (41) Stephenson, G. A.; Groleau, E. G.; Kleemann, R. L.; Xu, W.; Rigsbee, D. R. Formation of Isomorphic Desolvates: Creating a Molecular Vacuum. *J. Pharm. Sci.* **1998**, *87* (5), 536–542. <https://doi.org/10.1021/js970449z>.
- (42) Toraya, H. A New Method for Quantitative Phase Analysis Using X-Ray Powder Diffraction: Direct Derivation of Weight Fractions from Observed Integrated Intensities and Chemical Compositions of Individual Phases. *J. Appl. Crystallogr.* **2016**, *49* (5), 1508–1516. <https://doi.org/10.1107/S1600576716010451>.
- (43) Toraya, H. Direct Derivation (DD) of Weight Fractions of Individual Crystalline Phases from Observed Intensities and Chemical Composition Data: Incorporation of the DD Method into the Whole-Powder-Pattern Fitting Procedure. *J. Appl. Crystallogr.* **2018**, *51* (2), 446–455. <https://doi.org/10.1107/S1600576718001474>.
- (44) Noordik, J. H.; Beurskens, P. T.; Bennema, P. Crystal Structure, Polarity and Morphology of 4-O- $\beta$ -D-Galactopyranosyl- $\alpha$ -D-Glucopyranose Mono-Hydrate ( $\alpha$ -Lactose Monohydrate): A Redetermination. *Zeitschrift für Krist. - Cryst. Mater.* **1984**, *168*, 59–65.

## CONCLUSION

My PhD project is focused on crystal forms of API that are extremely important in pharmaceutical industry. Characterization and quantifications of polymorphs, solvates, and cocrystals are common requests from the regulatory bodies. In the chapter 2, I presented an interesting study on the cocrystal screening of Allantoin. Cocrystals are of particularly interest because of their potentially improvement in solubility and efficacy of drugs. The growing interest led the crystal engineering to develop statistical tools to identify molecular reactive sites, suitable coformers, and to evaluate the propensity to form cocrystal, as such as CSD-Materials module present within Mercury used for the study of Allantoin. The results obtained through CSD-Materials suggest propensity of Allantoin to form cocrystal with several molecules. Despite the favourable statistics, allantoin did not form cocrystal with any tested coformer. The allantoin's small dimension and the presence of groups able to hydrogen bond interactions encourage the generation of cocrystals, but the high stability of the crystal form of Allantoin (until now the only one) prevents the formation of the cocrystals. These results should deserve further investigation to understand which step is fallacious: the prediction step, which misses some important descriptors or the experimental part where correct conditions to form cocrystal have not found yet.

In chapter 3 I have described which are the source of errors and aberration which affect the analysis by X-ray powder Diffraction. The X-Ray diffraction is the lead technique for the study of the solid state because it provides easily and readily qualitative information about the polymorph. The knowledge of the source of errors and aberration in the analysis allows to optimize the measurement and prevent wrong conclusion. This technique is extremely useful also in case of quantitative analysis, as presented in chapter 4, in which several factors can be affected the analysis and the results as such as preferred orientation phenomenon, particle size, thickness, and amount of sample. Furthermore, the homogeneity of the calibration mixtures is extremely impacting and challenging aspect for solid-state quantification. The condition for successful quantitative method development is to obtain homogeneous mixture analysed using correct measurement settings. In chapter 5 I have compared the quantification by Standard Addition Method (SAM) with univariate and multivariate approach. Especially, the quantitative analysis of formulation and amorphous-crystalline are complicated, respectively due to the numerous peaks of excipients and the instability of the amorphous and the indirect quantification. In case of formulation the signal of the excipients was considered as matrix effect, inspired by the HPLC methods the standard addition method was used with satisfactory results. This method is extremely useful especially in case of no specific peaks, although it should be emphasised that this method requires preparation of standard addition mixtures and construction of calibration curve for each sample considerably extending the time of analysis.

Determination of the Crystalline fraction has been a fundamental part of the thesis and chapter 6 and 7 present the evaluation of different method of quantification and their application in a real case.

In case of amorphous-crystalline quantification it is important to monitor the eventually transition of the amorphous phase, for example promoted by mixing. Sometimes, the amorphous is not available for the preparation of mixture because of its instability. In these cases, the use of surrogate amorphous as such as hydroxypropyl methyl cellulose (HPMC) has demonstrated to be resolute. It is worth noting to take in consideration the difference in mass absorption coefficient between surrogate amorphous and crystalline phase. The use of surrogate amorphous is recommended exclusively when real amorphous is unreachable.

The study has evidenced the different response for various peaks in quantification with univariate analysis revealing that the choice of the quantification peak is significant. This aspect can be easily overcome using multivariate analysis that evaluates the whole pattern and unique specific peak is not necessary, extremely useful in case of formulation analysis. The PLS multivariate analysis has compensated the preferred orientation that slightly affect some peaks in crystalline lactose and the variability of the aliquots of the same standard mixtures. However, in X-Ray diffraction quantitative analysis it is recommended to use method based on whole pattern of this technique as such as direct derivation method. The direct derivation method is based on IC formula that can calculate the weight fraction of the individual phases in a mixture using only the chemical formulas of the mixture's constituents. Although, it is advisable to apply the unit cell parameters when available, because the studies have revealed the improvement in accuracy of the results. The direct derivation method is extremely adaptable, simple, advantageous, readily, and single point method. Its execution was extremely useful in the determination of highly complex sample, as formulation into catheter balloon, when no other method was feasible.